



सत्यमेव जयते

INDIAN AGRICULTURAL  
RESEARCH INSTITUTE, NEW DELHI

I.A.R. I.6.

GIP NLK—H-3 I.A.R.I.—10-5-55—15,000





# CANADIAN JOURNAL OF RESEARCH

VOLUME 25

1947

SECTION A



*Published by the*  
NATIONAL  
RESEARCH COUNCIL  
*of* CANADA



# Canadian Journal of Research

Issued by THE NATIONAL RESEARCH COUNCIL OF CANADA

VOL. 25, SEC. A.

JANUARY, 1947

NUMBER 1

## A MASS SPECTROMETER INVESTIGATION OF THE ISOTOPES OF XENON AND KRYPTON RESULTING FROM THE FISSION OF $U^{235}$ BY THERMAL NEUTRONS<sup>1</sup>

BY H. G. THODE<sup>2</sup> AND R. L. GRAHAM<sup>3</sup>

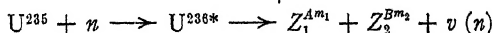
### Abstract

Mass spectrometer investigations have been made of rare gas fission products extracted from uranium irradiated with thermal neutrons. The irradiated uranium rods were allowed to stand for various periods of time after irradiation to permit the decay of most fission product chains to stable isotopes. Four stable isotopes of xenon were found having mass numbers 131, 132, 134, and 136, and three stable isotopes of krypton with mass numbers 83, 84, and 86.  $Kr^{86}$ , the most abundant of the latter group, is probably formed directly in fission. In addition a long lived krypton with mass 85 was discovered which is isomeric with a 4.0 hr.  $Kr^{85}$  reported previously.

The relative abundances of these isotopes which are related directly to fission yields of the corresponding mass chains have been determined with an accuracy of 1% or better. The mass numbers of these fission chains can now be identified with certainty by comparing mass spectrometer abundance data with known yield values of the active chain members. Finally, the half-life of krypton 85 was determined by comparing its concentration to that of a stable isotope over a period of time.

### Introduction

In the uranium fission process a thermal neutron is captured by the  $U^{235}$  nucleus. This gives rise to an activated compound nucleus  $U^{236*}$ , which in turn splits into two fragments or fission products in addition to several neutrons. The process can be represented by the following equation



where  $Z_1 + Z_2 = 92$ , and  $m_1 + m_2 + vn = 236$ .

The primary fission products  $A$  and  $B$  have more neutrons for their charge than the stable nuclei and undergo  $\beta$ -disintegrations in several steps ending in stable nuclear structures. Some 64 such fission chains are now known.†

Most of the work with fission products has involved a study of the activity of the separated active products. The difficulties involved in getting clean-cut separations of active products, in determining mass numbers of fission

<sup>1</sup> Manuscript received September 24, 1946.

<sup>2</sup> Contribution from the Department of Chemistry, McMaster University, Hamilton, Ont.

<sup>3</sup> Professor.

<sup>4</sup> Physicist, Division of Atomic Energy, National Research Council of Canada.

\* The fission product work reported here was done at McMaster University, Hamilton, between December 1944 and December 1945, in connection with the Canadian atomic energy project under the National Research Council of Canada.

† Address by C. Coryell at nuclear chemistry symposium held by the American Chemical Society at Atlantic City (April, 1946).

product chains, and, finally, in determining accurate fission yield data by these methods, are well known. The availability in Canada of small samples of rare gas mixtures (0.001 cc. of gas at N.T.P.) extracted from irradiated uranium for volume measurements and counting (2) experiments, made possible for the first time a mass spectrometer study of certain stable isotopes resulting from fission product chains. Because of the large number of stable isotopes of xenon and krypton which block further  $\beta$ -disintegration of fission product chains, the mass spectrometer experiments were expected to give important information about a relatively large number of these chains.

Some six rare gas mixtures extracted from irradiated uranium rods were investigated up to December 1945. These samples contained about  $10^{-3}$  cc. of xenon and about  $10^{-4}$  cc. of krypton. Altogether eight isotopes of krypton and xenon were found, seven stable and one active. Since the rods were allowed to stand for six to nine months, only long lived active isotopes will be present with the stable ones. Relative abundances of these isotopes were obtained with an accuracy of 1% or better. Details of the investigations are reported in this paper.

## Experimental

### *Rare Gas Samples*

The rare gases investigated were prepared by Drs. Arrol, Chackett, and Epstein (2), who had apparatus set up for the extraction and fractionation of rare gas mixtures for volume determinations. Details of the simple extraction are given in their papers. The uranium used was in the form of a composite rod made up of disks varying in weight. Two such rods were irradiated with neutrons in a pile. Rod 2 was irradiated at 1.5 times the neutron intensity of Rod 1, but for only two-thirds the exposure time.

Preliminary mass spectrometer investigations showed 1 cu. mm. of extracted gas to be contaminated with about 60% of argon. The 1 cu. mm. samples therefore contained less than 0.0004 cu. cm. of krypton and xenon from uranium fission. The gas sample line (see Fig. 1) was designed to handle these small samples of gas. It consists of a capillary line of 1 cc. volume leading to a capillary leak which introduces gas samples directly into the ionization chamber of the ion source system (see Fig. 2). This small volume is connected to a sample tube manifold by means of glass break seals that can be opened for pumping and for the introduction of samples. In addition, the line is fitted with a large reservoir mercury pump that is used to pump samples into the small volume behind the mass spectrometer leak. This pump is also used to mix the gas sample and to regulate the pressure of gas behind the leak, so as to obtain suitable ion currents for identification of isotopes and for abundance measurements. The small 1 cc. volume can be sealed off from the rest of the line at the second break seal manifold after the sample has been introduced into the large reservoir of the mercury pump. After the investigation of each sample, the residual gas can be condensed in a charcoal liquid air trap and stored for further work.

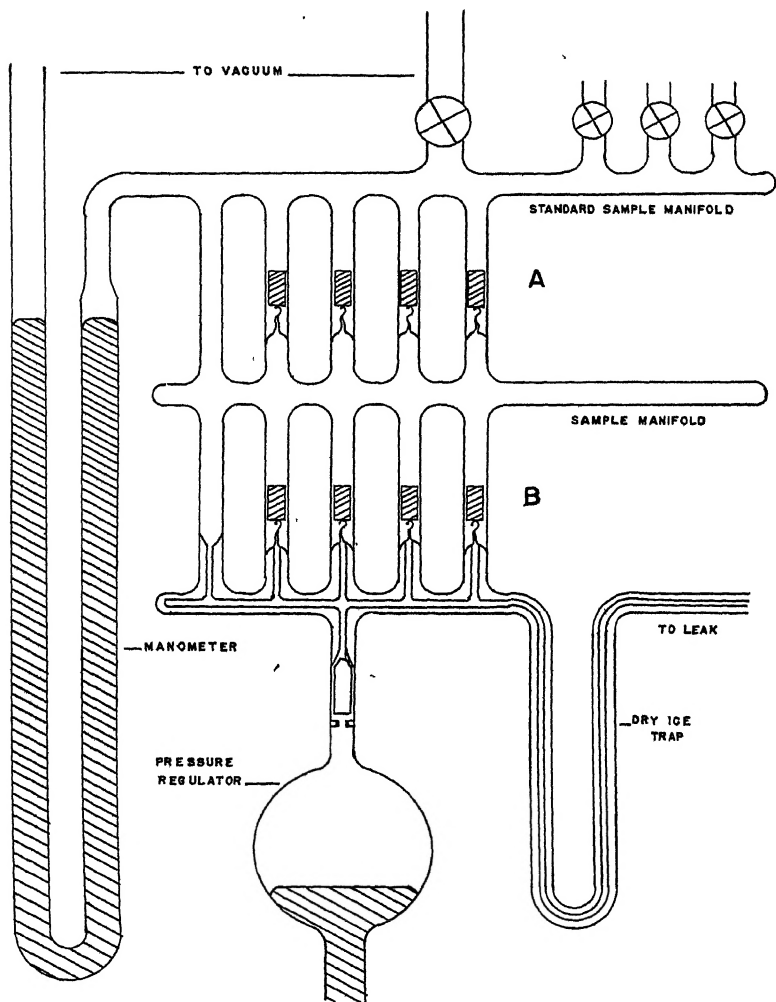


FIG. 1. Mass spectrometer sample line for rare gas samples.

### Mass Spectrometer

The mass spectrometer used is a 180 degree Nier type described previously (6, 7, 10). The ion source system and part of analyser tube are shown in Fig. 2. Plate *A* is a supporting plate and forms the top of the ionization chamber. Plate *C* contains the first collimating slit, 8 mm. long and 0.35 mm. wide. Between Plates *A* and *C* is located a box through which electrons pass from a filament through a 0.2 mm. slit and ionization chamber to a collector box or trap, *T*. Plate *B*, mounted in the ionization chamber over the first collimating slit, is made 1 to 5 volts more positive than Plate *C*, in order to

draw the ions out of the chamber. Plate *D* contains the final collimating slit of 0.25 mm. in width through which the ions enter the analyser tube. The tube, which included an ion source assembly, an analyser plate assembly, and a 180 degree 5-in. radius of curvature analyser tube, is completely enclosed in

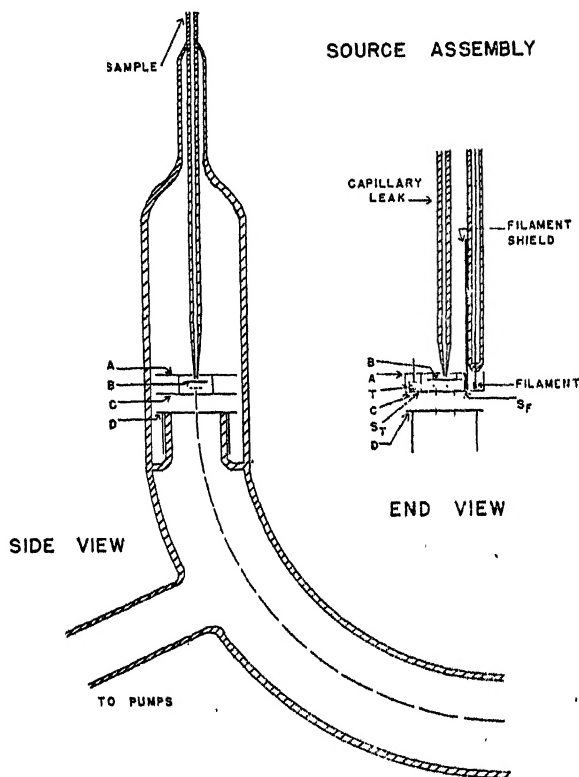


FIG. 2. *Mass spectrometer tube.*

a glass envelope. The glass envelope is wrapped with a heating element so that the tube can be thoroughly baked. The vacuum pump leak is connected directly to the analyser tube to ensure a low pressure in this region, and thereby reduce scattering of the ion beams to a minimum. With this arrangement there exists a pressure gradient between the source end and the analyser tube, which are connected by means of the slit in Plate *D*, and between the ionization chamber where the gas samples enter and the source end of the tube, since this chamber is enclosed but for two small slits.

A d-c. amplifier with linear feedback is used to measure the ion currents. This unit, in addition to the electronic equipment for control of electron emission, accelerating of ions, and stabilization of magnetic current, have been designed to operate from standard a-c. power lines. Details of these units and a discussion of their performances are described elsewhere (5).

## Results and Discussion

### Mass Spectrograms

Figs. 3 and 4 show typical mass spectrograms for normal and fission product xenon, and Figs. 5 and 6 for normal and fission product krypton, respectively. In each case the ion current is plotted against the ion accelerating voltage, which is given in terms of the corresponding mass number. As can be seen from the figures, the mass peaks are completely resolved. A check on the abundances of the xenon isotopes in standard mixtures was made before the investigation of a fission product sample. In each case the mass spectrometer ratios agreed with known values within the limits of accuracy (1%). Fig. 4 shows the existence of four xenon isotopes in the fission product sample, masses 131, 132, 134, and 136, and Fig. 6 shows the existence of four isotopes of

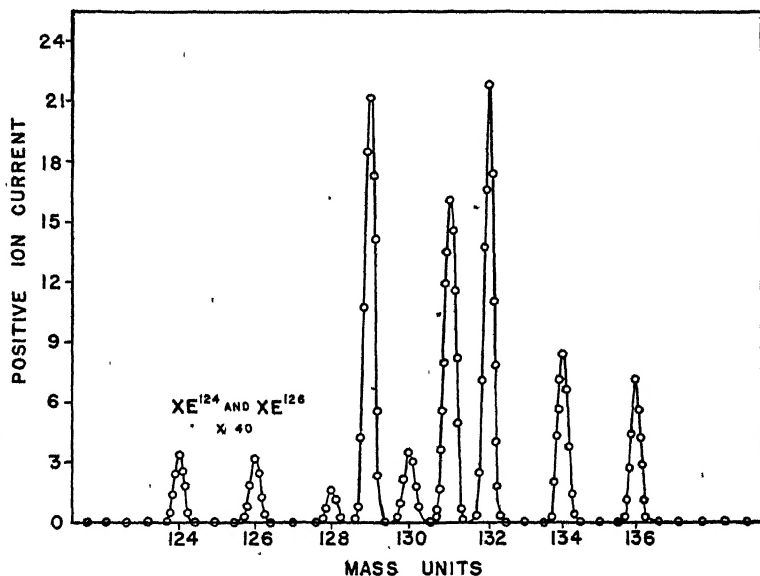


FIG. 3. A mass spectrogram for normal xenon gas.

krypton with masses 83, 84, 85, and 86. In the identification of these masses, all the usual precautions were taken and the possibility of contamination was investigated thoroughly. In the first sample investigated, xenon 129 was found to be present to the extent of 1 part in 2000 of the total number of xenon atoms. However, contamination with normal xenon was suspected because of the high concentration of  $Xe^{129}$  in naturally occurring xenon. Later work showed this to be the case. Contaminated samples were found to have traces of  $Xe^{129}$  and  $Xe^{130}$  in proportion to their abundances in normal xenon. Other samples free of contamination contained less than 1 part in 40,000 of these two isotopes, which is the limit of detection for the instrument with the size of samples available. The largest samples investigated showed the

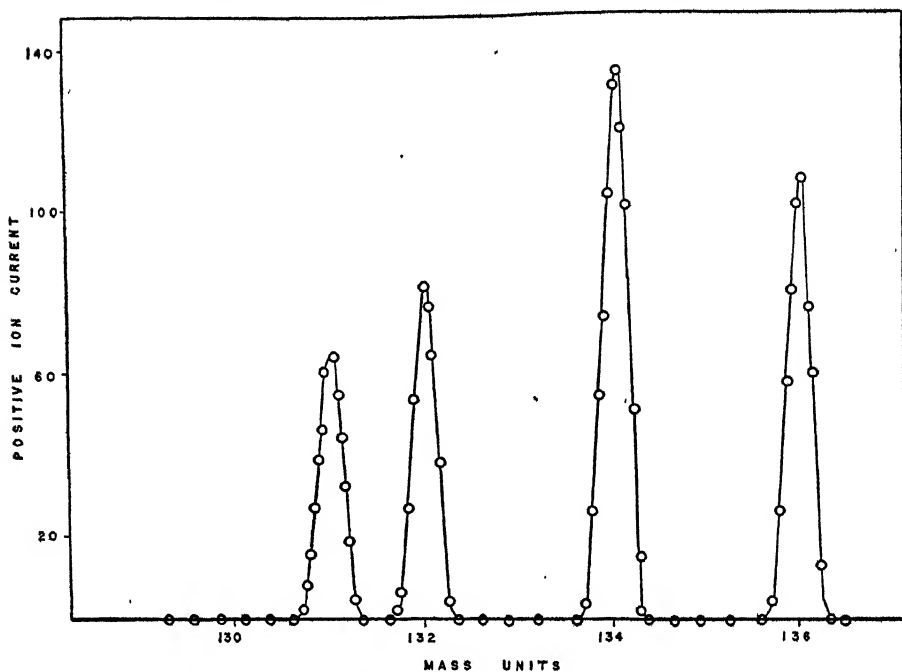


FIG. 4. A mass spectrogram for fission product xenon gas.

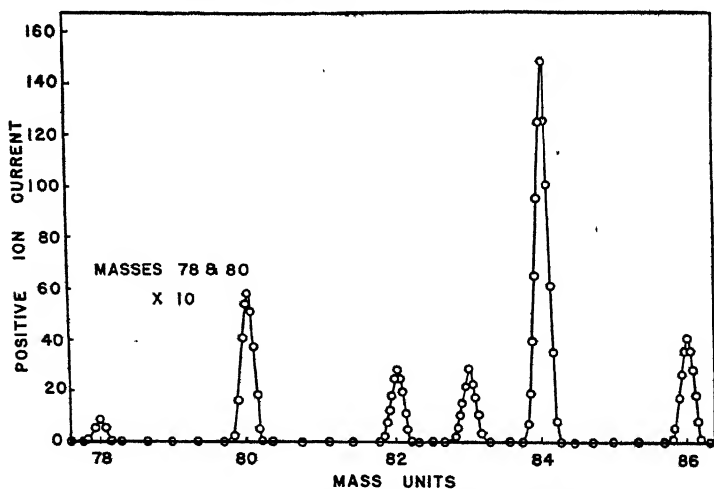


FIG. 5. A mass spectrogram for normal krypton gas.

existence of trace amounts of krypton 80 and 82. These traces amounted to less than 1 part in 8000 and 5000, respectively, in terms of total krypton.

#### *Isotope Abundances and Fission Yields*

The samples investigated contained only from  $1 \times 10^{-4}$  to  $1 \times 10^{-3}$  cc. of xenon and krypton. It was therefore necessary to use a very small volume

behind the mass spectrometer leak and operate at relatively low pressures. Because of this the ion currents decreased slowly with time. However, by making time corrections, quite precise abundance data were obtained. The

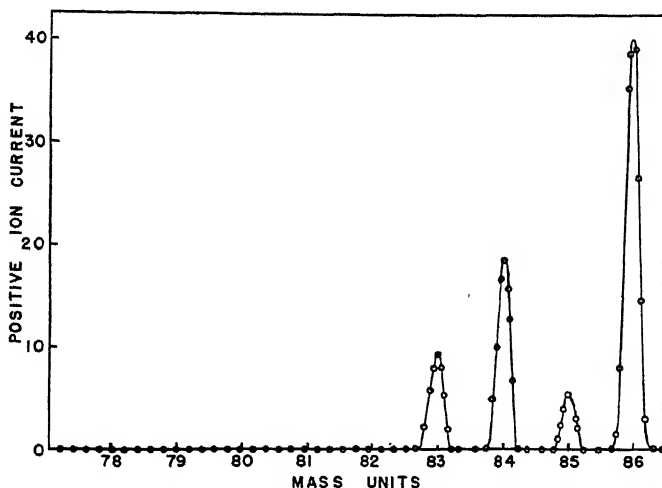


FIG. 6. A mass spectrogram for fission product krypton.

ion currents for the different isotopes were compared. Tables I and II give typical abundance data obtained for the isotopes of xenon and krypton in a mixture of rare gas fission products (Rod 1).

TABLE I

TYPICAL MASS SPECTROMETER ABUNDANCE DATA FOR ISOTOPES OF FISSION PRODUCT XENON\*

Mass unit	131		132		134		136	
Set	Ion** current	Atom per cent	Ion current	Atom per cent	Ion current	Atom per cent	Ion current	Atom per cent
1	255	13.67	370.5	20.35	670	35.92	560	30.02
2	241	13.76	358.9	20.52	633.1	36.18	516	29.49
3	236.4	13.76	351.6	20.47	620.3	36.09	509	29.73
4	1083.6	13.75	1602.4	20.33*	2838.0	36.00	2355	29.87
5	204.4	13.73	301.4	20.25	553.8	35.87	448	30.10
Average		13.73 ± 0.03		20.38 ± 0.08		36.01 ± 0.1		29.82 ± 0.2

\* Sample extracted 407 days after the irradiation period.

\*\* Ion current given in terms of galvanometer deflection in centimetres.

Tables III and IV give a summary of stable isotope abundances obtained with five samples of rare gas mixtures. Samples 1 to 4 were extracted from the centre disk of a single uranium rod referred to as Rod 1. Sample 5 was extracted from centre disk in Rod 2, which was irradiated at  $1\frac{1}{2}$  times the

TABLE II

TYPICAL MASS SPECTROMETER ABUNDANCE DATA FOR ISOTOPES OF FISSION PRODUCT KRYPTON\*

Mass unit	83		84		85**		86	
Set	Ion current	Atom per cent	Ion current	Atom per cent	Ion current	Atom per cent	Ion current	Atom per cent
1	215	14.3	401	26.61	106.2	7.06	781	51.90
2	204.6	14.25	383	26.70	102.5	7.13	744	51.75
3	186.5	14.10	353	26.75	93.0	7.06	686	52.0
4	540.0	13.82	1067	27.2	273.5	7.0	2026	51.8
Average		14.12 $\pm$ 0.15		26.81 $\pm$ 0.2		7.06 $\pm$ 0.04		51.86 $\pm$ 0.08

\* Sample extracted for analysis 407 days after irradiation period.

\*\* Kr<sup>85</sup> not a stable isotope (half-life 10 years) (see below).

TABLE III

SUMMARY OF ABUNDANCE DATA FOR ISOTOPES OF FISSION PRODUCT XENON

Sample	Mass unit			
	131	132	134	136
1 (Rod 1)	13.9 $\pm$ 0.1	20.4 $\pm$ 0.1	36.0 $\pm$ 0.1	29.7 $\pm$ 0.1
2	13.7 $\pm$ 0.1	20.25 $\pm$ 0.1	36.0 $\pm$ 0.1	30.1 $\pm$ 0.1
3	13.68 $\pm$ 0.04	20.45 $\pm$ 0.03	36.05 $\pm$ 0.06	29.84 $\pm$ 0.03
4	13.73 $\pm$ 0.03	20.38 $\pm$ 0.08	36.01 $\pm$ 0.1	29.82 $\pm$ 0.2
Average	13.73 $\pm$ 0.04	20.37 $\pm$ 0.05	36.04 $\pm$ 0.04	29.86 $\pm$ 0.09
1 (Rod 2)*	13.38 $\pm$ 0.04	20.09 $\pm$ 0.04	35.76 $\pm$ 0.04	30.77 $\pm$ 0.04

\* Rod 2 was irradiated at 1.5 times the neutron intensity of Rod 1 but only for two-thirds of the exposure time.

TABLE IV

SUMMARY OF ABUNDANCE DATA FOR STABLE ISOTOPES OF FISSION PRODUCT KRYPTON\*

Sample	Mass unit		
	83	84	86
1 (Rod 1)	14.1	28.3	57.6
2	15.8	29.2	55.0
3	15.1	28.7	56.2
Average (1-3)	15.0 $\pm$ 0.5	28.7 $\pm$ 0.3	56.3 $\pm$ 1.2
4 (Rod 1)	15.23 $\pm$ 0.15	28.90 $\pm$ 0.2	55.87 $\pm$ 0.1
1 (Rod 2)	15.39 $\pm$ 0.05	28.91 $\pm$ 0.05	55.70 $\pm$ 0.05

\* Active krypton 85 not included since its concentration is a function of time and would vary from sample to sample.

neutron density for two-thirds as long an irradiation time. The first three samples contained such small amounts of krypton that it was difficult to estimate the precision of the abundance data. These three sets of data have been averaged for comparison with results for Sample 4, which was considerably larger and permitted an estimation of the precision. Because of the higher concentration of xenon in the samples, about six times that for krypton, higher ion currents and therefore higher precision could be obtained for the xenon isotope abundances.

$Kr^{85}$ , which appears along with  $Kr^{83}$ ,  $Kr^{84}$ , and  $Kr^{86}$ , is not included in Table IV since it is radioactive and its concentration changes with time. In each case the uranium rods were allowed to stand for a number of months after irradiation to permit the different fission product chains to decay to stable xenon and krypton isotopes. Samples 1 to 4 extracted from Rod 1 over a period of 10 months, the first about nine months after irradiation, do not show any variation in the stable isotopic abundances within the limits of our precision.

TABLE V

COMPARISON OF XENON ISOTOPE RATIOS FOR GAS SAMPLES EXTRACTED FROM URANIUM RODS IRRADIATED UNDER SLIGHTLY DIFFERENT POWER CONDITIONS

Rod No.	Mass ratio		
	132/131	134/131	136/131
1	1.48	2.63	2.17
2	1.50	2.67	2.30
Difference, %	1.3	1.5	6.0

TABLE VI

COMPARISON OF KRYPTON ISOTOPE RATIOS FOR GAS SAMPLES EXTRACTED FROM URANIUM RODS IRRADIATED UNDER SLIGHTLY DIFFERENT POWER CONDITIONS

Rod No.	Mass ratio	
	84/83	86/83
1	1.90	3.66
2	1.88	3.62
Difference, %	1.0	1.1

In Tables V and VI, the stable isotopic ratios for fission product xenon and krypton obtained for Rods 1 and 2 are compared. These results show that stable krypton isotope ratios for the two agree well within the limits of our precision, but that the xenon isotope ratios differ for the two by as much as

6%. It would appear that even the small variations in the 132/131 and 134/131 ratios are significant, in view of the high internal precision of the measurements. Certainly the large difference in the 136/131 ratio is significant and cannot be explained on the basis of mass discriminations in the mass spectrometer. If this explanation were true, larger discrepancies would have shown up for the krypton isotope ratios, which were examined at the same time. Further, the variations indicated in Table V are not a linear function of the masses.

### *Krypton 85*

Ion currents appeared corresponding to mass 85 in all krypton fission product samples. Purification of the krypton samples did not alter the results of relative abundance measurements and there was no evidence for contamination in the mass spectrometer tube or the sample line that could give rise to a mass 85 ion current. A number of samples have been investigated and it is now quite clear that  $\text{Kr}^{85}$  is a product of the fission process and is radioactive with a half-life of about 10 years.

The discovery of this isotope was a little surprising in view of the existence of a four hour  $\text{Kr}^{85}$  reported previously. The new isotope is obviously an isomer of the four hour  $\text{Kr}^{85}$  with a long half-life. A sample of krypton extracted from a uranium rod 407 days after its irradiation with neutrons formed in a pile was found to contain  $7.06 \pm 0.04\%$  of the active  $\text{Kr}^{85}$  isotope (see Table II). This concentration was found to be less in older samples and greater in younger samples, indicating a definite activity. This activity was also investigated by Arrol, Chackett, and Epstein, who pumped fission product krypton into a gas counter (3). Recently the existence of a long lived krypton isotope was mentioned in an address by C. Coryell†, its discovery being attributed to N. Sugarman and C. Hoagland. Undoubtedly, this isotope, found independently by counting experiments, is the active  $\text{Kr}^{85}$  positively identified by mass spectrometer methods.

The decrease in the  $\text{Kr}^{85}$  concentration with time relative to one or more of the stable krypton isotopes was measured and its half-life calculated. The results are given in Table VII. In these calculations the assumption is made that variations in the  $\text{Kr}^{85}$  concentration relative to the stable isotopes from sample to sample are due wholly to the decay of  $\text{Kr}^{85}$  with time, and not due to variations in the distribution of fission product isotopes. This assumption seems justified for the first two calculations made, Rows 1 and 2, Table VII, since the samples investigated were extracted in each case from the centre disks of the same uranium rods, and the relative abundance measurements did not show any significant variations in the distribution of the stable isotopes of krypton and xenon that result from fission. The third calculation made from data in Row 3, Table VII, is perhaps less justified since the 144 day sample came from a uranium rod different from that of the 407 day one, and the relative abundance measurements for the two samples did show signifi-

†See footnote, page 1.

TABLE VII  
 $Kr^{85}$  HALF-LIFE FROM MASS SPECTROMETER ABUNDANCE DATA

Ratio	Time after irradiation, days			$Kr^{85}$ half-life calculated, years
	144	407	619	
Stable $Kr^{80}$ /active $Kr^{85}$	—	7.35	7.6	11
Stable $Kr^{84}$ /active $Kr^{85}$	—	3.80	3.96	9
Stable $Kr^{83} + ^{84} + ^{80}$ Active $Kr^{85}$	12.44*	13.16	—	9

\* This sample from uranium rod No. 2, all others from rod No. 1.

cant variations in the  $Xe^{136}$  concentration. However, the variations in the relative concentrations of the other stable isotopes of xenon and krypton were small and perhaps not significant.

The results of the three half-life calculations agree fairly well, considering the small changes in the  $Kr^{85}$  concentration measured. The assumptions made in above calculations become unnecessary when abundance measurements can be made on the same sample of rare gas. A larger sample, which will be sufficient for several investigations, and which can be studied over many months, is therefore being prepared.

The fission yield of the 10 year  $Kr^{85}$  can be calculated in terms of  $Kr^{83}$  from the data in Table II. Considering the half-life to be 10 years and the sample 407 days old, the ratio of  $84/85$  turns out to be 3.50.

#### *Ratio of Xenon to Krypton*

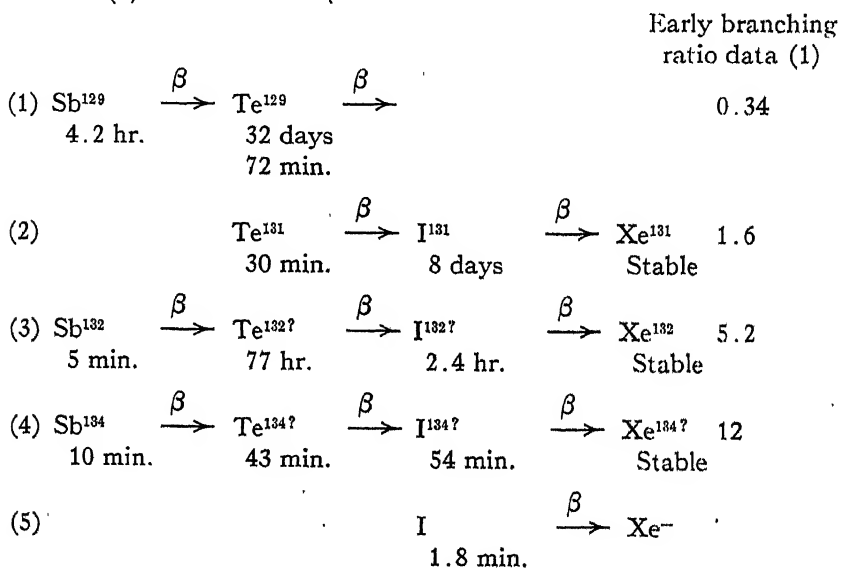
To date it has been difficult to determine with high accuracy the ratio of total xenon to total krypton with the mass spectrometer, because of the small size of the rare gas samples available and the difficulties encountered in calibrating the instrument with standard rare gas samples of that size. It was found that, under the conditions necessary to handle these small samples, there was considerable fractionation of the sample at the capillary leak. However, by extensive calibration of the instrument with small standard rare gas mixtures, a preliminary value of 6.2 has been obtained for the ratio of xenon to krypton. This compares with 5.0 obtained by Arrol, Chackett, and Epstein (2), who fractionated rare gas fission product mixtures and measured the volumes of the different components. A knowledge of this ratio together with the isotopic abundances makes it possible to tie in fission yield data for mass chains ending in xenon of the heavy fission product group with those ending in krypton in the light group.

### Discussion

The relative abundances of the stable isotopes found in fission material give the relative fission yields of the different mass chains directly. In view of the direct character and accuracy of the measurements, these fission yield

values should make it possible to draw the fission yield-mass number curve with greater certainty. Actually fission yield data obtained by counting experiments is only good to  $\pm 10\%$ . From a knowledge of the absolute fission yield of the 131 mass chain obtained for the 8 day  $I^{131}$ , fission yields for mass chains 132, 134, 136, and 83, 84, 86, follow directly from our data. This would give seven points on the curve. Actually these points have been fitted to the best available curve†, and, with the exception of one point the values agree consistently. This one discrepancy is decidedly significant and indicates some sort of branching from one mass chain to another. The problem is being investigated further.

The following series compiled from Seaborg's table of isotopes may lead to stable xenon (8).



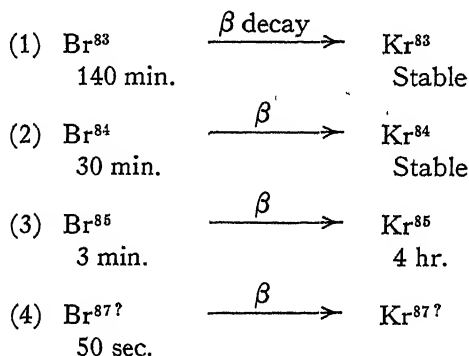
Seaborg in his 1944 table of isotopes refers to the mass numbers for 3 and 4 as  $> 131$ . Since only four isotopes of xenon have been identified with the mass spectrometer, and  $Xe^{131}$  is definitely associated with the eight day  $I^{131}$ , the  $Xe^{132}$ ,  $Xe^{134}$ ,  $Xe^{136}$ , must be associated with the series 3, 4, and 5 above, respectively. The order seems fairly certain, since one might expect the iodines to become less stable with increasing mass. Further fission yield data reported for the above series should agree with the relative abundances obtained for the corresponding xenon isotopes, and in this way the mass numbers can be assigned to the various series with certainty.

$Xe^{129}$ , as mentioned above, does not exist in fission product xenon within detection limits 1 part in 40,000. On the other hand, the fission yield of the 129 series determined from the activities of Sb and Te (Anderson, Fermi, and Grosse (1)) is 0.34%. This suggests the existence of a long lived  $I^{129}$ , which

†See footnote, page 1.

has been suspected for some time since no activity that could be attributed to  $I^{129}$  has yet been found.

The following fission product chains previously indicated (8) might give rise to stable Kr.



From the mass spectrometer results, we can conclude that only four stable isotopes of krypton exist in fission material in more than trace amounts,  $Kr^{83}$ ,  $Kr^{84}$ ,  $Kr^{85}$ , and  $Kr^{86}$ . The presence of  $Kr^{83}$  and  $Kr^{84}$  was expected since the mass numbers for Series 1 and 2 above had been definitely established previously by  $Se(d, n)Br^{83}$  and  $Rb(n, \alpha)Br^{84}$  reactions, respectively (4, 9). However, no previous mention had been made of the possible production of  $Kr^{86}$ , and  $Kr^{85}$  was entirely unsuspected in view of the known four hour  $Kr^{85}$ , which would have completely decayed in the 10 month period that elapsed between the time of irradiation and analysis. The assignment of mass number 85 to Series 3 is considered certain by Seaborg (8). The  $Kr^{85}$  discovered with the mass spectrometer must therefore be an isomer of the four hour  $Kr^{85}$  with a long half-life. This conclusion led to the half-life determinations given in Table VII. Further counting experiments of Arrol, Chackett, and Epstein on fission product krypton gas revealed an active krypton with a long period (3).

There is no known evidence for  $Br^{86}$ , which would be a parent to  $Kr^{86}$ . Therefore either the parent of  $Kr^{86}$  has a very short half-life and has escaped detection, or  $Kr^{86}$  is formed directly in fission, or both.

The mass spectrometer method is particularly suited to the study of fission products. It is the only method that gives information about the stable isotopes that grow from active products and that may form directly in fission. Mass numbers can be positively identified and relative fission yield data for the stable isotopes give a good deal of information about chain relations and possible decay mechanisms. Further, active products with long half-lives can be investigated and their periods determined. By extracting fission product samples from irradiated uranium soon after irradiation, the method can be extended to the short period isotopes as well. It is planned to explore this method further with the investigation of active rare gas samples. It will be of considerable interest also to follow changes in the relative abundances

of the different fission product isotopes as a function of time after irradiation and as a function of the pile irradiation intensity. Indications are that significant variations occur in the distribution of fission products, depending on the intensity of irradiation (see Table V). Further, the accurate mass spectrometer determination of the krypton isotope abundances furnishes a very sensitive method for detecting changes in fission product distribution effected by changes in the energy of neutrons in the irradiation process, since the krypton isotopes fall on the steep part of the fission yield-mass curve.

### References

1. ANDERSON, H. L., FERMI, E., and GROSSE, A. V. *Phys. Rev.* 59 : 52-56. 1941.
2. ARROL, W. J., CHACKETT, K. F., and EPSTEIN, S. Private communication.
3. ARROL, W. J., CHACKETT, K. F., and EPSTEIN, S. Unpublished work.
4. BORN, H. J. and SEELMANN-EGGEBERT, W. *Naturwissenschaften*, 31 : 420. 1943.
5. GRAHAM, R. L., HARKNESS, A. L., and THODE, H. G. *J. Sci. Instruments*. In press.
6. NIER, A. O. *Phys. Rev.* 52 : 933-937. 1937.
7. NIER, A. O. *Rev. Sci. Instruments*, 11 : 212-216. 1940.
8. SEABORG, G. T. *Rev. Modern Phys.* 16 : 1-32. 1944.
9. SNELL, A. H. *Phys. Rev.* 52 : 1007-1022. 1937.
10. THODE, H. G., GRAHAM, R. L., and ZIEGLER, J. A. *Can. J. Research, B*, 23 : 40-47. 1945.

# MEASUREMENT OF THE DIFFUSION LENGTH OF THERMAL NEUTRONS IN GRAPHITE<sup>1</sup>

By H. G. HEReward<sup>2</sup>, G. C. LAURENCE<sup>3</sup>, H. R. PANETH<sup>2</sup>, AND B. W. SARGENT<sup>3</sup>

## Abstract

The theory and method of measuring the diffusion length of thermal neutrons in graphite are discussed in detail. The graphite pile was a rectangular parallelepiped, 185.8 cm. square and 153.6 cm. high. The source was 1.2 gm. of radium mixed with beryllium. Part of the pile was used to slow down the neutrons to thermal velocities, and the density distribution of thermal neutrons was explored in the remainder of the pile with detectors of dysprosium oxide. The diffusion length of thermal neutrons in this graphite of average pile density 1.55 gm. per cc. was found to be 51 cm., with a probable error of 3 cm.

## Introduction

The diffusion length of graphite is required in the design of graphite-uranium piles, reflectors, and thermal columns. It has also been used as an index of the purity of commercial graphites. In the early work leading up to chain reacting piles of the heterogeneous graphite-uranium type it was clear that only with some difficulty could the value of the multiplication constant  $k$  be brought above unity and the neutron density in the pile be made to diverge. Of the various steps taken to increase  $k$ , one was to increase the thermal utilization, one of the factors making up  $k$ . This was brought about by improving the purities of the uranium metal and the graphite moderator, thus minimizing the parasitic capture of thermal neutrons (see Smyth report (4)).

This paper contains an account of the measurement\* of the diffusion length of thermal neutrons in a commercial graphite produced in Canada. The measurements were made in the Montreal Laboratory during June and July, 1943, and the final report was issued on October 29, 1943. It will be made clear later that the accuracy of the diffusion length depends a great deal on the size of the graphite pile. As we had at that time only nine tons in which to slow down the neutrons from a mixed radium and beryllium source and to measure their diffusion length while thermal, the accuracy was somewhat disappointing.

## Description of Graphite Pile

The graphite pile weighed 9.1 short tons and was built up of unplaned bars approximately 36 by 2 by 2 in., which were cross-piled as shown in Fig. 1. The rectangular parallelepiped formed by the 29 layers of 70 bars each was

<sup>1</sup> Manuscript received August 22, 1946.

Contribution from the Physics Branch, Montreal Laboratory, Atomic Energy Division, National Research Council of Canada. Issued as N.R.C. No. 1468.

<sup>2</sup> Member of United Kingdom Staff.

<sup>3</sup> Physicist, National Research Council; now at the Chalk River Laboratory.

\* We were aware at the time of this experiment that similar work had been done in the United States.

185.8 cm. square and 153.6 cm. high. The average pile density was 1.55 gm. per cc. while the densities of 10 planed bars taken at random were found to range from 1.58 to 1.65, with the average 1.62 gm. per cc. The pile rested on cadmium sheet, 0.3 mm. thick, covered with wrapping paper, which served to define its lower boundary for thermal neutrons.

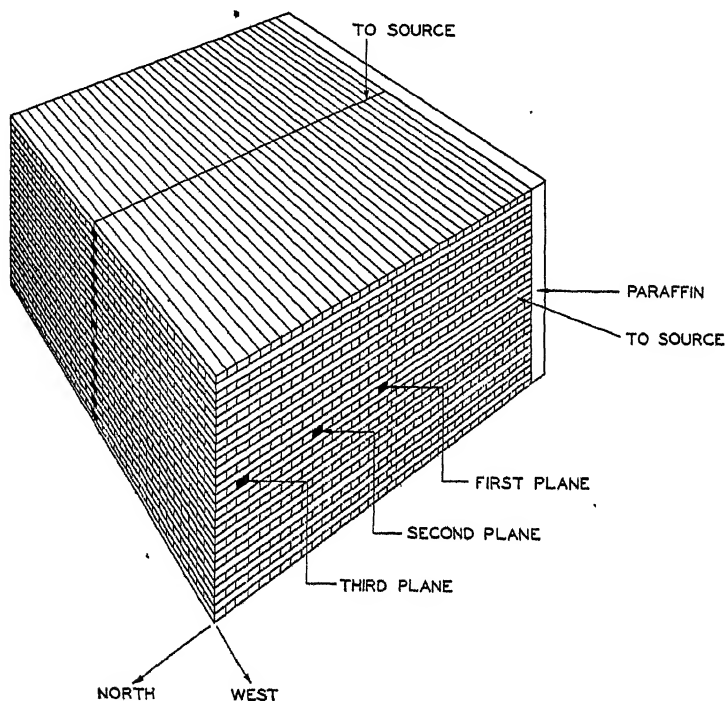


FIG. 1. *Graphite pile.*

The neutron source, 1.2 gm. of radium mixed with beryllium, was placed about 18 cm. from the south face of the pile. This face was covered with paraffin wax, about 12 cm. thick, to reduce the number of neutrons escaping from it and reaching other parts of the pile by scattering from the walls of the room.

### Experimental Method

The density distribution of thermal neutrons in the pile was measured with dysprosium detectors along the central north-south axis, on which the source was placed, and in the vertical and horizontal lines that intercept this axis normally at 13.5, 50.4, and 87.2 cm. from the north face. These lines may also be described as the defining lines of three vertical east-west planes, labelled first, second, and third planes in order towards the north end of the pile. The planed movable bars into which the detectors were placed are distinguished in Fig. 1 by the shading on their ends. The perpendicular

distances from the source to the three vertical planes of measurement and the north face were 81.3, 118.1, 155.0, and 168.5 cm., respectively. This disposition of source and planes of measurement was chosen to give a volume of reasonable length (about 1.7 diffusion lengths) in which the density distribution of thermal neutrons could be explored, and at the same time to locate this volume at a sufficient distance from the source of fast neutrons that the correction for the thermal sources within it was small. The evaluation of the diffusion length therefore did not require the precise value of the slowing-down length of the neutrons from the source.

A set of 10 detectors was used. Each consisted of 280 mgm. of dysprosium oxide in a shallow aluminium tray, 23 by 11 mm. The detectors, wrapped in aluminium foil, were wedged in holes in the movable bars with half-cylindrical graphite plugs, and always faced south in the pile. In order to avoid the influence of one detector on the activity acquired by another, adjacent ones at a given time in the pile were never less than 18 cm. apart.

The relative sensitivities of the detectors were determined by exposing them in turn to neutrons under constant geometrical conditions in the pile and comparing their  $\beta$ -emission with that from a radium ( $D + E$ ) preparation. Such standards were used systematically throughout the measurements to minimize errors due to variations in the behaviour of the Geiger-Müller counters and associated amplifiers and scales-of-32.

After the activity had approximately reached saturation at a point in the pile, eight minutes from the instant of removal was allowed to elapse for short-period activity to vanish, and the dysprosium activity was compared with a radium ( $D + E$ ) standard by bracketing for about two hours. The density of thermal neutrons was (arbitrarily) expressed as the counting rate ( $\beta$ -particles per minute), corrected to saturation, at the instant of removal from the pile, taking 140 min. for the half-period of dysprosium. Corrections were also applied for any activity remaining from the previous activation, and for the long period activity (perhaps contamination) of the detector. The latter was from two to four  $\beta$ -particles per minute from a single detector. The half-period of dysprosium was checked to about 1% by comparing decay-curves with those of actinium active deposit, the half-period of which (36.1 min.) is accurately known.

Corrections had to be applied to the measured distribution of neutrons to allow for two extraneous effects, which would have been greatly reduced if we had had sufficient cadmium sheet and covered the pile. (i) Some neutrons entered the pile from external sources, used in other experiments in the same room. (ii) Some neutrons from the source in the pile were reflected from the walls of the room back into the pile. The contribution of these neutrons to the measurements was investigated with the dysprosium detectors by measuring the densities ( $a$ ) at a few points in the pile in the absence of external sources, and ( $b$ ) at many points in the pile in the presence of external sources and with our source placed in a paraffin wax box on the floor beyond the south face. In arrangement ( $b$ ) our source was retained in the room to reproduce,

at least in part, the effect of scattered neutrons from the walls of the room. The final correction, representing the effects of all neutrons from outside the pile, of course varied from point to point in the pile but never exceeded nine  $\beta$ -particles per minute. When these intensities were subtracted from the original intensities, the extrapolated distributions vanished at the theoretical bounding planes for such a pile *in vacuo*.

We shall now examine our fundamental assumption that the density of thermal neutrons is proportional to the saturation activity of our detectors facing south in the pile. In order to have reasonably high counting rates we were obliged to choose rather thick detectors having a high capture cross-section per atom. When a stronger source became available, the 280 mgm. detectors, orientated in several directions, were compared with 28 mgm. detectors of dysprosium oxide at a number of points on the north-south axis of the pile. The 280 mgm. detectors acquired about 1% more activity when facing south and 1% less activity when facing north than the average for different orientations, at points between the first and third planes. The 28 mgm. detectors showed no measurable orientation effect. The ratio of the averaged activities acquired by thick and thin detectors was constant at 4.6 within experimental error. The 280 mgm. detectors, as used in this experiment, therefore give sufficiently accurate measurements of the density of thermal neutrons. A small departure from the  $1/v$  law of capture of neutrons by dysprosium, suspected by some experimenters, can scarcely be of importance here.

### Elementary Diffusion Theory

The diffusion equation for thermal neutrons may be simply derived from the idea of continuity in the steady state:

production = capture + outflow,

$$\text{or in symbols, } q = \frac{\rho}{\tau} + \text{div } j. \quad (1)$$

$q$  is the number of thermal neutrons produced by slowing down per  $\text{cm}^3$  per sec.

$\rho$  is the density or number of thermal neutrons per  $\text{cm}^3$ .

$\tau$  is the mean lifetime with respect to capture.

$j$  is the current or net number per  $\text{cm}^2$  per sec.

If in analogy with the kinetic theory of gas diffusion we introduce the diffusion coefficient  $D$  and the assumption  $j = -D \text{ grad } \rho$ , the equation of continuity becomes:

$$\nabla^2 \rho - \frac{\rho}{D\tau} = - \frac{q}{D}. \quad (2)$$

The product  $D\tau$ , having the dimensions of the square of a length, is written as  $L^2$ , where  $L$  is defined as the diffusion length. Equation (2) becomes:

$$\nabla^2 \rho - \frac{\rho}{L^2} = - \frac{q\tau}{L^2}. \quad (3)$$

If we assume that there are no fast neutrons in the region beyond the first plane, which is 81.3 cm. from the source, Equation (3) becomes:

$$\nabla^2 \rho - \frac{\rho}{L^2} = 0. \quad (4)$$

In order to proceed to find  $\rho$  as a function of the co-ordinates, the origin is chosen at the lower north-east corner of the pile, with the positive direction of the  $X$ -axis westward, the  $Y$ -axis upward, and the  $Z$ -axis southward into the pile. The solution of the diffusion Equation (4) is subject to the boundary conditions:

$$\rho = 0 \text{ for } x = 0, a; \rho = 0 \text{ for } y = 0, b; \text{ and } \rho = 0 \text{ for } z = 0;$$

where  $a = 189.4$  cm.,  $b = 157.2$  cm. are the two dimensions of the pile corrected for the breakdown of the diffusion theory near the boundaries. This correction amounts to a shift of the theoretical boundary to vacuum by a distance 0.71 times the transport mean free path. This theoretical result was brought to our attention by Placzek and Seidel's work on Milne's problem in transport theory (3) (see also Hopf (1)). The remaining boundary condition is given by the densities measured in the first plane, which may be analysed into Fourier components:

$$\rho = \sum_{l,m} K_{lm} \sin \frac{l\pi x}{a} \sin \frac{m\pi y}{b} \text{ at } z = d = .89 \text{ cm.}$$

where  $l, m = 1, 3, 5, 7, \dots$

The distribution is assumed to be symmetrical about the north-south axis of the pile, which was confirmed experimentally. The required solution of Equation (4) is:

$$\rho = \sum_{l,m} K_{lm} \sin \frac{l\pi x}{a} \sin \frac{m\pi y}{b} \frac{\sinh \frac{z}{L_{lm}}}{\sinh \frac{d}{L_{lm}}} \quad (5)$$

$$\text{or } \rho = \sum_{l,m} A_{lm}(z, L) \sin \frac{l\pi x}{a} \sin \frac{m\pi y}{b}, \quad (6)$$

$$\text{where } \frac{1}{L_{lm}^2} = \frac{1}{L^2} + \pi^2 \left( \frac{l^2}{a^2} + \frac{m^2}{b^2} \right) \quad (7)$$

The  $L_{lm}$ 's are called the relaxation lengths of the pile for the various components. The analysis of the measurements aims at isolating and evaluating  $L_{11}$  and in turn the diffusion length  $L$  through Equation (7).

### Experimental Results

Fig. 2 shows the densities of thermal neutrons plotted against distances measured vertically and horizontally from the north-south axis of the pile. The density at each point was measured twice, and, taking corresponding points on opposite sides of the axis together, each density plotted in Fig. 2 is

the average of four measurements. The ordinates are the counting rates in  $\beta$ -particles per minute. For points in the first and second planes, where the counting rates are reasonably high, separate determinations agreed to about 3%.

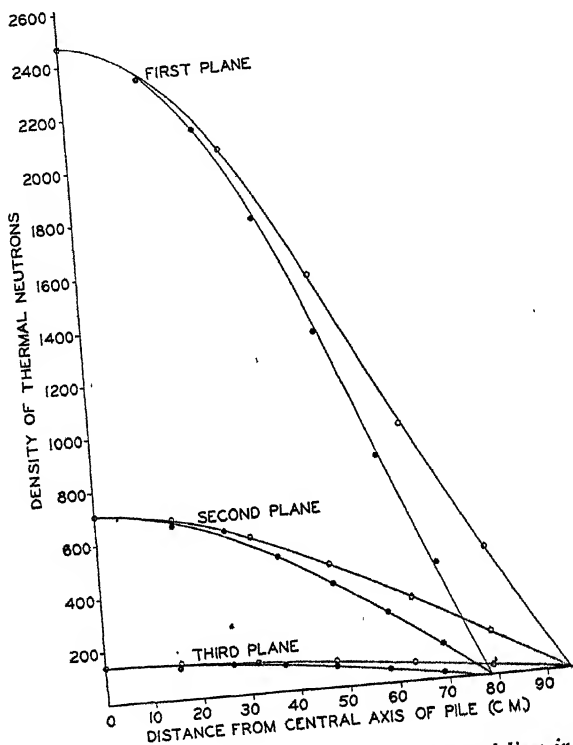


FIG. 2. Measured densities of thermal neutrons along horizontal lines in three vertical planes are shown by unfilled circles, and those along vertical lines in the same planes are shown by filled circles. The curves shown are those for best fit according to the method of least squares.

The amplitudes  $A_{lm}$  were found from the amplitudes of the trigonometric functions required to fit the experimental data along each axis of each plane. The method of least squares was used. Neglecting  $A_{33}$  and higher Fourier terms, the following coefficients were obtained.

First plane ( $z = 89.0$  cm.)

$$A_{11} = 2290, A_{31} = 166.5, A_{13} = 68.1 \quad (A'_{51} = -26.1, A'_{15} = -28.4).$$

Second plane ( $z = 52.2$  cm.)

$$A'_{11} = 673.3, A'_{31} = 25.7, A'_{13} = 9.7 \quad (A'_{51} = 0.4, A'_{15} = -3.6).$$

Third plane ( $z = 15.3$  cm.)

$$A''_{11} = 135.6 \quad (A''_{31} = -0.1, A''_{13} = 0.5).$$

The fit of these values is shown by the curves drawn in Fig. 2.

From Equation (5)

$$\frac{A_{11}}{A'_{11}} = \frac{2290}{673.3} = \frac{\sinh \frac{89.0}{L_{11}}}{\sinh \frac{52.2}{L_{11}}}$$

Hence

$$L_{11} = 30.9 \text{ cm. and } L = 52 \text{ cm.}$$

Similarly,

$$\frac{A'_{11}}{A''_{11}} = \frac{673.3}{135.6} = \frac{\sinh \frac{52.2}{L_{11}}}{\sinh \frac{15.3}{L_{11}}}$$

Hence

$$L_{11} = 31.8 \text{ cm. and } L = 57 \text{ cm.}$$

The latter values are less reliable than the former owing to the difficulty of measuring the small intensities in the third plane. A correction for thermal sources near the first plane must be applied, and this matter will be dealt with in the next section.

The densities measured along the central north-south axis of the pile are shown in Fig. 3. Each point represents the average of at least two measurements. A few points were remeasured later with a stronger source, and these results are distinguished by filled circles. These activities, averaged for different orientations of the detectors, were normalized to fit the earlier measurements at the first point. The curves were calculated for  $L = 48, 52$ , and  $56$  cm. and a slowing-down length of  $20.8$  cm.

### Corrections for Sources of Thermal Neutrons

Consideration of the effect of thermal sources on the derived diffusion length will be based on the slowing-down theory. It is convenient to divide the discussion into three parts.

#### (1) *Effect of the Paraffin Wax at the South Face*

The wax did not increase the number of epithermal neutrons beyond the first plane of measurement to any extent, for the total distance from the radium source to the wax and back to the first plane is  $117$  cm. or more than five slowing-down lengths. The wax may have increased the number of thermal neutrons in the region of measurement, compared with the case where the south face is a boundary to air. This point was tested experimentally, and it was found that the removal of the wax caused a maximum reduction in density of  $10\%$  in the first plane.

The experimental arrangement with the wax reflector was closer to the case of a square pile, bounded by air on all sides, than to the case of a semi-infinite pile in the  $z$ -direction, for calculation shows that the density of thermal neutrons at the first plane would be reduced by about  $40\%$  in going from the semi-infinite to the square pile. The effect of the wax was therefore to reduce

the ratio of fast to slow neutrons in the region of measurement up to 10%; and hence a slightly smaller correction for thermal sources is required than in the case of the finite pile.

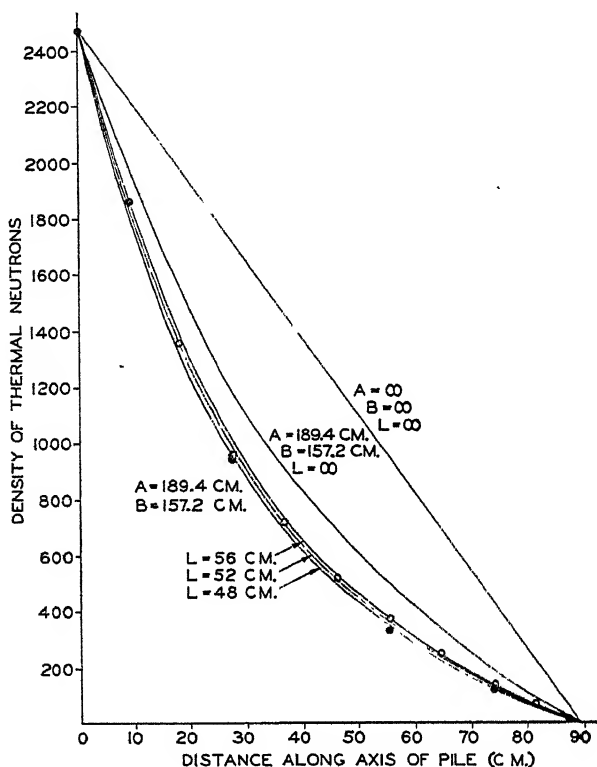


FIG. 3. Measured densities of thermal neutrons along the central axis of the pile are shown by unfilled circles. Repetitions using a stronger source and after normalization with the previous measurements at the first plane are shown by filled circles. The lowest curves are those calculated for  $L = 48, 52,$  and  $56$  cm. and a slowing-down length of  $20.8$  cm. In addition, the curve is shown for  $L = \infty$  (no capture), and the straight line for a pile infinite in the  $x$ - and  $y$ -directions and having  $L = \infty$ . Note that  $A = a$  and  $B = b$ , the small letters being used in the text for two of the pile dimensions.

## (2) Correction for Thermal Sources in the Case of the Finite Pile on the Basis of Elementary Slowing-down Theory

The equation for  $\chi$ , the number of neutrons per unit volume passing through the symbolic age  $\theta = \int_0^t D dt$  in unit time, is

$$\frac{\partial \chi}{\partial \theta} = \nabla^2 \chi - \epsilon(\theta) \frac{\chi}{L^2} + S \delta \left( x - \frac{a}{2} \right) \delta \left( y - \frac{b}{2} \right) \delta(z - z_1) \delta(\theta + L_s^2) \quad (8)$$

(change of  $\chi$  with age = influx - capture + source), where  $\delta$  is Dirac's delta-operator,  $\epsilon(\theta) = 0$  for  $\theta < 0$  and  $\epsilon(\theta) = 1$  for  $\theta > 0$ .  $\theta = 0$  denotes the age at which neutrons become thermal and liable to be captured.  $L_s$  is the

slowing-down length to thermal velocities.  $S$  is the strength of the source (neutrons emitted per second) situated at  $x = \frac{a}{2}$ ,  $y = \frac{b}{2}$ ,  $z = z_1$ .

The boundary conditions for Equation (8) are  $\chi = 0$  at  $x = 0, a$ ;  $\chi = 0$  at  $y = 0, b$ ; and  $\chi = 0$  at  $z = 0, c$ , where  $c = 189.4$  cm. is the length of the pile in the  $z$ -direction.

We take, at first, the case of a pile infinite in the  $z$ -direction and later use images to fulfil the boundary conditions on  $z$ . The solution at  $\theta = 0$  is

$$\begin{aligned}\chi(0) &= \sum_{l,m} \frac{4}{ab} \frac{S}{\sqrt{4\pi L_s^2}} e^{-\frac{(x-z_1)^2}{4L_s^2}} e^{-\pi^2 L_s^2 \left(\frac{l^2}{a^2} + \frac{m^2}{b^2}\right)} \sin \frac{l\pi x}{a} \sin \frac{m\pi y}{b} \\ &= \sum_{l,m} B_{lm}(x, y) \frac{e^{-\frac{(x-z_1)^2}{4L_s^2}}}{\sqrt{L_s^2}}\end{aligned}$$

where  $l, m = 1, 3, 5, \dots$

This solution, representing the distribution of sources of thermal neutrons, is used as a boundary condition in solving Equation (8) for thermal neutrons ( $\epsilon(\theta) = 1$ ). We obtain

$$\chi(\theta) = \sum_{l,m} \chi_{lm}(\theta) \quad \text{with} \quad \chi_{lm}(\theta) = B_{lm} \frac{e^{-\frac{(x-z_1)^2}{4(L_s^2 + \theta)}} - \frac{\theta}{L_{lm}^2}}{\sqrt{L_s^2 + \theta}}.$$

Since  $\chi(\theta) d\theta$  is the number of neutrons per unit volume passing through an age  $\theta$  in time  $dt$ , the number of neutrons per unit volume in an age interval  $d\theta$  is given by

$$\chi(\theta) d\theta = \chi(\theta) \frac{dt}{d\theta} d\theta = \frac{\chi(\theta)}{D} d\theta,$$

and the total density of thermal neutrons is given by  $\rho = \int_0^\infty \frac{\chi(\theta)}{D} d\theta$ , where  $D$  is the diffusion coefficient of thermal neutrons.

$$\rho = \frac{1}{D} \int_0^\infty \sum_{l,m} \chi_{lm}(\theta) d\theta = \sum_{l,m} \rho_{lm},$$

where

$$\rho_{lm} = \frac{1}{D} \int_0^\infty \chi_{lm}(\theta) d\theta.$$

$$\begin{aligned}\rho_{lm} &= B_{lm} \frac{e^{L_s^2/L_{lm}^2}}{D} L_{lm} \sqrt{\frac{\pi}{2}} \left\{ e^{\frac{z_1-z}{L_{lm}}} \left[ 1 - \operatorname{erf} \left( \frac{L_s}{L_{lm}} + \frac{z_1-z}{2L_s} \right) \right] \right. \\ &\quad \left. + e^{-\frac{(z_1-z)}{L_{lm}}} \left[ 1 - \operatorname{erf} \left( \frac{L_s}{L_{lm}} - \frac{z_1-z}{2L_s} \right) \right] \right\}.\end{aligned}$$

An equivalent treatment has been given by Wallace and LeCaine (5).

The boundary conditions in the  $z$ -direction are now introduced by superposing the solutions for image sources about the two boundaries, viz., for

sources of alternate sign at distances  $\pm (2nc - z_1)$ , where  $n$  is an integer. For the region  $15 < z < 89$  cm., between the first and third planes, we need only consider the primary source and three images. The first Fourier component of the density for the four sources is the only term for which the correction for thermal sources may be a significant fraction of the total density. Neglecting contributions of less than 0.1%, it reduces to the following:

$$\rho_{11} = C_{11} \left\{ 4 \left( e^{\frac{-z_1}{L_{11}}} - e^{\frac{-(2s - z_1)}{L_{11}}} \right) \sinh \frac{z}{L_{11}} + e^{\frac{z_1 - z}{L_{11}}} \left[ 1 - \operatorname{erf} \left( \frac{L_s}{L_{11}} + \frac{z_1 - z}{2L_s} \right) \right] - e^{\frac{-(z_1 - z)}{L_{11}}} \left[ 1 - \operatorname{erf} \left( \frac{z_1 - z}{2L_s} - \frac{L_s}{L_{11}} \right) \right] \right\}, \quad (9)$$

where

$$C_{11} = B_{11} \frac{e^{\frac{L_s^2}{2D}} L_{11}}{2D} \sqrt{\pi}.$$

An estimate of the slowing-down length  $L_s$  may be made from measurements taken by Dr. L. G. Elliott. He used indium resonance detectors and the same source in this pile. It is sufficient for the present purpose to state that a single Gaussian curve fits the measured distribution near the source if the slowing-down length to indium resonance (1.44 ev. (2)) is taken between 16 and 17 cm. A single Gaussian curve fits the measured points farther from the source if the slowing-down length is taken to be 19 cm. Allowing for slowing-down from the indium resonance region to the region of capture by dysprosium,  $L_s$  was taken to be between 18 and 21 cm.

Equation (9) for  $\rho_{11}$  differs from Equation (5), where the variation of  $\rho_{11}$  with  $z$  is given by  $\sinh \frac{z}{L_{11}}$ , by the last two terms in the bracket. Using  $L = 50$  cm., we find that these two terms amount to  $-2.2\%$  for  $L_s = 20.8$  cm.,  $-1.5\%$  for  $L_s = 20$  cm., and  $-0.7\%$  for  $L_s = 18.5$  cm. at the first plane, and become negligibly small for distances from the source greater than 100 cm., i.e., in the region of the second plane.

The curves of Fig. 3 were computed using  $L_s = 20.8$  cm. in Equation (9) for  $\rho_{11}$ , and the higher components from Equation (5).

### (3) *Modification of the Slowing-down Theory*

In Part (2) the contribution of thermal sources to the density was calculated on the basis of elementary slowing-down theory. Using a better approximation of the transport theory, for which we are indebted to Dr. R. E. Marshak, it is found that the additional correction to the density up to distances of 100 cm. from the source never amounts to more than 25% of the correction found in Part (2).

The final correction to the density for thermal sources is approximately 1% at the first plane, and if  $A_{11}$  is increased by this amount, the value of  $L$  calculated from the ratio  $A_{11}/A'_{11}$  is reduced to 51 cm.

In Fig. 3 the calculated curves are normalized to the density at the first plane. The best value of  $L$  to fit the points on the central axis between 18 and 65 cm. from the first plane (i.e., in the region where the sensitivity of  $L$  is greatest) is 51 cm., with a probable error of about 3 cm.

For this graphite of average pile density 1.55 gm. per cc. the diffusion length is  $51 \pm 3$  cm.

### Limitation of Accuracy

The density measurements were limited in accuracy by the rather low counting rates, instability of the counter sensitivity, and the unsatisfactory reproducibility of geometry at the counter.

The size of the graphite pile was insufficient for good accuracy, which may be seen from Fig. 3. The straight line shown in this figure represents the variation of density along the axis of a pile infinite in the  $x$ - and  $y$ -directions (no leakage of neutrons through its sides) and  $L = \infty$  (no capture). The next curve refers to the experimental pile as regards dimensions (same leakage) but having  $L = \infty$  (no capture). It is clear that for a pile with this cross-section the leakage of neutrons is more important than the capture within the graphite. The same point may be shown algebraically. The relaxation length  $L_{11}$  of the first component in the harmonic analysis is given by

$$\frac{1}{L_{11}^2} = \frac{1}{L^2} + \pi^2 \left( \frac{1}{a^2} + \frac{1}{b^2} \right) = 384 \times 10^{-6} + 675 \times 10^{-6}, \text{ or } L_{11} = 30.7 \text{ cm.}$$

The second or leakage term is 1.8 times the first or capture term.

### Acknowledgments

We are grateful for permission to refer to unpublished work of the following:

Dr. G. Placzek, Dr. W. Seidel, Dr. P. R. Wallace, Dr. Jeanne LeCaine, Dr. R. E. Marshak, and Dr. L. G. Elliott.

We have been greatly assisted by Miss E. O'Brien, who did part of the counting.

### References

1. HOFF, L. Mathematical problems of radiative equilibrium. Cambridge tract No. 31 : 85. 1934.
2. MARSHALL, J. Bull. Am. Phys. Soc. 21 (3) : 12. 1946.
3. PLACZEK, G. and SEIDEL, W. Milne's problem in transport theory. Montreal report. 1943.
4. SMYTH, H. D. Atomic energy for military purposes. Princeton Univ. Press. Princeton, N.J. 1945.
5. WALLACE, P. R. and LECANE, J. Elementary approximations in the theory of neutron diffusion. Montreal report. 1943.

# THE DIFFUSION LENGTH OF THERMAL NEUTRONS IN HEAVY WATER CONTAINING LITHIUM CARBONATE<sup>1</sup>

BY H. G. HEReward<sup>2</sup>, G. C. LAURENCE<sup>3</sup>, A. M. MUNN<sup>4</sup>,  
H. R. PANETH<sup>2</sup>, AND B. W. SARGENT<sup>3</sup>

## Abstract

The density distribution of thermal neutrons was measured with a small boron trifluoride chamber in a cylindrical tank containing 113 litres of heavy water in which lithium carbonate was dissolved. The diffusion length was found to be 22.7 cm. in this solution containing  $7.70 \times 10^{-4}$  atoms of lithium per molecule of heavy water (99.4 atom % D). After corrections were applied for the capture of neutrons in the heavy water and light hydrogen, the capture cross-section of lithium was found to be  $59 \times 10^{-24}$  cm.<sup>2</sup> per atom for neutrons of standard velocity 2200 m. per sec. from the measured diffusion length and known transport mean free path.

## Introduction

The diffusion length of thermal neutrons in a solution of a uranium compound in heavy water is not easy to measure directly owing to multiplication. If the ratio of the capture cross-section of uranium to that of boron or lithium is known, measurement of the diffusion length in a solution of a boron or lithium compound leads to the diffusion length in a uranium solution.

While the cross-section of boron is perhaps better known than that of lithium, there is a strong reason against its use and in favour of the use of lithium. Not only must the compound to be dissolved in heavy water be free of ordinary water and impurities that capture thermal neutrons strongly, but it must be possible to remove it completely from the heavy water by distillation. Mr. J. Hébert and Dr. A. G. Maddock (7) have kindly investigated these points for us, and found that the distillates from borax solutions contain boron, but that the lithium carbonate available in this laboratory meets all the requirements.

The density distribution of thermal neutrons was explored with a small boron trifluoride chamber in a cylindrical tank containing 113 litres of heavy water in which was dissolved sufficient lithium carbonate to reduce the diffusion length to a suitable value for measurement. In this solution containing  $7.70 \times 10^{-4}$  atoms of lithium per molecule of water (99.4 atom % D), the diffusion length was found to be 22.7 cm. This experiment was done in the Montreal Laboratory during the winter of 1944 and described in a report bearing the date May 16, 1944.

<sup>1</sup> Manuscript received August 29, 1946.

*Contribution from the Physics Branch, Montreal Laboratory, Atomic Energy Division of the National Research Council of Canada. Publication has been delayed owing to security restrictions. Issued as N.R.C. No. 1470.*

<sup>2</sup> Member of United Kingdom Staff.

<sup>3</sup> Research Physicist, National Research Council, now at Chalk River, Ont.

<sup>4</sup> Junior Research Physicist, National Research Council, now at McGill University, Montreal, Que.

### Theory of the Experiment

The diffusion equation in the absence of thermal sources is

$$\nabla^2 \rho - \frac{\rho}{L^2} = 0, \quad (1)$$

where  $\rho$ , the density of thermal neutrons, is a function of the co-ordinates, and  $L$  is the diffusion length (8). Equation (1) written in cylindrical co-ordinates  $r$  and  $z$  is

$$\frac{\partial^2 \rho}{\partial r^2} + \frac{1}{r} \frac{\partial \rho}{\partial r} + \frac{\partial^2 \rho}{\partial z^2} - \frac{\rho}{L^2} = 0. \quad (2)$$

The origin is taken at the centre of a horizontal cross-section near the bottom of the tank, and the positive direction of the  $z$ -axis is upwards along the axis of the tank. The term involving the angular co-ordinate  $\theta$  is omitted from Equation (2). Any angular asymmetry found experimentally can be allowed for by taking the angular average of the measured density  $\rho$  for a given radial distance  $r$  and given height  $z$ .

The solution of Equation (2) is subject to four boundary conditions.

(1) The density  $\rho$  is finite on the axis of the cylinder.

(2) The density vanishes at the surface of a vertical coaxial cylinder of radius  $R$ , where  $R$  (evaluated later) is the effective radius of the tank;

$$\text{i.e. } \rho(r, z) = 0 \text{ for } r = R.$$

(3) The density vanishes at a horizontal plane a short distance above the surface of the liquid;

$$\text{i.e. } \rho(r, z) = 0 \text{ for } z = h \text{ (to be evaluated later).}$$

(4) The density distribution in the horizontal plane through the origin is given by measurement.

The desired solution of Equation (2) is

$$\rho = \sum_{n=1,2,3,\dots} A_n J_0(\lambda_n r) \frac{\sinh \frac{h-z}{b_n}}{\sinh \frac{h}{b_n}}, \quad (3)$$

where

$$\frac{1}{b_n^2} = \lambda_n^2 + \frac{1}{L^2}. \quad (4)$$

The  $b_n$ 's are the relaxation lengths of the various Fourier-Bessel components.

The  $\lambda_n$ 's can be found from the roots of the equation:  $J_0(\lambda_n R) = 0$ ;

$$\text{i.e. } \lambda_1 = \frac{2.4048}{R}, \quad \lambda_2 = \frac{5.5201}{R}, \quad \lambda_3 = \frac{8.6537}{R},$$

$$\lambda_4 = \frac{11.792}{R}, \quad \lambda_5 = \frac{14.931}{R}, \text{ etc.}$$

Boundary condition (4) may be written

$$\rho(r, z = 0) = \sum A_n J_0(\lambda_n r). \quad (5)$$

This horizontal plane containing the origin must be taken a few scattering mean free paths above the bottom of the tank to avoid effects of scattering in the materials below the heavy water.

The density distribution was measured in three horizontal planes spaced at 12-cm. intervals, and along the central axis. The lowest or first plane was approximately 4.2 cm. above the bottom of the tank. The distributions were analysed transversely into Fourier-Bessel series, and the first component was thereby isolated. Its diminution in the vertical direction permitted  $b$  and  $h$  to be found according to Equation (3). The diffusion length was derived from Equation (4).

### Experimental Details

The source of thermal neutrons was a graphite pile 186 cm. by 186 cm. in horizontal section and 274 cm. high. On the vertical axis of the pile and 100 cm. from the top was placed 2.2 gm. of radium mixed with beryllium. Since the distance from this source of fast neutrons to the cylindrical tank on top of the pile was five slowing-down lengths, neutrons entering the tank were almost entirely thermal ( $> 99\%$  in number).

The graphite pile was covered on its sides, top, and bottom with cadmium sheet, 0.4 mm. thick. A wooden platform, 3.5 cm. thick, rested on the cadmium on top of the pile. Circular holes, 65 cm. in diameter, in the cadmium top and in the platform, were centred roughly on the axis of the pile. A circular aluminium tray, 91 cm. in diameter, was placed symmetrically over these holes to catch any leakage of heavy water in case of accidents, after the space between the graphite blocks and the upper surface of the wooden platform had been packed with petroleum coke and levelled. The experimental tank (Fig. 1) was centred in the tray. This tank was made of aluminium of wall thickness 3.3 mm. and 45.4 cm. high. Its internal diameter was measured in several directions and at various heights with a suitable inside caliper made for the purpose. The individual measurements were between 61.16 and 60.94 cm., and the average diameter was 61.01 cm.

The cover of the tank was designed with the assistance of Dr. S. G. Bauer. A glass disk, 7 mm. thick and 69.7 cm. in diameter, rested on the upper flange of the tank, and the joint was sealed with Apiezon grease *M*. A radial slot, 35 cm. long and 2.6 cm. wide, along which the boron chamber could be moved, was cut in the disk. A glass slab, 42 by 10 cm., with an identical slot, was cemented on to the disk so that the two slots coincided. A second slab, 76 by 13 cm., with a conical hole for the gland supporting the boron chamber, rested on the upper greased surface of the first slab. A tall box housing the head amplifier and gland for the boron chamber was clamped on the movable slab. The sides of the tank were tightly wrapped with cadmium sheets, and similar sheets were placed on top of the glass disk and slabs.

A number of excellent boron chambers were made for us by Mr. N. A. Veall (11); one of these is shown in Fig. 2. The chambers were made of lead glass, 5 mm. in internal diameter and 0.45 cc. in volume, and were filled with boron

trifluoride to a pressure of about 2 atm. The guard-rings were grounded in the solution. The first chamber was sealed to the lower end of a single glass tube housing the lead to the central anode. The high tension lead to the platinum cathode was a rubber-insulated wire to the lower end of the chamber and the joint was made water-tight with rubber Bostik. After some time the

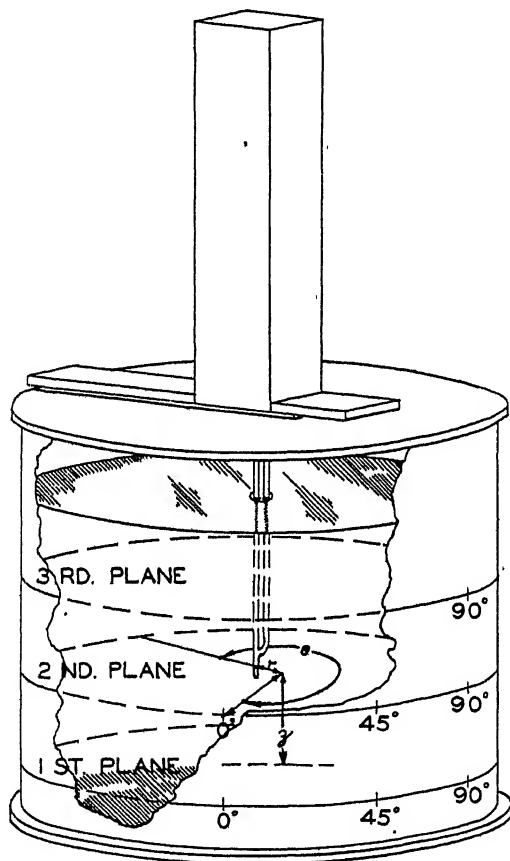


FIG. 1. *Experimental tank. The boron chamber and head amplifier box are shown.*

insulation failed, and this chamber was replaced by a second chamber sealed to two parallel glass tubes, one tube housing the lead to the anode, and the other the high tension wire to the cathode (Fig. 2). The latter tube was filled with some of the solution to reduce the disturbance in the neutron distribution caused by the channel. The glass tubes to the chamber were clamped in a gland, and the height was adjustable. The gland for the second boron chamber, designed by Mr. N. Q. Lawrence and Mr. N. A. Veall, is shown in Fig. 3.

The counting equipment was supplied by Mr. H. F. Freundlich. It consisted of a head amplifier (5), mounted as closely as possible to the boron

chamber, a linear amplifier of four stages, a discriminator to reject pulses below a chosen size, a scale-of-32, and an oscilloscope. A stabilized high

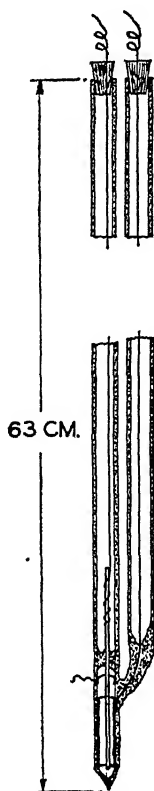


FIG. 2. Small boron trifluoride chamber.

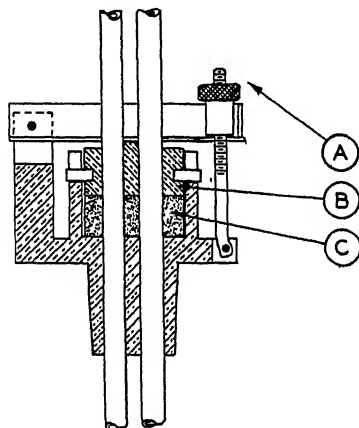


FIG. 3. Gland to support boron chamber. Tightening the nut A pushes the brass piece B on to the graphitized rubber gasket C, thus making a tight joint.

voltage (usually about 800 v.) was applied to the boron chambers. All electrical leads were shielded, and all units were brought to a common ground.

The solution of lithium carbonate was made by stirring 179.73 gm. of the carbonate in  $125.2 \pm 0.1$  kgm. of heavy water for a period of three hours. A portion (125.1 kgm.) of the solution was placed in the experimental tank. After the experiment had been completed, Mr. Hébert analysed two samples of the solution for us and found 1.566 and 1.575 gm. of lithium carbonate per litre, which may be compared with 1.585 gm. per litre from the original weights of the components.

The cylindrical co-ordinates of the approximate centre of sensitivity of the boron chamber in the tank were specified as follows (Fig. 1). The angular co-ordinate  $\theta$  was read at the axial slot on the circular scale painted around the tank. The radial distance  $r$  was found from the displacement of the movable glass plate supporting the boron chamber, the glass disk being centred through measurements between its edge and the upper flange of the tank. The height of the boron chamber above the first plane was measured from a mark on the gland to a mark on the glass tube.

### Experimental Results

At any point ( $r, z, \theta$ ) the counting was carried out in two parts, (i) with the boron chamber and gland in a given position, and (ii) with the boron chamber and gland rotated through  $180^\circ$  from the first position. The average of the two readings in counts per minute was taken as a measure of the density of thermal neutrons at the point. This method eliminated possible error due to the fact that the chamber was not situated accurately below the centre of the gland. Sufficient particles were counted at each point for the statistical error to be less than 1%.

Most of our measurements in the three planes are summarized in Table I. In the first plane, readings were taken along eight radii spaced at  $45^\circ$  intervals. That is, for  $z = 0$ , the densities at values of  $r = 5, 10, 15, 17.5$  cm., etc. were compared with the density at  $r = 0$  for eight different angles  $\theta$ . The readings were normalized to a count at the centre of 700 particles per minute, which was approximately the observed counting rate. Similar measurements were made in the second plane, which was 12 cm. above the first plane. In this case readings were normalized to a count at the centre of 270 particles per minute (see Table II). A slight angular asymmetry appeared in both planes, and it was traced to variations in depth due to the fact that the bottom of the tank was not perfectly flat and also to a slight error in levelling. The asymmetry was removed by averaging the densities for a given  $r$  and  $z$  over the angle  $\theta$ . In the third plane, 12 cm. above the second, it was sufficient to measure along four radii. These readings were normalized to a count at the centre of 91 particles per minute (see Table II). The average densities are plotted against the radial distances in Fig. 4.

TABLE I  
EXPERIMENTAL RESULTS  
DENSITY  $\rho$  AT VARIOUS ANGLES  $\theta$

$r$ , cm.	0°	45°	90°	135°	180°	225°	270°	315°	*Av.
<i>First plane</i>									
0	700	700	700	700	700	700	700	700	700
5	690	682	—	683	691	—	—	—	686
10	637	637	640	649	652	636	641	641	642
15	567	568	568	585	578	571	574	560	571
17.5	520	516	535	532	532	530	517	520	525
20	457	458	470	481	472	460	460	463	465
22.5	392	393	409	415	406	405	390	394	401
25	314	320	331	330	328	322	307	308	320
27.5	—	—	—	—	—	—	218	—	222
<i>Second plane</i>									
0	270	270	270	270	270	270	270	270	270
5	—	263	—	263	261	—	—	258	261
10	235	240	241	238	244	242	236	235	239
15	197	208	210	207	207	206	202	207	205
17.5	184	181	—	181	181	—	181	178	181
20	153	153	160	161	160	158	157	151	157
22.5	124	125	129	126	128	—	125	—	126
25	92.7	96.4	97.0	99.0	96.5	100	94.8	92.0	96.0
27.5	—	—	—	—	—	—	62.0	—	62.5
<i>Third plane</i>									
$r$ , cm.	0°	90°	180°	270°	*Av.				
0	91	91	91	91	91				
5	85.5	89.5	87.5	86.7	87.3				
10	80.5	78.1	79.0	79.6	79.3				
15	67.0	68.6	65.9	65.4	66.7				
17.5	—	59.5	58.5	60.5	59.5				
20	48.5	50.6	49.0	49.4	49.4				
22.5	—	39.5	—	39.8	39.6				
25	—	30.3	29.4	29.8	29.8				
27.5	—	—	—	18.0	18.0				

\* In the last line ( $r = 27.5$  cm.), where there is a single measurement at  $\theta = 270^\circ$ , the average over all angular positions takes into account the angular asymmetry in this position judged from the measurements at neighbouring points and the contour map of the bottom of the tank.

The density distribution along the central axis was also measured with the two boron chambers, and the averages at points spaced at 2-cm. intervals are plotted in Fig. 5. The densities at the centres of the second and third planes were each compared many times with the density at the centre of the first plane. These results including the averages of the residuals are given in Column 2 of Table II.

TABLE II

COMPARISON OF THE DENSITIES OF THERMAL NEUTRONS AT THE CENTRES OF THREE PLANES

Plane No.	Boron chamber at end of vertical tubes		Boron chamber at end of L-shaped tubes	
	Density	No. of comparisons	Density	No. of comparisons
1	700	—	700	—
2	$270 \pm 3$	11	$271 \pm 4$	11
3	$91.0 \pm 1.9$	12	$89.3 \pm 2.3$	8

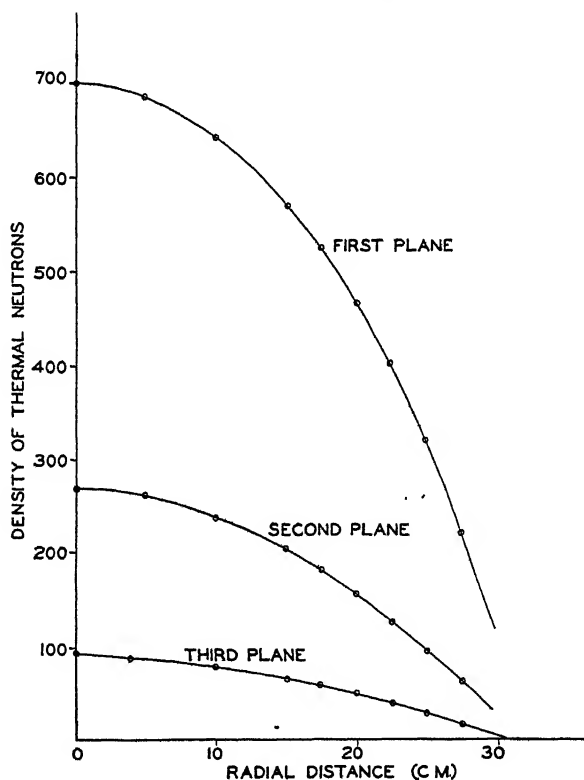


FIG. 4. The radial distribution of the density of thermal neutrons.

All measurements taken with the two different boron chambers agreed closely and were independent of the bias-setting of the discriminator and of the potential difference across the boron chambers. In order to ascertain whether there was any disturbance in the neutron density caused by the hollow glass tube supporting the boron chamber, the tubes of the second boron chamber were bent into an L-shape so that the centre of sensitivity of the chamber was displaced 10.2 cm. horizontally from the vertical supporting

tubes, and the intensities at the centres of the three planes were again compared. From a comparison of these results in Column 4 with those in Column 2 of Table II it is clear that the channel effect is small.

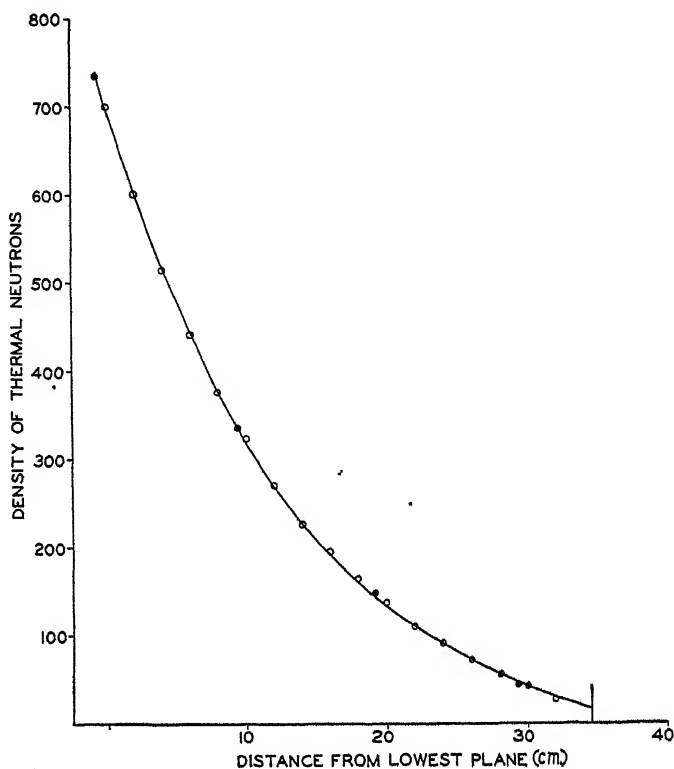


FIG. 5. The axial distribution of the density of thermal neutrons, unfilled circles representing measurements with the boron chambers and filled circles those with dysprosium detectors. The position of the liquid surface is indicated by the line segment at  $z = 34.6$  cm.

A few measurements along the central axis were made with dysprosium detectors. Each detector consisted of 280 mgm. of dysprosium oxide in an aluminium tray, 2.3 by 1.1 cm. Several of these detectors were spaced on a thin strip of aluminium, which was slid into an aluminium sheath of oblong cross-section and of wall thickness 5 mils. This sheath was supported at its top by a cone that fitted into the hole in the movable glass slab. Our counting procedure for activated detectors has been described in a previous paper (8). The measurements with the dysprosium detectors are fitted to the measurements with the boron chambers in Fig. 5, where the agreement is seen to be satisfactory.

### Analysis of the Experimental Results

Before the transverse measurements could be analysed into Fourier-Bessel series the parameters  $\lambda_n$  had to be estimated. This step required the value of the effective radius  $R$ . In our first analysis,  $R$  was taken to be equal to

the internal radius of the tank, plus 0.05 cm. for the aluminium wall of actual thickness 0.33 cm., plus 1.65 cm. This last length was the intercept of the curve, showing the density of thermal neutrons in a sample of the same heavy water as a function of the distance from a flat cadmium boundary, obtained in an experiment by Auger, Munn, and Pontecorvo (1).

$$R = 30.50 + 0.05 + 1.65 = 32.2 \text{ cm.}$$

$$\lambda_1 = 0.074684, \lambda_2 = 0.17143, \lambda_3 = 0.26875, \lambda_4 = 0.36620, \lambda_5 = 0.46369 \text{ cm.}^{-1}$$

The density distribution in each plane may be written

$$\rho = \sum_{n=1,2,3,\dots} A_n(z) J_0(\lambda_n r), \quad (6)$$

where

$$A_n(z) = A_n(z=0) \frac{\sinh \frac{h-z}{b_n}}{\sinh \frac{h}{b_n}}$$

The experimental values of  $\rho$  and  $r$  were substituted in Equation (6) to form a set of experimental equations for the amplitudes  $A_n(z)$ . Legendre's method of least squares was applied to these equations. The amplitudes, derived from the normal equations, are shown in Table III. The curves shown in Fig. 4 were drawn from Equation (6) with these amplitudes.

TABLE III  
FIRST ANALYSIS

Amplitude	First plane $z = 0$	Second plane $z = 12 \text{ cm.}$	Third plane $z = 24 \text{ cm.}$
$A_1(z) =$	814	287	94
$A_2(z) =$	-156	-22	-3
$A_3(z) =$	57	4	—
$A_4(z) =$	-23	(1)	—
$A_5(z) =$	8	—	—

The reduction in the amplitude of the first component of the Fourier-Bessel analysis with increasing  $z$  is used to find the relaxation length. When the three planes are equally spaced, two useful formulae can be derived from Equation (3). Let  $A_1(z_1)$ ,  $A_1(z_1 + c)$ , and  $A_1(z_1 + 2c)$  be the amplitudes of the first component in the planes having vertical co-ordinates  $z_1$ ,  $z_1 + c$ , and  $z_1 + 2c$ , respectively. It is easy to show that

$$\cosh \frac{c}{b_1} = \frac{1}{2} \frac{A_1(z_1) + A_1(z_1 + 2c)}{A_1(z_1 + c)} \quad (7)$$

$$\text{and } \tanh \frac{h-z_1-c}{b_1} = \frac{A_1(z_1) + A_1(z_1 + 2c)}{A_1(z_1) - A_1(z_1 + 2c)} \tanh \frac{c}{b_1}. \quad (8)$$

Similar expressions may be written for other components. From Equations (7) and (8) and the amplitudes (before rounding off their values for Table III)

$$b_1 = 11.63 \text{ cm.}$$

$$h = 37.6 \text{ cm.}$$

$$\text{From Equation (4)} \quad L = 23.5 \text{ cm.}$$

If the corresponding equations are applied to the second and third components, we find that  $L$  is imaginary. Two possible explanations for this behaviour may be suggested. (i) Since the relaxation length for the second component is only 5.7 cm., as compared with 2.3 cm. for the transport mean free path, the diffusion theory may be greatly in error for components higher than the first. (ii) Since  $1/L^2$  is only 6% of  $\lambda_2^2$  (but 33% of  $\lambda_1^2$ ), the determination of  $L$  from the second (and higher components) is too dependent on  $\lambda$  and hence on the effective radius. As there is some doubt regarding the contribution of the aluminium wall of the tank to the effective radius, a value of 32.5 cm. for the radius is admissible. Using  $R = 32.5$  cm. and

$$\lambda_1 = 0.073995, \lambda_2 = 0.16985, \lambda_3 = 0.26627, \lambda_4 = 0.36282, \lambda_5 = 0.45941 \text{ cm.}^{-1}$$

the amplitudes  $A_n(z)$  of Table IV were obtained by the method of least squares. From Equations (7), (8), and (4)

TABLE IV  
SECOND ANALYSIS

Amplitude	First plane $z = 0$	Second plane $z = 12 \text{ cm.}$	Third plane $z = 24 \text{ cm.}$
$A_1(z) =$	808	285	93
$A_2(z) =$	-144	-18	-2
$A_3(z) =$	47	2	—
$A_4(z) =$	-15	—	—
$A_5(z) =$	4	—	—

and the amplitudes (before rounding off their values for Table IV)

$$b_1 = 11.62 \text{ cm.}$$

$$h = 37.7 \text{ cm.}$$

$$L = 22.7 \text{ cm.}$$

$$b_2 = 5.78 \text{ cm.}$$

$$L = 30 \text{ cm.}$$

It would be possible to derive a perfectly consistent set of values of  $L$  from the first and second components by choosing a suitable value of  $R$  very close to 32.5 cm.

A comparison of the analyses for radii of 32.2 and 32.5 cm. with the experimental results in Table V shows that it is impossible to choose between them on the basis of best fit. However, a change of 1% in the effective radius

TABLE V  
COMPARISON OF EXPERIMENTAL RESULTS AND ANALYSES

$r$ , cm.	$\rho$ , exp.	$\rho$ , calc.	
		$R = 32.2$ cm.	$R = 32.5$ cm.
<i>First plane</i>			
0	700	700	700
5	686	684	685
10	642	643	643
15	571	571	571
17.5	525	523	523
20	465	466	467
22.5	401	401	400
25	320	321	319
27.5	222	222	222
<i>Second plane</i>			
0	270	270	269
5	261	262	262
10	239	239	240
15	205	204	204
17.5	181	182	181
20	157	156	155
22.5	126	127	127
25	96.0	95.4	95.8
27.5	62.5	62.1	63.7
<i>Third plane</i>			
0	91.0	91.0	91.0
5	87.3	88.3	88.2
10	79.3	80.2	79.9
15	66.7	67.0	66.6
17.5	59.5	58.7	58.4
20	49.4	49.6	49.4
22.5	39.6	39.7	39.7
25	29.8	29.4	29.6
27.5	18.0	18.9	19.5

causes only a 4% change in  $L$  derived from the first component. We have no information on the breakdown of diffusion theory for components higher than the first, which was mentioned as a possible explanation of the internal inconsistency found in the first analysis. Accordingly, we slightly prefer the second analysis with its better internal consistency, and shall write for the final result:

$$L = 22.7 \text{ cm.}$$

The axial measurements support, but do not throw new light on, the value of the diffusion length just derived. In Fig. 5 the measurements taken at

2-cm. intervals are shown to be in good agreement with the curve plotted from Equation (3) with the following constants:

$$R = 32.5 \text{ cm.}, L = 22.7 \text{ cm.}, h = 37.7 \text{ cm.},$$

$$A_1 = 808, A_2 = -144, A_3 = 47, A_4 = -15 \text{ and } A_5 = 4.$$

While the liquid surface is shown in Fig. 5 at 34.6 cm. above the first plane, this value can be only approximate, as the centre of sensitivity of the boron chamber was not accurately located. (The chamber counts over a length between 2.0 and 2.6 cm.) Owing to this reason and to the scattering of neutrons from the glass cover it is not possible to evaluate  $h$  from the position of the liquid surface and the value of the cut-off distance in the absence of back-scattering. From an inspection of Fig. 5,  $h$  must lie between 36.0 and 38.5 cm. However, the diffusion length is determined mainly from the measurements deep within the solution and is therefore not very much dependent on  $h$ .

The effect of errors in the observations on the derived diffusion length can be seen from the following considerations. The density distribution of thermal neutrons obeys the differential Equation (2), which may be written:

$$\frac{1}{L^2} = \frac{\frac{\partial^2 \rho}{\partial r^2} + \frac{1}{r} \frac{\partial \rho}{\partial r}}{\rho} + \frac{\partial^2 \rho}{\partial z^2}. \quad (9)$$

With reference to Fig. 4, it is found by trial that if the curve is altered by changing  $\left(\frac{\partial^2 \rho}{\partial r^2} + \frac{1}{r} \frac{\partial \rho}{\partial r}\right) / \rho$  by 3% throughout its length, it no longer fits the experimental points well. Similarly, a change of 3% in  $\frac{\partial^2 \rho}{\partial z^2} / \rho$  in the curve of Fig. 5 gives a poor fit with the points. The two right-hand terms in Equation (9) are roughly in the ratio  $-3 : 4$  or better, except near the wall of the tank where less weight is attached to the observations. From the separate estimates the resulting error in  $L$  cannot exceed

$$\left\{ \frac{-3}{4-3} 3\% + \frac{1}{4-3} 3\% \right\} = 10\%.$$

Other errors, such as that in the concentration of lithium, and those due to the channel effect and shift of the centre of sensitivity of the boron chamber as it is raised in the solution, are comparatively negligible (Table II). By calculation it is found that the shift of the centre of sensitivity of the chamber causes a change in the counting rate of less than 0.1%, which is beyond detection.

### Discussion

On the basis of diffusion theory it is possible to calculate any one of the three quantities — diffusion length  $L$ , transport mean free path  $l_t$ , and capture mean free path  $l_c$  — provided that the others are given, for

$$L^2 = \frac{1}{3} l_t l_c. \quad (10)$$

Auger, Munn, and Pontecorvo (1) have found  $l_t$  to be 2.31 cm. in a sample of the same heavy water as used here for the measurement of the diffusion length. Since the amount of lithium carbonate dissolved in the water is too small to affect its scattering properties,  $l_t = 2.31$  cm. in the solution. Substituting  $L = 22.7$  cm. and  $l_t = 2.31$  cm. in Equation (10),

$$l_o = 669 \text{ cm.}$$

$$\text{and } \Sigma n\sigma = \frac{1}{l_o} = 149 \times 10^{-5} \text{ cm.}^{-1}$$

$n$  is the number of atoms (or molecules) per cubic centimetre of the constituent, and  $\sigma$  is the capture cross-section per atom (or per molecule), the sum being taken for the constituents  $D_2O$ ,  $H_2O$ , and  $Li_2CO_3$  in the solution. In order to derive the capture cross-section of lithium, we shall allow for the capture of neutrons by the heavy and light water,\* and neglect the capture by the carbon and oxygen of the carbonate and the oxygen of the light water present.

For  $D_2O$   $n = 3.33 \times 10^{22}$  molecules per cc.

For  $H_2O$   $n = \frac{0.60}{100} \times 3.33 \times 10^{22} = 2.0 \times 10^{20}$  molecules per cc.,

based on mass spectroscopic analyses carried out in Dr. H. G. Thode's laboratory. For lithium carbonate, 1.57 gm. per litre of solution,

$$n = 2.58 \times 10^{19} \text{ atoms lithium per cc.}$$

According to an argument to be given later, the capture cross-sections to be used here should be those for neutrons of velocity† 2500 m. per sec. Booker, Cavanagh, Hereward, Niemi, and Sargent (2) have found from a measurement of the diffusion length in heavy water that the capture cross-section is  $0.81 \times 10^{-27}$  cm.<sup>2</sup> per molecule  $D_2O$  for neutrons of velocity 2500 m. per sec.

The capture cross-section of hydrogen will be found from the absolute cross-section of boron and the ratio of the cross-sections of boron and hydrogen. Dr. Fermi (4) informed us that the capture cross-section of boron is  $705 \times 10^{-24}$  cm.<sup>2</sup> per atom for neutrons of velocity 2200 m. per sec. (Recently Marshall (9) has published his value of  $710 \times 10^{-24}$  cm.<sup>2</sup> per atom, measured some time ago at the Argonne Laboratory.) The best measurement of  $\sigma_B / \sigma_H$  known to us is 2270, obtained by Whitehouse and Graham (12) of the Montreal Laboratory. From these results  $\sigma = 0.548 \times 10^{-24}$  cm.<sup>2</sup> per molecule  $H_2O$  for neutrons of velocity 2500 m. per sec.

For  $D_2O$  and  $H_2O$  together  $\Sigma n\sigma = 14 \times 10^{-5}$  cm.<sup>-1</sup>, which leaves  $135 \times 10^{-5}$  cm.<sup>-1</sup> for the  $n\sigma$  of lithium.

The capture cross-section of lithium follows:

$$\sigma = 52 \times 10^{-24} \text{ cm.}^2 \text{ per atom.}$$

\*For cross-section calculations it is immaterial whether we consider 1.2% HDO or its equivalent 0.6%  $H_2O$ .

†We do not make the classic distinction between velocity and speed.

It will be seen from the considerations that follow that the cross-section found from the diffusion length and transport mean free path corresponds approximately to the average velocity of the neutron spectrum, which is about 2500 m. per sec. at room temperature. We assume that the transport mean free path in heavy water is independent of the neutron velocity, and therefore the diffusion coefficient

$$D = \frac{1}{3} l_t \bar{v},$$

where  $\bar{v}$  is the average speed of the Maxwellian distribution of neutrons at room temperature. The diffusion length  $L$  may be written in terms of the diffusion coefficient  $D$  and the mean lifetime

$$\tau = \frac{1}{\Sigma n \sigma v}$$

Since the capture cross-section of lithium varies inversely as the velocity, according to the measurements of Havens and Rainwater (6, 10),  $\tau$  is independent of the velocity. Therefore

$$L^2 = D\tau = \frac{1}{3} l_t \bar{v} \tau = \frac{1}{3} l_t l_c,$$

where  $l_c = \bar{v} \tau$  is the capture mean free path for the average velocity of the neutron spectrum, and hence  $\sigma$  found above is the capture cross-section corresponding to that velocity. Referring to a standard velocity of 2200 m. per sec., we have

$$\sigma (\text{lithium}) = 59 \times 10^{-24} \text{ cm.}^2 \text{ per atom.}$$

In view of the assumptions and probable errors in the combined physical data just used, we conclude that this value is in agreement with  $65 \times 10^{-24} \text{ cm.}^2$  communicated to us by Dr. Fermi (4) and  $67 \times 10^{-24} \text{ cm.}^2$  obtained by Fenning, Graham, and Seligman (3) from their measured ratio  $\sigma_B / \sigma_{Li}$  and the Argonne Laboratory value  $\sigma_B = 705 \times 10^{-24} \text{ cm.}^2$ . On the other hand, Havens and Rainwater (6, 10) have found higher values:  $\sigma_B = 740 \times 10^{-24} \text{ cm.}^2$  and  $\sigma_{Li} = 72 \times 10^{-24} \text{ cm.}^2$  for neutrons of velocity 2200 m. per sec.

### Acknowledgments

We wish to thank our colleagues named in this paper for assistance in the design and construction of parts of the apparatus and in chemical and mass spectroscopic analyses. We are also grateful to several of our colleagues for permission to use unpublished information, and to Dr. E. Fermi for information privately communicated.

### References

1. AUGER, P., MUNN, A. M., and PONTECORVO, B. The transport mean free path of thermal neutrons in heavy water. Montreal report. 1944.
2. BOOKER, D. V., CAVANAGH, P. E., HEReward, H. G., NIEMI, N. J., and SARGENT, B. W. The diffusion length of thermal neutrons in heavy water. Montreal report. 1946.
3. FENNING, F. W., GRAHAM, G. A. R., and SELIGMAN, H. Ratio of the capture cross-sections of boron and lithium. Montreal report. 1944.

4. FERMI, E. Private communications from Argonne Laboratory. 1944.
5. FREUNDLICH, H. F. and LAWRENCE, N. Q. Report on design and construction of head amplifiers used at the Montreal Laboratory. 1944.
6. HAVENS, W. W., JR. and RAINWATER, J. Bull. Am. Phys. Soc. 21 (3) : 13. 1946.
7. HÉBERT, J. and MADDOCK, A. G. Relative merits of boron and lithium compounds as contaminating agents. Montreal report. 1944.
8. HERWARD, H. G., LAURENCE, G. C., PANETH, H. R., and SARGENT, B. W. , Can. J. Research, A, 25 : 15-25. 1947.
9. MARSHALL, J. Bull. Am. Phys. Soc. 21 (3) : 12. 1946.
10. RAINWATER, J. and HAVENS, W. W., JR. Bull. Am. Phys. Soc. 21 (3) : 13. 1946.
11. VEALL, N. A. On the construction of small boron chambers. Montreal report. 1944.
12. WHITEHOUSE, W. J. and GRAHAM, G. A. R. Ratio of the neutron absorption cross-sections of boron and hydrogen. Montreal report. 1945.

# THE CALCULATION OF LINE STRENGTHS FROM LABORATORY DATA<sup>1</sup>

BY WILLIAM PETRIE<sup>2</sup>

## Abstract

A. S. King has made extensive intensity estimates of spectral lines in furnace and arc spectra, and these data provide useful material for determining line strengths. The estimates have been made for many elements of astrophysical interest, and are reduced to line strengths for FeI, TiI, and TiII.

## Introduction

It is well to distinguish between two quantities, the strength, and the intensity, of a spectral line. The strength of a line is defined as the sum of the absolute squares of the matrix elements of electric moment joining the sets of states in question. On the other hand, the intensity of a line is proportional to the number of atoms in any one of the states of its initial level, the fourth power of its frequency, and its strength.

The line strength of the transition from an initial to a final level defined by the quantum numbers  $\gamma LSJ$  and  $\gamma' L'SJ'$ , respectively, is

$$[(a | P | b)]^2 = \sum_{MM'} [(\gamma LSJM | P | \gamma' L'SJ'M')]^2, \quad (1)$$

where  $L$  = the orbital quantum number,

$S$  = the spin quantum number,

$J$  = the inner quantum number,

$M$  = the magnetic quantum number,

$\gamma$  = the sum of quantities other than  $LSJM$  necessary to define a state.

Expression (1) enables one to calculate the relative strengths of the lines within a multiplet when  $LS$  coupling holds. Such line strengths have been calculated by White (8) and Russell (6).

Line strengths have also been obtained from solar data. The method has been fully described by Menzel (5) and more recently by Wright (9). The method is to obtain the so-called 'curve of growth' for a number of lines of the solar Fraunhofer spectrum, by plotting the theoretical strength of each line against the corresponding measured equivalent width. The equivalent width is a measure of the energy removed from the continuous spectrum by the absorption line. From the 'curve of growth,' the strength of any line may be obtained from the measured equivalent width. Solar line strengths are more numerous than the theoretical values, since all lines that have measurable equivalent widths are used. The solar line strengths also include intercombination lines, and these are absent from the theoretical values.

<sup>1</sup> Manuscript received May 14, 1946.

Contribution from the Department of Physics, University of Saskatchewan, Saskatoon, Sask.

<sup>2</sup> Associate Professor.

Beginning in 1913, and continuing the work over a long period of years, A. S. King has estimated the intensities of thousands of lines in the electric furnace and arc spectra. A description of the apparatus used and the procedure followed (1) in estimating intensities has been given. The eye estimates were made on a remarkably consistent scale, and self-reversal effects were indicated and allowed for when present. These data are useful for obtaining line strengths. It was pointed out by Russell (7) in 1925 that the square of King's estimated intensities are very nearly proportional to theoretical line strengths. This relation makes it possible to interpret King's estimated intensities in terms of line strengths. It will be indicated later that emission line theory yields the same results.

### Calibration of the King Intensity Scale

The elements chosen for the initial work are FeI, TiI, and TiII. The lines are first divided into groups of the same excitation potential. For the lines of each group, a logarithmic plot is made between the squares of King's arc intensities as abscissae and the solar line strengths as ordinates. The solar line strength is called  $X_0$ . Each resulting line segment now differs by the Boltzmann factor,  $\frac{5040 \Delta\chi}{T}$ , which we call  $B$ .  $\Delta\chi$  = the difference in excitation potential in electron volts of the lines in each group;  $T$  = the excitation temperature in degrees absolute of the arc. The excitation temperature of the arc is determined from the shift required to superimpose each line segment on the segment for the spectral lines of lowest excitation potential. If the shift is called  $\Delta y$ , then

$$\Delta y = \frac{5040 \Delta\chi}{T}. \quad (2)$$

This relation makes it possible to determine the excitation temperature of the arc.

Fig. 1 shows the resulting curves for FeI after superimposing the line segments. The points that are far off the line are probably affected by blending, and the general scatter is partly the result of departures from  $LS$  coupling. The wave-length range for each plot was chosen after studying the sensitivity curve of the photographic plates used by King. The range in sensitivity of the plates used for the wave-length regions chosen is small. Trial and error methods also show that the best curves are obtained when the data are divided in this manner.

Fig. 2 shows the temperature of the arc in degrees absolute as obtained from the data in the chosen wave-length regions. The temperature is seen to be a function of the excitation potential of the upper level involved in the production of each group of lines considered, which means that the arc is not in thermodynamic equilibrium. The excitation potential of the upper level is denoted by  $EP_H$ .

When the temperature of the arc is known from Fig. 2 we obtain values of line strengths from Fig. 1. For a given line we read off the value corresponding to the square of the logarithm of King's intensity, and then add the Boltzmann factor obtained from the temperature of the arc and the excitation

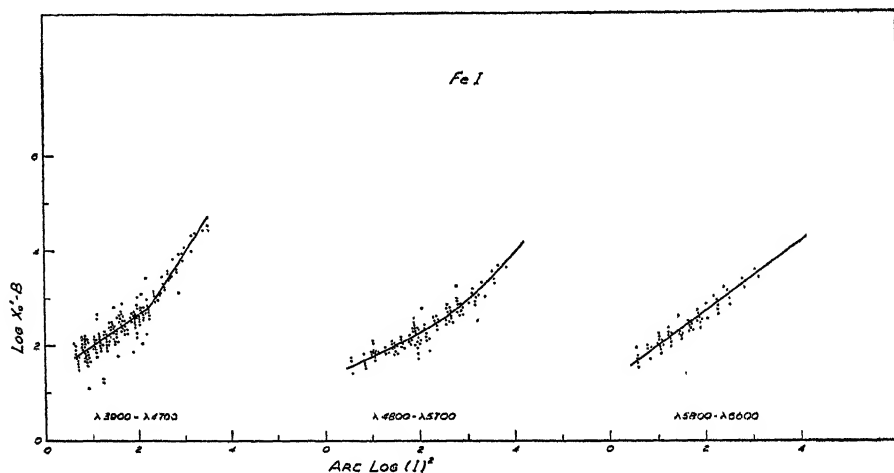


FIG. 1. Calibration of the King intensity estimates.

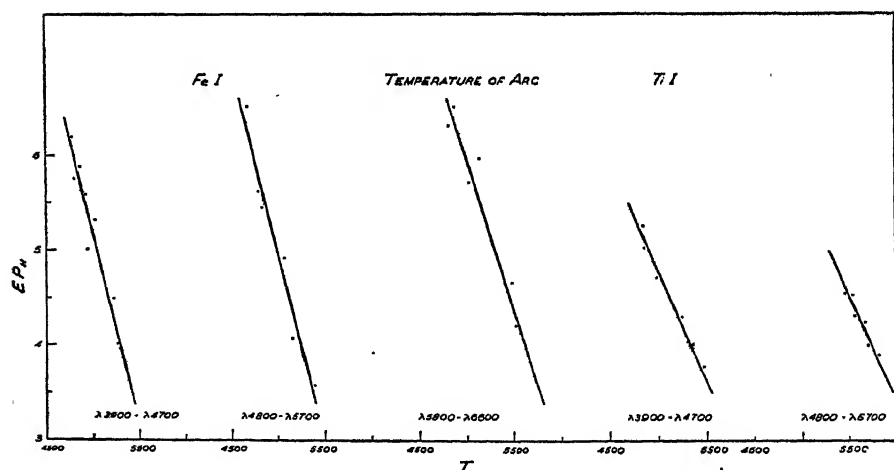


FIG. 2. Excitation temperature of the arc.

potential of the upper level involved in the production of the line. This calibration is extremely useful, since we can now obtain strengths for many hundreds of lines of FeI in the wave-length range  $\lambda$  3900- $\lambda$  6600. In order to facilitate more rapid use of the calibration, a double entry table is constructed. Tables I(a), I(b), and I(c) give the value of the line strength design-

nated as  $X'_0$ , corresponding to a given arc intensity and a given excitation potential. Tables II(a), II(b), II(c), and III give the same quantity for TiI and TiII.

TABLE I (a)  
FeI—LOG  $X'_0$  VALUES  
 $EP_H$

King (I) arc		3.0	3.4	3.8	4.2	4.6	5.0	5.4	5.8	6.2	6.6	7.0
2	1.89	2.25	2.63	3.04	3.44	3.87	4.32	4.78	5.26	5.80	6.26	
4	2.26	2.62	3.00	3.41	3.81	4.24	4.69	5.15	5.63	6.17	6.66	
6	2.47	2.83	3.21	3.62	4.02	4.45	4.90	5.36	5.84	6.38	6.87	
8	2.62	2.98	3.36	3.77	4.17	4.60	5.05	5.51	5.99	6.53	7.02	
10	2.74	3.10	3.48	3.89	4.29	4.72	5.17	5.63	6.11	6.65	7.14	
12	2.91	3.27	3.65	4.06	4.46	4.89	5.34	5.80	6.28	6.82	7.31	
20	3.54	3.90	4.28	4.69	5.09	5.52	5.97	6.43	6.91	7.45	7.94	
30	4.09	4.45	4.83	5.24	5.64	6.07	6.52	6.98	7.46	8.00	8.49	
40	4.43	4.79	5.17	5.57	5.98	6.41	6.86	7.32	7.80	8.34	8.83	
50	4.71	5.07	5.45	5.86	6.26	6.69	7.14	7.60	8.08	8.62	9.11	

$\lambda$  3900 —  $\lambda$  4700

TABLE I (b)  
FeI—LOG  $X'_0$  VALUES  
 $EP_H$

King (I) arc		3.0	3.4	3.8	4.2	4.6	5.0	5.4	5.8	6.2	6.6	7.0
2	2.08	2.46	2.85	3.26	3.68	4.12	4.57	5.05	5.52	6.02	6.56	
4	2.39	2.77	3.16	3.57	3.99	4.43	4.88	5.36	5.83	6.33	6.87	
6	2.57	2.95	3.34	3.75	4.17	4.61	5.06	5.54	6.01	6.51	7.05	
8	2.70	3.08	3.47	3.88	4.30	4.74	5.19	5.67	6.14	6.64	7.18	
10	2.82	3.20	3.59	4.00	4.42	4.86	5.31	5.79	6.26	6.76	7.30	
12	2.93	3.31	3.70	4.11	4.53	4.97	5.42	5.90	6.37	6.87	7.41	
15	3.08	3.46	3.85	4.26	4.68	5.12	5.57	6.05	6.52	7.02	7.56	
20	3.25	3.63	4.02	4.43	4.85	5.29	5.74	6.22	6.69	7.19	7.73	
25	3.40	3.78	4.17	4.58	5.00	5.44	5.89	6.37	6.84	7.34	7.88	
30	3.52	3.90	4.29	4.70	5.12	5.56	6.01	6.49	6.96	7.46	8.00	
35	3.64	4.02	4.41	4.82	5.24	5.68	6.13	6.61	7.08	7.58	8.12	
40	3.74	4.12	4.51	4.92	5.34	5.78	6.23	6.71	7.18	7.68	8.22	
50	3.92	4.30	4.69	5.10	5.52	5.96	6.41	6.89	7.36	7.86	8.40	
60	4.07	4.45	4.84	5.25	5.67	6.11	6.56	7.04	7.51	8.01	8.55	
75	4.27	4.65	5.04	5.45	5.87	6.31	6.76	7.24	7.71	8.21	8.75	
100	4.52	4.90	5.29	5.70	6.12	6.56	7.01	7.49	7.96	8.46	9.00	

$\lambda$  4800 —  $\lambda$  5700

The question arises whether or not the approximation  $(I)^2$  proportional to line strength is sufficiently accurate. The emission in a spectral line in ergs per second from an emitting volume of 1 cm.<sup>3</sup> is given by the following relation:

$$I = \frac{64 \pi^4 \nu^4}{3c^3} \frac{N_0}{\tilde{\omega}_0} e^{-X_n/kT} S \quad (3)$$

$\nu$  = the frequency of the line,

$N_0$  = the number of atoms in the ground level for a particular stage of ionization of the element in question,

$\tilde{\omega}_0$  = the statistical weight of the ground level,

$\chi_n$  = the excitation potential of the upper level involved in the production of the line,

$T$  = the excitation temperature of the emitting volume,

$S$  = the theoretical line strength.

TABLE I (c)  
FeI—LOG  $X'_0$  VALUES  
 $EP_H$

King ( $I$ ) arc		3.0	3.4	3.8	4.2	4.6	5.0	5.4	5.8	6.2	6.6	7.0
2	1.90	2.25	2.61	2.98	3.36	3.78	4.21	4.64	5.09	5.58	6.08	
4	2.34	2.69	3.05	3.42	3.81	4.22	4.65	5.08	5.53	6.02	6.52	
6	2.60	2.95	3.31	3.68	4.07	4.48	4.91	5.34	5.79	6.28	6.78	
8	2.76	3.11	3.47	3.84	4.23	4.64	5.07	5.50	5.95	6.44	6.94	
10	2.92	3.27	3.63	4.00	4.39	4.80	5.23	5.66	6.11	6.60	7.10	
12	3.03	3.38	3.74	4.11	4.50	4.91	5.34	5.77	6.22	6.71	7.21	
15	3.17	3.52	3.88	4.25	4.64	5.05	5.48	5.91	6.36	6.85	7.35	
20	3.34	3.69	4.05	4.42	4.81	5.22	5.65	6.08	6.53	7.02	7.52	
25	3.50	3.85	4.21	4.58	4.97	5.38	5.81	6.24	6.69	7.18	7.68	
30	3.60	3.95	4.31	4.68	5.07	5.48	5.91	6.34	6.79	7.28	7.78	
35	3.71	4.06	4.42	4.79	5.18	5.59	6.02	6.45	6.90	7.39	7.89	
40	3.79	4.14	4.50	4.87	5.26	5.67	6.10	6.53	6.98	7.47	7.97	
45	3.86	4.21	4.57	4.94	5.33	5.74	6.17	6.60	7.05	7.54	8.04	
50	3.94	4.29	4.65	5.02	5.41	5.82	6.25	6.68	7.13	7.62	8.12	
60	4.04	4.39	4.75	5.12	5.51	5.92	6.35	6.78	7.23	7.72	8.22	
75	4.19	4.54	4.90	5.27	5.66	6.07	6.50	6.93	7.38	7.87	8.37	
100	4.37	4.72	5.08	5.45	5.84	6.25	6.68	7.11	7.56	8.05	8.55	

$\lambda$  5800 —  $\lambda$  6600

TABLE II (a)  
TiI—LOG  $X'_0$  VALUES  
 $EP_H$

King ( $I$ ) arc		2.80	3.20	3.60	4.00	4.40	4.80	5.20	5.60	6.00
3	-1.10	-0.74	-0.36	0.04	0.47	0.94	1.44	1.96	2.54	
4	-0.80	-0.44	-0.06	0.34	0.77	1.24	1.74	2.26	2.84	
6	-0.37	-0.01	0.37	0.77	1.20	1.67	2.17	2.69	3.27	
8	-0.07	0.29	0.67	1.07	1.50	1.97	2.47	2.99	3.57	
10	0.17	0.53	0.91	1.31	1.74	2.21	2.71	3.23	3.81	
12	0.37	0.73	1.11	1.51	1.94	2.41	2.91	3.43	4.01	
15	0.62	0.98	1.36	1.76	2.19	2.66	3.16	3.68	4.26	
20	0.92	1.28	1.66	2.06	2.49	2.96	3.46	3.98	4.56	
25	1.17	1.53	1.91	2.31	2.74	3.21	3.71	4.23	4.81	
30	1.35	1.71	2.09	2.49	2.92	3.39	3.89	4.41	4.99	
35	1.50	1.86	2.24	2.64	3.07	3.54	4.04	4.56	5.14	
40	1.65	2.01	2.39	2.79	3.22	3.69	4.19	4.71	5.29	
45	1.77	2.13	2.51	2.91	3.34	3.81	4.31	4.83	5.41	
50	1.90	2.26	2.64	3.04	3.47	3.94	4.44	4.96	5.54	
60	2.09	2.45	2.83	3.23	3.66	4.13	4.63	5.15	5.73	
75	2.34	2.70	3.08	3.48	3.91	4.38	4.88	5.40	5.98	
100	2.65	3.01	3.39	3.79	4.22	4.69	5.19	5.71	6.29	

$\lambda$  3900 —  $\lambda$  4700

Equation (3) shows that for an accurate calibration of the King intensities, one should plot  $\log I$  against  $(4 \log \nu + \log S - B)$ . The writer has done this using FeI values, and the results are not appreciably different from those obtained using the approximation already discussed.

The King (1, 2, 3, 4) eye estimates needed for the tables are found in the references.

TABLE II (b)

 $EP_H$ TiI— $\log X'_0$  VALUES

	2.50	2.90	3.20	3.60	4.00	4.40	4.80	5.20	5.60	6.00
King ( $I$ ) arc										
5	-0.21	0.11	0.37	0.73	1.12	1.52	1.96	2.43	2.93	3.48
6	-0.11	0.21	0.47	0.83	1.22	1.62	2.06	2.53	3.03	3.58
8	0.18	0.50	0.76	1.12	1.51	1.91	2.35	2.82	3.32	3.87
10	0.39	0.71	0.97	1.41	1.72	2.12	2.56	3.03	3.53	4.08
12	0.57	0.89	1.15	1.59	1.90	2.30	2.74	3.21	3.71	4.26
15	0.78	1.10	1.36	1.80	2.11	2.51	2.95	3.42	3.92	4.47
20	1.05	1.37	1.63	2.07	2.38	2.78	3.22	3.69	4.19	4.74
25	1.27	1.59	1.85	2.29	2.60	3.00	3.44	3.91	4.41	4.96
30	1.44	1.76	2.02	2.46	2.77	3.17	3.61	4.08	4.58	5.13
35	1.58	1.90	2.16	2.60	2.91	3.31	3.75	4.22	4.72	5.27
40	1.70	2.02	2.28	2.72	3.03	3.43	3.87	4.34	4.84	5.39
45	1.81	2.13	2.39	2.83	3.14	3.54	3.98	4.45	4.95	5.50
50	1.92	2.24	2.50	2.94	3.25	3.65	4.09	4.56	5.06	5.61
60	2.09	2.41	2.67	3.11	3.42	3.82	4.26	4.73	5.23	5.78
75	2.31	2.63	2.89	3.33	3.64	4.04	4.48	4.95	5.45	6.00
100	2.57	2.89	3.15	3.59	3.90	4.30	4.74	5.21	5.71	6.26

 $\lambda 4800 - \lambda 5700$ 

TABLE II (c)

 $EP_H$ TiI— $\log X'_0$  VALUES

	3.10	3.20	3.60	4.00	4.40	4.80	5.20	5.60	6.00
King ( $I$ ) arc									
5	-0.04	0.03	0.40	0.77	1.13	1.50	1.87	2.23	2.60
6	0.14	0.21	0.58	0.95	1.31	1.68	2.05	2.41	2.78
8	0.35	0.42	0.79	1.16	1.52	1.89	2.26	2.62	2.99
10	0.52	0.59	0.96	1.33	1.69	2.06	2.43	2.79	3.16
12	0.66	0.73	1.10	1.47	1.83	2.20	2.57	2.93	3.30
15	0.83	0.90	1.27	1.64	2.00	2.37	2.74	3.10	3.47
20	1.05	1.12	1.49	1.86	2.22	2.59	2.96	3.32	3.69
25	1.22	1.29	1.66	2.03	2.39	2.76	3.13	3.49	3.86
30	1.35	1.42	1.79	2.16	2.52	2.89	3.26	3.62	3.99
35	1.46	1.53	1.90	2.27	2.63	3.00	3.37	3.73	4.10
40	1.56	1.63	2.00	2.37	2.73	3.10	3.47	3.83	4.20
45	1.66	1.73	2.10	2.47	2.83	3.20	3.57	3.93	4.30
50	1.74	1.81	2.18	2.55	2.91	3.28	3.65	4.01	4.38
60	1.88	1.95	2.32	2.69	3.05	3.42	3.79	4.15	4.52
75	2.05	2.12	2.49	2.86	3.22	3.59	3.96	4.32	4.69
100	2.26	2.33	2.70	3.07	3.43	3.80	4.17	4.53	4.90

 $\lambda 5800 - \lambda 6600$

TABLE III  
TiII—LOG  $X'_0$  VALUES  
 $EP_H$

King ( $J$ ) arc		3.8	4.2	4.6	5.0	5.4	5.8	6.2
2	2.56	2.92	3.27	3.63	3.98	4.33	4.69	
4	2.86	3.22	3.57	3.93	4.28	4.63	4.99	
6	3.02	3.39	3.74	4.10	4.45	4.80	5.16	
8	3.15	3.51	3.86	4.22	4.57	4.94	5.28	
10	3.25	3.61	3.96	4.32	4.67	5.02	5.38	
12	3.32	3.68	4.03	4.40	4.74	5.09	5.45	
15	3.42	3.78	4.13	4.50	4.84	5.19	5.55	
20	3.54	3.90	4.25	4.62	4.96	5.31	5.67	
25	3.64	4.00	4.35	4.72	5.06	5.41	5.77	
30	3.71	4.07	4.42	4.79	5.13	5.48	5.84	
35	3.77	4.13	4.48	4.85	5.19	5.54	5.90	
40	3.83	4.19	4.54	4.91	5.25	5.60	5.96	
45	3.87	4.23	4.58	4.95	5.29	5.64	6.00	
50	3.93	4.29	4.64	5.01	5.35	5.70	6.06	
60	4.00	4.36	4.71	5.08	5.42	5.77	6.13	
75	4.10	4.46	4.81	5.18	5.52	5.87	6.23	

$\lambda 4000 - \lambda 5000$

### References

1. KING, A. S. *Astrophys. J.* 37 : 239-281. 1913.
2. KING, A. S. *Astrophys. J.* 39 : 139-165. 1914.
3. KING, A. S. *Astrophys. J.* 56 : 318-339. 1922.
4. KING, A. S. *Astrophys. J.* 59 : 155-176. 1924.
5. MENZEL, D. H., BAKER, J. G., and GOLDBERG, L. *Astrophys. J.* 87 : 81-101. 1938.
6. RUSSELL, H. N. *Proc. Nat. Acad. Sci. U.S.* 11 : 314-322. 1925.
7. RUSSELL, H. N. *Proc. Nat. Acad. Sci. U.S.* 11 : 322-328. 1925.
8. WHITE, H. *Phys. Rev.* 44 : 753-756. 1933.
9. WRIGHT, K. O. *Astrophys. J.* 99 : 249-255. 1944.

# A LABORATORY STUDY OF VISIBILITY THROUGH CLOUDS<sup>1</sup>

BY G. O. LANGSTROTH<sup>2</sup>, M. W. JOHNS<sup>3</sup>, J. L. WOLFSON<sup>4</sup>, AND H. F. BATHO<sup>5</sup>

## Abstract

Various opinions have been expressed regarding the importance of such factors as a 'diffusing effect' due to small angle scattering in determining the visual range in a cloud. If a reduction of apparent contrast and an influence on brightness level are the only important factors, conditions at the obscuration point should be described by,

$$P = CB_i 10^{-\mu D} / (B_i 10^{-\mu D} + B_c),$$

where  $B_i$  denotes the brightness of an object which has a contrast  $C$  with its background,  $B_c$  and  $\mu D$  represent respectively the cloud brightness and optical density in the line of sight, and  $P$  denotes the contrast limen value. Experiments to test this relation have been performed with an ammonium chloride smoke in a chamber 1.8 m. long. The results indicate that the equation is adequate and that factors not taken into consideration in it play a negligible role in total obscuration under laboratory conditions. The experiments were performed at various brightness levels within the 1 to 100 millilambert range.

The theory of the visual range in a cloud such as smoke or fog has received considerable attention (for a summary see reference (7)). The presence of a cloud between an observer and an object influences the brightness level at which the observer's eye must operate and results in an apparent contrast between the object and its background that is less than the actual value. Furthermore, the cloud may operate to obscure the object through additional factors such as the production by small angle scattering of apparently diffuse object boundaries. This 'diffusing effect' has been stated (1) to play an important part in obscuration but a more recent theoretical calculation (8) indicates the converse.

If the obscuring effect of a cloud is determined solely by the reduction of apparent contrast and the influence on the brightness level, it follows that at the obscuration point,

$$P = CB_i 10^{-\mu D} / (B_i 10^{-\mu D} + B_c), \quad (1)$$

where  $B_i$  denotes the actual brightness of the object (assumed greater than that of the background,  $B_b$ ), and  $B_c$  and  $\mu D$  denote respectively the cloud brightness and optical density in the line of sight.  $C$  represents the actual contrast between the object and its background, and is defined by

$$C = (B_i - B_b) / B_b. \quad (2)$$

<sup>1</sup> Manuscript received June 3, 1946.

The experimental work on which this article is based was performed in the Department of Physics, University of Manitoba, Winnipeg, Man.

<sup>2</sup> Professor of Physics, University of Alberta, Edmonton, Alta.

<sup>3</sup> Physicist, National Research Council, Chalk River Laboratory.

<sup>4</sup> Holder of a Bursary under the National Research Council of Canada.

<sup>5</sup> Associate Research Physicist, British Columbia Research Council, Vancouver, B.C.  
Mr. S. C. Fultz and Mr. Allen Kahn contributed to this work as student research assistants.

The 'contrast limen'  $P$  denotes the maximum contrast that is imperceptible to the observer. It is a function of the brightness level and the angular size of the object, and is determined by the observer's visual ability and not by any characteristic of the cloud. If the obscuring effect of a cloud is dependent on other factors Equation (1) must be extended by the addition of appropriate terms. The experiments on which this report is based were performed to ascertain whether the addition of such extra terms is necessary to describe obscuration data obtained in a smoke chamber, i.e., whether reduction of apparent contrast and influence on the brightness level are the only important factors determining the obscuring effect of a cloud under laboratory conditions.

Equation (1) may be rewritten

$$\mu D = \log \left( \frac{C - P}{P} \right) + \log(B_i/B_e). \quad (3)$$

Since  $P$  may vary, it can be expressed as  $P = \phi \cdot P_0$ , where  $\phi$  is some function of the object's subtended angle and the brightness level, and  $P_0$  denotes the value of the limen at some selected angle and brightness level. Equation (3) then reduces to

$$\mu D + \log \phi = A + \log(B_i/B_e), \quad (4)$$

where  $A = \log \left( \frac{C - P}{P_0} \right)$ . For brightness levels greater than about 1 m.L. and subtended angles greater than  $0.6^\circ$ ,  $P$  is 0.01 or less. Under these conditions little error is made in regarding  $A$  as a constant for objects having a contrast of 0.5 or more. A plot against  $\log(B_i/B_e)$  of the optical density  $\mu D$  of smoke required to obscure an object (with a small correction for the  $\log \phi$  term) should on this basis yield a straight line of unit slope and constant  $A$  consistent with an acceptable value of the limen  $P_0$ . If the underlying assumptions are inadequate (i.e., if factors other than the reduction of apparent contrast and the influence on brightness level are important) departures from these characteristics may be expected. Such considerations formed the basis for the experiments.

## 1. Apparatus and Procedure

### (a) The Smoke Chamber

The main features of the smoke chamber and its accessory apparatus are shown diagrammatically in Fig. 1. The dimensions of the chamber were 1.83 by 1.22 by 1.22 m<sup>3</sup>. It was painted flat black inside. The observer, seated at  $O$ , made his observations through the glass window  $W_e$ . The brightness of the smoke to the observer was brought to the desired value by shining light from banks of incandescent lamps  $G$  and  $G'$  into the smoke through the glass windows  $W$ . All windows were fitted outside metal slides in the chamber walls so that they could be cleaned at any time during an experiment without disturbing the smoke. The test object  $T$ , of the form shown in Fig. 2, was enclosed in a smoke-tight box having a glass window  $W''$ . It was illuminated by shielded 6 v. battery-operated lamps  $L$  and  $L'$ . Since the test object was illuminated also by light scattered from the smoke, provi-

sion was made for measuring the illumination intensity on it by swinging photocell  $P$  into a position before section No. 1 when desired. Both the box and the window  $W_0$  were located centrally in the cross-section of the chamber. The former could be moved along the chamber axis by means of a pipe  $R$ , which also served as a conduit for connecting wires. The pipe carried a scale from which the depth of the smoke layer between the observation window  $W_0$  and the test object could be determined. The chamber was fitted with a

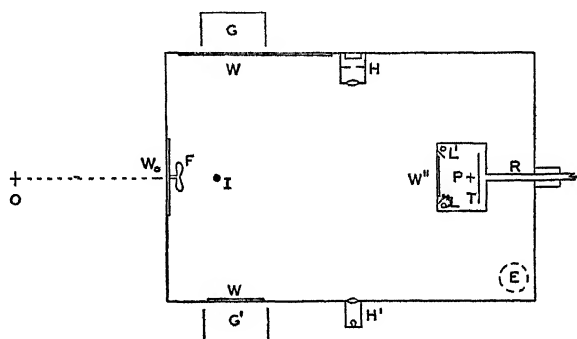


FIG. 1. Smoke chamber and accessory apparatus; top view, approximately to scale.

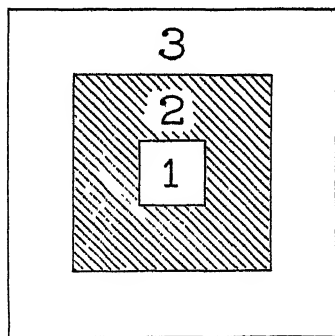


FIG. 2. The test object. Sections Nos. 1 and 3 were white and section No. 2 was painted a uniform grey. The numerals shown were not included. The brightness contrast between sections Nos. 1 and 2 was for the most part 0.65.

photoelectric parallel-beam device  $H, H'$  for measuring the extinction coefficient of the smoke (5). Smoke was introduced through inlet  $I$  in the bottom of the chamber and removed when desired through outlet  $E$  with the aid of a centrifugal blower. A fan  $F$  mounted just below the observation window served to dilute the smoke during production and to stir the contents of the chamber when desired.

#### (b) Production of Smoke

The apparatus used for producing ammonium chloride smoke is shown diagrammatically in Fig. 3. The rate of flow of air introduced at  $A$  from a compressor was controlled by valves  $E$  and  $C$  and measured by the flowmeter

F. The meter was a modification of a device (2) used for measuring the velocity of air currents not bounded by confining walls. The air was preheated to an exit temperature of  $300^{\circ}\text{C}$ . in passing through a lagged Pyrex tube *II*, 55 cm. long, containing an internal 51 ohm heating coil. To maintain this exit temperature the power dissipation was about 430 watts for an air flow of 0.36 litres per second. Ammonium chloride was placed in a Pyrex tube forming the inner walls of the 20 ohm resistance furnace *X*. Six grams was decomposed in 11 min. with a power input of 230 w. The decomposition products mixed with preheated air flowed through the lagged Pyrex tube *L*, 40 cm. long, which had a 33 ohm external heating coil sufficient to maintain the

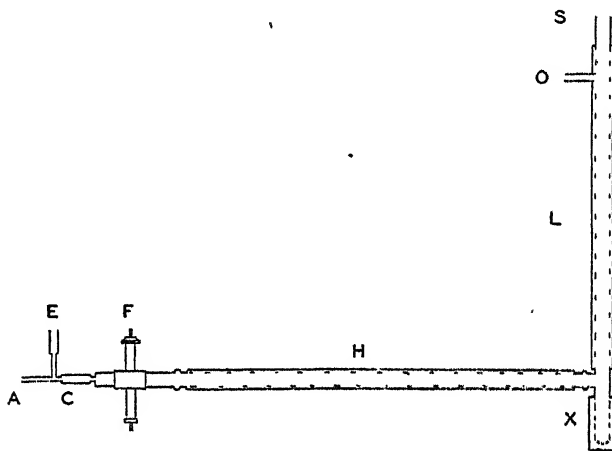


FIG. 3. Ammonium chloride smoke generator; side view, approximately to scale.

temperature at  $300^{\circ}\text{C}$ . While the furnace was heating, preheated air escaped through the outlet *O* but when smoke appeared this was closed and the outlet *S* into the chamber opened. The mixture of decomposition products and hot air was rapidly diluted and cooled by a blast from the fan (*F*, Fig. 1) blowing directly across the outlet *S*. The temperature rise within the chamber was about  $3^{\circ}\text{C}$ . during the production of a cloud of high optical density (e.g., 2 to 3).

### (c) Procedure

In general two types of experiment, each consisting of a long series of observations, were performed. In the first type the cloud brightness  $B_c$  was maintained constant throughout the series, the test object brightness  $B_t$  (or the depth of the smoke layer before the test object) was set successively to various selected values, and the depth  $D$  of the smoke layer (or the test object brightness) was adjusted at each step until the test object was just invisible to the observer. In the second type of experiment,  $B_t$  was left unaltered throughout a series of measurements except for variations due to changes in the scattered light incident on the test object,  $B_c$  was set at various selected values and obscuration was obtained at each by adjustment of  $D$ . In judging

the obscuration point, observations were made by each of two criteria, (a) total disappearance, and (b) loss of definition. For the former, conditions were adjusted until the test object was entirely invisible; for the latter they were adjusted until section No. 1 of the object appeared as a light patch of undefined shape. While observers were perfectly adapted to the prevailing brightness level in experiments characterized by a constant  $B_o$  value, there may have been slight departures from complete adaptation in experiments in which  $B_o$  was varied.

A cycle of observations consisting of measurements at all selected values of the predetermined quantity was repeated three to five times during the life of a smoke, yielding 25 to 60 determinations of the conditions required for obscuration. Since the size and number of the smoke particles varied with time, determinations of the extinction coefficient were made at intervals

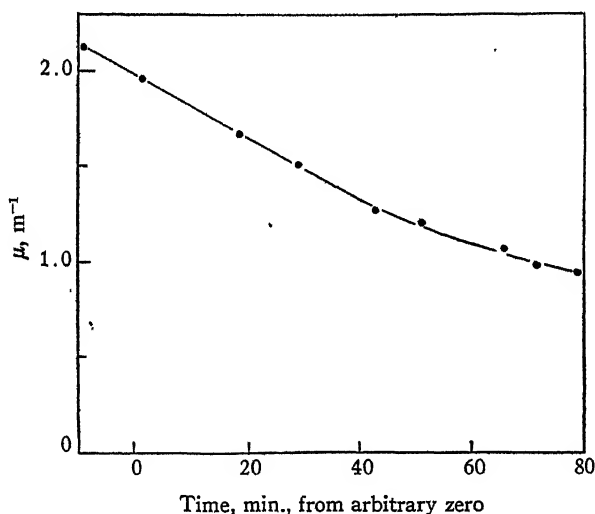


FIG. 4. A typical extinction coefficient vs. time curve.

and the value of  $\mu$  at the time of each observation was read from a ' $\mu$  vs. time' curve plotted from the results. A typical curve is shown in Fig. 4. For the same reason, frequent adjustments were required in the illumination provided by the bank of lamps ( $G, G'$ , Fig. 1) to give the desired cloud brightness. The adjustments were made by changing the number of lamps in each bank and, in order to avoid noticeable colour differences in the illumination, only minor current variations were used. Adjustment of the test object brightness was made by varying the current through the lamps  $L, L'$  (Fig. 1).

A measurement of cloud brightness was made immediately before each obscuration determination with the aid of a flicker brightness meter (4) sighted through the observation window from a position just behind the observer. Similarly a reading of the test object brightness was made by swinging the photocell ( $P$ , Fig. 1) into position in front of the test object and

reading the response on a microammeter; the response was converted to terms of the brightness of section No. 1 with the aid of a calibration curve for 'response vs. brightness of section No. 1' as read with a flicker brightness meter in the absence of smoke. The brightness contrast  $C$  between sections Nos. 1 and 2 of the target was calculated from numerous flicker meter readings in the absence of smoke.

The experiments provide data on the values of  $\mu$ ,  $D$ ,  $B_t$ , and  $B_e$  at obscuration over wide ranges of all these variables. All brightness values were based essentially on the readings of the flicker meter. The relative values of brightness (which are of primary importance in this work) are in error by not more than 3% (4). The absolute values may be more greatly in error since absolute calibration of the meter was made against a commercial illumination meter with the aid of a magnesium oxide screen.

(d) *Correction for Limen Variations*

Although variations in the limen with the angle  $\alpha$  subtended by section No. 1 of the test object (i.e., with  $D$ ) and with  $B_e$  were not excessive in these experiments, they could not be disregarded. The  $\log \phi$  term of Equation (4) may be regarded as a correction to be applied to the observed  $\mu D$  values. The size of the correction was in some cases as great as 10%, though generally it was much less (cf. Table I).

In order to obtain correction data the observers determined relative limen values for various  $\alpha$ -values in the brightness level range of the experiments.

TABLE I  
DETAILED DATA FOR EXPERIMENT 61A\*

$t$	$\mu$	$D$	$\alpha$	$B_e$	$B_t$	$\mu D$	
						Uncorr.	Corr.
6	1.87	0.50	0.92	111	5.16	0.94	0.95
12	1.76	0.76	0.82	44.1	5.23	1.34	1.37
16	1.70	0.97	0.76	12.9	5.00	1.65	1.71
22	1.60	1.28	0.69	5.20	4.95	2.05	2.18
26	1.52	1.45	0.65	2.04	3.01	2.20	2.41
32	1.46	0.72	0.84	106	6.60	1.05	1.07
36	1.40	0.93	0.77	39.8	5.60	1.30	1.35
40	1.34	1.25	0.69	12.3	5.02	1.68	1.79
46	1.26	1.45	0.65	4.86	2.05	1.83	2.01
50	1.22	1.45	0.65	2.00	1.29	1.77	1.99
55	1.15	0.89	0.78	99	7.31	1.03	1.06
59	1.11	0.98	0.76	37.8	4.00	1.09	1.14
63	1.06	1.24	0.69	13.5	2.61	1.32	1.43
77	0.95	1.16	0.72	96.2	9.5	1.10	1.16

\*  $B_e$  was set to selected values and  $D$  adjusted to obscuration at each. Corrections to the  $\mu D$  values have been made with the aid of Fig. 5. The time  $t$  (minutes) at which the observation was made was reckoned from an arbitrary zero set soon after the production of smoke was complete. Brightness is given in millilamberts, distance in metres, subtended angle in degrees, and extinction coefficient in  $\text{metres}^{-1}$ . The data refer to total obscuration. The observer was G.L.

A sheet of glass was placed before the observation window at an angle of  $45^\circ$  to the line of sight. A large brightly illuminated white card was so placed that the observer saw its image superimposed on the test object. With no smoke in the chamber, the apparent contrast of section No. 1 was reduced until it was just imperceptible; this was done either by increasing the brightness of the veiling glare provided by the white card or by decreasing the brightness of the test object. The limen was calculated from  $P = CB_t/(B_t + B')$ , where  $B'$  denotes the brightness of the veiling glare. Determinations were made at various test-object-to-observer distances using total disappearance in judging the critical point. The average results obtained were as follows.

Subtended angle:	$0.99^\circ$	$0.84^\circ$	$0.73^\circ$	$0.65^\circ$
Relative limen:	1.00	1.03	1.15	1.36

The angle refers to that subtended by a side of section No. 1. Data on the relative limen values at various brightness levels were taken from the literature (3, 6, 9\*, 10). The average values for subtended angles of  $1^\circ$  or more are as follows.

Brightness level, mL.: 100	33	10	3.3	1.0	
Relative limen:	1.00	1.01	1.04	1.13	1.34

Combined with the preceding figures for angle variation these yield data for  $\phi$  of Equation (4).  $P_0$  was taken as the limen for a brightness level of 100 mL and a subtended angle of  $0.99^\circ$ . The data as used in making the corrections

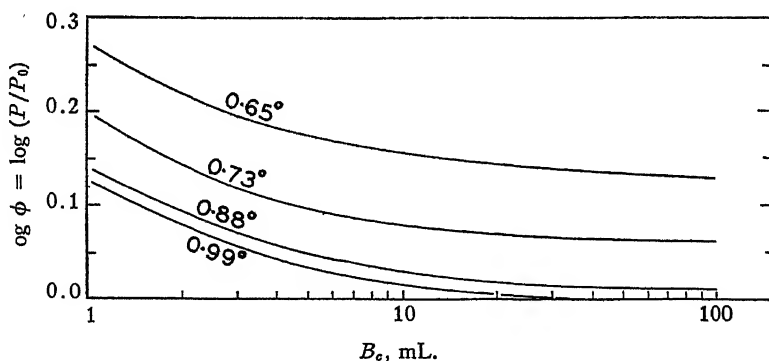


FIG. 5. Variation of the limen with subtended angle and brightness level as used in correcting observed  $\mu D$  values.

are presented in Fig. 5. The appropriate  $\log \phi$  values were added to the observed  $\mu D$  values. The absolute values of the limen did not enter into the considerations.

## 2. Results

The data for a typical experiment are given in Table I. In this experiment, as in all others, the angle subtended at the observer by a side of the illuminated

\* See paper by J. Blanchard (*Phys. Rev.* 11 : 81. 1918) for the brightness units appropriate to König and Brodhun's limen data.

patch of smoke (i.e., the observation window) was about  $15^\circ$ . The surround beyond the window was relatively dark. The typical scatter encountered in these experiments is indicated by the Table I data as plotted in Fig. 6. A summary of the results of six experiments by three observers is given in Table II.

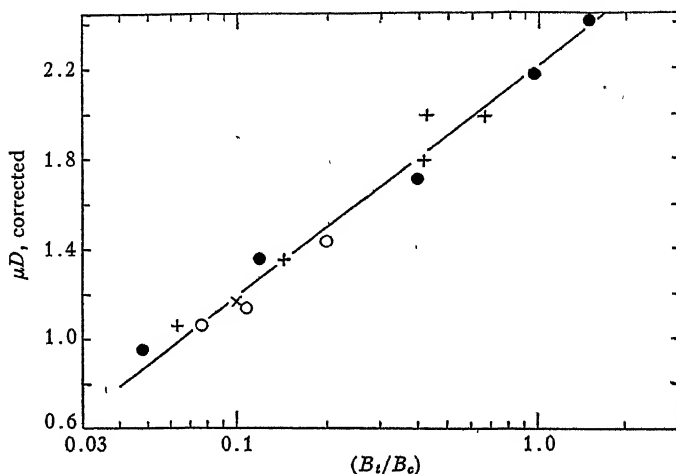


FIG. 6. A typical plot of observed data (Expt. 61A, observer GL) illustrating the linearity of the relation, the scatter of observations, and the range covered. The points for each cycle of measurements are represented by a separate symbol.

TABLE II

A SUMMARY OF THE RESULTS OF SIX EXPERIMENTS\*

Experiment	54A	55A	56A	62A	60A	61A
Observer	JW	JW	GL	MJ	JW	GL
$B_e$ range, mL.	16.8	17.5	20.6	1.7 -62	1.3 -76	2.0 -111
$B_t$ range, mL.	0.50-24	0.98-34	0.77-15	0.50-7.0	0.35-6.3	1.3 -9.5
$D$ range, m.	0.30-1.39	0.30-1.25	0.30-1.30	0.62-1.45	0.40-1.45	0.40-1.45
$\mu$ range, $m^{-1}$	1.93-1.15	2.07-1.05	1.85-0.97	1.70-0.72	1.48-0.77	1.91-0.95
$A$ ( $\mu D$ uncorr.)	1.76	1.82	1.79	1.81	1.69	2.04
$E$ ( $\mu D$ uncorr.)	0.82	0.86	0.80	0.76	0.85	0.85
$A$ ( $\mu D$ corr.)	1.93	1.94	1.90	2.04	1.80	2.22
$E$ ( $\mu D$ corr.)	0.99	0.95	0.88	0.95	1.00	1.02

Averages

Uncorrected    Corrected

$A$     1.82    1.99

$E$     0.82    0.97

\* The data refer to total obscuration. They are described by the relation  $\mu D = A + E \log (B_t/B_e)$ , whether  $\mu D$  is corrected for limen variation with subtended angle and brightness level or not.

### 3. Discussion

The experimental data exhibit a moderately large scatter as illustrated by the typical example shown in Fig. 6. The scatter is largely the result of momentary fluctuations in the visual ability of observers (cf. (3)) and can hardly be avoided in experiments of this kind. On the average, however, the relation between the various observed quantities is well represented by the data of Table II.

The range covered by the data is reasonably wide, i.e. brightness level, 1.3–111 mL.; test object brightness, 0.35–34 mL.; extinction coefficient, 0.72–2.47 m.<sup>-1</sup>; optical density, 0.44 to 2.28; depth of smoke, 0.30 to 1.45 m. For total obscuration of the object, the results are described by

$$\mu D = 1.99 + 0.97 \log(B_i/B_e),$$

where  $\mu D$  has been 'corrected' by the addition of the  $\log \phi$  term to the observed values. The equation is identical in form with Equation (4) and the coefficient of the  $\log (B_i/B_e)$  term is unity within the limits of experimental error. Furthermore, equating  $\log(C/P_0)$  with  $C = 0.65$  to the constant term one obtains a value of 0.0067 for the limen at 100 mL. and 0.99°. This is in excellent agreement with the average value for unrestricted binocular vision (0.0068) as determined in an extensive series of measurements (3). It is therefore concluded that Equation (1) is adequate and that factors such as 'diffusing effect' caused by small angle scattering play a negligible role in total obscuration under laboratory conditions.

Observations on the apparent loss of definition of test objects as contrasted with total disappearance are discussed in the following article.

### References

1. BENNETT, M. G. *Quart. J. Roy. Met. Soc.* 56 : 1-26. 1930.
2. HELD, E. F. M. VANDER and MULDER, L. L. *Koninkl. Akad. Wetenschappen Amsterdam*, 35 : 267. 1932.
3. LANGSTROTH, G. O., BATHO, H. F., JOHNS, M. W., and WOLFSON, J. L. In preparation.
4. LANGSTROTH, G. O., JOHNS, M. W., WOLFSON, J. L., and BATHO, H. F. In preparation.
5. LANGSTROTH, G. O. and WOLFSON, J. L. *Can. J. Research, A*, 25 : 62-67. 1947.
6. LOWRY, E. M. *J. Optical Soc. Am.* 21 : 132-136. 1931.
7. MIDDLETON, W. E. K. *Visibility in meteorology*. 2nd ed. Univ. of Toronto Press, Toronto. 1941.
8. MIDDLETON, W. E. K. *J. Optical Soc. Am.* 32 : 139-143. 1942.
9. NUTTING, P. G. *Bull. Bur. Standards*, 5 : 261-308. 1909.
10. STILES, W. S. and CRAWFORD, B. H. *Proc. Roy. Soc. Ser. B*, 116 : 55-102. 1934.

## THE RECOGNITION OF OBJECTS NEARLY OBSCURED BY A CLOUD<sup>1</sup>

BY G. O. LANGSTROTH<sup>2</sup>, M. W. JOHNS<sup>3</sup>, J. L. WOLFSON<sup>4</sup>, and H. F. BATHO<sup>5</sup>

### Abstract

As the apparent contrast of a square test object situated behind a smoke layer is decreased in laboratory experiments a point is reached at which the object appears as a light patch of unrecognizable shape. On decreasing the apparent contrast a little further the object becomes completely invisible. A study of the conditions under which the apparent loss of definition occurs was carried on simultaneously with the study of total obscuration described in the preceding paper. The optical density of smoke required to produce loss of definition was found to be linearly related to the logarithm of the ratio of object to cloud brightness, in close correspondence with the relation found for total obscuration. Over the range of our experiments the minimum optical density of smoke associated with loss of definition was from 12 to 23% less than that associated with total obscuration, the magnitude of the difference depending on brightness conditions. Since the phenomenon of loss of definition is observable in the presence of a veiling glare without smoke, it is probably of physiological origin.

Experiments on the total obscuration of a square test object by ammonium chloride smoke of determined extinction coefficient have been described in the preceding paper. In the experiments the layer depth or the brightness of the smoke or the illumination incident on the object was adjusted until the object became just invisible. Information was obtained on the brightness conditions and optical density of smoke required for complete obscuration over a fairly wide range of the variables involved. In the same experiments analogous data were obtained on the conditions associated with apparent loss of definition. The adjustments were made until the shape of the object became just unrecognizable although its presence was still indicated by a light patch of undefined shape. The apparatus and procedure are described in the preceding article. It is the purpose of this note to place the data on record.

### Results

Data for a typical experiment are presented in Table I and Fig. 1. Table I and Fig. 6 of the preceding paper contain the corresponding data for complete obscuration in the same experiment. Table II, corresponding to Table II of the preceding paper, contains a summary of the results of seven experiments by three observers. The symbols  $\mu$ ,  $B_t$ , and  $B_o$  have their previous significance.  $D'$  denotes the minimum depth of smoke layer required to produce a loss of definition.

<sup>1</sup> Manuscript received October 16, 1946.

The experimental work on which this article is based was performed in the Department of Physics, University of Manitoba, Winnipeg.

<sup>2</sup> Professor of Physics, University of Alberta, Edmonton, Alta.

<sup>3</sup> Physicist, National Research Council, Chalk River Laboratory.

<sup>4</sup> Holder of a Bursary under the National Research Council of Canada.

<sup>5</sup> Associate Research Physicist, British Columbia Research Council, Vancouver, B.C. Mr. S. C. Fultz and Mr. Allan Kahn contributed to this work as student research assistants.

TABLE I  
DETAILED DATA FOR EXPERIMENT 61A\*

$t$	$\mu$	$D'$	$\alpha$	$B_e$	$B_t$	$\mu D'$
4	1.91	0.40	0.95	89.1	5.40	0.76
10	1.80	0.60	0.87	43.6	5.70	1.08
15	1.71	0.82	0.80	13.2	5.28	1.40
20	1.63	1.11	0.72	5.00	5.40	1.81
24	1.56	1.37	0.67	2.06	5.55	2.14
30	1.49	0.60	0.87	101	6.12	0.89
35	1.41	0.80	0.91	40.8	5.68	1.13
39	1.35	1.10	0.73	12.6	5.28	1.48
45	1.27	1.36	0.67	5.28	5.49	1.73
48	1.24	1.45	0.65	2.00	2.98	1.80
53	1.18	0.64	0.85	92.9	4.27	0.76
57	1.13	0.81	0.80	37.2	2.43	0.92
61	1.09	1.06	0.73	13.8	2.86	1.16
75	0.96	0.87	0.79	94.5	7.60	0.83

\* $B_e$  was set to selected values and  $D'$  adjusted to the point of loss of definition at each. The times  $t$  (min.) at which the observations were made were reckoned from an arbitrary zero set soon after production of smoke was complete. Brightness is given in millilamberts, distance in metres, subtended angle ( $\alpha$ ) in degrees, and extinction coefficient in  $\text{metres}^{-1}$ . The observer was G.L. The total obscuration data for this experiment are given in Table I of the preceding paper.

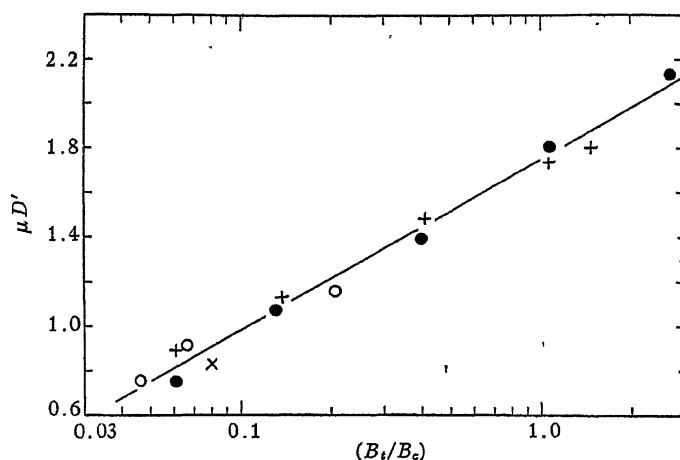


FIG. 1. A typical plot of observed data (Expt. 61A, observer G.L.). The points for each cycle of measurements are represented by a separate symbol.

## Discussion

A plot of  $\mu D'$  vs.  $\log(B_t/B_e)$  shows a linear relation in all experiments. Fig. 1 provides a typical example. The scatter of plotted points is comparable to that obtained in total obscuration determinations (compare Fig. 1 with

TABLE II

A SUMMARY OF THE RESULTS OF SEVEN EXPERIMENTS\*

Experiment	54A	55A	56A	62A	60A	61A	52A
Observer	JW	JW	GL	MJ	JW	GL	GL
$B_e$ range, mL.	16.8	17.5	20.6	1.7-62	1.3-76	2.0-111	12.3
$B_i$ range, mL.	0.50-24	0.98-34	0.77-15	0.50-7.0	0.35-6.3	1.3-9.5	0.54-34
$D'$ range, m.	0.30-1.39	0.30-1.25	0.30-1.30	0.62-1.45	0.40-1.45	0.40-1.45	0.30-1.36
$\mu$ range, m. <sup>-1</sup>	1.93-1.15	2.07-1.05	1.85-0.97	1.70-0.72	1.48-0.77	1.91-0.95	2.47-1.45
$A'$	1.55	1.55	1.62	1.56	1.37	1.77	1.71
$E'$	0.77	0.83	0.80	0.70	0.71	0.77	0.78
Averages	$A' = 1.59$			$E' = 0.77$			

\* The data plotted for each experiment were found to be well described by the relation  $\mu D' = A' + E' \log(B_i/B_e)$ ; see Fig. 1. The data on total obscuration for the above experiments may be found in Table II of the preceding paper.

Fig. 6 of the preceding paper). Using the average results given in Table II, the minimum optical density required to produce a loss of definition is described by

$$\mu D' = 1.59 + 0.77 \log (B_i/B_e). \quad (1)$$

This equation is simply a statement of average experimental results; no correction to  $\mu D'$ , corresponding to the correction for limen variation applied to  $\mu D$  in the preceding paper, has been made. The equation therefore includes any variations originating in changes in subtended angle (about  $0.6^\circ$  to  $1^\circ$ ) and brightness level (about 2 to 110 mL.).

A comparison between the optical density required for a loss of definition and that required for complete obscuration is readily made. The latter is described by Equation (1) with  $\mu D'$ , 1.59, and 0.77 replaced respectively by  $\mu D$ , 1.82, and 0.82 (Table II of the preceding paper). The  $\mu D$  values are uncorrected for limen variation. Subtraction of the two equations yields,

$$\Delta \mu D = 0.23 + 0.05 \log(B_i/B_e), \quad (2)$$

where  $\Delta \mu D$  denotes the difference between the optical density required to produce complete obscuration and that required for loss of definition under the particular conditions of our experiments. At the lowest and highest  $B_i/B_e$  ratios used (0.044 and 3.16) the  $\mu D'$  values were respectively 23 and 12% less than the  $\mu D$  values. Any effect produced by variation in subtended angle of the test object is contained implicitly in Equation (2).

As described in the preceding paper, corrections for limen variations with subtended angle and brightness level were applied to the total obscuration data. No corresponding corrections have been attempted for the loss of definition data because of the lack of appropriate information. In determining limen values with the aid of a veiling glare in the absence of smoke, however, it was noted that loss of definition preceded total disappearance as the

apparent contrast of the object was gradually decreased. The corners of the square test object became indistinct so that it might easily have been confused with a disk although its presence was not in doubt. Since the phenomenon of loss of definition was observed in the absence of smoke, it is considered to be of physiological origin; it is probably not connected with any objective factor such as a diffusing effect caused by the smoke.

# A NOTE ON THE DETERMINATION OF THE EXTINCTION COEFFICIENT OF AEROSOLS<sup>1</sup>

BY G. O. LANGSTROTH<sup>2</sup> AND J. L. WOLFSON<sup>3</sup>

## Abstract

Difficulties were encountered in smoke chamber experiments in obtaining reliable extinction coefficient data by methods based on brightness measurements of bright and 'black' surfaces seen through the smoke. These difficulties led to an investigation of the reliability of a commonly used method employing a parallel light beam and a photoelectric cell. The results indicate that the method is capable of yielding extinction coefficient data with an accuracy of 1 to 2% under the conditions of our experiments.

A surface of brightness  $B_0$  seen through a smoke layer of depth  $d$  and extinction coefficient  $\mu$  has an apparent brightness  $B$  given by

$$B = B_e + B_0 10^{-\mu d},$$

where  $B_e$  denotes the smoke brightness in the line of sight. The extinction coefficient is described by

$$\mu = 1/d \cdot \log(B_0/(B - B_e)),$$

and can be determined if the other quantities are measured. An attempt to use this method in smoke chamber experiments with smokes having coefficients in the range 0.7 to 2.5 m.<sup>-1</sup> proved unsuccessful. The 20 by 20 cm.<sup>2</sup> surface was located about 20 cm. behind the glass window of a small smoke-tight box that could be moved along the chamber axis to alter the  $d$ -value, and was illuminated by shielded lamps within the box. The smoke chamber is described elsewhere (1). Brightness measurements were made with a flicker brightness meter (2). Determinations of  $B_e$  made with the meter sighted just beyond the boundary of the surface led to  $\mu$ -values which depended on  $B_0$  and were obviously incorrect. When the  $B_e$  determinations were made with the meter sighted on the opening of a 4 cm. diameter tube located near the centre of the surface and serving as a 'black' body, the resulting  $\mu$ -values were acceptable in this respect. They were however 20 to 30% lower than those expected from the slope of curves for 'log  $B_0$  vs. layer depth at obscuration' as obtained with a constant veiling glare produced by the reflection of an illuminated white card in a 45° glass sheet in front of the observer. These difficulties were associated with an inability to make

<sup>1</sup> Manuscript received June 3, 1946.

The experimental work on which this article is based was performed in the Department of Physics, University of Manitoba, Winnipeg, Man.

<sup>2</sup> Professor of Physics, University of Alberta, Edmonton, Alta.

<sup>3</sup> Holder of a Bursary under the National Research Council of Canada. Mr. S. C. Fultz and Mr. Allan Kahn contributed to this work as student research assistants.

appropriate determinations of cloud brightness, and led to an investigation of a method employing a parallel beam of light and a photocell. The investigation forms the basis of this report.

## 1. The Nature of the Experiments

(a) *The photoelectric parallel-beam method.*—This method, which is not original with us, has been used in several laboratories, but we do not know the name of the originator. The experimental arrangement used by us is shown diagrammatically in Fig. 1. A collimating and a condensing lens ( $L$

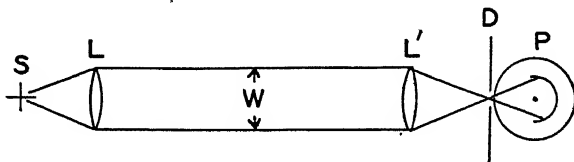


FIG. 1. Diagram of the experimental arrangement for the parallel-beam method of extinction coefficient measurement.

and  $L'$ , focal length 10 cm.) were placed at the opposite sides of the smoke chamber, a distance of 1.30 m. apart. A 21 cp. automobile lamp placed at the principal focus of the lens  $L$  and operated at constant voltage served as the light source  $S$ . A screen  $D$  containing a small opening was placed at the principal focus of the lens  $L'$ . The purpose of the screen was to prevent as much of the scattered light as possible from reaching the vacuum photocell  $P$  while permitting the directly transmitted light forming the image of the filament of  $S$  to do so. The relation between the amplified photoelectric current and the light energy incident on the cell was determined over the required range with the aid of large Nicol prisms inserted between  $L$  and  $L'$ . Denoting the light energy incident on the cell in the presence and in the absence of smoke by  $I$  and  $I_0$ , respectively, the extinction coefficient of the smoke was calculated from  $\mu = \log(I_0/I)/1.30$ .

(b) *Dependence of  $\mu$  on the width  $W$  of the collimated light beam.*—In order for the method to prove satisfactory the contribution of directly transmitted light to the energy incident on the photocell must predominate. Compared to it the contribution of light that has undergone scattering within the beam, or has been scattered back from regions outside, must be negligibly small. The directly transmitted light forms an image of the lamp filament in the plane of the screen but the scattered light is incapable of doing so. The contribution of scattered light to the total incident on the photocell is expected to depend on the beam width  $W$  (Fig. 1), approaching zero for an infinitely narrow beam. An observed dependence of  $\mu$  on beam width might therefore be taken as an indication that scattered light cannot be neglected. Experiments to test this point were performed with the aid of diaphragms of various

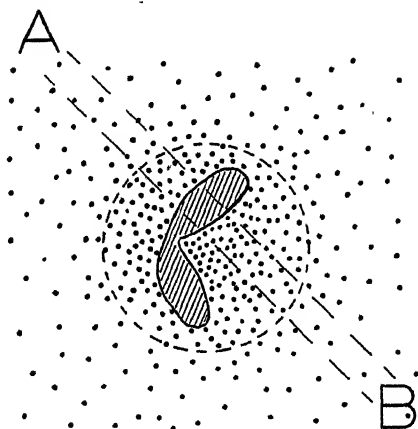


FIG. 2. Sketch of the surface distribution of light incident on a photographic plate placed in the plane of the screen D (Fig. 1). The image formed by directly transmitted light is shaded, and the incidence of scattered light is indicated by the dotted area. The dashed circle indicates the position of the opening in the screen. The plate was photometered along the band AB.

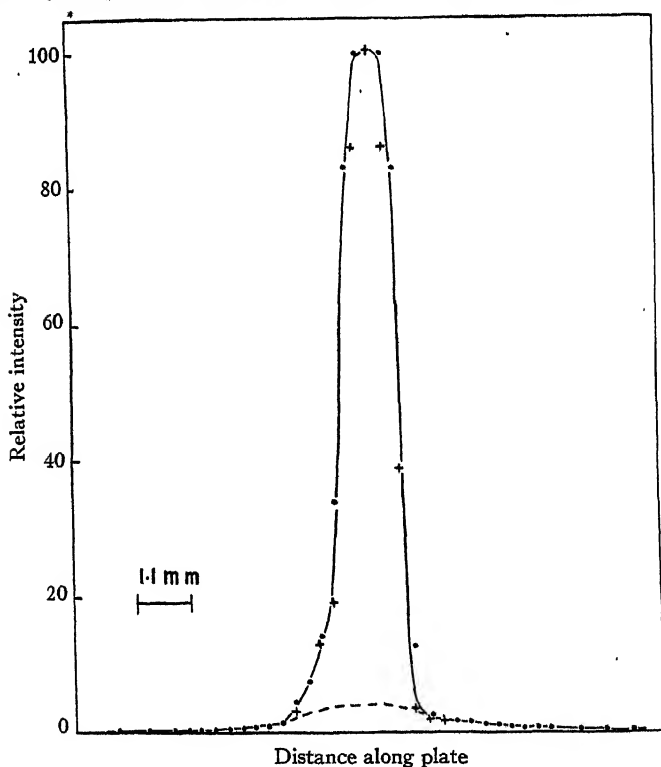


FIG. 3. Intensity contour obtained by photometering two photographic plates. Outside the main image the intensity is low, and measurements indicated elsewhere by + have been omitted to avoid confusion. The unplots points fall closely along those plotted. The dashed line suggests an upper limit for the intensity of scattered light in the area occupied by the filament image.

sizes inserted at the collimating lens. Typical results are given in Table I of Section 2.

(c) *Estimation of an upper limit for the contribution of scattered light.*—In order to obtain an estimate of the relative energies associated with directly transmitted and scattered light admitted to the photocell, the screen *D* (Fig. 1) was replaced by a photographic plate. A short exposure was made in the early stages of a smoke using a beam width of 3.9 cm. Calibration marks were placed on the plate with the aid of an adjustable high speed sector and a light source of appropriate energy-wave-length distribution. These permitted photographic densities on the plate to be converted to terms of the relative light energies incident. The plate (Eastman 40) was somewhat under-developed to produce low contrast, care being taken to minimize the Eberhardt effect. Microphotometric determinations of the photographic density were made at intervals of 0.28 mm. along the band *AB* indicated in Fig. 2. The determined distribution of light energy along the band *AB* of Fig. 2 is shown in Fig. 3 of Section 2.

(d) *The dependence of  $\mu$  on the angle of divergence of a non-parallel beam.*—If permissible, the use of a somewhat divergent beam of light has certain advantages since the adjustments are less critical and the apparatus consequently more rugged. Series of measurements of  $\mu$  were made with beams of various divergence. The divergence was controlled by adjusting the distance between the light source and the collimating lens. Typical results are given in Table II of Section 2.

## 2. Results

TABLE I

A COMPARISON OF THE  $\mu$ -VALUES OBTAINED WITH PARALLEL BEAMS OF VARIOUS WIDTHS IN TYPICAL EXPERIMENTS\*

Experiment	<i>t</i>	$\mu$ -Values for beam widths of				
		3.94	3.30	2.06	1.31	0.88
47A	6- 8.5	1.82	1.80	1.90	1.95	1.84
	16- 20	1.87	1.85	1.90	1.93	1.88
	52- 56	1.74	1.72	1.79	1.75	1.68
	71- 75	1.67	1.64	1.69	1.64	1.65
	106-110	1.48	1.45	1.49	1.50	1.47
49A	12- 15	2.39	2.38	2.38	2.33	—
	65- 68	1.77	1.76	1.76	1.76	—
48A	3.5-6	2.81	2.88	2.95	2.88	—
	40- 42.5	2.80	2.86	2.87	2.85	—
	111-112.5	2.37	2.42	2.45	2.43	—

\* Beam width is given in cm., and *t* denotes the time interval (min.) in which the observations were made as reckoned from an arbitrary zero set soon after complete generation of ammonium chloride smoke.

TABLE II

A COMPARISON OF  $\mu$ -VALUES OBTAINED WITH BEAMS OF VARIOUS ANGLES OF DIVERGENCE\*

$t$	$\mu$ -Values for divergence angles (degrees) of								
	0.0	2.6	4.6	7.6	10.0	15.6	20.0	24.0	30.0
13-19	1.85	1.85	1.84	1.71	1.67	1.63	1.59	1.56	1.54
30-36	1.63	1.64	1.62	1.55	1.53	1.50	1.45	1.44	1.43
53-59	1.47	1.47	1.43	1.34	1.31	1.27	1.22	1.21	1.19

\* The angle  $\theta$  referred to is the plane angle at the apex of the cone formed by projecting backward the boundaries of the ray bundle between the collimating and condensing lenses. The time interval  $t$  has the same significance as in Table I. For  $\theta$  values of 4.6° or less the collimating lens was diaphragmed down to a diameter of 1.31 cm.; for the others the diameter of the diaphragm was 3.94 cm.

### 3. Discussion

The particulate characteristics of a smoke change with time. In the experiments each group of measurements to be compared was made as rapidly as possible to minimize this factor. Examination of the decrease in extinction coefficient with time for a given beam width (Table I) indicates that changes in smoke characteristics during the time interval required for a group of comparative determinations caused a decrease of not more than 0.01 to 0.02 in the extinction coefficient value.

The results of Table I show no systematic variation of the determined extinction coefficient value with beam width. The average deviation of individual  $\mu$ -values from the means for the groups is 1.2%. This evidence supports the view that the contribution of scattered light to the energy incident on the photocell is negligible in the parallel-beam method.

The contour of Fig. 3 indicates the surface distribution of energy incident on the screen before the photocell. A probable upper limit for the scattered energy in the region of the filament image is indicated by the dashed line in the figure. A comparison of the energies of scattered and directly transmitted light admitted to the photocell was made by integration under the respective contours over the area of the screen opening. The result indicates that the former was less than 7% of the latter. This value is an upper limit. The occurrence of halation and diffusion of light in traversing the emulsion are factors that would influence the extrapolation of the scattered light contour toward spuriously high values, and the use of a colour blind emulsion probably favoured the scattered at the expense of the transmitted light. The Eberhardt effect would operate in the opposite direction, but no evidence of its presence is detectable in the contour of Fig. 3. At worst, a 7% error in transmitted energy introduces an error of 1% in an extinction coefficient of 2.00 and an error of 2% in a coefficient of 1.00. The result indicates that the parallel-beam method is capable of yielding accurate values for the extinction coefficient.

The results quoted in Table II show that it is not important to use a strictly parallel beam under the conditions of these experiments. Divergences of as much as  $5^\circ$  appear permissible.

Extinction coefficients measured by the parallel-beam method were found to be about 20% higher than those determined with the aid of a brightness meter, an illuminated surface, and a 'black' body as described in the introduction. As mentioned there, this finding is in accord with the results of obscuration data.

### References

1. LANGSTROTH, G. O., JOHNS, M. W., WOLFSON, J. L., and BATHO, H. F. *Can. J. Research, A*, 25 : 49-57. 1947.
2. LANGSTROTH, G. O., JOHNS, M. W., WOLFSON, J. L., and BATHO, H. F. In preparation.

# A NOTE ON PHASE CORRECTION IN ELECTRICAL DELAY NETWORKS<sup>1</sup>

BY ALEX. J. FERGUSON<sup>2</sup>

## Abstract

The standard method of correcting the phase characteristic of low-pass networks by introducing mutual inductance between the coils is extended. By means of mutual inductance between the coils and a capacity across them, it is possible to eliminate the third and fifth order terms in the variation of the phase shift with frequency. The relation required between the circuit constants for this result is given, and is found to be very simple.

There are a number of systems that may be used to provide a small delay for a video signal. These may be divided roughly into two categories; those with distributed constants, and those with lumped constants. In the first category are concentric lines with coiled inner conductors and the 'condensed cables' suggested by Kallmann (2). These are simple devices, fairly readily constructed, and they provide a reasonably good solution to the problem. Their performance is not perfect—they suffer phase defects at frequencies for which the wave-length along the structure is comparable with its diameter. In the second category are wave filters and standard artificial lines. It is with a network of this type that this report is concerned. Holcomb (1) has described an elaborate bridged-T delay network with excellent phase characteristics, which, however, is much too complicated for high frequency ranges.

It is well known (3, p. 245) that the phase characteristic of a simple low-pass filter can be improved by introducing mutual inductance between adjacent coils as shown in Fig. 1. Let  $\theta$  be the phase shift of a single section and  $\omega$  the radian frequency.  $\theta$  is an odd function of  $\omega$ , so that if  $\theta$  is expanded in a Maclaurin series, we obtain

$$\theta = \theta_1 \omega + \theta_3 \omega^3 + \theta_5 \omega^5 + \dots \quad (1)$$

$\theta_1, \theta_3, \theta_5, \dots$  are the Maclaurin coefficients and are functions of the network parameters. We may choose the mutual inductance so that  $\theta_3$  vanishes, removing the third order term in  $\omega$ . The condition for this is\*

$$L - 6M = 0 \quad (2)$$

Some attention must be given the sign of  $M$ . Equation (2) implies that the coils are series-aiding.

<sup>1</sup> Manuscript received June 7, 1946.

Contribution from the Radio Branch, Division of Physics and Electrical Engineering, National Research Laboratories, Ottawa, Canada. Issued as N.R.C. No. 1474.

<sup>2</sup> Physicist.

\* The network is essentially equivalent to a series  $m$ -derived filter with  $m = \sqrt{1.5}$ . Starr recommends  $m = \sqrt{2}$ , which is over-corrected in the sense taken here. It should be noted that a chain of  $m$ -type sections would produce a network with the inductances divided in halves in the manner suggested at the end of the paper.

It will be shown how to introduce another circuit parameter to obtain yet another order of phase correction, the word 'correction' here having the significance used above, i.e., the removal of successive non-linear terms of Equation (1). The circuit is that of Fig. 2, the added element being a condenser  $C_1$  across the inductance  $L$ .  $C_1$  and  $M$  may be chosen so that the  $\theta_s$  and  $\theta_5$  for this circuit both vanish. The required conditions reduce to a very simple form, namely

$$L - 6.439 M = 0 \quad (3)$$

$$C_2 - 28.439 C_1 = 0 \quad (4)$$

Here again it is found that the coils are series-aiding.

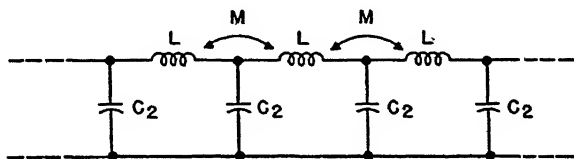


FIG. 1. Simple low-pass filter delay network with mutual inductance for phase correction.

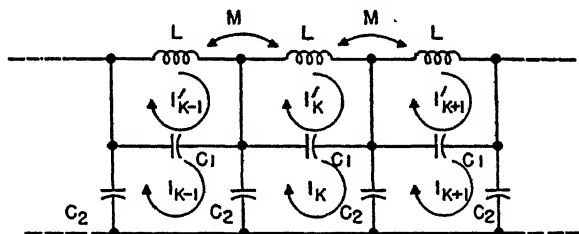


FIG. 2. Low-pass delay network using both mutual inductance and a capacity,  $C_1$ , for phase correction.

This result is obtained by laborious but straightforward algebra. Only an outline of the calculation will be given. The network equations are:

$$I_k \left( \frac{2}{j\omega C_2} + \frac{1}{j\omega C_1} \right) - \frac{I'_k}{j\omega C_1} - \frac{1}{j\omega C_2} (I_{k-1} + I_{k+1}) = 0. \quad (5)$$

$$I'_k \left( j\omega L + \frac{1}{j\omega C_1} \right) - \frac{I_k}{j\omega C_1} + j\omega M (I'_{k-1} + I'_{k+1}) = 0. \quad (6)$$

If we put

$$I_k = A e^{k\gamma} \\ I'_k = A' e^{k\gamma},$$

where  $A$  and  $A'$  are arbitrary constants and  $\gamma$  the propagation constant, then the consistency of Equations (5) and (6) requires that

$$\cosh^2 \gamma - \frac{1}{2} \left\{ \frac{C_2}{C_1} + 2 - \frac{L}{M} + \frac{1}{\omega^2 M C_1} \right\} \cosh \gamma \\ - \frac{1}{4} \left\{ \frac{L}{M} \left( \frac{C_2}{C_1} + 2 \right) - \frac{2}{\omega^2 M C_1} \right\} = 0. \quad (7)$$

Equation (7) determines the propagation constant  $\gamma$ .

As there are two solutions for  $\cosh \gamma$ , there are two modes of transmission. One of these is rapidly attenuated at all frequencies and does not concern us. The other mode has a low-pass filter type of behaviour that is susceptible of the improvement obtained by choosing the circuit constants properly.

In the pass band,  $\gamma$  is purely imaginary and equal to  $j\theta$ . The solution of Equation (7) then gives us  $\cos \theta$ . This solution may be expanded as a Maclaurin series in  $\omega$ :

$$\begin{aligned}\cos \theta &= 1 + a_2 \omega^2 + a_4 \omega^4 + a_6 \omega^6 + \dots \\ &= 1 + \frac{a_2}{\theta_1^2} (\theta_1 \omega)^2 + \frac{a_4}{\theta_1^4} (\theta_1 \omega)^4 + \frac{a_6}{\theta_1^6} (\theta_1 \omega)^6 + \dots\end{aligned}\quad (8)$$

The coefficients  $a_2, a_4, a_6, \dots$  are all functions of the network parameters.  $\theta_1$  may be regarded as an additional arbitrary parameter.

At this point we could apply Taylor's theorem to Equation (7) or (8) to obtain an expansion of the form (1), and then equate  $\theta_3$  and  $\theta_5$  to zero to get our desired conditions. However, it is much easier to proceed as follows. We have

$$\cos \theta = 1 - \frac{\theta^2}{2!} + \frac{\theta^4}{4!} - \frac{\theta^6}{6!} + \dots\quad (9)$$

The required result is obtained by identifying the coefficients of Equations (8) and (9) up to and including the sixth degree terms. That is, we put

$$\begin{aligned}\frac{a_2}{\theta_1^2} &= -\frac{1}{2!} \\ \frac{a_4}{\theta_1^4} &= \frac{1}{4!} \\ \frac{a_6}{\theta_1^6} &= -\frac{1}{6!}\end{aligned}$$

Eliminating  $\theta_1$  between these equations gives us two equations for the circuit parameters,  $M$  and  $C_1$ . These can be reduced to

$$\begin{aligned}L &= 6.439 M \\ C_2 &= 28.439 C_1\end{aligned}$$

that is, Equations (3) and (4).

Turning to other important constants of the circuit, we may readily find that the cut-off frequency is

$$\omega_0 = \frac{2}{\sqrt{(L - 2M)(C_2 + 4C_1)}}.$$

The question of the characteristic impedance or the proper terminating impedance is more difficult. If the mutually coupled coils be replaced by their  $T$  equivalents, it will be seen that the ladder becomes not a chain of four-terminal networks, but of six-terminal networks. It is this fact that is responsible for the two modes of propagation. Such a network requires two characteristic impedances.

In a practical case the line will probably be broken off at one of the junction points as they appear in Fig. 2. This procedure destroys the six-terminal character of the last section, but there does not seem to be any good reason for attempting to preserve it. The terminating admittance which will remove the reflected propagated wave for such an arrangement can be calculated. The result appears to be complicated—it has not been carried through in any case. It will undoubtedly be mainly resistive, of a value close to  $\sqrt{L/C_2}$ . Experience with networks with a cut-off frequency of 5 megacycles per second indicates that the results are uncritical to the termination.

It has been assumed that there is no mutual inductance between any pairs of coils except adjacent ones. If the coils are mounted coaxially, this will not be true, i.e. there will be interaction between non-adjacent coils. The effect of this has not been considered, but it will probably be small. If any concern were felt about this point, it is possible to divide each coil in half and then to arrange the parts so that a half-coil in one section interacts only with the adjacent half-coil in the next section.

### References

1. HOLCOMB, R. T. Bell Labs. Record, 9 : 229-232. 1931.
2. KALLMANN, H. E. Proc. Inst. Radio Engrs. 28 : 302-310. 1940.
3. STARR, A. T. Electric circuits and wave filters. 2nd ed. Sir Isaac Pitman & Sons, Ltd., London. 1938.



# Canadian Journal of Research

Issued by THE NATIONAL RESEARCH COUNCIL OF CANADA

VOL. 25, SEC. A.

MARCH, 1947

NUMBER 2

## THE RATIO OF THE CAPTURE CROSS-SECTIONS OF LITHIUM AND BORON FOR THERMAL NEUTRONS<sup>1</sup>

BY F. W. FENNING,<sup>2</sup> G. A. R. GRAHAM,<sup>3</sup> AND H. SELIGMAN<sup>2</sup>

### Abstract

A small boron trifluoride chamber is used to obtain the spatial distribution and density integrals of thermal neutrons produced by a source in aqueous solutions of compounds of lithium and boron. The effects of the finite size of the boron chamber are minimized by adjusting the concentrations of the solutions so that the mean life of thermal neutrons is the same in both. The scattering mean free paths are also almost identical. The final result is

$$\sigma_{Li}/\sigma_B = 0.0948 \pm 0.0013.$$

Taking  $\sigma_B = 705 \times 10^{-24}$  cm.<sup>2</sup> per atom,  $\sigma_{Li} = (66.8 \pm 1.0) \times 10^{-24}$  cm.<sup>2</sup> per atom.

### Introduction

Early measurements of the capture cross-section of lithium for thermal neutrons are in considerable disagreement, largely owing to uncertainties in the mean energies of the neutron spectra concerned. Usually the capture cross-sections for boron and lithium have been determined by the same authors with the same geometry and spectrum, so that even if the values for any one of these substances are in disagreement, the ratio  $\sigma_{Li}/\sigma_B$  should be independent of the spectrum if we can assume a  $1/v$  variation of cross-section with neutron velocity for both substances. However, even these ratios do not agree, so that when certain experiments requiring knowledge of the cross-section of lithium were planned in this laboratory, it was also decided to determine the ratio  $\sigma_{Li}/\sigma_B$  by the method used earlier by Frisch, Halban, and Koch (2), and by ourselves in determining  $\sigma_B/\sigma_H$  (1).

As in the work mentioned above (1), a small boron chamber is used to obtain integrals of the thermal neutron density produced by a source in aqueous solutions of compounds of the elements concerned. The chief source of error in this method comes from the effect of the finite size of the boron chamber, which effect may be different in two solutions of different capturing and scattering properties. In the present experiment these effects are brought to a minimum by adjusting the concentrations of the solutions used (one

<sup>1</sup> Manuscript received August 29, 1946.

Contribution from the Nuclear Physics Branch of the Montreal Laboratory, Atomic Energy Division of the National Research Council of Canada. Montreal report, MP-71, dated June 29, 1944. Issued as N.R.C. No. 1497.

<sup>2</sup> Member of United Kingdom staff.

<sup>3</sup> Physicist.

containing lithium, the other containing boron) so that the mean life of thermal neutrons is the same in both. In the two solutions used the scattering mean free paths were also almost identical.

### Apparatus

The boron chamber was prepared by Mr. N. Veall and has been described (5), its dimensions being 0.6 cm. in diameter and 2 cm. in length. It was mounted on a brass tube through which the lead from the collecting electrode passed to the head amplifier. The high tension lead passed through a glass tube a few centimetres from the brass tube.

Two identical tanks, 80 by 40 by 30 cm., contained the two solutions. A frame which was not attached to any tank and which carried the source and the chamber was used for the measurements in both solutions. Source and chamber could move on rails fixed to the frame. The distance between source and chamber was read off a mirror scale attached to the frame behind indicators fixed to the source and chamber supports.

The source was contained in a lead and brass box (1 cm. of lead, 0.1 cm. of brass). The lead served to reduce the 'noise' due to  $\gamma$ -rays in the chamber. The usual linear amplifier and scaling circuits were used for counting the impulses from the boron chamber.

### Experimental Procedure

On the basis of existing data, solutions of boric acid and lithium acetate were so prepared as to reduce the mean life of thermal neutrons in each to about one-fifth of that in water. In these solutions boron chamber counts

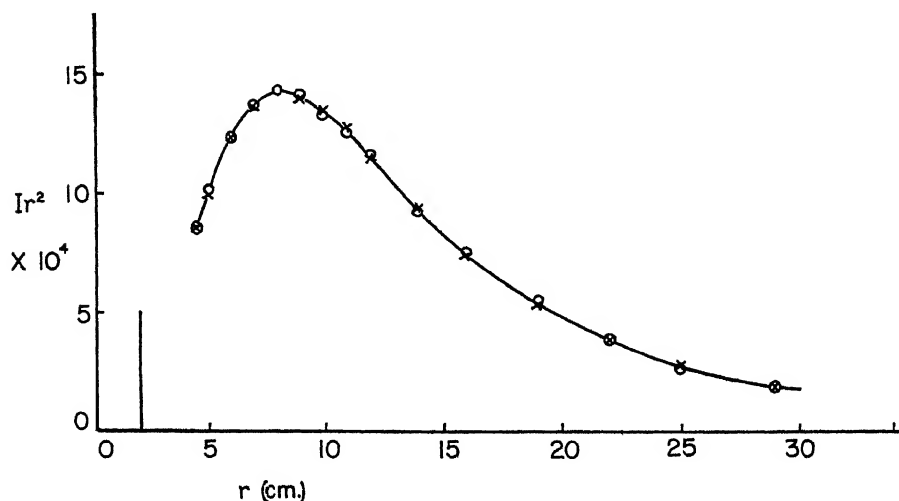


FIG. 1. Spatial distribution of thermal neutrons around a Ra- $\alpha$ -Be source (0.6 gm. Ra). Solution I: boric acid in water ( $C_B = 0.197$  gm-atoms per litre). Measurements shown by circles. Solution II: lithium acetate in water ( $C_L = 2.095$  gm-atoms per litre). Measurements shown by crosses.

were taken at several distances from the source. From the ratio of intensities in the two solutions for given separations of source and chamber it was possible to see by how much the concentration of one of the solutions would have to be changed in order to bring their capture probabilities to the same value. After a few preliminary adjustments of this type, complete density distribution curves were obtained by plotting  $I r^2$  against  $r$  for each solution.  $I$  represents the density of thermal neutrons at a distance  $r$  from the source, measured in counts per minute from the boron chamber. Sufficient counts were taken to give better than 1% statistical accuracy to the more important points, while the weaker intensities far from the source were progressively less accurate. To safeguard against drift in the counting apparatus, measurements were made in the two solutions alternately, but no significant change was apparent.

The final measurements were carried out in the course of one day. Immediately after these measurements were finished, samples of the two solutions were taken for chemical analysis. We wish to thank Mr. A. C. English and Mr. J. Hébert for carrying out these analyses of the lithium and boron content.

## Results

It can be seen from the curve of Fig. 1 that to the accuracy of the measurements the two solutions had the *same* mean life for thermal neutrons. Then the mean life  $\tau$  is inversely proportional to  $\sum C_i \sigma_i$ , where  $C_i$  represents the concentration in gm-atoms per litre of a capturing nucleus of cross-section  $\sigma_i$ .

$\therefore C_B \sigma_B + C_H \sigma_H = C_{L_1} \sigma_{L_1} + C'_H \sigma_H$ , if we neglect the small amount of absorption in oxygen and carbon present.

$$\begin{array}{ll} \text{From the analysis} & C_B = 0.197 \\ & C_H = 110.7 \end{array} \qquad \begin{array}{ll} & C_{L_1} = 2.095 \\ & C'_H = 107.0 \end{array}$$

$$\therefore \frac{\sigma_{L_1}}{\sigma_B} = \frac{C_B}{C_{L_1}} + \frac{(C_H - C'_H) \sigma_H}{C_{L_1} \sigma_B} = 0.09403 + 0.00078 = 0.0948,$$

using the known value of  $\sigma_H$  and taking  $\sigma_B(kT) = 705 \times 10^{-24}$  cm.<sup>2</sup> per atom (private communication from the Chicago group early in 1944) to obtain the hydrogen correction term.

Hence  $\sigma_{L_1}(kT) = 66.8 \times 10^{-24}$  cm.<sup>2</sup> per atom.

Recently it has been shown that both lithium and boron have capture cross-sections that are inversely proportional to the velocity of the neutrons (3, 4). Therefore it follows that the ratio of their capture cross-sections is independent of the neutron spectrum.

## Accuracy of Measurement

Previous measurements of this type have frequently shown that a particular density distribution curve can be reproduced to an accuracy of about  $\frac{1}{2}\%$  in the area underneath the curve. Hence it is reasonable to say that the mean life in the two solutions was the same to about 0.7%. The chemical analyses were carried out by two independent observers by slightly different methods,

each observer giving a reproducibility figure of about  $\frac{1}{2}\%$ . Their results actually differed by about  $1\%$  in absolute value, but only  $\frac{1}{4}\%$  in the ratio  $C_{Li}/C_B$ . Hence from errors in the analysis we may expect an uncertainty of about  $0.7\%$  in the ratio  $\sigma_{Li}/\sigma_B$ . Consequently we get

$$\sigma_{Li}/\sigma_B = 0.0948 \pm 0.0013,$$

or taking  $\sigma_B = 705 \times 10^{-24}$  cm.<sup>2</sup> per atom,

$$\sigma_{Li} = (66.8 \pm 1.0) \times 10^{-24} \text{ cm.}^2 \text{ per atom.}$$

### References

1. FENNING, F. W., HALBAN, H. v., JR., and SELIGMAN, H. Unpublished report, Br.-135. The ratio of the absorption cross-sections of boron and hydrogen. British Atomic Energy Project. Jan. 1943.
2. FRISCH, O. R., HALBAN, H. v., JR., and KOCH, J. Kgl. Danske Videnskab. Selskab. Math. fys. Medd. 15 (10). 1938.
3. HAVENS, W. W., JR. and RAINWATER, J. Phys. Rev. 70 : 154-173. 1946.
4. RAINWATER, J. and HAVENS, W. W., JR. Phys. Rev. 70 : 136-153. 1946.
5. VEALL, N. Unpublished report, MP-60. On the construction of small boron chambers. National Research Council of Canada. May. 1944.

# EVIDENCE FOR AN $(n, \alpha)$ REACTION INDUCED IN $O^{17}$ BY THERMAL NEUTRONS<sup>1</sup>

BY A. N. MAY<sup>2</sup> AND E. P. HINCKS<sup>3</sup>

## Abstract

It can be shown from the masses involved that the reaction  $O^{17}(n, \alpha)C^{14}$  should be exothermic by 1.72 Mev., and should therefore occur with thermal neutrons. As an attempt to detect the reaction an investigation was made of the pulse spectrum produced when an ionization chamber containing oxygen was placed in a flux of thermal neutrons. The pulses were amplified and then counted in a series of energy bands by means of a kicksorter. Two oxygen samples were compared, one being enriched (three times normal), and the other impoverished (0.5 times normal), in  $O^{17}$ . Differences between runs with these two gases showed a considerable number of pulses between 1 and 2 Mev., with a maximum at 1.4 Mev. Reasons are given for assigning these pulses to the above reaction, including considerations of the possibility that other exothermic neutron reactions occur. By comparing the number of pulses with the number produced by  $N^{14}(n, p)C^{14}$  when the chamber contained air, a value of  $(1.9 \pm 0.5) \times 10^{-28}$  cm.<sup>2</sup> for the cross-section for the  $O^{17}(n, \alpha)C^{14}$  reaction in ordinary oxygen was deduced. This gives a cross-section of  $(0.46 \pm 0.11) \times 10^{-24}$  cm.<sup>2</sup> per atom of the pure isotope  $O^{17}$ . The effect measured is about 20% of the total thermal neutron capture cross-section that has been reported for ordinary oxygen.

## Introduction

The thermal neutron capture cross-section of oxygen is known to be very small. Recent experimental determinations have given a value  $\sigma = 1 \times 10^{-27}$  cm.<sup>2</sup>\* Among the possible neutron-induced reactions with any of the three stable oxygen isotopes ( $O^{16}$ ,  $O^{17}$ ,  $O^{18}$ ) which give known products the reaction



is unique in that it should be exothermic, and so should occur with thermal neutrons. Using the masses given by Mattauch (6), ( $O^{17} = 17.00450$ ,  $n^1 = 1.00895$ ,  $C^{14} = 14.00774$ ,  $He^4 = 4.00386$ ), it may be shown that the above reaction should have a  $Q = +1.72$  Mev.

The experiment described in this paper was carried out in an attempt to measure the cross-section for the reaction  $O^{17}(n, \alpha)C^{14}$  with thermal neutrons. This will show to what extent it contributes to the total capture cross-section of oxygen, a question that is of special interest because of the use of heavy water as a pile moderator. Since  $O^{17}$  is only 0.041% of natural oxygen, the  $(n, \alpha)$  reaction would not be expected to compete seriously with simple capture unless the cross-section per atom of the isotope were relatively high, or the capture  $(n, \gamma)$  cross-sections for the more abundant isotopes were extremely low.

<sup>1</sup> Manuscript received October 15, 1946.

Contribution from the Nuclear Physics Branch, Montreal Laboratory, Atomic Energy Division of the National Research Council of Canada. Issued as N.R.C. No. 1504.

<sup>2</sup> Member of the United Kingdom Staff until September 1945.

<sup>3</sup> Physicist, National Research Council; now at the Chalk River Laboratory.

\* Report from Manhattan Project, to be published. Table of cross-sections compiled by Dr. H. Goldsmith.

## Experimental Method

The method used was to expose the oxygen (gas) in a pulse ionization chamber to a flux of thermal neutrons, and to look for pulses whose size corresponded roughly to 1.7 Mev. Two oxygen samples of different isotopic constitution were used for most of the experiment; one was enriched (three times normal) and the other impoverished (0.5 times normal) in  $O^{17}$ . Differences between counts obtained with the two samples were taken to give a result due to  $O^{17}$ . Other devices such as discrimination of pulses according to their energies, variation of the gas pressure in the chamber, and variation of the neutron flux were used to guard against spurious results.

The pulses produced in the chamber were fed through a linear amplifier (gain  $\sim 10^5$ ) to a kicksorter which sorted them according to their size, and counted them on mechanical counters. The kicksorter biases were arranged so that the anticipated energy ( $\sim 1.7$  Mev.) fell at about the middle of the range; the probability of distinguishing a small effect due to  $O^{17}$  from a large background of both larger and smaller pulses was thus enhanced.

The experiment was carried out twice, the first time in the Montreal Laboratory at the beginning of 1944, with a 'natural' neutron source. Then, in April 1944, the measurements were repeated in the Argonne Laboratory at Chicago, using the much more intense flux of neutrons from the thermal column of the graphite pile. Here much more dependable results with better 'statistics', were obtained and they form the chief basis for the conclusions reached below.

## Apparatus

The same apparatus was used for the Montreal and Argonne experiments, except for the kicksorter. (A newly designed instrument was used at the Argonne Laboratory.) The actual experimental runs in the two cases were, however, somewhat different because of the vast difference in the neutron intensities and counting rates.

The ionization chamber was a high-pressure pulse chamber designed by one of the authors (A. N. M.) for fast neutron recoil work. The sectional sketch, Fig. 1, shows the construction. The chamber is cylindrical, with a useful volume of 55 cc. The electrodes—the inner one is the negative ion collector—are of thin copper, and the surfaces facing the collecting volume were silver-plated to reduce the background. Soldering was avoided where possible in the construction, and the soldered joints that remained were very carefully plated to contain any  $\alpha$ -particles produced by neutrons on boron or lithium that might have been left by the soldering flux. The polystyrene electrode support was designed to minimize the possibility of the production of pulses in the chamber by recoil protons from fast neutrons.

The negative high tension for the outer electrode was supplied by a 0–5000 volt supply of conventional design with full-wave rectifier and degenerative pentode stabilization. The collecting voltage normally used was between 2000 and 3000 v.

The chamber was evacuated and filled through the filling tube shown in Fig. 1. The method generally used for filling to pressures up to 2 atm. is obvious from Fig. 2. Here  $C$  is the chamber,  $M$  an ordinary mercury-glass manometer,  $T$  a trap that can be immersed in liquid air boiling at reduced

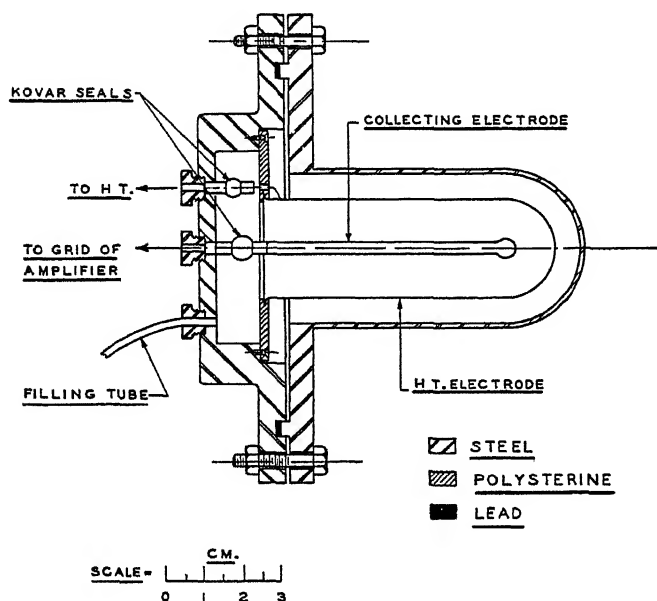


FIG. 1. Section of pressure chamber.

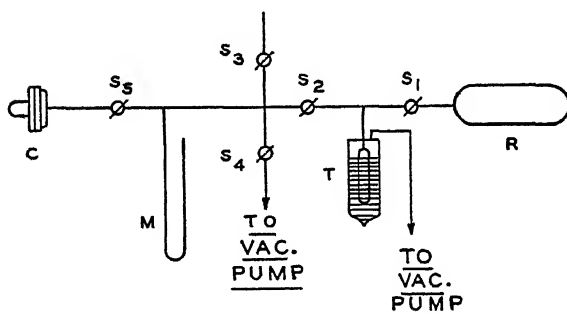


FIG. 2. Chamber filling system.  $C$ , chamber;  $M$ , manometer;  $T$ , liquid air cooled trap;  $R$ , oxygen reservoir;  $S_1 \dots S_5$ , stopcocks.

pressure,  $R$  the oxygen reservoir ( $1\frac{1}{2}$  litre flask), and  $S_1 \dots S_5$  are stopcocks. The following sequence of operations fills the chamber. With the system evacuated to the left of  $S_2$  and between  $S_1$  and  $S_2$  ( $S_1$ ,  $S_2$ ,  $S_3$ , and  $S_4$  closed),  $S_1$  is opened and oxygen condensed in  $T$ . Then  $S_1$  is closed and  $S_2$  opened, and  $T$  warmed until the required pressure is reached in the chamber as shown by  $M$ . Finally  $T$  is cooled with  $S_2$  closed, and surplus oxygen in  $T$

may be boiled off through  $S_1$  back into  $R$ . By a similar process the oxygen in the chamber may be almost completely recovered, and returned to  $R$  via  $T$ . In practice a sequence of counts were taken with alternate flasks of enriched and impoverished oxygen at  $R$ , all other conditions remaining constant. Care was taken not to admit any air into the chamber during successive fillings. At the beginning and end of a sequence air could be admitted through  $S_2$  for calibration purposes as described below.

The linear amplifier was one of the standard type used in the Montreal Laboratory. It consisted of five stages with resistance-capacity coupling, and with a variable time-constant 'quick stage'. The first stage is in a separate box placed close to the chamber, and is designed to have low noise and to be non-microphonic. The linear amplifier output could be monitored visually with a cathode-ray oscilloscope.

The pulses from the amplifier were fed to a kicksorter. This instrument sorts pulses into a number of classes according to their amplitude—the limits being determined by pre-set voltages—and records the number counted in each class. The kicksorter used in the Montreal experiments had 12 channels and was built by H. F. Freundlich in Cambridge, England, in 1942. That used at Argonne was a new model (3) built in 1943-44 in the Montreal Laboratory, and was specially adapted to counting the broad pulses produced by the slow collection of ions in oxygen. Twelve channels were used. A separate discriminator and scale-of-32 operated in parallel with the kicksorter served to monitor the total count, and so check against the possibility of losses or double counts.

In the Montreal experiments, since the counting rates obtained with the natural source were of the order of a few per hour, rather elaborate precautions were taken to minimize the number of spurious counts from extraneous electrical and mechanical disturbances. The experiment was carried out in an electrically screened room, and filters were placed in the 110 v. mains supply to cut out pulses that might be fed into the amplifier from outside. Some care was taken to find the best earthing system for the apparatus. Sponge rubber was used liberally to reduce microphonic effects in the chamber and amplifier.

Calibrations of the kicksorter bias voltages in terms of energy were made by introducing air into the chamber, and observing the pulses from the reaction  $N^{14}(n, p)C^{14}$ . This gave a single point at about 0.6 Mev., which was sufficient, assuming the linearity of the whole system. (The linearity was actually checked by introducing artificial pulses of various sizes on to the collecting electrode and grid of the first tube through a small ( $\sim 1 \mu\text{mf.}$ ) condenser.) The number of pulses observed under given conditions could also be used as a measure of the product of neutron flux and effective chamber volume, and permitted an estimation of the cross-section for the oxygen reaction to be made in terms of the nitrogen cross-section.

A schematic diagram of the arrangement of apparatus is given in Fig. 3.

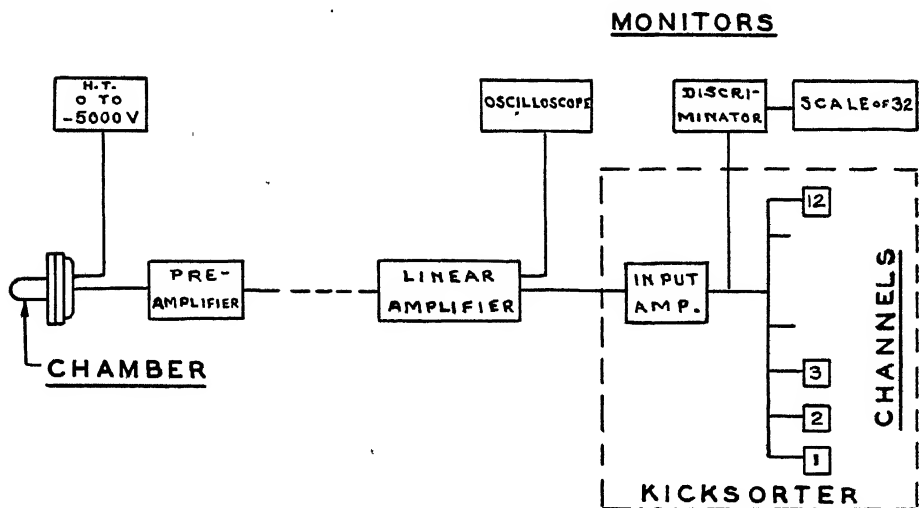


FIG. 3. Schematic arrangement of counting apparatus.

### Experimental Results

#### A. Montreal Laboratory

A series of measurements was made in Montreal over a period of several months using 2.4 gm. of radium at the centre of an 11 cm. beryllium cube as a source of neutrons. This, together with the chamber, was surrounded by paraffin wax, with some lead between source and chamber to reduce the  $\gamma$  background. Runs were made with both natural (electrolytic) oxygen and enriched oxygen (three times normal in  $O^{17}$ ), in each case at several different pressures. Each run was repeated with cadmium shielding around the chamber. Measurements were made at night as much as possible to avoid disturbances, and the total length of each run was 25 to 35 hr.

All pulses between about 0.6 and 2.5 Mev. were counted, and cadmium differences taken. Since variations in gain of the amplifier during the long runs were unavoidable, and since the chance of recording spurious counts was high, while the total number of pulses observed was small, the results of this experiment were very uncertain. It did seem apparent, however, that for a given pressure there were more pulses due to C neutrons from the enriched gas than from the ordinary, and that this difference increased with the pressure. The average difference (enriched minus ordinary) was between four and six counts per hour per atmosphere. Since 14,000 counts per hour were obtained from the nitrogen ( $n, p$ ) reaction under the same conditions with the oxygen replaced by one atmosphere of air, this suggested a cross-section of about 0.0003 times the thermal capture cross-section of nitrogen for a 'twice-enriched' oxygen.

#### B. Argonne Laboratory

In the Argonne experiments the chamber was placed in a hole in the thermal column of the graphite pile, and advantage was taken both of the higher

neutron flux available and of the case of varying the flux by known amounts. It was decided as a result of the Montreal experiment that the correlation of results obtained at different pressures was unreliable, since the collection of ions in oxygen is slow and it is difficult to ensure that the pulse size for a given energy is independent of pressure. All runs with oxygen were therefore made at the same pressure—2 atm. The gases compared were enriched (three times normal) and impoverished (0.5 times normal) in  $O^{17}$ . The nitrogen calibrations were made as before with 1 atm. of air.

Three separate determinations were made of the  $O^{17}$  effect. Calling them (I), (II), and (III), they consisted respectively of the following measurements.

(I). With 2 atm. of enriched oxygen, runs were made at pile power levels of 90, 180, 350, and 820 w. The neutron flux at the chamber must increase proportionally. The number of counts per minute in each channel was corrected where necessary for the loss occurring in the mechanical counter. (This correction was made for all the Argonne results, and will be assumed hereafter.) With 2 atm. of impoverished oxygen, similar runs were made at each of the same four power levels, and finally the series was repeated for the enriched gas. When the 'impoverished' values were subtracted from suitably chosen means of the two sets of 'enriched' values (adjusted for variation in amplifier gain), a set of results  $N_i(P)$  per min. (enriched minus impoverished) were obtained for each kicksorter channel (number  $i$ ) at each of four powers. The values  $N_i(P)$  for each channel were then plotted against the power  $P$  and straight lines were drawn from the origin through the appropriate points. This was generally easy, but an exception occurred in the case of the lowest few channels, where at higher powers the points rose rapidly above a certain power. It was obvious during the experiment that this effect was due to a piling up of small pulses which occurred in great number, even producing an effect in the difference (enriched minus impoverished). Their origin will be discussed below, and the points affected were disregarded in drawing the best straight lines. From the series of straight lines, characteristic values  $N_i(1)$  = number of counts per minute at 1 kw. were obtained, and these plotted against the channel number,  $i$ , give the spectrum shown in Fig. 4 (A) (Expt. I). Here the majority of pulses occurred at the low end of the kicksorter range, and a considerable part of the curve had to be extrapolated with the assumption that the peak was roughly symmetrical. The area under the peak was then determined to get a measure of the oxygen effect.

Finally, a 'nitrogen calibration' was made with 1 atm. of air in the chamber. The gain of the amplifier was increased to bring the proton pulses into the kicksorter range, and the pile power was reduced to give a reasonable counting rate. The area under the well defined nitrogen peak (Fig. 5) was then corrected to a value corresponding to 1 kw. power and to 2 atm. of pure nitrogen. The ratio of the final result for oxygen to the corrected result for nitrogen gives directly the ratio of the cross-section ( $\sigma_E$ ) for a 2.5 times enriched oxygen to that ( $\sigma_N$ ) for nitrogen. These results are given in the first line of Table I. From the position of the nitrogen peak, and adopting the value

0.55 Mev. for the disintegration energy of the ( $n, p$ ) reaction (6), the energy scale shown at the bottom of Fig. 4 (A) was deduced. The oxygen peak falls at approximately 1.4 Mev.

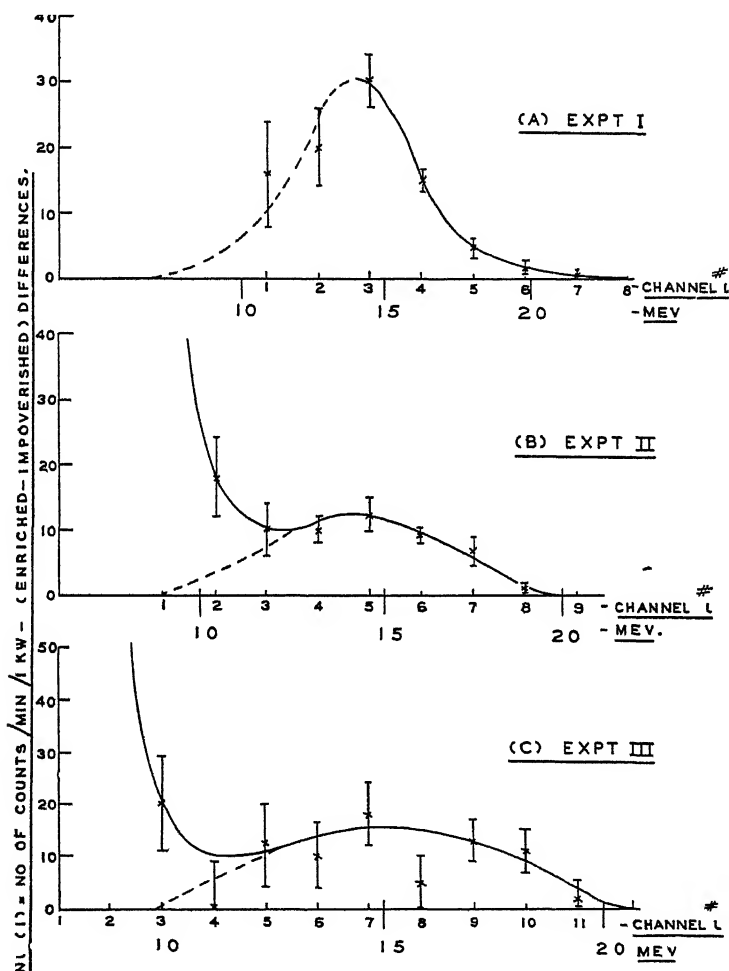


FIG 4 Distribution of pulses due to oxygen effect for the three Argonne Laboratory experiments

(II). In order to shift the oxygen pulses nearer the middle of the kicksorter range the kicksorter biases were altered, and the experiment repeated. The sequence of operations was exactly as described under (I), except that the second set of runs with enriched gas was omitted. The final spectrum obtained is shown in Fig. 4 (B) (Expt. II). It is apparent that actually little was gained, this time it was quite impossible to allow for the piling up of pulses into the lower channels, and again a large extrapolation had to be made. However, the presence of a peak—again at about 1.4 Mev.—is unquestionable, although a determination of the number of pulses belonging to it is difficult.

(III). Finally, in an attempt to avoid the 'piling up' difficulty, much longer runs were made with both enriched and impoverished oxygen at very low

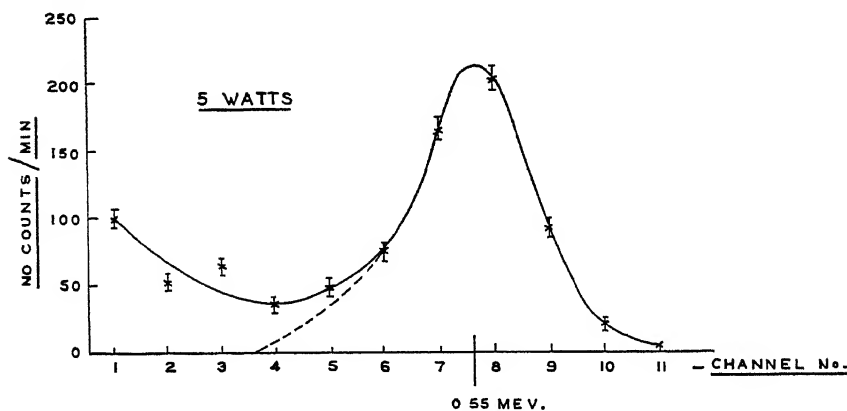


FIG. 5. Distribution of pulses due to nitrogen ( $n, p$ ) disintegrations used for calibration (Expt. I).

power (17.6 w.). The differences are plotted in Fig. 4 (C) (Expt. III), and again a peak is apparent with the low energy rise still present. A run with cadmium surrounding the chamber was also made which verified that the effect observed was due to C neutrons.

The results of Experiments (I), (II), and (III) are summarized in Table I.

TABLE I

Experiment	No counts/min / 1 kw / 2 atm.		Ratio $\frac{\sigma_E}{\sigma_N} \times 10^4$	Energy of oxygen peak or $Q$ , Mev
	Oxygen	Nitrogen		
(I)	$94 \pm 20$	$2.94 \times 10^5$	$3.2 \pm 0.7$	1.4
(II)	$54 \pm 12$	$2.94 \times 10^5$	$1.8 \pm 0.4$	1.4
(III)	$92 \pm 24$	$2.67 \times 10^5$	$3.4 \pm 0.9$	1.5

The mean value of  $\frac{\sigma_E}{\sigma_N}$  is  $(2.8 \pm 0.7) \times 10^{-4}$ , and the mean  $Q$  is 1.4 Mev. Taking  $\sigma_N = 1.7 \times 10^{-24}$  cm<sup>2</sup> per atom,\* we get

$$\sigma_E = (4.8 \pm 1.2) \times 10^{-28} \text{ cm}^2$$

Since this refers to an oxygen enriched 2.5 times in  $O^{17}$ , we find, assuming that the whole of the effect measured is due to  $O^{17}$ , the cross-section per atom of normal oxygen to be

$$\begin{aligned} \sigma_o &= \frac{4.8}{2.5} \times 10^{-28} \text{ cm}^2 \\ &= (1.9 \pm 0.5) \times 10^{-28} \text{ cm}^2 \end{aligned}$$

\* See footnote, page 77.

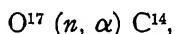
Moreover, from the natural abundance of  $O^{17}$  (0.041 %), we deduce the cross-section per atom of the isotope to be

$$\sigma_{O^{17}} = (0.46 \pm 0.11) \times 10^{-24} \text{ cm.}^2$$

It will be noted that this should contribute approximately 20% of the total oxygen capture cross-section that has been reported ( $1 \times 10^{-27} \text{ cm.}^2$  \*).

### Discussion of Results

We have observed an effect produced by thermal neutrons in a pulse ionization chamber containing oxygen. When the concentration of  $O^{17}$  and  $O^{18}$  is increased, the pulse size distribution shows a significant increase in number between 1 and 2 Mev. with a maximum at 1.4 Mev. This can be attributed to the reaction



which should be exothermic ( $Q = + 1.72$  Mev.) according to the masses.

The following considerations prompted the assignment of the observed effect to this reaction.

(1). The effect is observed as a difference between results obtained with two samples of oxygen, both produced in the same way by the electrolysis of heavy water. One sample was enriched, and the other impoverished in  $O^{17}$ . The only other difference should be in their  $O^{18}$  concentration, e.g., the first sample was also enriched (seven times normal) in  $O^{18}$ . The effect increases with pressure of the gas in the chamber.

(2). By the use of cadmium shielding, and by varying the neutron flux by known amounts, the effect was found to be due to thermal neutrons.

(3). The effect appears as a peak in the pulse spectrum lying between 1 and 2 Mev., with a maximum at 1.4 Mev. The anticipated energy for the reaction is 1.72 Mev. The discrepancy is not considered to be significant since the following questionable assumptions were made for the experimental energy calibration. The effect of the recombination and slow collection of ions in the chamber on the pulse size was assumed to be the same for 2 atm. of oxygen as for 1 atm. of air; moreover, the number of electron volts required to produce one ion pair was assumed to be the same for the different ionizing particles involved under these different conditions.

The most likely impurity in the oxygen samples is nitrogen, which should produce pulses of only  $\frac{1}{2}$  to  $\frac{1}{4}$  the size of those observed.

(4). The possibility of other exothermic reactions with the three stable oxygen isotopes has been considered. A summary of all possible ( $n, p$ ) and ( $n, \alpha$ ) reactions in oxygen is given in Table II, with their calculated  $Q$ 's. It will be seen that the reaction  $O^{17} (n, \alpha) C^{14}$  is the only one giving a known product that can be exothermic by mass considerations. The  $O^{18}$  reactions are excluded anyway by the experimental method.

\* See footnote, page 77.

TABLE II

Reaction	Mass of oxygen isotope (Mattauch (6))	Mass of product			Q, Mev.
		Mattauch (6)	Empirical	Barkas (1)	
$O^{16}(n, p)N^{15}$	16 00000	16 00645			-5 25
$O^{16}(n, \alpha)C^{13}$	16 00000	13 00756			-2 30
$O^{17}(n, \alpha)C^{14}$	17.00450	14 00774			+1 72
$O^{17}(n, p)N^{17} ?$	17.00450		>17 011		<-5
				17 0136	-7.7
$O^{18}(n, p)N^{18} ?$	18 00485		>18 011	—	<-5
				18 027	-20
$O^{18}(n, \alpha)C^{15} ?$	18 00485		>15 005	—	<+5
				15 0165	-6 1

The last three reactions in the table, if they occurred, would produce unknown isotopes of nitrogen and carbon. It may be readily seen from a table of masses of isotopes that in cases in which the appropriate group of masses is known, the following rule generally holds:

$$M_Z^A - M_{Z+1}^A > M_Z^{A-1} - M_{Z+1}^{A-1},$$

where  $M_Z^A$  is the mass of an isotope of element  $Z$  with mass number  $A$ . (It is true for every known group below  $Z = 13$  (Al).) By means of this rule lower limits for the masses of  $N^{17}$ ,  $N^{18}$ , and  $C^{15}$  were deduced, and are given in the table as 'empirical' masses. For example,

$$N^{17} - O^{17} > N^{18} - O^{18} = + 0.00645$$

and so

$$N^{17} > 0.00645 + O^{17} = 17.011.$$

Barkas (1) has calculated the masses of  $N^{17}$  and  $C^{15}$  based on theoretical considerations of nuclear binding energies. These are also shown in Table II, along with a value for  $N^{18}$  which has been calculated by the authors by the same method. The values of  $Q$  corresponding to the various estimated masses are given in the last column. It is apparent that each of the three reactions should be endothermic, with the possible but improbable exception of the reaction  $O^{18}(n, \alpha)C^{15}$ .

The value  $Q = 0.55$  Mev. for the reaction  $N^{14}(n, p)C^{14}$  is quoted by Mattauch (6), and is due to an ionization chamber measurement by Huber, Huber, and Scherrer (4). Livingston and Bethe (5) have calculated the value 0.62 Mev. from the results of Bonner and Brubaker (2), who made range measurements in a cloud chamber. If the higher value (0.62 Mev.) is used for the energy calibration, the oxygen peak is shifted to 1.6 Mev. Such a change is, however, inconsequential, since little accuracy is attached to our energy measurement as pointed out above.

The determination of the cross-section could have been made to a much greater accuracy had it not been for the large background of small kicks that merged with the lower end of the  $O^{17}$  peak and was particularly disturbing at

higher powers. That their effect still persisted in the (enriched minus impoverished) differences has already been noted. It seems most likely that this was due to nitrogen impurity in the samples, the contamination being greater for some reason in the enriched gas. Thus there were an appreciable number of pulses belonging to a large nitrogen peak which, owing to background noise, piling up effect, etc., were recorded in the channels up to  $\sim 1$  Mev. or higher. There was also a small background of pulses above 2 Mev. but this remained roughly constant, being eliminated by the (enriched minus impoverished) differences, and may have been due to boron contamination on the chamber walls.

### Acknowledgment

We wish to express our gratitude to the Manhattan Project Directors, who made the facilities of the Argonne Laboratory available to us, and to members of the Argonne Staff for their generous co-operation and assistance.

### References

1. BARKAS, W. H. Phys. Rev. 55 : 691-698. 1939.
2. BONNER, T. W. and BRUBAKER, W. M. Phys. Rev. 49 : 778. 1936.
3. FREUNDLICH, H. F., HINCKS, E. P., and OZEROFF, W. J. Rev. Sci. Instruments. In press.
4. HUBER, O., HUBER, P., and SCHERRER, P. Helv. Phys. Acta, 13 : 209-211. 1940.
5. LIVINGSTON, M. S. and BETHE, H. A. Rev. Modern Phys. 9 : 245-390 1937.
6. MATTAUCH, J. Kernphysikalische Tabellen. Springer-Verlag, Berlin. 1942.

# SONIC DETERMINATION OF THE ELASTIC PROPERTIES OF ICE<sup>1</sup>

By T. D. NORTHWOOD<sup>2</sup>

## Abstract

By measuring the velocity of various types of elastic waves in a solid it is possible to deduce Young's modulus and Poisson's ratio. Longitudinal, extensional, and Rayleigh wave velocities were measured in ice, the first by resonance in a rod and the other two by a pulsing technique. The value obtained for Young's modulus was  $9.8 \times 10^{10}$  dynes per cm.<sup>2</sup> and for Poisson's ratio was 0.33.

## Introduction

The author was recently concerned with the design of an instrument for measuring the thickness of ice by supersonic echo-ranging. Since it was desirable at the outset to know the velocity of sound in an extended mass of ice, a search was made for velocity data or the elastic constants from which the velocity could be deduced. Some values of Young's modulus were found, and although they were very scattered the more recent ones seemed reliable enough. However, there was no satisfactory information on Poisson's ratio, which was also required in this application. Consequently, it was necessary to make velocity measurements as the equipment developed. In view of the fragmentary nature of the published information it was considered worth while to extend the measurements sufficiently to obtain the elastic constants of ice.

## General Method

The expression for the velocity of sound in any medium is

$$v = \sqrt{\frac{\text{Elasticity of medium}}{\text{Density of medium}}},$$

using the modulus of elasticity appropriate to the mode of propagation. In a solid, several modes of propagation, associated with the various elastic moduli, are commonly encountered. For example, the velocity of sound travelling longitudinally in a long wire or thin rod will be given by using Young's modulus in the above formula, whereas in other circumstances the modulus of rigidity or the extensional modulus, or some modification of these, might be applicable.

The elastic moduli may all be expressed in terms of Young's modulus and Poisson's ratio, and it is usual to regard these two quantities as the fundamental elastic constants of a material. Young's modulus may readily be measured directly, but Poisson's ratio is usually determined indirectly, from the relations between the elastic moduli.

<sup>1</sup> Manuscript received in original form, September 27, 1946, and as revised, January 2, 1947.  
Contribution from the Division of Physics and Electrical Engineering, National Research Council of Canada, Ottawa. Issued as N.R.C. No. 1507.

<sup>2</sup> Physicist.

In the present work three types of propagation were studied. The relations between them are discussed briefly below.

The velocity in an infinitely long rod, commonly called the 'longitudinal' velocity, is given by the familiar expression:

$$v_0 = \sqrt{\frac{E}{\rho}}, \quad (1)$$

where  $E$  is Young's modulus and  $\rho$  is the density of the material.

The velocity through an infinite solid medium ('extensional' velocity) is given by:

$$v_e = \sqrt{\frac{E(1-\sigma)}{\rho(1+\sigma)(1-2\sigma)}} \quad (2)$$

$$= v_0 \sqrt{\frac{(1-\sigma)}{(1+\sigma)(1-2\sigma)}}, \quad (3)$$

where  $\sigma$  is Poisson's ratio.

The transverse wave over the surface of an extended solid is related to the shear wave, which occurs in thin plates. Vibrations of this type were first discussed by Rayleigh (9, p. 441) and are commonly called 'Rayleigh waves'. A mathematical treatment is given by Love (8, p. 307). The velocity may be written:

$$v_r = K \sqrt{\frac{E}{\rho} \cdot \frac{1}{2(1+\sigma)}}, \quad (4)$$

$$= v_0 \cdot K \sqrt{\frac{1}{2(1+\sigma)}}. \quad (5)$$

It differs from the shear velocity by the factor  $K$ , a complicated function of Poisson's ratio, which however is readily evaluated for  $\sigma = \frac{1}{4}, \frac{1}{3}, \frac{1}{2}$ . These three values adequately define the function in the important range of Poisson's ratio. The resulting curve is shown in Fig. 1.

Also shown in Fig. 1 are the ratios  $v_r/v_0$ ,  $v_0/v_e$ , and  $v_r/v_e$ . It will be noted that  $v_r/v_0$  is almost independent of Poisson's ratio, and  $v_r$  is therefore almost as useful as  $v_0$  for determining Young's modulus. The other two ratios are fairly sensitive to changes in Poisson's ratio, and are therefore used to determine this quantity.

### Longitudinal Velocity

The longitudinal velocity was measured by determining the resonance frequencies of long rods cut from the ice. The procedure was simply to drive one end of the rod with a Rochelle salt transducer, and pick up the vibration at the other end with a similar transducer. The driver consisted of an audio oscillator with considerable output power and good frequency stability. The pick-up system consisted of transducer, amplifier, and cathode ray oscillograph. Frequency determinations were made by connecting to the horizontal deflection plates of the oscillograph a beat-frequency oscillator of considerable stability, whose calibration was adjusted frequently against the Research Council's 1000 cycle standard. After the driver oscillator had been tuned to

resonance, the beat-frequency oscillator was adjusted to give a Lissajous figure on the oscillograph.

Equation (1) for longitudinal velocity applies to the case of an infinite rod, where  $r^2/l^2$  is a negligible quantity. It was not feasible to meet this condition,

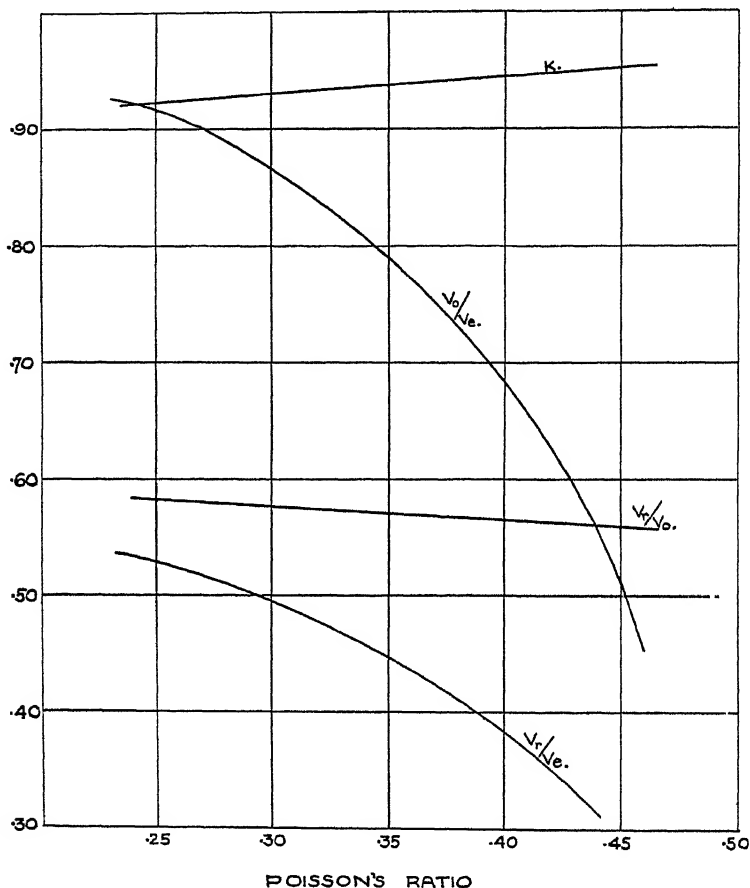


FIG 1. Curves showing relations between the three velocities as functions of Poisson's ratio.  $K$  is the ratio of Rayleigh wave velocity ( $v_r$ ) vs. shear velocity.

and it was therefore necessary to apply the correction worked out by Rayleigh (10, p. 251), who shows that the resonant frequency of a rod is lowered by the factor

$$1 - \frac{\pi^2 \sigma^2}{4} \cdot \frac{r^2}{l^2}.$$

The procedure in the present investigation was to start with the longest possible rods and take a series of observations for progressively shorter lengths. These were plotted against  $r^2/l^2$ , and the resulting straight line extrapolated to obtain the infinite-rod value,  $v_0$ . The maximum length, limited by the

capacity of the available constant temperature chamber, was about 40 cm. While the  $r/l$  correction could also be reduced by reducing the diameter of the rod, other complications appeared, such as the end-loading effect of the transducers, which made it advisable to work with a diameter of at least 5 cm.

It was first considered that Rayleigh's correction might itself be used as a method of determining Poisson's ratio, by measuring velocities for a series of values of  $r/l$ . However, when  $r/l$  becomes large enough to give accurate results, an additional factor, the radial resonance of the rod, begins to affect the velocity (4).

### Extensional Velocity

The extensional velocity was measured with the use of a pulsing technique. A 300 kc. pulse was applied by a Rochelle salt transducer on one face of a block of ice and received on the opposite face. The transit time was measured by applying initial and received pulses to an oscillograph. The details are as follows. The pulsing system was an overloaded audio amplifier, converting an audio-frequency sine-wave into a square wave and eventually (via a small coupling capacitor in the last stage) into a series of very sharp pulses. The sharp pulses were introduced on the grid of the overbiased 6AC7 tube whose plate load comprised an r f. choke in parallel with the crystal transmitter unit. The output circuit was thus shock-excited during each positive pulse on the grid of the 6AC7, producing a damped 300 kc. signal, three or four cycles long, from the transmitter.

The pinging system was driven by a Hewlett Packard Model 205-A oscillator, at as high a frequency as possible without undue 'reverberation' due to multiple reflections within the sample. This was a few hundred cycles in the case of the ice samples.

The ice blocks used were, of course, large enough to provide a practically infinite medium for the 300 kc. pulse, so that Equation (3) applied directly.

### Rayleigh Wave Velocity

Measurements of Rayleigh waves were made by the same method as for extensional waves, except that the transducers were both on the same face of the ice block. The separation of the transducers was varied from about 1 to 40 cm., giving a linear relation between pulse-time intervals and transducer spacing, whose slope is the Rayleigh wave velocity.

### Miscellaneous Details

The ice samples used for these experiments were cut from the Ottawa River or obtained from a local ice manufacturer. It was assumed that in all cases the crystallization was sufficiently rapid that the ice consisted of many crystals, variously oriented, and could be considered isotropic. This is borne out by the fact that although specimens were cut in a variety of directions from the ice-blocks, no great variation was noted from sample to sample. Such minor variations as were observed could be explained by internal flaws which were present in some specimens.

Temperature was controlled by using a temperature controlled test chamber. The specimens were enclosed in a copper case around which air cooled by passage over 'dry ice' was circulated when necessary. For most of the measurements a temperature of  $-15^{\circ}\text{C}.$  was maintained, although some observations of the variation in longitudinal velocity with temperature were made.

### Discussion of Results

The following velocity measurements were obtained:

$$v_0 = 3.28 \pm 0.02 \times 10^5 \text{ cm. per sec.}$$

$$v_e = 3.98 \pm 0.02 \times 10^5 \text{ cm. per sec.}$$

$$v_r = 1.85 \pm 0.05 \times 10^5 \text{ cm. per sec.}$$

Poisson's ratio was determined from the ratios  $v_0/v_e$  and  $v_r/v_e$  using the curves of Fig. 1:

$$v_0/v_e = 0.824, \text{ whence } \sigma = 0.33$$

and

$$v_r/v_e = 0.464, \text{ whence } \sigma = 0.34.$$

Young's modulus was determined from the observed value of  $v_0$ :

$$E = 9.9 \times 10^{10} \text{ dynes per cm.}^2,$$

and from the value of  $v_r$  and Poisson's ratio:—

$$E = 9.7 \times 10^{10} \text{ dynes per cm.}^2.$$

The extensional and Rayleigh wave velocities, measured by the pulsing technique, were sufficient in themselves to obtain the two elastic constants. However, it was desired to verify the method by obtaining the third velocity, involving as it did a different experimental approach and measurement of the wave velocity rather than the group velocity. The agreement obtained is most gratifying.

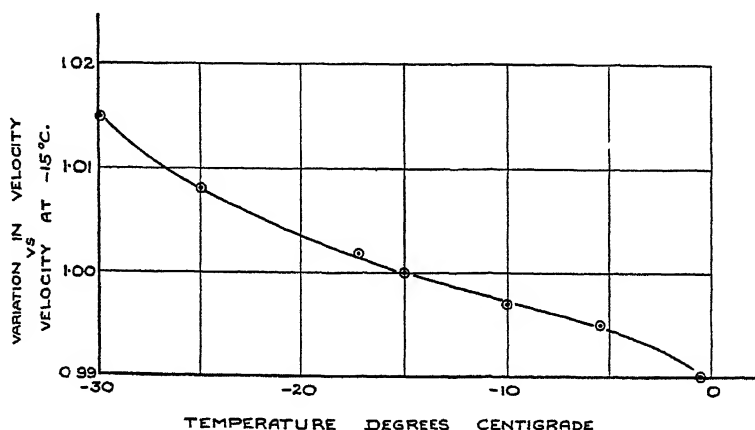


FIG. 2. Variation in longitudinal velocity with temperature.

The variation in longitudinal velocity with temperature is shown in Fig. 2. It will be seen that the velocity decreases very slowly with increasing temperature in this range.

## Absorption

As mentioned above, the pulsing frequency used in the extensional velocity measurements was limited by reverberation, due to multiple reflections within the ice. In some preliminary work on similar samples of duralumin the reverberation was much worse, and it was therefore concluded that the absorption of the wave in ice was much greater than in duralumin. This suggests the possibility of measuring absorption in solids by applying the ordinary reverberation theory used in architectural acoustics.

It was also observed that the absorption increased greatly as the temperature approached the freezing point.

Reference should be made to the possible effect of dispersion on the pulsing experiments, since group velocities were measured. This subject has been thoroughly dealt with by several investigators (5), and it is known that certain boundary conditions give rise to selective absorption and dispersion. Such conditions were, of course, avoided in the present work. Inspection of the received 300 kc. pulse showed experimentally that no dispersion occurred.

## Comparison with Previously Published Results

A wide variety of values for the elasticity of ice have been given by various investigators. Most of the early measurements were made by static methods, and the results were so scattered that there appears to be something inherently wrong with the method (6, 7). Dorsey (2, pp. 444, 398-417) suggests that plastic flow may occur in ice at even the most moderate static loads, thus invalidating the static measurements. However, this does not explain the statical experiments of Koch (7), who, after obtaining two sets of results that did not agree, repeated the work with the same apparatus but with extreme caution about temperature variations. He then obtained a value of Young's modulus that agrees very well with recent sonic measurements.

It is probable that a great deal of the variation could be attributed to the effects of varying temperature. Most of the early work was done only a few degrees below the freezing point, and was dependent upon winter weather for maintaining a steady temperature. In these circumstances the samples were probably subject to a certain amount of thawing from time to time, and would by no means be the perfect single crystals that they were assumed to be. And whereas the sonic method is relatively insensitive to small inhomogeneities, the static method depends greatly on uniformity of the sample throughout.

The most complete sonic measurements of Young's modulus appear to be those of Boyle and Sproule (1), who measured the resonant frequencies of rods, much as was done in the present work. Their results are shown in Table I. They agree substantially with the present work at  $-15^{\circ}\text{C.}$ , although greater variation with temperature was noted.

The authors remark that they also were handicapped by dependence upon outdoor weather conditions, and that there seemed to be a time lag in the

TABLE I  
VALUES OF YOUNG'S MODULUS

Author	Ref.	Temp., ° C.	Orientation of rod with respect to freezing surface	$E$ , dynes/cm. <sup>2</sup>
Koch	(7)	Not stated	Parallel	$9.4 \times 10^{10}$
			Perpendicular	11 2
Boyle and Sproule	(1)	-35	Perpendicular	10 9
		-30	"	10 2
		-10	"	9.48
		- 9	"	9 28
Ewing, Crary, and Thorne	(3)	0 to -5	Average of parallel and perpendicular samples	9 17
Author's value	—	-15	Various	9.8

change in  $E$  with temperature. This might have been attributed to the slowness of the interior of a sample to arrive at a new ambient temperature, but it was noted that the effect was equally noticeable in large and in small samples. Hence, it would rather appear to be a slow structural change in the ice that occurred after a change of temperature.

In the present work, a similar phenomenon was observed. Results obtained immediately after a temperature change were quite erratic. Hence measurements were made several hours after the temperature had changed.

Measurements were also made by Boyle and Sproule of the variation in elasticity with crystal orientation. However, the variation with orientation appeared to be less than that from sample to sample. Possibly a significant difference could be found if the temperature were held constant.

Work done by Ewing, Crary, and Thorne (3) for temperatures between 0° and -5° C., gives slightly lower results than those of Boyle and Sproule. These are also included in Table I.

From these various results and those reported in the present paper, it would appear that ice is highly susceptible to thermal effects, at least in the range -30° to 0° C. The elasticity seems variable during a period of temperature change, but under steady-state conditions there is no great change with temperature.

In this connection, Dorsey (2, pp. 444, 398-417) has collected a great variety of opinions on the physical structure of ice that illustrate the difficulty of understanding even this relatively simple and very common material. It is considered that the supersonic pulsing scheme used here, combined with a temperature controlled test chamber, would be a useful tool for a detailed investigation of the structural nature of solids, especially near their critical points.

### Acknowledgment

The author wishes to acknowledge the advice and criticism of Dr. G. S. Field of this laboratory, whose wide experience with vibrations in solids was called upon frequently during the project.

### References

1. BOYLE, R. W. and SPROULE, D. O. *Can. J. Research*, 5 : 601-618. 1931.
2. DORSEY, N. E. *Properties of ordinary water-substance in all its phases: water-vapor, water and all the ices.* Reinhold Publishing Corporation, New York. 1940.
3. EWING, M., CRARY, A. P., and THORNE, A. M., JR. *Physics*, 5 : 165-168. 1934.
4. FIELD, G. S. *Can. J. Research*, 5 : 619-624. 1931.
5. FIELD, G. S. *Phys. Rev.* 12 : 1188. 1940.
6. HESS, H. *Ann. Physik.* 8 : 405-431. 1902.
7. KOCH, K. R. *Ann. Physik.* 45 : 237-258. 1914.
8. LOVE, A. E. H. *A treatise on the mathematical theory of elasticity.* 4th ed. Cambridge University Press. 1927.
9. RAYLEIGH, BARON J. W. S. *Scientific papers.* Vol. 2. Cambridge University Press. 1900.
10. RAYLEIGH, BARON J. W. S. *Theory of sound.* Vol. 1. 2nd ed. Macmillan, London. 1896.

# THE FOUNDATIONS AND PHILOSOPHICAL IMPLICATIONS OF WAVE MECHANICS<sup>1</sup>

BY SEYUAN SHU<sup>2</sup>

## Abstract

This paper attempts to show:

(a) The nature of the basic assumptions made either explicitly or implicitly by L. de Broglie in arriving at the fundamental formula,  $\lambda = \frac{h}{p}$ , of wave mechanics, and that at least some of these assumptions are open to criticism.

(b) That it is a little too hasty to regard as demonstrated the non-localization of photons or electrons in motion and the lack of determinism with respect to them.

(c) That the presuppositions which lead to the 'relations of incertitude' involve highly arbitrary elements and these 'relations' are read into or arbitrarily imposed upon the physical world rather than really found to be in it.

(d) That it is an unwarranted claim that the new mechanics can contribute to the solution of the age-long philosophical problem of free will.

(e) That it is possible to render the foundations of wave mechanics logically independent of the theory of relativity.

## I. The Basic Ideas of Wave Mechanics

Since 1927, experimental proofs have been repeatedly obtained by physicists concerning the undulatory nature of electrons (and even of other material particles such as protons and atoms). The scientific world considers therefore as fully established the basic ideas of wave mechanics first propounded by Louis de Broglie during 1923-24. There is no fault to find with these experimental results, nor can one entertain any doubt as to the soundness of de Broglie's main thesis that, like photons, electrons (and indeed other elementary material particles) partake of the nature of waves. But the arguments that de Broglie employs in establishing the formula for the wave-length of a material particle in motion seem to be quite unsatisfactory, and one cannot help deeming highly debatable the foundations of wave mechanics.

De Broglie's formula for the wave-length of a material particle in motion,

$$\lambda = \frac{h}{p},$$

where  $\lambda$  is the wave-length,  $p$  the momentum of the particle, and  $h$  Planck's constant, can be deduced only by admitting as premises the following four propositions:

(1) Einstein's transformation equation for time-co-ordinates,

$$t' = \frac{t - \frac{vx}{c^2}}{\sqrt{1 - \frac{v^2}{c^2}}},$$

is valid.

<sup>1</sup> Manuscript received in original form December 11, 1945, and, as revised, September 16, 1946.

<sup>2</sup> Correspondent Member of the Chinese National Academy, Peiping. Professor of Philosophy, National Central University, Nanking.

(2) Einstein has really proved that all material body of mass  $m_0$  has an energy content equal to  $m_0c^2$ .

(3) The letter  $W$  in Einstein's formula for the photon,  $W = fh$ , must be interpreted as representing not only the kinetic energy of the photon but also its internal energy. (Einstein deduces from his formula  $W = fh$  another formula,  $p = \frac{fh}{c}$ ,  $p$  being here the momentum of the photon, by assuming  $W = \frac{m_0c^2}{\sqrt{1 - \frac{v^2}{c^2}}}$ . But one can also derive the formula  $p = \frac{fh}{c}$  from the formula

$W = fh$  by regarding  $W$  as consisting of nothing but kinetic energy, for the 'internal energy' of a photon does not differ practically from zero.)

(4) The energy (kinetic and internal) of a material particle in motion, which is taken to be equal to  $\frac{m_0c^2}{\sqrt{1 - \frac{v^2}{c^2}}}$ , must be equal to Planck's constant multiplied by the frequency of its associated wave.

(A)

Here we shall discuss the first point. If Einstein's special theory, or more precisely, Einstein's transformation equation for time-co-ordinates were wrong, it would be impossible for de Broglie to obtain for the phase velocity of the associated wave the formula  $V = \frac{c^2}{v}$  from which the formula  $\lambda = \frac{h}{p}$  is derived. In fact, de Broglie would then be utterly unable to obtain any formula at all for the so-called phase velocity of a material wave. If it should prove impossible to establish such a formula, there would be lacking at least one of the theoretical foundations for wave mechanics. It has been elsewhere shown (8, Chaps. III and VII) in detail that one is bound to reject Einstein's Special Theory as contrary to concrete reality, and the arguments will not be repeated here.

(B)

With regard to the second point, it must be said that the assertion that a material body of mass  $m_0$  has an energy content of  $m_0c^2$  is an altogether unwarranted extrapolation, far from being a logical consequence of Einstein's Special Theory. Even if one accepts the Special Theory, one can yet refuse to credit such an assertion. For the above assertion to be valid one has to show beforehand that all matter with its elementary constituents, such as neutrons and protons, could be *entirely* transformed into radiant energy with no residue of matter or 'mass at rest'. Clearly, there is no justification for such a statement. It seems likely that a pair of electrons of opposite sign can be transformed into a photon, but the same thing cannot be said of neutrons and protons. In the observed phenomena of material radiation, the protons emitted still preserve their mass  $m_0$ , which is not transformed into energy. There is not the slightest empirical basis for the affirmation that the

mass  $m_0$  of a proton or a neutron could be converted into a sum of radiant energy equal to  $m_0c^2$ . As the mass of a material object consists almost entirely of its protons or neutrons, evidently it would be idle talk to pretend that all matter could be transformed into energy. (It has been observed that certain stars during their long course of evolution have lost nine-tenths of their original substance. This forms, however, no decisive argument in favour of the possibility of converting protons and neutrons into radiant energy. Stars may have lost part of their substance in protons, neutrons, etc., through material radiation, but there is no indication whatever that these elementary material particles have become either photons or pure mechanical energy.)

In the article first published in 1905, *Does the Inertia of a Body Depend on its Energy-content?* (6, pp. 69-71), Einstein claims to have proved that after an emission of luminous energy equal to  $L$  a material body at rest will lose a quantity of mass equal to  $\frac{L}{c^2}$ . This result is generally regarded as the basis for the assertion that a body of mass  $m_0$  has an energy content equal to  $m_0c^2$ . Now, according to the present writer, the 'proof' given by Einstein in the above-mentioned article is altogether unsatisfactory. Einstein has not really succeeded in showing that a quantity of radiant or luminous energy equal to  $L$  possesses a mass equal to  $\frac{L}{c^2}$ . (One could justify the assertion that an amount of luminous energy equal to  $L$  possesses a mass equal to  $\frac{L}{c^2}$  as being a logical consequence of Lorentz's formula concerning the variation of mass as a function of velocity only by assuming that luminous energy is nothing but a transformation of subatomic *kinetic* energy.) Strictly speaking, Einstein has not been able even to show the inertia of light. Still less is there any ground for the belief that Einstein has proved that matter, or the mass of a body, could be entirely transformed into energy. If there is no theoretical support for such a belief, one has to reject as groundless the assertion that a body of mass  $m$  has an energy content equal to  $m_0c^2$ .

Even if the 'proof' were rigorous, it could not be applied to the case of material radiation. In this case the protons or neutrons radiated still preserve their 'mass at rest', which is neither transformed into photons nor into pure mechanical energy, while in the case of electromagnetic radiation (including the radiation in the form of visible light) the 'mass at rest' of photons is generally taken to be zero. In the so-called proof, the letter  $L$  must represent an energy with no residue of any 'mass at rest'; hence its inapplicability to the case of material radiation, unless it could first be shown that protons or neutrons were capable of being entirely transformed into photons or into pure mechanical energy.

Einstein believes that in his article, *Does the Inertia of a Body Depend on its Energy-content?*, he has proved that a quantity of radiant energy equal to  $L$  possesses a mass equal to  $\frac{L}{c^2}$ . The 'proof' given in this regard is, as we

have said, quite unacceptable. It is far from rigorous, though it seems to be perfectly so. The premises which Einstein uses are:

(1) A certain quantity of radiant energy, if it is  $L$  when measured with reference to a 'stationary' system, will be  $\frac{L}{\sqrt{1 - \frac{v^2}{c^2}}}$  when measured with reference

to a system possessing the velocity  $v$  (Doppler effect).

(2) A quantity of kinetic energy equal to  $E$  possesses a mass equal to  $\frac{E}{c^2}$ .

The present writer wants to point out that it is illogical to base the proof on the above two premises. In fact, no deduction from these premises could justify even the assertion that radiant energy possesses mass. (It must, however, be remarked that what we reject is the proof given by Einstein; there is no reason to doubt the inertia of radiant energy. It is certain that radiant energy possesses mass, and it is also very likely that a quantity of radiant energy equal to  $L$  possesses a mass not differing materially from  $\frac{L}{c^2}$ ).

Let us consider a body emitting a certain quantity of radiant energy. If that quantity is  $L$  when the measurements are made with respect to a system in which the emitting body is at rest, it will be  $\frac{L}{\sqrt{1 - \frac{v^2}{c^2}}}$  when the measurements

are made with respect to a system in which the emitting body moves with a velocity  $v$  (here one presupposes the validity of the Lorentz transformation). This difference is due to the Doppler effect. We shall now consider it from the point of view of the second system. The body moves with the velocity  $v$ , and the sum of radiant energy it has emitted is  $\frac{L}{\sqrt{1 - \frac{v^2}{c^2}}}$ . Since the notion

of internal energy is based on the phenomena of radiation and at least a part of radiant energy must be regarded as being but a transformation of internal energy, the internal energy of the emitting body must have naturally decreased after the body has emitted a quantity of radiant energy equal to  $\frac{L}{\sqrt{1 - \frac{v^2}{c^2}}}$ .

But has its kinetic energy also somewhat diminished after the emission? Has one any right to consider the quantity of radiant energy equal to  $L \left( \frac{1}{\sqrt{1 - \frac{v^2}{c^2}}} - 1 \right)$  as being entirely or at least in part but a transformation of a

portion of the kinetic energy of the emitting body which moves with the velocity  $v$ ? (The expressions for the same quantity of radiant energy differ according to whether the emitting body is at rest or in motion; the difference between the two cases is  $L \left( \frac{1}{\sqrt{1 - \frac{v^2}{c^2}}} - 1 \right)$ , which sum may therefore be con-

sidered as being due to the velocity  $v$ .) To the two above questions, if one knows the facts, one ought certainly to answer in the affirmative, because in point of fact radiant energy does possess mass. But premises (1) and (2) contain absolutely nothing that might justify one in doing so. From these premises it is impossible for Einstein to draw the conclusion ( $a$ ) that any emission of radiant energy must have caused a diminution of the kinetic energy of the emitting body (or that a part of the radiant energy  $\frac{L}{\sqrt{1 - \frac{v^2}{c^2}}}$  must

be due to kinetic energy). Einstein has therefore not the slightest justification for making the further conclusion ( $b$ ) that an amount of radiant energy equal to  $L\left(\frac{1}{\sqrt{1 - \frac{v^2}{c^2}}} - 1\right)$  (which is due to the velocity  $v$ ) must be regarded as resulting

from the transformation of a part of the kinetic energy of the emitting body. ("Due to velocity" is not necessarily the same as "due to kinetic energy". This is a very important distinction.) To affirm ( $a$ ) would be the same as to affirm the proposition ( $a'$ ) that radiant energy possesses mass. To affirm ( $b$ ) would be the same as to affirm the proposition ( $b'$ ) that a quantity of radiant energy equal to  $L$  possesses a mass equal to  $\frac{L}{c^2}$ , the very proposition that has to be proved. Propositions ( $a'$ ) and ( $b'$ ) can be deduced from ( $a$ ) and ( $b$ ) but not from (1) and (2), the two premises that Einstein has assumed. Premises (1) and (2) are equally consistent with non-( $a$ ) and non-( $b$ ) as with ( $a$ ) and ( $b$ ). In order to arrive at Einstein's conclusions ( $a'$ ) that radiant energy possesses mass and ( $b'$ ) that a quantity of radiant energy  $L$  possesses a mass equal to  $\frac{L}{c^2}$ , propositions ( $a$ ) and ( $b$ ) have first to be supposed as true. ( $a$ ) and ( $b$ ) may well correspond to experiment, but they are to be based upon theoretical and empirical grounds other than those that could be deduced from the Doppler effect plus the special theory of relativity.) But in the proof given by Einstein, there is not the least trace of such a presupposition. So one has to reject his proof as entirely unsatisfactory, and even as fallacious.

Now look at the problem from another point of view. In his article (1905) Einstein seems to take it for granted at the outset, perhaps without being fully aware of it, that the 'internal energy' of a body, which is taken to be the cause of radiant energy, must depend on its mass and on its mass alone. Thus, internal energy is considered as a function of one variable, that is, a function of mass,  $f(m)$ , and as completely independent of the velocity of the body. Now since radiation is a concrete phenomenon, one may admit as legitimate the notion of 'internal energy' (which is to be considered as the cause or source of radiant energy and indeed whose existence is assumed chiefly for the purpose of accounting for the latter). But here one has to deal with an empirical datum, not with a simple question of definition. It would be quite unscientific to determine a priori the factors on which must

depend the so-called internal energy. Of course, one can freely imagine that the internal energy of a body, being the source of radiant energy, may be intimately related to its mass; but until further informed by experimental evidence one has no right to affirm dogmatically that internal energy must be a function of mass and of mass alone. There is not the slightest reason, either theoretical or empirical, which might warrant the assumption that the internal energy must always be the same when measured with regard to different co-ordinate systems. It would be also unjustifiable to affirm that a new sort of energy, if it should depend also on velocity, like ordinary kinetic energy, ought to be called kinetic instead of 'internal'. There is no justification for the omission of the letter  $v$  from the formula for a different sort of energy, simply because it has already appeared in the formula for kinetic energy. The notion of internal energy is based on the phenomena of radiation. It serves rather as an explanation for the phenomena of radiation. The idea is that what manifests itself as radiant energy must already exist as a sort of subatomic energy which is therefore termed internal energy. One calls this sort of energy internal, because one supposes it exists within the atom, but this does not suggest that it must be something constant and independent of all reference systems. (The dependence of internal energy on velocity might be physically false, that is, might be contrary to reality; but logically, it is as conceivable as the dependence of mass on velocity. To a superficial observer, it might seem to contradict the principle of the conservation of energy. But here the contradiction is only apparent, not real. 'Internal energy' is only a possible form of energy; it has not actually become energy, so long as it has not been transformed into radiant energy. The principle of the conservation of energy requires that any actual energy lost by a system must produce work; it does not imply that any possible energy lost must also produce work.) It is only in assuming tacitly the dependence of internal energy on mass and on mass alone that Einstein can deduce the result  $m_0 = \frac{L}{c^2}$  from the two initial equations:  $E_0 = E_1 + L$ ,  $H_0 = H_1 + \frac{L}{\sqrt{1 - \frac{v^2}{c^2}}}$  (see the article to which reference has already been made). If internal energy is a function of both mass and velocity, then one can deduce from the above two equations the following result:

$$m_0 = \frac{L}{c^2} \left( \frac{1}{\sqrt{1 - \frac{v^2}{c^2}}} - \frac{1}{\alpha} \right) / \left( \frac{1}{\sqrt{1 - \frac{v^2}{c^2}}} - 1 \right).$$

(In this formula  $\alpha$  is an undetermined function of  $v$ . A quantity of internal energy equal to  $E_0$  with reference to the system at rest will be  $\frac{E_0}{\alpha}$  with regard to a system possessing the velocity  $v$ .)

It is only in the case  $\alpha = 1$ , that is, only by assuming the independence of internal energy relative to reference systems, that one could, like Einstein,

obtain the formula  $m_0 = \frac{L}{c^2}$ . In fact, Einstein can by no means even arrive at the conclusion that radiant energy possesses mass, because he has no right to assume  $\alpha$  is necessarily different from  $\sqrt{1 - \frac{v^2}{c^2}}$ . At any rate, nothing justifies Einstein in taking for granted that  $\alpha$  must be equal to 1. It is only in assuming  $\alpha = 1$  that one could deduce from the above-mentioned two equations the result that "If a body gives off the energy  $L$  in the form of radiation, its mass diminishes by  $\frac{L}{c^2}$ ". From what has been said above, it will not be difficult to see that if internal energy depends on mass but not on velocity, then propositions (a) and (b) will be valid. On the other hand, if (a) and (b) are valid, internal energy must be independent of velocity. In a word, Einstein believes that, if one takes into consideration the Doppler effect, one could deduce as a logical consequence of the special theory of relativity the conclusion that a quantity of radiant energy  $L$  possesses a mass equal to  $\frac{L}{c^2}$ , whereas the contention of the present writer is that the inertia of radiant energy could not be deduced from the special theory, even when one also accepts the Doppler effect.

(C)

We shall now discuss the third point. It is an experimental fact that the formula for a photon or a light-quantum,  $W = fh$ , agrees well with the measured quantities. But is there any reason to suppose that the letter  $W$  in this formula must be interpreted as representing the kinetic energy of the photon plus its internal energy  $m_0c^2$ ? This interpretation is justifiable only on the condition that one could first establish the proposition that a particle of mass  $m_0$  has an energy content equal to  $m_0c^2$ . As has been shown in the preceding section, this proposition is without the least theoretical support. So one is bound to abandon such an interpretation. In fact, in the case of photons, as far as the magnitude of  $W$  is concerned, it makes no difference whether one interprets  $W$  as representing both the kinetic energy and the 'internal energy'  $m_0c^2$ , or as representing simply the kinetic energy, because the mass at rest of a photon is generally considered as being infinitely small and its 'internal energy', the term  $m_0c^2$ , does not differ practically from zero. It is therefore evident that if the formula  $W = fh$  as interpreted by Einstein agrees well with experiment it must also agree with experiment when one interprets it as representing only the kinetic energy of the photon. But one has to reject Einstein's interpretation, because it involves at least the entirely unwarranted affirmation that a particle of mass  $m_0$  has an energy content equal to  $m_0c^2$ .

We must here add a remark. If one interprets  $W$  as consisting simply of kinetic energy, one can also deduce from the formula  $W = fh$  the other

formula,  $p = \frac{f\hbar}{c}$ , which is generally regarded as being confirmed experimentally by the Compton effect. As the formula  $p = \frac{f\hbar}{c}$  can be obtained without reference to the notion of internal energy, it is plain that the Compton effect can never be considered as constituting a proof for the assertion that a body or a particle of mass  $m_0$  has an energy content equal to  $m_0c^2$ .

## (D)

According to de Broglie, the formula for the energy of a material particle will be the same as Einstein's formula for photons.  $W = f\hbar$ . Here de Broglie is guided simply by analogy. As pointed out above, in the case of photons  $W$  can be interpreted as consisting only of kinetic energy without causing any conflict with experiment. But with regard to de Broglie's formula of the same form, if one is bound to interpret  $W$  as consisting only of the kinetic energy of the material particle, the result would be disastrous for de Broglie's theory (because the wave frequency of the material particle would thus be zero whether the particle be at rest or in motion). De Broglie found it necessary to interpret the letter  $W$  (in his own formula as well as in Einstein's formula for photons) as representing not only the kinetic energy but also the internal energy  $m_0c^2$  of the particle. But de Broglie has no right to make such an interpretation, unless the statement that a particle of mass  $m_0$  has an energy content equal to  $m_0c^2$  could be justified. Now this statement, as has been shown in Section (B), is quite groundless. So one has to reject de Broglie's formula  $W = f\hbar$ ,  $W$  being interpreted by its author

as representing the total energy  $\frac{m_0c^2}{\sqrt{1 - \frac{v^2}{c^2}}}$  of the material particle

It has been pointed out at the beginning of this essay that the fundamental formula of wave mechanics,  $\lambda = \frac{h}{p}$ , can be deduced only by admitting as premises the four propositions, which have been dealt with one by one but none of which appears to be valid. Now if the formula  $\lambda = \frac{h}{p}$  is without real theoretical foundation, the whole edifice of wave mechanics with its whole set of Schroedinger's equations, as well as the formulae expressing the so-called relations of incertitude such as  $\Delta x \Delta p \geq h$ , would be nothing but conjecture.

It cannot be denied that de Broglie's formula  $\lambda = \frac{h}{p}$  does possess some empirical value. What the present writer has tried to do is only to show the emptiness of the reasons given by de Broglie for arriving at that formula. It is therefore de Broglie's theory only that is here repudiated.

It was doubtless a rare intuition to have surmised the undulatory nature of electrons. As in the case of photons, the formula  $\lambda = \frac{h}{p}$  agrees well with

experiment—it has been remarked that this formula can also be obtained without assuming the ‘internal energy’  $m_0c^2$  of a particle of mass  $m_0$ —so de Broglie might on the simple strength of analogy assume this formula to be valid also in the case of electrons. In an address delivered in Stockholm, de Broglie said that with regard to the formula for the total energy of an electron it is “natural” to write it as  $W = fh$ . It would apparently be no less “natural” to write the formula for the wave-length of an electron, directly, as  $\lambda = \frac{h}{p}$ . This would certainly much simplify the matter.

## II. Determinism or Indeterminism

According to the present writer, rigorous determinism is an abstract ideal like a geometrical entity such as a ‘straight line’, or a ‘circle’, etc. Man’s experiments are by their very nature incapable of yielding any proof that rigorous determinism does really exist in nature, just as no experiments can prove the perfect realizability of certain geometrical entities. The possibility of rigorous determinism depends at least on the condition that with respect to every particle in motion one could always speak of it as having a definite position at every particular instant and describing a definite trajectory. Now the utmost one can say is that, so far as ordinary physical phenomena are concerned, their course of evolution seems to observe a rigorous determinism.

The recent developments in microphysics tend to break up the rigid frames of the time-honoured scientific determinism. In fact, the only empirical basis that seems to justify such a radical change of opinion is a series of experiments that seem to indicate that photons (or electrons), even when arriving *one by one* at the interference apparatus, can still produce the phenomena of interference (2, pp. 152-164; 3, pp. 31-36, 61-63). If in these experiments the phenomena of interference are really due to photons (or electrons) which come singly one after another in contact with the apparatus, and if it could also be shown that these photons (or electrons) must have identical initial states—if these two conditions are fulfilled, one is bound to recognize that photons or electrons in motion are not only non-localizable but also essentially ‘non-localized’, and one has to admit frankly that no rigorous determinism exists, at least with respect to photons or electrons in motion. But if only the first of the above two conditions is fulfilled, that is to say, in the case that the initial states of the photons or electrons in question may not be identical, then one may still cherish the hope of being able to determine, from the particular initial states (supposed to be knowable) of a photon or an electron, the particular spot on the posterior screen of the interference apparatus where the photon or electron must finally show itself. In this case a photon or electron in motion could not be considered as non-localizable or non-localized, except when it passes through the two tiny holes on the anterior screen. Still there will always be a mystery, something contrary to expectation, if photons or electrons can arrive singly at the interference apparatus and yet produce the phenomena of interference. For though it must be the tiny

holes that let the photon or the electron pass, yet one cannot maintain that it passes through either one of these two holes. One is forced to admit that when the photon or the electron comes near the two holes it behaves as if it could pass through the two holes at the same time, thus relinquishing, at least for the moment, its particulate nature and becoming 'non-localized'.

In short, if it is empirically certain that photons or electrons possessing identical initial states and arriving singly at the apparatus can produce the phenomena of interference, then the non-localization of photons or electrons in motion must be regarded as proved; and, as the classical scientific determinism is incompatible with the non-localization of particles, one has to abandon rigorous determinism at least with respect to photons or electrons in motion. But who could guarantee the absolute singleness of photons or electrons arriving successively at the apparatus in the experiments and also the identity of their initial states? No doubt, it would be a little too hasty to regard as demonstrated the non-localization of photons or electrons in motion and the lack of determinism with respect to these particles.

### III. The Relations of Incertitude

The so-called relations of incertitude depend at least on the validity of the following propositions:

- (A) What is associated with a particle in motion is not a single monochromatic wave but a group or a packet of superposed monochromatic waves.
- (B) The variations of position and velocity (or momentum) of a particle can be adequately represented by the expansion or contraction of its associated packet of superposed monochromatic waves.

With regard to proposition (A), one must readily acknowledge that "nothing compels us to suppose that the wave  $\Psi$  (the wave associated with a particle) must be a monochromatic wave; it may well consist of . . . the superposition of plane monochromatic waves and forms a train of waves" (4, pp. 198-199). But the reason here given by de Broglie is purely negative. One might say with equal reason: "Nothing compels us to suppose that what is associated with a particle in motion must be a group of superposed monochromatic waves; it may well consist of a single monochromatic wave". One is here free to choose between the alternatives; but, evidently, the supposition that only a single monochromatic wave is associated with the particle is the simpler of the two. De Broglie could give no better reason than the one cited. Another reason has indeed been given but it is not more convincing. It is urged that a group of superposed monochromatic waves is necessarily limited in space, while a single wave can theoretically fill the entire space; so, according to de Broglie, it would seem better to associate with a moving particle a group of waves, instead of a single wave. This argument is certainly not cogent. A wave of infinite extension is but an abstract ideal; every concrete single wave is always limited in space. Every concrete wave has always a

beginning, and within a definite time the wave must have a definite space-limit. There is not the slightest ground to suppose that when one wants to associate a single monochromatic wave with a concrete moving particle, one would have to associate with it an abstract wave of infinite extension, instead of a concrete monochromatic wave of varying dimensions.

With regard to proposition (*A*), the conclusion is as follows:

So far as theoretical considerations are concerned, with a moving particle one may associate a group of waves or a single wave, as one pleases. In this case there is not the slightest reason for preferring a group of waves to a single wave. It is completely arbitrary to associate with the particle a group of waves instead of a single wave, although this arbitrariness does not constitute a valid argument against the procedure.

With regard to proposition (*B*), a little reflection shows that it depends on proposition (*A*) as one of its necessary premises. In fact, proposition (*B*) asserts that a particle in motion, such as a photon or an electron, must have a multiplicity of probable positions and of probable velocities, that is, the particle is not only non-localized but also has no definite velocity. We have analysed the necessary conditions of the notion of the non-localization of photons or electrons. Now, though it would be difficult to regard a non-localized particle as having a definite velocity, yet there is no basis whatever (either theoretical or empirical) for maintaining that a non-localized moving particle must have at every instant a multiplicity of probable velocities. This is not a logical consequence but an arbitrary interpretation of the proposition (*A*) that the associated wave must be a group or a packet of superposed monochromatic waves. Doubtless, it is only because quantum physicists would endow the particle at every instant with a multiplicity of velocities that they have devised the very ingenious and curious method of associating with it a packet of superposed monochromatic waves. But here a sort of arbitrary interpretation is needed for the purpose.

In short, nothing suggests that one must associate with a moving particle a packet of superposed monochromatic waves, and it is certainly no less arbitrary to interpret the artificially introduced packet of monochromatic waves as signifying that the particle in question has a multiplicity of velocities or rather a multiple velocity.

Proposition (*B*) asserts the multiplicity of position as well as the multiplicity of velocity with regard to a particle in motion and also the particular relations between these two multiplicities. Its validity involves necessarily an antagonism of precision concerning the measurements relative to the position and the velocity of an electron in motion. If one accepts as true proposition

(*B*) and also de Broglie's formula  $\lambda = \frac{h}{p}$ , then one can logically deduce from them the well known formulae expressing the so-called relations of incertitude, such as  $\Delta x \Delta p \geq h$ , etc. Briefly, these formulae imply at least the validity of the following assertions:

(1) Photons or electrons, even when such particles arrive one by one at the interference apparatus, can produce the phenomena of interference.

(2) The initial states of the successively arriving photons or electrons mentioned in the preceding assertion are identical.

(3) One must associate with a moving particle a packet of superposed monochromatic waves, instead of a single monochromatic wave.

(4) The fact of its being associated with a packet of superposed monochromatic waves means that the particle has no definite velocity but a multiplicity of probable velocities (or rather a multiple velocity).

(5) De Broglie's formula,  $\lambda = \frac{h}{p}$ , is well founded theoretically.

Now as regards assertion (1), some element of doubt may still be possible because of the extreme smallness of photons and electrons. Can one truly be sure that a certain visible effect is due to the action of a *single* photon or electron without making any hypothesis? Assertion (2) is a pure assumption. Assertions (3) and (4) are also purely arbitrary assumptions. As to assertion (5), though one cannot deny that the formula has a certain empirical value, yet it has been deduced by de Broglie from premises that are certainly fallacious (see Part I of the present essay). So one must infer that the so-called relations of incertitude and the well known formulae expressing them are invalid. There is not the slightest ground for believing them to have been well established either theoretically or empirically. It would be an egregious error to maintain that these 'relations' and the formulae expressing them are the necessary consequences of the existence of the quantum of action. In order to make the matter clearer, it is advisable to add the following remarks.

The existence of the 'relations of incertitude' was first pointed out by Heisenberg and Bohr, and they have given besides some examples of measurements, each tending, according to them, to show the reality of these supposed 'relations.' Most of the examples given by de Broglie in the 12th chapter of his *Introduction à l'Etude de la Mécanique Ondulatoire* (2, pp. 152-164) have been advanced by Heisenberg and Bohr. Now, according to the present writer, it is impossible to arrive at the relations of incertitude without first making the assumption, among others, that the associated wave is not a single monochromatic wave but a group of superposed monochromatic waves. Among the examples given by de Broglie, some are logically correct only because in these examples one has made either explicitly or implicitly the above assumption. Where no such assumption is made, the argument must necessarily prove to be false. In the 12th chapter of de Broglie's book the examples given in Sections III and IV all depend on that assumption. In the second section (pp. 167-168) one finds reference to a modified form of the well known theoretical microscope originally conceived by Heisenberg. In this form there is no trace of the above-mentioned assumption, but the argument is certainly false. It states:  $mv_x mv'_x = \alpha \frac{h}{\lambda}$ . Now  $\alpha$  is a magnitude that can be determined, if  $\lambda$  and  $v$  are known (in fact,  $\alpha$  can be as small as one likes),

and it cannot be said to have necessarily an incertitude of  $2\epsilon$ . If the value of  $\alpha$  is known with greater accuracy, obviously here the formula  $\Delta x \Delta p \geq h$  cannot be deduced.

In the first section of the 12th chapter, de Broglie argues in general terms that in the determination of the position of a particle by means of a microscope one must necessarily arrive at the relations of incertitude. We try to show the fallacy involved in his argument.

There are three different conditions:

(1) The modification of position that an electron undergoes as the result of the impact of a photon.

(2) The uncertainty in regard to the position of an electron when illuminated and viewed through a microscope.

Condition (1) must not be confounded with condition (2). They are completely independent.

(3) The modification of momentum of the electron due to the impact of a photon.

If one takes  $\Delta x$  to be the modification of position, then (1), *certainly not* (2), is to be represented by  $\Delta x$ . Condition (2) could be represented by  $\Delta x$ , as in the formula  $\Delta x \Delta p \geq h$ , only on the condition that (2) is to be regarded as the limits of a packet of superposed monochromatic waves associated with the electron. If one does not here assume such a packet of waves, one has to admit that  $\Delta p$ , the modification of momentum of an electron, is in proportion to  $\Delta x$ , the modification of its position. Thus the precisions concerning  $\Delta x$  and  $\Delta p$  would be convergent instead of antagonistic. (In the present example, de Broglie talks of (1), the modification of position, while in fact what he has in mind is (2).)

### Conclusion

The advent of the new mechanics has rendered, according to its initiators, all forms of rigorous determinism untenable. Ever since, many learned people talk passionately about 'indeterminism' (or indeterminacy), but have no very precise ideas. In fact, one can attach at least three different meanings to the same word 'indeterminism' with regard to the new mechanics:

(1) According to de Broglie (4, p. 125) an experiment, carried out by Taylor, shows that interferential phenomena can be produced by photons that come singly one after another into the apparatus. If the usual interpretation of this experiment is correct, then a single particular photon (or electron), when it encounters no material body, or at least when it comes into the neighbourhood of the two tiny holes pierced on the fore-screen of the interference apparatus, will cease to behave as a localized particle and will manifest only its undulatory aspect. (For, if the photon or electron in question is then still a particle, it ought to traverse one and only one of the two holes, but experiments seem to prove that the photon or electron may have come to the other side of the screen through the two holes at once, yet without

having passed *through* either of these holes.) According to the accepted interpretation of the Taylor experiment (or any similar experiment with electrons), one has to recognize that photons (or electrons) are, sometimes at least, not only non-localizable but also non-localized. Now rigorous determinism requires first of all that one can speak of a particle or a material body as occupying a definite position at any given instant. According to J. J. Trillat (9, pp. 23-32) the undulatory nature is not peculiar to photons and electrons; even protons and neutral atoms behave like waves. If one supposes that the protons and atoms imprisoned in a material body do not differ essentially from those concerned in radiation, one would then have to admit that not only elementary particles but also physical bodies are not always strictly localized, which admission might be considered as a fatal blow to rigorous determinism. Thus one might speak with some apparent reason of indeterminism, when one deems as being proved by facts the non-localization of photons and material particles.

(2) But, when one speaks of indeterminism, what one has in mind may be not only the non-localization of particles; one might also take it for granted that the photons or electrons which come one by one into the interference apparatus must all be identical with respect to their inner structures, initial states, etc. Consequently one has to accept not only indeterminism but also essential probabilism, or rather to consider this sort of probabilism as forming a part of indeterminism. Thus understood, the word 'indeterminism' will have a richer content than has been envisaged in the preceding case.

(3) Still, one might prefer to base the doctrine of indeterminism on Heisenberg's relations of incertitude. Understood in this sense, the term 'indeterminism' will appear to be yet richer in content, for then it must involve as its premises not only the non-localization of particles and essential probabilism, but also other assumptions. We readily acknowledge that rigorous determinism is incapable of any empirical proof; but the arguments for indeterminism are at least equally far from convincing. To be able to arrive at the relations of incertitude, one has to make a large number of postulates, none of which is entirely justifiable. One can maintain a sort of essential probabilism only on the condition that one presupposes the absolute identity of photons (and also of electrons), which is evidently an altogether unwarrantable assumption. In fact, the mechanism of radiation yet remains unknown. Photons (and also electrons) individually may be very dissimilar; the structures of these particles may be no less complex than those of living organisms. At the present stage of scientific knowledge it would certainly be rash to affirm that photons (or electrons) passing through an interference apparatus can be identified with respect to their size, structure, initial state, etc. So nothing compels one to accept as scientifically established that sort of essential probabilism concerning the eventual localizations of photons or electrons in motion.

In what concerns the phenomenon of radioactivity, which one among the myriads of atoms will next explode is regarded by some physicists of the

newest school as a problem of pure probability. According to these scientists, though the average life of a particular atom can be calculated fairly accurately, yet there is absolutely no reason why one atom among the myriads should explode earlier than another. In their opinion, the myriads of atoms, of which some explode at this very instant and others will explode only thousands of years hence, are absolutely identical with respect to both inner and outer conditions. The present writer cannot but think this supposed identity to be pure conjecture. It would certainly be more reasonable and more discreet to recognize that there must be an adequate reason why a particular atom explodes just at this instant and at no other. The fact that people do not at present know anything about such a reason does not mean that it is non-existent. At least there is no reason to believe that all atoms, electrons, and photons should belong to the same pattern and be absolutely identical. To accept as true a sort of inherent and fundamental probabilism with respect to the localization of photons or electrons, or with respect to the explosion of particular atoms, would be the same as to declare that so far as certain micro-physical phenomena are concerned no determining factors can ever be assigned, that is, the principle of sufficient reason must be here in default (which would mean that an event might happen without an adequate cause). Plainly, it would be more prudent to avoid such an extremist attitude, and it would be more in the interests of science to avow one's ignorance as to the causes by which certain phenomena are produced than declare such causes to be non-existent.

As to the non-localization of photons (or electrons), all depends on the interpretation of the Taylor experiment. Since photons (even if such particles do exist as individuals) are inconceivably small, could one be sure that certain interferential phenomena are really produced by photons which come singly one after another into the apparatus? At least some doubt is here permissible. One might put also the question whether the elementary particles (such as electrons, protons, etc.), when regarded as the constituents of a material body, are the same as those in the free state. From the fact that there are no photons as individuals within the atom, one might argue by analogy that there are no electrons as individuals within the atoms. One might perhaps conceive the photons, electrons, etc. (which are capable of interferential phenomena), as a sort of physical entity separate and distinct from matter, and in any case as not being the elementary constituents of material bodies. If one could thus argue, the indeterminism of particles in the free state would be inapplicable to material bodies and their constituents. In fact, one might reasonably consider photons, electrons, etc., as belonging to a particular class of physical entities that behave under certain conditions like waves and under others like particles; they are at times *exclusively* waves and at others *exclusively* particles. If they are sometimes not localized, it is simply because they are then not particles—there is nothing surprising in this. When they are waves, they must be considered as being nothing but waves. Clearly, the simple truism that waves are waves, not particles, must not be turned

into an argument for indeterminism. (If one considers a photon in propagation to be exclusively a sort of wave, it may well come to the other side of the screen of an interference apparatus without having had to choose one of the two tiny holes in the screen for its passage through.)

Our conclusion is: Though no experiment can ever establish rigorous determinism, just as no experiment can prove the perfect realizability of geometrical entities such as straight lines or planes (because principles or ideas created by the mind aim at absolute precision, the very condition unobtainable in experimental work), yet the arguments the new physicists can offer for indeterminism contain invariably some arbitrary or even artificial elements, which render these arguments far from convincing.

## APPENDIX I

### COMMENTS AND CONTROVERSIES

#### (A) *Sir A. S. Eddington*

According to Sir A. S. Eddington, determinism has been definitely disproved by the so-called relations of incertitude. The foregoing essay has pointed out the arbitrary and artificial elements which are involved in the premises of these relations. Yet Eddington's chief grievance against determinism is not that it has been found incompatible with the new mechanics. He thinks the belief in determinism to be utterly unfounded and gratuitous and holds the opinion that the physicist is not acquainted with a single law in the physical world that might justify the belief in determinism (5, p. 11).

Now, though determinism (as opposed to essential probabilism) or the principle of causality cannot be rigorously proved by experiment (Eddington is not exacting in this regard), yet one is bound to accept it as the fundamental principle of scientific knowledge. No science is possible without admitting as true the principle of causality in one form or another. So far as wave mechanics is concerned, indeterminism or probabilism (inherent and fundamental) may mean that, in the microscopic world, the principle of causality (which may be regarded as affirming that identical causes must produce identical effects) is no longer valid. In the foregoing pages the writer has dwelt on the fragility of the reasons given in support of the essential probabilism and the so-called relations of incertitude. If one adheres to this sort of probabilism the following question naturally presents itself: Is this probabilism rigorous or not? There are three possible answers: (1) It is absolutely rigorous, (2) sufficiently rigorous, or (3) not rigorous at all. An example will be given to make this clear.

We shall, first of all, elucidate somewhat the meaning of probability in connection with that sort of essential probabilism envisaged by the new microphysics. In what concerns the play of heads or tails, for instance, the use of the theory of probability does not mean that there is no certainty or no strict determinism; it is simply an extremely convenient and also the only possible method of calculation, in view of the complexity and minuteness of

the causes. This differs completely from the inherent and essential probabilism of the new microphysics. According to the latter, for a particle, such as a photon or electron, to appear finally at a particular point is a question of pure probability; even should one know all the possible data concerning the physical world at that instant, one would still be unable to predict with certainty the behaviour of a single photon or electron; here the probabilism must be regarded as inherent in the nature of things. If the probability that an individual photon (or electron) will appear at a certain point is calculated to be  $\frac{1}{n}$ , it is not at all certain that among  $n$  identical photons one will eventually arrive at that point; but when an extremely great number, say a billion, are concerned, one can be pretty certain that almost exactly the fraction  $\frac{1}{n}$  of this number of photons will show themselves at that point. The movement of an individual photon is entirely unpredictable; one cannot explain why it appears precisely there and not elsewhere. But in all macroscopic phenomena, the submicroscopic indeterminism is completely masked and everything happens as if there exists rigorous determinism. In pre-quantum physics, even where microscopic phenomena alone are concerned, identical causes must produce identical effects and identical effects must be attributed to identical causes: whereas, according to the quantum school, in the domain of microphysics identical causes may produce very dissimilar effects (for photons or electrons which are assumed to be identical in all respects, when emitted by the same source, will show themselves at different points on the rear screen of the interference apparatus)—so here one is bound to accept a certain kind of indeterminism; but, so far as macroscopic phenomena are concerned, identical causes will produce extremely similar, though not absolutely identical, effects (for, when one is concerned with an extremely great number of photons or electrons, the laws governing the probabilities of distribution are always approximately, if not rigorously, verified)—this explains why for practical purposes all physical phenomena may be considered to be completely determined. One might therefore say that, according to the new mechanics, microscopic phenomena are indetermined, while ordinary physical phenomena are approximately determined. But since macroscopic phenomena are made up of microscopic phenomena, one might regard the latter as having some subtle connection with the laws governing the former. Perhaps even the microphysical world is not indetermined to such an extent as the new physicists suppose. At all events, it is only partially true that the new mechanics is incompatible with determinism. And one has also to recognize that if one accepts the new mechanics the principle of causality seems to be invalidated only so far as microscopic phenomena are concerned, and this principle must be deemed to be at least approximately true with regard to ordinary physical phenomena. (Besides, if one accepts only a sort of probabilism with respect to the localization of photons or electrons and rejects the relations of incertitude, it will be at least logically possible to conceive the laws governing microscopic physical phenomena as rigorously deterministic.)

According to de Broglie, the interferential phenomena in the Taylor experiment are really produced by photons which come singly one after another across the forescreen of the interference apparatus. And according to Eddington (5, p. 12) "by means of an instrument called Geiger Counter, electrons can in fact be counted one by one in the same manner as an observer counts, one by one, the stars in the firmament." If their opinions are reliable in this respect, one has doubtless to regard photons or electrons as endowed with individuality. But, on the other hand, if one gives full credit to Pauli's principle, one must deny individuality to electrons. Perhaps, it would be wise to consider this problem as still unsolved. Langevin would save rigorous determinism with respect to all physical phenomena by denying the individuality of elementary particles, but unfortunately he could give no decisive arguments against results obtained with the Geiger counter or in the Taylor experiment.

*(B) Planck, Langevin, Einstein*

Planck does not think rigorous determinism or the principle of strict causality could be proved, but considers this principle to be the safest guide in scientific research (7, p. 259). Planck is less vehemently anti-indeterministic than Einstein, who regards the very concept of indeterminism as illogical. The latter's opinion is clearly untenable. Rigorous determinism is nothing but one of man's mental constructions. It can neither be proved by experiment nor be deduced by pure logical reasoning. Since determinism has no logical necessity, its opposite, indeterminism, involves at least no logical contradiction. Since determinism is neither empirically nor logically proved, one is bound to admit indeterminism as an idea whose realization is possible at least within certain limits.

People like Langevin and Einstein apparently want to save rigorous determinism at all costs, but the arguments given are sentimental rather than logical. The new physicists, while denying strict determinism to microscopic phenomena, emphasize, however, the fact that, practically, one may regard all ordinary physical phenomena as being subject to a sufficiently rigorous determinism. It would, consequently, be incorrect to consider even the most ardent advocates of the new mechanics, such as Bohr and Heisenberg, to be thoroughgoing indeterminists. Even these two physicists cannot dispense with a sort of approximate determinism. It is not the indeterminism with respect to microscopic phenomena, but unlimited and thoroughgoing indeterminism, which would be incompatible with science. (The latter type would deny completely the principle of causality, and, if it should prove to be true, no prediction with regard to natural phenomena would be possible and cosmos would in no way differ from chaos.) The chasm between Langevin and Einstein on one hand, and Bohr and Heisenberg on the other, would be much less wide than the chasm between the latter two and a thoroughgoing indeterminist, to whom scientific laws would be impossible. In short, whether the concrete physical world is subject to strict determinism or not remains in our opinion an open question; yet one may well be assured that wherever there

are mathematical formulae, there must be presumed to exist some sort of determinism.

Among the initiators of indeterminism the most prominent are Bohr, de Broglie, and Heisenberg. It has been shown in the course of this essay that most of the arguments for indeterminism given by the above-mentioned physicists are far from satisfactory. It is now time to point out a very misleading and unfounded affirmation originally made by Bohr and Heisenberg and often thoughtlessly repeated by physicists of the quantum school. They maintain that the principle of indeterminacy and, in particular, the so-called relations of incertitude have arisen from the fact that physical phenomena are inevitably altered by observation, that is, no pure objectivity is possible; they thus attribute a highly metaphysical significance to their doctrine of indeterminism. Nothing supports such an interpretation. The relations of incertitude are entirely contained in the two postulates, namely, the association of a packet of superposed monochromatic waves with a moving particle and the interpretation of the modifications of its position and velocity by the contraction or expansion of the packet. In all this there is absolutely no connection with the age-long metaphysical problem of the objectivity of our knowledge concerning the external world.

## APPENDIX II

### INDETERMINISM AND FREE WILL

The problem of free will is one of the central problems, perhaps the most difficult, of Western philosophy, for it was Kant who said that to solve this problem "centuries have laboured in vain". Since Heisenberg first made known in 1927 his so-called principle of indeterminacy (or relations of incertitude, as de Broglie prefers to call it) not only many idealist philosophers have exulted at the supposed death-blow dealt at the adversary of free will (they have even gone so far as to think indeterminism scientifically proved), but also some prominent scientists have come to hold firmly the opinion that the possibility of moral freedom is for the first time demonstrated by the mathematical formulae of the new mechanics. Sir A. S. Eddington was inclined to think that the year 1927 would mark an important epoch in the development of scientific thought, for, in his opinion, since 1927 religion has become acceptable to a reasonable, scientific mind. One sees how a close relation is supposed to exist between the problem of free will and the principle of indeterminacy of the new physics. Now, according to the writer, this principle, even if it is fully established, does not in the least prove the reality of free will and has in fact nothing to contribute to the solution of that problem.

To refute free will as an objective fact (not the mere consciousness of freedom), one has to make the two following postulates: (1) The world (including living beings) is governed by physico-chemical laws, and (2) all physico-chemical laws are strictly deterministic. If there are non-physico-chemical laws (for example, 'laws of configuration or structure', which might

perhaps be needed to account for the divers behaviours of living beings, if one adopts something like a holistic or emergent-evolutionist point of view), then postulate (1) is denied and one has to admit the possibility of free will, even if postulate (2) is still valid. In case postulate (1) is false and (2) is true, then there will also be possibility but no certainty of free will, for moral freedom might manifest itself as a sort of 'higher' law which would of course conflict with physico-chemical laws but in no way interfere with the supposed rigour of the latter, just as electric force might move a cable car to the summit of Mont Blanc without interfering with the rigour of the law of gravitation. In this case free will is possible, but here it will have nothing to do with the indeterminism of Heisenberg. If postulate (1) is true and (2) is false, then freedom is possible but not certain, it might have its cause in the lack of rigour of physico-chemical laws. Now, if one admits as valid Heisenberg's principle of indeterminacy or the relations of incertitude as well as postulate (1), one has yet no right to regard free will as automatically established. For, according to the new mechanics, indeterminism is manifested only in individual submicroscopic phenomena; with respect to macroscopic physical phenomena there exists a sufficiently rigorous determinism. Now indeterminism limited to the domain of microphysics does not permit freedom of will, unless here one supposes the existence in nature of a non-physico-chemical principle which could reinforce and enlarge the microscopic indeterminism. But such a principle is denied by postulate (1). It is evident that so long as one assumes postulate (1) to be valid, Heisenberg's relations of incertitude are unable to establish the possibility of free will. If one rejects postulate (1), then one ought to admit the possibility of free will, even if Heisenberg's doctrine is refuted. One has therefore to repudiate as groundless the affirmation that the alleged indeterminism with respect to individual microphysical phenomena is to be regarded as a scientific argument for moral freedom.

If the principle of causality should be completely denied, then no phenomena could be explained or predicted, and there would exist no connection whatever between physical events (one would thus have to accept universal freedom or chaos, not merely the freedom of will, for in the complete absence of causality any phenomenon could succeed any other phenomenon). Yet this would be, evidently, also incompatible with the relations of incertitude.

### APPENDIX III

#### CAN WAVE MECHANICS BE RENDERED INDEPENDENT OF THE THEORY OF RELATIVITY ?

The equations (of propagation) of wave mechanics may assume two forms, one non-relativistic, proposed by Schroedinger, and the other relativistic, advanced by Dirac. But whatever form they assume, its basic ideas must have, according to de Broglie, an intimate connection with Einstein's theory. In the first section of the present essay a complete analysis has been given with regard to the presuppositions that de Broglie has made in order to

arrive at his equation for the energy of an electron in motion:  $\lambda = \frac{h}{p}$  (the equation that serves as the foundation of wave mechanics). De Broglie accepts in this regard: (i) the Lorentz transformation equation for time-co-ordinates, (ii) the assertion that a body of mass  $m_0$  has an energy content equal to  $m_0c^2$ , and (iii) Einstein's interpretation of the letter  $W$  in the equation (for a photon or light-quantum)  $W = fh$ , while (iv) he asserts that by reason of analogy it is very natural to write the equation for the energy of an electron in motion also as  $W = fh$ .

It has been shown in Section I that there is no reason to accept the first three points, and that one might regard the letter  $W$  in Einstein's equation as representing only kinetic energy. As to the fourth point, inasmuch as de Broglie thinks it very natural by reason of analogy to write the equation for the energy of an electron in exactly the same form as Einstein's first equation for photons; one may by the same reasoning write the equation for the wave-length of an electron directly as  $\lambda = \frac{h}{p}$  (which is Einstein's second equation for the photon derived by him from the first). This procedure would certainly be no less natural. Thus one might arrive at the fundamental equation of wave mechanics without making the three above-mentioned premises. In case these three premises should prove unjustifiable, it would still be possible to preserve that fundamental equation; and one might speculate on the possibility of rendering the bases of wave mechanics wholly independent of relativity.

Doubtless, all relativists would declare unanimously the impossibility of detaching the bases of wave mechanics from the theory of relativity. It would doubtless be urged that Einstein's second equation (concerning the wave-length of a photon),  $\lambda = \frac{h}{p}$ , could be deduced from the first equation  $W = fh$  (no matter how one interprets the letter  $W$ ) only by assuming the validity of the Lorentz transformation. According to the writer, this opinion, though apparently well founded, is contestable. To deduce the equation  $\lambda = \frac{h}{p}$  from the equation  $W = fh$ , Einstein has to make use of the equation

$$W = \frac{m_0c^2}{\sqrt{1 - \frac{v^2}{c^2}}} \quad \left[ \text{or } E = m_0c^2 \left( \frac{1}{\sqrt{1 - \frac{v^2}{c^2}}} - 1 \right) \right],$$

and it is indispensable for him to suppose the dependence of mass on velocity which is a consequence of the Lorentz transformation. There is no doubt that the increase of mass in proportion to velocity is a law that has been amply verified by experiment, and one might regard it as a fundamental physical fact. But this dependence of mass on velocity is no theory but a fact discovered several years before the special theory of relativity was first announced. One has certainly the right to contemplate it apart from relativity and, as it is a fact, also apart from all scientific theories (including Lorentz's theory). It

has been shown (8, Chap. III) that one must reject the special theory of relativity, and it has also been made clear (8, Chap. I) that if Einstein's theory is incorrect, Lorentz's must automatically be rejected. But the increase of mass in proportion to velocity is, let it be repeated, no theory but a fact that cannot be denied. It might well be a fundamental fact, irreducible and irrational. Anyhow, there is absolutely no need to 'explain' it by a false theory or to regard it as one of its 'verifications'. When some physical facts seem to be more or less fundamental, one must either accept them such as they are (because really fundamental facts do not admit of further explanations), or avow frankly one's ignorance for the moment with regard to their possible explanations. Now, if mass should be deemed to be something constant as in classical physics, then from the first equation for photons,  $W = fh$ , one would derive the second equation as  $\lambda = \frac{1}{2} \frac{h}{p}$ , which is certainly incorrect, since the variability of mass has been empirically proved. But one may write the second equation for photons as  $\lambda = k \frac{h}{p}$  ( $k$  is here an unknown constant), and by reason of analogy one may assume this equation to be valid for electrons also. Now  $k$  must be greater than  $\frac{1}{2}$ , at least this is certain. As to its exact magnitude, experience alone can determine it. To all appearances, it is approximately 1 (as C. Guye's experiments seem indirectly to show), but one is unable to say that it must be 1, unless one accepts either Lorentz's or Einstein's theory. (It must be remarked that from Lorentz's or Einstein's theory one can deduce the formula  $k = 1$ , but not the converse). But one will certainly be justified in assuming  $k = 1$ , at least provisionally, as a conclusion directly based on facts. Thus one can render the bases of wave mechanics wholly independent of relativity. (Einstein's theory is decidedly unsatisfactory, but the variation of mass as a function of velocity is a fact. When one deals with particles having an extremely great velocity, doubtless one has to adopt something like the relativistic equations.)

### References

1. BROGLIE, L. DE. *Matière et lumière*. Albin Michel, Paris. 1937.
2. BROGLIE, L. DE. *Introduction à l'étude de la mécanique ondulatoire*. Hermann et Cie, Paris. 1930.
3. BROGLIE, L. DE. *Continu et discontinu en physique moderne*. Albin Michel, Paris. 1940.
4. BROGLIE, L. DE. *La physique nouvelle et les quanta*. Flammarion Fils, Paris. 1937.
5. EDDINGTON, A. S. *Sur le problème du déterminisme*. Hermann et Cie, Paris. 1934.
6. EINSTEIN AND OTHERS. *The principle of relativity*. Methuen & Co., London. 1923.
7. PLANCK, M. *Wege zur physikalischen Erkenntnis*. S. Hirzel, Leipzig. 1934.
8. SHU, S. *Etudes critiques sur la théorie de la relativité*. Bosc et Riou, Lyons. 1942.
9. TRILLAT, J. J. *Les preuves expérimentales de la mécanique ondulatoire. La diffraction des électrons et des particules matérielles*. Hermann et Cie, Paris. 1934.



# Canadian Journal of Research

Issued by THE NATIONAL RESEARCH COUNCIL OF CANADA

VOL. 25,

MAY, 1947

NUMBER 3

## A NOTE ON THE ELECTRON MICROSCOPE EXAMINATION OF GREASES<sup>1</sup>

BY S. G. ELLIS<sup>2</sup>

### Abstract

A method is described for examining the soap component of lubricating greases with the electron microscope. The soap component is mounted on Formvar films from a dispersion in ether. The specimen is shadow cast by the method of Williams and Wyckoff. The deduction of the shape of the soap particles is discussed.

### Introduction

For the purpose of this note a grease is considered as a suspension of soap particles in oil. The properties of the grease that are of commercial importance, such, for instance, as the viscosity, depend in part on the form, number, and mode of aggregation of the soap particles. These, in turn, depend on the chemical nature of the soap and the thermal and mechanical treatment of the grease during manufacture.

The prime problem to be solved by the electron microscopic examination of the grease is the determination of the size and shape of the soap particles. Since the oil components of the grease, if of sufficiently high vapour pressure, will evaporate in the electron microscope, any conclusions as to the state of aggregation of the soap particles in the grease must be inferred from the micrographs of the residual soap component.

The electron microscopic examination may be considered in three stages, the preparation of the specimen, the production of the micrograph, and the interpretation of the micrograph. This is a subdivision for convenience of discussion, since the deductions made in the last stage must be influenced by what has been done in the previous two stages. For this reason it is desirable, as a matter of practice, for one person to perform all these stages of the work.

### Previous Work

In early work by Drs. Beatrice M. Deacon, L. Newman, and J. H. L. Watson at this laboratory the specimens were prepared by the following method. A film of 'Formvar' about 200 Å thick was formed on a glass

<sup>1</sup> Manuscript received July 3, 1946.

Contribution from the McLennan Laboratory, Department of Physics, University of Toronto, Toronto, Ont. Section D (a) of a thesis submitted in partial fulfilment of the requirements governing the award of the degree of Doctor of Philosophy at the University of Toronto.

<sup>2</sup> Holder of a Fellowship under the National Research Council of Canada, 1945-1946.

microscope slide by the usual method (3). A small amount of grease (less than  $10^{-3}$  cc.) was placed on this film, while it was still attached to the glass slide, and was spread out with either a razor blade or a camel's-hair brush. Alternatively it can be squashed and smeared out with a dust-free microscope cover slide. The Formvar film was then cut, floated off on to water, picked up and transferred to a 200 mesh screen, with the grease side away from the screen. The films were manipulated to bring the edges of the grease smears over the mesh in order to obtain areas thin enough to transmit electrons. Preliminary examination of the mounted specimens under a dark field light microscope at  $\times 100$  aided in selecting suitable mounts. The specimens were examined in the first electron microscope built in this laboratory (2), without the aid of an aperture limiting diaphragm in the objective.

Two difficulties were encountered with this method of mounting. It was not easy to mount the specimens by this method without tearing the Formvar film, and the micrographs were difficult to interpret.

### Later Work

All the micrographs shown in this note are of the same grease sample. It is chosen, here, because it led to unusual difficulties of interpretation. The soap is a calcium base soap.

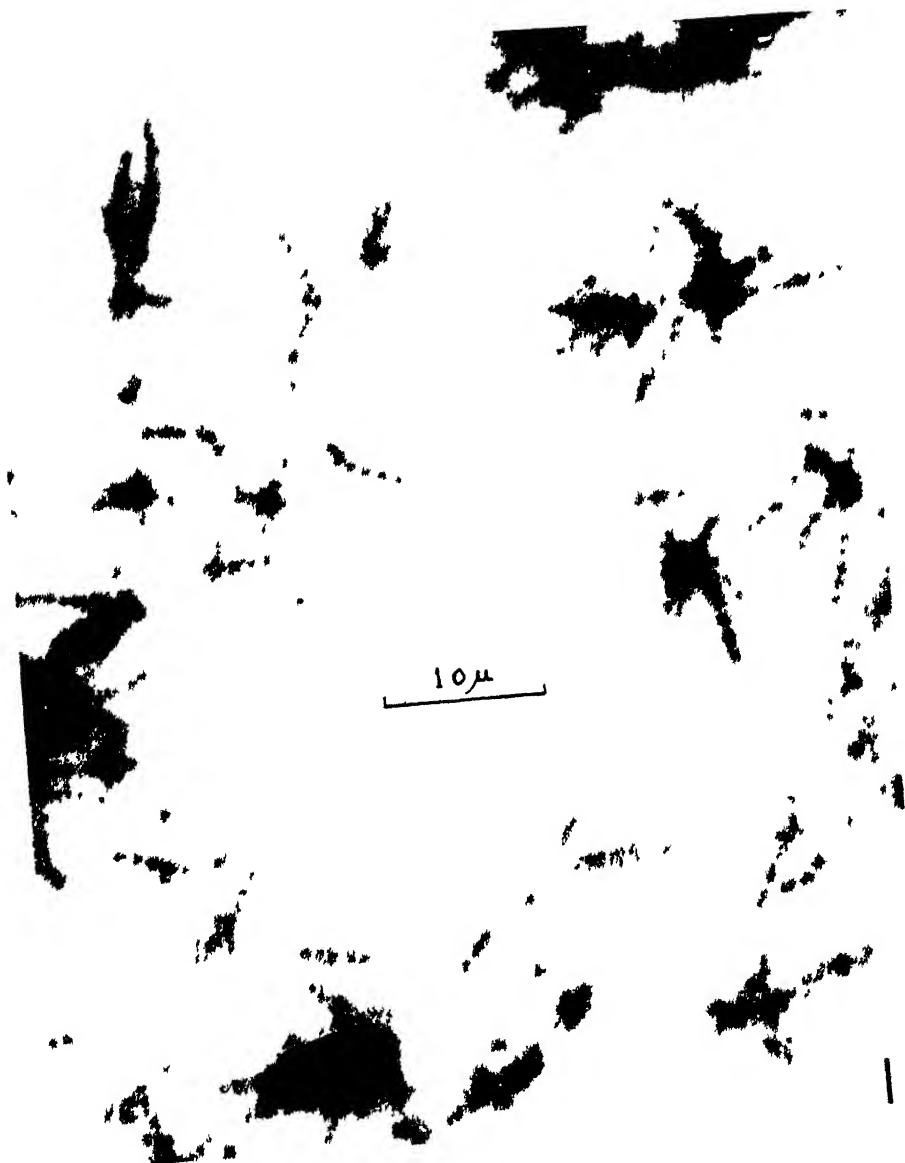
Fig. 1 was obtained by the method described above. It is seen that this soap exists in a fibre form with a periodic variation in either thickness or density along the fibre. From our knowledge of soaps the variation in thickness would appear to be more probable. The spacing of the spots is not uniform but is of the order  $1100 \text{ \AA}$ . The details of the structure are not resolved, and this is not due to optical deficiencies in the microscope, since holes in the film were sharply focused. In some micrographs the photographic density between the spots was the same as that of the general background due to the Formvar film itself.

Since some of the lack of contrast in the micrographs might be due to low vapour pressure components of the oil remaining on the film in the microscope, the grease was mounted from a suspension in ether.

Formvar films,  $200 \text{ \AA}$  thick, mounted on meshes, were attached film up, to a glass microscope slide with small spots of rubber cement.\* These were chilled by inverting the slide over liquid air and leaving them in the cold air above the liquid for a few minutes. Meanwhile some grease (about  $10^{-3}$  cc.) was taken on a needle and shaken with 2 cc. of ether. The slide with the Formvar films was placed on the bench and breathed upon to coat the Formvar with a thin protective film of moisture. A small drop of the ether suspension

\* The dried rubber cement is a good insulator and should not be allowed to enter the electron microscope subsequently.

FIG. 1. Electron micrograph of soap fibres from calcium base grease.





(recently shaken) was withdrawn by means of a micropipette and immediately touched to the top of the Formvar film near the edge before the moisture could evaporate, and was immediately blown upon to promote evaporation of the ether. Close to the point at which the ether first touched the film were areas of film destruction but, outside this, suitable deposits of the soap fibres were found. Dark field examination in the light microscope helped in selecting the best mount for the electron microscope.

These mounts were examined in the new 1944 electron microscope designed by Drs. L. Newman and J. H. L. Watson and constructed in this laboratory (1). In this microscope a diaphragm can be accurately centred to the optical axis of the objective near the exit pupil of the lens while the microscope is in operation. These specimens were photographed at a magnification of  $\times 5000$  in the electron microscope. The resolution in the micrographs obtained with this method of mounting, and with an objective diaphragm, was very little better than that previously attained with smeared preparations and no objective diaphragm. Two types of fibre were observed. That sketched in Fig. 2 was the more common, but a few fibres of the type sketched in Fig. 3 were found on examining several plates.



FIG. 2.



FIG. 3.

By displacing the objective diaphragm laterally to cut off all but the scattered electrons and thereby producing a dark field image, it was observed that the soap fibres scattered electrons not much more than did the supporting film.

Since the structure was still not readily interpretable it was decided to apply the shadow casting technique of Williams and Wyckoff (4, 5). To this end the soap was mounted from ether suspension on top of a Formvar film on a mesh as described above. It was shadow cast with from 60 Å to 100 Å of chromium to produce shadows from two to four times as long as the height of the fibres. Fig. 4 is a micrograph of such a preparation.

The micrographs of shadow cast preparations (Figs. 4 and 8) have been prepared by the following method. Contact positive transparencies have been made from the original negatives produced in the microscope, and the figures shown here are of prints made from the contact positive transparencies. This is done in order to obtain shadows that are dark in the prints and thus enhance the appearance of relief, and simplify interpretation.

The increase in resolution in the micrograph is evident (Fig. 4). The form of the fibres is that of a two stranded rope. Both right- and left-handed spirals are present in approximately equal proportions. When one of the fibres is straight (see *A* of Fig. 4) it produces the type of image sketched in Fig. 3, in the non-shadow cast preparations.

It is interesting to note that images of the form sketched in Fig. 5 have not been observed with either the smeared or the ether-mounted specimens without shadow casting. Yet the mass distribution of a twisted fibre projected on to a plane perpendicular to the beam of the electron microscope is symmetrical about the projection of the axis of the fibre. This can be seen from Fig. 6, which is an X-ray photograph of a model of a fibre made from Plasticine into which brass filings have been mixed. In this sense the images of Fig. 1 are not of the form to be expected from the two stranded fibres shown in Fig. 4.

To resolve this point a specimen of the grease was mounted by the smearing method and photographed (Fig. 7). The sample was then shadow cast with chromium and the same field photographed again (Fig. 8). It can be seen from Fig. 8 that most of the soap fibres are embedded in the Formvar film.



FIG. 5.

Comparing the two plates it is seen that the embedded parts (*B* of Fig. 7 and *C* of Fig. 8) scatter electrons little more than would the Formvar they have displaced. In many fields of the ether-mounted specimens the fibres are similarly embedded in the film. This may be due to a solvent effect of the ether on the Formvar film. In both cases the embedded parts of the fibres, since they scatter electrons little more than the rest of the Formvar film, contribute little to the image formation. Consequently at points such as *B* in Fig. 7, between the spots, the photographic density in the micrograph does not differ greatly from the general background due to the Formvar film. It was this factor that confused the interpretation of the micrographs from non-shadow cast specimens.

Had the preparations been made on silica films it appears likely that this difficulty would have been avoided.

### Location of Fields

The duplication of certain fields of the specimen is best done by mounting the specimen and film on a mesh that has been pierced with three holes as shown in Fig. 9. Nickel or copper meshes are suitable in this application. The holes should be spaced so that they can be seen on the intermediate screen of the microscope. The holes serve both in orienting the mesh in the object cartridge of the microscope, and as reference points for finding any desired part of the specimen. If a sketch map of the image on the intermediate screen is made it aids in finding the same fields again.

FIG. 4. *Electron micrograph of soap fibres from calcium base grease, shadow cast with chromium.*

FIG. 6. *X-ray photograph of model of soap fibre.*

FIG. 7. *Electron micrograph of soap fibres from calcium base grease.*

FIG. 8. *Same field as Fig. 7 after shadow casting with chromium.*

## Conclusions

The conclusions as to the nature of these particular soap fibres have been given above as an illustration of the general method. The more general interpretation of the pictures must be made by co-ordinating these results with those of other experiments on the grease, and by extending the studies to other greases. This will be done in a later paper.

The techniques described here are not limited in their applications to greases alone and may aid in the general study of soaps. The study reported here serves to emphasize the importance of care in the interpretation of electron micrographs. This is particularly the case if the specimen scatters

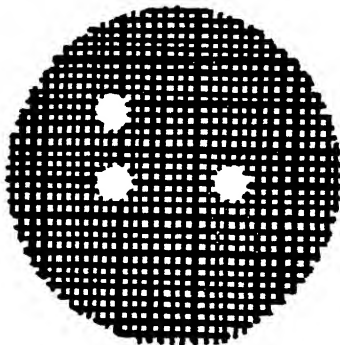


FIG. 9. Screen pierced to aid in duplication of field.

electrons only a little more than does the supporting film, or if the film is cast from a suspension of the particles in a solution of Formvar, and some parts of the particles scatter but little more than the Formvar. It is also evident that the value of the shadow casting techniques is by no means limited to study of very small particles.

## Acknowledgments

The writer has received much encouragement from Prof. E. F. Burton of this laboratory, and from Mr. L. W. Sproule of Imperial Oil Ltd. of Sarnia, Ont. He is indebted to Dr. R. K. Stratford of Imperial Oil Ltd. for permission to publish these results, and he wishes to thank Dr. Elizabeth Allin who aided in the preparation of Fig. 6. Imperial Oil Ltd. made a grant towards this work.

## References

1. BURTON, E. F. and KOHL, W. H. The electron microscope; an introduction to its fundamental principles and applications. 2nd ed. Reinhold Publishing Corporation, New York. 1946.
2. PREBUS, A. and HILLIER, J. Can. J. Research, A, 17 : 49-63. 1939.
3. SCHAEFER, V. J. and HARKER, D. J. Applied Phys. 13 : 427-433. 1942.
4. WILLIAMS, R. C. and WYCKOFF, R. W. G. J. Applied Phys. 15 : 712-716. 1944.
5. WILLIAMS, R. C. and WYCKOFF, R. W. G. J. Applied Phys. 17 : 23-33. 1946.

# THE USE OF HIGH PERMEABILITY MATERIALS IN MAGNETOMETERS. THE APPLICATION OF A SATURATED CORE TYPE MAGNETOMETER TO AN AUTOMATIC STEERING CONTROL<sup>1</sup>

BY L. D. ARMSTRONG<sup>2</sup>

## Abstract

Two types of magnetometers using high permeability materials are described—first, those using a field leaving the material in an unsaturated condition and giving a second harmonic output, and, second, those using the saturated core method, resulting in a peak signal output. The application of the saturated core type magnetometer to the particular problem of an automatic steering control is described in detail.

## Introduction

The principle of the use of high permeability materials in apparatus for the detection of small magnetic fields was used extensively during the war years in both U.S.A. and Canada. This paper is based on work done at the National Research Laboratories in Ottawa on magnetometers using transformers with high permeability, low hysteresis core materials as detection elements. The development and application of the unsaturated core type magnetometer was the work chiefly of Dr. A. C. Young\* and Mr. C. K. Jones\*. The saturated core type was developed and applied to the particular problem of an automatic steering control by the author in conjunction with Dr. D. G. Hurst\*.

Magnetometers are devices for measuring some or all of the following:

1. Direction of magnetic fields;
2. Magnitude of magnetic fields;
3. The gradient of a magnetic field;
4. Changes in any of 1, 2, or 3.

The use of the recently developed magnetic materials of very high permeability yields magnetometers more sensitive than those previously available.

The magnetometers herein described consist of two identical open-core transformers, each having primary and secondary windings that are wound over a core of high permeability material. These transformers are mounted parallel to each other, and the secondary windings connected in opposition to each other. If the transformers are excited by an a-c. voltage applied to the primaries, their output will be modified in the presence of an external magnetic field, owing to the magnetic bias imposed on the core material by the external field. This modified output may then be amplified in a suitable amplifier, and recorded or used as desired.

<sup>1</sup> Manuscript received June 29, 1946.

Contribution from the Division of Physics and Electrical Engineering, National Research Laboratories, Ottawa, Canada. Issued as N.R.C. No. 1538.

<sup>2</sup> Physicist.

\* Physicist, National Research Laboratories, Ottawa, Canada.

There are two general modes of operation used in this type of magnetometer. The a-c. voltage impressed on the primary may be such as to saturate the core material twice during each cycle, or it may be small enough to leave the core always in an unsaturated condition.

For ferromagnetic material operated upon by an alternating magnetic field and in the absence of a steady magnetic field, the flux  $B$  curve may be given by a Fourier series of both sine and cosine odd harmonic terms (1, pp. 173-177).

That is, if  $B$  = the flux density associated with a current  $i = i_0 \sin \omega t$  then

$$B = A_1 \cos \omega t + A_3 \cos 3\omega t + A_n \cos n\omega t \\ + C_1 \sin \omega t + C_3 \sin 3\omega t + C_n \sin n\omega t, \quad (1)$$

where  $n$  is any odd integer.

The addition of a steady magnetic field  $H_0$  results in an unsymmetrical distortion to the original wave form, the equation for which will therefore be modified by the inclusion of even harmonic terms of the form  $K H_0 \frac{\sin}{\cos} 2M \omega t$ , where  $M$  is an integer. By maintaining the flux density of the core material well below saturation and suitably choosing the origin, the higher harmonics become of small effect and  $B$  can be represented to a first approximation by an even function of the form

$$B_1 = A_1 \cos \omega t + A_3 \cos 3\omega t + K H_0 \cos 2 \omega t. \quad (2)$$

For a transformer with the primary winding in the opposite direction

$$B_2 = -A_1 \cos \omega t - A_3 \cos 3\omega t + K H_0 \cos 2 \omega t. \quad (3)$$

Hence, with two transformers connected with primaries in opposition, and the secondaries in series, and so placed that the same steady magnetic field is imposed on both of them, the net e.m.f. is given by

$$E = E_1 + E_2 = \frac{d}{dt} (B_1 + B_2) = \frac{d}{dt} (2K H_0 \cos 2\omega t) \\ = -4K H_0 \omega \sin 2\omega t. \quad (4)$$

This is a second harmonic of magnitude directly proportional to  $H_0$ , the steady magnetic field through the transformers. As may be noted, the phase of the output depends on the direction of  $H_0$  through the transformers, the phase shift being  $180^\circ$  on reversal of the direction of  $H_0$ . Thus, by using a phase sensitive input in an amplifier, the direction of  $H_0$  may be ascertained.

The harmonic distortion of the  $B$  curve on the addition of a constant magnetic field is small for ordinary ferromagnetic materials, and consequently the impressed  $H_0$  must be of considerable magnitude for the output  $E$  to be significantly affected. However, the permeability of permalloy materials is very great in comparison with that of ordinary iron, and the subsequent effect on  $B$  is correspondingly large. Thus, such materials are suitable as cores in equipment for the detection of small magnetic fields or small changes in them.

In practice the output of an unsaturated core magnetometer is a distorted second harmonic chiefly because the equation for  $B$  should contain higher harmonics. As saturation is approached the increasing harmonic content adds in such a way as to form a sharp pulse twice for each cycle of the exciting field, and the sign of the pulse is the same each time but dependent on the direction of the constant field. A more satisfactory explanation of the operation of the saturated core type magnetometer is the descriptive one that follows.

In this mode of operation, which was used in the steering control described later in this paper, the transformers operate on a magnetic cycle that carries the core material through saturation and hence brings it to standard states of magnetization twice during each cycle. This method thus eliminates difficulties due to variations in the permanent magnetization of the two cores

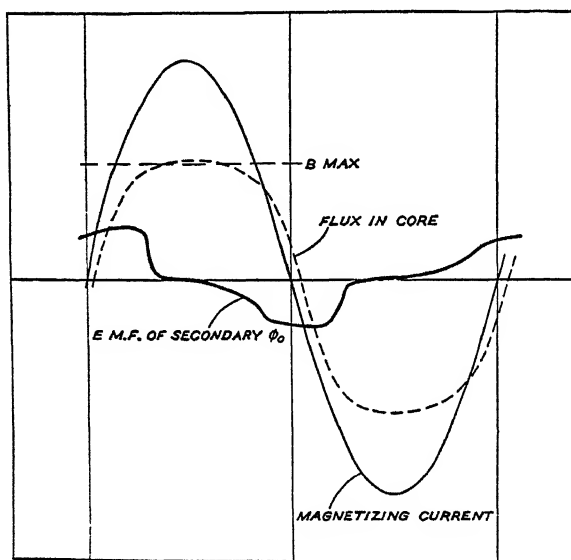


FIG. 1.

Fig. 1 shows a typical magnetization cycle of a core of high permeability material excited approximately to saturation  $B_{max}$  by an exciting field  $H$ . Such a magnetization cycle will induce in the secondary winding around the core an e.m.f. having a wave form approximating the curve  $\phi_0$ . The important feature of the induced e.m.f. is the discontinuity, corresponding to the point  $B_{max}$  (Fig. 1) on the magnetization curve, at which point the induced voltage drops from its maximum value rapidly toward zero.

If now a steady external magnetic field is applied along the direction of the axis of the core, the result corresponds to a magnetic bias such that the magnetizing current required to reach saturation is reduced on one half of the cycle and increased on the other half. While the wave form is not fundamentally changed, a shift in the wave pattern results (Fig. 2), the magnitude

of which depends upon the strength of the applied external field and the steepness of the magnetization curve. The time lag of the induced e.m.f. is slightly advanced in one half of the cycle and correspondingly retarded in the other half cycle, the direction and magnitude of the shift depending upon the direction and magnitude of the external field with respect to the impressed magnetizing force.

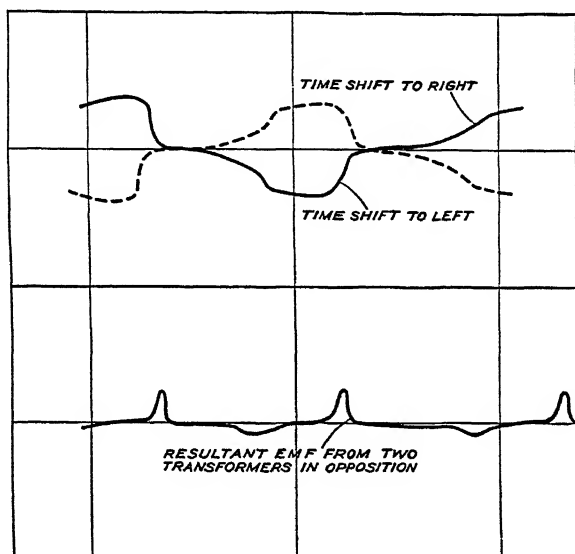


FIG. 2.

If two of these transformers are operated simultaneously and connected so that the induced e.m.f.'s are in opposition, the resulting e.m.f. will be zero when the external field is zero. The application of an external field will, however, result in a phase shift between these induced e.m.f.'s, and the net output will no longer be zero (Fig. 2). The magnitude and direction of the resulting e.m.f. depend upon the strength and direction of the external field.

The necessary features for a resulting e.m.f. are (i) the time shift in the wave pattern of the induced e.m.f. wave, (ii) the asymmetry of the wave pattern due to hysteresis in the magnetic core. This hysteresis effect gives an e.m.f. curve of small slope on the portion corresponding to the change from the state of saturation toward zero, and of steep slope on the portion corresponding to the attainment of the state of saturation. When two e.m.f.'s in opposition are given a phase shift with respect to each other, the resulting e.m.f. curve is as shown in Fig. 2. It consists of a low voltage peak and a high voltage peak. A circuit with a peak rectified output will then give a d-c. output voltage, the sign and magnitude of which correspond to those of the high peak voltage. The height depends on the amount of the phase shift and hence on the strength of the external field.

Two methods are commonly used for measuring magnetic fields with such transformers. The first is to measure the output of the amplifier, using a proportionality factor between the impressed magnetic field and the output. This method is generally used for measurements on small magnetic fields (0 to 0.1 gauss). The second is to balance out the magnetic field by passing a current through the secondary coils; the current is then an accurate measurement of the magnetic field. This current can be obtained either through manual control or by using feedback from the amplifier itself to drive its output toward zero. In this way higher amplification can be used in the amplifier since its operation is always maintained at the same point in the characteristic.

Measurements can be made with an indicating sensitivity of  $1 \times 10^{-5}$  gauss using equipment of this nature. The accuracy of the measurements is limited chiefly by consistent fluctuations in the earth's field, which average between  $2 \times 10^{-5}$  and  $10 \times 10^{-5}$  gauss, and frequently are as great as  $1 \times 10^{-3}$  gauss. For a detection instrument set in the earth's field, these fluctuations are imposed on the measurements, limiting the readable accuracy.

More accurate measurements of the direction of magnetic fields may be obtained by indicating in directions at right angles to the field. Deviation in position relative to the field then results in an output proportional to the sine of the angle  $d\theta$ , i.e.,  $H \sin d\theta \approx H d\theta$ , whereas if measurement is made in the direction of the field the output is proportional to  $H \cos d\theta \approx 0$  for small angles.

### The Application of Saturated Core Magnetometers to Automatic Steering Controls for Ships

If a magnetometer is suspended with the two magnetic elements horizontal and parallel to each other, but free to rotate together about a vertical axis in the earth's magnetic field, it is evident that the signal output from these coils will vary from zero when the axis of the coils lies along the east-west magnetic line to a maximum when the coils are in the north-south direction. Also the sign of the output will depend upon whether the coils are pointed south or north. Thus the signal resulting from such a pair of coils can be used to control the rudder of a craft in such a way as to keep the axis of the coils in an east-west direction.

Stability equations for the use of such a signal in controlling a ship's steering are derived as follows.

The assumptions upon which this analysis is based are:—

1. The rate of turning of the ship is proportional to the rudder angle

$$P\theta = K_s M, \quad (5)$$

where  $P$  is the operator  $\frac{d}{dt}$ ,

$\theta$  is the ship angle,

$K_s$  is a constant,

$M$  is the rudder angle.

This assumption holds accurately for small, light craft. For the larger sea-going ships there is an additional inertia term which, however, has small effect on the final equations.

2. The output of the amplifier is given by

$$A = \frac{-G(\theta - \theta_0)}{1 + t_2 p}, \quad (6)$$

where  $G$  is the amplification factor,

$t_2$  is the circuit time constant,

$\theta - \theta_0$  is the input signal.

3. The rudder position  $M$  may be represented by the equation

$$M = \frac{K_2 A}{L + t_1 p}, \quad (7)$$

where  $K_2$  is a proportionality factor,

$A$  is the amplifier output mentioned above,

$t_1$  may be regarded as a time constant, depending on the speed of the motor driving the rudder.

These relations may be resolved into a single equation.

$$\left( \frac{t_1 t_2}{K_5} p^3 + \frac{t_1 + t_2}{K_5} p^2 + \frac{p}{K_5} \right) \theta = K_2 G \theta_0 \quad (8)$$

With flux coils held horizontally by gravity loading, there is an added effect on certain courses, as the centrifugal force of the ship's turning gives a false vertical. This may be represented in the amplifier equation:—

$$A \text{ corrected} = \frac{(G(\theta - \theta_0) + K_3 M)}{(1 + t_2 p)}, \quad (6b)$$

where  $K_3$  is a variable, the maximum value of which depends upon the ship's rate of turning and on the value of the vertical component of the earth's magnetic field. It is a maximum for south and north courses and with a positive sign on north course.

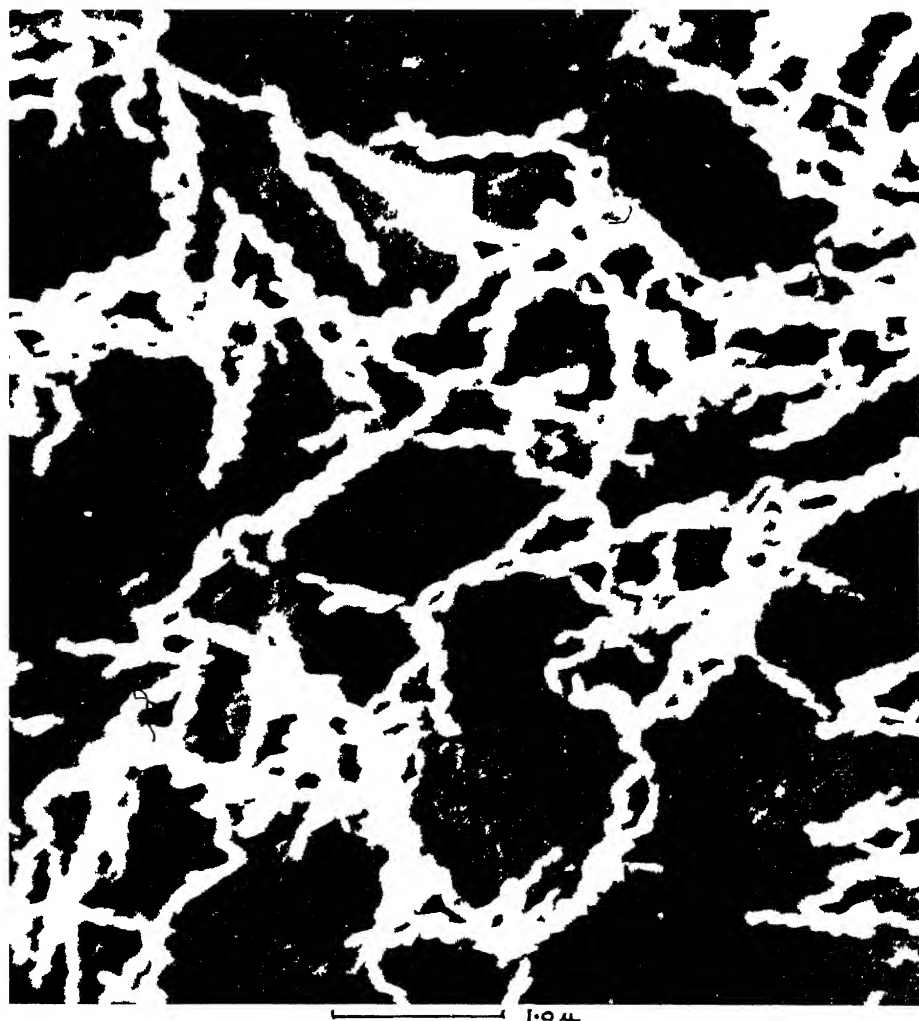
The  $P$  equation then becomes

$$\left( \frac{t_1 t_2}{K_5} p^3 + \frac{t_1 t_2}{K_5} p^2 + \left( \frac{1}{K_5} - \frac{K_2 K_3}{K_5} \right) p + K_2 G \right) \theta = K_2 G \theta_0, \quad (8b)$$

the positive value of  $K_3$  being used, as the most unstable condition. Stability requires that all the roots of the Equation (8b), with  $p$  considered as an algebraic unknown, must have negative real parts.

The effect of this false vertical is thus to decrease the coefficient of the  $p$  term on the north courses. The effect can be counteracted by the addition of a feedback of such a nature as to decrease the last term in the equation. Such a feedback was found to be necessary on the first application, a high speed hydrofoil craft, but unnecessary in applications on the larger sea-going types of ships.





1.0  $\mu$

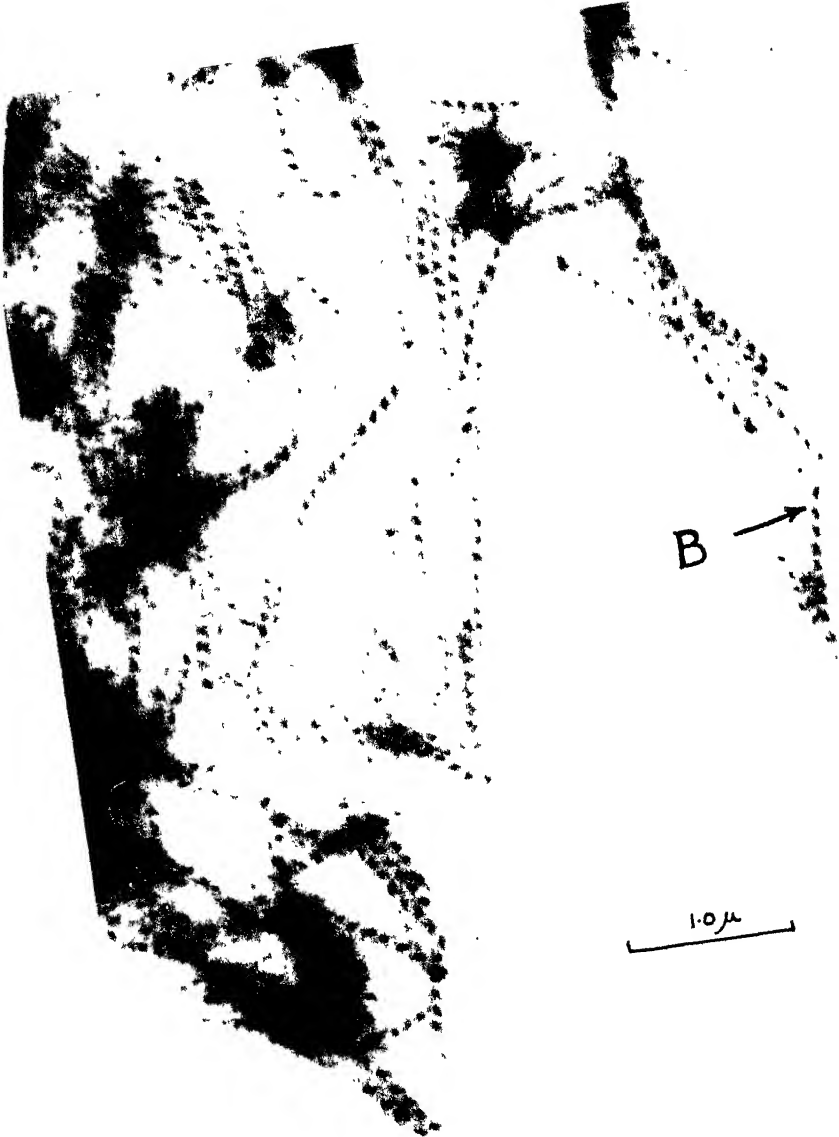


PLATE III



6

PLATE IV







In the mechanism involved in this unit

$t_2$  is of the order of  $\frac{1}{2}$  sec.,

$t_1$  is widely variable, depending upon the driving motor arrangements ( $\frac{1}{2}$  sec. to 1 min.),

$K_2$  depends upon the effective signal amplification and can be rather widely variable,

$K_5$  is a constant of the ship being controlled,

$K_3$  is a constant of any given set of conditions.

An automatic steering control based on these equations was built and trials were made with it in two types of craft, a high speed hydrofoil craft and a Fairmile M.L. ship of the Canadian Navy. The saturated core mode of operation was used because of the simpler design of the amplifier.

### Steering Control Equipment

A schematic diagram of the control system is shown in Fig. 3. The essential parts were:

1. The magnetometer coil unit, which consisted of the two gimbal mounted transformers with parallel axes. The axes of the transformers could be fixed at any desired angle with respect to the fore and aft axis of the boat. The transformers were used in the saturated core mode of operation for two reasons. The type of amplifier is smaller and simpler and it was considered that the effect of variations in the magnetic state of the core material could be reduced in this way.

2. The signal from the coil unit was passed, via slip-ring connections, to the amplifier. The wiring diagram is shown in Fig. 4.

3. The output from the amplifier controlled the motor which drove the rudder. The motor drove as well a set of switches which limited its motion to the desired maximum rudder swing. A feedback from the motor output was returned to the amplifier so as to maintain the condition of proportionality between the rudder deflection and input signal.

4. The rudder position caused the boat to turn so that signal from the coils became smaller and the rudder would move toward its zero position.

The gimbal mount must be free to rotate about the axis perpendicular to the boat, so that the pick up coils may be set at any desired angle to the fore and aft axis of the boat. To allow for this rotation it was necessary to use slip rings to carry the signals to and from the coils. An air damping unit to damp out spurious oscillations was incorporated on the gimbal. A sketch of the coil unit, as used in the Fairmile trials, is shown in Fig. 5.

The amplifier used could be powered either by a 6 v. battery vibrator system, or by 110 v. a-c. power, if available. It consisted of a customary a-c. amplification stage, double rectifier, followed by a d-c. amplifier stabilized against variations in the supply voltage. The output of the d-c. amplifier actuated a relay connected to the driving motor.

A potentiometer, driven by the gimbal axis, gave a signal which, after being amplified, fed a current to the secondaries of the transformers so as to compensate for the tilt on the gimbal mount due to centrifugal force developed by the turning of the boat. This signal was coupled so as to decrease to zero with a large time constant (40 sec. was used). Thus the steady state values were maintained at the correct point.

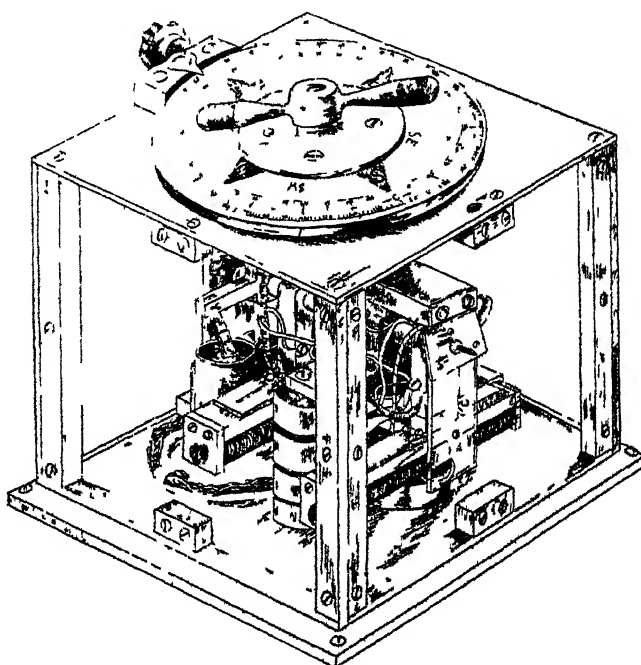


FIG. 5

The driving system maintained a small hunt on the rudder at all times. The magnitude of the hunt was small enough to give no noticeable effect on the course of the ship. In this way, errors due to the finite size of a null point were avoided.

The values of the constants used in the experimental set-up on the Fairmile ship were as follows:—

$$\begin{aligned} t_2 &= \frac{1}{2} \text{ sec.} \\ t_1 &= 4 \text{ sec.} \\ K_2 K_3 &= \frac{1}{3} \text{ sec.} \\ K_5 &= 3/20^\circ/\text{sec.}/\text{degree} \\ K_2 G &= 1. \end{aligned}$$

When these values are substituted in the stability Equation (8), it becomes

$$\left( \frac{40}{3} p^3 + \frac{80}{3} p^2 + \frac{40}{9} p + 1 \right) \theta = K_2 G \theta_0, \quad (9)$$

and if  $\frac{40}{3} p^3 = r^3$ , where  $r$  is a new operator, the equation becomes

$$(r^3 + 48r^2 + 1.9r + 1) \theta = K_2 G \theta_0, \quad (10)$$

which is the equation of a stable system with slight overshoot on changes (2).

The experimental results were satisfactory in both applications of the equipment, the accuracy of steering being  $\pm \frac{1}{2}^\circ$  or better. The stability of the control system was in general accord with theoretical expectations, although it was difficult to evaluate exactly and measure the factors involved.

### Acknowledgment

The author wishes to acknowledge the assistance of Dr. D. G. Hurst and Mr. J. C. Beynon in designing and testing the equipment, and expresses appreciation to Lt.-Comm. D. Hodgson, R.C.N.V.R., for excellent co-operation in arranging for and assisting in experimental trials.

### References

1. MASSACHUSETTS INSTITUTE OF TECHNOLOGY, Department of Electrical Engineering. Magnetic circuits and transformers. John Wiley & Sons, Inc., New York. 1943.
2. JAHNKE, E. and EMDE, F. Tables of functions with formulae and curves. [Funktionen-tafeln mit Formeln und Kurven]. Dover Publications, New York. 1943.

## THE DIFFUSION LENGTH OF THERMAL NEUTRONS IN HEAVY WATER<sup>1</sup>

BY B. W. SARGENT,<sup>2</sup> D. V. BOOKER,<sup>3</sup> P. E. CAVANAGH,<sup>3</sup> H. G. HEReward,<sup>3</sup>  
AND N. J. NIEMI<sup>4</sup>

### Abstract

A continuous flux of thermal neutrons was passed into a large cylindrical tank of heavy water that sat on a graphite column containing a source of photoneutrons. The neutron density in the tank was explored with small indium detectors at selected points along two diameters at right angles in each of three horizontal planes and at 10-cm. intervals along the axis of the tank. The transverse measurements were fitted to Fourier-Bessel series in which the amplitudes of the harmonics were relatively small. The effective radius derived from the transverse analysis was the same in the three planes. The relaxation length of the first component was found from the axial measurements. Corrections were applied for the absorption of neutrons in the axial detector tube, enclosed framework, and indium detectors, and in the light hydrogen in the heavy water. The final value of the diffusion length of thermal neutrons in heavy water (100% D<sub>2</sub>O) is  $171 \pm 20$  cm. Combining this with the known transport mean free path, the capture cross-section is  $(0.92 \pm 0.22) \times 10^{-27}$  cm.<sup>2</sup> per molecule D<sub>2</sub>O for neutrons of velocity 2200 m. per second.

### Introduction

In the search for a suitable moderator to reduce the non-fission capture of neutrons by uranium and thereby to improve the chances of a chain reaction, the lightest elements were naturally considered. The hydrogenous substances—water and paraffin wax—had already been extensively used to slow down neutrons from laboratory sources. It was recognized, however, that a good moderator for a chain reaction would have to combine good slowing-down properties with small neutron capture. In view of both requirements one of the most promising moderators appeared to be heavy hydrogen or deuterium. It was assumed that the deuterium would be used in the form of heavy water, as the capture cross-section of oxygen was believed to be low. Early experiments designed to measure the capture cross-sections of deuterium and heavy water showed that these were indeed small and consequently difficult to measure. As the result of a series of experiments on uranium compounds and heavy water, the British group became convinced in 1940 that a chain reaction would go. Since 1943 a number of piles containing uranium and heavy water have been built and operated.

If any two of the three related quantities—capture cross-section, transport mean free path, and diffusion length of thermal neutrons in heavy water are measured experimentally, the third follows. This paper is concerned with the direct measurement of the diffusion length of heavy water, which is one of

<sup>1</sup> Manuscript received November 30, 1946.

Contribution from the Nuclear Physics Branch, Montreal Laboratory, Atomic Energy Division of the National Research Council of Canada. Issued as N.R.C. No. 1523.

<sup>2</sup> Physicist; now at the Chalk River Laboratory.

<sup>3</sup> Physicist, United Kingdom Staff.

<sup>4</sup> Physicist.

the nuclear physical quantities required in the design of chain-reacting piles that contain this moderator. Previous attempts to measure directly the diffusion length had indicated that it is very great, and if a reliable estimate were to be obtained a much larger quantity of heavy water than had been used hitherto would be necessary. Last year, when 7600 lb. of heavy water was on hand, the opportunity was presented for such a measurement. This paper contains a brief account\* of the method and the final results of the experiment carried out between April 17 and May 12, 1945.

### Theory of the Experiment

Suppose that the heavy water is contained in a cylindrical tank on the top of a graphite column and that thermal neutrons are continuously fed into the tank from a source in the graphite. It is convenient to use a system of cylindrical co-ordinates with the origin located near the bottom of the tank and the positive direction of the  $z$ -axis vertically upwards along its axis. The radial distance  $r$  is measured from this axis, and the angle  $\varphi$  is measured from a vertical plane containing the  $z$ -axis.

The diffusion of thermal neutrons may be described by the differential equation

$$\nabla^2 \rho - \frac{\rho}{L^2} = 0 \quad (1)$$

in the absence of thermal sources, where  $\rho$  is the density of thermal neutrons and  $L$  is their diffusion length. Written in cylindrical co-ordinates, Equation (1) becomes:

$$\frac{\partial^2 \rho}{\partial r^2} + \frac{1}{r} \frac{\partial \rho}{\partial r} + \frac{1}{r^2} \frac{\partial^2 \rho}{\partial \varphi^2} + \frac{\partial^2 \rho}{\partial z^2} - \frac{\rho}{L^2} = 0. \quad (2)$$

The solution of Equation (2) is required subject to the boundary conditions:

- (1)  $\rho$  is finite on the axis of the cylinder,
- (2)  $\rho = 0$  at an effective radius  $r = R$  (to be evaluated experimentally),
- (3)  $\rho = 0$  at  $z = h$  (to be evaluated experimentally),
- (4)  $\rho$  is representable by a measured distribution expressed as a Fourier-Bessel series in the plane  $z = 0$ .

The desired solution of Equation (2) is

$$\rho = \sum_{\substack{l=0,1,2,\dots \\ m=1,2,3,\dots}} (A_{lm} \cos l\varphi + B_{lm} \sin l\varphi) J_l(\lambda_{lm}r) \frac{\sinh \frac{h-z}{b_{lm}}}{\sinh \frac{h}{b_{lm}}}, \quad (3)$$

where the relaxation lengths  $b_{lm}$  are given by:

$$\frac{1}{b_{lm}^2} = \lambda_{lm}^2 + \frac{1}{L^2}. \quad (4)$$

If the experiment is well devised the first term in the Fourier-Bessel Series (3) dominates all others in a large part of the cylinder. In that case the

\* Owing to security restrictions many of the experimental data have been omitted.

harmonics ( $l = 0, m \neq 1$ ), ( $l \neq 0$ , any  $m$ ) are at most small corrections on the dominant term:

$$\rho = A_{01} J_0(\lambda_{01} r) \frac{\sinh \frac{h-z}{b_{01}}}{\sinh \frac{h}{b_{01}}} . \quad (5)$$

In Equation (5)

$$\lambda_{01} = \frac{2.4048}{R} ,$$

and the diffusion length  $L$  follows from

$$\frac{1}{L^2} = \frac{1}{b_{01}^2} - \left( \frac{2.4048}{R} \right)^2 . \quad (6)$$

The experimental procedure was to explore the density of thermal neutrons transversely and vertically in the tank. From the transverse analysis the effective radius  $R$  of the tank was found, and from the vertical analysis the values of  $h$  and  $b_{01}$  were derived.

### Experimental Details

The experimental tank was made of mild steel with welded seams. The thickness of the wall was 0.4 cm. and that of the bottom and cover 1.1 cm. The inside surfaces were coated with Lithcote enamel to prevent corrosion. The internal radius of the tank was  $79.9 \pm 0.3$  cm. and the height 165 cm.

The tank containing the heavy water sat on a graphite pedestal having approximately the same shape and diameter as the tank and a height of 28 cm. This pedestal surmounted a rectangular parallelepiped of graphite 270 by 186 cm. in horizontal section and 228 cm. high. When neutrons flow from the parallelepiped of large cross-section into the column of sharply smaller cross-section the harmonics in the density distribution become important. The purpose of the pedestal was to allow the amplitudes of the harmonics to fall off relative to the first component as the neutrons diffuse upwards, and thus simplify the distribution of neutrons across the tank.

The source of neutrons was a block of beryllium at the end of the tube of a General Electric X-ray generator (2) operated at 2000 kv. peak and 1.4 ma. The beryllium was located on the axis of the pile at an average distance of 86 cm. below the centre of the bottom of the tank. This distance was sufficient to ensure that the neutrons entering the tank had reached thermal energies by slowing-down collisions in the graphite. (This point will be examined more closely later.) The exposed surfaces of the graphite pile and tank were covered with cadmium sheet, 0.4 mm. thick, to prevent the escape of thermal neutrons from the system and their entry into the tank after being reflected from the walls of the room.

Indium detectors were used to explore the neutron density in the heavy water. The vertical detector tubes, in which the detectors were placed for activation, were positioned near their lower ends by holes in a horizontal

aluminium grid (3.2 mm. thick) and at their upper ends by holes in the cover of the tank. The grid rested on a narrow flange, tack-welded to the wall of the tank, 8 cm. above the bottom. The detector tubes were made of thin-walled aluminium, and were closed at their lower ends with welded plugs and filled with heavy water to the same level as that in the tank.

The indium foils were 1 cm. square and weighed about 88 mgm. each. These were cemented on aluminium rectangles (2.6 cm. by 2.1 cm. by 0.53 mm.) for convenience in handling. The detectors were positioned on light aluminium frameworks and lowered into the detector tubes. Vertical measurements on the detectors were made with a cathetometer, and radial distances were determined by the holes in the aluminium grid and cover of the tank. Similar indium foils were used to monitor the output of the source of neutrons and were placed for activation at a standard position 126 cm. below the middle of the beryllium block in the graphite parallelepiped. The foils activated in the tank were counted against the corresponding monitoring foil. The half-period of indium activity was taken to be 54.5 min., as measured in this laboratory. The relative sensitivities of the detectors were measured and taken into account. The geometry at the Geiger-Müller counters was accurately reproducible, and the behaviour of the counters, high tension supplies, and scales-of-128 was very satisfactory. The initial counting rate of the monitors was approximately 2500  $\beta$ -particles per minute after the X-ray generator had been operated at full voltage and current for 1.5 hr. The corresponding rate for a foil activated at the lowest point selected in the tank was 2175  $\beta$ -particles per minute.

The experiment was performed with two different quantities of heavy water. When 5800 lb. of heavy water was in the tank the neutron density was measured at approximately 10-cm. intervals along the axis of the tank and at selected points along two diameters at right angles in three approximately horizontal planes spaced at 20 and 30-cm. intervals. Six indium detectors were used in each run, three being in one detector tube and three in another. The two detector tubes were usually kept 50 cm. or more apart to avoid any influence of the neutron capture by one tube on the neutron density being measured in the other. The indium foils in a given tube were spaced at 20-cm. intervals to reduce to a negligible amount (estimated at 0.03%) the influence of one foil on the activity acquired by another. The density of neutrons at each point on the axis was measured six to ten times and at the other points four times. In half of the runs the indium foils faced the axis of the tank, and in the other half they faced the wall. The slight dependence of the activity on the neutron current drops out in the average, which is a measure of the neutron density.

When the supply of heavy water was increased to 7600 lb. some of the measurements were repeated. The neutron density was measured at approximately 10-cm. intervals along the axis of the tank using six indium foils spaced at 20-cm. intervals in a given run. Each point was measured six

times. The agreement obtained in the various runs was satisfactory, the probable error in the mean being about  $\frac{1}{2}\%$  for all except a few points where the neutron density was low.

### Experimental Results

Two minor corrections were applied to the averaged density measurements at the various points.

(1) While the vertical positioning of the detectors in the tank was measured to 0.1 mm., it was impracticable to obtain better reproducibility of vertical positioning in different runs than  $\pm 5$  mm. Consequently, the variations  $\Delta z$  of points from the horizontal planes chosen at  $z = 0, 20.00$ , and  $50.00$  cm. were allowed for. The corrections to  $\rho$  were based on the assumption of a single term for the neutron density:

$$\rho = A_{01}J_0(\lambda_{01}r) \frac{\sinh \frac{h-z}{b_{01}}}{\sinh \frac{h}{b_{01}}}, \quad (5)$$

from which

$$\frac{\Delta \rho}{\rho} = - \frac{\Delta z}{b_{01}} \coth \frac{h-z}{b_{01}} \quad (7)$$

with sufficient accuracy. ( $\Delta z$  was always less than 1 cm.)

(2) Though the detector tubes were straight, they were not exactly parallel to the vertical axis of the tank. The radial distances measured at the grid and just above the cover (160 cm. above the grid) did not differ by more than 5 mm., and the former set was adopted as standard. The correction to  $\rho$  for a departure  $\Delta r$  from a standard distance  $r$  was taken to be:

$$\frac{\Delta \rho}{\rho} = - \lambda_{01} \Delta r \frac{J_1(\lambda_{01}r)}{J_0(\lambda_{01}r)}. \quad (8)$$

Approximate values of  $b_{01}$ ,  $h$  and  $R$  (hence  $\lambda_{01}$ ) were sufficient for these two corrections.

The measurements of the neutron density were analysed according to the Distribution (3), which was derived as the solution of the diffusion Equation (1) in which the thermal source term was set equal to zero. The validity of this assumption will now be considered. If the threshold for the photodisintegration of the beryllium nucleus is 1.63 Mev. the *maximum* energy of the photoneutrons is 330 kev. when the X-ray generator is operated at 2.0 Mv. peak. According to the calculations of Marshak (5), the slowing-down length from this initial energy to thermal energies is about 16.3 cm. in graphite (density 1.6 gm. per cc.). It can be shown from slowing-down and diffusion theory that the fraction of epithermal neutrons is very small and their effect on the thermal distribution negligible after the neutrons have traversed 86 cm. of graphite (5.3 slowing-down lengths) between the middle of the beryllium block and the bottom of the tank. In addition, the neutrons had to traverse 6.4 cm. of heavy water to reach the lowest point in the tank

at which their density was measured, and thus they suffered further slowing-down collisions. The sources of thermal neutrons within the volume of heavy water actually used for measurements may therefore be neglected. Moreover, the activity acquired by absorption of neutrons of resonance energy (1.44 ev. (4)) in the indium foils may also be neglected. This latter point was substantiated by a few measurements with indium foils shielded by 1 mm. of cadmium.

The transverse measurements in the plane  $z = 0$  were first examined graphically, and the symmetrical part of the density was found to be well represented by

$$A_{01}J_0(\lambda_{01}r) + A_{02}J_0(\lambda_{02}r) + A_{03}J_0(\lambda_{03}r), \quad (9)$$

where  $A_{02}/A_{01} = 2\%$  and  $A_{03}/A_{01} = 1\%$ . Secondly, the relaxation lengths  $b_{02}$  and  $b_{03}$  were estimated from Equation (4) using approximate values of  $L$  and  $R$ ; and the contributions of these two harmonics were calculated and subtracted from the measured densities in the planes  $z = 0, 20.00$ , and  $50.00$  cm. Thirdly, the remainders were fitted by the method of least squares to the expression:

$$\rho = A'_{01}(z)J_0(\lambda_{01}r) + (A'_{11}(z) \cos \varphi + B'_{11}(z) \sin \varphi)J_1(\lambda_{11}r), \quad (10)$$

yielding the values of the amplitudes and effective radius  $R$  of the tank in each of the three planes. Details are as follows. Since the amplitudes  $A'_{11}(z)$  and  $B'_{11}(z)$  are small in comparison with  $A'_{01}(z)$  and the effective radius is close to 82.8 cm., we set

$$\lambda_{11} = \frac{3}{82} \frac{8317}{8} \text{ cm.}^{-1}.$$

The variables that remain to be determined are  $A'_{01}(z)$ ,  $A'_{11}(z)$ ,  $B'_{11}(z)$  and  $\lambda_{01}$  (or  $R$ ).  $J_0(\lambda_{01}r)$  is expanded to two terms in a Taylor's series about  $\lambda'_{01}r$ , where

$$\lambda'_{01} = \frac{2}{82} \frac{4048}{8} \text{ cm.}^{-1}.$$

Equation (10) becomes:

$$\rho = A'_{01}(z)J_0(\lambda'_{01}r) + A'_{01}(z) \frac{\delta R}{R} \lambda'_{01}r J_1(\lambda'_{01}r) + (A'_{11}(z) \cos \varphi + B'_{11}(z) \sin \varphi)J_1(\lambda_{11}r). \quad (11)$$

It is convenient to regard  $A'_{01}(z)$ ,  $A'_{01}(z) \frac{\delta R}{R}$ ,  $A'_{11}(z)$ , and  $B'_{11}(z)$  as independent variables, for the normal equations derived from the application of the method of least squares to the experimental equations are then linear. In the plane  $z = 0$ ,  $A_{11}/A_{01} = 7.4\%$  and  $B_{11}/A_{01} = 7.2\%$ . The effective radius  $R$  is given in Table I.

The effective radius is therefore  $82.56 - 79.9 = 2.66$  cm. greater than the average internal radius of the steel tank tightly wrapped on the outside with cadmium. Auger, Munn, and Pontecorvo (1) determined the extrapolated cut-off distance to be 1.64 cm. from the curve of the density of thermal neutrons in heavy water below a flat cadmium plate. Since the

effect of the small curvature of the tank is believed to be negligible, the whole difference 1.0 cm. is attributed to the neutron scattering by the steel wall of thickness 0.4 cm.

TABLE I

$z$ , cm.	$R$ , cm
0	82 56
20	82 47
50	82 65
	Average 82 56

An approximate value of the relaxation length  $b_{01}$  was obtained from the sets of densities measured at the same  $r$  and  $\varphi$  in the three planes. After these densities had been corrected for the harmonics  $J_0(\lambda_{02}r)$ ,  $J_0(\lambda_{03}r)$  and  $J_1(\lambda_{11}r)$  they were substituted into Formula (5):

$$\rho = A_{01}''(r) \frac{\sinh \frac{h-z}{b_{01}}}{\sinh \frac{h}{b_{01}}} \quad (5a)$$

A more accurate value of the relaxation length  $b_{01}$  was found from the two sets of measurements at 10-cm. intervals along the axis of the tank. First, these were corrected for the harmonics  $J_0(\lambda_{02}r)$  and  $J_0(\lambda_{03}r)$ , using the amplitudes found in the transverse analysis for  $z = 0$  and the estimated relaxation lengths. Second, the vertical distance  $h$  from the chosen origin to the horizontal plane at which the neutron density vanishes was estimated from the second set of measurements at points nearest this plane. As a first approximation this plane was assumed to be 3 cm. above the surface of the heavy water. Therefore

$$\rho = \left( A_{01} / \sinh \frac{h}{b_{01}} \right) \sinh \left( \frac{h' + \delta - z}{b_{01}} \right), \quad (5b)$$

where  $\delta$  is the correction to the first approximation  $h'$ , and  $b_{01}$  is approximately known. The densities  $\rho$  measured at three points, four points, etc., to seven points, counting downward from the plane of vanishing density, were used in turn in this expression and  $\delta$  found by the method of least squares. The final result was  $\delta = -0.1 \pm 0.1$  cm. Third, using the appropriate value of  $h$ , the relaxation length  $b_{01}$  was derived from each set of axial measurements. The densities  $\rho$  (corrected for the harmonics) should be represented by:

$$\rho = A_{01} \frac{\sinh \frac{h-z}{b_{01}}}{\sinh \frac{h}{b_{01}}}, \quad (5)$$

which may be rewritten:

$$\rho = A_{01} e^{-z/b_{01}} \left( \frac{1 - e^{-2(h-z)/b_{01}}}{1 - e^{-2h/b_{01}}} \right). \quad (5c)$$

The last factor may be regarded as the end-correction for the finite length of the column of heavy water. It was evaluated for  $h$  and a likely value of  $b_{01}$  and applied as a correction to  $\rho$ . The method of least squares was then applied to the logarithms of the  $\rho$ 's (so corrected) to yield  $b_{01}$ . If we write  $b_{01}$  (assumed) for the value substituted in the end-correction, and  $b_{01}$  (derived) for the value derived from the least squares solution, it is found that  $b_{01}$  (derived) varies linearly with  $b_{01}$  (assumed). This is a useful property in arriving at the final result, at which  $b_{01}$  (derived) =  $b_{01}$  (assumed).

Up to this point we have neglected the effect of the neutron capture by the axial detector tube, enclosed framework, and indium detectors. The diffusion theory was applied to give the necessary correction (+ 2%) to the diffusion length derived from Equation (6).

Finally, the diffusion length, measured in the heavy water of known isotopic composition, was corrected for the neutron capture in the light hydrogen present to yield the diffusion length in pure heavy water (100% D<sub>2</sub>O).

The capture cross-section of hydrogen was derived from the following measurements. Whitehouse and Graham (8) have found

$$\sigma_B/\sigma_H = 2270$$

in a series of careful measurements. The  $1/v$  law of neutron capture by boron has been well substantiated by Rainwater and Havens (7). From work at the Argonne Laboratory (3, 6)

$$\sigma_B = 705 \times 10^{-24} \text{ cm}^2/\text{atom}$$

for neutrons of velocity 2200 m. per sec. From these data

$$\sigma_H = 0.273 \times 10^{-24} \text{ cm}^2/\text{atom}$$

for neutrons of velocity 2500 m. per second.

The diffusion length  $L$  is related to the transport mean free path  $l_t$  and the mean free path for capture  $l_c$  by the diffusion formula:

$$L^2 = \frac{1}{3} l_t l_c, \quad (12)$$

where  $l_c = v\tau$ ,  $\tau$  being the mean lifetime of thermal neutrons in heavy water and  $v$  their average velocity (2500 m. per sec.) at room temperature. Setting  $l_t = 2.4 \pm 0.1$  cm., as measured by Auger, Munn, and Pontecorvo (1), and correcting for neutron capture in the light hydrogen present, we find that

$$L = 171 \pm 20 \text{ cm.}$$

in heavy water of 100% purity, and that the capture cross-section is  $(0.81 \pm 0.19) \times 10^{-27} \text{ cm}^2$  per molecule D<sub>2</sub>O for neutrons of velocity 2500 m. per second. Assuming a  $1/v$  law of capture,

$$\sigma_c = (0.92 \pm 0.22) \times 10^{-27} \text{ cm}^2/\text{molecule D}_2\text{O}$$

for neutrons of standard velocity 2200 m. per second.

### Acknowledgments

The Geiger-Müller counters were made for us by Mr. N. Veall, and the stabilized high tension supplies and scales-of-128 by Mr. H. F. Freundlich and staff. Mr. F. W. Fenning made the indium detectors and devised the detector holders that fitted over the Geiger-Müller counters in the course of some earlier experiments in which he collaborated with us. We are grateful for their assistance.

We should also like to thank Miss E. O'Brien for operating the X-ray generator and Miss Y. Diamond, Miss G. Despins, Mrs. S. Courant, and Miss H. Zackon for counting.

### References

1. AUGER, P., MUNN, A. M., and PONTECORVO, B. *Can. J. Research*, A, 25 : 143-156. 1947.
2. CHARLTON, E. E. and WESTENDORP, W. F. *Electronics*, 17(12) : 128-133. 1944.
3. FERMI, E. Private communication. 1944.
4. HAVENS, W. W., JR. and RAINWATER, J. *Phys. Rev.* 70 : 154-173. 1946.
5. MARSHAK, R. E. Unpublished report, MT-18. On the moments of the distribution function of neutrons slowed down in heavy elements. National Research Council of Canada. 1943.
6. MARSHALL, J. *Bull. Am. Phys. Soc.* 21(3) : 12, F4. 1946.
7. RAINWATER, J. and HAVENS, W. W., JR. *Phys. Rev.* 70 : 136-153. 1946.
8. WHITEHOUSE, W. J. and GRAHAM, G. A. R. Unpublished report, MP-172. The ratio of the neutron absorption cross-sections of boron and hydrogen. National Research Council of Canada. 1945.

# THE TRANSPORT MEAN FREE PATH OF THERMAL NEUTRONS IN HEAVY WATER<sup>1</sup>

BY P. AUGER,<sup>2</sup> A. M. MUNN,<sup>3</sup> AND B. PONTECORVO<sup>4</sup>

## Abstract

The transport mean free path of thermal neutrons in heavy water is determined from measurements of the neutron density in heavy water (99.4 atoms of deuterium per 100 atoms of hydrogen element) at various distances from a cadmium plate. In the region investigated, the density is found to be a linear function of the distance from the cadmium plate. When this straight line is extrapolated, the density vanishes at a distance  $d = 1.64$  cm. behind the plate. On the basis of transport theory it is known that  $d = 0.71l_t$ , where  $l_t$  is the transport mean free path in the medium. The final result is  $l_t = 2.4$  cm. in pure heavy water. The measurements of the neutron density show that it falls below the straight line as the cadmium surface is very closely approached, in agreement with transport theory.

## Introduction

Let  $l(v)$  be the scattering mean free path in a medium for neutrons of velocity  $v$ . The corresponding transport mean free path,  $l_t(v)$ , is defined by the relation

$$l_t(v) = \frac{l(v)}{1 - (\cos \theta)_{av}}, \quad (1)$$

where  $(\cos \theta)_{av}$ , the mean cosine of the scattering angle  $\theta$  in single collisions, represents quantitatively the amount of coherence between two successive free paths in the medium considered. From the Definition (1) it is recognized that the transport mean free path, rather than the scattering mean free path, enters fundamentally in problems of neutron diffusion. When the scattering is isotropic,  $l_t$  is equal to  $l$ .

It should be noticed that the scattering mean free path and, consequently, the transport mean free path, may vary considerably with the neutron velocity in the *thermal region*. In the case of crystalline matter, for example, only the mean free path of monokinetic neutrons, impinging upon the crystal at a given incidence, is a well defined quantity, while the notion of mean free path (and of transport mean free path) of *thermal neutrons* has not a precise meaning. One should expect to find different results according to the various experimental conditions affecting the mean neutron velocity. In a liquid like heavy water, however, rapid variations of the scattering cross-section with the neutron energy within the thermal region are hardly expected, and the notion of transport mean free path of thermal neutrons has a definite meaning.

<sup>1</sup> Manuscript received September 17, 1946.

Contribution from the Montreal Laboratory, Nuclear Physics Branch, Division of Atomic Energy, National Research Council. (Work performed in 1943.) Issued as N.R.C. No. 1524.

<sup>2</sup> Member of the United Kingdom staff; now at the Ecole Normale Supérieure, Paris, France.

<sup>3</sup> Junior Research Physicist, National Research Council; now at McGill University, Montreal, Que.

<sup>4</sup> Member of the United Kingdom staff; now at the Chalk River Laboratory, Chalk River, Ontario.

One should accordingly get the same value of  $l_t$  for thermal neutrons in heavy water by changing the experimental conditions, thus slightly affecting the mean neutron velocity. In all considerations below it will be tacitly assumed that all the thermal neutrons have the same velocity  $v$  equal to their average velocity.

### Purpose of the Experiment

The experiment described in this paper was performed because with the knowledge of  $l_t$  the following information pertaining to heavy water can be derived.

(1) The value of the capture mean free path  $l_c$  of thermal neutrons can be derived from the well known relation of diffusion theory:

$$L^2 = \frac{1}{3} l_t l_c, \quad (2)$$

where  $L$ , the diffusion length of thermal neutrons in the medium, is known from a separate experiment. Conversely, the value of  $L$  can be derived when  $l_t$  and  $l_c$  are known.

(2) The correct boundary condition\* for the neutron density can be written in problems concerning the diffusion of neutrons. Examples are experiments designed to measure diffusion lengths, exponential experiments with multiplying media, and technical problems concerning reflectors for chain reacting piles and concerning thermal utilization of neutrons in heterogeneous chain reacting systems.

(3) The value of  $(\cos \theta)_{av}$  can be derived from Equation (1). This is an interesting quantity, characteristic of the scattering of thermal neutrons in heavy water.

### Methods That May Be Used for Determining $l_t$

Since  $l_t$  and  $l$  are not expected to differ much in value, an experimental measurement of  $l_t$  will definitely distinguish it from  $l$  only if the method is capable of good accuracy, say to 5%. This consideration and the fact that only 13 litres of heavy water was available have been weighed in selecting the experimental method from the five described below.

(1) The study of the angular distribution of thermal neutrons after single collisions in heavy water provides a direct method of measuring  $(\cos \theta)_{av}$  and consequently, by Equation (1), the transport mean free path. The neutron sources available were not sufficiently strong to provide the extremely intense and well collimated beam of thermal neutrons that this method requires.

(2) If the diffusion length  $L$  and the mean lifetime  $\tau$  of thermal neutrons in a heavy water medium are known from experiments, the diffusion coefficient  $D$  can be deduced from the diffusion Relation (2), which may be written:

$$L^2 = D\tau = \frac{1}{3} l_t v \tau. \quad (3)$$

\* This will be explained later.

The diffusion length of thermal neutrons in heavy water is so great that it cannot be measured when only a quantity of the order of 100 litres is available. Hereward, Laurence, Munn, Paneth, and Sargent (6) have, however, measured the diffusion length in heavy water containing lithium carbonate. The neutron capture by the lithium reduced the diffusion length to such a value that it could be measured in a quantity of the order of 100 litres. Since the mean free path is not appreciably changed by the addition of lithium carbonate, the diffusion coefficient  $D$  follows from Equation (3) when  $L$  and  $\tau$  are substituted. For this purpose  $\tau$  would be estimated from the known capture cross-sections and numbers of atoms per cubic centimetre of the constituents. It should be noticed that this method yields directly the diffusion coefficient, and the transport mean free path follows only after a value of the neutron velocity  $v$  is assumed. In spite of the uncertainty in the neutron velocity that is appropriate, the value of  $l_t$  obtained in the present experiment and the values of  $L$  and  $\tau$  in Reference (6) satisfy Equation (3) fairly well.

(3) Suppose that a thermal neutron detector, geometrically thin but infinitely thick with respect to thermal neutrons, is placed deep within the scattering medium with its faces normal to the gradient of the neutron density. If the area of the detector is so small that the neutron field is not modified, it can be shown that the sum  $S$  of the  $\beta$ -activities,  $I_1$  and  $I_2$ , of the two faces is proportional to the neutron density  $\rho$ , while the difference  $\Delta$ ,  $I_1 - I_2$ , is proportional to the neutron current density  $j$ :

$$S = I_1 + I_2 = \frac{1}{2} k \rho v \quad (4)$$

$$\Delta = I_1 - I_2 = k j. \quad (5)$$

The constant  $k$  of proportionality is the same in the two equations except for a small correction that arises from the fact that the neutrons impinging on the two sides of the detector have slightly different angular distributions. When Equations (4) and (5) are combined with the expression for the current density in diffusion theory:

$$j = -D \text{grad } \rho = -\frac{1}{3} l_v \text{grad } \rho, \quad (6)$$

it follows that

$$\Delta = -\frac{2}{3} l_t \text{grad } S. \quad (7)$$

This experimental method of measuring  $l_t$  therefore consists of measuring the difference of the  $\beta$ -activities of the two faces and the gradient of their sum and using Equation (7).

It is not possible to use an infinitely thick detector, but a moderately thick detector of small area backed by a (strongly absorbing) cadmium sheet of the same area would meet the requirements. This method was not used because, with the neutron sources available, the  $\beta$ -activities were too small for measurement when the linear dimensions of the detector were a small fraction of the scattering mean free path in the medium.

(4) Suppose that the scattering medium is bounded by a plane surface, which is a perfectly absorbing sheet or a boundary to vacuum. If  $\rho_s$  represents the density of thermal neutrons and  $j_s$  the current density, both at the surface, on the basis of an isotropic scattering law it follows exactly (11) that

$$\rho_s = \sqrt{3}j_s/v. \quad (8)$$

If the scattering law is more complicated, Equation (8) is a good approximation (8).

Owing to continuity,  $j_s$  is approximately equal to the current density at points distant a few scattering mean free paths from the boundary. At this depth, however, diffusion theory is valid and Equation (6) can be applied. Therefore

$$j_s = v\rho_s/\sqrt{3} = -\frac{1}{3}l_v \text{ grad } \rho,$$

or

$$l_t = -\sqrt{3} \rho_s / \text{grad } \rho, \quad (9)$$

where  $\text{grad } \rho$  stands for the gradient of the density at a point close to the boundary, but far enough from it to permit the use of diffusion theory.

While in principle this method is simple and very accurate, in practice a serious difficulty arises. An extremely thin detector of neutrons is required, since the neutron density must be measured within the medium where the distribution of neutron velocities is almost isotropic and also at the boundary where the distribution is very anisotropic.

(5) The principle of this method, which was adopted for measuring  $l_t$  in heavy water, had been used before by Amaldi and Fermi (1) in their work on the motion of neutrons in hydrogenous materials. The theory will be presented in detail in the next section. It will be seen later that this method possesses some practical advantages.

### Principle of the Method Selected for Determining $l_t$ in Heavy Water

Suppose that a plane source of thermal neutrons at infinity produces a stream of neutrons of velocity  $v$  in a semi-infinite scattering medium, limited to the right at  $z = 0$  by a perfectly absorbing sheet or a vacuum. If no capture of neutrons takes place in the medium the current density  $j$  is constant everywhere. In regions far from the boundary (a few mean free paths) diffusion theory may be applied. Under these assumptions it can easily be shown that the neutron density  $\rho(z)$  is a linear function of  $z$ . Near the boundary, however, only transport considerations may be applied. It has been shown theoretically that  $\rho(z)$  falls below the straight line near the boundary and its gradient becomes infinite there (10, 11). If the straight line is extrapolated outside the medium the density vanishes at a certain distance from the boundary. This distance  $d$  is related to  $l_t$  by a numerical relation, obtained by Placzek and collaborators (8-11), which is known to good accuracy as stated below.

Let the scattering law be represented by the function  $f(\cos \theta)$  such that  $f(\cos \theta) d(\cos \theta)$  is the probability that the cosine of the scattering angle  $\theta$  in one collision lies between  $\cos \theta$  and  $\cos \theta + d(\cos \theta)$ . By definition,

$$\int_{-1}^1 f(\cos \theta) d(\cos \theta) = 1 \quad (10)$$

and

$$(\cos \theta)_{av} = \int_{-1}^1 \cos \theta f(\cos \theta) d(\cos \theta). \quad (11)$$

If  $f(\cos \theta)$  is expanded in terms of Legendre polynomials  $P_l(\cos \theta)$ ,

$$\begin{aligned} f(\cos \theta) &= A_0 + A_1 P_1(\cos \theta) + A_2 P_2(\cos \theta) + \dots \\ &= A_0 + A_1 \cos \theta + \frac{1}{2} A_2 (3 \cos^2 \theta - 1) + \dots, \end{aligned} \quad (12)$$

the coefficients  $A_0$  and  $A_1$  are derived by substituting Equation (12) in Equations (10) and (11) respectively and carrying out the integrations. Equation (12) can therefore be written:

$$f(\cos \theta) = \frac{1}{2} [1 + 3(\cos \theta)_{av} \cos \theta + A_2 (3 \cos^2 \theta - 1) + \dots]. \quad (13)$$

The relation between  $d$  and  $l_t$  for several scattering laws has been investigated by Mark (9). When the scattering is isotropic ( $f = \frac{1}{2}$  and  $l = l_t$ ), the relation, according to Placzek and Seidel (11), is

$$d = 0.71 l_t. \quad (14)$$

When the scattering law is represented by

$$f(\cos \theta) = \frac{1}{2} [1 + 3(\cos \theta)_{av} \cos \theta]$$

Mark shows that

$$d = 0.71 l_t. \quad (15)$$

When the next Legendre polynomial is included in the scattering law,

$$f(\cos \theta) = \frac{1}{2} [1 + 3(\cos \theta)_{av} \cos \theta + A_2 (3 \cos^2 \theta - 1)],$$

Mark obtains

$$d = 0.71 l_t [1 + a(A_2)] \quad (16)$$

with  $a(A_2) < 0.005$ .\*

From a comparison of Expressions (14), (15), and (16), it is reasonable to assume that even for a scattering law in which higher moments of the angular distribution function are not negligible,  $d$  is not very different from (15).

Fermi's relation (4),

$$d = l/\sqrt{3} = 0.58 l, \quad (17)$$

which was used in the original work of Amaldi and Fermi (1) with paraffin, is not accurate, although the original law for the angular distribution of neutrons emerging from a plane surface,

$$\cos \theta + \sqrt{3} \cos^2 \theta,$$

is a very good approximation, as shown by Placzek (10).

\* It is easy to see that there is a limitation to the value of  $A_2$ , for  $f(\cos \theta)$  must be greater or equal to zero. The value of  $a = 0.005$  holds for the maximum value of  $A_2$ .

In the experimental method adopted for determining  $l_t$ , the density of thermal neutrons is measured at various distances from a plane boundary but in the region where diffusion theory is applicable. The measured distribution is extrapolated to the point of zero density, which determines  $d$  and in turn  $l_t$  from Equation (15). Since the detector of thermal neutrons is not to be used close to the boundary, the requirements of its properties are less severe than in Method (4). A small boron trifluoride chamber, having the practical advantage of almost zero background, may be used in spite of the fact that its presence makes a sizable hole in the medium.

In order to simulate the ideal conditions described in presenting the principle of the method, the following conditions must be fulfilled.

- (1) There must be no sources of thermal neutrons in the heavy water.
- (2) The boundary of the heavy water must be plane and sharply defined. (There must be no back scattering.)
- (3) In the region where density measurements are made  $\rho(z)$  must be a linear function of  $z$  to an accuracy such that the departure from linearity is smaller than the experimental error.

Condition (1) was fulfilled by placing the source of fast neutrons in a graphite pile at a distance from the tank of heavy water so great that epithermal neutrons were practically non-existent in the heavy water (13, pp. 55-56, para. 4.2 and 4.6 (a)). Condition (2) was fulfilled by defining the heavy water boundary with a thick cadmium plate. Since the capture mean free path in cadmium is of the order of 0.1 mm., practically no neutrons are reflected. Condition (3) is fulfilled if the relaxation length  $L_r$  of the pile is sufficiently great. At large distances from the source, the density of thermal neutrons in the graphite is given by

$$\rho(z) = A \sinh \frac{z+d}{L_r} = A \left( \frac{z+d}{L_r} \right) \left[ 1 + \frac{1}{6} \left( \frac{z+d}{L_r} \right)^2 + \dots \right], \quad (18)$$

where  $A$  is a constant and  $z$  is measured from the plane boundary.\* The term that represents the first order departure of  $\rho(z)$  from linearity,  $\frac{1}{6}[(z+d)/L_r]^3$ , is sufficiently small if  $L_r$  is sufficiently large.

Since the relaxation length  $L_r$  of thermal neutrons in a square pile of moderator can be related (see for example Reference (7)) to the diffusion length  $L$  and the side length  $a$  of the pile:

$$\frac{1}{L_r^2} = \frac{1}{L^2} + \frac{2\pi^2}{a^2}, \quad (19)$$

a large value of  $L_r$  is obtained when  $a$  is large, i.e., when the loss of neutrons through the sides is small. Since only 13 litres of heavy water was available, it was necessary to reduce the leakage of neutrons through the sides of the tank by an artificial means. This was accomplished by embedding the tank in the

\* Equation (18) may be regarded as a definition of the relaxation length  $L_r$  of neutrons in the graphite pile.

graphite (Fig. 1). In this way the escape of neutrons through the sides of the tank is essentially determined by the dimension  $a$  of the graphite pile. Since the diffusion length of thermal neutrons in heavy water is greater than in graphite, the relaxation length in the heavy water is at least as great as in the graphite pile with graphite replacing the heavy water. Setting  $L = 51$  cm. and  $a = 190$  cm. in Equation (19),  $L_r = 33$  cm. for thermal neutrons in this graphite pile. It is necessary, however, that the radius of the tank be large in comparison with the transport mean free path in heavy water.

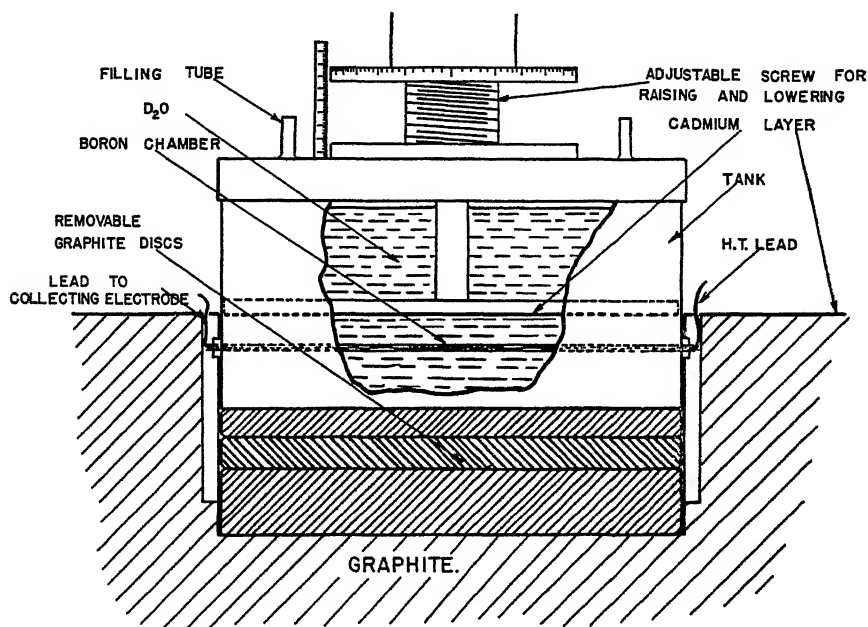


FIG. 1. *Experimental arrangement.*

### Experimental Arrangement

The experimental arrangement is shown in Fig. 1. The graphite pile was 250 cm. high and of square cross-section, 188 cm. on the side.

The source of neutrons was 2.4 gm. of radium mixed with beryllium. It was placed on the vertical axis of the pile 97 cm. below the top of the graphite and hence 97 cm. below the heavy water boundary. In one experiment, however, the source was placed 132 cm. below the common boundary. The upper surface of the pile was covered with cadmium sheet approximately 1 mm. thick.

The aluminium tank containing 11.32 kgm. of heavy water had an internal diameter of 29.9 cm., a wall thickness of 1.5 mm., and a height of 16 cm. The aluminium lid was sealed in place with wax. The rod used to raise and lower the cadmium plate passed through a central hole in the lid, which was made air-tight with a rubber gasket. An aluminium tube, 6.35 mm. in

outside diameter, and of wall thickness 0.85 mm., crossed the tank along a diameter 4.45 cm. above the bottom. This tube housed a boron trifluoride chamber, 4 mm. in outside diameter, at its middle point

The heavy water boundary was defined by the lower surface of a cadmium layer, 1 mm. in thickness, sprayed on a horizontal steel disk, 8 mm. thick, which was fixed to the vertical rod. By means of the micrometer screw the disk could be moved over a distance of 9 cm.

In order to vary the distance of the chamber from the cadmium surface and at the same time keep the cadmium level with the graphite surface, the disk was displaced by means of the micrometer screw and the tank raised or lowered to compensate for the former displacement. Graphite disks of graded thicknesses, 1, 2, 5 cm., were used under the tank to bring about the necessary compensation. In this way the neutron density was explored at a number of distances between the cadmium boundary and the boron chamber.

The alternative to the method adopted for varying the distance between the chamber and boundary would have been to move the boron chamber with respect to a stationary cadmium plate. The method adopted has the following advantages. (1) The very fragile chamber remains undisturbed inside the aluminium tube, and hence there is little chance of breakage. (2) The distance between the cadmium plate and the aluminium tube, which is an essential parameter in the measurements, can be measured with a micrometer screw to a high degree of accuracy. It is safe to state that the distance  $a$  of the tube from the plate was known to  $\pm 0.1$  mm.

The distance  $z$  from the plate to the chamber was taken to be

$$z = a + \text{half the outer diameter of the tube.}$$

The possibility that errors arise in this procedure, and experiments to test the validity of the procedure, will be discussed later.

The interior of the tank and the other surfaces in contact with the heavy water had been painted with a zinc chromate primer to protect the metals against corrosion. The thickness of this coat on the cadmium was such a small fraction of the scattering mean free path in the primer that its presence introduced no error. No corrosion of the cadmium took place for no drift in the counting rate of the chamber was observed (at a given position) over a period of three weeks.

During the series of measurements the temperature of the heavy water was fairly constant at 22° C.

### Neutron Detector

For the measurement of neutron densities a boron trifluoride chamber was chosen in preference to a detector having the property of becoming radioactive under neutron bombardment for the following reasons.

(1) For a given neutron absorption a boron trifluoride chamber has a greater efficiency (number of pulses counted per neutron absorbed) than any

detector having the property of becoming  $\beta$ -active. Moreover, there is some practical advantage in being able to count in the presence of the source.

(2) For the low counting rates that are encountered in this experiment, the fact that the chamber has practically no background is a great advantage. The background of the chambers used was about one count per hour. Moreover, the neutron counting rates do not drift over long periods of time

(3) Although the boron trifluoride chamber has dimensions that cannot be reduced beyond a certain practical limit, *relative* measurements of neutron density can be made without error in the present experiment where the density is a linear function of  $z$ . Under this condition, in fact, the counting rate is altered through the finite dimensions of the chamber by a factor that is independent of  $z$ . The  $z$ -co-ordinate defining the position of the chamber can be identified as that of its geometrical centre, provided that the symmetry about the axis of the chamber is perfect. It will be shown that this requirement was met.

The boron trifluoride chambers, one of which is shown in Fig. 2, were of a series made by Mr. N. Veall (14). They were filled with boron trifluoride to a pressure of 2 atm. The cathode, anode, and guard-ring were made of platinum. The collecting voltage was 600 in most of the experiments.

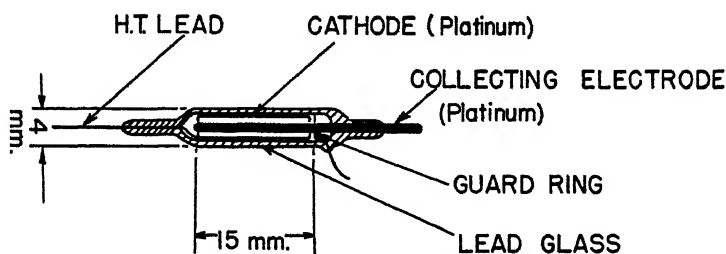


FIG. 2. Boron trifluoride chamber.

The chamber was connected to a linear amplifier of conventional design, the first tube of which was situated as close as possible to the chamber. The amplifier was followed by a discriminator, to reject pulses smaller than a chosen size, and a scale-of-32. Counting rates were reproducible within the statistical accuracy during the whole series of measurements, which lasted one month.

In order to estimate the neutron absorption in the chamber as a whole, the lead glass (Corning G-12) used to make the envelope was analysed. Taking the known capture cross-sections and numbers of nuclei in the constituents (boron, fluorine, oxygen, aluminium, silicon, sodium, potassium, lead, and platinum) of the chamber and an equal length of the enclosing aluminium tube, the chamber was found to be equivalent in absorption to about 1 mgm. of boron.

The error arising from the perturbation of the neutron density by the detector must be estimated because this perturbation would cause the density to be underestimated by a factor that is larger the farther the detector is from the boundary. Consequently the measured cut-off distance  $d$  would be too great, if the error under consideration were not negligible. The following considerations show, however, that the detector was so thin with respect to neutron capture that its perturbation introduces negligible errors in comparison with the statistical errors. For convenience, the actual case is reduced to simple geometry by supposing that the chamber is replaced by an equivalent absorbing disk of boron having a radius of 1 cm. and a mass of 1 mgm. A calculation by Skyrme (12) can then be used to estimate the perturbation, on the assumptions that the scattering medium is infinite in extent and that the neutron velocities are distributed isotropically, for a disk of mass absorption coefficient  $k$ , thickness  $t$ , and radius  $r$ . The elementary expression for the rate of neutron capture,

$$A = \pi r^2 \rho v k t,$$

is replaced by

$$A(1 - 0.03 - 0.007)$$

for the boron disk under consideration ( $k = 39 \text{ cm}^2 \text{ per gm.}$ ,  $t = 0.003 \text{ gm. per cm}^2$ ,  $r = 1 \text{ cm.}$ ) and far from any boundary. The first term represents the 'undisturbed' rate of capture (infinitely thin detector), the second term is a function of  $k$  and  $t$ , and is consequently a property of the detector only, taking into account its finite thickness. The third term depends on the properties of the medium and of the detector, namely, it is a function of  $k$ ,  $t$ ,  $r$ , scattering mean free path (about 2 cm.), and the diffusion length (greater than 50 cm.) of the heavy water. Suppose that the equivalent boron disk is used in a region close to the boundary but far enough from it for the neutron velocities to be distributed almost isotropically. The rate of neutron capture in the detector will be approximately equal to  $A(1 - 0.03 - f(z))$ , with  $f(z) \ll 0.007$  at any point  $z$  of the region investigated. In fact, the third term in the expression for the rate of absorption of neutrons is 0.007 at a distance of more than one diffusion length from the boundary and must approach zero as the boundary is approached. Consequently, this term must be less than 0.007, and it cannot change much over a distance much less than one diffusion length. The effective sensitivity of the boron chamber, which is proportional to the rate of capture of thermal neutrons, is therefore independent of  $z$  to high accuracy.\*

In the Appendix some experiments using dysprosium oxide and a boron trifluoride chamber as detectors of thermal neutrons in graphite are compared. Since no significant difference in the cut-off distance was found, it is concluded that the electrical leads to the chamber do not introduce errors.

\* If the equivalent boron disk is assumed to have a radius of 0.5 cm the third term is about 0.01 inside the medium

### Discussion of the Results

Several independent series of measurements were made; each one consisted of determining the density at various distances from the cadmium plate. In Fig. 3 the results of three typical series are plotted. One can see from the figure that the departure of  $\rho(z)$  from linearity (in the region for  $z$  between

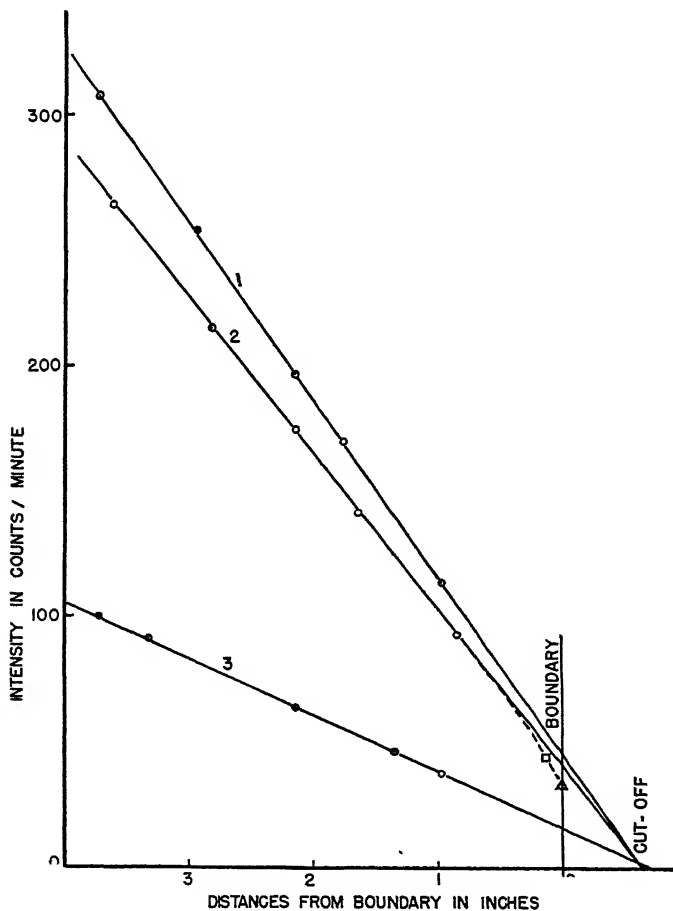


FIG. 3. Curves representing the density of neutrons at various distances from the boundary heavy water - cadmium.

Curve No. 1—Source 97 cm. below boundary, boron trifluoride chamber No. 1.

Curve No. 2—Source 97 cm. below boundary, boron trifluoride chamber No. 2.

Curve No. 3—Source 132 cm. below boundary, boron trifluoride chamber No. 2.

The dotted curve is the theoretical representation of the densities near the boundary. The point marked with a triangle is the theoretical value of the density at the boundary, according to Placzek and Mark. The point marked with a square is experimental.

2.5 and 9 cm.) is not detectable: this is due to the fact that the relaxation length  $L_r$  is certainly longer than 33 cm. The closest point to the boundary which was used for measuring  $l_t$  was at a distance of one mean free path from

the cadmium plate, because  $\rho(z)$  is expected to depart from a straight line at distances from the boundary smaller than the transport mean free path. However, it was thought worth while to detect the curvature of  $\rho(z)$  near the boundary because, to the authors' knowledge, the departure from the linearity near the boundary had never been observed. The neutron density was therefore measured when the cadmium plate was in contact with the aluminium tube ( $z = 3.2$  mm.). The measured point, marked with a square in Fig. 3, is definitely below the straight line. Of course, the accuracy to which this point is measured is rather bad since here  $\rho$  is no longer a linear function of  $z$  and consequently the 'effective' position of the chamber is not accurately known. It is interesting to notice, however, that the theory predicts a departure of  $\rho(z)$  from linearity about equal to the observed one (9, 10). In Fig. 3 a triangle indicates the theoretical value of  $\rho$  at the surface.

The curvature of the neutron density was roughly measured in the horizontal direction at three selected distances from the boundary. The density on the vertical axis of the tank was between 2 and 3.5% higher than at a point 9 cm. from that axis, measured along the aluminium tube. This is about the amount expected at distances over 100 cm. from the source in this graphite pile if graphite replaced the tank of heavy water.

It has been stated already that in a region where the density is linear, the effective distance between the ionization chamber and the heavy water boundary is correctly expressed by the distance from the axis of the boron trifluoride chamber to the cadmium plate, provided that the chamber has cylindrical symmetry around its geometrical axis. That this was the case is shown by the following experiments.

(1) Two series of measurements, made with two different chambers of similar construction, yielded the same value of the cut-off distance within experimental error.

(2) The effect of rotating a chamber through  $180^\circ$  was investigated. At a distance of 1.48 cm. from the cadmium plate, the counting rate was  $85.7 \pm 0.7$  pulses per minute when the chamber was orientated as usual and  $86.1 \pm 0.7$  pulses per minute when the chamber was rotated through  $180^\circ$ . From the slope of the straight line, at the point investigated a displacement of 1 mm. corresponds to a change in counting rate of three pulses per minute. The error in the cut-off distance is probably less than 0.3 mm. owing to this uncertainty in position, and hence is much less than the statistical error, which is given in Table I.

TABLE I

Experiment	Extrapolated cut-off distance, cm.
1	$1.57 \pm 0.12$
2	$1.63 \pm 0.08$
3	$1.62 \pm 0.08$
4	$1.71 \pm 0.09$

A straight line was fitted by the method of least squares to each of four independent sets of measurements.\* The values of the cut-off distance  $d$  are given in Table I. The final results are

$$d = 1.64 \pm 0.06 \text{ cm.}$$

and

$$l_t = 2.31 \pm 0.09 \text{ cm.}$$

According to a mass spectroscopic analysis performed by Dr. H. G. Thode and his collaborators, the heavy water used in these experiments contained 99.4 atoms of deuterium per 100 atoms of hydrogen element. When a correction is applied for the neutron scattering by the light hydrogen present,† it is found that

$$l_t(100\% \text{ D}_2\text{O}) = 2.4 \pm 0.1 \text{ cm.}$$

This value may be compared with the ordinary mean free path, which, according to several authors (2, 3, 5), is

$$l = 2 \text{ cm.}$$

It follows that

$$(\cos \theta)_{av} = 0.17,$$

with an error of about 25%.

### Acknowledgments

The authors wish to thank Drs. C. Mark, G. Placzek, B. W. Sargent, and P. Wallace for their interest and co-operation.

### APPENDIX

Before the measurements in heavy water were initiated, similar experiments were performed with graphite. The main purpose was to compare measurements obtained with a boron trifluoride chamber and with a dysprosium detector. The latter was a disk of aluminium, 1.6 cm. in diameter, on which was deposited 14 mgm. of dysprosium oxide. The agreement between the following results for graphite of density 1.68 gm. per cc. is seen to be satisfactory:

$$d_{\text{graphite}} = 1.72 \pm 0.13 \text{ cm. with dysprosium detector}$$

$$d_{\text{graphite}} = 1.69 \pm 0.06 \text{ cm. with boron trifluoride chamber.}$$

As stated at the beginning of this paper, the transport mean free path of thermal neutrons in a crystalline substance is not a well defined quantity; consequently no attempt has been made to evaluate, from the results of such experiments, the transport mean free path of thermal neutrons in graphite.

\* Each density was measured to better than 1%. When the method of least squares was applied, each density was given a weight inversely proportional to the square of its absolute statistical error. The time taken to make a complete set of measurements was about 48 hr.

† The mean free path in ordinary water is about 3.2 mm.

## References

1. AMALDI, E. and FERMI, E. Phys. Rev. 50 : 899-928. 1936.
2. BEYER, H. G. and WHITAKER, M. D. Phys. Rev. 57 : 976-981. 1940.
3. CARROLL, H. Phys. Rev. 60 : 702-709. 1941.
4. FERMI, E. Ricerca sci. 7 : 13-52. 1936.
5. HANSTEIN, H. B. Phys. Rev. 59 : 489-497. 1941.
6. HEReward, H. G., LAURENCE, G. C., MUNN, A. M., PANETH, H. R., and SARGENT, B. W. Can. J. Research, A, 25 : 26-41. 1947.
7. HEReward, H. G., LAURENCE, G. C., PANETH, H. R., and SARGENT, B. W. Can. J. Research, A, 25 : 15-25. 1947.
8. MARK, C. Unpublished report, MT-26. Milne's problem for anisotropic scattering. National Research Council of Canada. 1944.
9. MARK, C. Unpublished report, MT-50. The neutron density near a plane surface. National Research Council of Canada. 1944.
10. PLACZEK, G. Unpublished report, MT-16. The neutron density near a plane surface. National Research Council of Canada. 1943.
11. PLACZEK, G. and SEIDEL, W. Unpublished report, MT-5. Milne's problem in transport theory. National Research Council of Canada. 1943.
12. SKYRME, T. H. R. Unpublished report, MS-91. Reduction in neutron density caused by an absorbing disc. British Atomic Energy Project. 1944.
13. SMYTH, H. De W. Atomic energy for military purposes. 2nd ed. Princeton Univ. Press, Princeton, N.J. 1945.
14. VEALL, N. Unpublished report, MP-60. On the construction of small boron chambers. National Research Council of Canada. 1944.

## SPATIAL DISTRIBUTION OF NEUTRONS IN HYDROGENOUS MEDIA CONTAINING BISMUTH, LEAD, AND IRON<sup>1</sup>

BY A. M. MUNN<sup>2</sup> AND B. PONTECORVO<sup>3</sup>

### Abstract

The spatial distributions of thermal neutrons (as measured by dysprosium detectors) and of resonance neutrons (indium detectors protected by cadmium) have been investigated in several media, consisting of water and heavy elements in a heterogeneous arrangement, with two different neutron sources (Ra- $\alpha$ -Be and Ra- $\gamma$ -Be). The experimental results are summarized in tables where the values of the mean square distances from the source of neutrons are given, for the various media, detectors, and sources used. It was found that among all the media investigated, a mixture of water and iron is the most efficient shield for neutron generating machines such as piles and cyclotrons.

### Introduction

The distribution in space of slow neutrons which are produced when a source of fast neutrons is introduced in a moderating medium has been studied in a systematic way only in media containing essentially light elements, such as paraffin, water and heavy water. The object of the present work is to investigate hydrogenous substances containing high concentrations of heavy elements. The knowledge of the neutron spatial distribution in such media is not only interesting in itself, but is also very useful in solving the problem of shielding neutron generating machines such as cyclotrons and chain reacting piles. In fact, a good shield against the radiations from a neutron generating machine must combine the following properties. It must rapidly slow down neutrons and also strongly absorb the  $\gamma$ -radiation arising when neutrons are captured. In addition to these sources of  $\gamma$ -rays distributed throughout the moderating and capturing medium, in the case of the chain reacting pile the accumulated fission products emit strong  $\gamma$ -radiation. The necessity for strong absorption of  $\gamma$ -radiation by the shield suggests heavy elements. The choice is further limited by the requirement that the material must be inexpensive, for in a practical case the quantity needed may be very large. On these grounds iron and lead should be considered. On the other hand, the need for an efficient and inexpensive moderator for neutrons suggests immediately a substance containing hydrogen, such as water or wood. A mixture of water with iron or lead should therefore be a good shield against both neutrons and  $\gamma$ -rays. Mixtures of water with bismuth are also interesting for the general understanding of the process of moderation and diffusion of neutrons.

<sup>1</sup> Manuscript received October 16, 1946.

Contribution from the Montreal Laboratory, Nuclear Physics Branch, Division of Atomic Energy, National Research Council of Canada. (Work performed in 1943.) Issued as N.R.C. No. 1525.

<sup>2</sup> Physicist; now at McGill University, Montreal, Que.

<sup>3</sup> Member of the United Kingdom staff, now at the Chalk River Laboratory, Chalk River, Ont.

In a discussion of the effect of heavy atoms in a hydrogenous material on the spatial distribution of neutrons, two points should be kept in mind. First, if fast neutrons are scattered inelastically by the heavy nuclei, the slowing down efficiency is increased. The spatial distribution of slow neutrons around a source in the scattering medium may therefore be affected by inelastic collisions if the neutrons from the source are sufficiently energetic. The neutrons from a mixed radium and beryllium source (Ra- $\alpha$ -Be) are certainly sufficiently energetic and undergo inelastic collisions against heavy nuclei. On the contrary, the photoneutrons from a radium and beryllium source (Ra- $\gamma$ -Be), having a much smaller energy, may be incapable of exciting nuclei and undergoing inelastic collisions. Secondly, elastic collisions must be considered. Although a neutron loses a small fraction of its energy in an elastic collision with a heavy nucleus, the effect of such collisions upon their spatial distribution is far from negligible for the following reasons. (1) Since the elastic scattering cross-section of a heavy element does not decrease with increasing energy of the neutrons as rapidly as in the case of hydrogen, collisions against the heavy nuclei are comparatively frequent at high energies. (2) After neutrons make collisions against heavy nuclei, their velocities are distributed isotropically, while in the case of hydrogen their velocities are predominantly forward.

The effect of elastic collisions in nuclei heavier than hydrogen was first described by Fermi (4) in his original theoretical derivation of the mean square distance of neutrons in water. The effects of inelastic and elastic scattering collisions of neutrons with heavy nuclei will be discussed in detail later.

In the absence of inelastic collisions, in principle, the mean square distance of neutrons of a given energy from a source of fast neutrons embedded in a scattering medium could be calculated. Prerequisite data, such as the energy distribution of the neutrons from the source and the scattering cross-sections of all types of nuclei present at various energies of the neutrons, are however not well known. Under these circumstances, a simple experimental approach seemed likely to yield information of theoretical and practical value in a short time. Since high concentrations of the elements iron, lead, and bismuth in water were required, solutions of their compounds could not be used. A heterogeneous mixture, and a lattice, resembling a checkerboard, of water and the heavy element was adopted. The spatial distributions of thermal and indium resonance neutrons were explored in several lattices using two different sources of fast neutrons (Ra- $\alpha$ -Be) and (Ra- $\gamma$ -Be).

### Experimental Method

The Ra- $\alpha$ -Be source consisted of 1 gm. of radium bromide mixed with beryllium, enclosed by a brass cylinder of radius 1.8 cm. and height 1.8 cm. The Ra- $\gamma$ -Be source consisted of 1 gm. of radium at the middle of a cube of beryllium, 4.9 cm. edge. This cube had to be large in order to get sufficient neutron intensity, although its size makes the results more difficult to interpret.

The experimental arrangement is shown in Fig. 1. The tank was made of galvanized iron, painted on the inside to prevent corrosion. Its dimensions were: 90 cm. long, 45 cm. wide, and 45 cm. deep. The square rods, arranged in a checkerboard pattern, were supported on end in the tank by a grid of wires. The lead and bismuth rods were 32 by 2 by 2 cm. and the iron rods 32 by 1.87 by 1.87 cm. The latter were nickel plated. The depth of water in the tank was 32 cm. By varying the arrangement of the rods, various ratios of volume of water to metal could be obtained (1 : 2, 1 : 1, 2 : 1 for bismuth and lead, 1.3 : 1 for iron).

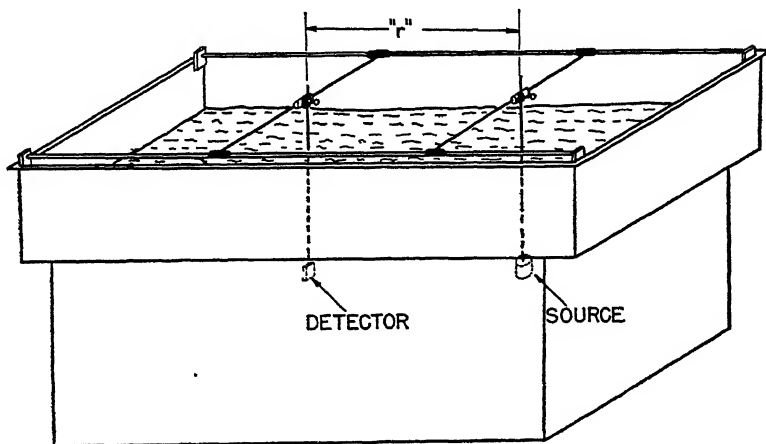


FIG. 1. Sketch of the tank, in which  $H_2O + Bi$ ,  $H_2O + Pb$ ,  $H_2O + Fe$  lattices were studied in a checkerboard arrangement.

The source and the boxes for the detectors were supported by a system giving three dimensional motion. These were placed halfway down in the water. The source was placed in a fixed position about 20 cm. from one end of the tank, while the detectors were irradiated at various distances  $r$  from the centre of the source, measured in several directions. The minimum distance between a detector and the nearest boundary of the mixture of water and metal was 15 cm.

The detectors of thermal neutrons consisted of 70 mgm. each of dysprosium oxide on an aluminium tray, 2 by 2.5 cm. The detectors of resonance neutrons were made of indium, 45 mgm. each on an aluminium backing, 2 by 2.5 cm. The dysprosium detectors were activated in flat watertight aluminium boxes, the indium in similar cadmium boxes of wall thickness 0.6 mm. Following the irradiation of the detectors by neutrons, their  $\beta$ -activities were measured on a thin-walled aluminium counter. Corrections were applied for decay during measurement and lack of saturation at the end of the irradiation, using 138 and 54 min. respectively for the half-periods of dysprosium and indium.

### Experimental Results

Let  $I$  represent the saturation  $\beta$ -activity of a detector, measured in counts per minute of the Geiger-Muller counter, after the detector has been exposed to neutrons at a distance  $r$  from the source. Now,  $I$  is directly proportional to the density of thermal neutrons in the case of a dysprosium detector or to the density of resonance neutrons in the case of an indium detector under cadmium. The number of neutrons of the type considered found in a shell of constant thickness and mean radius  $r$  about the source is therefore directly proportional to  $I r^2$ , if the system is spherically symmetrical. A plot of  $I r^2$  against  $r$  is a convenient way of representing the spatial distribution (1). Examples are shown in Figs. 2 and 3.

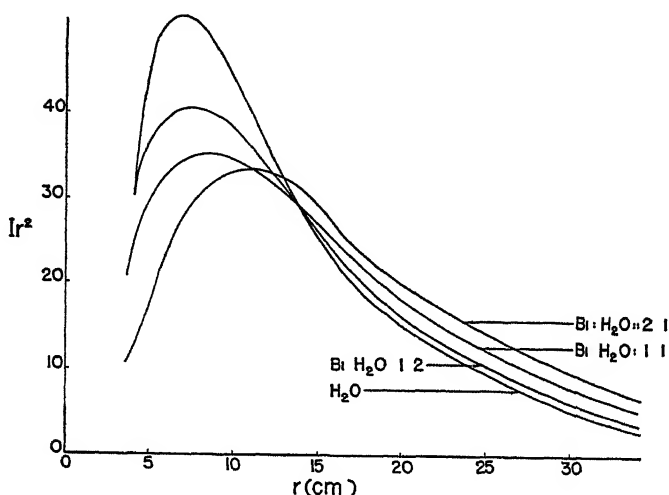


FIG. 2. Spatial distribution of In resonance neutrons. Source: Ra- $\alpha$ -Be.

Although some detail is sacrificed in the process, a single parameter is usually derived from the spatial distribution, for convenience in discussion. This parameter is the mean square distance from the source,  $(r^2)_{av}$ , of the neutrons of the type considered. A characteristic length  $L_c$  in the medium, simply related to  $(r^2)_{av}$ , may be defined for convenience. The mean square distance is found from the obvious relation:

$$(r^2)_{av} = 4\pi \int_0^\infty I(r) r^4 dr / 4\pi \int_0^\infty I(r) r^2 dr. \quad (1)$$

The characteristic length  $L_c$  is defined by

$$L_c^2 = \frac{1}{6} (r^2)_{av}. \quad (2)$$

The following assumptions are implied: (1) the source is effectively a point, (2) the material of the source has the same slowing down properties as the

mixture of water and metal, and (3) the neutron density is spherically symmetrical around the source, as it would be if the medium were homogeneous. The last assumption holds sufficiently well, for the tank was large enough and the neutron densities were measured at corresponding points in the lattice.

The experimental results are summarized in Tables I and II. The Ra- $\alpha$ -Be source conforms sufficiently to the assumption of a point source, but the Ra- $\gamma$ -Be source does not. The geometrical error in the mean square distance caused by the departure of the source distribution from a point is estimated at less than 10% for the beryllium cube in any of the media investigated. The correction for the difference in the slowing down properties of beryllium and

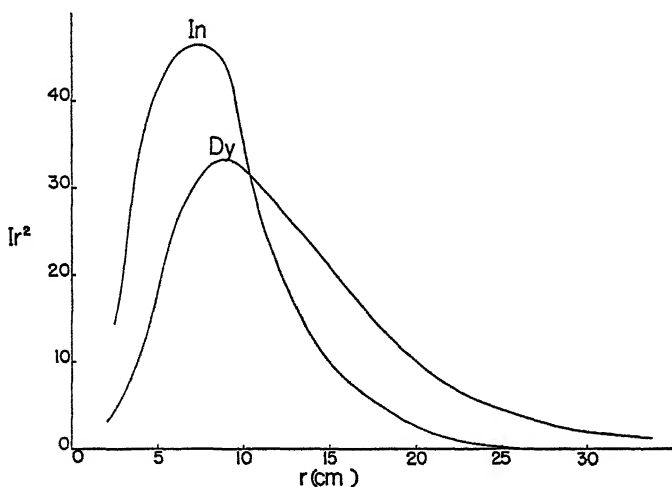


FIG 3. Spatial distribution of resonance neutrons (*In*) and of thermal neutrons (*Dy*) in  $H_2O + B_2$  (1:1 by volume). Source: Ra- $\gamma$ -Be. (The side of the Be cube is 4.9 cm.)

the surrounding medium was more serious and was estimated as follows. The average energy of the photoneutrons was assumed to be 130 kev. According to a calculation by Marshak (7), which was based on known scattering cross-sections,  $(r^2)_{av} = 38 \text{ cm.}^2$  in water for neutrons of energy 130 kev. This value is  $20 \text{ cm.}^2$  smaller than the measured  $58 \text{ cm.}^2$  in water (Table II). The slowing down properties of the mixtures of water and metal are more similar to those of water than to those of beryllium. A rough order of magnitude calculation indicates that the correction is about  $18 \text{ cm.}^2$  for all the media investigated. The observed values of  $(r^2)_{av}$  in Table II have been reduced by  $18 \text{ cm.}^2$

Since the measurements could not be carried out at very large values of  $r$ , owing to lack of intensity, some extrapolation of the spatial distribution was necessary in evaluating  $(r^2)_{av}$ . At large values of  $r$  the quantity  $Ir^2$  decreases according to  $e^{-r/\lambda}$ , where  $\lambda$ , defined as the relaxation length, is an important parameter in shielding considerations. Although in fact  $\lambda$  increases slowly

with  $r$ , for the purpose of extrapolation  $\lambda$  was estimated at the last part of the measured distribution, and  $Ir^2$  assumed to decrease with this relaxation length.

TABLE I  
SOURCE: RA- $\alpha$ -Be

Medium (volume ratio)	Concentrations, $C$ , gm-atoms/l.	Detector	$(r^2)_{av}$ , cm. <sup>2</sup>	$L_c$ , cm.
H <sub>2</sub> O	$C_H = 111$	Dy	330	$7.4 \pm 0.2$
*H <sub>2</sub> O	$C_H = 111$	Rh(Cd difference)	327	7.4
H <sub>2</sub> O	$C_H = 111$	In resonance	278	$6.8 \pm 0.2$
*H <sub>2</sub> O	$C_H = 111$	Rh resonance	277	6.8
H <sub>2</sub> O : Bi :: 1 : 1	$C_H = 56$ $C_{Bi} = 23$	Dy	562	$9.7 \pm 0.4$
H <sub>2</sub> O : Bi :: 2 : 1	$C_H = 74$ $C_{Bi} = 15$	In resonance	398	$8.1 \pm 0.3$
H <sub>2</sub> O : Bi :: 1 : 1	$C_H = 56$ $C_{Bi} = 23$	In resonance	477	$8.9 \pm 0.4$
H <sub>2</sub> O : Bi :: 1 : 2	$C_H = 37$ $C_{Bi} = 30$	In resonance	517	$9.3 \pm 0.4$
H <sub>2</sub> O : Pb :: 1 : 1	$C_H = 56$ $C_{Pb} = 27$	In resonance	437	$8.5 \pm 0.3$
H <sub>2</sub> O : Fe :: 1.3 : 1	$C_H = 63$ $C_{Fe} = 60$	In resonance	319	$7.3 \pm 0.3$

\* Measured by Amaldi and Fermi (1), using a Rn- $\alpha$ -Be source.

TABLE II  
SOURCE: RA- $\gamma$ -Be  
DETECTOR: IN UNDER Cd

Medium (volume ratio)	Concentrations, $C$ , gm-atoms/l.	$(r^2)_{av}$ , cm. <sup>2</sup>		$L_c$ , cm.
		Observed	Corrected	
H <sub>2</sub> O	$C_H = 111$	58	38	2.5
H <sub>2</sub> O : Bi :: 2 : 1	$C_H = 74$ $C_{Bi} = 15$	87	69	3.4
H <sub>2</sub> O : Bi :: 1 : 1	$C_H = 56$ $C_{Bi} = 23$	95	77	3.6
H <sub>2</sub> O : Pb :: 1 : 1	$C_H = 56$ $C_{Pb} = 27$	87	69	3.4
H <sub>2</sub> O : Fe :: 1.3 : 1	$C_H = 63$ $C_{Fe} = 60$	79	61	3.2

In conclusion, it should be emphasized that the values of  $(r^2)_{av}$  in Tables I and II are by no means equally accurate. Since the Ra- $\alpha$ -Be source has small dimensions and the values of  $(r^2)_{av}$  are comparatively high, Table I is satisfactory. On the other hand, Table II is unsatisfactory for the opposite reasons, and only close comparisons of  $(r^2)_{av}$  within the table should be attempted. No attempt was made to estimate the error affecting the values of  $L_c$  in Table II.

### Discussion

The values of  $(r^2)_{av}$  and  $L_c$  for  $C$  or cadmium absorbable neutrons and for rhodium resonance neutrons obtained with a Rn- $\alpha$ -Be source in water by Amaldi and Fermi (1) are included in Table I. The agreement with the present results is very good.

It is seen that the characteristic length  $L_c$  is greater when dysprosium is used as a detector of neutrons than when indium shielded by cadmium is used, the source and medium being the same (Table I). This is due to the fact that the motion of neutrons consists of two phases: (i) the slowing down phase, where the neutrons are slowed down from their average initial energy to the beginning of the thermal energy region, which is associated with a characteristic length  $L_s$  called the slowing down length, and (ii) the diffusion phase, associated with a characteristic length  $L$  called the diffusion length. Since dysprosium detects thermal neutrons, it is easy to see that with this detector

$$L_c^2(\text{Dy}) = L_s^2 + L^2.$$

In the case of the indium detector shielded by cadmium, the neutrons are detected at the resonance energies of indium that lie above the strong absorption region of cadmium. The strongest resonance band of indium is at 1.44 ev. The characteristic length  $L_c$  is therefore the slowing down length to 1.44 ev., which may be called  $L'_s (< L_s)$ . Since the squares of such lengths are additive,

$$L_c^2(\text{Dy}) - L_c^2(\text{In}) = L_s^2 + L^2 - L_s'^2,$$

which qualitatively explains the differences noted above for water and a mixture of water and bismuth. The difference for water and bismuth is much greater than the difference for water (first observed and explained by Amaldi and Fermi (1)), because of the increase in the diffusion length when bismuth replaces part of the water, the capture cross-section of bismuth for thermal neutrons being low.

The very great difference in the spatial distributions of thermal and indium resonance neutrons may be seen directly. The greater spread of the former is shown in Fig. 3, where the two are compared in a lattice of water and bismuth around a Ra- $\gamma$ -Be source. (Owing to the perturbation by the mass of beryllium, the mean square distance of thermal neutrons has been omitted from Table II.)

For a further discussion of the experimental results in Tables I and II it will be convenient to use values of the scattering cross-sections in hydrogen, iron, lead, and bismuth for neutrons of several energies (2, 3, 5, 6). From

these, given in Table III, the scattering mean free paths of Table IV were calculated for the mixtures of water and metal used in these experiments. Although the lattice spacings are comparable to the scattering mean free paths, it is necessary to ignore the heterogeneity and consider each lattice replaced by a homogeneous medium having the same atomic composition and density.

TABLE III

SCATTERING CROSS-SECTIONS  $\sigma$  (IN UNITS OF  $10^{-24}$  CM.<sup>2</sup>) AT VARIOUS NEUTRON ENERGIES FOR THE SUBSTANCES DENOTED BY THEIR CHEMICAL SYMBOLS

Neutron energy, ev.	$\sigma$				
	H	H <sub>2</sub> O	Fe	Pb	Bi
1	20.5	46.0	11.1	9.6	8.7
$130 \times 10^3$	11.5	28.6	3.5	7.3	8.1
$220 \times 10^3$	8.0	24.0	3.6	6.2	8.4
$460 \times 10^3$	6.3	16.6	—	5.8	6.7
$900 \times 10^3$	4.5	13.8	3.1	5.1	5.4
$2.7 \times 10^6$	2.5	6.0	3.1	6.4	6.5
$3 \times 10^6$	2.3	5.6	—	6.7	6.7
$5 \times 10^6$	1.6	4.6	—	—	—

TABLE IV

SCATTERING MEAN FREE PATH, IN CM., IN HOMOGENEOUS MEDIA HAVING THE SAME ATOMIC COMPOSITION AND DENSITY AS THE LATTICES INVESTIGATED

Neutron energy, ev.	Scattering mean free path, cm.					
	H <sub>2</sub> O	H <sub>2</sub> O + Bi (2 : 1)	H <sub>2</sub> O + Bi (1 : 1)	H <sub>2</sub> O + Bi (1 : 2)	H <sub>2</sub> O + Fe (1.3 : 1)	H <sub>2</sub> O + Pb (1 : 1)
1	0.65	0.98	1.1	1.4	0.8	1.05
$130 \times 10^3$	1.05	1.4	1.7	2.1	1.5	1.7
$220 \times 10^3$	1.25	1.6	1.9	2.3	1.7	2.0
$460 \times 10^3$	1.80	2.3	2.6	3.2	—	2.7
$900 \times 10^3$	2.15	2.7	3.2	3.8	2.7	3.2
$3 \times 10^6$	5.3	5.3	5.4	5.4	4.7	4.9
$5 \times 10^6$	6.5	—	—	—	—	—

It is worth while mentioning the following points.

(1) The spatial distributions in Fig. 2 and Tables I and II show that the mean square distance is increased when iron, lead, or bismuth is added to water. This observation is in qualitative agreement with the increase in the mean free path which is caused by the addition of the metal (Table IV) for all but the very high neutron energies.

(2) The least values of  $(r^2)_{av}$  obtained in the hydrogenous media containing heavy metals were those for water and iron (Tables I and II), which fact is to be explained by the high atomic concentration in iron and the consequently reduced mean free path (Table IV).

(3) The ratio  $R$  of the mean square distance obtained with a Ra- $\alpha$ -Be source to that obtained with a Ra- $\gamma$ -Be source is smallest in water and iron (Table V). This fact indicates that probably inelastic collisions are relatively most important in iron. However, no certain conclusion can be drawn on this point, since the smallness of the mean free path at very high neutron energy

TABLE V  
DETECTOR: IN UNDER Cd

Medium	$R = \frac{(r^2)_{\alpha}(\text{Ra-}\alpha\text{-Be})}{(r^2)_{\gamma}(\text{Ra-}\gamma\text{-Be})}$
H <sub>2</sub> O	7.3
H <sub>2</sub> O : Bi :: 2 : 1	5.8
H <sub>2</sub> O : Bi :: 1 : 1	6.2
H <sub>2</sub> O : Pb :: 1 : 1	6.3
H <sub>2</sub> O : Fe :: 1.3 : 1	5.2

in water and iron might be sufficient to explain the observations. The fact that the highest value of  $R$  is in water is due to the very rapid increase of the mean free path with the neutron energy, characteristic of hydrogen.\*

(4) The shielding properties of a medium for neutrons are determined jointly by the mean square distance and the relaxation length at large distances. In the lattices of water and bismuth and water and lead the relaxation lengths at large distances from the Ra- $\alpha$ -Be source are larger than that in water. On the other hand, in the lattice of water and iron the relaxation length (9.4 cm.) is somewhat smaller than—more exactly within experimental error equal to—the value in water. At greater distances from the source than those that could be used in the experiment, the 'hardening' of the radiation should be more pronounced in water than in water and iron for the following reasons. The cross-section of very energetic neutrons is low in hydrogen but fairly high in iron, and inelastic collisions in iron become important for energetic neutrons. It is clear, therefore, that water and iron constitutes a very good shield for neutron generating machines.

It is possible to estimate the mean square distance of neutrons of a given energy on the basis of Fermi's age-velocity theory. Unfortunately, in the case of hydrogenous media, the scattering mean free path of energetic neutrons changes too rapidly for a change of the neutron energy corresponding to the average energy loss per collision. For this reason the age-velocity theory will be more reliable for the photoneutrons from a Ra- $\gamma$ -Be source than for the more energetic neutrons from a Ra- $\alpha$ -Be source.

\* Incidentally it seems worth while to point out here that water would be completely inadequate for shielding very high energy neutrons produced by the newly developed frequency modulated cyclotrons. Water and iron, on the contrary, appears to be very promising for shielding such instruments.

Suppose the source is emitting neutrons of average initial energy  $E_*$  in a medium composed of elements of several types  $k$ . The following symbols are needed:

- $M_k$  = nuclear mass of type  $k$ ,
- $C_k$  = atomic concentration for type  $k$ ,
- $a_k$  = average logarithmic energy loss in elastic collisions (8) between neutrons and nuclei of type  $k$  ( $a_{\text{hydrogen}} = 1$ ,  $a_{\text{oxygen}} = 0.12$ ,  $a_{\text{iron}} = 0.036 \dots$ ),
- $\sigma_l(E')$  = total cross-section of nuclei of type  $k$  at the neutron energy  $E'$ ,
- $l(E')$  = total mean free path in the medium for neutrons of energy  $E'$ ,
- $p_k(E')$  = probability that a neutron of energy  $E'$  makes a collision with a nucleus of type  $k$ ,
- $p_k(E') = \frac{C_k \sigma_k(E')}{\sum C_k \sigma_k(E')}.$

The mean square distance traversed by neutrons in slowing down from  $E_*$  to  $E$ , on the age-velocity theory, is given by

$$(r^2)_{av} = 2 \int_E^{E_*} \frac{l^2(E') dE'}{(\sum p_k a_k) \left(1 - \frac{2}{3} \sum \frac{p_k}{M_k}\right) E'} \quad (3)$$

Owing to the small loss of energy in collisions with heavy nuclei and their large mass in comparison with hydrogen, Equation (3) can be written in the simple approximate form:

$$(r^2)_{av} = 2 \int_E^{E_*} \frac{l^2(E') dE'}{p_H \left(1 - \frac{2}{3} p_H\right) E'} \quad (4)$$

Using the values of the cross-sections given in Table III,  $p_H$  and  $p_H(1 - \frac{2}{3} p_H)$  as shown in Table VI were obtained. The quantity  $p_H$  can vary only between zero (no hydrogen) and unity (pure hydrogen), and the quantity  $1 - \frac{2}{3} p_H$  between unity and 0.33. Consequently, the quantity  $p_H(1 - \frac{2}{3} p_H)$  rises from zero where  $p_H = 0$  and eventually reaches a flat maximum of 0.37 at  $p_H = 0.75$ . As shown in Table VI,  $p_H(1 - \frac{2}{3} p_H)$  is practically constant at 0.37 in all media used in the experiments, for neutron energies from 1 volt to 100 kev. Consequently, for neutrons from a Ra- $\gamma$ -Be source, this part of the denominator of the integral (Equation (4)) can be taken outside the integral sign, leaving  $(r^2)_{av}$  dependent on the medium only through the mean free path.

If the ratio

$$\frac{(r^2)_{av}(\text{H}_2\text{O} + \text{heavy element})}{(r^2)_{av}(\text{H}_2\text{O})}$$

of the experimental, corrected values of the mean square distances given in Table II is compared with the ratio of the square of the 'average' mean free path at low energies in the corresponding media (Table IV), qualitative agreement is found, within the various experimental errors and approximations involved.

TABLE VI

VALUES OF  $p_H$  AND  $p_H(1 - \frac{2}{3} p_H) = q_H$  FOR HOMOGENEOUS MEDIA HAVING THE SAME ATOMIC COMPOSITION AS THE HETEROGENEOUS ONES INVESTIGATED

Neutron energy, ev.	H <sub>2</sub> O		H <sub>2</sub> O + Bi (2 : 1)		H <sub>2</sub> O + Bi (1 : 1)		H <sub>2</sub> O + Bi (1 : 2)		H <sub>2</sub> O + Fe (1.3 : 1)		H <sub>2</sub> O + Pb (1 : 1)	
	$p_H$	$q_H$	$p_H$	$q_H$	$p_H$	$q_H$	$p_H$	$q_H$	$p_H$	$q_H$	$p_H$	$q_H$
1	0.89	0.36	0.83	0.37	0.77	0.37	0.68	0.37	0.60	0.36	0.74	0.37
$130 \times 10^3$	0.81	0.37	0.72	0.37	0.66	0.37	0.55	0.35	0.64	0.37	0.64	0.37
$220 \times 10^3$	0.67	0.37	0.59	0.36	0.52	0.34	0.43	0.31	0.52	0.34	0.53	0.35
$460 \times 10^3$	0.76	0.37	0.65	0.37	0.57	0.36	0.46	0.32	—	—	0.57	0.36
$900 \times 10^3$	0.65	0.37	0.56	0.35	0.50	0.33	0.40	0.29	0.45	0.32	0.47	0.32
$2.7 \times 10^6$	0.83	0.37	0.58	0.36	0.44	0.31	0.31	0.25	—	—	0.41	0.29
$3 \times 10^6$	0.83	0.37	0.56	0.35	0.42	0.30	0.29	0.23	0.39	0.29	0.38	0.28
$5 \times 10^6$	0.70	0.37	—	—	—	—	—	—	—	—	—	—

### Acknowledgments

The authors wish to thank Dr. H. Halban and Dr. B. W. Sargent for their interest and co-operation.

### References

1. AMALDI, E. and FERMI, E. Phys. Rev. 50 : 899-928. 1936.
2. BRETSCHER, E. and MURRELL, E. B. M. Unpublished report, Br-136. The total neutron collision areas of some heavy metals. British Atomic Energy Project. 1943.
3. BRETSCHER, E. and MURRELL, E. B. M. Unpublished report, Br-137. Determination of the total neutron collision cross-section for hydrogen and carbon. British Atomic Energy Project. 1943.
4. FERMI, E. Ricerca sci. 7 : 13-52. 1936.
5. HANSTEIN, H. B. Phys. Rev. 59 : 489-497. 1941.
6. LEIPUNSKY, A. I. J. Phys. U.S.S.R. 3 : 230-236. 1940.
7. MARSHAK, R. E. Unpublished report, MT-17. On the slowing-down length of neutrons in water. National Research Council of Canada. 1944.
8. PLACZEK, G. Phys. Rev. 69 : 423-438. 1946.



# Canadian Journal of Research

Issued by THE NATIONAL RESEARCH COUNCIL OF CANADA

OL. 25, SEC. A.

JULY, 1947

NUMBER

## THE EFFECT OF WIND ON THE THERMAL RESISTANCE OF CLOTHING WITH SPECIAL REFERENCE TO THE PROTECTION GIVEN BY COVERALL FABRICS OF VARIOUS PERMEABILITIES<sup>1</sup>

P. LAROSE<sup>2</sup>

### Abstract

The thermal resistance of a pile fabric uncovered and covered with thin fabrics of various permeabilities was measured under different conditions of wind velocities and wind direction. Wind velocities up to 30 m.p.h. were used and tests were carried out with winds striking the surface of the material at 0°, 30°, 45°, and 90°. The permeabilities of the covers varied between 0 and 193 cu. ft. per sq. ft. per min., under a pressure difference of  $\frac{1}{2}$  in. of water across the fabric. The effects of varying the conditions of the thermal resistance of the boundary air layer are discussed and corrections applied to the results for the resistance of this air layer. The results show that for low wind velocities, the permeability, within wide limits, is relatively of little importance, but with higher wind velocities it is advantageous to employ a covering fabric of as low a permeability as possible.

### Introduction

During the war, the thermal insulation of clothing assumed an increased importance as a result of the wide range of climatic conditions under which the fighting forces had to operate. This applied particularly to the airmen who, sometimes within a matter of minutes, had to change from a tropical atmosphere to one in which the temperature was well below freezing point. The question of warm clothing was also of great concern to mountain troops. The necessity of suitable clothing, if the greatest efficiency was to be obtained from the soldiers, was well recognized, and the problem of maintaining men in comfort in various climatic surroundings was one that occupied the attention of physiologists.

One of the climatic factors that affect the protection afforded by clothing is wind. Very little work had been done, prior to the war, on the effect of wind on thermal insulation of clothing. The work that had been carried out involved experiments with a very limited range of air velocities, and in most tests the results reported did not lend themselves to a calculation of the direct changes caused by the air movement. Moreover, in most of the experiments, a single material or fabric was tested at one time whereas in practice clothing usually consists of several layers of fabrics superposed and differing one from

<sup>1</sup> Manuscript received March 12, 1947.

Contribution from the Textile Section, National Research Laboratories, Ottawa, Canada.  
Issued as N.R.C. No. 1559.

<sup>2</sup> Chemist.

another. More particularly if protection against wind is desired, one usually wears an outer shell of some fabric generally designated as 'wind-proof'. It was the thermal protection given by this particular layer in which we were specially interested, and the determination of the relation between the degree of protection given by the 'coverall' fabric, the velocity of the air or wind striking the material, and the permeability of this material. Most experiments carried out previously had taken no account of the air permeability of the textile materials tested. The experiments described in this paper were therefore designed with the view to determining the effect of wind velocity, wind direction, and permeability of coverall on its thermal resistance in combination with a comparatively thick underlying fabric.

### Methods

The apparatus used for measuring the heat transmission through the combination of fabrics investigated was similar, except in method of control and in size, to that described by Cleveland (1) and used at the National Bureau of Standards, Washington. It consisted of a central brass plate, 10 in. square,  $\frac{3}{16}$  in. thick, surrounded by a guard ring 2 in. wide of the same thickness as the central plate and placed in the same plane. An air space about  $\frac{1}{12}$  in. wide separated the guard ring from the central plate. Both guard ring and central plate were painted a dull black. Another brass plate, 14 in. square, was placed 3 in. below and parallel to the central plate and guard ring. A number of reflecting aluminium foil layers spaced about  $\frac{1}{2}$  in. apart divided the space between the bottom and top plates. The brass plates, guard ring, and foil were encased in a wooden frame  $2\frac{1}{2}$  in. thick and fitted with a bottom 1 in. thick. The bottom plate, central plate, and guard ring were heated independently of one another by means of electric resistances placed directly below them. The current through these various heater resistances was controlled by means of hand-manipulated rheostats. During the initial stage of an experiment, the rheostats were adjusted frequently to maintain equality of temperature of the guard ring, central plate, and bottom plate, but after some time the plates would reach a practically steady state and little adjustment was required from then on. The fabrics were placed directly on top of the plate and guard ring. The samples, 20 in. square, were sufficiently large to cover the whole top of the apparatus, including the wooden frame.

The earlier tests carried out with low air velocities were performed in a room maintained under controlled conditions of temperature and humidity. Under such conditions it was possible to bring the apparatus to an equilibrium state in a relatively short time, but later, when higher wind speeds were desired, it was found impractical to carry out the experiments in the air-conditioned room, and, under the varying conditions of the laboratory, equilibrium was reached in a more or less longer time depending on the steadiness of the ambient conditions. It was possible, however, to carry out one test per day on the average.

Conducting the tests in the ordinary laboratory with no temperature control resulted also in some uncertainty regarding the temperature of the room. This point will be dealt with in discussing the results.

Temperatures were measured by means of thermocouples but, except in some of the later experiments, temperature differences between the various points were determined and not the absolute temperatures since these were not required for the calculations in which we were interested. The temperature of the air was taken as that of a  $\frac{1}{2}$  in. mesh grid placed above the sample. In some of the later experiments, a copper wire ring was used but there was no significant difference between the results obtained in this way and the results obtained with the grid, other conditions being equal. The grid (or ring) was placed about 1 in. above the surface of the fabric and parallel to it. A thermometer placed on the grid, at one side, served to show at a glance, any variation in the temperature of the grid during the tests. In the earlier experiments, it was thought that the grid was at a distance from the top of the fabric sufficient to have it take up the temperature of the room and to use its temperature as that of the room, but it was found in later experiments that, apparently owing to convection currents, the grid was in fact warmer than the air in the room, and a correction based on the results of these experiments was applied to arrive at the air temperature in the earlier experiments. However, some degree of uncertainty is attached to this correction, for reasons to be explained later. The difference in temperatures between the central plate and the guard ring was measured with four sets of thermocouples connected in series, one set to each side of the plate, so that the potential difference indicated on the potentiometer corresponded to the sum total of the temperature differences across each thermocouple between plate and guard. The other measurements taken were the temperature differences between central plate and bottom plate, and between the central plate and grid (air). In some of the later experiments, the temperature differences between central plate and surface of fabric was also determined. The potentiometer and thermocouples used allowed temperature differences to be read to within  $0.02^{\circ}\text{C}$ .

In the initial experiments an ordinary 12 in. propeller type fan with axial flow was used to produce the air circulation. It was placed with its centre about 8 in. away from the outside edge of the apparatus and slightly above it for the horizontal wind, and in corresponding positions but higher up for winds of  $30^{\circ}$  and  $45^{\circ}$  to the horizontal. With it, speeds up to 11 m.p.h. could be obtained but when higher speeds were required, a centrifugal fan with a 6 in. diameter outlet giving radial flow was used. This produced winds up to 30 m.p.h. The position of the fan was such that the outlet was about 24 in. above the sample being tested. Although the outlet of the fan was only 6 in., at 24 in. distance it exerted a fairly uniform effect over the whole central plate. Since the speed of the fan motor could not readily be altered, the variation in wind velocity was obtained by placing diaphragms of different sizes in the inlet opening of the fan.

The wind velocities recorded in the initial experiments, in which the propeller fan was used, were obtained by measurement with a vane-anemometer placed over the centre of the samples. Measurements made at various points between the fan and the surface of the fabric showed quite a variation with a rapid drop as the anemometer approached the fabric, when the fan was placed above the surface of the fabric. This was to be expected in view of the change in direction of the air as it approached the flat surface of the test piece. Arbitrarily the wind velocity was taken as that 4 in. above the surface of the fabric.

It should be kept in mind that the vane-anemometer measures only streamline flow and gives no indication of eddy currents or turbulent flow, but turbulent flow would not be expected to have much bearing on the thermal resistance except in disturbing the protecting air layer above the fabric. The effect of the wind on the air going through the fabric would be expected to depend only on the vertical component. However, air current measurements were also made with a katathermometer. The results obtained in this way checked fairly well with the anemometer figures arbitrarily chosen as described above, except for one of the lower velocities. This tended to show that there was little turbulent flow. Nevertheless, it was thought desirable to measure the velocity of the wind by a third method giving directly the pressure exerted on the fabric due to the wind. It would appear that this pressure is the most important factor affecting the heat loss by penetration of air through the covering fabric. In this latter method a dummy 'hot-plate' and 'guard ring' was built of beaver board of the same dimensions as those of the metal plates used in the thermal insulating apparatus. The fan was placed directly above this in the same relative position that it had over the hot-plate. The 'central plate' was balanced on a trip scale and the force necessary to maintain it in position with the various velocities was measured. The force for the lower velocities was however very small and difficult to measure accurately with this rather crude installation. The wind velocities calculated in this way agreed closely with those obtained by the other two methods.

The permeabilities reported for the various coveralls are those obtained with the 'Frazier' apparatus described by Schiefer and Boyland (10) and refer to air flow through the fabric with a pressure gradient across it equivalent to  $\frac{1}{2}$  in. of water. The permeability  $P$  will always be in cubic feet of air per square foot per minute for that pressure difference.

### Materials

As coverall fabrics, light cotton materials were used where the given permeabilities are 8 to 66 cu. ft. per sq. ft. per min., parachute canopy fabrics for the higher permeabilities, and plastic coated cotton materials for those stated as having zero permeability. The colour of the cotton fabrics having permeabilities  $P=8$  and  $P=13$  was white and that of the others khaki.

The parachute fabrics were white, while one of the coated fabrics was khaki, the other green.

The basic material used below the coverall fabric was, for most experiments, a single mohair pile fabric with a thickness of 0.51 in. under no pressure and 0.45 in. under a pressure of 0.1 lb. per sq. in. The number of tuft ends per square inch was 50. The tufts were bound with a cotton ground fabric. The total weight of the fabric was  $35\frac{1}{2}$  oz. per sq. yd., of which  $22\frac{1}{2}$  oz. was mohair pile. The apparent density of the pile was therefore of the order of 4.0 lb. per cu. ft. The double pile fabric used in some of the later experiments was one in which the pile was 2/18's worsted yarn of 60's quality wool, woven on to a cotton ground fabric. The number of tufts per square inch was 160. Since the construction was such that the tufts were continuous from one side to the other, the number of tuft ends were the same on either side. The weight of this fabric was 23 oz. per sq. yd., of which 14 oz. was wool pile. The thickness for all practical purposes was the same as that of the mohair fabric except that the tufts were more irregular in length.

## Results

### *Wind Velocity*

In order to show how the wind velocity measured varied according to the method employed in measuring it, the following table summarizes the results of a number of tests in which the wind velocity was determined by the three

TABLE I  
WIND VELOCITIES IN MILES PER HOUR OBTAINED BY DIFFERENT METHODS

Test	Vane-anemometer	Katathermometer	Dynamic pressure
A	$3\frac{1}{2}$	4	4
B	$4\frac{1}{2}$	$4\frac{1}{2}$	$3\frac{1}{2}$
C	9	6	$6\frac{1}{2}$
D	14	$12\frac{1}{2}$	$12\frac{1}{2}$
E	16	15	14
F	22	22	21
G	26	$26\frac{1}{2}$	23

different methods referred to previously. In reporting the wind velocity in Table IV, and others that follow, the results obtained with the katathermometer will be given because the readings obtained with the vane-anemometer varied somewhat with the position of the instrument, and it was not convenient to use the direct pressure method for the regular determination of velocity.

### *Initial Thermal Resistance Tests*

These tests were conducted, as mentioned before, with a propeller fan so placed that it produced a wind parallel to the surface of the material in one series of tests and a wind at  $30^\circ$  to the surface for the next series of tests. In

the first series, several textile materials were used to obtain a rough idea of the effect of the horizontal wind on the thermal resistance, but the second series was carried out with the definite purpose of finding out the effect of covers of various permeabilities, and the underlying fabrics were limited to two double pile fabrics of similar construction but differing somewhat in the quality of the pile and in thickness.

The results of the initial tests with a horizontal wind are given in Tables II and III.

TABLE II  
THERMAL RESISTANCE OF VARIOUS MATERIALS IN STILL AIR<sup>1</sup>  
AND IN A HORIZONTAL WIND

Material	Thermal resistance, clo <sup>2</sup>	
	In still air	With wind (velocity in parentheses)
Overcoating	1 91	1 45 ( 7 m.p.h.)
Loose pad of wool (thickness 1 in. +)	6 42	5 13 ( 7 m.p.h.)
Very loose pad of wool	5 40	2 33 ( 7 m.p.h.)
Same with fine cotton cover	5 68	5 43 ( 7 m.p.h.)
Double pile fabric A ( $\frac{1}{2}$ in.)	2 83	{ 2 47 ( 8 m.p.h.) 2 06 (12 m.p.h.) }
Same with cotton cover	3 35	2 77 (12 m.p.h.)
Cover alone	0 53	
Double pile fabric B ( $\frac{1}{2}$ in.)	2 44	{ 2 08 ( 9 m.p.h.) 2 10 (12 m.p.h.) 2 04 (13 m.p.h.) }
Single pile fabric ( $\frac{1}{2}$ in.)	1 35	0 88 (11 m.p.h.)

<sup>1</sup> Although the vane-anemometer did not register any air movement when the fan was not in motion, there was some air circulation in the room, perhaps around 0.2 m.p.h., caused by the conditioning system. The anemometer did not register at speeds lower than 0.3 m.p.h. The term 'still air' is, therefore, only relative. The same remark applies to later tests.

<sup>2</sup> As this paper deals with clothing materials, the clo unit, proposed by Gagge, Burton, and Bazett (2) has been used to express thermal resistance. This unit has been defined as the thermal resistance of the clothing necessary to maintain in comfort a sitting-resting subject in a normally ventilated room (air movement 20 ft. per min.) at a temperature of 70° F. and a humidity of the air that is less than 50%. It is equivalent to 0.18  $\frac{\text{Cal.}/\text{hr.}/\text{sq. m.}}{^{\circ}\text{C.}}$  or 0.88  $\frac{\text{B.t.u.}/\text{hr.}/\text{sq. ft.}}{^{\circ}\text{F.}}$ .

The use of thermal resistance as a measure of the thermal insulation given by fabrics offers many advantages over that of thermal conductance, which has been most widely used by those concerned with the heat transmission through insulating materials.

#### Tests with Higher Wind Velocities and Various Angles of Incidence

Although the initial results indicated an appreciable drop in thermal resistance due to winds up to 11 m.p.h. when the permeability of the cover was high, it was considered desirable to experiment with a wider range of wind velocities in order to differentiate more closely between the effects of the low permeability covers. More information was also desirable on the effect of wind direction, and it was decided to try the effect of wind striking

TABLE III

THERMAL RESISTANCE OF DOUBLE PILE FABRICS WITH AND WITHOUT COVER IN STILL AIR AND IN WIND OF 11 m.p.h., 30° TO SURFACE

Test No.	Permeability of cover	Air movement	Underlying fabric	
			A	B
1	No cover	No wind	2.70	2.44
2	No cover	Wind	1.71	1.42
3	0	No wind	2.95	2.70
4	0	Wind	2.52	2.32
5	33	Wind	2.21	—
6	66	No wind	—	2.70
7	66	Wind	—	2.02
8	100	Wind	2.04	—
9	165	Wind	2.00	—
10	205	Wind	1.97	—

the surface at angles of 90° and 45°, as well as at 30°. The results of these experiments are given in Tables IV and V. The same results are presented in another form in Tables VI and VII, in which they have been corrected so as to represent the thermal resistance of the fabrics only, without that of the air over them. The correction is explained in the discussion that follows.

#### *Thermal Resistance of Boundary Air Layer*

The thermal resistance determined in most of our tests was that of the fabric and the boundary air layer combined. In order to calculate the resistance of the fabric itself, it is necessary to know that of the air layer. The correction could have been made by the use of data obtained by others, but the information published was meagre and there was some doubt as to the extent to which it was applicable to our experiments. It was thought preferable to repeat some of the experiments and measure the surface temperature of the fabric as well as that of the air. In this way it was possible to calculate the thermal transmission through the fabric separately from that through the air layer. Although the calculation of the resistance of the fabric offered no difficulty, the calculation of the resistance of the air layer necessitated a knowledge of the air temperature. In our initial experiments, the air temperature was taken as that of the grid, and, to apply a correction to the results, it would be sufficient to know the value of the resistance of the air between the surface of the fabric and the grid under the conditions of the experiments. However, in order to compare the results with theoretical figures or with results reported by other investigators the temperature of the air or room is required.

Measurement of the temperature of the air or of the walls of the room was not as easy as anticipated. Attempts made to measure the temperature of the room showed that there were appreciable variations due to drafts, and the temperatures of the walls varied significantly with the position of the thermocouple. The ceiling, 14 ft. above the floor, was generally a few degrees

TABLE IV

THERMAL RESISTANCE (CLOS) OF PILE FABRIC WITH AND WITHOUT COVER AND FOR VARIOUS WIND VELOCITIES (UNCORRECTED)

Wind velocity, m.p.h.	Permeability of cover					
	0	8	13	38	193	$\infty$
	Thermal resistance, clos					
<i>Wind at 90°</i>						
0	2.30 (2.26)	—	2.31 —	2.21 (2.38)	2.24 (2.36)	1.96 (1.95)
3	1.75 (1.84)	—	—	—	—	1.36
5	—	1.74	1.68 (1.96)	—	(1.78)	—
6	—	—	(1.72)	(1.83)	(1.73)	—
8	1.80 (1.74)	—	—	—	(1.75) 1.46	0.73
9	—	—	—	1.70	—	—
11	1.76	—	—	—	—	—
13	1.68	—	—	1.22	—	—
14	—	1.50	—	—	1.06	—
15	—	—	1.42	—	—	0.69
16	—	1.44	—	1.19	0.94	—
18	1.66	1.42	—	—	—	—
19	1.71	—	—	—	—	—
20	—	—	0.99	0.78	—	—
22	1.60	1.16	—	0.75	0.57	0.53
	—	1.14	—	—	—	—
24	—	1.15	—	—	—	0.50
26	1.64 (1.53)	1.08	—	(0.62)	0.54	0.49
30	1.54	—	0.80	—	0.49	0.46
<i>Wind at 45°</i>						
30	1.66 1.62	— —	1.10 —	0.93 0.96	0.70 —	0.55 —
<i>Wind at 30°</i>						
8	2.08	—	—	—	1.78	—
9	2.05	—	—	—	—	—
10	1.98	—	—	—	—	1.35
13	1.85	—	—	1.70	1.67	1.17
	1.81	—	—	—	—	—
18	—	—	—	—	1.47	—
20	1.76	—	—	—	—	0.84
25	1.74	—	—	—	1.34	0.83
30	1.70	—	—	—	1.03	0.68
	1.69	—	—	—	1.05	—
<i>Parallel wind</i>						
3	(1.89)	—	—	—	—	—
3½	(1.90)	—	—	—	—	—
4½	(1.89)	—	—	—	—	—

NOTE.—Figures in parentheses are those obtained when temperature of surface was measured directly in later experiments.

TABLE V

THERMAL RESISTANCE (CLOS) OF DOUBLE PILE FABRIC *B* WITH AND WITHOUT COVER  
AND FOR VARIOUS WIND VELOCITIES (UNCORRECTED)

Wind velocity, m.p.h.	Permeability of cover			
	$\infty$	44	8	0
	Thermal resistance, clos			
0	2 40 <sup>1</sup>	—	2 44	2 69 <sup>1</sup>
2	—	—	—	2 45
3½	2 10	—	—	2 32
4½	{ 1 95 }	—	—	—
6½	{ 1 97 }	—	—	—
9	1 43	—	—	—
9	1 26	1 91	2 30	{ 2 30 }
				2 33
26	0 37	0 61	1 22	{ 2 14 }
				2 11

<sup>1</sup> Mean of five measurements.

warmer than the walls. The temperature variation around the room was also appreciable and there was sometimes a difference of a few degrees between the temperature of the walls and that of the air, the air being generally cooler at such times. As the apparatus was in a corner of the room in close proximity to two walls, it was decided to use the temperature of these walls, a short distance above the level of the apparatus, as the air temperature. Where there was an induced air movement to simulate the effect of wind, the air temperature was measured directly in front of the fan.

#### *Air Resistance with No Wind*

The thermal resistance provided by the boundary air layer and determined as above under comparatively still air conditions was found to vary in the different tests from 0.53 to 0.64 clo for surface to grid and between 0.68 and 0.76 clo for surface to wall, with mean values of 0.58 and 0.72 clo, respectively. These values are for a temperature gradient of about 12° F. from surface to air, this temperature gradient being that which applied to most of our earlier experiments.

In order to find out how the resistance of the air layer varied with temperature, a number of tests were carried out in which the heat input was varied within fairly wide limits in order to give different temperature gradients. The results of one particular set of tests are given in Table VIII while results of all such tests are given in Fig. 1, in which a straight line has been drawn through the points. This line has an intercept of 1.6° F. on the temperature axis and a slope of 1.79 B.t.u. per degree corresponding to 0.63 clo insulation. These results will be discussed presently.

TABLE VI  
THERMAL RESISTANCE (CORRECTED) OF PILE FABRIC WITH AND WITHOUT COVER AND  
FOR VARIOUS WIND VELOCITIES

Wind velocity, m.p.h.	Permeability of cover					
	0	8	13	38	193	$\infty$
	Thermal resistance, clos					
<i>Wind at 90°</i>						
0	1.72 (1.67)	—	1.73 —	1.63 (1.63)	1.66 (1.67)	1.38 (1.35)
3	1.51 (1.69)	—	—	—	—	1.12
5	—	1.56	1.50 (1.64)	— (1.64)	(1.56) <sup>1</sup>	—
6	—	—	(1.59)	—	1.67	—
8	1.65 (1.64)	—	—	—	1.30	0.57
9	—	—	—	1.56	—	—
11	1.65	—	—	—	—	—
13	1.59	—	—	1.11	—	—
14	—	1.42	—	—	0.95	—
15	—	—	1.34	—	—	0.57
16	—	1.38	—	1.10	0.84	—
18	1.63	1.38	—	—	—	—
19	1.68	—	—	—	—	—
20	—	—	0.97	0.71	—	—
22	1.60	1.15 <sup>1</sup>	—	0.70	0.49	0.43
24	—	1.12	—	—	—	0.40
26	1.70 (1.63)	1.14	—	(0.74)	0.49	0.40
30	1.65	—	0.86	—	0.45	0.37
<i>Wind at 45°</i>						
30	1.65 <sup>1</sup>	—	1.16	0.90 <sup>1</sup>	0.64	0.46
<i>Wind at 30°</i>						
8	1.92	—	—	—	1.62	—
9	1.90	—	—	—	—	—
10	1.82	—	—	—	—	1.20
13	1.71 <sup>1</sup>	—	—	1.58	1.54	1.04
18	—	—	—	—	1.36	—
20	1.67	—	—	—	—	0.73
25	1.68	—	—	—	1.26	0.74
30	1.66 <sup>1</sup>	—	—	—	0.96 <sup>1</sup>	0.59
<i>Parallel wind</i>						
3	(1.74)					
3½	(1.74)					
4½	(1.67)					

<sup>1</sup> Mean of two measurements.

NOTE.—Figures in parentheses are those obtained directly from surface temperature measurements and not by difference from Table IV.

TABLE VII

THERMAL RESISTANCE (CORRECTED) OF DOUBLE PILE FABRIC *B* WITH AND WITHOUT COVER AND FOR VARIOUS WIND VELOCITIES

Wind velocity, m.p.h.	Permeability of cover			
	$\infty$	44	8	0
	Thermal resistance, clos			
0	1.82	—	1.86	2.11
2	—	—	—	2.17
3½	1.87	—	—	2.09
4½	{ 1.75 1.77 }	—	—	—
6½	1.26	—	—	—
9	1.11	1.77	2.16	{ 2.16 2.19 }
26	0.28	0.59	1.28	{ 2.20 2.17 }
				Mean 2.14

TABLE VIII

PROTECTION GIVEN BY BOUNDARY AIR FOR VARIOUS TEMPERATURE GRADIENTS BETWEEN SURFACE AND AIR

$\Delta t$ , surface to air, ° F.	Thermal resistance, clos	
	Surface-grid	Total
12.5	0.60	0.74
15.7	0.57	0.71
17.9	0.57	0.70
22.3	0.55	0.69
25.4	0.51	0.66

Determinations of the thermal resistance were also made with the grid at various distances from the surface, with results given in Table IX.

These results show that the position of the grid between ½ in. and 2 in. above the surface of the fabric was not critical and that its temperature was practically constant between these limits.

The results obtained for the air resistance might be compared with those given for flat plates by other investigators. In order to compare results, it is desirable to break up the heat lost from the surface into heat lost by radiation and heat lost by convection. The heat lost by radiation is readily obtained from theoretical considerations. Assuming that, for the difference in temperature with which we are concerned, the heat radiated is proportional to the temperature difference,  $\theta$ , between surface and air, we can write  $H_r = h_r \theta$ , where  $H_r$  is the total heat loss per square foot per hour and  $h_r$  represents the

heat loss per square foot per hour per degree difference in temperature. If  $\theta$  is of the order of  $10^\circ$  to  $12^\circ$  F. as in most of our experiments,  $h_r = 1.10$  B.t.u. when the emissivity is 1.0. As the emissivity of the fabrics used in our experiments was probably closer to 0.90,  $h_r$  might be taken as 1.0 B.t.u.

TABLE IX  
VARIATION OF AIR RESISTANCE BETWEEN SURFACE  
AND GRID FOR DIFFERENT POSITIONS OF THE GRID

Distance above surface, in.	Thermal resistance, clo
0.2	0.38
0.3	0.48
0.6	0.53
0.9	0.52
1.2	0.51
1.5	0.53
1.8	0.54
8	0.58
18 (to one side near wall)	0.68

To calculate the heat lost by convection, we may similarly use  $H_c$  as the heat loss per square foot per hour and  $h_c$  as the heat loss per square foot per hour per degree difference in temperature.

However, in this case,  $h_c$  itself is dependent on temperature. To find  $h_c$  we may use Nussel's formula  $h_c = 0.39 \theta^{1/4}$  for loss of heat from a vertical pipe, applying the correction  $+6\%$  suggested by Rosin for plane surfaces (9, p. 96). This gives  $h_c = 0.77$  B.t.u. when  $\theta = 12^\circ$  F. Griffiths and Davis (3) use a similar formula in which the coefficient is 0.38 instead of 0.39 while King (5) gives a coefficient of 0.36 ( $0.275 + 30\%$  correction for horizontal surfaces). These two coefficients yield values of  $h_c = 0.71$  and 0.67 B.t.u., respectively. Hampton (4) uses a formula of the same type which gives  $h_c = 0.60$  B.t.u. The sum of  $h_r + h_c$  can therefore be taken as somewhere between 1.60 and 1.77 B.t.u. This corresponds to a resistance of 0.71 to 0.64 clo. Our figures are therefore in good agreement with those generally accepted.

It follows from the above that  $H_c = 0.38 \theta^{3/4}$ , using the coefficient 0.38 given by Griffiths and Davis, and  $H_r = 1.0 \theta$ , so that  $H_c + H_r$  is not a linear function of temperature and the straight line drawn in Fig. 1 is only an approximation, while the slope of the line represents simply a mean of the experimental values of  $\frac{H_r + H_c}{\theta}$  within the range of temperatures investigated.

The values calculated from the formula  $H_r + H_c = 1.0 \theta + 0.38 \theta^{3/4}$  have been represented by open circles in Fig. 1. Taking the extreme temperature differences used to obtain Fig. 1, we have for a  $26^\circ$  difference a heat loss of 1.85 B.t.u. per hr. per ft.<sup>2</sup> per  $^\circ$  F. corresponding to a resistance of 0.61 clo, and for a  $6^\circ$  difference, a heat loss of 1.60 B.t.u. per hr. per ft.<sup>2</sup> per  $^\circ$  F.,

corresponding to a resistance of 0.71 clo. The resistance calculated from the slope of the line in Fig. 1 is 0.63 clo. The calculated values for  $H_c + H_r$  are somewhat higher than most of the experimental values found. The deviation may be due to the factor 0.38 being too high or the emissivity might be lower than the 0.90 assumed. However, it might be pointed out also that the temperature difference that controls the radiation loss in our experiments is not necessarily the same as that affecting the convection losses, since the latter would depend mostly on the air temperature around the apparatus, while the radiation would depend more on the temperature of the walls or other surfaces in the room. In other words  $H_r + H_c = 1.0 \theta_1 + 0.38 \theta_2^{3/4}$ , where  $\theta_2$  is different from and generally smaller than  $\theta_1$  in our experiments. Since  $\theta_1$ , the temperature difference between the surface of the fabric and the

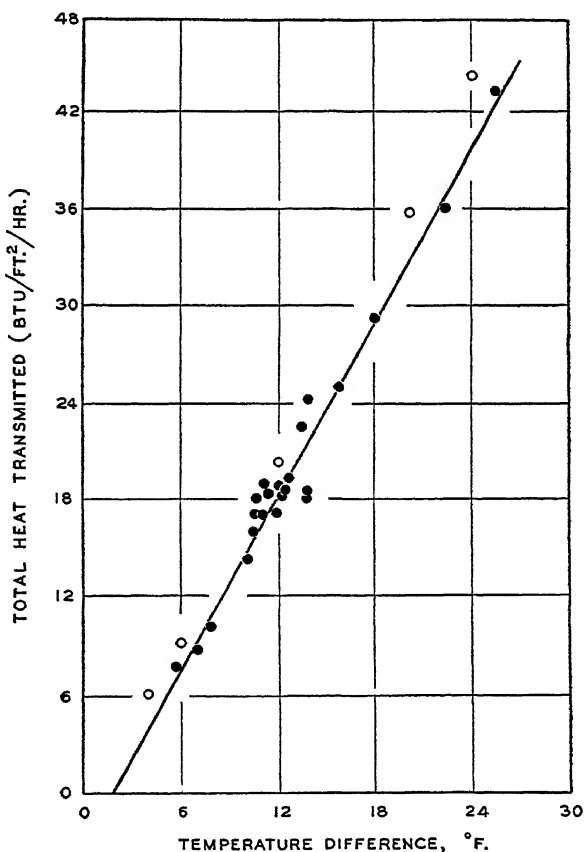


FIG 1. Relation of heat loss to temperature difference between surface of fabric and room.

walls of the room, was used in plotting Fig. 1, the experimental points would be expected to be too high with respect to temperature if the above explanation is correct. It is of course possible that all three factors just mentioned are

jointly responsible for the deviations noted, but, whichever explanation is correct, it is evident that the line expressing the relation between heat loss and temperature difference should pass through the origin. The intercept of 1.6° F. on the temperature axis given by our curve indicates that our temperature differences were either too high, at least for the lower points, or that the line changes direction for low temperature differences. This point was not considered of sufficient importance to merit further study.

In order to obtain the resistance of the fabric itself under 'no wind' conditions, it was decided then to subtract 0.58 clo from the total for fabric plus boundary air layer, between surface and grid, this figure being considered the most probable mean value under the conditions of our test. The results given in Table IV thus yield 1.72 clo for the resistance of the pile fabric covered with the impermeable cover. This is the figure reported in Table VI, which contains such corrected values for all other tests. The repeated tests in which the surface temperature was measured directly gave 1.67 clo as the mean of six determinations, in good agreement with the previous result. The correction is further justified by the agreement between the direct measurements and those calculated by difference for covers of permeability 38, 193, and  $\infty$ .

#### *Resistance of Air Under Circulation*

The resistance of the boundary air layer discussed in the preceding section was for so-called 'still air', but it is evident that any body at a different temperature from the ambient air cannot be surrounded by still air since there will always be convection currents resulting from the difference in temperature. The term 'still air' or 'no wind' is therefore relative only and signifies that there was no deliberately induced air movement.

The correction to be applied for the air layer in the results obtained with various wind velocities is not so readily calculated as for conditions of no wind. However, the thermal resistance of the air in such cases is quite small and any small error in the correction would have little effect on the total resistance. As before, tests were repeated in which surface temperatures were determined while the material was subjected to air movement. It was not deemed necessary to carry out a wide series of such experiments, as the initial tests indicated that the thermal resistance of the air became quite small even at low wind velocities. The results are given in Table X.

Available formulae for calculating the heat loss through forced convection apply either to wind parallel to plane surfaces or to pipes. Data obtained by Winslow, Gagge, and Herrington (11) can also be used, but the formulae apply to the human body and not to a flat surface. Nevertheless, work on heat loss by natural convection has shown that a plane horizontal surface has a heat loss comparable to that of a pipe 4 in. or more in diameter. Assuming that this similarity holds for forced air circulation, then one could justify the use of a formula derived from data on the human body, as Rees (7) has done.

TABLE X

THERMAL RESISTANCE OF BOUNDARY AIR LAYER UNDER WIND CONDITIONS

Wind velocity, m.p.h.	Permeability of cover, cu. ft./ft. <sup>2</sup> /min. at $\frac{1}{2}$ in. water pressure	Thermal resistance of air layer, clo		
		Surface-grid	Total	Total calc.
0.4	0	0.58	0.72	0.71
0.6	0	0.33	0.35	0.63
1.1	0	0.33	0.43	0.52
2.4	0	0.25	0.30	0.39
3.5	0	0.18	0.32	0.34
4.5	0	0.13	0.29	0.30
4.5	0	0.17	0.31	0.30
4.5	13	0.20	0.32	0.30
4.5	160	0.10	0.15	0.30
5.5	38	0.20	0.27	0.28
6.0	0	0.18	0.28	0.27
6.0	13	0.16	0.20	0.27
6.0	160	0.08	0.16	0.27
14	>750	0.05	0.06	0.19
26	0	0.06	0.09	0.14
26	38	0.03	0.04	0.14

Using the data of Winslow, Gagge, and Herrington, namely, a radiation loss of 3.35 kgm-cal. per m.<sup>2</sup> per hr. per °C. and a convection loss of  $1.043 \sqrt{v}$  kgm-cal. per m.<sup>2</sup> per hr. per °C. where  $v$  is the air velocity in centimetres per second, one gets by change of units a thermal resistance  $R = \frac{1}{0.61 + 1.25 \sqrt{v}}$  where  $v$  is in miles per hour.

The calculated values from this equation are given in the last column of Table X. Considering the difficulties involved in measuring such low resistances with any precision and the possible error in the determination of the wind velocity itself, it can be assumed that the above formula is applicable to our results obtained with an impermeable cover and for velocities above 1 to 2 m.p.h. For low velocities, the effect of natural convection currents predominates over the effect of forced air circulation, and the relation no longer holds, as Winslow, Gagge, and Herrington have pointed out in their paper.

The rate of heat loss by convection was calculated as follows from our observations under various wind velocities with the impermeable cover over the pile fabric. The value 1.65 clo, representing the thermal resistance of the fabrics, was subtracted from the total resistance found. The difference was taken as the resistance of the air over the fabric. The rate of heat loss by radiation was assumed to be 1.0 B.t.u. per sq. ft. per hr. per °F., and, by subtracting this from the total heat loss through the air, the rate of heat loss by convection,  $h_c$ , was obtained. The various values of  $h_c$  thus found have been used in Fig. 2. The full dots in the upper curve represent values

calculated from a smooth curve drawn through the resistances found experimentally when plotted against  $\sqrt{v}$ , while the open circles are points derived directly from some of the observations. The upper curve represents the

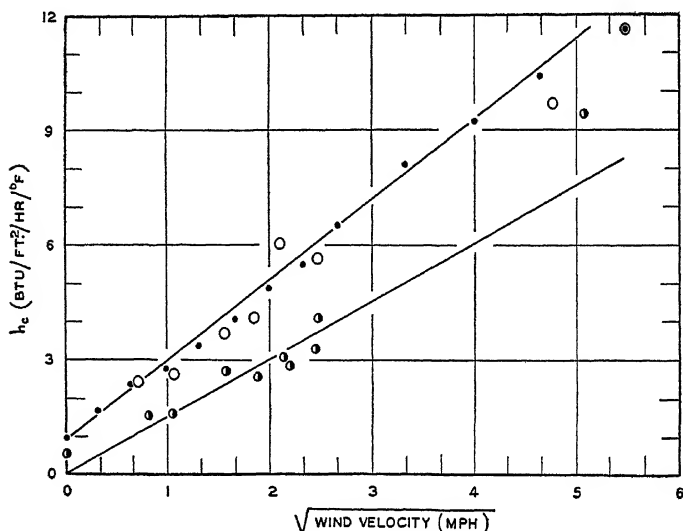


FIG. 2 Relation between convective heat loss and wind velocity for the boundary air layer.  
Upper curve for layer between surface of fabric and grid  
Lower curve for entire air layer

conductance for the air layer between surface and grid. The lower curve was drawn through points obtained in the later experiments when the surface temperature was measured directly, and it represents the conductance of the total boundary air layer (i.e., air layer between fabric and grid + the effective layer above the grid). It should be pointed out that owing to the difficulty in determining the air temperature between surface and air in most cases, the values for  $h_c$  are subject to a relatively large error. The values for conditions of 'no wind' have been placed at  $v = 0$ , but these points actually represent conductances with air under some movement. In Table X, the agreement between experimental values and calculated values is good if we take  $v = 0.4$  m.p.h. for the 'no wind' condition. The slope of the lower line in Fig. 2 is 1.50. Although this is only approximate it gives an equation for the thermal resistance,  $R = \frac{1}{0.88 + 1.32\sqrt{v}}$  clo, that compares with  $R = \frac{1}{0.61 + 1.25\sqrt{v}}$  clo, obtained with the data of Winslow, Gagge, and Herrington. The average ratio of surface-to-grid resistance to the total air resistance is roughly  $\frac{2}{3}$ . The values calculated for the total resistance have therefore been multiplied by  $\frac{3}{2}$  to obtain the correction to be subtracted from the experimental results of Tables IV and V. The few tests carried out with the covers of permeabilities 38 and 160 seem to indicate that the air protection is appreciably less when

the outer fabric is quite permeable (cf. Table X). This is perhaps due to the fact that the convection effect extends below the surface of the fabric when the covering fabrics are permeable. The comparative roughness of the surface in such cases may also play a role in diminishing the thermal resistance of the air by increasing the convection effects. It is therefore much more difficult to correct for the air layer resistance in these instances. Fortunately the corrections are small and any error resulting from the use of the wrong values will be small in comparison to the total resistance of fabric plus air.

The corrections to be applied when the wind is not perpendicular to the surface but makes angles of  $30^\circ$  and  $45^\circ$  to the horizontal can be taken to be the same as for the  $90^\circ$  wind. Table XI gives the figures for a horizontal wind calculated from the formula proposed by King and Knaus (6) and compared with the values for a vertical wind calculated as before. It will be seen that the two sets of values are comparable and it seems logical therefore to assume that any wind direction would give similar results.

TABLE XI

THERMAL RESISTANCE OF AIR LAYER FOR A  $90^\circ$  WIND  
COMPARED WITH THE RESISTANCE IN A HORIZONTAL  
WIND PARALLEL TO SURFACE

Wind velocity, m.p.h.	Thermal resistance, clos	
	Vertical wind	Horizontal wind
3	0 36	0 45
5	0 29	0 35
8	0 24	0 27
11	0 21	0 23
13	0 20	0 21
16	0 18	0 18
24	0 15	0 14
30	0 13	0 12

The effect of wind direction on the surface coefficient of flat surfaces has been investigated by Rowley and Eckley (8). They found that for winds below 15 m.p.h., the heat loss was practically the same for all angles between  $15^\circ$  and  $90^\circ$  but slightly less than that for a parallel direction. Above 15 m.p.h., the conduction decreased somewhat as the angle of the wind increased but at 25 m.p.h. the results for a  $60^\circ$  wind and a  $90^\circ$  wind were still about the same. In view of the low value for the thermal resistance of the boundary air at high wind velocities, no serious error is introduced by assuming the same values for all directions of the wind.

There is another correction to be made that has no connection with the boundary air layer but that is dependent on the wind. This is the reduction in thermal resistance resulting from the change in thickness of the materials due to the compressional effect of the wind pressure. This pressure will be

proportional of course to the square of the wind velocity. Direct determination of the change in thickness by means of a cathetometer showed that a wind of 30 m.p.h. resulted in a compression of about 2.2 mm. corresponding to a change in resistance of 0.30 clo when the impermeable fabric covered the pile fabric. With a cover of permeability 38 the change in thickness was only about half that, and with the cover of permeability 193 it was only one-fourth. For winds of velocity lower than 30 m.p.h. the compression has been assumed to be proportional to the square of the velocity. For angles other than  $90^\circ$ , the vertical component of the velocity has been used to calculate the compressional effect. This correction is of opposite sign to that applied for the change in resistance of the boundary air layer, and has to be added to the experimental results.

The results corrected for boundary air resistance and for compression due to wind pressure are given in Tables VI and VII. These figures represent therefore the thermal resistance of the pile fabric itself with the covers of various permeabilities and under various wind conditions.

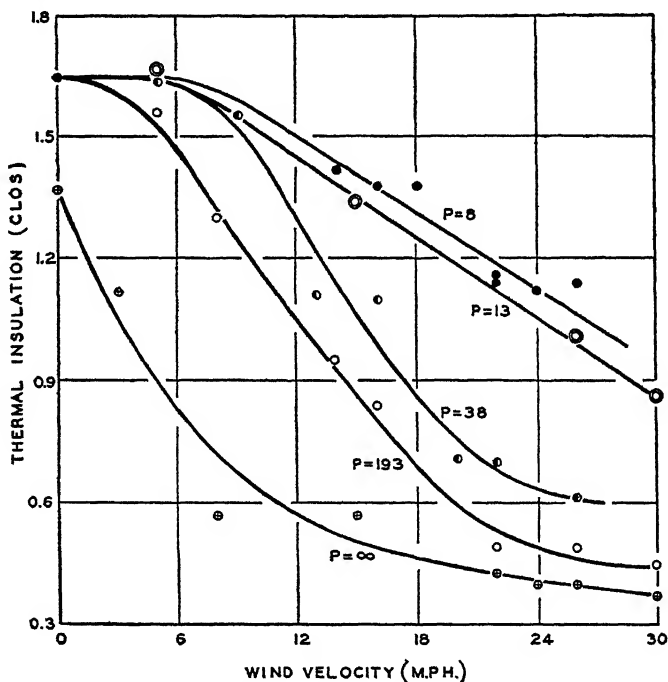


FIG. 3. Curves showing the relation between change in thermal insulation and wind velocity for covers of different permeabilities.

These results have been plotted in Figs. 3 and 4. Fig. 3 shows the variation in thermal resistance with varying wind velocity for covers of different permeabilities. In Fig. 4, the thermal resistance is given against the permeability for various wind velocities, the points having been taken from the curves of Fig. 3.

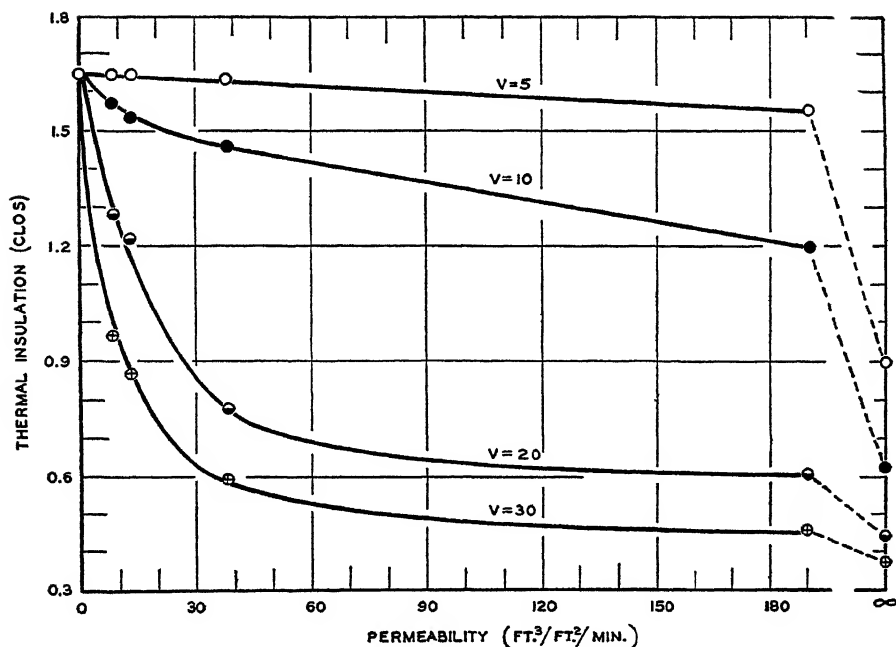


FIG. 4. Curves indicating the change in thermal insulation with permeability of cover for various wind velocities.

## Discussion of Results

### Effectiveness of Covers

Fig. 3 shows clearly that for low wind velocities, up to about 10 m.p.h., the permeability of the cover is not very important until a fairly high permeability is reached. It would appear also that as long as the permeability is not too high, say below 50 on our scale, the air behind the covering fabric is not appreciably disturbed when the wind velocity is not higher than 6 m.p.h. The sole effect of the wind up to this point is to change the resistance provided by the boundary air layer, and most of this change, as we have seen from Table X, occurs at low wind speeds.

Once the speed of the wind reaches 6 m.p.h., the reduction in thermal resistance of the fabric behind the cover is practically proportional to wind velocity for covers of low permeability, at least up to 30 m.p.h. It is evident, however, that this relation cannot hold for all velocities and that at some higher velocity the curves for the low permeability covers must level off and become asymptotic to the horizontal axis, as do the lines for the higher permeabilities at velocities of 24 to 30 m.p.h. The latter show a linear relation over a more limited range of wind velocities, and it would appear that the higher the permeability, the shorter the linear portion of the curve becomes.

It is also clear that at very high wind velocities the lines approach one another and that again the permeability becomes relatively unimportant, since the thermal resistance is small in any case. The curve for  $p = \infty$

(uncovered pile fabric) is a special case but it indicates the limit to which the other curves tend as the permeability is indefinitely increased.

The relative protection given by covers of different permeabilities will therefore depend on the wind velocity. For a wind of low velocity, the permeability is of little importance within fairly wide limits of permeability, but at high wind velocities, say 20 m.p.h. or more, to get the best protection one should employ a cover of as low a permeability as possible. This is probably best shown by the curves of Fig. 4, which indicate that at wind velocities of 20 to 30 m.p.h., most of the drop in thermal resistance occurs in the covers of low permeability.

Although the relation between change of resistance and permeability is not a linear one, for purposes of calculation within a narrow range of permeabilities it can be assumed that the reduction in thermal resistance is proportional to permeability. For example, for a wind of 30 m.p.h. and between zero permeability and a permeability of 10, the drop in resistance is about 0.70 clo and we can therefore say that the resistance decreases by 0.07 clo for every unit change in permeability. This sort of calculation is useful in comparing the efficacy of two or more windbreaks that differ somewhat in permeability but that are all low in permeability.

It should be borne in mind that the results given indicate only the general relation between wind, permeability of cover, and change in thermal resistance. The magnitude of the change will depend not only on the permeability of the cover but also on the nature of the fabric under the cover. This is shown by comparing the results for the double pile fabric with those obtained with the single pile. Whereas a change in resistance of 1.54 clo was obtained for the double pile fabric without cover when the wind was 26 m.p.h. as compared with the 'no-wind' condition, the single pile fabric showed only a corresponding drop of 0.98 clo. Comparing the figures for the cover of permeability 44 over the double pile with those for the cover of permeability 38 over the single pile and the change occurring when the wind is increased from 9 to 26 m.p.h., we have a drop of 1.18 clo for the double pile and 0.82 clo for the single pile fabric. This difference could hardly be due to the small difference in permeability. It is more likely due to the more open construction of the double pile and to the fact that the pile was much more uneven in thickness (fibre length) than in the single pile fabric of mohair fibres fairly closely packed and sheared so as to give a uniform pile thickness.

Differences due to the nature of the underlying fabric itself are also evident from the results given in Tables II and III. The results given in Table II show clearly that the more open the structure of the fabric, the larger the effect of the wind, as is to be expected. Table III indicates that fabric *A* was more open than fabric *B*, for the drop between 'no wind' and wind conditions with the cover of permeability 66 was 0.83 clo (interpolated) for fabric *A* versus 0.68 clo for fabric *B*. Comparison of the 12 m.p.h. results in Table II also reflect the more open structure of fabric *A* relative to fabric *B*.

Applying the corrections for the resistance of the boundary air layer to the results of Table II, it is possible to show that, except for the fabrics of more open structure, the effect of a horizontal wind is small. In the case of fabric *B* with no cover, for example, we have 1.86 clo for 'no wind', 1.93 clo for a wind of 9 m.p.h., 1.97 clo for a wind of 12 m.p.h., and 1.91 clo for a wind of 13 m.p.h.; on the other hand, fabric *A* shows a change from 2.25 clo for 'no wind' to 2.06 clo for a wind of 12 m.p.h., again indicating a more open structure for fabric *A*.

The advantage to be derived from a cover is well shown by the two results obtained for the loose pad of wool. While the thermal resistance decreased by only 0.25 clo with the cover, the change was 3.07 clo with no cover, for a horizontal wind of 7 m.p.h.

Regarding the effect of the angle at which the wind strikes the fabric, the number of tests carried out are insufficient to enable a generalization to be made but the results reported in Table VI seem to indicate that the effect is proportional to the vertical component of the wind; in other words the effect of the 30° wind is roughly the same as that obtained with a 90° wind of half the velocity, while the 45° results should correspond to that of a 90° wind with a velocity of 0.7 that of the 45° wind. For example, the insulation for  $P = \infty$  at 30 m.p.h. at 30° is 0.59 clo, while that for 15 m.p.h. at 90° is 0.57 clo. For 45° we have 0.46 clo, while for a 21 m.p.h. ( $0.7 \times 30$ ) wind at 90° we have 0.43+ clo. The relation apparently falls down at low wind velocities, but we have seen that convection currents interfere with the correction at low velocities and that the convection currents are also largely dependent on the openness of the fabric. If we take the figures for a cover of permeability  $P = 193$  we have, for 30 m.p.h. at 30°, 0.96 clo, and 0.90 clo for 15 m.p.h. at 90°, or 1.36 clo for 18 m.p.h. at 30° and  $\sim 1.26$  clo for 9 m.p.h. at 90°. The relation can be considered only a rough one, however, until more data are available. The results for the 45° wind, for example, do not agree so well with those for the 21 m.p.h. wind at 90°.

In conclusion it might be objected that the results given in this paper apply to flat surfaces only and may not be applicable to the same materials worn on the body. We hope to show in a later paper that the general conclusions drawn from our results also hold for vertical cylinders. However, it can be argued that the conditions under which clothing is worn are so variable that one cannot hope in ordinary laboratory experiments to duplicate exactly these conditions. The information obtained in the laboratory serves rather to evaluate the relative merits of different fabrics, and this can be done more conveniently on a flat plate apparatus than on a cylindrical one.

### References

1. CLEVELAND, R. S. J. Research Natl. Bur. Standards, 19 : 675-684. 1937.
2. GAGGE, A. P., BURTON, A. C., and BAZETT, H. C. Science, 94 : 428-430. 1941.
3. GRIFFITHS, E. and DAVIS, A. H. Food Investigation Board Special Report, 9. D.S.I.R. London. 1922.
4. HAMPTON, W. M. Nature, 481. 1946.

5. KING, W. J. Mech. Eng. 54:347-353. 1932.
6. KING, W. J. and KNAUS, W. L. Refrigerating Data Book, A.S.R.E. 1937-1938.
7. REES, W. H. J. Textile Inst. 37 : P132-P153. 1946.
8. ROWLEY, F. B. and ECKLEY, W. A. Heating, Piping, Air Conditioning, 3 : 870-874. 1931.
9. SCHACK, A. Industrial heat transfer. *Translated by* H. Goldschmidt and E. P. Partridge.  
John Wiley & Sons, Inc., New York. 1933.
10. SCHIEFER, H. F. and BOYLAND, P. M. J. Research Natl. Bur. Standards, 28 : 637-642.  
1942.
11. WINSLOW, C.-E. A., GAGGE, A. P., HERRINGTON, L. P. Am. J. Physiol. 127 : 505-518.  
1939.

## PERMEABILITY STUDIES

### II. SURFACE AREA MEASUREMENTS OF INORGANIC PIGMENT POWDERS<sup>1</sup>

By J. C. ARNELL<sup>2</sup>

#### Abstract

The modified Kozeny equation has been found to be satisfactory for the measurement of the specific surface of inorganic pigments having particle diameters of the order of 0.1 to 0.2  $\mu$  to within  $\pm 10\%$ . These powders were too fine for visual microscope counting or standard sedimentation methods of specific surface measurement. The results obtained from experimental data were checked against those calculated from electron microscope counting for two of the powders studied and found to be in satisfactory agreement.

#### Introduction

A modification of the Kozeny equation for the measurement of the specific surface of fine powders by permeability methods has been presented in a previous paper (3). This modification was introduced for the case of gases permeating through porous media, where the average size of the channels through the media was of the same order of magnitude as the mean free path of the gas. The modified equation may be written as:

$$Q = \frac{A h \rho_{Hg} g \epsilon}{L S_v (1 - \epsilon)} \left[ \frac{\epsilon^2}{k \eta S_v (1 - \epsilon)} + \frac{8}{3} \sqrt{\frac{2 R_0 T}{\pi M} \frac{\delta \alpha}{\bar{P} \rho_{Hg} g}} \right], \quad (1)$$

- where  $Q$  = rate of gas flow in cubic centimetres per second,  
 $A$  = cross-sectional area of the bed in square centimetres,  
 $h$  = pressure head in centimetres of mercury,  
 $\rho_{Hg}$  = density of mercury in grams per cubic centimetre,  
 $g$  = acceleration due to gravity,  
 $L$  = length of the bed in centimetres,  
 $\epsilon$  = volume of pore space per unit volume (porosity),  
 $S_v$  = specific surface of the powder in square centimetres per cubic centimetre,  
 $\alpha$  = fraction effective void area,  
 $k$  = shape factor,  
 $\eta$  = viscosity of the gas in poises,  
 $\delta$  = variable factor, having a value of approximately 0.9,  
 $R_0$  = gas constant,  
 $T$  = absolute temperature,  
 $M$  = molecular weight of the gas, and  
 $\bar{P}$  =  $(p_1 + p_2)/2$  = mean pressure in centimetres of mercury.

<sup>1</sup> Manuscript received February 2, 1947.

Contribution from the Defence Research Chemical Laboratories, Ottawa, Canada.

<sup>2</sup> Research Chemist.

This equation was tested against the data obtained from the flow of air through a bed of finely ground quartz at different mean pressures and also against the data of Hodgins, Flood, and Dacey (7), who measured the flow of both permanent and non-permanent gases through a sintered glass plug at different mean pressures.

In this paper, additional data are presented for the flow of air through beds of finely ground quartz and a number of inorganic pigments over a fairly wide range of porosities. These results permit a closer examination of the above equation and bring out some of the relations between the porosity and such variables as the shape factor, which cannot be determined accurately.

### Apparatus and Technique

The apparatus employed for the permeability studies is illustrated in Fig. 1, and was a modified form of that used by Rigden (9).

The powder to be studied was packed, in increments, in a small tube, *A*, by means of a hand press of the type used by Pechukas and Gage (8) to give a bed 1.00 cm. long. The first tubes used were made of lengths of glass tubing, selected with a uniform cross-section. These tubes were later discarded in favour of tubes machined out of Lucite rods. All the tubes used had a cross-sectional area of about 0.245 sq. cm. and were about 4.5 cm. long. The packed tube was attached to two glass adapters by means of rubber pressure tubing and mounted across the top of the two mercury towers, *B*.

The two mercury towers were about 110 cm. long and had a cross-sectional area of 3.99 sq. cm. They were connected across the bottom to form a large manometer and were half-filled with mercury. The right-hand tower was connected through a null manometer, *C*, to a mercury manometer, *D*.

The technique of measuring permeabilities was as follows. After the packed tube was in position, stopcock  $S_1$  was closed, and, with stopcock  $S_2$  open, the left-hand tower was slowly evacuated through stopcock  $S_3$ . The evacuation was continued until a pressure difference of between 12 and 20 cm. of mercury, depending on the mean pressure of the experiment, was attained across the two towers, and stopcock  $S_3$  was then closed. Stopcock  $S_4$  was closed when the mercury in the two arms of the null manometer was approximately level. The gas volume between the top of the mercury in the left-hand arm of the null manometer and stopcock  $S_4$  was sufficiently small as to be negligible when compared to the total gas volume in the mercury towers. Stopcock  $S_2$  was closed and stopcock  $S_1$  opened slowly to connect the two towers through the bed of powder. As the gas flowed through the bed of powder, the drop in the mercury level in the left-hand tower with time was followed by means of a cathetometer. The decrease in the pressure head was logarithmic with time and from a plot of the logarithm of the pressure head against time, the rate of gas flow could be calculated, by the method to

be given later in this paper, for any required pressure difference. When sufficient readings had been obtained, stopcock  $S_2$  was opened slowly and the equilibrium pressure,  $p_0$ , was obtained on the mercury manometer,  $D$ , by balancing the two arms of the null manometer,  $C$ , with stopcock  $S_4$  open, by the proper manipulation of stopcock  $S_3$ .

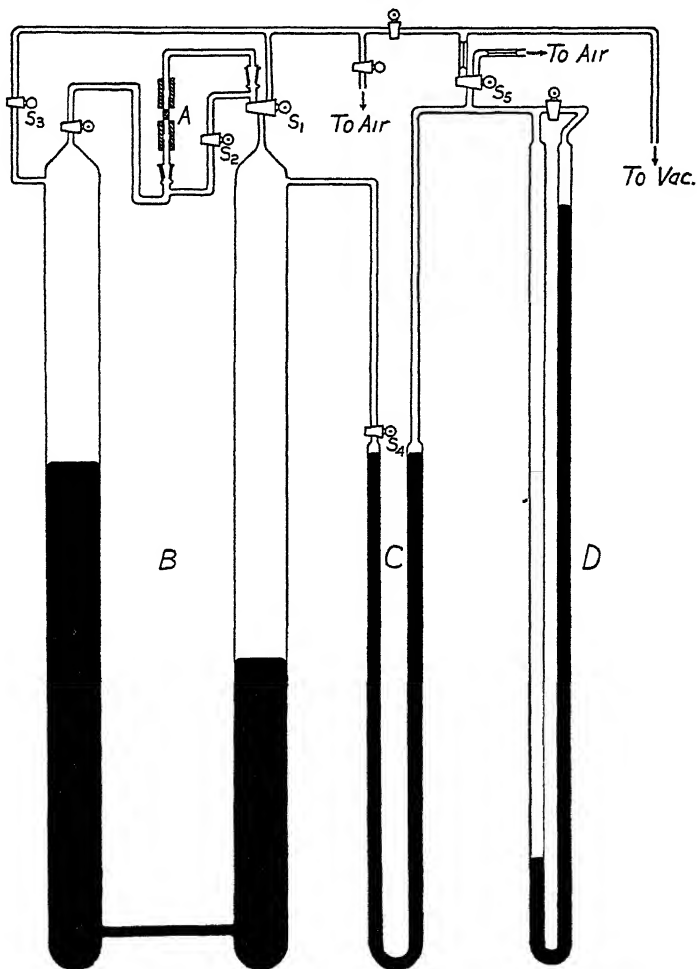


FIG. 1 Diagram of decay apparatus.

In the normal operation of the apparatus, the drop of the mercury level with time was generally followed from a pressure difference of just over 10 cm. of mercury to just under 5 cm. of mercury and the rates of flow were calculated for pressure heads of 5 and 10 cm. of mercury. If the pressure difference at the start of an experiment was higher than that desired, some gas was bled through stopcock  $S_2$  until the required difference was obtained.

### Theory of the Decay Apparatus

For the sake of completeness, the treatment followed here will be carried through the final integration, but, as will be shown later, the resulting equation has been used in its differential form.

In Fig. 1, if  $p_1$  and  $p_2$  are the pressures in centimetres of mercury, at any instant on the high and low pressure sides of the mercury towers respectively, and if  $h$  be the instantaneous pressure head in centimetres of mercury across the bed of powder, then

$$p_1 - p_2 = h. \quad (2)$$

Equating the sums of the masses of gas on both sides of the bed at any moment with the total mass of gas in the equilibrium position, and assuming isothermal conditions throughout, the following equation is obtained:

$$p_1(V_1 + A_0 h/2) \rho_1 + p_2(V_2 - A_0 h/2) \rho_1 = p_0(V_1 + V_2) \rho_1, \quad (3)$$

where  $V_1$  and  $V_2$  = equilibrium volumes of the high and low pressure sides of the mercury towers respectively in cubic centimetres,

$A_0$  = cross-sectional area of the towers in square centimetres,

$\rho_1 = \rho/p$  = density of the gas at unit pressure, and

$p_0$  = equilibrium pressure in centimetres of mercury.

Rearranging Equation (3),

$$p_1 V_1 + p_2 V_2 + (p_1 - p_2) A_0 h/2 = p_0(V_1 + V_2).$$

Eliminating  $p_2$  by substituting from Equation (2),

$$p_1(V_1 + V_2) - V_2 h + A_0 h^2/2 = p_0(V_1 + V_2),$$

and therefore,

$$p_1 = p_0 + \left( \frac{h}{V_1 + V_2} \right) \left( V_2 - \frac{A_0 h}{2} \right). \quad (4)$$

Similarly, eliminating  $p_1$ ,

$$p_2 = p_0 - \left( \frac{h}{V_1 + V_2} \right) \left( V_1 + \frac{A_0 h}{2} \right). \quad (5)$$

The mass of gas entering the bed per second at any moment is equal to the rate of change of the mass of gas in the high pressure tower, which is:

$$G = -\frac{d}{dt} [p_1(V_1 + A_0 h/2) \rho_1],$$

where  $G$  = rate of gas flow in grams per second.

Substituting for  $p_1$  from Equation (4),

$$G = -\frac{d}{dt} \left[ (V_1 + A_0 h/2) \left\{ p_0 + \left( \frac{h}{V_1 + V_2} \right) (V_2 - A_0 h/2) \right\} \rho_1 \right],$$

which on differentiation becomes

$$G = -\rho_1 \left[ \frac{A_0 p_0}{2} + \frac{V_1 V_2}{V_1 + V_2} - \frac{A_0 (V_1 - V_2) h}{V_1 + V_2} - \frac{3 A_0^2 h^2}{4 (V_1 + V_2)} \right] \frac{dh}{dt}. \quad (6)$$

Equation (6) has been used for all the calculations of gas flow reported in this paper. The equilibrium volumes,  $V_1$  and  $V_2$ , were determined by the

expansion of known volumes of air in the apparatus and the use of Boyle's law, and the cross-sectional area of the towers was determined by liquid displacement.

If  $v_1$  is the volume of gas entering the bed per second, and  $v_2$  is the volume of gas leaving the bed per second, and the flow of gas is assumed to be governed by the Poiseuille equation, then

$$p_1 v_1 = p_2 v_2 = \frac{(p_1 + p_2)}{2} (p_1 - p_2) X, \quad (7)$$

where  $X$  = a constant for any particular bed of powder, and is analogous to the constant  $\pi \rho_H g r^4 / 8 \eta L$  in the Poiseuille equation for the flow of a compressible fluid through a capillary tube.

The mass of gas entering the bed per second may also be represented by  $p_1 v_1 \rho_1$ , and therefore

$$G = p_1 v_1 \rho_1 = \frac{(p_1 + p_2)}{2} (p_1 - p_2) X \rho_1.$$

Substituting for  $p_1$  and  $p_2$  from Equations (4) and (5) and combining with Equation (6), the following equation is obtained:

$$\left[ p_0 - \frac{(V_1 - V_2)h}{2(V_1 + V_2)} - \frac{A_0 h^2}{2(V_1 + V_2)} \right] h X = - \left[ \frac{A_0 p_0}{2} + \frac{V_1 V_2}{V_1 + V_2} - \frac{A_0 (V_1 - V_2)h}{V_1 + V_2} - \frac{3A_0^2 h^2}{4(V_1 + V_2)} \right] \frac{dh}{dt}.$$

Rearranging and integrating

$$X \int_{h_1}^{h_2} dt = - \int_{h_1}^{h_2} \frac{\frac{A_0 p_0}{2} + \frac{V_1 V_2}{V_1 + V_2} - \frac{A_0 (V_1 - V_2)h}{V_1 + V_2} - \frac{3A_0^2 h^2}{4(V_1 + V_2)}}{p_0 - \frac{(V_1 - V_2)h}{2(V_1 + V_2)} - \frac{A_0 h^2}{2(V_1 + V_2)}} \cdot \frac{dh}{h}.$$

The right-hand side can be integrated by factoring in the form:

$$[Xt]_{t_1}^{t_2} = - \int_{h_1}^{h_2} \frac{B}{h} dh - \int_{h_1}^{h_2} \frac{Ch + D}{p_0 - \frac{(V_1 - V_2)h}{2(V_1 + V_2)} - \frac{A_0 h^2}{2(V_1 + V_2)}} dh,$$

where  $B$ ,  $C$ , and  $D$  are constants and have the values:

$$\begin{aligned} B &= \frac{A_0}{2} + \frac{V_1 V_2}{(V_1 + V_2)p_0}, \\ C &= \frac{A_0 V_1 V_2}{(V_1 + V_2)^2 p_0} - \frac{A_0^2}{2(V_1 + V_2)}, \text{ and} \\ D &= \frac{V_1 V_2 (V_1 - V_2)}{2(V_1 + V_2)^2 p_0} - \frac{3A_0 (V_1 - V_2)}{4(V_1 + V_2)}. \end{aligned}$$

Evaluation of these integrals and collection of terms leads to the following relation between the pressure head and the time:

$$[Xt]_h^{t_2} = \left[ \left\{ \frac{A_0}{2} + \frac{V_1 V_2}{(V_1 + V_2) p_0} \right\} \ln h - \left\{ \frac{V_1 V_2}{(V_1 + V_2) p_0} - \frac{A_0}{2} \right\} \ln \left\{ p_0 - \frac{(V_1 - V_2)h}{2(V_1 + V_2)} - \frac{A_0 h^2}{2(V_1 + V_2)} \right\} - \frac{A_0(V_1 - V_2)}{\sqrt{(V_1 - V_2)^2 + 8A_0 p_0(V_1 + V_2)}} \right. \\ \left. \ln \frac{2A_0 h + (V_1 - V_2) + \sqrt{(V_1 - V_2)^2 + 8A_0 p_0(V_1 + V_2)}}{2A_0 h + (V_1 - V_2) - \sqrt{(V_1 - V_2)^2 + 8A_0 p_0(V_1 + V_2)}} \right]_{h_2}^{h_1} \quad (8)$$

For all practical purposes, it was found that the second and third terms in the expression on the right-hand side of Equation (8) were sufficiently small in the region between  $h = 5$  cm. and  $h = 10$  cm. for the apparatus used, that they could be neglected and Equation (8) written:

$$[Xt]_h^{t_2} = \left[ \left\{ \frac{A_0}{2} + \frac{V_1 V_2}{(V_1 + V_2) p_0} \right\} \ln h \right]_{h_2}^{h_1} \quad (9)$$

With beds of very fine powders, such as were used in these experiments, the simple Poiseuille equation is no longer valid and a second term must be introduced to account for 'slip'. In the previous paper of this series (3), this matter was discussed and the simple Poiseuille equation was replaced by:

$$G = \frac{(p_1 + p_2)}{2} (p_1 - p_2) X \rho_1 + (p_1 - p_2) Y \rho_1 = p_1 v_1 \rho_1, \quad (10)$$

where  $Y =$  a constant for any particular bed of powder and is analogous to the Knudsen flow equation constant,  $\frac{4}{3} \sqrt{2\pi} \sqrt{\frac{R_0 T}{M}} \frac{r^3}{L}$ .

Equation (10) can be combined with Equation (6) and integrated in the same manner as above with Equation (7). This yields a more complicated result than Equation (8), but one having the same form. Again for all practical purposes, two terms on the right-hand side may be neglected for the apparatus used here, and the final simplified form is:

$$[t]_h^{t_2} = \left[ \left\{ \frac{A_0 p_0}{2} + \frac{V_1 V_2}{V_1 + V_2} \right\} \ln h \right]_{h_2}^{h_1} \quad (11)$$

When  $V$  becomes very small, Equation (11) reduces to Equation (9).

This equation can be readily checked against the flow of air through calibrated capillary tubes.

### Test of the Decay Apparatus Theory

Before any permeability measurements were made on beds of powder, the theory presented in the previous section was checked with three capillary tubes. Two of these capillary tubes consisted of thermometer tubing, while the third was a piece of fine Pyrex capillary tubing. The tubes had the following characteristics:

Type of tubing	Radius, cm.	Length, cm.
-50° C. to 50° C. alcohol thermometer	0.0311	25.4
Pyrex capillary tubing	0.0229	26.5
-10° C. to 110° C. thermometer	0.00816	20.0

With the apparatus filled with air, the capillary tube under test was mounted with suitable adapters across the top of the two mercury towers, *B*, and, after evacuating the left-hand tower, the air was allowed to flow through the capillary until equilibrium was attained. As the air was flowing through the capillary, the level of the mercury in the left-hand tower was periodically read on a cathetometer and the time of each reading noted on a stopwatch having two second hands for interval timing. From a knowledge of the cathetometer reading of the mercury level at equilibrium, it was possible to evaluate the pressure head corresponding to any reading of the mercury level in the left-hand tower, since a calibration showed that the cross-sectional areas of the two towers were sufficiently uniform that the expected linear relation between the pressure head and the reading of the mercury level in the left-hand tower held over the entire working range.

Fifteen runs were made with the alcohol thermometer capillary over an equilibrium pressure ( $p_0$ ) range of 0.9 to 20 cm. of mercury, six runs were made with the other thermometer capillary over an equilibrium pressure range of 14 to 64 cm. of mercury, and 11 runs were made with the Pyrex capillary tubing over an equilibrium pressure range of 0.5 to 26 cm. of mercury.

In all cases, when the logarithm of the pressure head was plotted against time, a straight line was obtained, which was considered sufficient justification for the use of Equations (9) and (11) above. Further, when the rates of gas flow in grams per second were calculated using Equation (6) for pressure heads of 1, 5, and 10 cm. of mercury, where such calculations were possible, and plotted against the corresponding mean pressures,  $(p_1 + p_2)/2$ , calculated from Equations (4) and (5), straight lines were obtained, which almost passed through the origin. This was as expected, since the correction for 'slip' in the Poiseuille equation is very small when applied to tubes of these radii.

As little is to be gained by reproducing all the data obtained with the capillary tubes, only data applying to the Pyrex capillary tubing is presented here.

Typical lines obtained when the logarithm of the pressure head was plotted against the time are shown in Fig. 2. It is possible to calculate the slopes of these lines from Equation (11) by introducing the necessary apparatus constants. The equilibrium volumes,  $V_1$  and  $V_2$ , of the apparatus, with the capillary tube adapters in place, were determined by inserting a solid glass rod in place of a capillary tube between the two adapters and observing the pressure change inside one half of the apparatus, when the mercury level was changed by varying the pressure in the other half. The accompanying volume change was calculated from the change in the mercury level and the cross-sectional area of the tower\* being calibrated. The equilibrium volume was then cal-

\* The two tubes that were used for the two towers were calibrated before the apparatus was built and were found to have an average cross-sectional area of 3.99 sq. cm. over the working length.

culated by means of Boyle's law. The equilibrium volumes were found to be:  $V_1 = 233$  cc. and  $V_2 = 265$  cc.

Introducing the Poiseuille and Knudsen flow equation constants in Equation (11) and letting  $\delta = 0.9$ , as recommended by Adzumi (1), the equation becomes:

$$[t]_{h_1}^{h_2} = \left\{ \frac{\frac{A_0 p_0}{2} + \frac{V_1 V_2}{V_1 + V_2}}{\left( \frac{\pi r^4}{8 \eta L} p_0 \rho_{Hg} g + 0.9 \times \frac{4}{3} \sqrt{2\pi} \sqrt{\frac{R_0 T}{M}} \frac{r^3}{L} \right)} \right\} \ln h \quad (12)$$

where  $r$  = radius of the capillary tube in centimetres. The term  $\rho_{Hg} g$  has been introduced into the denominator above to permit the use of centimetres of mercury as the unit of pressure head.

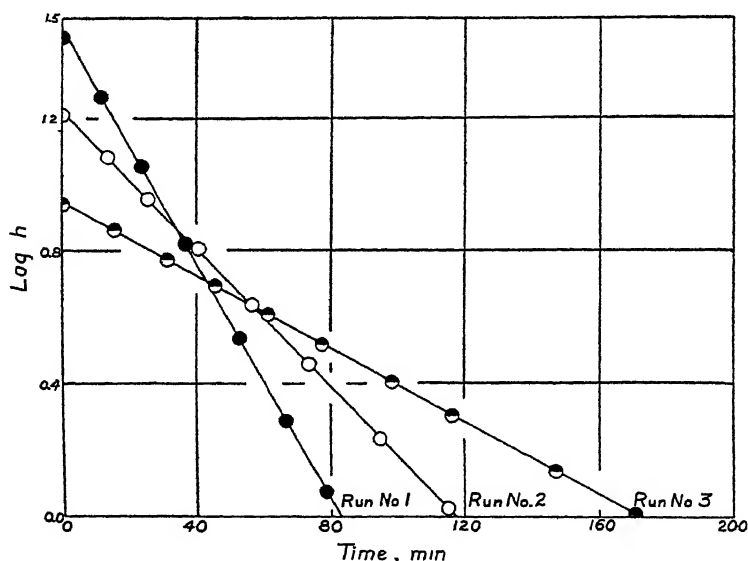


FIG. 2. Logarithm of pressure head plotted against time. Abscissa—Time, min. Ordinate— $\log h$ .

Rearranging Equation (12), it can be written:

$$\ln h = Kt + \ln h_0, \quad (13)$$

where  $1/K$  = the expression in the brace  $\{ \}$  in Equation (12), and  $h_0$  = pressure head at time  $t = 0$ .

From this it can be seen that the slopes obtained from the graphs of the logarithm of the pressure head versus the time should be given by the reciprocal of the expression in the brace in Equation (12). The calculated values of the slopes are listed with the experimental values in Table I, together with the rates of air flow in grams per second at a pressure head of 1.0 cm., calculated by means of Equation (6).

TABLE I  
FLOW OF AIR THROUGH PYREX CAPILLARY TUBE

Run No.	Equilibrium pressure, $p_0$ , cm. Hg.	Slope of $\ln h$ vs. $t$		Flow at $h = 1$ cm., $G$ , gm./sec.	Mean pressure at $h = 1$ cm., $\bar{P}$ , cm. Hg
		Observed	Calculated		
11	25.72	0.0431	0.0435	$11.92 \times 10^{-5}$	25.78
1	23.72	0.0411	0.0414	11.20	23.78
2	11.50	0.0239	0.0236	5.59	11.56
6	6.54	0.0141	0.0144	3.05	6.60
3	5.65	0.0126	0.0127	2.72	5.71
7	3.15	0.00749	0.00741	1.54	3.21
4	2.75	0.00666	0.00661	1.37	2.81
8	1.58	0.00397	0.00396	0.79 <sub>7</sub>	1.64
5	1.37	0.00349	0.00352	0.70 <sub>5</sub>	1.43
9	0.76	0.00207	0.00210	0.40 <sub>6</sub>	0.82
10	0.49	0.00146	0.00147	0.28 <sub>8</sub>	0.55

The relation between the rate of air flow,  $G$ , and the mean pressure,  $\bar{P}$ , is given by Equation (10), which may be rewritten with the capillary tube constants as:

$$G = \frac{\pi r^4}{8\eta L} h \rho_{H_2} g \rho_1 \bar{P} + 0.9 \times \frac{4}{3} \sqrt{2\pi} \sqrt{\frac{R_0 T}{M}} \frac{r^3}{L} h \rho_1. \quad (14)$$

Substituting for the various constants in Equation (14), the equation for the rate of air flow through the Pyrex capillary tube is found to be:

$$G = 4.74 \times 10^{-6} h \bar{P} + 6.33 \times 10^{-7} h. \quad (15)$$

The values of  $G$  from Table I are shown plotted against the mean pressure in Fig. 3, together with the line given by Equation (15).

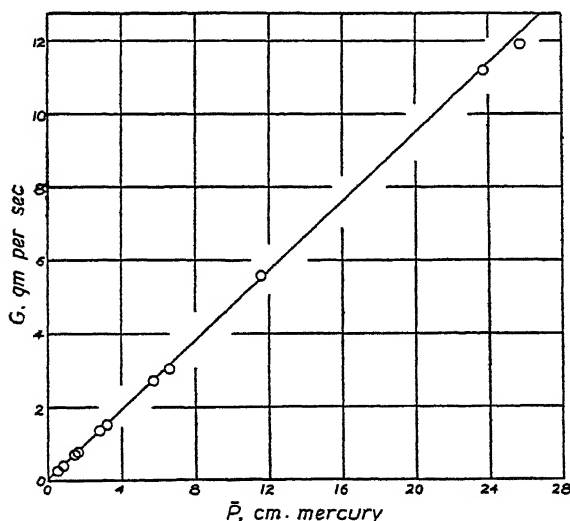


FIG. 3. Rate of mass flow plotted against mean pressure. Abscissa— $\bar{P}$  (centimetres of mercury). Ordinate— $G$  (grams per second).

From the results of these experiments, the equations developed for use with the decay apparatus appeared to be valid and the permeabilities of beds of fine powders were then investigated.

### Experimental Results

Decay curves were obtained on beds of finely ground quartz and a number of inorganic pigments over as wide a range of porosities as was feasible. The limiting values of porosity were governed by the minimum amount of powder that would form a solid bed and withstand a full atmosphere pressure difference across its length at high porosities, and by the maximum amount of powder that could be compressed into the required length using the small hand press at low porosities. In general, the decay curves were determined at five different mean pressures, all below atmospheric pressure, on each bed and further runs were made only when there appeared to be some discrepancy in the data.

From the decay curves, the rates of mass flow,  $G$ , were calculated using the Equation (6) for pressure heads of 5 and 10 cm. of mercury and these values were then plotted against the corresponding mean pressures  $\bar{P}$ . These plots all proved to be straight lines and could be expressed by an equation of the form:

$$G = \frac{Ah}{L} (B\bar{P} + C) . \quad (16)$$

The runs were all made at room temperature (20° to 25° C.), as it was found that the temperature seldom varied by more than 1° C. during the runs on any one bed, and the constants  $B$  and  $C$  of Equation (16) were all reduced to 20° C. to permit direct comparison between the different beds and powders studied.

The pertinent data for each of the powders studied are listed in Table II.

TABLE II  
DATA ON THE POWDERS USED FOR PERMEABILITY STUDIES

Kind of powder	Source	Density, gm./cc. <sup>1</sup>
Finely ground quartz	Laboratory preparation	2.65
Mapico Red No. 297	Binney and Smith, New York	5.18
Mapico Yellow Lemon	Binney and Smith, New York	3.82
Hydrated yellow iron oxide	C. K. Williams and Co., Easton, Pa.	4.0
Hydrated chromic oxide	C. K. Williams and Co., Easton, Pa.	3.12
Pure red iron oxide	C. K. Williams and Co., Easton, Pa.	5.15
Pure chromic oxide	C. K. Williams and Co., Easton, Pa.	5.2

<sup>1</sup> Except for the powdered quartz, the values of the densities of the powders were all supplied by the manufacturers.

The values of the apparatus constants that are needed for the calculation of the rate of mass flow and the porosity of the bed are given in Table III.

TABLE III  
CONSTANTS OF THE DECAY APPARATUS

Area of the permeability cell, sq. cm.	0.243
Length of the bed of powder, cm.	1.00
Area of the mercury towers, $B$ , sq. cm.	3.99
Equilibrium volume (with adapter), $V_1$ , cc.	234.5
Equilibrium volume (with adapter), $V_2$ , cc.	268.5

In Table IV are listed the constants  $B$  and  $C$  of Equation (16) and the porosities for the various beds studied.

TABLE IV  
SUMMARY OF EXPERIMENTAL DATA

Porosity	Constants—Equation (16) at 20° C.	
	$B$	$C$
<i>Powdered Quartz</i>		
0.610	$4.09 \times 10^{-8}$	$4.16 \times 10^{-8}$
0.621	6.53	5.02
0.604	4.18	3.68
0.584	3.35	3.32
0.619	4.31	4.17
0.585	2.97	3.13
0.528	1.51	2.29
0.514	1.47	2.11
0.498	1.05	1.83
0.439	0.85	1.55
0.537	2.16	2.76
0.428	0.63	1.32
0.517	1.45	2.15
0.545	2.21	2.80
0.475	1.41	2.10
0.510	1.24	1.99
0.425	0.60	1.23
0.475	1.03	1.66
0.563	3.54	3.63
<i>Mapico Red No. 297</i>		
0.766	$11.81 \times 10^{-9}$	$3.48 \times 10^{-8}$
0.752	14.08	2.80
0.718	7.60	2.29
0.692	4.25	1.88
0.677	4.24	1.99
0.721	6.81	2.31
0.636	2.05	1.54

TABLE IV—*Concluded*  
SUMMARY OF EXPERIMENTAL DATA—*Concluded*

Porosity	Constants—Equation (16) at 20° C.	
	<i>B</i>	<i>C</i>
<i>Mapico Yellow Lemon</i>		
0.807	$7.05 \times 10^{-8}$	$8.33 \times 10^{-6}$
0.780	3.01	5.72
0.754	2.77	4.88
0.767	2.54	4.83
0.704	1.37	3.35
0.700	1.08	2.81
0.676	0.95	2.60
<i>Hydrated yellow iron oxide</i>		
0.778	$2.68 \times 10^{-8}$	$4.08 \times 10^{-6}$
0.771	1.99	3.99
0.781	2.91	5.04
0.747	1.72	3.75
0.721	0.89	2.63
0.702	0.77	2.64
<i>Hydrated chromic oxide</i>		
0.682	$6.36 \times 10^{-9}$	$1.20 \times 10^{-6}$
0.664	7.26	1.24
0.656	4.07	0.80
0.711	38.85	3.30
0.706	26.85	2.52
0.691	15.51	1.92
<i>Pure red iron oxide</i>		
0.552	$12.80 \times 10^{-9}$	$2.15 \times 10^{-6}$
0.583	21.53	2.80
0.491	4.90	1.32
0.479	5.98	1.50
0.568	20.43	2.93
0.543	11.15	1.93
<i>Pure chromic oxide</i>		
0.526	$26.8 \times 10^{-9}$	$1.85 \times 10^{-6}$
0.464	3.53	1.08
0.521	23.5	1.91
0.487	7.27	1.28
0.493	5.64	1.49

### Discussion

In the derivation of Equation (1), which has been given in the preceding paper of this series (3), the fraction effective void area,  $\alpha$ , was introduced only into the term corresponding to Knudsen-type flow, and the part of the equation including the original Kozeny equation was left in its original form. The derivation of the original Kozeny equation contains a substitution of  $v/\epsilon$  for  $v_0$ , where  $v$  is the approach velocity of the fluid and  $v_0$  the mean velocity of the fluid in the bed. As the fraction effective void area,  $\alpha$ , is generally smaller than the fraction void volume,  $\epsilon$ , the  $v/\epsilon$  term should be replaced by  $v/\alpha$  in the above-mentioned substitution. This change would result in  $\alpha$  being introduced in place of an  $\epsilon$  in the first term of the right-hand side of the modified equation (Equation (1)) with a corresponding change in the shape factor  $k$ . As  $G = Q\bar{P}\rho_1$ , it is possible to rewrite Equation (1) with these modifications in terms of mass flow  $G$  as:

$$G = \frac{Ah\epsilon\alpha\rho_1}{LS_v(1-\epsilon)} \left[ \frac{\epsilon\rho_H g \bar{P}}{k_0\eta S_v(1-\epsilon)} + \delta \times \frac{8}{3} \sqrt{\frac{2}{\pi}} \sqrt{\frac{R_0 T}{M}} \right], \quad (17)$$

where  $k_0$  = a new shape factor.

It has already been pointed out that the experimental data can be represented by the equation:

$$G = \frac{Ah}{L} (B\bar{P} + C), \quad (16)$$

where  $B$  and  $C$  are constants.

From a comparison of Equations (16) and (17), the following relations are obtained:

$$B = \frac{\rho_H g \epsilon^2 \alpha \rho_1}{k_0 \eta S_v^2 (1-\epsilon)^2}, \quad (18)$$

and

$$C = \frac{8}{3} \sqrt{\frac{2}{\pi}} \sqrt{\frac{R_0 T}{M}} \frac{\delta \epsilon \alpha \rho_1}{S_v (1-\epsilon)}. \quad (19)$$

An expression for the specific surface,  $S_v$ , in terms of  $\epsilon$  and  $\alpha$  can be obtained by rearranging Equation (19) to give:

$$S_v = \frac{8}{3} \sqrt{\frac{2}{\pi}} \sqrt{\frac{R_0 T}{M}} \frac{\delta \epsilon \alpha \rho_1}{C(1-\epsilon)}. \quad (20)$$

It is possible to evaluate  $S_v$  using Equation (20), provided that the value of  $\alpha$ , the effective void area, is known. It appears to be very difficult to measure  $\alpha$  experimentally and little is known of its nature as a function of the porosity, although Furnas (6) has pointed out that  $\alpha$  generally has a value of 0.1 to 0.2 when  $\epsilon$  is 0.4 to 0.6. In the previous paper of this series (3), an empirical relation between  $\alpha$  and  $\epsilon$  was found to be satisfactory for the data under consideration and it can also be used here. This relation is:

$$\log \alpha = 1.41\epsilon - 1.40. \quad (21)$$

The values of  $S_v$ , calculated from the experimental data given in Table IV by means of Equations (20) and (21), are listed in Table V.

With a knowledge of the values of  $S_v$  for the different powders, it is now possible to determine the values of the shape factor,  $k_0$ , from Equation (18). The values obtained for  $k_0$  from the experimental data in Table IV are listed in Table V.

TABLE V

VALUES OF THE SPECIFIC SURFACE, THE SHAPE FACTOR, AND THE ADZUMI PORE RADIUS CALCULATED FROM THE EXPERIMENTAL DATA

Porosity	Specific surface, $S_v$ , sq. cm./cc.	Shape factor, $k_0$	Pore radius, $R$ , cm.
<i>Powdered quartz</i>			
0.610	$1.1 \times 10^5$	2.4	$2.98 \times 10^{-5}$
0.621	0.9	1.7	3.94
0.604	1.0	2.2	3.44
0.584	1.0	2.2	3.07
0.619	1.0	2.6	3.14
0.585	1.1	2.5	2.88
0.528	1.0	2.6	2.00
0.514	0.9	2.3	2.11
0.498	1.0	2.7	1.74
0.439	0.7	1.7	1.65
0.537	0.9	2.0	2.38
0.428	0.8	2.0	1.45
0.517	0.9	2.4	2.05
0.545	0.9	2.1	2.39
0.475	0.7	1.5	2.04
0.510	1.0	2.6	1.88
0.425	0.9	2.1	1.48
0.475	0.9	2.1	1.88
0.563	0.8	1.6	2.96
	$0.9_1 \times 10^5$	2.2	
<i>Mapico Red No. 297</i>			
0.766	$4.0 \times 10^5$	3.4	$1.03 \times 10^{-5}$
0.752	4.4	2.3	1.52
0.718	4.0	2.7	1.01
0.692	4.0	3.5	0.69
0.677	3.4	2.9	0.65
0.721	4.1	3.2	0.89
0.636	3.2	3.7	0.40
	$3.8_7 \times 10^5$	3.1	
<i>Mapico Yellow Lemon</i>			
0.807	$2.4 \times 10^5$	2.3	$2.56 \times 10^{-5}$
0.780	2.8	3.5	1.59
0.754	2.6	2.6	1.72
0.767	2.9	3.4	1.59
0.704	2.4	2.7	1.24
0.700	2.9	3.3	1.16
0.676	2.5	2.7	1.11
	$2.6_4 \times 10^5$	2.9	

TABLE V—*Concluded*VALUES OF THE SPECIFIC SURFACE, THE SHAPE FACTOR, AND THE ADZUMI PORE RADIUS CALCULATED FROM THE EXPERIMENTAL DATA—*Concluded*

Porosity	Specific surface, $S_r$ , sq. cm./cc.	Shape factor, $k_0$	Pore radius, $R$ , cm.
<i>Hydrated yellow iron oxide</i>			
0.778	$3.8 \times 10^5$	2.4	$1.99 \times 10^{-5}$
0.771	3.3	2.4	1.51
0.781	3.2	2.3	1.75
0.747	3.2	2.4	1.39
0.721	3.6	3.2	1.02
0.702	3.1	2.9	0.88
	$3.3_8 \times 10^5$	2.6	
<i>Hydrated chromic oxide</i>			
0.682	$5.8 \times 10^5$	—	$1.60 \times 10^{-5}$
0.664	4.9	—	1.78
0.656	7.1	—	1.55
0.711	2.7	—	3.56
0.706	3.3	—	3.23
0.691	3.9	—	2.42
	$4.6 \times 10^5$		
<i>Pure red iron oxide</i>			
0.552	$1.2 \times 10^5$	2.5	$1.80 \times 10^{-5}$
0.583	1.2	2.1	2.33
0.491	1.3	3.3	1.12
0.479	1.0	2.4	1.21
0.568	1.0	1.9	2.11
0.543	1.2	2.6	1.75
	$1.1_4 \times 10^5$	2.5	
<i>Pure chromic oxide</i>			
0.526	$1.1 \times 10^5$	0.9	$4.41 \times 10^{-5}$
0.464	1.3	3.4	1.00
0.521	1.1	1.0	3.72
0.487	1.3	2.1	1.72
0.493	1.1	2.9	1.15
	$1.1_6 \times 10^5$	2.1	

From Table V it can be seen that the values of the specific surface for any given powder show a maximum deviation of about  $\pm 10\%$ , which is the maximum error suggested by previous workers for specific surface measurements on coarse granules. The one exception in Table V is hydrated chromic oxide, which shows no consistent value for the specific surface. From electron microscope photographs, this powder appears to be extremely heterogeneous

and to have no definite form. It is therefore quite possible that some deformation of the particles occurred during the packing of the beds and that the resultant beds were of variable porosity throughout their length, which would render the values of the over-all porosity meaningless.

The average values of the shape factor vary from 2.2 to 3.1 for the different powders and appear to be of the right order of magnitude. In the original Kozeny equation, the shape factor,  $k$ , was taken as a constant equal to 5, but with the replacement of an  $\epsilon$  by an  $\alpha$  in the modified equation, the corresponding new shape factor,  $k_0$ , varies from 1.8 at  $\epsilon = 0.4$  to 3.5 at  $\epsilon = 0.8$ . It is also interesting to note that with most of the powders studied, the values of the shape factor for any given powder in Table V show a decrease with increasing porosity. As Carman (4) has pointed out, the shape factor embodies a term which relates the actual length of the conduits through the bed with the over-all length of the bed and which he considers to be a factor of about  $\sqrt{2}$ . It seems reasonable to assume that, as the porosity of a bed of powder increases, the ratio of the length of the conduits to the length of the bed would decrease and thus cause a decrease in the value of the shape factor, similar to that found experimentally.

A further comparison between Equation (17) and the equation put forward by Adzumi (2) is of particular interest. The Adzumi equation may be written as:

$$G = \frac{A h \rho_1}{L} \left[ \frac{\pi \rho_{H_2O} E_0 \bar{P}}{8 \eta} + \frac{4}{3} \sqrt{2\pi} \sqrt{\frac{R_0 T}{M}} \delta F_0 \right], \quad (22)$$

where  $E_0$  and  $F_0$  are constants for any given bed of porous media. Adzumi considered the significance of the constants  $E_0$  and  $F_0$  and concluded that the average radius of the pores ( $R$ ) in a porous bed was given by the ratio  $E_0/F_0$ . Evaluating the values of  $E_0$  and  $F_0$  in terms of Equation (17) and working out the ratio  $E_0/F_0$ , the following expression is obtained for the Adzumi pore radius:

$$R = \frac{4\epsilon}{k_0(1 - \epsilon)S_v}. \quad (23)$$

If the shape factor,  $k_0$ , has a value of 4 in Equation (23), the equation reduces to the definition of hydraulic radius, which forms the basis of both the original Kozeny equation and the modified equation being considered here. The value of the shape factor, as discussed above, appears to vary from 2 to 4 over the normal working range of porosities, and it therefore seems reasonable to conclude that the average pore radius arrived at by Adzumi by a method of summation applied to a system considered to be composed of a large number of fine circular capillaries, connected both in parallel and series, is practically the same as the hydraulic radius.

The value of the Adzumi pore radius in terms of the experimental data is useful for purposes of calculation and may be obtained from a comparison of Equations (16) and (22). This leads to the result:

$$R = \frac{32}{3} \sqrt{\frac{2}{\pi}} \sqrt{\frac{R_0 T}{M}} \frac{\delta B \eta}{\rho_{H_2O} g C}. \quad (24)$$

The values of the Adzumi pore radius calculated from Equation (24) using the data in Table IV are listed in Table V.

In order to check the calculated specific surface of several of the powders, a series of electron microscope photographs were taken of dispersions of two of the powders at a magnification of approximately 17,000 $\times$ . The plates were examined under a visual enlarger, which gave a final magnification of about 130,000 $\times$ . The diameters of the particles on a number of plates were measured across their horizontal axes, and the distributions of the particle diameters obtained are summarized in Table VI.

TABLE VI  
DISTRIBUTION OF PARTICLE DIAMETERS OF TWO OF THE POWDERS STUDIED

Size range	Number of particles	
	Mapico Red	Yellow iron oxide
Less than 0.05 $\mu$	5	58
Between 0.05 and 0.10 $\mu$	37	57
0.10 0.15	58	24
0.15 0.20	31	26
0.20 0.25	4	24
0.25 0.30		14
0.30 0.35		15
0.35 0.40		19
0.40 0.45		13
0.45 0.50		6
0.5 0.6		7
0.6 0.7		4
0.7 0.8		6
0.8 0.9		1
0.9 1.0		4
Total	135	278

Fair and Hatch (5) quote an expression for calculating the specific surface from a particle distribution, such as those above. This expression may be written:

$$S_v = K \frac{\sum nd^2}{\sum nd^3}, \quad (25)$$

where  $K$  is a shape factor depending on the form of the particles and varies from 6.0 for spheres to 7.7 for angular particles.

Equation (25) can be applied to the data in Table VI after a consideration of the particle shapes. From the electron microscope photographs, the Mapico Red particles are nearly spherical and appear to have smooth surfaces. These particles would be considered Rounded in the Fair and Hatch nomenclature and  $K$  would equal 6.1. The yellow iron oxide is in the form of needles, which appear on the average to be about eight times as long as they are wide. Fair and Hatch make no provision for particles of this shape, but an estimate of the shape factor can easily be made for different needle-like

shapes by comparing the surface of the shape under consideration with that of a sphere of equal volume and multiplying by 6, since the surface-volume ratio of a sphere is equal to 6 divided by the diameter of the sphere. Applying this method, the following shape factors are obtained for various figures having a length-width ratio of 8:

Shape of figure	Shape factor
Tetragonal prism	10.4
Triangular prism	13.4
Regular pyramid (octahedron)	21.3

From the shape of the yellow iron oxide crystals, which tend to be tapered towards the ends, it seems reasonable to assume a shape factor of 16 to 18 for  $K$ .

Substituting these values of the shape factor in Equation (25), together with the calculated sums of the squares and cubes of the diameters from Table VI, the specific surface of Mapico Red is found to be  $4.1 \times 10^5$  sq. cm. per cc. and of the yellow iron oxide to be 2.9 to  $3.3 \times 10^5$  sq. cm. per cc., both of which are in excellent agreement with the average values calculated from the permeability data (Table V).

It would appear that this method of measuring the specific surface of fine powders, which are too fine to be counted under an ordinary microscope and also too fine for measurements using the standard sedimentation methods, is reliable to within  $\pm 10\%$ . The greatest error with the method appears to lie in the packing of the bed, as slight changes in porosity through the bed are magnified in the values of the specific surface. Even though all the beds studied were packed in small increments, it was almost impossible to apply the same pressure to each increment during the packing with the small hand press used. If this could be done, it is quite possible that the error involved in the measurements would be appreciably reduced.

As the specific surface is calculated from the intercept of the mass flow equation (Equations (16) and (20)), which corresponds to the contribution that Knudsen-type flow makes to the total flow, it is very likely that the low pressure region, where the entire flow is of the Knudsen type, would be the most satisfactory for measurements of specific surface, if a suitable apparatus was used for the measurements.

### Acknowledgments

The author would like to express his thanks to Dr. W. M. Barss, Physics Division, National Research Council of Canada, for supplying the pigment samples and for the electron microscope photography; to former Lieut. G. O. Henneberry for assisting in the construction of the apparatus and for making some of the early measurements; and to Mr. J. W. McWade for assisting in some of the latter experimental work.

## References

1. ADZUMI, H. Bull. Chem. Soc. Japan, 12 : 292-303. 1937.
2. ADZUMI, H. Bull. Chem. Soc. Japan, 12 : 304-312. 1937.
3. ARNELL, J. C. Can. J. Research, A, 24 : 103-116. 1946.
4. CARMAN, P. C. Trans. Inst. Chem. Engrs. London, 15 : 150-166. 1937.
5. FAIR, G. M. and HATCH, L. P. J. Am. Water Works Assoc. 25 : 1551-1565. 1933.
6. FURNAS, C. C. Flow of gases through beds of broken solids. U.S. Department of Commerce, Bureau of Mines Bull. 307. 1929.
7. HODGINS, J. W., FLOOD, E. A., and DACEY, J. R. Can. J. Research, B, 24 : 167-177. 1946.
8. PECHUKAS, A. and GAGE, F. W. Ind. Eng. Chem., Anal. Ed. 18 : 370-373. 1946.
9. RIGDEN, P. J. J. Soc. Chem. Ind. 62 : 1T-4T. 1943.

## ERRATA

PERMEABILITY STUDIES. I. Surface Area Measurements Using A Modified Kozeny Equation.  
By J. C. Arnell. Can. J. Research, A, 24 : 103-116. November, 1946.

Page 104. Equation (3) should read:

$$Q = \frac{h \rho g A}{5 S_1^2 \eta L} \cdot \frac{\epsilon^3}{(1 - \epsilon)^2} \quad (3)$$

Page 105. Line 8 should read:

. . . a constriction may have the . . .

Page 108. Equation (16) should read:

$$Q = \frac{\pi(p_1 - p_2)}{8L} \left[ \frac{R^4}{\eta} + \frac{1 + c_1 p}{1 + c_2 p} \frac{32}{3\pi} \sqrt{2\pi} \sqrt{\frac{R_0 T}{M}} \frac{R^3}{p} \right] \quad (16)$$

Equation (17) should read:

$$Q = \frac{\pi(p_1 - p_2)E}{8\eta} + \gamma \frac{4}{3} \sqrt{2\pi} \sqrt{\frac{R_0 T}{M}} \frac{(p_1 - p_2)F}{p} \quad (17)$$

## THE GAMMA-RAY MEASUREMENT OF RADIUM ORE CONCENTRATES<sup>1</sup>

By W. J. HUSHLEY<sup>2</sup> AND W. R. DIXON<sup>2</sup>

### Abstract

A method is described for measuring the radium content of substances in which the radium concentration is of the order of micrograms per gram of material. The gamma-ray activities of the unknown material and of a standard radium capsule are compared by means of Geiger-Muller counters. Corrections for self-absorption and distance are given for rectangular and cylindrical sources. The effect of radiation scattered by the source into the detector is discussed. Synthetic bulk sources made up with known quantities of radium were used for the experimental work.

### Introduction

In order to measure a quantity of radium by comparing its gamma-radiation with that of a known standard, it is necessary to correct for the absorption of radiation in the radium-bearing material and its container. Several authors (2-7) have described methods of obtaining absorption corrections in the measurement of radium salts. In these methods the container is usually a cylinder less than a centimetre in diameter, and the radiation is measured in a direction from the cylinder that is at right angles to its axis. The total absorption correction may be a few per cent, most of which is due to the container, and the expected accuracy in the radium content is about 0.1%. The absorption coefficients must be obtained by measurements on other similar salts and containers.

It was the purpose of the present investigation to determine whether such techniques are applicable to the measurement of radium ore concentrates in which the radium concentration is of the order of micrograms per gram, and is to be determined to within 1%. In order to obtain a radiation intensity convenient to measure, a few hundred grams of the material is required. In comparing such bulk sources with the usual radium standards, absorption corrections as high as 30% may be necessary. Since the samples to be measured may vary considerably in density, size, and composition it might be thought desirable to measure the absorption coefficient of each independently rather than use predetermined coefficients. It was found, however, that over the range of densities and of sizes of containers studied, the measured value of the absorption coefficient usually gives a value of the absorption correction that is too high. The error for large sources is about 1% or greater and is believed to be due to radiation scattered from other parts of the bulk source into the detector. Thus in using this method for the determination of the

<sup>1</sup> Manuscript received in original form October 29, 1946, and, as revised, April 2, 1947.

Contribution from the Division of Physics, National Research Laboratories, Ottawa, Canada Issued as N.R.C. No. 1563.

<sup>2</sup> Physicist.

radium content it is desirable to have the source of a size for which the appropriate mass absorption coefficient is known or for which it is known that the measured value will give the proper correction.

### Form of Corrections

The accuracy of radium content determinations depends mostly upon the accuracy of the absorption corrections, since other sources of error may be largely eliminated. For bulk sources the correction for absorption in the radium-bearing material is much larger than the correction for absorption in the container; the latter correction may be made small by using a thin-walled container. For purposes of calculation it is assumed that the radium is uniformly distributed throughout the material in a container, that all the gamma-radiation is due to radium in equilibrium with its products of disintegration, and that the measured radiation is essentially homogeneous. It is also assumed that the distance between the source and the detector is several times larger than the maximum dimension of either the source or the detector, in order that corrections due to the finite extent of source and detector shall be small.

Cylindrical containers were used throughout as they were more readily obtained than those of other shapes. However, it is more convenient to measure the absorption coefficient and to calculate the absorption correction in an object having a rectangular cross-section. If a cylinder is placed with its axis in the line joining the source and the detector it will be referred to as a rectangular source; while if it is placed with its axis at right angles to the source-detector axis it will be referred to as a cylindrical source.

#### *Radiation from a Rectangular Source*

Referring to Figs. 1(a) and 1(b), consider a source whose cross-section is rectangular in the plane passing through both the source and the detector.

- Let  $L_c$  = distance from the centre of the source to the detector  $G$ ,
- $L_f$  = distance from the front face of the source to the detector  $G$ ,
- $h$  = length of source in the direction of the detector,
- $\mu$  = linear absorption coefficient of the source.

To calculate the correction due only to absorption in the source, consider the radiation from an element of thickness  $dx$  at a distance  $x$  from the origin  $O$  and integrate for the intensity over the length of the source. Then the ratio of the intensity received at  $G$  with absorption to the intensity with no absorption in the source is

$$1/P = (1/\mu h) (1 - e^{-\mu h}), \quad (1)$$

where  $P$  is the factor by which a measured radiation equivalent must be multiplied to correct it for absorption in the source. A source is said to be the radiation equivalent of a given quantity of radium, at the same or a given distance, if the intensity of its gamma-radiation is the same as that of the radium, provided there is no absorption of the radiation in the reference source

of radium or in its container. Expression (1) applies to both Figs. 1(a) and 1(b) and in effect replaces the bulk source with an equivalent surface source at the origin.

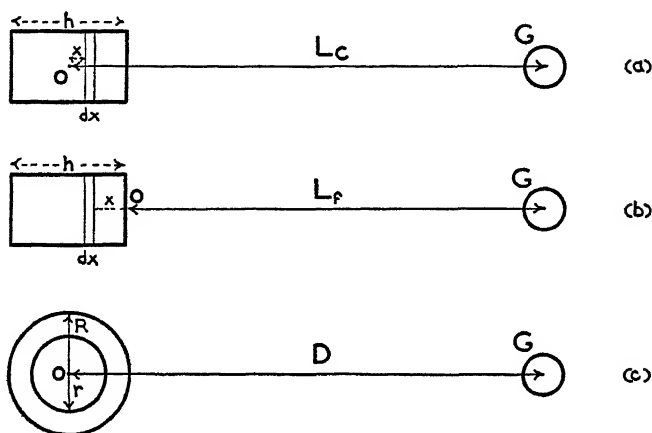


FIG. 1. Container cross-sections for which absorption corrections are considered.

Let  $t$  = the thickness of the container, and  $\lambda$  = linear absorption coefficient of the container material. Then the intensity is further reduced because of absorption in the container by a factor  $e^{-\lambda t}$ .

Since the various elements of the source are at different distances from the detector it may be necessary to apply an inverse square correction. If the distance  $L_c$  from the detector is measured to the centre of the source the ratio of intensities when the source is distributed throughout the container to that when it is concentrated in the plane  $x = 0$  is

$$\frac{1}{h} \int_{-h/2}^{h/2} \frac{L_c^2}{(L_c - x)^2} dx = \frac{1}{1 - h^2/4L_c^2}.$$

Combining the corrections for absorption in the sample and for distance as in Fig. 1(a), one obtains a ratio of measured to corrected intensities of

$$\begin{aligned} \frac{1}{P_c} &= \frac{1}{h} \int_{-h/2}^{h/2} e^{-\mu(h/2-x)} \frac{L_c^2}{(L_c - x)^2} dx \\ &= \frac{1}{\mu h} (1 - e^{-\mu h}) + \frac{h}{L_c} \left( \frac{\mu h}{6} - \frac{\mu^2 h^2}{12} + \frac{\mu^3 h^3}{40} + \dots \right) \\ &\quad + \frac{h^2}{4L_c^2} \left( 1 - \frac{\mu h}{2} + \frac{\mu^2 h^2}{5} - \frac{\mu^3 h^3}{120} + \dots \right) + \dots \end{aligned} \quad (2)$$

If  $\mu h$  and  $h/L_c$  are small it may be permissible to neglect the inverse square correction when distances are measured to the centre of the source. For example, if  $\mu h = 0.2$  and  $h/L_c = 0.05$ ,  $P = 1.1033$ , whereas  $P_c = 1.1014$ .

If the distance  $L_f$  is measured to the front face the ratio of intensities for the source distributed to the source concentrated in the plane  $x = 0$  is

$$\frac{1}{h} \int_0^h \frac{L_f^2}{(L_f + x)^2} dx = \frac{1}{1 + h/L_f}.$$

Combining the corrections for absorption in the sample and for distance as in Fig. 1(b), one obtains the ratio of measured to correct intensities,

$$\frac{1}{P_f} = \frac{1}{h} \int_0^h e^{-\mu x} L_f^2 / (L_f + x)^2 dx \quad (3)$$

$$= \frac{1 - e^{-\mu h}}{\mu h} - \frac{h/L_f}{1 + h/L_f} + \sum_{m=1}^{\infty} \frac{(-1)^m (\mu h)^m}{m!} \left[ \sum_{n=1}^{\infty} \frac{n+1}{n+m+1} (-1)^n (h/L_f)^n \right].$$

In Table I are given a few values of  $P_c$  and  $P_f$  for  $\mu h$  values up to 0.40 and for  $h/L$  values up to 0.10.

TABLE I

COMBINED CORRECTIONS FOR ABSORPTION IN THE SOURCE AND FOR THE DISTANCE EFFECT ALONG THE LENGTH OF THE SOURCE IN A RECTANGULAR SAMPLE.  $P_c$  AND  $P_f$  ARE THE CORRECTIONS WHEN THE DISTANCE IS MEASURED TO THE CENTRE AND TO THE FRONT FACE OF THE SAMPLE RESPECTIVELY

$\frac{h}{L}$ $\mu h$	$P$	$P_c$					$P_f$				
	0.00	0.02	0.04	0.06	0.08	0.10	0.02	0.04	0.06	0.08	0.10
0.00	1.000	0.9999	0.9996	0.9991	0.9984	0.9975	1.020	1.040	1.060	1.080	1.100
0.02	1.010	1.010	1.009	1.009	1.008	1.007	1.030	1.050	1.070	1.091	1.111
0.04	1.020	1.020	1.019	1.019	1.018	1.017	1.040	1.061	1.081	1.101	1.121
0.06	1.030	1.030	1.029	1.029	1.028	1.027	1.051	1.071	1.091	1.112	1.132
0.08	1.041	1.040	1.040	1.039	1.038	1.037	1.062	1.082	1.102	1.123	1.143
0.10	1.051	1.050	1.050	1.049	1.048	1.046	1.072	1.092	1.113	1.133	1.154
0.12	1.061	1.060	1.060	1.059	1.058	1.056	1.082	1.103	1.124	1.144	1.165
0.14	1.072	1.071	1.070	1.069	1.068	1.066	1.093	1.113	1.134	1.155	1.176
0.18	1.093	1.092	1.091	1.090	1.088	1.087	1.114	1.135	1.156	1.177	1.199
0.20	1.103	1.102	1.101	1.100	1.099	1.097	1.125	1.146	1.167	1.189	1.210
0.22	1.114	1.113	1.112	1.111	1.109	1.107	1.135	1.157	1.178	1.200	1.221
0.24	1.125	1.124	1.123	1.121	1.119	1.118	1.146	1.168	1.189	1.211	1.233
0.26	1.136	1.135	1.133	1.132	1.130	1.128	1.157	1.179	1.201	1.222	1.244
0.28	1.147	1.145	1.144	1.142	1.140	1.138	1.168	1.190	1.212	1.234	1.256
0.30	1.157	1.156	1.155	1.153	1.151	1.149	1.179	1.201	1.223	1.245	1.267
0.32	1.168	1.167	1.166	1.164	1.162	1.159	1.191	1.213	1.235	1.257	1.279
0.34	1.180	1.178	1.176	1.175	1.172	1.170	1.202	1.224	1.246	1.268	1.291
0.36	1.191	1.189	1.187	1.185	1.183	1.181	1.213	1.235	1.258	1.280	1.302
0.38	1.202	1.200	1.199	1.197	1.194	1.191	1.225	1.247	1.269	1.292	1.314
0.40	1.213	1.212	1.210	1.207	1.205	1.202	1.236	1.259	1.281	1.304	1.326

### Radiation from Cylindrical Source

Consider a cylinder of unit length whose axis is at right angles to the direction of the detector. Absorption corrections for this arrangement have been given by several authors (3-8) and are included here for comparison and

reference purposes only. Referring to Fig. 1 (c), let  $r$  and  $R$  be the inside and outside radii of a container that is completely filled with the source material. Let  $\mu$  and  $\lambda$  be the linear absorption coefficients of the source and container materials as before.

Considering absorption in the source only, let there be an element at  $(x, y)$  emitting gamma-radiation in the direction of the detector  $G$ . Then the ratio of the intensity with absorption in the source to that with no absorption is

$$\frac{2}{\pi r^2} \int_0^r \int_{-(r^2-y^2)^{\frac{1}{2}}}^{(r^2-y^2)^{\frac{1}{2}}} e^{-\mu\{(r^2-y^2)^{\frac{1}{2}}-x\}} dx dy \quad (4)$$

$$= 1 - (8/3\pi)\mu r + \frac{1}{2}\mu^2 r^2 - (32/45\pi)\mu^3 r^3 + \dots$$

The equivalent rectangular source is approximately that for which  $1 - (8/3\pi)\mu r = 1 - \mu h/2$ , or  $h = 1.68 r$ .

Considering the absorption in the circular container only, the ratio of the intensity with absorption to that with no absorption is

$$\frac{2}{\pi r^2} \int_0^r \int_{-(r^2-y^2)^{\frac{1}{2}}}^{(r^2-y^2)^{\frac{1}{2}}} e^{-\lambda\{(R^2-y^2)^{\frac{1}{2}}-(r^2-y^2)^{\frac{1}{2}}\}} dx dy$$

$$= 1 - \lambda R[1 - (8/3\pi)r/R - (1/8)r^2/R^2 - (1/64)r^4/R^4 - \dots] \quad (5)$$

$$+ \frac{\lambda^2 R^2}{2} [1 - (16/3\pi)r/R + \frac{1}{2}r^2/R^2 + (8/15\pi)r^3/R^3 + \dots] + \dots$$

If the container correction is small a good degree of approximation may be obtained by defining an effective thickness  $t$  by

$$t = R[1 - (8/3\pi)(r/R) - (1/8)(r^2/R^2) - \dots]. \quad (6)$$

and the absorption correction is then given by  $e^{-\lambda t}$ . For more accurate work a graphical integration is usually performed.

If the cylindrical source and container corrections are large and an accurate result is required the two expressions (4) and (5) must be combined before integration since the corrections cannot be applied separately as they can for a rectangular source.

### *Obliquity Corrections*

If the distance between the source and the detector is of the same order as the lateral dimensions of either the source or the detector, it may be necessary to apply obliquity corrections. The form of such corrections has been given by Backhurst (1). In the experimental work described here obliquity corrections were usually negligible.

## **Experimental**

Experimental work was performed on several bulk sources of known radium content, so that errors arising from using the wrong absorption coefficient, or from using an undesirable geometrical arrangement, would become evident.

Measurements were made of the radiation equivalent of each source as a rectangular source, and an absorption coefficient was measured to see whether it could be used to give the proper absorption correction. Typical results are given in Table III for the sources that are described below.

The direct measurement of the absorption coefficient of the bulk source was made by measuring the reduction in intensity of the radiation from a standard capsule placed behind it. Thus if

$I_s$  is the intensity due to the standard capsule alone;

$I_{su}$  is the intensity due to the standard capsule and to the unknown, placed so that radiation from the standard is absorbed in the unknown before reaching the detector;

and

$I_u$  is the intensity due to the unknown alone,  
then the measured value of  $\mu h$  is

$$\mu h = \ln I_s / (I_{su} - I_u) - 2\lambda t, \quad (7)$$

where  $\lambda t$  refers to the container walls. The measured values of  $\mu h$  given in Table III were obtained with the standard capsule touching the centre of the back face of the bulk source.

#### *Description of Sources*

The sources used in the experimental work are listed in Table II, U-1 to U-10 being especially prepared bulk sources, and S-1 to S-4 being National Research Council secondary radium standards.

Sources U-1, U-2, and U-3 were prepared from capsules of radium bromide that previously had been measured against the National Research Council secondary standards with both an ionization chamber and a Geiger-Müller counter. The contents of each capsule was dissolved in dilute hydrobromic acid and mixed with enough barium carbonate to give the desired concentration. The tools and dishes used in the mixing were sealed in another container and their radiation equivalent later measured to determine how much radium was lost. This amounted to a few micrograms. It is considered that the radium content of U-1, U-2, and U-3 is known with an accuracy of at least 0.5%.

Sources U-4 to U-8 were prepared to show the effect of containers of different sizes. The material used for each was from the same sample of radium ore concentrate, consisting of 92% barium carbonate and 7% aluminium oxide, which had been obtained from Eldorado Mining and Refining Co. Subsequent measurements of these five sources indicated that the most likely radium concentration was 11.00  $\mu\text{gm. per gm.}$ , and the true content of each source was calculated on this basis.

Sources U-9 and U-10 contain pitchblende ore that had been chemically analysed and then mixed with inert rock to contain 32.0 and 48.0%, respectively, of  $\text{U}_3\text{O}_8$ . These ore samples were obtained from the Bureau of Mines, Department of Mines and Resources, Ottawa. By assuming the ratio of

TABLE II

DESCRIPTION OF SOURCES. THE SOURCE MATERIALS ARE: *A*—MIXTURE OF RADIUM BROMIDE AND BARIUM CARBONATE; *B*—A SAMPLE OF RADIUM BARIUM CARBONATE OBTAINED IN THE REFINING OF ORE; *C*—CANADIAN PITCHBLEND ORE; *D*—RADIUM SULPHATE

Description of source					Description of container				
Source number	Radium content, mgm.	Material	Weight, gm.	Density, gm./cm. <sup>3</sup>	Material	Wall thickness, cm.	Inside diameter, cm.	Inside length, cm.	Volume, cm. <sup>3</sup>
U-1	1 118	<i>A</i>	125 6	1 39	Steel	0.025	5 49	3 81	90 2
U-2	2.150	<i>A</i>	179.7	1 97	Steel	0 025	5 49	3.86	91.4
U-3	2 070	<i>A</i>	131.3	1 49	Steel	0 025	5.49	3.71	87.8
U-4	0.656	<i>B</i>	59.6	1.85	Steel	0.025	3.79	2.85	32.2
U-5	1.262	<i>B</i>	114.7	1.88	Steel	0 025	4.79	3 38	60.9
U-6	1.811	<i>B</i>	164.6	1.80	Steel	0.025	5.49	3 86	91.4
U-7	2.486	<i>B</i>	226.0	1 85	Steel	0 025	6 04	4.27	122.3
U-8	1.103	<i>B</i>	100 3	1 66	Steel	0.025	7.59	1.34	60.6
U-9	0.025	<i>C</i>	267 5	2 05	Steel	0 025	7.50	2 95	130.3
U-10	0 050	<i>C</i>	363.3	2.68	Steel	0.025	7.50	3.07	135.6
S-1	Rad. Eq. 0.0906	<i>D</i>			Glass				
S-2	0.528	<i>D</i>			Glass				
S-3	0.942	<i>D</i>			Glass				
S-4	1.977	<i>D</i>			Glass				

TABLE III

TYPICAL EXPERIMENTAL RESULTS ON SOURCES DESCRIBED IN TABLE II. INTENSITIES ARE GIVEN AS COUNTING RATES PER MINUTE, SCALE-OF-64. FILTER WAS 1 CM. LEAD SURROUNDING THE G-M TUBE

Unknown source	Standard source	Distance unknown, $L_u$ , cm.	Distance standard, $L_s$ , cm.	Intensity unknown, $I_u$	Intensity standard, $I_s$	Radiation equiv., mgm. Ra	Measured $\mu_{m/h}$
U-1	S-3	75.0	75.0	87.6	81.5	1.013	0.199
U-2	S-4	110.0	110.0	73.7	78.0	1.868	.299
U-3	S-4	75.0	75.0	162.6	171.9	1.870	.203
U-4	S-2	70.0	70.0	56.0	50.2	0.589	.196
U-5	S-3	100.0	100.0	51.0	42.9	1.119	.230
U-6	S-4	97.6	100.0	80.4	95.0	1.594	.256
U-7	S-4	100.0	100.0	98.8	90.3	2.163	.292
U-8	S-4	100.0	100.0	47.6	89.8	1.048	.078
U-9	S-1	33.0	33.0	9.4	38.2	0.0223	.254
U-10	S-1	34.0	34.0	17.2	35.7	0.0436	.364

radium to uranium to be  $3.4 \times 10^{-7}$  the amount of radium in each of U-9 and U-10 was calculated.

For purposes of measurement a given sample of radium ore concentrate is thoroughly mixed to ensure a homogeneous distribution and packed into a container that is then sealed and put away until the disintegration products

come into equilibrium with the radium. Steel cylindrical containers of height about 4 cm., radius 2.5 cm., and wall thickness 0.025 cm. have been found convenient, since they were readily available commercially. These containers hold about 150 gm. of barium carbonate.

### Apparatus

The radiation intensities due to the radioactive sources were measured by means of Geiger-Müller counters. In order to minimize scattering from the walls and tables into the Geiger-Müller tube, the apparatus was located centrally in a room approximately 20 ft. square. The Geiger-Müller tube was mounted about twenty inches above the edge of one table, and the sources and filters were placed on an optical bench that stretched across to another table. Mountings to hold the Geiger-Müller tube and the sources were made of light wood. The usual distance between the sources and the counters was of the order of 100 cm. The general arrangement is shown in Fig. 2.

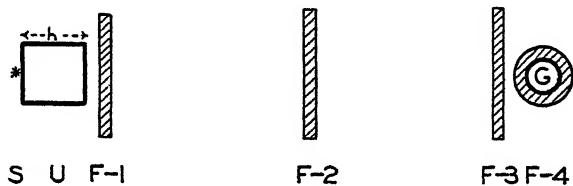


FIG. 2. Arrangement of standard radium capsule *S*, the unknown bulk source *U*, filters *F-1* to *F-4*, and Geiger-Müller counter *G*.

The detecting apparatus consisted of a self-quenching Geiger-Müller tube, a stabilized high voltage supply, a scaler, and a recorder. The G-M tubes were made with brass cathodes of cross-section 14 by 2 cm. Counting rates were of the order of 100 counts per sec. All the measurements were corrected for resolving time losses and the natural background, and sufficient counts were taken to reduce statistical errors to the order of 0.1%.

### Positions of Filters

Owing to the complex nature of the gamma-radiation emitted by the disintegration products of radium it is necessary to use a filter to improve the homogeneity of the radiation that reaches the detector. Four possible locations of the filter are illustrated in Fig. 2. In choosing the best arrangement of the filter, consideration must be given to the radiation scattered from the walls and tables, and to the radiation scattered from the filter itself into the counter.

The wall and table scattering was measured experimentally by placing a lead brick, 25 cm. long and 10 cm. square in cross-section, in the path of the direct radiation from a 5 mgm. source placed 150 cm. from the counter. The following counting rates were observed:

No filtering	238.0
25 cm. lead filter in direct beam	20.4
25 cm. lead filter in direct beam plus 3 mm. lead surrounding the G-M tube	2.7
25 cm. lead filter in direct beam plus 1 cm. lead surrounding the G-M tube	1.5
Natural background, 1 cm. lead surrounding G-M tube	1.4
Lead filter 1 cm. in direct beam	108.5

Thus the wall and table scatter comprises roughly 10% of the total radiation reaching the counter in this particular geometry, if no lead is used about the G-M tube. If a lead filter of 1 cm. thickness is used next to the source, and no lead is placed about the G-M tube, the wall and table scatter may be as much as 20% of the total. Three millimetres of lead about the G-M tube cuts out most of the scattered radiation since it is much softer than the direct, owing to the large angles through which it has been scattered.

Scattering from the lead filter itself may be as much as 10% of the total radiation reaching the counter. This may be demonstrated by placing a lead filter close to the source, Fig. 2, F-1; midway between the source and the counter, F-2; and close to the counter, F-3. The recorded counting rate is always less for the filter in the midway position. For a lead filter 18 cm. by 15 cm. and 1 cm. thick, the counting rate was observed to be 10% less than for either of the other two positions. This is to be expected from a consideration of the solid angles subtended by the filter at the source and by the counter at the filter. A more complete discussion of the radiation scattered into the detector from a filter has been given by Tarrant (8).

Since the amount of radiation scattered from the filter depends upon the distance between the filter and the source, the inverse square law as applied to distance between the source and the detector does not hold. Table IV gives results that were obtained with different positions of the filter and sources. It is seen that divergent values are obtained when use is made of

TABLE IV

EXPERIMENTAL RESULTS FOR SOURCES U-3 AND S-4 FOR DIFFERENT ARRANGEMENTS OF FILTERING AND DISTANCES. INTENSITIES ARE GIVEN AS COUNTING RATES PER MINUTE, SCALE-OF-64

Distance unknown, U-3, $L_c$ , cm.	Distance standard, S-4, $L_s$ , cm.	Lead filtering	Intensity unknown, $I_u$	Intensity standard, $I_s$	Calculated content, mgm. Ra
72.6	75.0	3 mm. F-4, 1 cm. F-1	130.5	126.5	2.116
97.6	100.0	" "	72.6	71.6	2.115
152.6	155.0	" "	30.2	30.6	2.093
72.6	70.7	" "	129.2	145.6	2.049
72.6	75.0	3 mm. F-4, 1 cm. F-2	119.2	117.3	2.083
152.6	155.0	" "	25.5	26.1	2.073
72.6	75.0	1 cm. F-4	173.5	171.9	2.070

the inverse square law, except when the filter is placed about the detector. The arrangement adopted has been to place a 1 cm. lead cylinder around the G-M tube even though there is considerable radiation scattered from the lead cylinder into the counter tube.

### Absorption Corrections

If the form of the absorption corrections given above is to be used, it is necessary to find that value of  $\mu h$  for which the corresponding  $P$  (Equation (1), (2), or (3)) gives the correct radium content. This value of  $\mu h$  is found most accurately from sources of which the true radium content is known, and of which the radiation equivalent has been measured. Coefficients obtained by other means then may be compared with this value.

It will be found convenient to distinguish three different absorption coefficients.  $\mu_p$  will be used to indicate the 'appropriate' coefficient which when used to calculate the correction factor  $P$  gives the correct result.  $\mu_m$  will be used to indicate the measured coefficient as calculated from Equation (7).  $\mu_t$  will be used to indicate the true coefficient, i.e., that which would be measured if radiation scattered from other parts of the source were not allowed to reach the detector. It has been found that  $\mu_m$  is usually less than  $\mu_t$  but greater than  $\mu_p$ , the differences being due to scattered radiation reaching the detector. Scattered radiation increases the apparent radiation equivalent of the bulk source, requiring a lower value of  $\mu_p$ , and this is not always compensated for by the scattered radiation which reaches the counters during the measurement of the coefficient  $\mu_m$ .

The appropriate corrections for absorption are shown for sources U-1 to U-10 in Table V. The corresponding value of  $\mu_p h$  was found from Table I, and the mass absorption coefficient  $\mu_p/\rho$  was found by dividing  $\mu_p h$  by  $h\rho$ , where  $\rho$  is the density. The results show that  $\mu_p/\rho$  varies with the dimensions

TABLE V

COMPARISON OF APPROPRIATE AND MEASURED ABSORPTION COEFFICIENTS AND ABSORPTION CORRECTIONS FOR SOURCES OF KNOWN RADIUM CONTENT CORRECTION FOR ABSORPTION IN THE CONTAINER WALL WAS TAKEN TO BE 1.010

Source No.	$h/L_c$	$P(\mu_p h)$	$\mu_p h$	$\mu_p/\rho$ , cm <sup>2</sup> /gm	$\mu_m/\rho$ , cm <sup>2</sup> /gm	$P(\mu_m h)$	$\frac{P(\mu_m h)}{P(\mu_p h)}$
U-1	0.051	1.093	0.185	0.035	0.038	1.100	1.007
U-2	0.035	1.139	0.272	0.036	0.039	1.155	1.013
U-3	0.050	1.096	0.191	0.035	0.037	1.102	1.006
U-4	0.041	1.103	0.203	0.038	0.037	1.099	0.996
U-5	0.034	1.117	0.229	0.036	0.036	1.118	1.001
U-6	0.040	1.125	0.244	0.035	0.037	1.131	1.005
U-7	0.043	1.138	0.270	0.034	0.037	1.151	1.011
U-8	0.013	1.042	0.083	0.037	0.035	1.039	0.997
U-9	0.090	1.098	0.200	0.033	0.042	1.124	1.024
U-10	0.090	1.143	0.287	0.035	0.044	1.184	1.036

of the sources. The radium content of the sources is not known accurately enough to determine whether it also varies with the density.

The accuracy with which  $\mu h$  must be known may be found by differentiating the correction factor

$$P = \mu h / (1 - e^{-\mu h})$$

with respect to  $\mu h$ . This gives

$$\Delta P / P = (1 - P e^{-\mu h}) \Delta \mu h / \mu h.$$

For  $\mu h = 0.10$ , the relative error in  $\mu h$  is about twenty times the relative error in  $P$ ; for  $\mu h = 0.20$ , about ten times; and for  $\mu h = 0.30$ , about seven times. The error in using a value  $\mu/\rho = 0.035 \pm 0.001$  cm.<sup>2</sup> per gm. for sources U-1 to U-3 is then about  $0.001 \times 0.1 \times 100 / 0.035 = \pm 0.3\%$ .

The measured values of  $\mu_m/\rho$  are also shown in Table V, but these values may have an appreciable error because the density within a bulk source may not be uniform. The observed coefficient  $\mu_m/\rho$  shows a significant decrease for a thin sample and is much higher for a small radius, a value of 0.045 being obtained when a lead brick with a hole through it of radius half a centimetre was placed in front of the absorbing sample. Increase of the radius beyond about two centimetres seemed to have little effect, probably because of the large angle through which the radiation had to be scattered in order to reach the counter. The measured coefficient also increases as the distance between the source and the absorber is increased owing to the smaller amount of scattered radiation reaching the counter.

The correction factor  $P$  calculated from the measured value  $\mu_m h$  is usually higher than the 'appropriate' value. The error in using the former value of  $P$  may be seen from the last column of Table V. Although this error is only a little greater than the experimental errors in measurement, a discussion is given below to show how it might arise.

### Effect of Scattered Radiation

The effect of scattered radiation in the determination of the 'appropriate' and measured coefficients may be written in terms of the fraction of radiation scattered. Let us consider the fraction  $J_s/I$ , arising in the direct measurement of the absorption coefficient, and the fraction  $J_u/I_0$  arising in the measurement of the radiation equivalent of a bulk source, where

$J_s$  is the intensity of the radiation from the standard capsule scattered into the counter during the measurement of  $\mu h$ ,

$I_s$  is the intensity of radiation due to the standard capsule alone,

$J_u$  is the intensity of the radiation from the unknown bulk source scattered into the counter from other parts of the source, and

$I_0$  is the intensity due to the unknown with no absorption.

If  $\mu_i$ ,  $\mu_m$ , and  $\mu_p$  are the coefficients already defined, then

$$\text{and} \quad J_s/I_s = e^{-\mu_m h} - e^{-\mu_i h}, \quad (8)$$

$$J_u/I_0 = 1/P(\mu_p h) - 1/P(\mu_i h). \quad (9)$$

Experimental values of these scattered fractions for sources U-1 to U-8 are shown in Table VI, as calculated from Equations (8) and (9), taking  $\mu_i/\rho = 0.050 \text{ cm.}^2 \text{ per gm.}$  This value of  $\mu_i/\rho$  was measured by using an absorbing sample of small cross-section and a separation of standard capsule and absorber of several centimetres. It agrees with a value obtained by Perry (7).

The 'appropriate' coefficient  $\mu_p/\rho$  may be written in terms of the measured coefficient  $\mu_m/\rho$  from Equations (8) and (9), if the approximations  $P = e^{\frac{1}{2}\mu h}$  and  $x = \ln(1 + x)$  for small  $x$  are used, giving

$$\mu_p/\rho = \mu_m/\rho + (1/h\rho) (J_s/I_s)e^{\mu_i h} - (2/h\rho) (J_u/I_0)e^{\frac{1}{2}\mu_i h}. \quad (10)$$

If a measured coefficient is to be used for the calculation of the absorption correction, it is then necessary that the approximate ratio of the scattered fractions be

$$\frac{J_s/I_s}{J_u/I_0} = 2 e^{-\frac{1}{2}\mu_i h}, \quad (11)$$

or, more accurately, simply the ratio of Equation (8) to Equation (9) with  $\mu_p$  substituted for  $\mu_m$ . The latter relation has been used to calculate the required ratio in Table VI. The experimental value of this ratio is also given in Table VI. Since  $J_u/I_0$  is fixed by the geometry of the unknown source it is necessary to find those conditions in the measurement of  $\mu h$  for which the scattering would compensate the effect of scattering in measuring the radiation equivalent of the bulk source, if a measured coefficient is to be used.

TABLE VI

FRACTIONS OF RADIATION SCATTERED IN MEASURING AN ABSORPTION COEFFICIENT AND A RADIATION EQUIVALENT OF A BULK SOURCE AND THEIR RATIO

Source	$J_s/I_s$ Equation (8)	$J_u/I_0$ Equation (9)	The ratio $(J_s/I_s)/(J_u/I_0)$	
			Exptl.	Req'd.
U-1	0.053	0.034	1.6	1.9
U-2	0.057	0.043	1.3	1.8
U-3	0.059	0.036	1.6	1.9
U-4	0.054	0.026	2.1	1.9
U-5	0.067	0.037	1.8	1.8
U-6	0.068	0.042	1.6	1.9
U-7	0.072	0.050	1.4	1.8
U-8	0.030	0.013	2.3	2.0

Scattering presumably also has an effect upon the correction for absorption in the container walls. However, the total wall correction for 0.025 cm. of steel is 1% so that variations in this correction due to scattering may be neglected. The effect of container walls was further investigated by measuring source U-2 with a brass collar 0.3 cm. thick fitting snugly around it. The collar increased the measured radiation equivalent by about 1% owing to increased scattering. A container wall of 0.025 cm. would, therefore, introduce no appreciable error.

## Conclusions

The main features of the experimental method for the determination of the radium content of unknown bulk sources are the measurement of the radiation equivalent of the source, as found by comparing the intensity of gamma-radiation from it to that from a standard radium capsule, and the correction for self-absorption made on the basis of an absorption coefficient measured with the capsule touching the centre of the back face of the bulk source. This method gives an error in the radium content that is less than 2% for the radium ore concentrates studied.

The measurements on the synthetic sources, consisting chiefly of barium carbonate, indicate that the mass absorption coefficient required to give the proper absorption correction varies with the dimensions of the source. An accurate value of a directly measured absorption coefficient is difficult to obtain, and, because this value frequently does not give an appropriate absorption correction, it is desirable to have the source of a size for which the appropriate mass absorption coefficients are known, or for which it is known that the measured value will give the proper correction. The error in using the directly measured absorption coefficient arises because scattering conditions in the measurement of the coefficient differ from those in the measurement of the radiation equivalent of a bulk source.

## References

1. BACKHURST, I. *Proc. Phys. Soc. London*, 38 : 277-290. 1926.
2. KAYE, G. W. C., ASTON, G. H., and PERRY, W. E. *Brit. J. Radiol.* 7 : 540-556. 1934.
3. ODDIE, T. H. *Proc. Phys. Soc. London*, 51 : 905-931. 1939.
4. OWEN, E. A. and FAGE, W. E. *Proc. Phys. Soc. London*, 34 : 27-32. 1921.
5. OWEN, E. A. and NAYLOR, B. *Proc. Phys. Soc. London*, 34 : 92-97. 1921.
6. PATERSON, C. C., WALSH, J. W. T., and HIGGINS, W. F. *Proc. Phys. Soc. London*, 29 : 215-246; discussion, 246-249. 1917.
7. PERRY, W. E. *Proc. Phys. Soc. London*, 57 : 178-190. 1945.
8. TARRANT, G. T. P. *Proc. Cambridge Phil. Soc.* 28 : 475-489. 1931.

# NEW PHOTOGRAPHIC EMULSIONS SHOWING IMPROVED TRACKS OF IONIZING PARTICLES<sup>1</sup>

BY PIERRE DEMERS<sup>2</sup>

## Abstract

The photographic emulsion method of registering the tracks of ionizing particles suffers from certain disadvantages that are mainly due to the relatively large size of grains forming the tracks and their large spacing. These disadvantages are mostly removed in new emulsions that have been prepared after numerous tests. The tracks of ionizing particles in these emulsions consist of grains of diameter  $\bar{d} \sim 0.2 \mu$ , which often form continuous lines.

Grain spacing is no longer the main cause of apparent straggling, except below a range of 3 to 4 mm. of air. The standard deviation in determining energy from a single measurement of range is 3.25 to 3.5% for protons of 0.6 to 2.4 Mev., and 1.3 to 1.9% for  $\alpha$ -rays of 4 to 8.5 Mev. The latter deviation is one-half to one-quarter that obtained in commercial emulsions. Ease of finding the tracks, especially of protons, is considerably increased. The tracks of fission fragments have a characteristic appearance and are easily found amidst the faint or invisible tracks of  $\alpha$ -rays and protons. Slow electron tracks have occasionally been seen.

The action of certain sensitizing and desensitizing chemicals is described and discussed in terms of the theory of the photographic process.

The grain spacing is related to the diameter of the grain, the concentration of silver bromide in the emulsion, and the average probability of development of the grains touched by the ionizing particle. A quantitative theory is given for the probability of development in terms of the specific energy loss and a sensitivity parameter of the emulsion. The observed variation of the grain spacing with residual range of protons,  $\alpha$ -rays, and fission fragments can be approximately explained by the theory.

## Introduction

### 1. General Remarks

The cloud chamber and the photographic emulsion methods were introduced as new techniques into nuclear physics at about the same time (1910-1912); both make visible the tracks of individual electrified particles. As is well known, the cloud chamber method is due to C. T. R. Wilson. The photographic emulsion method originated from the work of several authors, notably Kinoshita (11) and Reinganum (20). The principle is as follows. An ionizing particle passes through a layer of emulsion, which consists of silver bromide crystals embedded in gelatine, and leaves a modification called a latent image in some of the crystals, which renders them developable. After these crystals have been reduced to silver, the track is visible as a row of silver grains under a magnification of 100 to 1500 times. (In the processing some crystals are developed outside the track, thus producing what is called fog.)

<sup>1</sup> Manuscript received August 29, 1946.

Contribution from the Montreal Laboratory, Nuclear Physics Branch, Division of Atomic Energy of the National Research Council of Canada. Issued as N.R.C. No. 1450. This work was mostly done in 1945, the first original results being obtained in May 1945. Publication was withheld owing to security restrictions. In December 1945, a brief account was sent in the form of a Letter to the Editor for publication in the *Physical Review*, but its appearance was delayed until July 15, 1946. The results of this paper were briefly presented at the Toronto meeting (May 20, 1946) of the Royal Society of Canada.

<sup>2</sup> Physicist, National Research Council; now at the University of Montreal, Montreal, Que.

By this technique the tracks of mesotrons, protons, and heavier ions have been recorded by various experimenters. Electrons and  $\gamma$ -rays fog the emulsions without usually leaving recognizable tracks.

## 2. *Photographic Emulsions That Have Been Used to Record Tracks*

The properties of photographic materials are dealt with by Mees (13) and Webb (26), and emulsion-making by Baker (1), Wall (24), and Carroll (7). Shapiro (21) and Wilkins (27) have written useful reviews of the emulsion technique in nuclear physics.

Photographic emulsions usually contain about 40% silver bromide in the form of minute crystals or grains, the balance being gelatine, with occasional minor constituents. The diameter of the grains may range from a few hundredths of a micron to several microns. The mean diameter is smallest (about  $0.03 \mu$ ) in the Lippmann emulsions and largest ( $1$  to  $2 \mu$ ) in fast negative material. The dried emulsion forms a layer  $10$  to  $20 \mu$  thick on a support of glass or a cellulose derivative.

The early experimenters were able to record the tracks of  $\alpha$ -rays but not of protons. In 1925 Miss Blau (3) found that certain emulsions could be sensitized to protons by pinakryptol yellow or green. Plates are now commercially available that will respond to the action of protons without a sensitizing dye. Some of these are *Eastman fine grain  $\alpha$ -particle* (Eastman Kodak, U.S.A.) or *Eastman  $\alpha$*  for short, *Ilford Special Half-tone* (Ilford, U.K.) and *Agfa K* (Agfa, Germany). Ilford has recently produced a series of improved emulsions, which came to the writer's attention while this work was being written (19).

There is no information in the technical literature on how these commercial emulsions are made. Jdanov (10) has recommended one emulsion (called  $E_1$ ) for recording proton tracks, without giving its complete formula. Myssowsky and Tschishow (15) have discussed the recording of  $\alpha$ -ray tracks in an emulsion of given recipe.

## 3. *Advantages and Limitations of the Photographic Emulsion Technique*

In order to appreciate the value of the photographic emulsion technique, it may be compared with the cloud chamber method. The photographic emulsion acts as a continuously sensitive device for recording the tracks of ionizing particles, while a cloud chamber is sensitive only about one-thousandth of the time that it is in operation. The volume of air equivalent to the emulsion is usually greater than that contained in a cloud chamber. Moreover, the photographic plate has the great convenience of small size. On the other hand, when the thin thread-like tracks in a cloud chamber are compared with the tracks seen in the usual emulsions, the limitations of the latter are evident. Since the grains are large and relatively scarce, the tracks are hard to find and the accuracy possible in range and angular measurements is severely limited. These limitations may be seen in Figs. 13A, 13B and 18, which show tracks obtained in Eastman  $\alpha$ -plates. Powell (18) has found that  $\alpha$ -ray energies of a few million electron volts can be measured with a

standard deviation of 0.25 Mev. and protons with a standard deviation of 0.15 Mev. in Ilford halftone plates. The writer has found somewhat higher deviations in Eastman  $\alpha$ -plates. Moreover, in addition to the rather large standard deviations, there is usually little difference in appearance between the tracks of protons and  $\alpha$ -rays. Sometimes it has even been difficult to recognize the tracks of the strongly ionizing fission fragments among the tracks of  $\alpha$ -rays. Perfilov (17) and Borst and Floyd (6) have recently succeeded, however, in recording and recognizing the tracks of the fission fragments from uranium without confusion with the  $\alpha$ -rays.

#### 4. *Desired Improvements in Emulsions*

In view of the causes of the limitations pointed out in the previous section, the following improvements may be aimed at: (i) smaller grain size, and (ii) closer grains, which will result in a better definition of the track, (iii) differential sensitivity of the grains so that the various particles may be distinguished and identified, (iv) every grain touched by the ionizing particle must develop, and (v) excessive fog must be avoided. How these desired results may be brought about can be seen in part from the considerations that follow.

Jdanov (10) has introduced a useful relation that correlates the mean grain spacing  $\Delta$ , the grain diameter  $d$ , and the concentration  $c$ :

$$\Delta = 4.2 d/c.$$

It is easily derived from geometrical considerations on the assumptions that the grains are spherical, the track linear, and every grain touched by the track is ultimately developed.  $\Delta$  and  $d$  are conveniently expressed in microns and  $c$  in grams of silver bromide per cubic centimetre of emulsion. Owing to the absence of information on grain sizes before development, the apparent diameter after development will be used for  $d$  throughout this paper. If not every grain touched is developed but a fraction  $P$  of them, Jdanov's formula can be modified as follows:

$$\Delta = 4.2 d/cP = \Delta_0/P,$$

where  $\Delta_0$  is the expression written above. The variables  $d$ ,  $c$ , and  $P$  are not generally independent, for they are related through the process of emulsion making. The concentration  $c$  is usually determined by the quantities of chemicals used; how to effect changes in  $d$  and  $P$  is a complicated physico-chemical problem.\* While  $c$  is nearly 1 gm. of silver bromide per cc. of the usual emulsions, it may be increased to a maximum of 6.5 gm. per cc., which is the density of pure silver bromide. If  $P$  is less than unity, sensitizing the grains may be useful.

\* Very small values of  $d$ , about 0.03  $\mu$ , are found in Lippmann emulsions. Unsuccessful attempts have been made by Blau and Wambacher (4) and by Jdanov to show  $\alpha$ -ray tracks in these emulsions. Their failure may be attributed to the values of  $c$  and  $P$  being too small under their conditions.

## 5 *Brief Survey of the Present Work*

After making numerous tests, emulsions have been prepared that have very small grain size and grain spacing. In these the tracks of ionizing particles often look like narrow and continuous threads, except under high resolving power when the individual grains can be seen. The improvements effected may be judged from Figs. 13 to 34. Differential sensitivity has been attained.  $\beta$ - and  $\gamma$ -rays fog these plates quite slowly. In a few instances it is believed that the last few centimetres of the tracks of electrons have been seen.

Following a brief account of the microscopic technique, the preliminary work on previous kinds of emulsions will first be reviewed. Second, the making, processing, and application of new emulsions will be described. Third, some nuclear physical experiments using the emulsion technique will be described. Fourth, the actions of certain sensitizing and desensitizing substances will be included. Fifth, a quantitative theory that correlates grain spacing and several other factors will be put forward.

### Microscopic Technique

The best optical conditions are necessary to bring out the details in the finest grained emulsions. A Spencer binocular mono-objective microscope with inclined eyepieces was used. The illumination was provided by a Bausch and Lomb lantern, and the image of its diaphragm was accurately focused in the plane being examined by a 1.4 N.A. condenser. Oil immersion was used between the condenser and the plate and between the plate and the objective. The latter was a 1.3 N.A. 90 $\times$  Apochromat. The eyepieces were usually 12.5 $\times$  compensated, and the over-all magnification 1125. A scale divided into hundredths or into two-hundredths of a millimetre was used. The resolving power in white light should be approximately

$$1.22 \lambda / 2 \text{ N.A.} = 1.22 \times 0.55 \mu / 2.6 = 0.26 \mu.$$

In practice it was possible to detect the presence of as many as three or four grains per micron and to estimate the diameter of a grain down to 0.1  $\mu$ .

Photomicrographs were taken in white light, which showed a resolving power not as good as that calculated above (Figs. 13A and 26 to 34). Photographs were also taken with a blue filter, consisting of a liquid cell filled with a solution of copper nitrate and malachite green, which transmits a band around 0.48  $\mu$ . With this filter the theoretical resolving power of 0.24  $\mu$  was actually attained, judging from the enlargements (Figs. 13B to 25).

### Preliminary Work

#### 1. *Eastman $\alpha$*

The tracks of  $\alpha$ -rays were obtained in Eastman  $\alpha$ -emulsions (Fig. 18) by soaking the plates in dilute uranium or thorium nitrate, drying, and keeping them for some time before development. The emulsions were developed for 20 min. in Eastman's D-19 diluted 1 : 20. The mean grain spacing was

found to be  $1.6 \mu$  along the whole range of the  $\alpha$ -rays from thorium C'. The stopping power of the emulsion from measurements on these tracks was 1415 times that of air at  $15^\circ \text{C}$ . and a pressure of 1 atm.

Long proton tracks (Figs. 13A, 13B, 34) were obtained by irradiating plates with neutrons from a mixed polonium and beryllium source. The grain spacing  $\Delta$ , which varied from  $2.2 \mu$  to  $10 \mu$ , is plotted in Fig. 1A against the residual range of the proton in Figs. 13A and 13B.

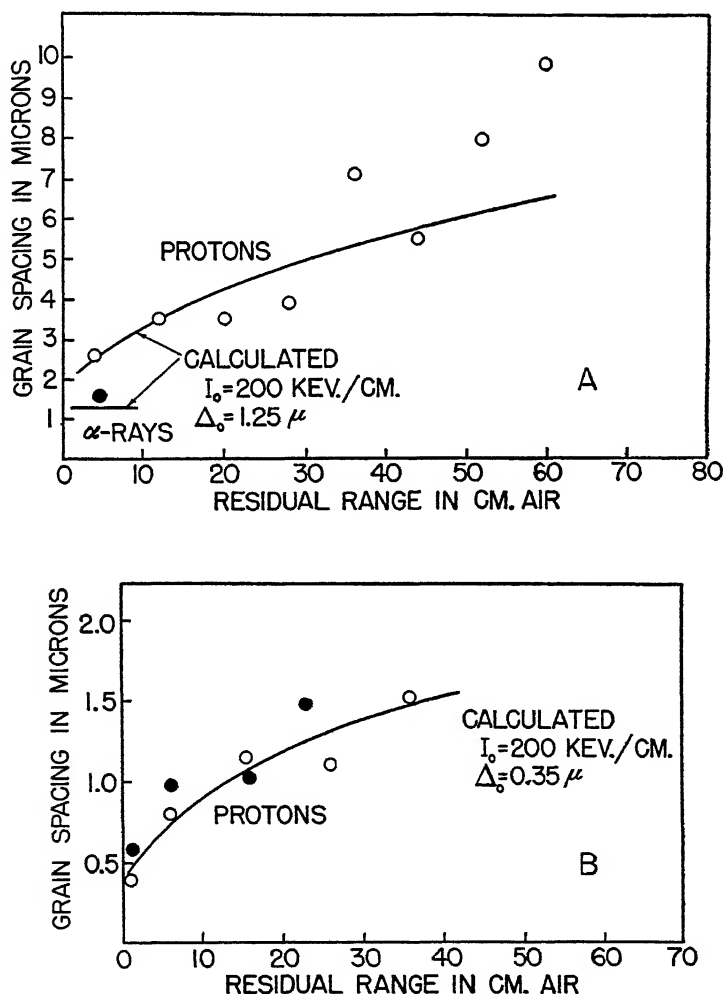


FIG. 1. A. Measured grain spacing in microns is plotted against the residual range in centimetres of air for tracks of protons and  $\alpha$ -rays in Eastman  $\alpha$ -emulsion. Concentration  $c = 1 \text{ gm. silver bromide per cc. emulsion}$ , and grain diameter  $d = 0.6 \mu$ . The curves were calculated from the proposed theory, using the indicated values of the parameters.

B. Measured grain spacing in microns is plotted against the residual range in centimetres of air for tracks of protons in Eastman  $\alpha$ -emulsion concentrated by centrifuging. Concentration  $c = 4 \text{ gm. silver bromide per cc. emulsion}$ , and grain diameter  $d = 0.6 \mu$ . The curve was calculated with one parameter the same as in A, the other parameter different.

The composition of the Eastman  $\alpha$ -emulsions was obtained as follows. The thickness of the gelatine layer on a plate was measured with the microscope. A plate was weighed, fixed, washed, dried, and weighed again. The loss in weight represents the silver bromide originally present. The weight of gelatine was obtained after the plate had been scrubbed free of gelatine and weighed again. The results were as follows:

Silver bromide: 40% of emulsion by weight

$c = 1.04$  gm. silver bromide per cc. emulsion

Density of emulsion = 9 mgm. per  $\text{cm}^2$ , 2.6 gm. per cc.

Thickness of emulsion =  $34.5 \mu$

Density of gelatine = 1.6 gm. per cc.

The developed grains were seen to be quite uniform and had a mean diameter of  $0.6 \mu$ . From these data the minimum spacing should be

$$\Delta_0 = 4.2 \times 0.6 \mu / 1.04 = 2.4 \mu,$$

which does not agree with the spacing of  $1.6 \mu$  found in  $\alpha$ -ray tracks. It seems unlikely that the composition was 50% in error, and a more likely explanation is that the mean grain diameter was only  $0.4 \mu$  before development.

## 2. Eastman $\alpha$ Centrifuged

In order to increase the concentration of silver bromide in an emulsion, centrifuging was tried. It was convenient to start with Eastman  $\alpha$ -plates and to remove the emulsion by soaking in water. When the melted emulsion was centrifuged, the silver bromide grains accumulated at the bottom of the tube, leaving a clear liquid above. The plug of silver bromide was melted, coated on a glass plate, and allowed to set and dry before use. The concentration was approximately 93% silver bromide or  $c = 5$  gm. silver bromide per cc. emulsion, which may be compared with  $c = 1$  gm. per cc. in the original emulsion. If the size and sensitivity of the grains have not been changed in the operations, the spacing should be one-fifth of its original value. The measured spacings along proton tracks, plotted in Figs. 1A and 1B, are approximately in this ratio. (Development was for 5 to 10 min. in D-19 at full strength.)

The effect of centrifuging on the appearance of proton tracks may be seen in Figs. 13B, 13C, 33, and 34. These show the proton tracks in Eastman  $\alpha$  and in centrifuged Eastman  $\alpha$ -emulsion. In the latter case the grains are practically contiguous. Fog was tolerable in the instance reproduced, although in other cases it was bad. Development spreads from isolated fog grains as well as from the grains in the tracks, thus producing black clumps. Although careful control of conditions might have led to consistently good results, it appeared preferable to avoid centrifuging and to try finer grained material.

## 3. Eastman Type V-O

Spectroscopic plates Type V are recommended for minimum graininess. Development was for 5 to 10 min. in D-19 at full strength. The tracks of

$\alpha$ -rays were seen in these plates with a grain size of  $0.8 \mu$  and a spacing of  $2.1 \mu$ . As these values are very high, no further work was done.

#### 4. Eastman Type 548

Eastman Type 548 emulsions are extremely fine grained (grain diameter not greater than  $0.1 \mu$ ) and have been recommended for making graticules. By the procedure described for Eastman  $\alpha$ -plates, it was found that the thickness of emulsion Type 548 is  $20 \mu$  and the composition about the same:  $c = 1.04$  gm. per cc. or 40% silver bromide. If  $d$  is taken to be  $0.1 \mu$ ,  $\Delta_0 = 0.4 \mu$ .

Some plates were irradiated with neutrons and then strongly developed for 15 min. in Eastman developer D-82. Proton tracks were occasionally seen, but they were weak and very difficult to find in the strong fog. Only a small fraction of the proton tracks present could be found. Figs. 2 and 3 show the grain spacing along the tracks, varying from  $0.9$  to  $1.6 \mu$ . The grain size after development was  $0.2 \mu$ .

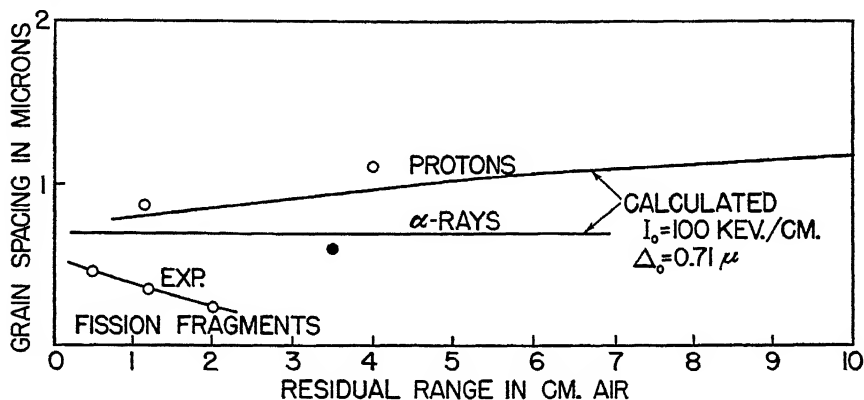


FIG. 2. Measured grain spacing in microns is plotted against the residual range in centimetres of air for tracks of protons,  $\alpha$ -rays, and fission fragments in Eastman 548 emulsion. Concentration  $c = 1$  gm. silver bromide per cc. emulsion, and grain diameter  $d \leq 0.1 \mu$ . The curves for protons and  $\alpha$ -rays were calculated with the common pair of parameters shown.

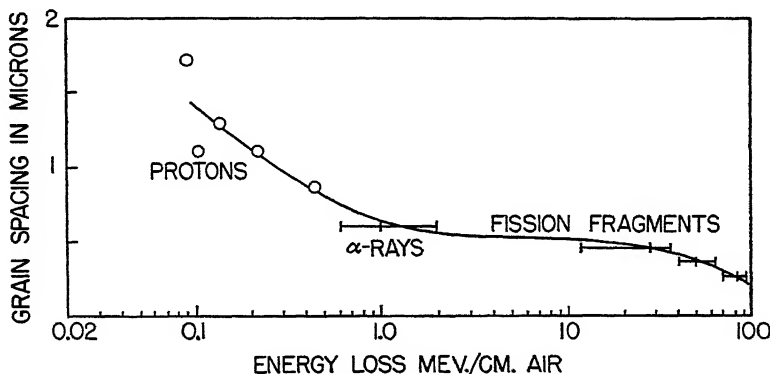


FIG. 3. Measured grain spacing in microns is plotted against the specific energy loss in million electron volts per centimetre of air on a logarithmic scale, for tracks of protons,  $\alpha$ -rays, and fission fragments in Eastman 548 emulsion.

The tracks of  $\alpha$ -rays could be brought out with a five minute development in D-19, which is insufficient to bring out proton tracks. The grain spacing along the  $\alpha$ -ray tracks was  $0.6 \mu$  (Figs. 2, 3), and the size of the grain increased with increasing development. The stopping power of the emulsion for the  $\alpha$ -rays of thorium C' was 1415 times that of air. The standard deviation on the range of these  $\alpha$ -rays was found to be 1.8%, while it was 2.5% on the shorter tracks of the  $\alpha$ -rays of thorium C.

Reasonably good tracks of fission fragments were obtained in this emulsion (Fig. 26); a more complete description of this work will be given later.

### 5. Emulsions Made by Jdanov

The first series of emulsions to be made from the separate constituents followed the lines indicated by Jdanov (10), whose results, reproduced in Table I, will be discussed in this section. Two solutions are made up; Solution I

TABLE I  
EMULSIONS MADE BY JDANOV (10)

#### EMULSION E<sub>1</sub>

Solution I: 4 gm. potassium bromide, 3.5 gm. gelatine, 52.5 cc. water.

Solution II: 5 gm. silver nitrate, 1.75 gm. gelatine, 52.5 cc. water.

Add Solution II to Solution I at 60° C.

Emulsions E<sub>2</sub>, E<sub>3</sub>, and E<sub>4</sub> are made from similar recipes.

#### EMULSION L

Solution I: 5 gm. potassium bromide, 20 gm. gelatine, 300 cc. water.

Solution II: 6 gm. silver nitrate, 10 gm. gelatine, 300 cc. water.

Add Solution II to Solution I at 39° C.

Emulsions L<sub>1</sub>, L<sub>2</sub>, L<sub>3</sub>, L<sub>4</sub>, and L<sub>5</sub> are mixed at other temperatures.

Type	Temp., <i>t</i> , ° C.	<i>d</i> , $\mu$	Concentration of AgBr in emulsion <sup>1</sup>			$\Delta_0$ , $\mu$	$\alpha$ -Rays $\Delta$ , $\mu$	Protons $\Delta$ , $\mu$
			<i>c</i> , gm./cc.	% vol.	% wt.			
E <sub>1</sub>	60	1	1.4	22	51	3.0	2.7	Weak
E <sub>2</sub>	60	0.4	0.7	11	33	2.2	2.2	—
E <sub>3</sub>	60	0.8	2.5	39	72	1.2	1.5	2-4 2 <sup>2</sup>
E <sub>4</sub>	60	1.2	3.7	57	84	1.2	1.4	None <sup>2</sup>
L	39	0.03				0.43	None	—
L <sub>1</sub>	40	—	0.34	5.2	18	—	Very weak	
L <sub>2</sub>	45	—					Weak	
L <sub>3</sub>	50	—	(0.30) <sup>3</sup>	(4.7) <sup>3</sup>	(16) <sup>3</sup>	—	Moderate	
L <sub>4</sub>	55	—					Clear	
L <sub>5</sub>	60	0.2- 0.4				4.3	~4.3 clear	—

<sup>1</sup> Washed to remove soluble salts and dried.

<sup>2</sup> No proton tracks were observed after an 8 to 10 min. treatment with pinakryptol yellow in concentrations 1/5000 to 1/2000, and a 40 to 50 min. washing in running water.

<sup>3</sup> Calculated for the emulsions dried but not washed.

contains potassium bromide and gelatine, and Solution II contains silver nitrate and gelatine. Solution II is added to Solution I while stirring proceeds. Concentrations and excess of bromide over silver vary from one emulsion to another, as well as the temperature  $t$  at which mixing is done. Emulsion E<sub>3</sub>, used by Jdanov and co-workers, was recommended for proton tracks. The L-series of emulsions is interesting for the diameter  $d$  of the grains is varied from 0.03 to 0.3  $\mu$  by changing the temperature  $t$  while the concentration  $c$  is held constant at 0.3 gm. silver bromide per cc. emulsion. In this case

$$\Delta = \frac{4}{0.3} \frac{2}{\bar{P}} \frac{d}{P}.$$

The probability  $P$  of development is nearly unity when  $d = 0.3 \mu$ , and must be very small when  $d = 0.03 \mu$  for then no tracks were seen (Table I).

#### 6. Extension of Jdanov's Work

The writer followed Jdanov's formula for the L-emulsions and confirmed his results. In addition to repeating the work on these emulsions, the writer made exhaustive tests on the possibilities of formulas of the same type, which are labelled X1, X2, X3, X4, and X10 and which contain twice, three times, etc., respectively, the amounts of salts in the two solutions used for X1. The emulsions were poured on glass plates (7 cc. on a plate 8 by 11 cm.) and allowed to set. While X1 and X2 dried satisfactorily, the more concentrated ones containing too much soluble salts had to be washed and dried before use. If the temperature is low during the mixing of the two solutions or the concentrations of salts high, the gelatine may partially set during the reaction and a dirty emulsion results. Table II contains the information obtained from these experiments. It is seen that the average grain size increases as the temperature at the time of mixing is raised and also as the concentration of silver bromide is increased.

A modified series of X-emulsions was prepared in which about 5% of the silver was present as the iodide. (Such a proportion is often found in commercial light-sensitive emulsions.) The only noticeable change was a slight reduction in the size of grain.

The emulsions of the X-series were tested for recording the tracks of  $\alpha$ -rays and fission fragments. A uranium disk was placed on the surface of the plate and irradiated with slow neutrons. The plate was developed for five minutes in D-19. In the case of  $\alpha$ -ray tracks in X2 it is seen (Table II) that the grain spacing  $\Delta$  decreases at first and then increases as the temperature  $t$  at the time of mixing is raised. The tracks of  $\alpha$ -rays and fission fragments can be distinguished when  $\Delta$  has nearly its minimum value; for larger grain sizes all tracks are alike, while for still smaller sizes, the tracks are invisible. Fig. 4 shows these results graphically; in plotting it plausible assumptions have been made on grain size, as exact measurements are not feasible below 0.2  $\mu$ .

If a comparison is made between X2 and Eastman 548, which have about the same values of  $c$  and  $d$ , the latter is better as regards differentiation of

TABLE II  
EXTENSION OF JDANOV'S WORK  
EMULSION XI

Solution I: 0.5 gm. potassium bromide, 2 gm. gelatine, 30 cc. water.

Solution II: 0.6 gm. silver nitrate, 1 gm. gelatine, 30 cc. water.

Add Solution II to Solution I while stirring continuously.

Emulsions X2, X3, X4 and X10 are made with 2, 3, 4, and 10 times amounts of salts used for Emulsion X1.

$d$ ,  $\Delta$  and  $\Delta_0$  are expressed in microns.

Emulsion	X1				X2				X3				X4				X10			
Gm. AgBr/gm. emulsion, %	18.1				30.7				39.9				46.9				69.0			
Cc. AgBr/cc. emulsion, %	5.15				9.8				14.0				17.8				35.2			
Gm. AgBr/cc. emulsion, c	0.335				0.637				0.912				1.16				2.29			
Temp., °C.	$d$	$\Delta_0$	$\Delta$	$\Delta_f$	$d$	$\Delta_0$	$\Delta$	$\Delta_f$	$d$	$\Delta_0$	$\Delta$	$\Delta_f$	$d$	$\Delta_0$	$\Delta$	$\Delta_f$	$d$	$\Delta_0$	$\Delta$	$\Delta_f$
20, 25	—	—	—	—	$\leq 0.2$ $d$	$\leq 1.3$	$i$	$i$	—	—	—	—	$\leq 0.2$ $d$	$\leq 1.1$	0.9	—	—	—	—	—
30	—	—	—	—	$\leq 0.2$	$\leq 1.3$	$w$	$w$	—	—	—	—	—	—	—	—	$0.3$ $d$	0.6	0.8	—
35	—	—	—	—	$\leq 0.2$	$\leq 1.3$	$w$	$w$	—	—	—	—	—	—	—	—	$0.3$ $d$	0.6	0.8	—
40	$\leq 0.2$ $c$	$\leq 2.5$	$i$	$i$	$\leq 0.2$	$\leq 1.3$	0.8	0.5	—	—	—	—	0.3	1.1	1	—	$0.3$ $d$	0.6	0.8	—
45	—	—	—	—	$\leq 0.2$	$\leq 1.3$	1.0	$i$	—	—	—	—	—	—	—	—	$0.4$ $d$	0.8	1.0	—
50	$\leq 0.2$ $c$	$\leq 3.8$	$> 5$	$i$	—	—	—	—	0.2	0.9	1.6	$i$	—	—	—	—	—	—	—	—
65	—	—	—	—	0.2	1.3	1.3	—	—	—	—	—	0.5	1.8	1.1	—	—	—	—	—
80	$0.3$ $c$	3.8	5	—	—	—	—	—	—	—	—	—	—	—	—	—	—	—	—	—

Code:  $\alpha$  =  $\alpha$ -ray tracks,  $f$  = fission fragment tracks,

$i$  = invisible tracks,  $d$  = dirty emulsion,

$w$  = weak tracks,  $c$  = clear tracks.

track, spacing of grains, and amount of fog. It is possible that the differences are due to the rather large range of grain sizes in X2.

Some tests were made on X2- and X4-emulsions centrifuged at about 50° C. Grains smaller than 0.2  $\mu$  in diameter did not settle completely. The mass formed at the bottom of the tube of the centrifuge, after being washed and

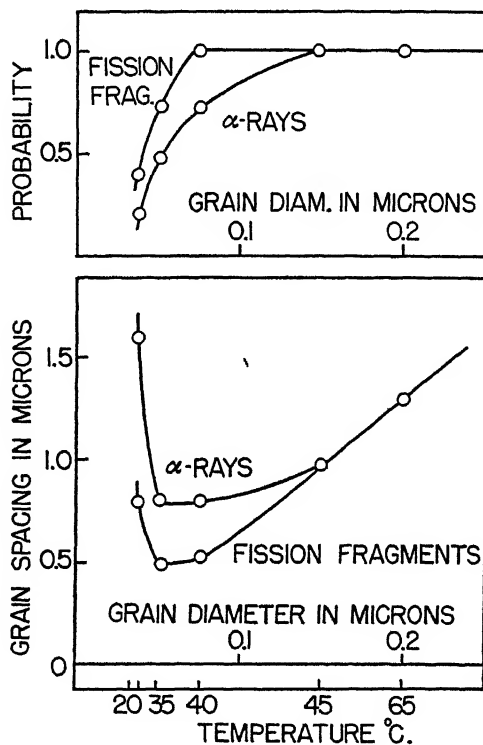


FIG. 4. Upper. Probability of development is plotted against the grain diameter in microns for tracks of  $\alpha$ -rays and fission fragments in Emulsion X2

Lower. Measured grain spacing in microns is plotted against the grain diameter in microns for tracks of  $\alpha$ -rays and fission fragments in Emulsion X2.

The grain diameter is varied by changing the temperature at which the emulsion is made. The curves are not accurate, but their general behaviour is significant.

dried, had the following typical composition: 93% silver bromide by weight, 76.5% silver bromide by volume, and  $c = 5.17$  gm. silver bromide per cc. emulsion. This emulsion does not melt or dissolve easily, hence it is difficult to spread it evenly on a plate.

In one case an X4-emulsion made at 40° C., in which  $d$  was 0.2  $\mu$  and  $\Delta$  was 0.8  $\mu$  in the tracks of  $\alpha$ -rays, was centrifuged, and in the concentrated emulsion  $d$  was 0.3  $\mu$  and  $\Delta$  was 0.4  $\mu$ . The grains were practically contiguous in the track. Emulsions having the smaller grain sizes were chosen from the series X2 and X4 and were centrifuged. These showed improved tracks of fission fragments (Figs. 27A and 27B), which were clearer and better

defined than those seen in Eastman 548 emulsion. (The stopping power was about 1800 times that of air.)

It should be noted that the vertical dip of tracks is modified by the shrinkage of these concentrated emulsions that occurs in processing. The thickness of the gelatine layer is reduced to  $\frac{1}{2}$  to  $\frac{1}{4}$  of its original value in fixing.

In agreement with the tests on Eastman  $\alpha$ -emulsions that had been concentrated by centrifuging, spreading development often occurred in the centrifuged X-emulsions if the grain size was greater than  $0.2 \mu$ . Sometimes the development spreads from the track to large numbers of surrounding grains, which then form a huge black object in the field (Fig. 31). There may also be a broadening of the track, which happens preferentially near the end where the ionizing power of the  $\alpha$ -ray is great, producing a club-like appearance. It is well known that grains clumped together in much coarser grained emulsions have a tendency to develop as a unit (13, p. 832).

### New Emulsions

If the solutions mixed to form silver bromide grains in gelatine are concentrated, the first grains are large and grow by Ostwald ripening, because the concentrated bromide solution favours the formation and growth of large crystals and the last grains formed are small. Since very small and uniform grains are desired in conjunction with a high concentration, the precipitation of silver bromide should proceed between *dilute* reagents from beginning to end. The procedure used was suggested by a remark by Carroll (7); it has also been described for making positive emulsions by Baker (1, p. 100), and is similar in principle to the one followed by Sheppard, Lambert, and Swinchart (23) to obtain dilute silver bromide sols in the absence of gelatine.

The new emulsions were prepared from three solutions as follows. Equivalent volumes of silver (*A*) and bromide (*B*) solutions are run simultaneously and at equal rates into a solution of gelatine (*C*), which is stirred continuously and as vigorously as possible without excessive foam production. The details for six new emulsions are given in Table III. The rates of flow are controlled so that there is a small excess of soluble bromide over silver; for example Solution *B* should be 0.5 to 1 cc. ahead of *A*, although an occasional slight excess of *A* over *B* is not important. For the quantities shown in Table III, it takes about 30 min. to add *A* and *B* to *C*. The rates of flow are controlled by drawn capillaries of adjusted length below the stopcocks on the burettes containing *A* and *B* or preferably by stainless-steel needle-valves. Solution *C* is kept in a tray of thermostatically controlled water usually at  $40^{\circ}\text{C}$ .

The emulsion is poured into a flat tray, 12 by 18 in., cooled in ice water to set. It is then washed with running cold water for six to eight hours to remove the large amount of potassium nitrate present. The emulsion is removed, melted, and coated on a glass slide (1 cc. on 2.5 by 7.5 cm.) and left to set. (Such a layer measures about  $40 \mu$  at the centre when dry). The relative humidity of the air should be 60 to 80%, otherwise the emulsion

TABLE III  
NEW EMULSIONS

Solution A: 0.6 gm. silver nitrate per cc.  
 Solution B: 0.42 gm. potassium bromide per cc.

Formula	Solution			% AgBr	gm. AgBr/cc.	$d$ , $\mu$
	A, cc.	B, cc.	C			
I	30	30.5	75 cc. H <sub>2</sub> O 4.5 gm. gel.	81.6	3.34	$\leq 0.1$
II	30	30.5	50 cc. H <sub>2</sub> O <sup>1</sup> 4.5 gm. gel. 25 cc. alcohol	81.6	3.34	$\leq 0.1$
III <sup>2</sup>	30	30.5	75 cc. H <sub>2</sub> O 4.5 gm. gel.	81.6	3.34	0.1-0.2
IV	30	30.5	25 cc. H <sub>2</sub> O 1.5 gm. gel.	93	5.17	0.1-0.15
V	30	30.5	25 cc. H <sub>2</sub> O 0.75 gm. gel.	96.4	5.6	$\sim 0.2$
VI <sup>3</sup>	30	30.5	I or II	—	—	—

<sup>1</sup> Melt gelatine in water, then add alcohol while solution is stirred.

<sup>2</sup> Temperature control was different from that in I and II.

<sup>3</sup> Chlorine or iodine partly or wholly replacing bromine in Solution B.

is likely to peel off its glass support. This tendency to peel off, which is due to the high concentration of silver bromide, is reduced if the layer is thinner and of smaller area. As these emulsions are not very sensitive to light, all operations listed above can be performed in red or amber light.

Digesting occurs on keeping the emulsions; the sensitivity rises in the course of a few days whether the emulsion be in the form of a jelly or dried on plates. Since fog increases with time it is advisable to keep the plates in an ice-box.

Excellent tracks were obtained in Emulsions I and II: Formula II is most highly recommended. The use of denatured alcohol was suggested by Wall's statement that it prevents coarse grain formation in emulsions containing ammonia (24). Although the present emulsions contain no ammonia, alcohol does greatly reduce fog and clump formation. Very reproducible results were obtained.

Unlike Emulsion I, II after washing occasionally does not melt when heated. Syneresis occurs, the emulsion contracting by one-tenth to one-fifth of its volume and giving off a liquid that contains little or no gelatine. If the supernatant liquid is expelled, the remaining gel may be melted by heating and stirring.

Emulsion III is the same as I except for temperature control. Several tests were made in which Solution C was brought up to 50° C., then Solutions A and B were added while the temperature fell to 20° to 30° C. Froth appeared or the gelatine partially set below 30° C., and the resulting emulsion was dirty. Sometimes excellent proton tracks were obtained after weak development, and still denser tracks were obtained if the emulsion was concentrated by centrifuging (Fig. 32A, B, C). Even by mixing the solutions at a chosen temperature, consistently good emulsions of this character could not be produced.

Emulsion IV contains 93% silver bromide, which is the same as that obtained by centrifuging III. When heated after washing it suffers syneresis, the volume contracting to  $\frac{1}{3}$ ; and when coated on glass it has a tendency to peel off. Good proton tracks have been recorded in IV.

Emulsion V suffers syneresis during the mixing of Solutions A and B into C. Since it does not adhere to glass very well it is not satisfactory.

Emulsion VI was made with iodine or chlorine partly or wholly replacing the bromine. Pure iodide emulsions are insensitive even to fission tracks. Pure chloride emulsions have occasionally shown proton tracks, but they fog too easily. If 25% of the bromine atoms are replaced by iodine, fission tracks can be recorded, but the emulsion is insensitive to other particles. If a few per cent of the bromine atoms are replaced by iodine or chlorine or both, no worthwhile improvement in sensitivity is found.

Development was for 5 to 15 min. in Eastman's D-19. A still stronger development was occasionally used 5, 10, or even 15 min. in Eastman's D-82. Too strong a development brings out excessive fog; on the other hand, if it is too weak, only fission tracks appear. Fixing may be lengthy if the coating is thick, stirring of the fixing bath is then helpful.

### Nuclear Physics Experiments with Emulsions

Some of the nuclear physics experiments were carried out in preliminary work and have been described in part above. Most of the best tracks were recorded in the new emulsions. Tables IV and V show some collected results.

#### 1. $\alpha$ -Rays of Uranium and Thorium C'

Fig. 17 shows the track of an  $\alpha$ -ray from uranium in the new Emulsion II. Standard deviations on the range and energy have been determined by measuring about 60 tracks in each case (see Table V). The two  $\alpha$ -ray groups of  $U^{238}$  and  $U^{234}$ , which were recorded simultaneously, are easily distinguished. For the  $\alpha$ -rays of thorium C' the standard deviation is 2% on the range or 1.3% on the energy. In Eastman 548, which contains less silver bromide, the corresponding values are 1.8% and 1.1%; but the visibility of the tracks is not as good as in Emulsion II. The main cause of these deviations is not the grain spacing but straggling of the range, which is known to increase with atomic weight. Gelatine shift may be a contributing cause of the deviations in range.

## 2. Protons from $N^{14} (n, p) C^{14}$

As gelatine contains 5 to 15% nitrogen, emulsions irradiated with slow neutrons show numerous short proton tracks from the reaction  $N^{14} (n, p) C^{14}$ . Figs. 15A, B, C are examples obtained with Emulsion II. The standard deviations are small for such short tracks, 5.2% on the range (1.06 cm.) and 3.5% on the energy (0.62 Mev. (12)). The deviations are nearly four times as great in Eastman  $\alpha$ .

## 3. Proton Recoils from $D^2 (d, n) He^3$ Neutrons

Proton recoil tracks were recorded in emulsions placed near the target of the Ottawa high tension set. The neutrons from the reaction  $D^2 (d, n) He^3$  that are emitted at an angle of 110 degrees from the beam of deuterons are monokinetic (2.4 Mev.). The proton recoils in the forward direction have therefore a small energy spread. The standard deviations were 3.35% on the energy and 5.4% on the range in the new emulsions.

## 4. Proton Recoils from $Po-\alpha-Be$ Neutrons

A large number of proton tracks, each equivalent to several cm. of air, have been seen. Figs. 13D, E show the beginning and end of a proton track having a range of 60 cm. in air (Emulsion II). The end of a proton track is usually defined within  $\frac{1}{2}$  mm. of air; the beginning of tracks 60 to 100 cm. long is usually defined within 1 to 2 mm. of air and sometimes within  $\frac{1}{2}$  mm. as in the example shown.

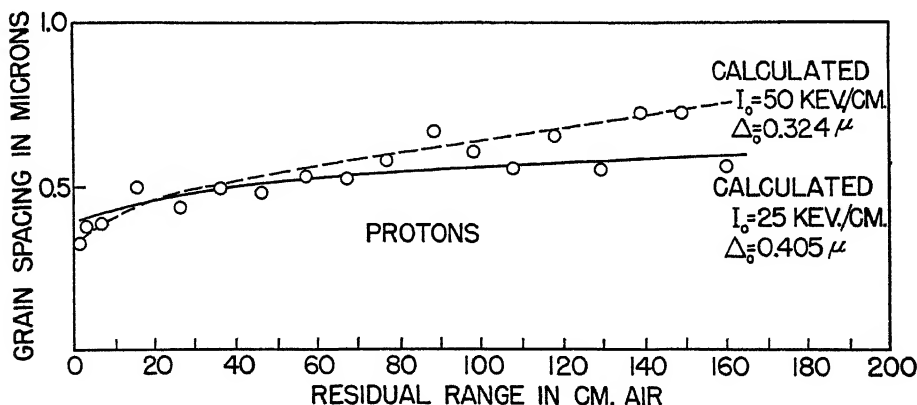


FIG. 5. Measured grain spacing in microns is plotted against the residual range in cm. air for tracks of protons in Emulsion II. Concentration  $c = 3.3$  gm. silver bromide per cc. emulsion, grain size  $d \leq 0.1 \mu$ . The two curves were calculated from the proposed theory, using the parameters shown. These indicate the range of permissible choice.

The advantage of the new emulsions is more marked on the short ranges. Reasonably good measurements are possible at 3 mm. of air, which corresponds to an energy of 200 kev. for protons and 400 kev. for  $\alpha$ -particles. Grain spacing, grain size, and resolving power are the limiting factors. Grain spacing along proton tracks is plotted in Fig. 5.

The directions of proton tracks can now be ascertained very accurately. Deviations are visible in Figs. 32*A*, *B*, and *C*, especially near the end of the range. Four forks representing proton-proton collisions have been seen. Two of these nearly right-angled forks are shown in Figs. 28 and 29.

#### 5. *Particles from the Reaction $Li^6(n, \alpha)H^3$*

Fig. 16 shows the tracks of an  $\alpha$ -ray and a triton, obtained by irradiating Emulsion II containing lithium chloride with slow neutrons. This is a good example of differential sensitivity.

#### 6. *Fission Tracks*

The tracks of fission fragments have been recorded in photographic emulsions by Myssowsky and Jdanov (14), Perfilov (17), and Borst and Floyd (6).

The writer has obtained numerous examples of the tracks of fission fragments in Eastman 548 and the new emulsions. Two variations of the technique have been employed. In the first method a disk of uranium metal was laid upon the emulsion, the two wrapped in black paper, and exposed to neutrons. In the early work the irradiation was performed for several hours in a paraffin box containing a source of neutrons consisting of 1 gm. of radium mixed with beryllium. The plate was shielded from the direct action of the  $\gamma$ -rays by 5 cm. of lead. Eastman 548 plates were processed in D-19 for five minutes. In nearly every field of view a few thick tracks were visible, which started at the surface and dipped into the emulsion. Their appearance is characteristic of fission fragments, as the tracks become thinner towards the end of the range, in agreement with the known ionizing properties. The effect of the  $\alpha$ -rays was to form a netted background of light fog. The fog caused by  $\gamma$ -rays was tolerable until the plate had received a few hundred roentgens. The longest fission tracks recorded were about  $17\ \mu$  or 2.4 cm. of air, which may be compared with 2.85 cm. obtained in a cloud chamber (5). The mean spacing  $\Delta$  in the Eastman 548 emulsion was about  $0.4\ \mu$ .

The same procedure was used with Emulsions X2 or X4 centrifuged. The fission tracks stand out prominently among the  $\alpha$ -ray tracks and are much clearer than in Eastman 548 (Figs. 27*A*, *B*), as they appear like unbroken lines.

In the second method the complete tracks of pairs of fission fragments were recorded. Plates were soaked in uranium nitrate solution for five minutes, dried, and irradiated with slow neutrons from a chain reacting pile. The best concentration of uranium nitrate is 1/16%  $UO(NO_3)_2 \cdot 6H_2O$ . A smaller concentration shows too few tracks, while a larger concentration desensitizes the emulsion and the tracks contain fewer grains. Several complete tracks were measured. Their lengths show a distribution with a standard deviation of 5% from the mean value. This deviation is due mostly to the diverse mass and energy of the fragments, and not as in the cases of  $\alpha$ -rays and protons to the ordinary straggling of ranges.

Fig. 26 shows the complete tracks of pairs of fission fragments in Eastman 548 emulsion, while Figs. 19 to 25 show complete tracks in the new emulsions.

It will be noted that the fission tracks stand out prominently amidst the tracks of  $\alpha$ -rays and protons; an  $\alpha$ -ray track is visible in Fig. 19. Figs. 17 and 19 show the tracks of  $\alpha$ -rays and fission fragments in the same emulsion. The variation of the specific ionization from the centre of the pair of fission fragment tracks, where fission occurred, to the ends is clearly shown by the varying width. The point of fission cannot, however, be located very exactly by visual inspection. In Eastman 548 the grain spacing varied between  $0.6 \mu$  and  $0.2 \mu$  along the track. In the new emulsions the tracks are so well marked and dense that the single grains are not always recognizable and that grain spacing cannot be determined with its usual meaning.

Cloud chamber pictures of fission tracks, such as those of Bøggild, Brostrøm, and Lauritsen (5), show clearly numerous deviations and short side branches due to projected nuclei. Although the tracks in emulsions do not show as much of the detail, there are many examples of deviations and side branches, which may be due to hydrogen, carbon, nitrogen, oxygen, bromine, and silver nuclei (Figs 19 to 24).

Figs. 25, A to F, show a complete pattern of tracks, which are not all contained in one plane. The three branches have comparable specific ionizations, possibly nearly the same mass, and not very different ranges (1 cm. for one track and 1.5 to 2.0 cm. for the others). The angles suggest conservation of momentum between three particles of about equal mass. If triple fission occurred the appearance could be like this. However, one of the branches may well be a silver or bromine nucleus knocked on by one of the pair of fragments, near the point of common origin.

The fission of thorium by fast neutrons was also shown by the emulsion technique. Thorium metal was laid on Eastman 548 emulsion, and irradiated for several days with a strong Po- $\alpha$ -Be source of neutrons. Dense tracks dipping into the emulsion, similar to those obtained from uranium, were seen after development.

## 7. Electrons

Whenever a very sensitive emulsion had been obtained, where grain spacing was very small at the beginning of long proton tracks, some faint complicated

TABLE IV  
COMPARISON OF EMULSIONS

	New emulsions	Eastman $\alpha$ centrifuged	Eastman $\alpha$	Iford halftone
% AgBr, wt	81.6	80-90	40	~ 40
Conc. c AgBr, gm/cc	3.3	3-4	1.0	~ 1
Stopping power (rel. to air)	1600	1800	1400	~ 1400
Developed grain diam., $\mu$	0.1-0.3	0.6	0.6	~ 0.5
$\Delta$ , cm air, end of proton track	0.05	0.1	0.3	—
$\Delta$ , cm of air, beginning 6 Mev. proton track	0.05-0.1	0.3	1	—

TABLE V  
COMPARISON OF TRACKS

$\sigma_1$  = standard deviation on range in centimetres air.

$\sigma_2$  = standard deviation on energy in Mev

Particles	New emulsions		Eastman $\alpha$	Ilford half-tone	Cloud chamber
	$\sigma_1$	$\sigma_2$	$\sigma_2$	$\sigma_2$	$\sigma_2$
UI $\alpha$ , 2.6 cm, 4.09 Mev	0.065 2.5%	0.075 1.8%	0.24 5-6%	0.25 (18) —	— 0.4-0.6%
UII $\alpha$ , 3.2 cm, 4.7 Mev	0.09 2.8%	0.09 1.9%	— —	— —	— —
ThC' $\alpha$ , 8.5 cm, 8.78 Mev.	0.18 2%	0.16 1.3%	0.3 2.5%	— —	— —
Protons, 1.06 cm, 0.62 Mev	0.055 5.2%	0.02 3.5%	0.08 14%	— —	— —
Protons, 9.0 cm, 2.4 Mev	0.49 5.4%	0.08 3.35%	— —	0.15-0.2 6-8% (28)	— ~1.1%

tracks consistently appeared. These are attributed to electrons in the last one or two centimetres of their range, usually due to  $\gamma$ -rays or cosmic rays. One instance is reproduced in Fig 30, although it is realized that the loss of detail in reproduction will make the track difficult to see.

### Action of Various Chemicals on Emulsions

Emulsions to be tested were prepared according to Formula I or II, and sensitivity changes between treated and untreated parts of the same plate or of the same batch were estimated from the grain spacing in proton tracks. The treatment preceded irradiation.

#### 1. Dyes

In some cases the dye was added to the emulsion before coating and amounted to 0.05% dye when dry, in other cases the dried plate was soaked in a 1 or  $\frac{1}{2}$ % solution of the dye for three minutes

No effect on sensitivity was observed from the following:

- Acid fuchsin
- Alizarin red S. (leaves reddish masses)
- Bromo cresol green
- Bromothymol blue
- Chlorophenol red
- Chromotropic acid (leaves yellow crystals)
- Meta cresol purple
- Phenol red.

Methylene blue induces a strong fog. The following dyes, which are known desensitizers, decrease the size of the grains either in the tracks or in the fog, and reduce sensitivity to some extent:

Neutral red  
Rhodamine B  
Rhodamine 6G.

Two dyes that are known to act either as sensitizers or as desensitizers occasionally reduced and never increased sensitivity in the tests:

Pinakryptol green  
Pinakryptol yellow.

Three other dyes, the second of which is a known desensitizer, reduced sensitivity:

Diphenylamine blue  
Phenosafranine (marked effect)  
Tartrazine.

The following dyes improve sensitivity; they are listed in the approximate order of increasing effect observed:

Fluorescein  
Dichloro R fluorescein  
Chromotrope F 4B  
Erythrosin (tetraiodofluorescein)  
Methyl violet  
Rose bengal  
Eosin (tetrabromofluorescein).

Sensitizing occurred only when the emulsion was actually stained. A positive or negative effect on sensitivity appeared only with dyes that have known ability to be adsorbed on silver halides (Yoe and Sarver (29)). Eosin seems to be the most useful of these sensitizers. Fig. 6 was obtained from measurements on tracks in the two halves of the same plate, one untreated, one treated with eosin and dried. The best conditions are to bathe the plate

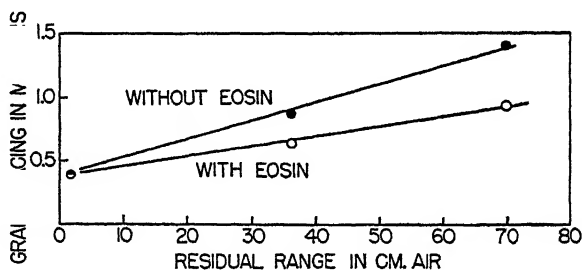


FIG. 6. The reduction in grain spacing, brought about by eosin treatment, is shown for proton tracks in Emulsion II. Concentration  $c = 3.3$  gm. silver bromide per cc. emulsion, grain size  $d \leq 0.1 \mu$ .

3 to 10 min. in a 1% solution of eosin. Prolonged treatment reduced the sensitivity, while a 0.001% solution has very little effect. It is not advantageous to add the dye to Solution C before making the emulsion.

## 2. Nitrogen Compounds

Since several nitrogen compounds produce complex salts with silver halides, some action is expected. Ammonia and triethanolamine are known to hypersensitize emulsions containing a colour sensitizing dye. Hypersensitizing may increase that part of the spectral sensitivity that is due to the action of the dye and even the part in the blue and violet region. Bathing plates already stained with various dyes in 1% ammonia for three minutes brought about an increase in sensitivity in all cases. The same effect of ammonia was also found for unstained emulsions.

The action of several organic compounds containing nitrogen was studied. Either 1% aqueous solutions or saturated solutions in weak alcohol were used. The treatment lasted three minutes. Nearly all substances having basic properties were active. The following decreased sensitivity and increased fog:

Diaminophenol hydrochloride (saturated)

Hydroxylamine hydrochloride.

Hydrazine induced strong fog and even blackened the undeveloped dried emulsion when it stood overnight, after soaking in a 1% solution. The following had little effect or decreased the sensitivity:

Diphenylamine (saturated solution)

Pyridine

Urea.

Ethylenediamine and hydroxyethylethylenediamine occasionally increase sensitivity, but they also increase grain size in the developed emulsion and may induce strong fog. The first is the more active. The following increased sensitivity without much increase in fog:

Acetonitrile

Aniline

Diethylamine

Diethylaniline

Hydroxyethylorthotoluidine (saturated solution)

$\alpha$ -Naphthylamine (saturated solution)

Triethanolamine

Trimethylamine.

Of these, the most promising are diethylamine, triethylamine, and triethanolamine, which are even more active than eosin and do not stain the emulsions. As the three act very much alike and the first two have objectionable smells, triethanolamine is most convenient to use. Prolonged treatment reduces both sensitivity and fog, which action is different from digesting. Plates treated with triethanolamine develop less fog on keeping than those treated with ammonia.

## 3. Hydrogen Peroxide

Hydrogen peroxide is a known intensifier of the latent image, if applied between irradiation and development (Nebllette (16)). This effect on proton

tracks was observed, following a one- to five-minute treatment in 0.01% hydrogen peroxide.

#### 4. *Chromic Acid*

(1) Chromic trioxide (2%) with sulphuric acid (1%) destroys sensitivity centres in five minutes according to Sheppard (22). Such a treatment was applied to Eastman  $\alpha$ , Eastman 548, and X4 plates, which were then washed thoroughly. The Eastman  $\alpha$ -plates showed  $\alpha$ -ray tracks with increased grain spacing and no proton tracks, while the other plates recorded  $\alpha$ -ray and fission tracks without much change. This is in general agreement with Wambacher (25), who found that chromic acid reduces sensitivity of certain emulsions to  $\alpha$ -rays.

These experiments should now be interpreted as showing the importance of active centres in promoting sensitivity to protons and to a lesser extent to heavier particles. Presumably the same active centres are responsible for sensitivity to light and to ionizing particles.

(2) A one-minute treatment with 5% chromic trioxide and 2.5% sulphuric acid applied to Emulsions I or II removed fog to a remarkable extent, but it had little effect on sensitivity. On the other hand, a 15 min. treatment with  $\frac{1}{2}$ % chromic trioxide and  $\frac{1}{4}$ % sulphuric acid removed fog to the same degree, but it considerably affected sensitivity. These tests show that a chemical difference exists between fog or development centres, and active centres, in accord with other evidence. Further study by similar methods on the kinetics of the removal of both should bring important information on their nature. Active centres are known to contain less silver and more silver sulphide than development centres.

An emulsion so treated has lost to a variable degree its original sensitivity. Sensitivity may then be improved or restored by ageing or by a triethanolamine treatment in such a way that very dense proton tracks with very small grain size can be obtained with almost no visible fog.

(3) Emulsions may be prepared, coated, and dried in white light if they are afterwards treated with chromic acid in red light, which removes the latent fog. Emulsions suitable for recording the tracks of fission fragments against little background can be prepared in this way. Sensitivity to protons is negligible after this treatment, but it may increase with time.

#### 5. *Ammonium Persulphate*

Concentrations of 0.002 to 2% ammonium persulphate removed fog from emulsions but reduced sensitivity more than chromic acid for the same amount of fog removed.

### Effect of Ionizing Particles on the Photographic Grain

#### 1. *Proposed Mechanism*

In the theory of Gurney and Mott (9), which has also been described by Webb (26) and Berg (2), the action of light in forming a latent image is essentially as follows. A quantum of light of suitable wave-length is absorbed

by resonance in the silver bromide, and by photoelectric effect brings an electron from its normal state in a  $\text{Br}^-$  ion to an energy level in the conduction band of silver bromide. The electron may then migrate through the lattice, leaving behind a neutral bromine atom, which is a positively charged potential hole. The electron may become trapped on an active centre owing to its lower potential energy there. Active centres are specks of silver sulphide and silver on the crystal, which are essential for its sensitivity. The active centre, being negatively charged, attracts  $\text{Ag}^+$  ions, which have the ability to migrate. In this way neutral silver atoms can accumulate on the active centre, which becomes a development centre if sufficiently enlarged with silver.

In the case of ionizing particles, the mechanism should be the same except for the first stage. Electrons are brought into the conduction band not by the photoelectric effect but by ionization by collision in the crystal. A few electrons may also come into the crystal after being produced in the gelatine immediately surrounding it. In gases the energy spent by a fast particle in producing an ion pair is about the same for all gases and all particles, about 30 ev. Professor N. F. Mott has pointed out to the writer that in silver bromide this energy should be much less. Nearly all the energy should be spent ultimately in bringing electrons into the conduction band, which requires a minimum expenditure of 3 ev. If an electron in this band possesses kinetic energy in excess of 3 ev., it will bring another electron into the conduction band. We may, therefore, expect a total energy of 3 to 6 ev, say 5 ev, spent per electron brought into the conduction band.

These views could be tested by experiments on the amount of visible image formation or on the photoconductance in silver bromide under the influence of  $\alpha$ -rays, protons,  $\beta$ -rays, or  $\gamma$ -rays.\*

An ordinary silver bromide grain to become developable requires the absorption of at least a few, say 10, and at most a few thousand quanta of light of about 3 ev., the average number being 100 or a total energy of 300 ev. It is interesting to compare this with the sensitivity of emulsions to the effect of various radiations. According to Eggert and Noddack (8), some 150 kev. energy is spent by X-rays per grain developed in one commercial emulsion. In one of the writer's emulsions the energy spent was 470 kev. for 100 grains developed, near the beginning of the track of a 12 Mev. proton. Since half of the volume was gelatine, about 250 kev. was spent in silver bromide or 2500 ev per grain developed. Since not all the grains traversed by the proton were developed, but only a fraction of the order of one-fifth or one-tenth, the energy spent in each grain was therefore 250 to 500 ev. This corresponds to the release of 50 to 100 electrons if the energy spent per electron is 5 ev. If the energy spent per electron were 30 ev., it would correspond to 9 to 18 electrons released; such a sensitivity of the grain appears too high

\* Note added at the proof reading stage — Van Heerden has proved that these views are correct, by measurement of the ionization current in silver chloride crystals caused by single rays. P. J. Van Heerden. "The crystal counter, a new instrument in nuclear physics". Thesis, Utrecht, 1944

From the following two effects we would expect that the number of electrons required to be set free in a grain before it will develop is greater in the case of ionizing particles than in the case of light of a suitable intensity level.

The first effect is related to the failure of the reciprocity law at high intensity of illumination. It is known that in general a given flux of light will be most effective on an emulsion, when applied in a continuous exposure of duration  $t$ , for a certain optimum value of  $t$ . If the same total flux is applied using either a shorter time and a higher intensity, or a longer time and a lower intensity, the exposed plate is not blackened so much. The effect of an ionizing particle is completed in an exceedingly short time as compared with the times practicable in the case of light. The primary effect of the passing particle may last only  $10^{-13}$  sec. or less. We may therefore expect as low an efficiency as can be obtained by reducing the exposure time  $t$  to the utmost.

The second effect has no exact parallel in the case of light. It is one of recombination of ions, and at present there is no direct experimental proof of its importance. Electrons and positive holes of potential when formed by the passing particle in the crystal are all located initially near a linear axis inside a cylinder of very small diameter in the silver bromide grain. The electrons tend at once to migrate away and reach the active centres; but this tendency may be strongly opposed by the high linear density of positive holes left in the crystal, if the latter migrate but slowly as is probable. This positive core creates a strong attractive field for the electrons, which have therefore a great chance of staying in that core, and of recombining with a positive hole, being then lost for the photographic process. Suppose the same number of electrons are created by light absorption in the same time; they would appear at points distributed at random throughout the volume of the crystal or on the surface, leaving on the average no particular regions where the positive holes of potential are densely grouped. Electrons produced by light, even under conditions of high intensity of illumination, are therefore more likely not to recombine with the positive holes, and to contribute finally to latent image formation.

Such an effect, which may be called a positive charge concentration effect, may come into play if the energy loss per unit length is large enough, and if the actual diameter of the cylindrical space where ionization is set up is small enough with respect to the dimensions of the crystal. These conditions are probably nearly fulfilled in the cases of  $\alpha$ -rays and of protons of a few million electron volts energy, in emulsions of not too small grains.

With the proposed mechanism, we may try to explain the sensitizing and the desensitizing effects observed. They are due exclusively to substances liable to be adsorbed, or forming compounds with the silver halide, in agreement with Vogel's law.

Optical sensitizing is due to increased absorption of light at the surface of the crystal, but as the stopping power is not changed by sensitizing, the improvement cannot be ascribed to increased production of electrons. It is not definitely connected with fluorescence, as the most active fluors are not

the best sensitizers. It appears rather to be connected with improved collection of electrons, and then of silver ions, by the active centres, whether the influence be through a modification of the active centre itself, of the surface, or of the mass of the crystal. A surface change seems most probable. That it is not due to an intensification of the latent image after its formation or to an effect enhancing development has been checked directly in the cases of eosin, ammonia, and triethanolamine.

The desensitizing effect is now accepted to be in most cases an oxidation phenomenon leading to regression of the latent image, and it does not seem impossible that the same substance be a sensitizer enhancing formation of an efficient latent image, and a desensitizer later oxidizing it, whether in the presence of air or not. Such consideration might explain the dual properties of pinakryptol yellow and green.

The fact that prolonged triethanolamine treatment decreases sensitivity and fog, while prolonged digesting decreases sensitivity and increases fog, suggests that sensitizing does not affect the formation and growth of the active centres in the same way as digesting. However, there may be an indication to the contrary in the following observation. The two effects seem to be complementary; a fully ripened emulsion is little improved by sensitizing, and a sensitized emulsion is little improved by ripening.

## 2. Quantitative Theory

The following theory gives a fair account in most cases of the grain spacings observed, while it is insufficient to explain certain other features

Let  $l$  be the length of path of an ionizing particle in a grain, and  $E_l$  the corresponding energy spent by the particle. The path varies between zero and  $d$ , the diameter of the grain, which is assumed to be spherical. If  $E$  is the maximum energy that is spent in the grain ( $l = d$ ) and  $I$  is the mean energy loss per unit length,

$$E_l = Il = El/d.$$

We shall assume that a grain having received energy  $E_l$  has the following probability of being developed:

$$1 - e^{-E_l/E_0},$$

where  $E_0$  is a constant of the emulsion. Let  $P$  be the probability that a grain be developed if the ionizing path goes through it at random. Assuming that equal elements of cross-section in the sphere have equal chances of being hit by the particle, whose track is assumed to be linear,

$$\begin{aligned} P &= \int_0^d (1 - e^{-El/I_0d}) \frac{2l \, dl}{d^2} \bigg/ \int_0^d \frac{2l \, dl}{d^2} \\ &= 1 - (2/x^2) (1 - e^{-x} - xe^{-x}) \\ &= 2x/3 - x^2/4 + x^3/15 - x^4/72 \dots, \end{aligned}$$

where  $x = E/E_0 = I/I_0$ .

In the formula for the grain spacing,

$$\Delta = \Delta_0/P = 4.2 d/cP,$$

we may regard  $P$  as a function of  $E/E_0$  or  $I/I_0$ , where  $I$  is the mean energy loss per unit length at the point considered, and  $I_0$  is a constant. Sensitivity may be defined as the reciprocal of  $I_0$ . In this form, which contains only one adjustable parameter ( $I_0$ ), the theory does not hold except as a rough approximation for large grains. On the other hand, if  $\Delta_0$  and  $I_0$  are both regarded

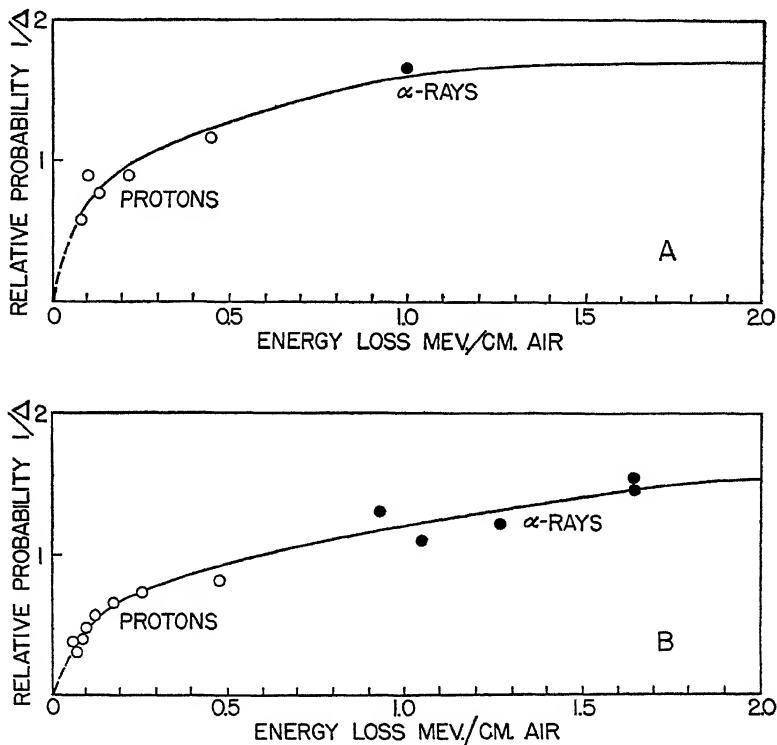


FIG. 7. A. Relative probability of development or reciprocal of grain spacing is plotted against the specific energy loss in million electron volts per centimetre of air for tracks of protons and  $\alpha$ -rays in Eastman 548 emulsion.

B. Similar plot for Emulsion II with gelatine added. Concentration  $c = 1$  gm. silver bromide per cc. emulsion and grain diameter  $d \leq 0.1 \mu$ , for both emulsions.

as adjustable parameters the measured grain spacing can be approximately fitted for protons,  $\alpha$ -rays, and fission fragments in most emulsions used.

For convenience, the probability  $P$  of development of the grains is plotted from the expression above against  $x (= I/I_0)$  in Fig. 8. The specific energy loss in million electron volts per centimetre of air, calculated from theoretical formulae (5, 12), is shown as a function of the residual range for protons,  $\alpha$ -rays, and fission fragments in Fig. 9. These two figures are useful in fitting

experimental results to the theory and deriving the best values of the parameters  $\Delta_0$  and  $I_0$ .

Calculated curves with suitable parameters are seen to fit the measured grain spacing plotted in Figs. 1, 2, and 5 for several emulsions. The similarity of the calculated probability curve (Fig. 8) with the experimental curves in

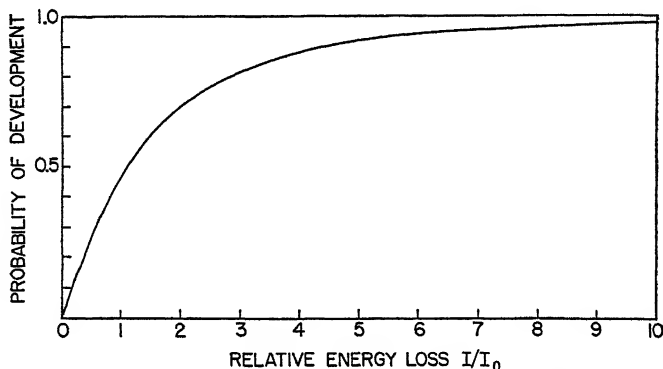


FIG. 8. Probability of development is plotted against the relative energy loss  $I/I_0$ , on the basis of the proposed theory. The constant  $I_0$  is a reciprocal sensitivity factor of the emulsion. The shape of the curve is similar to that of the experimental curves in Figs. 7A and 7B.

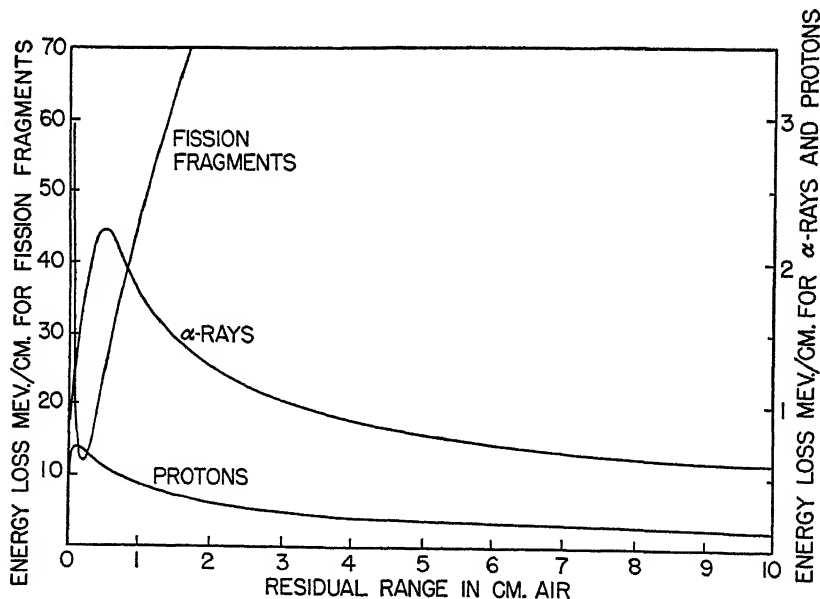


FIG. 9. Specific energy loss in million electron volts per centimetre of air is plotted against the residual range in centimetres of air for protons,  $\alpha$ -rays, and fission fragments. Theoretical formulas were used (5, 12).

Figs. 7A and 7B should be noted. The values of  $I_0$  required to fit the experimental results range from 25 kev. to 10 Mev. per cm. of air. In these emulsions proton tracks show well only if  $I_0 < 100$  kev. per cm. Figs. 10, 11, and 12

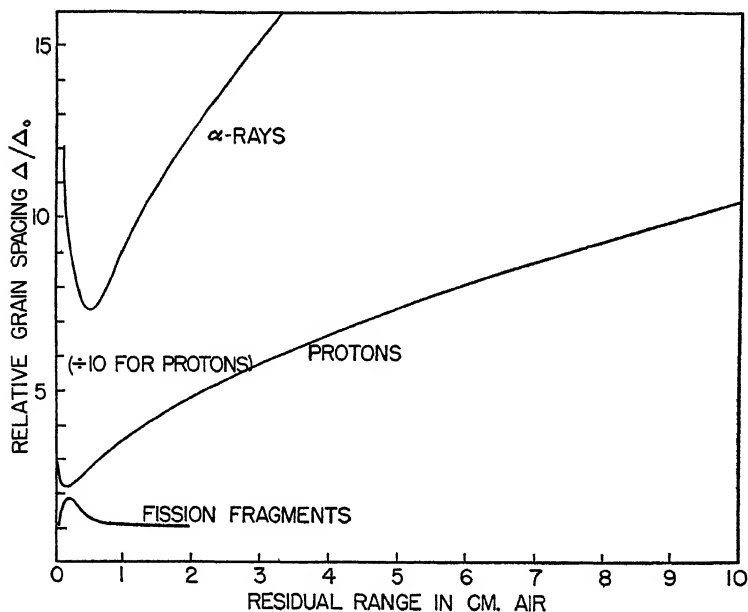


FIG. 10. Relative grain spacing or  $\Delta/\Delta_0$ , calculated from the proposed theory (Figs. 8 and 9), is plotted against the residual range for tracks of protons,  $\alpha$ -rays, and fission fragments. The parameter  $I_0 = 10$  Mev. per cm. air.

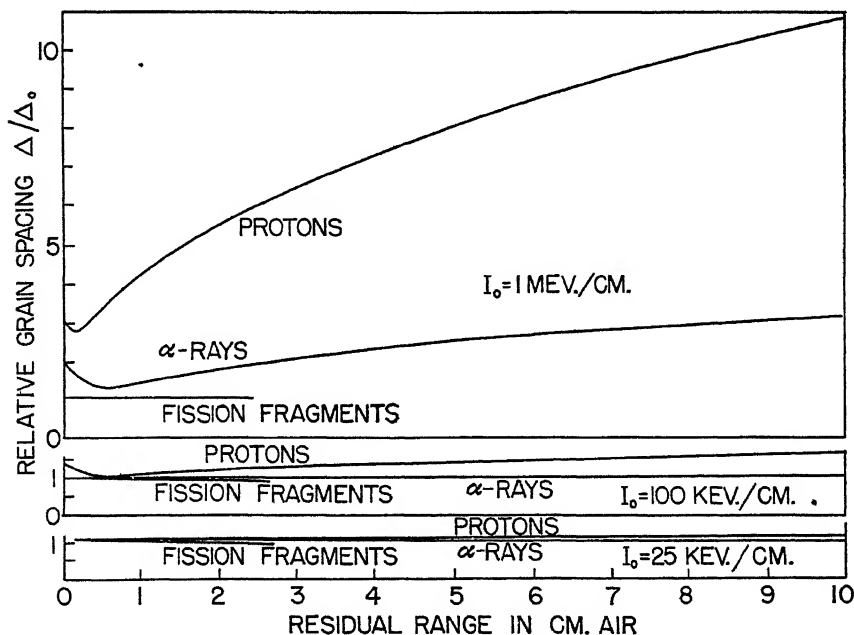


FIG. 11. Relative grain spacing or  $\Delta/\Delta_0$ , calculated from the proposed theory (Figs. 8 and 9), is plotted against the residual range for tracks of protons,  $\alpha$ -rays, and fission fragments. Chosen values of  $I_0$  are 1 Mev. per cm., 100 kev. per cm., and 25 kev. per cm. air.

show calculated curves of relative grain spacing plotted against the residual range of protons,  $\alpha$ -rays, and fission fragments for values of  $I_0$  likely to be encountered.

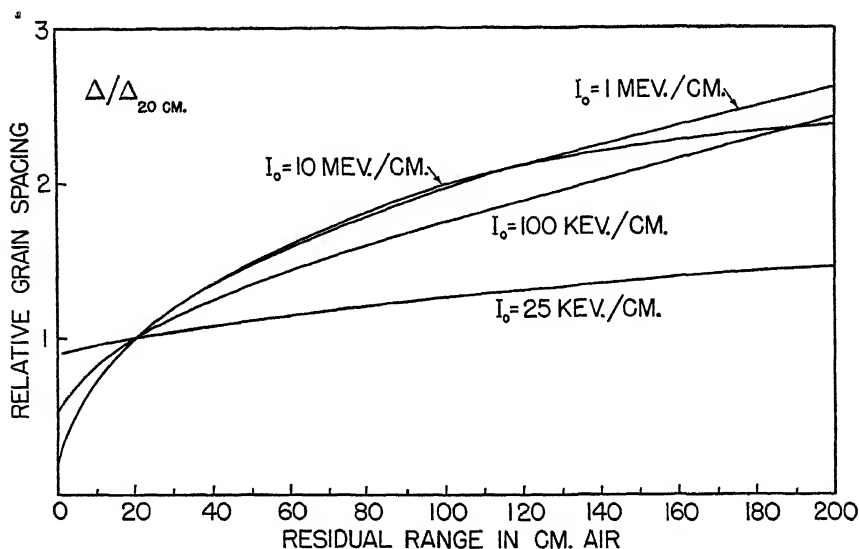


FIG 12 Relative grain spacing or  $\Delta/\Delta_0$  cm., calculated from the proposed theory (Figs 8 and 9), is plotted against the residual range of energetic protons. The variation in shape arising from the inverse sensitivity parameter  $I_0$  is shown.  $\Delta_0$  cm.  $\Delta_0 = 105, 110, 20,$  and  $1.11$  at  $10, 1, 1/2, 1,$  and  $0.025$  Mev per cm, respectively.

The theory is not wholly satisfactory for the following reasons. (i) Certain curves of grain spacing as a function of residual range of protons cannot be fitted. These were obtained in very insensitive emulsions, in which the spacing was excessive at high energy. (ii) One pair of parameters  $\Delta_0$  and  $I_0$  is not generally sufficient to fit the results for protons,  $\alpha$ -rays, and fission fragments in the same emulsion. Usually the highest value of  $I_0$  is required for the most strongly ionizing path. A very strong ionization appears therefore to bring a reaction from less sensitive grains.

### Acknowledgments

The author wishes to thank Dr. J. D. Cockcroft and Dr. B. W. Sargent for their interest and encouragement in this work; also Prof. N. F. Mott, who read critically the part of the manuscript dealing with the formation of the latent image and modified several of the author's views on the subject.

Through the courtesy of the following, plates have been irradiated at various times: the group at the graphite pile of the Argonne Laboratory, the group at

---

*Note*—Photomicrographs for Figs 13A and 26 to 34 were taken with white light, those for Figs 13B to 25 were taken with a blue-green filter, and show a better definition.

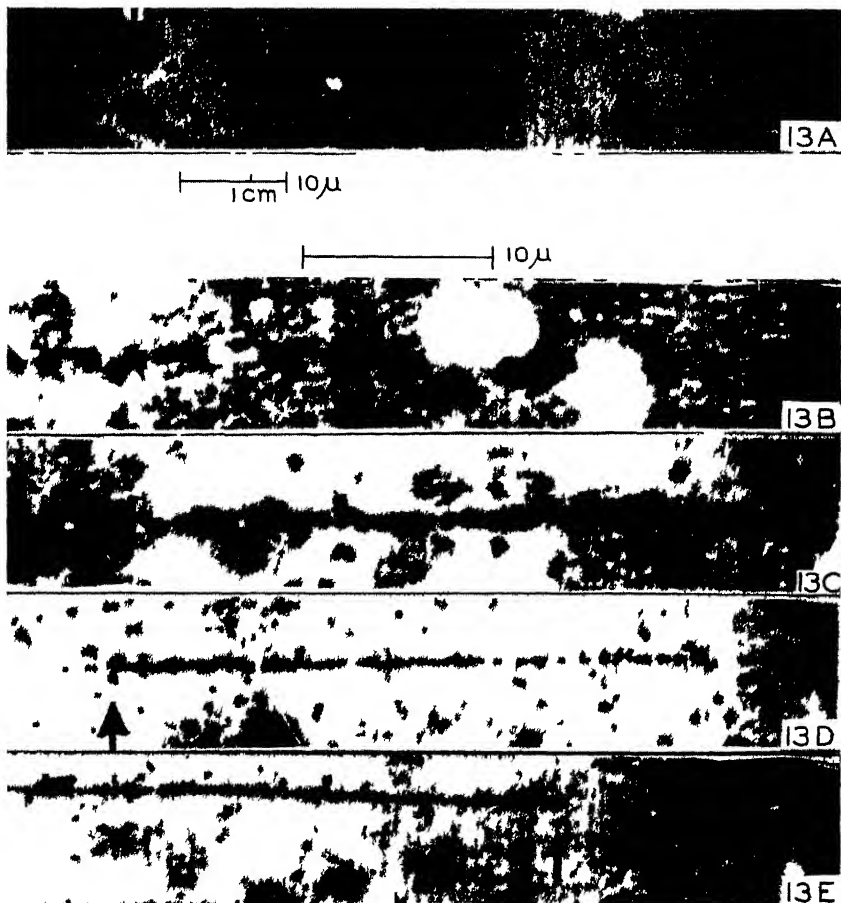
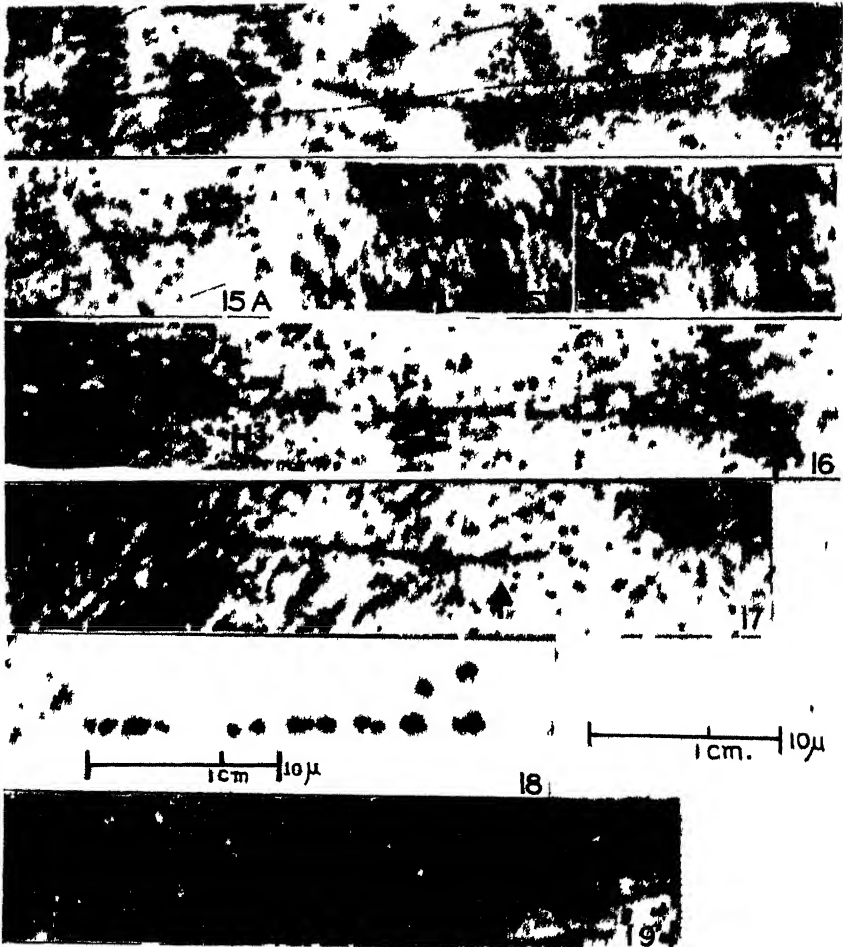
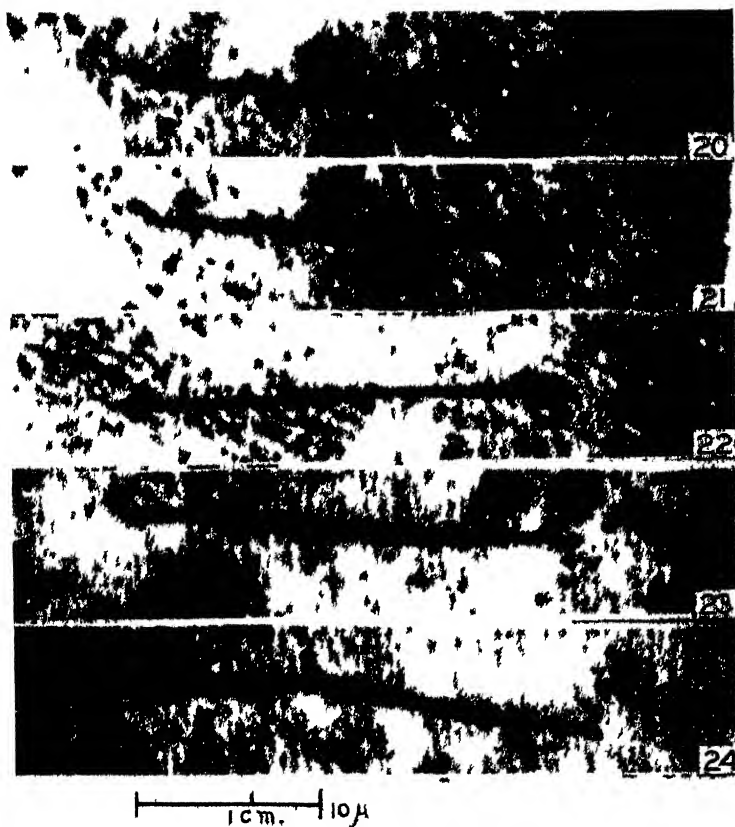


FIG 13A Beginning of proton track of residual range 30 cm air in Eastman  $\alpha$  emulsion  
 FIG 13B End of proton track partly shown in Fig 13A  
 FIG 13C End of proton track in centrifuged Eastman  $\alpha$  emulsion  
 FIG 13D Beginning of proton track of residual range 60 cm air in Emulsion II  
 FIG 13E End of proton track partly shown in Fig 13D



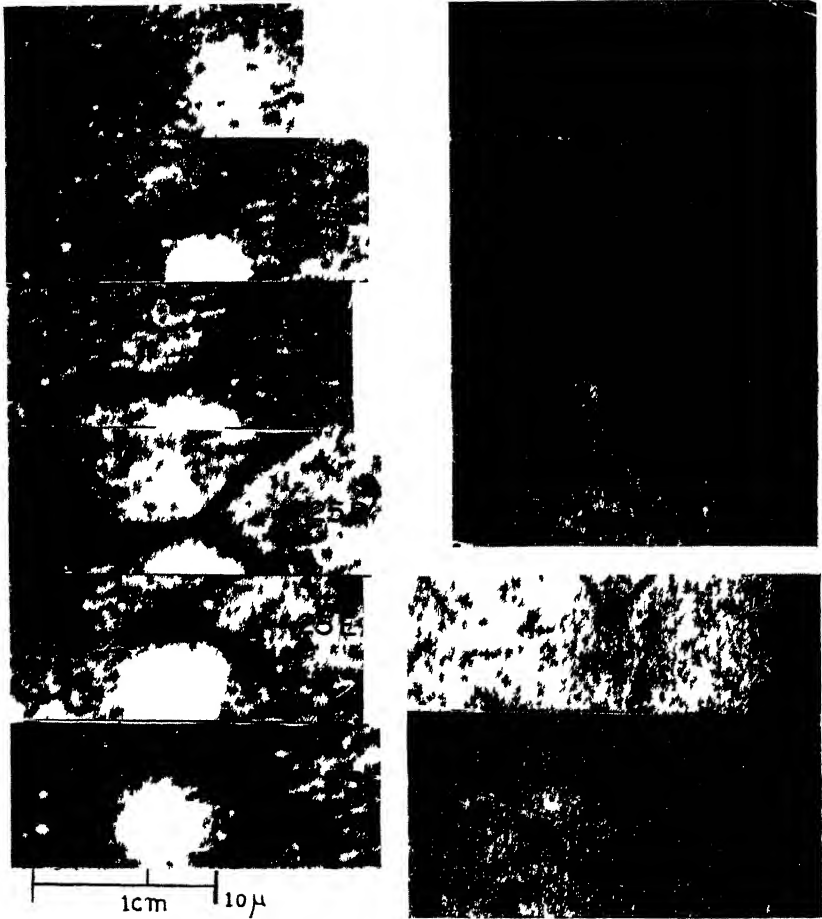
- FIG 14 End of proton track in Emulsion II containing lithium chloride
- FIGS 15A B C Proton tracks of range 1.06 cm air and energy 0.62 Mev from reaction  $N^{14} (n, p) C^{14}$  in Emulsion II containing lithium chloride (same plate as Fig 14)
- FIG 16  $\alpha$  and  $H^1$  tracks from reaction  $Li^7 (n, \alpha) H$  in Emulsion II containing lithium chloride (same plate as Figs 14 15A C) Differential sensitivity has been obtained
- FIG 17 Track of  $\alpha$  ray from uranium in Emulsion II
- FIG 18 Track of  $\alpha$  ray from uranium in Eastman  $\alpha$  emulsion
- FIG 19 Tracks of a pair of fission fragments in Emulsion II An  $\alpha$  ray track can be seen

PLATE III



FIGS 20 21 Tracks of a pair of fission fragments in Emulsion II to o focusings  
 FIGS 22 23 24 Tracks of pairs of fission fragments in Emulsion II

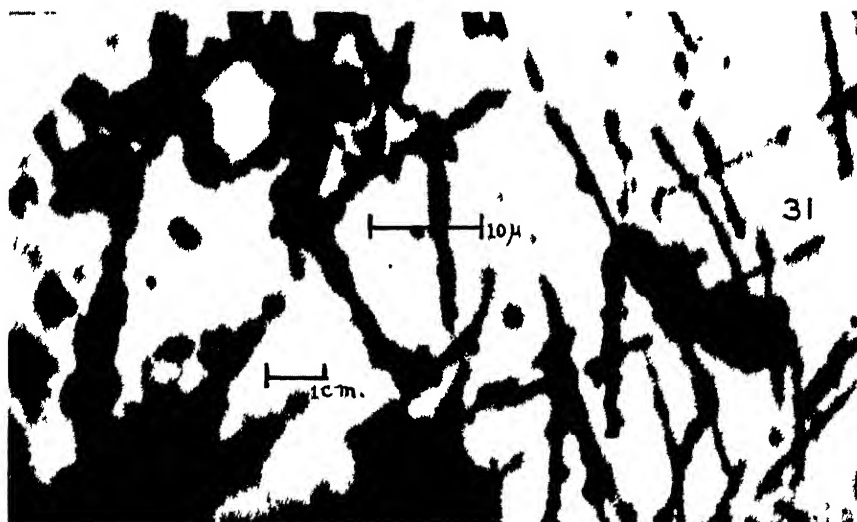
PLATE IV



FIGS. 25A-D Tracks of fission fragments, three branches of comparable appearance in focusings

FIG. 26 Tracks of pairs of fission fragments in Eastman 548 emulsion

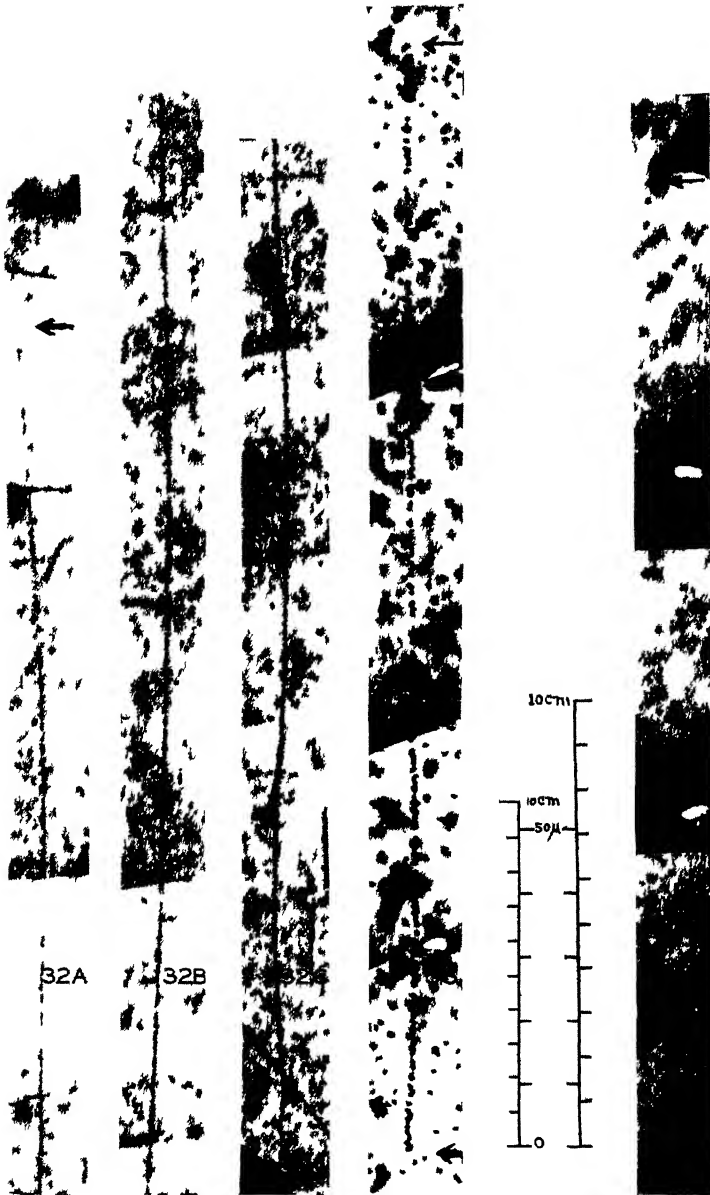
FIGS. 27A-B Tracks of fission fragments and  $\alpha$  rays dipping into emulsion from uranium disk lying on it, Emulsion X2 or X4 centrifuged



FIGS 28, 29 Torked tracks caused by proton-proton collisions in Emulsion I

FIG 30 Track attributed to an electron in Emulsion I At the top a proton track is out of focus

FIG 31  $\alpha$ -ray tracks in Emulsion V4 centrifuged Development has spread from tracks and fog grains to produce the club-like appearance and lumps of various sizes



FIGS 32A C Proton track of range 85 cm air and initial energy 8.9 Mev begins on Fig 32A and ends on Fig 32C Emulsion III centrifuged

FIG 33 Proton track of range 30 cm air in centrifuged Eastman emulsion

FIG 34 Proton track of range 25 cm air in Eastman  $\alpha$  emulsion

the low power, heavy water pile of the Chalk River Laboratory, and Dr. H. M. Cave and his collaborators in charge of the high tension set in Ottawa. Their assistance is gratefully acknowledged.

Miss E. O'Brien, Miss E. Mooney, and Mr. G. Gauron have assisted in preparing emulsions at various times.

The author is grateful to Dr. Marietta Blau, Dr. C. F. Powell, Dr. D. L. Livesey, and Mr. D. H. Wilkinson for private information.

The Ciba Company of Montreal has kindly given several of the dyes used in this work.

### References

1. BAKLR, T. T. Photographic emulsion technique. American Photographic Publishing Company, Boston. 1941.
2. BERG, W. F. Trans. Faraday Soc. 39 : 115-134. 1943.
3. BLAU, M. J. phys. radium, 5 : 61-66. 1934.
4. BLAU, M. and WAMBACHER, H. Z. wiss. Phot. 31 : 243-250. 1933.
5. BØGGILD, J. K., BROSTRØM, K. J., and LAURITSEN, T. Kgl. Danske Videnskab. Selskab. Math.-fys. Medd. 18 (4) : 1-32. 1940.
6. BORST, L. B. and FLOYD, J. J. Bull. Am. Phys. Soc. 21 (3) : 13. 1946.
7. CARROLL, B. H. J. Chem. Education, 8 : 2341-2367. 1931.
8. GEGERT, J. and NODDACK, W. Z. Physik, 43 : 222-229. 1927.
9. GURNEY, R. W. and MOTT, N. F. Proc. Roy. Soc. London, A, 164 : 151-167. 1938.
10. JÐANOV, A. J. phys. radium, 6 : 233-241. 1935.
11. KINOSHITA, S. Proc. Roy. Soc. London, A, 83 : 432-453. 1910.
12. LIVINGSTON, M. S. and BETHE, H. A. Rev. Modern Phys. 9 : 245-390. 1937.
13. MEES, C. E. K. Theory of the photographic process. The Macmillan Company, New York. 1944.
14. MYŚKOWSKY, L. and JÐANOFF, A. Nature, 143 : 794-795. 1939.
15. MYŚKOWSKY, L. and TSCHISHOW, P. Z. Physik, 44 : 408-420. 1927.
16. NEBLEHIN, C. B. Photography, its principles and practice. 4th ed. D. Van Nostrand Company, Inc., New York. 1942.
17. PERFILOV, N. A. Compt. rend. acad. sci. U.R.S.S. 47 : 623-626. 1945.
18. POWELL, C. F. Proc. Roy. Soc. London, A, 181 : 344-359. 1943.
19. POWELL, C. F., OCCHIALINI, G. P. S., LIVESY, D. L., and CHILTON, L. V. J. Sci. Instruments, 23 : 102-106. 1946.
20. REINGANUM, M. Physik. Z. 12 : 1076-1077. 1911.
21. SHAPIRO, M. M. Rev. Modern Phys. 13 : 58-71. 1941.
22. SHEPPARD, S. E. Cited in Theory and application of colloidal behaviour. Vol. 2. Edited by R. H. Bogue. McGraw-Hill Book Company, New York. 1924.
23. SHEPPARD, S. E., LAMBERT, R. H., and SWINEHART, D. J. Chem. Phys. 13 : 372-377. 1945.
24. WALL, E. J. Photographic emulsions, their preparation and coating on glass, celluloid and paper, experimentally and on the large scale. American Photographic Publishing Company, Boston. 1929.
25. WAMBACHER, H. Sitzber. Akad. Wiss. Wien, Math.-naturw. Klasse, 140 (Abt. IIa) : 271-291. 1931.
26. WEBB, J. H. J. Applied Phys. 11 : 18-34. 1940.
27. WILKINS, T. R. J. Applied Phys. 11 : 35-45. 1940.
28. WILKINSON, D. H. Private communication.
29. YOE, J. H. and SÄRVER, L. A. Organic analytical reagents. John Wiley & Sons, Inc., New York. 1941.

## A METHOD FOR COMPUTING TRANSFORMATIONS IN RADIOACTIVE SERIES<sup>1</sup>

BY W. H. WATSON<sup>2</sup>

### Abstract

A direct computational procedure is given for finding the coefficients of the exponential terms in the expressions for the time dependence of the amounts of the various products in a given radioactive series. The method is based on the partition of a matrix which can be written down directly from the diagram of the series. After the explanation of simple applications, an example involving double branching with 10 members of the series is considered in order to exhibit the generality and directness of the method.

### Introduction

The laws of radioactive transformation are linear differential equations. If they are treated by operator methods, the problem of finding the changes in time of the amounts of the various products requires the solution of linear algebraic equations and the interpretation of the operators in series of exponential functions of the time. When more than a few products are involved, the labour of computation is exceedingly tedious. The present note shows how the coefficients of the exponential terms in the expressions for the amounts of the various products can be obtained by a direct computational procedure using matrix representation to manage the algebra.

First we write down the matrix ( $C$ ) which transforms the column vector, whose elements are the masses at time  $t$  arranged in suitable order, into the column vector composed of the corresponding initial masses. One can easily see after consideration of the few examples exhibited below how this matrix may be written down immediately from a diagram of the sequence of transformations in the particular series to be treated. Next we have to compute the reciprocal matrix ( $U$ ): rules are given here for writing it down *directly from the diagram of the series*.

We now split  $U$  into a sum of matrices each of which contains one exponential function of the time as a factor. Again rules are given for finding the elements of these partial matrices in terms of the various half-lives involved in the series. It is then possible to derive by matrix multiplication the explicit time dependence of the masses of any or all of the products. This, of course, requires only simple multiplication and addition. The advantages of this method are that the errors caused by approximation can be immediately assessed, and that the general result for a particular series is best left in matrix form.

<sup>1</sup> Manuscript received February 11, 1947.

Contribution from Atomic Energy Project, Chalk River Laboratory, Ont. Issued as N.R.C. No. 1564.

<sup>2</sup> Head of Theoretical Physics Branch.

We shall deal first with a series in which no branching occurs, then we shall treat  $\triangle$ -branching and  $\diamond$ -branching.

In principle the method is applicable to the growth of fission products in a reacting pile and to their subsequent decay when power is shut off. Obviously the method will apply to any system of first order linear differential equations representable by a matrix of the same general form as that imposed by the laws of radioactive transformation.

### 1. Series Without Branching

Suppose the series of products named in order by the subscripts 1, 2, . . . ,  $r$ , . . .  $n$ . Let the  $r$ th member have decay constant  $\lambda_r$ , half-life  $T_r$ ; let the amount of it at time  $t$  be  $x_r$ , and let  $a_r$  be the amount at  $t = 0$ . In operational form (1, 2) the equations governing decay are

$$(p + \lambda_r)x_r = a_r + \lambda_{r-1}x_{r-1} \quad (1)$$

$$(r = 1, 2, \dots, n, \lambda_0 = 0).$$

This set of equations may be represented in matrix form thus:

$$\begin{pmatrix} p + \lambda_1 & 0 & 0 & 0 & \dots & 0 \\ -\lambda_1 & p + \lambda_2 & 0 & 0 & \dots & 0 \\ 0 & -\lambda_2 & p + \lambda_3 & 0 & \dots & 0 \\ 0 & 0 & -\lambda_3 & p + \lambda_4 & \dots & 0 \\ - & - & - & - & - & - \\ & & & & & (p + \lambda_n) \end{pmatrix} \begin{pmatrix} x_1 \\ x_2 \\ x_3 \\ x_4 \\ \vdots \\ x_n \end{pmatrix} = \begin{pmatrix} a_1 \\ a_2 \\ a_3 \\ a_4 \\ \vdots \\ a_n \end{pmatrix} \quad (2)$$

or

$$C(x) = (a).$$

The inverse transformation is

$$(x) = U(a).$$

If we write

$$q_r = \frac{1}{p + \lambda_r} \quad (3)$$

and

$$s_r = \frac{\lambda_r}{p + \lambda_r} \quad (4)$$

we find for  $U$  the form

$$U = \begin{pmatrix} q_1 & 0 & 0 & 0 & . & . & . \\ s_1 q_2 & q_2 & 0 & 0 & . & . & . \\ s_1 s_2 q_3 & s_2 q_3 & q_3 & 0 & . & . & . \\ s_1 s_2 s_3 q_4 & s_2 s_3 q_4 & s_3 q_4 & q_4 & . & . & . \\ - & - & - & - & - & - & - \\ - & - & - & - & - & - & q_n \end{pmatrix} \quad (5)$$

Now the operator  $s_1 s_2 s_3 q_4$ , for example, is

$$\begin{aligned} & \frac{\lambda_1 \lambda_2 \lambda_3}{(p + \lambda_1)(p + \lambda_2)(p + \lambda_3)(p + \lambda_4)}, \text{ leading to the function} \\ & \frac{\lambda_1 \lambda_2 \lambda_3 e^{-\lambda_1 t}}{(\lambda_2 - \lambda_1)(\lambda_3 - \lambda_1)(\lambda_4 - \lambda_1)} + 3 \text{ like terms} \\ & = \frac{T_4 T_1^2}{(T_1 - T_2)(T_1 - T_3)(T_1 - T_4)} \left(\frac{1}{2}\right)^{t/T_1} + 3 \text{ like terms} \end{aligned}$$

Accordingly we may split the matrix  $U$  as follows

$$U = \left(\frac{1}{2}\right)^{t/T_1} u_1 + \left(\frac{1}{2}\right)^{t/T_2} u_2 + \left(\frac{1}{2}\right)^{t/T_3} u_3 + \dots \quad (6)$$

where

$$\begin{aligned} u_1 &= \begin{bmatrix} 1 & 0 & 0 & 0 \\ \frac{T_2}{T_1 - T_2} & 0 & 0 & 0 \\ \frac{T_3 T_1}{(T_1 - T_2)(T_1 - T_3)} & 0 & 0 & 0 \\ - & - & - & - \end{bmatrix} \\ u_2 &= \begin{bmatrix} 0 & 0 & 0 & 0 \\ \frac{T_2}{T_2 - T_1} & 1 & 0 & 0 \\ \frac{T_2 T_3}{(T_2 - T_1)(T_2 - T_3)} & \frac{T_1}{T_2 - T_3} & 0 & 0 \\ - & - & 0 & - \end{bmatrix} \\ u_3 &= \begin{bmatrix} 0 & 0 & 0 & 0 \\ 0 & 0 & 0 & 0 \\ \frac{T_3^2}{(T_3 - T_1)(T_3 - T_2)} & \frac{T_3}{T_3 - T_2} & 1 & 0 \\ - & - & - & - \end{bmatrix} \end{aligned}$$

and so on

**Rule** (i) To find the matrix  $u_k$ , put equal to zero all the elements in  $U$  which do not contain  $q_k$  or  $s_k$ .

(ii) Replace  $s_m$  by  $\frac{T_k}{T_k - T_m}$  and  $q_m$  by  $\frac{T_m T_k}{T_k - T_m}$ .

(iii) Omit  $q_k$  and replace  $s_k$  by  $\frac{1}{T_k}$ .

Ex. In  $u_3$

$$\begin{aligned} s_1 s_2 q_3 &\rightarrow \frac{T_3}{T_3 - T_1} \cdot \frac{T_3}{T_3 - T_2} = \frac{T_3^2}{(T_3 - T_2)(T_3 - T_1)} \\ s_1 s_2 s_3 q_4 &\rightarrow \frac{1}{T_3} \cdot \frac{T_3}{T_3 - T_2} \cdot \frac{T_3}{T_3 - T_1} \cdot \frac{T_3 T_4}{T_3 - T_4} \\ &= \frac{T_4 T_3^2}{(T_3 - T_1)(T_3 - T_2)(T_3 - T_4)}. \end{aligned}$$

In this way we may read off the coefficients of the various powers of  $\frac{1}{2}$ , for we have only to multiply the given column vector ( $a$ ) by the appropriate  $u_k$ , to obtain the contributions to ( $x$ ) which vary as  $\left(\frac{1}{2}\right)^{1/r_k}$ .

## 2. Branching

We consider first the introduction of a  $\Delta$ -branch connecting the  $r$ th and  $(r+1)$ th products in the series. This is represented in Fig. 1. We denote the intermediate product by  $(\alpha r)$ ,  $\alpha$  being the fraction of  $r$  atoms disintegrating which go to the branch product,  $\beta$  is the complementary fraction ( $\alpha + \beta = 1$ ) disintegrating to the product  $(r+1)$  directly.

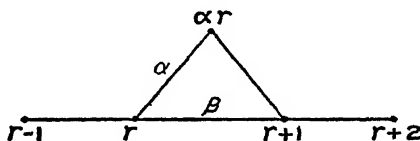


FIG. 1

The relevant equations to be considered are:

$$\begin{aligned} (p + \lambda_r)x_r &= a_r + \lambda_{r-1}x_{r-1} \\ (p + \lambda_{\alpha r})x_{\alpha r} &= a_{\alpha r} + \alpha\lambda_r x_r \\ (p + \lambda_{r+1})x_{r+1} &= a_{r+1} + \lambda_{\alpha r}x_{\alpha r} + \beta\lambda_r x_r. \end{aligned} \quad (7)$$

Thus the matrix operator  $C$  and Equation (2) are modified as follows:

$$\begin{pmatrix} \dots & \dots & \dots & \dots & \dots & \dots & \dots \\ \dots & p + \lambda_{r-1} & 0 & 0 & 0 & 0 & \dots \\ \dots & -\lambda_{r-1} & p + \lambda_r & 0 & 0 & 0 & \dots \\ \dots & 0 & -\alpha\lambda_r & p + \lambda_{\alpha r} & 0 & 0 & \dots \\ \dots & 0 & -\beta\lambda_r & -\lambda_{\alpha r} & p + \lambda_{r+1} & 0 & \dots \\ \dots & 0 & 0 & 0 & -\lambda_{r+1} & p + \lambda_{r+2} & \dots \\ \dots & \dots & \dots & \dots & \dots & \dots & \dots \end{pmatrix} \begin{pmatrix} \dots \\ x_{r-1} \\ x_r \\ x_{\alpha r} \\ x_{r+1} \\ \dots \\ \dots \end{pmatrix} = \begin{pmatrix} \dots \\ a_{r-1} \\ a_r \\ a_{\alpha r} \\ a_{r+1} \\ \dots \\ \dots \end{pmatrix} \quad (8)$$

The introduction of the off-diagonal element  $-\beta\lambda_r$  still leaves the determinant of the matrix  $C$  equal to the product of its principal diagonal elements.



1. Replace the principal diagonal elements of  $C$  by their reciprocals, i.e., insert  $q_k$  in the  $k$ th place in the diagonal.

2. All elements to the right of the principal diagonal are zero. It is unnecessary, therefore, to write them down.

3. On the left, build up each row from the principal diagonal. Each step to the left in the matrix corresponds to the transition from the member of the series named by the index of the column from which we start to that named by the adjacent column on its left. When these two members are related as daughter and parent multiply the element of  $U$  on the right by the  $s$  for the element on the left when there is no branching. If the two members are not related in this way write zero for the corresponding element of  $U$ .

When the column of  $U$  corresponds to a point of branching the element to be written down represents the complete series of transitions between the point of branching and the member represented by the principal diagonal element on the same row. For instance in (9) above in the second column and fourth row we find the element  $s_r(\alpha s_{\alpha r} + \beta)q_{r+1}$ . So the procedure is to write down a  $q$ -factor for the series member naming the row of the matrix and an  $s$ -factor for each step when simple and when the branching occurs the obvious linear combination of  $s$ -factors in the proportion of the branching ratio.

Thus we can write down  $U$  by inspection from the diagram of the series once we have decided how to number the members of the series.

For the convenience of the reader we shall treat  $\diamond$ -branching explicitly (see Fig. 2).

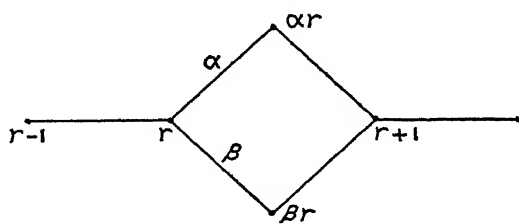


FIG. 2

In operational form the equations governing decay are

$$\begin{aligned}
 (p + \lambda_r)x_r &= a_r + \lambda_{r-1}x_{r-1} \\
 (p + \lambda_{\alpha r})x_{\alpha r} &= a_{\alpha r} + \alpha\lambda_r x_r \\
 (p + \lambda_{\beta r})x_{\beta r} &= a_{\beta r} + \beta\lambda_r x_r \\
 (p + \lambda_{r+1})x_{r+1} &= a_{r+1} + \lambda_{\alpha r}x_{\alpha r} + \lambda_{\beta r}x_{\beta r}
 \end{aligned} \tag{10}$$

The relevant part of the matrix  $C$  is

$$\begin{array}{ccccc}
 -\lambda_{r-1} & p + \lambda_r & 0 & 0 & 0 \\
 0 & -\alpha\lambda_r & p + \lambda_{\alpha r} & 0 & 0 \\
 0 & -\beta\lambda_r & 0 & p + \lambda_{\beta r} & 0 \\
 0 & 0 & -\lambda_{\alpha r} & -\lambda_{\beta r} & p + \lambda_{r+1} \\
 0 & 0 & 0 & 0 & -\lambda_{r+1}
 \end{array} \tag{11}$$

To check the computing of the reciprocal matrix by the rules given above, consider

$$\text{Let } \begin{pmatrix} a_1 & 0 & 0 & 0 & 0 & 0 \\ -a_2 & b_1 & 0 & 0 & 0 & 0 \\ 0 & -b_2 & c_1 & 0 & 0 & 0 \\ 0 & -b_3 & 0 & d_1 & 0 & 0 \\ 0 & 0 & -c_2 & -d_2 & e_1 & 0 \\ 0 & 0 & 0 & 0 & -e_2 & f_1 \end{pmatrix} = C.$$

$$\Delta = - \begin{vmatrix} b_2 & c_1 & 0 \\ -b_3 & 0 & d_1 \\ 0 & -c_2 & d_2 \end{vmatrix}$$

Compute  $U$ , the reciprocal of  $C$  following the rules of matrix theory. The result is

$$U = \begin{pmatrix} \frac{1}{a_1} & 0 & 0 & 0 & 0 & 0 \\ \frac{a_2}{a_1 b_1} & \frac{1}{b_1} & 0 & 0 & 0 & 0 \\ \frac{a_2 b_2}{a_1 b_1 c_1} & \frac{b_2}{b_1 c_1} & \frac{1}{c_1} & 0 & 0 & 0 \\ \frac{a_2 b_3}{a_1 b_1 c_1} & \frac{b_3}{b_1 d_1} & 0 & \frac{1}{d_1} & 0 & 0 \\ \frac{a_2 \Delta}{a_1 b_1 c_1 d_1 e_1} & \frac{\Delta}{b_1 c_1 d_1 e_1} & \frac{c_2}{c_1 e_1} & \frac{d_2}{d_1 e_1} & \frac{1}{e_1} & 0 \\ \frac{a_2 \Delta e_2}{a_1 b_1 c_1 d_1 e_1 f_1} & \frac{\Delta e_2}{b_1 c_1 d_1 e_1 f_1} & \frac{c_2 e_2}{c_1 e_1 f_1} & \frac{d_2 e_2}{d_1 e_1 f_1} & \frac{e_2}{e_1 f_1} & \frac{1}{f_1} \end{pmatrix}$$

Apply this result to matrix (11) to find

$$\begin{array}{ccccccc} q_{r-1} & & & & & & \\ s_{r-1} q_r & & q_r & & & & \\ s_{r-1} \alpha s_r q_{ar} & & \alpha s_r q_{ar} & & q_{ar} & & \\ s_{r-1} \beta s_r q_{\beta r} & & \beta s_r q_{\beta r} & & 0 & & q_{\beta r} \\ s_{r-1} s_r (\alpha s_{ar} + \beta s_{\beta r}) q_{r+1} & s_r (\alpha s_{ar} + \beta s_{\beta r}) q_{r+1} & s_{ar} q_{r+1} & s_{\beta r} q_{r+1} & q_{r+1} & & \\ - & - & - & - & - & - & s_{r+1} q_{r+2} \quad q_{r+2} \end{array}$$

This is the result which could have been written down directly from Fig. 2.

$q_1$	$q_2$	$q_3$	$q_4$	$q_5$	$q_6$	$q_7$	$q_8$	$q_9$	$q_{10}$
$s_1 q_2$	$\alpha s_2 q_3$	$\gamma s_3 q_4$	$\delta s_4 q_5$	$s_5 q_6$	$s_6 q_7$	$s_7 q_8$	$s_8 q_9$	$s_9 q_{10}$	
$s_1 \alpha s_2 q_3$	$\alpha s_2 \gamma s_3 q_4$	$\delta s_3 q_5$	$s_4 q_6$	$s_5 \gamma s_4 + \delta s_5 q_6$	$s_6 q_7$	$s_7 q_8$	$s_8 q_9$	$s_9 q_{10}$	
$s_1 \alpha s_2 \delta s_3 q_5$	$\alpha s_2 \delta s_3 q_5$	$s_4 q_6$	$s_5 \gamma s_4 + \delta s_5 q_6$	$s_6 q_7$	$s_7 q_8$	$s_8 q_9$	$s_9 q_{10}$	$s_{10} q_{11}$	
$s_1 \alpha s_2 s_3 (\gamma s_4 + \delta s_5 q_6)$	$s_2 \alpha s_3 (\gamma s_4 + \delta s_5 q_6)$	$s_3 \gamma s_4 + \delta s_5 q_6$	$s_4 q_6$	$s_5 \gamma s_4 + \delta s_5 q_6$	$s_6 q_7$	$s_7 q_8$	$s_8 q_9$	$s_9 q_{10}$	
$s_1 \beta s_2 q_7$	$\beta s_2 q_7$	$s_3 q_8$	$s_4 q_9$	$s_5 q_{10}$	$s_6 q_{11}$	$s_7 q_{12}$	$s_8 q_{13}$	$s_9 q_{14}$	$s_{10} q_{15}$
$s_1 \beta s_2 s_3 q_8$	$\beta s_2 s_3 q_8$	$s_3 q_8$	$s_4 q_9$	$s_5 q_{10}$	$s_6 q_{11}$	$s_7 q_{12}$	$s_8 q_{13}$	$s_9 q_{14}$	$s_{10} q_{15}$
$A$	$B$	$s_3 (\gamma s_4 + \delta s_5) s_6 q_9$	$s_4 s_5 q_{10}$	$s_5 s_6 q_{11}$	$s_6 s_7 q_{12}$	$s_7 s_8 q_{13}$	$s_8 s_9 q_{14}$	$s_9 s_{10} q_{15}$	$s_{10} s_{11} q_{16}$
$C$	$D$	$s_3 (\gamma s_4 + \delta s_5) s_6 s_7 q_{10}$	$s_4 s_5 s_6 q_{11}$	$s_5 s_6 s_7 q_{12}$	$s_6 s_7 s_8 q_{13}$	$s_7 s_8 s_9 q_{14}$	$s_8 s_9 s_{10} q_{15}$	$s_9 s_{10} s_{11} q_{16}$	$s_{10} s_{11} s_{12} q_{17}$

where

$$A = s_1 s_2 [\alpha s_3 (\gamma s_4 + \delta s_5) s_6 + \beta s_7 s_8] q_9, \quad B = s_2 \alpha s_3 (\gamma s_4 + \delta s_5) s_6 q_9,$$

$$C = s_1 s_2 [\alpha s_3 (\gamma s_4 + \delta s_5) s_6 + \beta s_7 s_8] s_9 q_{10}, \quad D = s_2 \alpha s_3 (\gamma s_4 + \delta s_5) s_6 s_9 q_{10}.$$

As a further example to show the directness of the method we shall choose the quite complicated series shown in Fig. 3 and write down  $U$ .

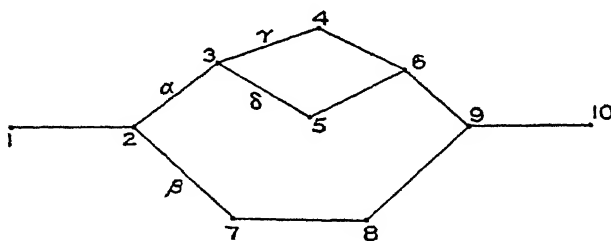


FIG. 3

The result is shown on p. 259.

It remains to remark that in carrying out the numerical computation of the partial matrices  $u_k$  we should take advantage of the recurrence of common factors and economize in the number of elementary operations of multiplication. This can be done by evaluating the  $s_m$  and  $q_m$  for a particular  $k$  and following the complete matrix  $U$  as a guide, after noting the elements to be put equal to zero in accordance with the rule given above.

### References

1. BERG, C. J. Heaviside's operational calculus as applied to engineering and physics. 2nd ed. McGraw-Hill Book Co., Inc., New York. 1936.
2. CARSLAW, H. S. and JAEGER, J. C. Operational methods in applied mathematics. Oxford University Press, New York. 1941.

# RATIO OF NEUTRON ABSORPTION CROSS-SECTIONS OF BORON AND HYDROGEN<sup>1</sup>

By W. J. WHITEHOUSE<sup>2</sup> AND G. A. R. GRAHAM<sup>3</sup>

## Abstract

Using a Ra- $\alpha$ -Be source and a small boron trifluoride chamber as detector, the ratio of the neutron absorption cross-sections of boron and hydrogen,  $\sigma_B/\sigma_H$ , has been measured by the integration method in water and in aqueous solutions of boric acid. The result is

$$\sigma_B/\sigma_H = 2270$$

with a statistical error of  $\pm 30$ . Subsidiary experiments have been made which fix at about 3% the upper limit of the systematic error caused by perturbation of the neutron density in the neighbourhood of the ionization chamber.

## Introduction

The integration method used in this experiment is due to Frisch, Halban, and Koch (4). Using a small boron-lined chamber as detector they obtained the result  $\sigma_B/\sigma_H = 1940 \pm 100$ , where  $\sigma_B$  and  $\sigma_H$  are the absorption cross-sections of boron and hydrogen. Fenning, Halban, and Seligman (3) repeated the measurement using boron trifluoride chambers as detectors and found the ratio  $\sigma_B/\sigma_H$  to be  $2160 \pm 30$ . In both measurements no correction has been applied to the final result for the perturbation by the detector of the neutron density in its neighbourhood.

Kubitschek (6, 7) has carried out an extensive series of measurements using thin manganese foils as detectors and found the ratio  $\sigma_B/\sigma_H$  to be  $2380 \pm 70$ . This result has been corrected for perturbation effects by an extrapolation to infinitely thin foils.

Recently Schulz and Goldhaber (8) have obtained the value  $\sigma_B/\sigma_H = 1954 \pm 24$ ; details of the method are not given.

In view of the diversity of results obtained in previous experiments it was decided to make still another determination of the ratio, using as detector a much smaller boron trifluoride chamber than that previously used. It was hoped, in particular, to remove the discrepancy between the results obtained with boron trifluoride chambers and with foils.

The theory of the experiment has been adequately treated in several papers (3, 4, 6, 7) and will not be reproduced in detail here. The neutron density ( $I$ ) is measured in an effectively infinite bath at a number of distances ( $R$ ) from a neutron source. The measurements are made first in distilled water and then in a dilute boric acid solution. (The neutron capture by oxygen is

<sup>1</sup> Manuscript received in original form November 6, 1946, and, as revised, May 1, 1947.

Contribution from the Nuclear Physics Branch, Montreal Laboratory, Atomic Energy Division of the National Research Council of Canada. Publication of this work done in 1945 has been delayed owing to security restrictions. Issued as N.R.C. No. 1573.

<sup>2</sup> Physicist, United Kingdom Staff; now at the Atomic Energy Research Establishment, Harwell, England.

<sup>3</sup> Assistant Research Physicist, National Research Council of Canada; now at the University of Rochester, Rochester, N.Y.

negligible.) If the  $1/v$  law of capture is obeyed by hydrogen and boron, the ratio of the capture cross-sections is independent of the velocity of the neutrons and is given by the formula:

$$\sigma_B/\sigma_H = \frac{C_H}{C_B} \left( \frac{S_H}{S_B} - \frac{C'_H}{C_H} \right), \quad (1a)$$

where

- $\sigma_B$  = absorption cross-section of boron,
- $\sigma_H$  = absorption cross-section of hydrogen,
- $C_H$  = volume concentration of hydrogen atoms in water,
- $C'_H$  = volume concentration of hydrogen atoms in the solution,
- $C_B$  = volume concentration of boron atoms in the solution,
- $S_H$  = area under curve  $IR^2$  vs.  $R$  for water,

and

- $S_B$  = area under curve  $IR^2$  vs.  $R$  for the solution.

Since  $C_H \simeq C'_H$  in this experiment, this formula may be written

$$\sigma_B/\sigma_H = \frac{C_H}{C_B} \left( \frac{S_H}{S_B} - 1 \right). \quad (1b)$$

(The error so introduced is less than 1 part in 500.)

### Scope of Present Experiments

The present experiments may be separated into the following sections:

- IA. (1) Measurement in distilled water,
- (2) Measurement in 1% boric acid solution,
- (3) Measurement in 2% boric acid solution.
- IB. (1) Measurement in distilled water,
- (2) Measurement in 0.4% boric acid solution,
- (3) Measurement in 3% boric acid solution.

(The measurements of Section IA were carried out using one boron trifluoride chamber, and those of Section IB with a different chamber of about the same dimensions.)

- II. Comparative measurements with boron trifluoride chambers and manganese foils.

### Measurements with Boron Trifluoride Chambers

A boron trifluoride chamber was chosen in preference to foils as a detector of neutrons for the principal measurement because of the advantages of very low background and the possibility of long uninterrupted counts. The chambers were constructed by Mr. N. Veall (10). They had the dimensions 0.4 cm. in diameter, 1.5 cm. long, and were filled with boron trifluoride to 1.5 atm. The chamber was mounted on a brass tube (diameter, 0.5 cm.), the opposite end of which was attached to the carriage supporting the head amplifier. The carriage rode upon two rails, which were part of a rigid steel framework. The latter also supported the source on another carriage. The source and

chamber were arranged with their centres on a horizontal line corresponding to the central axis of the tank, which was contained within the framework. For convenience the distance between the chamber and source was varied by moving the source only. The separation, chamber to source, could be read from a mirror scale attached to the framework using indicators fixed to the two carriages. The scale was first calibrated by measuring the separation with a cathetometer at several distances.

The tank containing the solutions was made of stainless steel. Its cross-section had a U-shape, and the dimensions were: length 78 cm., width 40 cm., and greatest depth 41 cm. A second tank, rectangular in shape (87 by 42 by 42 cm.) contained ordinary water, to be used for check measurements. The whole frame, bearing source and chamber, could be moved readily from one tank to the other. The conventional linear amplifier, discriminator, and scaling units were used to count the impulses from the chamber.

For intensity reasons and to eliminate the effect of ' $\gamma$ -noise' two Ra- $\alpha$ -Be sources were used.

- (a) A 110 mgm. source, contained in a thin brass cylinder approximately 3 cm. long and 1.3 cm. in diameter, was used for measurements up to a separation of 12 cm.
- (b) A 600 mgm. source, contained in a thin brass cylinder approximately 3 cm. long and 2.3 cm. in diameter, was used for all measurements with separations greater than 12 cm.

The ratio of the neutron intensities of the two sources was measured and all readings adjusted to values appropriate to the smaller source (see below).

The solutions were prepared in the stainless steel tank by dissolving a weighed quantity of Baker's analytical boric acid in a measured volume of distilled water. The concentrations were determined chemically by Mr. A. C. English and Mr. A. H. Booth of the Chemistry Branch. A description of their analyses is contained in Appendix I.

The intensity  $I$  (counts per min.) was measured at various distances  $R$  (separation source - chamber in cm.). The readings are given in full in Tables I and II, together with the statistical accuracy of each count. The readings in Column 4 have all been adjusted by multiplying by the ratio of the neutron intensities of the two sources.

The results are also presented graphically in Figs. 1 and 2, where the graphs are smaller and less accurate than those under which the areas were actually measured. The constancy of the counting apparatus was checked frequently by a measurement at the closest point. A further check was made by measurements in the auxiliary tank of water each day. Some drift occurred within a few hours of switching on the electronic equipment, but subsequently no drift could be detected within the statistical accuracy of the counts (usually 1%). The apparatus ran continuously during the course of each experiment.

In certain cases the separation  $R$  was slightly different for the two sources, and to allow for this difference an adjustment to  $I$ , based on the graph of

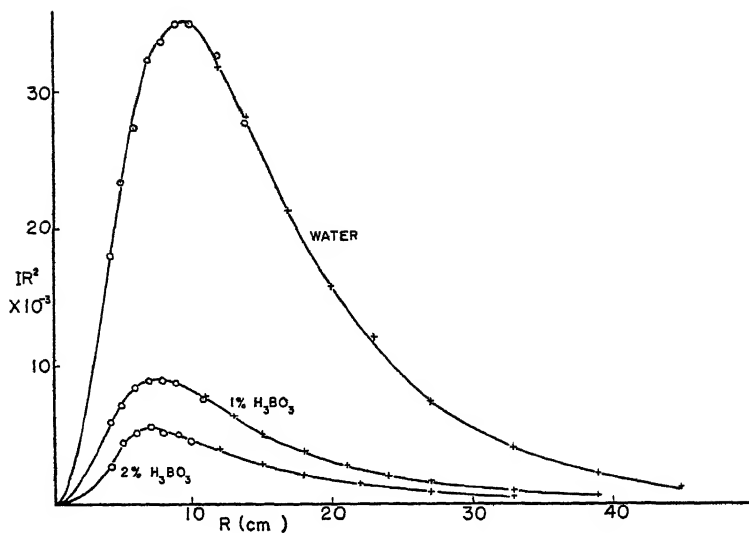


FIG. 1. Distribution of neutron density,  $I$ , multiplied by  $R^2$ . Circles indicate measurements with 110 mgm. source; crosses those with 600 mgm. source.

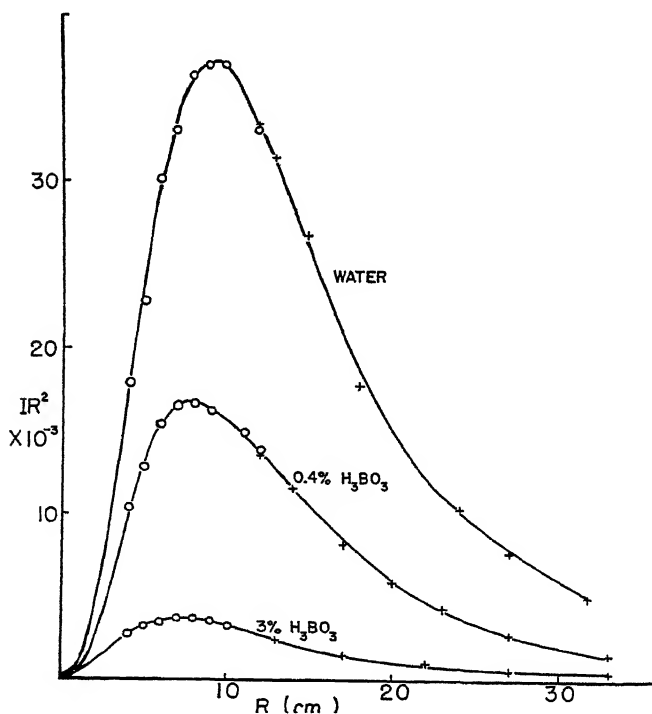


FIG. 2. Distribution of neutron density,  $I$ , multiplied by  $R^2$ . Circles indicate measurements with 110 mgm. source; crosses those with 600 mgm. source.

TABLE I

READINGS WITH BORON TRIFLUORIDE CHAMBER, TAKEN IN EXPERIMENT IA

Source	$R$ , cm.	$I$ , Counts/min.	$I$ , Adjusted	$IR^2 \times 10^{-3}$	Statistical error, %
<i>Medium: Water</i>					
110 mgm.	4.1	1077	—	18.1	1
"	4.9	975	—	23.4	1
"	5.9	810	—	27.3	1
"	6.9	677	—	32.2	1
"	7.9	538	—	33.6	1
"	8.9	440	—	34.8	1
"	9.9	356	—	34.9	1
"	10.9	280	—	33.2	1
"	11.9	229*	—	32.5	1
"	13.9	143*	—	27.6	1
"	16.9	74.5*	—	21.4	1
600 mgm.	12.0	1203*	220.5	31.7	1
"	14.0	780*	143	28.0	1
"	17.0	400*	73.2	21.1	1
"	20.0	—	39.2	15.7	1½
"	23.0	—	22.7	12.0	1½
"	27.0	—	10	7.3	1½
"	32.9	—	3.7	4.0	3
"	38.9	—	1.46	2.2	6
"	44.9	—	0.62	1.2	13
<i>Medium: 1% boric acid solution (10.07 gm. per litre)</i>					
110 mgm.	4.1	492	—	5.86	1
"	4.9	297	—	7.14	1
"	5.9	239	—	8.34	1
"	6.9	185	—	8.80	1
"	7.9	142	—	8.85	1
"	8.9	110	—	8.72	1
"	10.9	64.2*	—	7.63	1
600 mgm.	11.0	345*	63.2	7.66	1
"	13.0	—	37.1	6.27	1
"	15.0	—	22.3	5.02	1
"	18.0	—	11.5	3.73	1½
"	21.0	—	6.1	2.69	1½
"	24.0	—	3.36	1.94	3
"	27.0	—	2.18	1.59	3½
"	32.9	—	0.75	0.81	5
"	38.9	—	0.34	0.51	13
<i>Medium: 2% boric acid solution (20.2 gm. per litre)</i>					
110 mgm.	4.1	213	—	3.58	1
"	5.0	174.5	—	4.36	1
"	6.0	137.5	—	4.95	1
"	7.0	105.5	—	5.47	1
"	8.0	80.4	—	5.14	1
"	9.0	61.7	—	5.00	1
"	10.0	45.2	—	4.52	1
600 mgm.	12.0	—	26.7	3.84	1
"	15.0	—	12.35	2.78	1½
"	18.0	—	6.14	1.98	2½
"	22.0	—	2.72	1.31	2
"	27.0	—	1.09	0.80	3½
"	33.0	—	0.40	0.44	8½

$\log I$  vs.  $R$ , has been applied to obtain the proper ratio. The readings from which the ratio of the strengths of the two sources was obtained are marked with an asterisk in Tables I and II. They are collected in Table III.

TABLE II

READINGS WITH BORON TRIFLUORIDE CHAMBER TAKEN IN EXPERIMENT IB

Source	$R$ , cm.	$I$ , Counts/min.	$I$ , Adjusted	$IR^2 \times 10^{-3}$	Statistical error, %
<i>Medium: Water</i>					
110 mgm.	4.1	1122	—	18.9	1
"	5.0	994	—	24.8	1
"	6.0	826	—	30.1	1
"	7.0	673	—	33.0	1
"	8.0	554	—	36.4	1
"	9.0	454	—	36.8	1
"	10.0	369	—	36.9	1
"	11.0	292	—	36.3	1
"	12.0	229*	—	33.0	1
600 mgm.	12.0	1277*	232.5	33.4	1
"	13.0	—	186.5	31.4	1
"	15.0	—	118.5	26.7	1
"	19.0	—	49.0	17.7	1
"	24.0	—	18.0	10.4	1
"	27.0	—	10.5	7.7	1 $\frac{3}{4}$
"	31.8	—	4.5	4.9	3
<i>Medium: 0.4% boric acid solution (4.02 gm. per litre)</i>					
110 mgm.	4.1	607	—	10.25	1
"	5.0	513	—	12.8	1
"	6.0	426	—	15.35	1
"	7.0	337	—	16.5	1
"	8.0	260	—	16.6	1
"	9.0	201	—	16.25	1
"	11.0	123	—	14.9	1
"	12.0	96*	—	13.8	1
600 mgm.	12.0	515*	93.8	13.5	1
"	14.0	—	58.9	11.55	1
"	17.0	—	28.5	8.25	1
"	20.0	—	14.7	5.9	1 $\frac{1}{2}$
"	23.0	—	8.2	4.33	2
"	27.0	—	3.82	2.7	2 $\frac{1}{2}$
"	33.0	—	1.47	1.6	3
<i>Medium: 3% boric acid solution (30.17 gm. per litre)</i>					
110 mgm.	4.1	159	—	2.67	1
"	5.0	126.5	—	3.16	1
"	6.0	95.9	—	3.49	1
"	7.0	76.0	—	3.72	1
"	8.0	58.6	—	3.75	1
"	9.0	43.8	—	3.55	1
"	10.0	32.9	—	3.29	1
600 mgm.	13.0	—	14.6	2.47	1
"	17.0	—	5.66	1.63	1
"	22.0	—	1.98	0.96	2
"	27.0	—	0.84	0.61	3
"	33.0	—	0.41	0.45	4 $\frac{1}{2}$

TABLE III

RATIO OF INTENSITIES OF THE TWO SOURCES

Medium	110 mgm. source			600 mgm source		Ratio $\frac{110 \text{ mgm. source}}{600 \text{ mgm. source}}$
	$R$ , cm.	$I$ , Counts/min	$I$ , Adjusted	$R$ , cm.	$I$ , Counts/min.	
H <sub>2</sub> O	11.9	229	224	12.0	1203	0.186
H <sub>2</sub> O	13.9	143	140	14.0	780	0.180
H <sub>2</sub> O	16.9	74.5	72.8	17.0	400	0.182
1% H <sub>3</sub> BO <sub>3</sub>	10.9	64.2	61.7	11.0	345	0.179
H <sub>2</sub> O	12.0	229	229	12.0	1277	0.179
0.4% H <sub>3</sub> BO <sub>3</sub>	12.0	96	96	12.0	515	0.186
						$0.182 \pm 0.0012 \text{ (s.d.)}$

The error to be attributed to the measured ratio  $\sigma_B/\sigma_H$  in each case was determined from the individual errors. Let the percentage errors in the separate quantities be as follows:  $\epsilon$  in  $\sigma_B/\sigma_H$ ,  $\alpha_1$  in  $S_H$ ,  $\alpha_2$  in  $S_B$ ,  $\gamma_1$  in  $C_H$ , and  $\gamma_2$  in  $C_B$ . The following formula was used to combine the errors:

$$\epsilon^2 = \gamma_1^2 + \gamma_2^2 + \left( \frac{S_H}{S_H - S_B} \right)^2 (\alpha_1^2 + \alpha_2^2). \quad (2)$$

The errors in the concentrations are given in Appendix I. However, since a small amount of evaporation and replacement of water occurred during the course of each experiment, an accuracy of only  $\pm 0.5\%$  is claimed in the concentration, although the chemical analysis is more accurate than this.

In estimating the error to be attributed to the area under each density distribution curve several factors must be considered.

- (a) Since all the important points on the curves have a statistical accuracy of 1%, the error in the area will be much less on this account. The error in  $R$  is negligible, cathetometer measurements indicating an accuracy of  $\pm 0.05$  cm. Since the boron trifluoride chamber has a small cross-sectional area, the measured separation,  $R$ , from the centre of chamber to centre of source may be used without correction. The use of two sources may also introduce a small error of the order of  $\frac{1}{2}\%$ , but this affects each area equally and does not contribute fully to the final result. We have allowed an error of 1% in the area in each case for all the above factors including any possible drift of the counting apparatus.
- (b) Secondly, the exponential nature of the curve for  $R > 20$  cm. approximately, was investigated fully only in the case of the first water curve, for which the relaxation length is 10.1 cm. In the other cases the relaxation lengths agree within 5% with this value in the portions of the curves measured. In each case an extrapolation has been made beyond the last measured point using this value of the relaxation length.

The error in the area under the tail of the curve has been estimated taking 5% error in the relaxation length together with the statistical error of the last measured point on the curve.

- (c) Lastly, since we were unable to measure at separations less than  $R = 4.1$  cm. because of 'γ noise', the portion of the curve near the origin has been drawn on the basis of previous experience. This introduces an additional error for which we have allowed arbitrarily.

In Table IV, Columns (a), (b), and (c) give the percentage errors attributed to the causes discussed in the similarly lettered paragraphs above. The total error\*  $\alpha$  in the area, given by

$$\alpha^2 = a^2 + b^2 + c^2, \quad (3)$$

is entered in Column 5. The error in the corresponding value of  $\sigma_B/\sigma_H$  is given in the last column.

TABLE IV  
ERRORS IN DETERMINATION OF  $\sigma_B/\sigma_H$

Curve	Percentage errors in areas				$\epsilon, \%$
	Drift, etc. (a)	Tail (b)	Portion near origin (c)	Total $\alpha$	
1st H <sub>2</sub> O	1	0	0	1	—
1% H <sub>3</sub> BO <sub>3</sub>	1	0.72	0	1.25	2.2
2% H <sub>3</sub> BO <sub>3</sub>	1	0.8	0.5	1.35	2.1
2nd H <sub>2</sub> O	1	0.6	0	1.20	—
0.4% H <sub>3</sub> BO <sub>3</sub>	1	0.7	0	1.20	2.8
3% H <sub>3</sub> BO <sub>3</sub>	1	0.8	1	1.7	2.3

The final results calculated on the basis of Equation (1b) are contained in Table V.

TABLE V

Expt.	Solution	$C_H$ , gm-atoms/litre	$C_B$ , gm-atoms/litre	$S_H$ arbitrary	$S_B$ units	$\sigma_B/\sigma_H$
IA	H <sub>2</sub> O	111	0	60.72	—	—
	1% H <sub>3</sub> BO <sub>3</sub>	111	0.1628	—	14.11	2250 ± 50
	2% H <sub>3</sub> BO <sub>3</sub>	111	0.327	—	7.99	2240 ± 45
IB	H <sub>2</sub> O	111	0	64.03	—	—
	0.4% H <sub>3</sub> BO <sub>3</sub>	111	0.0650	—	26.95	2350 ± 65
	3% H <sub>3</sub> BO <sub>3</sub>	111	0.488	—	5.81	2280 ± 50

\* The error  $\alpha$  stands for  $\alpha_1$  or  $\alpha_2$ , as defined above.

Taking the weighted mean we arrive at the result:

$$\sigma_B/\sigma_H = 2270 \pm 30.$$

It must be emphasized that this result is not corrected for perturbation effects due to the detector.

### Comparative Measurements with Boron Trifluoride Chamber and Manganese Foils

In the experiments to be described here the ratio of the readings of the boron chamber and of an 'ideal' detector is measured in water and in a 1% boric acid solution. If there were no perturbation of the neutron density owing to the absorption by, and the finite size of, the boron chamber, we would expect this ratio to be independent of the medium. Further, since both detectors obey the  $1/v$  law of capture we would expect the ratio also to be independent of the velocity distribution of the neutrons, i.e., in this case, of the distance from the source.

Manganese foils can be considered as 'ideal' detectors only after two conditions are fulfilled. (1) The foils must be so thin that there is no disturbance of the neutron density in the neighbourhood, or else a correction for this disturbance must be applied. (2) A correction must be made for the resonance absorption of manganese. The first condition is met in these experiments by choosing very thin foils. Activation measurements are consequently limited to points of high neutron density. The correction for resonance activity is described later. It introduces a factor of the order of 3% in a 1% boric acid solution, and would become serious in the stronger solutions. The activation measurements have therefore been restricted to water and a 1% boric acid solution. The small statistical errors and good agreement of the results in Table V show that the perturbation by the boron chamber does not vary significantly from one solution to another.

Two foils of manganese alloy were used, each 2 by 1.6 cm. and having a mass of 0.02 gm. per cm.<sup>2</sup> Calculations based on a formula given by Skyrme (9) show that these foils produce negligible perturbation of the neutron density in the aqueous media. The foils were mounted upon bakelite plates of thickness 0.38 mm., which had machined edges, and could be accurately held in position near the Geiger-Müller counter by a spring mechanism. During the irradiation in the liquids the detectors were held in frames of beryllium-copper wire of diameter 0.51 mm. In a subsidiary experiment it was shown that the bakelite plates caused no perturbation of the neutron density in the aqueous media. The foils were covered with a thin layer of cellulose cement to prevent oxidation.

All counts were made to a statistical accuracy of about 1%. (Actually 7500 particles was the smallest number counted.) Thus the statistical error in the comparison between the boron trifluoride chamber and the foil is about 2%, and to this must be added an error of the order of 1% due to possible differences in position.

Owing to the small size of the manganese foils, their activities acquired when shielded by cadmium were too small for measurement. Instead, Kubitschek's experimental results (6, 7) for the cadmium difference were used in the calculation of our resonance correction.

The correction for resonance absorption in manganese requires an estimate, experimental or otherwise, of the percentage of neutrons having energies above the cadmium cut-off, which exist in the whole space surrounding the source. A measurement, made in paraffin oil, with a boron trifluoride chamber under cadmium, gave this quantity as 0.93% (2). Since the scattering and absorption of neutrons, both in water and paraffin oil, are mainly due to hydrogen, the same percentage may be used for water.

If the scattering and capture mean free paths are compared with each other both in water and a 1% boric acid solution, for neutrons at various energies above the cadmium cut-off, it is found that the capture mean free path is the greater. Even at the cadmium cut-off the scattering mean free path in water is about 0.5 cm., while the capture mean free path in a 1% boric acid solution is about 10 cm. Neutrons are therefore removed from the energy region above the cadmium limit almost exclusively by scattering. It is reasonable therefore to assume that the actual *number* of neutrons having energies above the cadmium limit in the space surrounding a given source is almost the same in dilute boric acid solutions as in water.

The total *number* of neutrons in the medium is  $Q\tau$ , where  $Q$  is the number of neutrons per second emitted by the source, and  $\tau$  is the mean lifetime of the neutrons in the medium concerned. It follows, therefore, that the *percentage* of neutrons with energies above the cadmium limit in the boron solution is  $0.93 \tau_H/\tau_B$ , where  $\tau_H$  and  $\tau_B$  are the mean lifetimes of neutrons in water and the boric acid solution respectively. This value is entered under Method I in Column 4 of Table VI. A more detailed calculation is not easy to make with accuracy, owing to the uncertain nature of the available constants, particularly the variation of the scattering cross-section of hydrogen in water with the energy of the neutrons.

An alternative method of estimating the percentage of neutrons above the cadmium limit is as follows. Let  $P$  be the probability that a neutron escapes capture during the slowing-down process to the energy of the cadmium cut-off in the boric acid solution. The number  $QP$  of neutrons per second reach the cadmium limit, and may be regarded as a source of slow neutrons. Hence the number of slow neutrons is  $QP\tau$ , and the percentage below the cadmium cut-off is  $100P$ . The probability  $P$  was calculated from Equation (2) of Appendix II. The results obtained by this method are shown in Column 5 of Table VI. The agreement between the two different methods is satisfactory (Columns 4 and 5).

Kubitschek (7) gives a graph of the neutron distribution ( $IR^2$ ) measured in water by a manganese foil under cadmium. The area under this curve is not a correct measure of the total number of neutrons with energies above

TABLE VI

Medium	Molar fraction of boron	$\tau$ , sec.	Percentage of neutrons above cadmium limit	
			Calculated by Method I	Calculated by Equation (2) of Appendix II
Water	—	$219 \times 10^{-8}$	0.93	0.90
1% $\text{H}_3\text{BO}_3$	$1.455 \times 10^{-3}$	$51 \times 10^{-8}$	4.00	3.88

the cadmium limit, but is an overestimate owing to the extra sensitivity of the manganese foil for neutrons of resonance energy. In fact the area under this curve is 1.7% of the area obtained when the C-group of neutrons is considered, whereas it should be about 0.9% (Table VI). We may artificially divide the neutrons absorbed by a manganese foil in water into the following three groups. (1) A fraction  $t$  is absorbed with energies below the cadmium cut-off according to the  $1/v$  law. (2) A fraction  $f$  is assumed to be absorbed with energies above the cadmium cut-off according to the  $1/v$  law. (3) A fraction  $r$  is assumed to be absorbed in the resonance band. We have now the following approximate relations between  $t$ ,  $f$ , and  $r$ :

$$\frac{f}{t+f} = \frac{0.93}{100}; \quad \frac{f+r}{t} = \frac{1.7}{100}; \quad f+t+r = 1; \quad (4)$$

whence

$$t = 0.984, \quad f = 0.009, \quad r = 0.007, \quad \frac{r}{f+r} = 0.44. \quad (5)$$

We shall now assume that the fractions  $f$  and  $r$ , which refer to the population of neutrons, can also be applied to each reading of the manganese foil, no matter what its distance from the source may be. This amounts to an assumption that the spatial distribution of epithermal neutrons of all energies is the same, i.e., that the amount by which the cadmium-enclosed foil overestimates the neutron density is independent of position. Within the very wide limits of accuracy sufficient in applying this correction, the assumption is permissible. (See, for example, the curves of the distribution of neutrons of several energies in water around a point source, obtained by Amaldi and Fermi (1).)

It is now possible to correct the reading of a manganese foil to that of an ideal detector, simply by subtracting the fraction  $r$  from its reading. This is done in Table VII. The figures in the first three columns were obtained by Kubitschek (7). Both Kubitschek's and our notation are given in the headings to this table.

The results of comparative experiments with manganese foils and the boron trifluoride chamber are given in Table VIII, where the counts for the boron trifluoride chamber are in the same units as in Tables I and II. (The readings in Tables I and II and VIII do not agree exactly owing to readjustment of the

apparatus between experiments.) The counts given by the foils are in arbitrary units, being expressed in terms of a standard  $\beta$ -ray source. The resonance correction has been explained above.

TABLE VII

Distance from source	Intensity measured with bare Mn foil	Intensity measured by Mn foil under Cd	$r$	Resonance Correction
$\sqrt{r^2}$	$A_{\text{bare}}$	$A_{\text{res}}$		$r/(t + f + r)$
$R$ , cm.	$t + f + r$	$f + r$		
2.19	21620	798	350	0.016
4.10	17650	478	210	0.012
6.06	12600	286	126	0.010
8.05	8361	142	62	0.0074
10.04	5320	72	32	0.0060
12.03	3340	55	24	0.0072
10.18	36010	554	244	0.0068
10.18	35780	550	242	0.0068
10.18	35680	550	242	0.0068
20.09	3954	48	21	0.0053
20.09	3945	47.7	21	0.0053
20.09	4026	47.7	21	0.0052

$R$ , cm.	5.8	7	12
$r/(t + f + r)$ interpolated	0.010	0.008	0.0055

TABLE VIII

Distance from source, cm.	Medium	Count $I_{Ch}$ with $BF_3$ chamber	Count with Mn foils					$\frac{I_{Ch}}{I_{Mn}}$	$K = \frac{(I_{Ch}/I_{Mn})B}{(I_{Ch}/I_{Mn})H_2O}$
			First foil	Second foil	Mean $t+f+r$	$r$	$t+f$		
12	Water	1240	531	525	528	3	525	2.36	1.03
	1% $H_3BO_3$	267	110	115	113	3	110	2.43	
5.8	Water	835	340	347	344	3	341	2.45	1.03
	1% $H_3BO_3$	250	102	102	102	3	99	2.53	
12	Water	1220	513	506	510	3	507	2.41	1.03
	1% $H_3BO_3$	272	114	112	113	3	110	2.47	
7	Water	665	274	269	272	2	270	2.46	0.975
	1% $H_3BO_3$	187	78.7	80.8	79.7	2	79.9	2.40	

From the last column it is seen that the mean of the ratio  $K$ , of  $I_{Ch}/I_{Mn}$  in boric acid solution to  $I_{Ch}/I_{Mn}$  in water, is not significantly different from unity.

The accuracy of these experiments is only sufficient to show that the perturbation error, if it exists, is less than  $\pm 3\%$ . Greater accuracy could have been obtained only by a long series of experiments which would have been very largely a duplication of Kubitschek's work (7). We do not consider it justifiable to make any modification to our result for  $\sigma_B/\sigma_H$  on the basis of the results shown in Table VIII.

### Conclusion

The result of the integration experiment with the boron trifluoride chamber,

$$\sigma_B/\sigma_H = 2270,$$

has a statistical error of approximately 1%. The systematic error that might exist because of perturbation by the boron trifluoride chamber of the neutron density has been shown to be less than 3% if it exists. It is, therefore, not felt justifiable to correct the ratio given above on this account.

Within the errors of measurement this result is in agreement with Kubitschek's (7), and it is felt that the former discrepancy between measurements with boron trifluoride chambers and with foils has been removed.

In view of the difficulties inherent in the method used in the experiment, it is considered improbable that, in a reasonable time, the method would yield a value more accurate than either of the above results.

### APPENDIX I

#### Analyses of Boric Acid Solutions

By A. H. BOOTH AND A. C. ENGLISH

Standard solutions of Analar boric acid were made up at the concentrations of the samples to be analysed so that in no case was the difference greater than 1%. Standard and sample were then estimated by the titration of the boric acid, in the presence of excess glycerine, by sodium hydroxide to the phenolphthalein end-point. The same pipette was used for both and the same burette over the same range. Quantities of glycerine and phenolphthalein added were constant and the end-point was taken by comparing the pink colour in 100 ml. Nessler tubes.

Using this technique, the absolute value obtained is dependent solely on the graduated flask, the weighing of the boric acid and its quality.

The average deviation of single titrations was less than 0.05 ml in 40 ml. and the errors given are obtained by combining titration figures for standard and sample in the most unfavourable manner.

The results were:  $(0.402 \pm 0.001)\%$  for 0.4% solution,  $(1.007 \pm 0.002)\%$  for 1% solution,  $(2.020 \pm 0.005)\%$  for 2% solution, and  $(3.017 \pm 0.007)\%$  for 3% solution.

## APPENDIX II

## Calculation of the Probability that a Neutron Escapes Capture During the Slowing-down Process

The following formulae are essentially the same as those used by Kubitschek (6, 7) and are derived from the work of Wigner (11).

The probability  $P$  that a neutron escapes capture during the process of slowing-down from an initial energy  $E_I$  to the energy  $E_{Cd}$  of the cadmium cut-off in a boric acid solution may be written as follows:

$$P = \exp \left\{ - \int_{E_{Cd}}^{E_I} \frac{\sigma_B(E)C_B + \sigma_H(E)C_H}{\sigma_s C_H} \frac{dE}{\xi E} \right\} \quad (1)$$

where  $\sigma_B(E)$  and  $\sigma_H(E)$  are the absorption cross-sections of boron and hydrogen, respectively, at energy  $E$ ,  $\sigma_s$  the scattering cross-section of hydrogen,  $C_B$  and  $C_H$  the concentrations of boron and hydrogen respectively, and  $\xi$  the average logarithmic energy loss for neutron collisions with hydrogen. The effect of the oxygen has been neglected.

Writing  $\sigma(E) = \sigma(kT) \sqrt{E_{kT}/E}$  for the absorption cross-sections of boron and hydrogen, and assuming that  $\sigma_s$  and  $\xi$  are constant, we obtain the approximate formula:

$$P = \exp \left\{ - \frac{2}{\xi \sigma_s} \sqrt{\frac{E_{kT}}{E_{Cd}}} \left[ \sigma_B(kT) \frac{C_B}{C_H} + \sigma_H(kT) \right] \right\}. \quad (2)$$

This formula is used to calculate the percentage of neutrons in the solution that have energies below that of the cadmium cut-off. The following numerical values, partly taken from Goldsmith's tables (5), were used in the calculations:

$$E_{kT} = 0.025 \text{ ev.}, \quad E_{Cd} = 0.3 \text{ ev.}$$

$$\sigma_B(kT) = 705 \times 10^{-24} \text{ cm.}^2 \text{ per atom,}$$

$$\sigma_H(kT) = 0.31 \times 10^{-24} \text{ cm.}^2 \text{ per atom,}$$

$$\xi = 1,$$

$$\sigma_s = 20 \times 10^{-24} \text{ cm.}^2 \text{ per atom.}$$

The last is an approximate average value for neutrons with energies greater than 0.3 ev.

## References

1. AMALDI, E. and FERMI, E. Phys. Rev. 50 : 899-928. 1936.
2. ELLIOTT, L. G. Private communication.
3. FENNING, F. W., HALBAN, H. v., JR., and SELIGMAN, H. Unpublished report, Br-135. The ratio between absorption cross-sections of boron and hydrogen. British Atomic Energy Project. 1943.
4. FRISCH, O. R., HALBAN, H. v., JR., and KOCH, J. Kgl. Danske Videnskab. Selskab. Math.-fys. Medd. 15 (10) : 1-37. 1938.
5. GOLDSMITH, H. H. Unpublished report, CL-697. A critical survey of neutron cross-sections. Manhattan District Project. 1944.
6. KUBITSCHKE, H. Unpublished report, CP-972. Absorption cross-section ratio of boron and hydrogen. Manhattan District Project. 1943.

7. KUBITSCHKE, H. Unpublished report, CP-1824. Absorption cross-section ratio of boron to hydrogen. Manhattan District Project. 1944.
8. SCHULZ, L. G. and GOLDBERGER, M. Phys. Rev. 67 : 202. 1945.
9. SKYRME, T. H. R. Unpublished report, MS-91. Reduction in neutron density caused by an absorbing disc. British Atomic Energy Project. 1944.
10. VEALL, N. Unpublished report, MP-60. On the construction of small boron chambers. National Research Council of Canada. 1944.
11. WIGNER, E. P. Unpublished report, C-1. Discussion of the homogeneous and lattice arrangements for power plants. Manhattan District Project. 1942.

# A THEOREM ON NEUTRON MULTIPLICATION<sup>1</sup>

BY G. PLACZEK<sup>2</sup> AND G. VOLKOFF<sup>3</sup>

## Abstract

The asymptotic behaviour of the neutron distribution due to a point source in an infinite homogeneous medium in which a convergent chain reaction (multiplication constant  $k < 1$ ) takes place is investigated without special assumptions about the properties of the medium and the mechanism of neutron diffusion. It is shown under very general assumptions that at large distances  $r$  from the point source the neutron distribution always has the form

$$\frac{A}{r} \exp(-\mu r).$$

General expressions for the constants  $\mu$  and  $A$  of this asymptotic form of the distribution are given for any  $k < 1$  in terms of the Fourier transform of the spatial distribution of primary fission neutrons. These expressions reduce to particularly simple form for  $(1 - k) \ll 1$ . The exact expression for the neutron distribution throughout the medium is given in integral form. Four special frequently occurring cases are discussed as illustrations of the general result.

## 1. Introduction

This paper reports work done at the Montreal Laboratory, National Research Council of Canada, in 1943 and early 1944. An investigation is made of the behaviour far from a source of the neutron distribution in an infinite homogeneous medium in which a convergent chain reaction (multiplication factor  $k < 1$ ) takes place.

The discussion is restricted to the simplest case of a plane source of neutrons at  $z = 0$  since once the neutron distribution is known for this case the point source neutron distribution in an infinite medium may be obtained from it in the usual manner by differentiation. The neutron distribution in an infinite medium corresponding to any other arbitrary source distribution may then be expressed in terms of the point source distribution.

The problem of finding the neutron distribution due to a plane source in an infinite multiplying medium is formulated in Section 2 in terms of an inhomogeneous integral equation. In Section 3 an elementary method of finding the approximate solution for  $(1 - k) \ll 1$  is given. In Section 4 the exact solution for any  $k < 1$  is obtained in integral form, and its asymptotic expression is shown to be of the form  $C \exp(-\mu |z|)$  at distances  $|z|$  from the plane source large compared to a characteristic length  $M$  (defined below in Section 2) for the diffusion of neutrons of a single generation. The theorem proved in Section 4 is that this exponential form of the asymptotic solution is *independent* of detailed assumptions about the nature of the medium and of

<sup>1</sup> Manuscript received February 17, 1947.

Contribution from the Division of Atomic Energy, National Research Council of Canada, Chalk River, Ont. Issued as N.R.C. No. 1576.

<sup>2</sup> Formerly with the Montreal Laboratory, National Research Council; now with the Research Laboratory, General Electric Company, Schenectady, New York.

<sup>3</sup> Formerly with the Montreal and Chalk River Laboratories of the National Research Council; now Professor of Physics, University of British Columbia, Vancouver, B.C.

the process of neutron diffusion. The value of the ratio of the relaxation length  $1/\mu$  of this asymptotic solution to the characteristic length  $M$  referred to above depends, for a general  $k < 1$ , not only on the value of  $k$  but also on the mechanism of diffusion of a single generation of neutrons, e.g., on the nature of the slowing down mechanism. However, as  $k \rightarrow 1$  this ratio approaches  $(1 - k)^{-1/2}$  *independently* of the mechanism assumed. Likewise the value of  $C$  as  $k \rightarrow 1$  is found to approach

$$C = \frac{Qs}{2M\sqrt{1 - k}}, \quad (1.1)$$

(where  $Q$  is the source strength and  $s$  is a constant defined in Section 2) independently of the nature of the diffusion mechanism assumed, although the dependence of  $C$  on  $k$  for general values of  $k < 1$  is affected by the diffusion mechanism.

In Section 5 four special cases based on specific models of the diffusion of a single generation of neutrons are discussed. Explicit expressions for the constants in the asymptotic form of the solution of the integral equation in these four cases are given as illustrations of the general theorem.

## 2. Formulation of the Problem

We define  $G(|z|)dz$  to be the number of *primary* fission neutrons of all energies created (as the result of direct absorption of source neutrons only) between  $z$  and  $z+dz$  per neutron emitted by a plane source of neutrons placed at  $z = 0$  in the multiplying medium.  $G(|z|)$  will depend on the properties of the multiplying medium with respect to the diffusion, capture, relative fission probability, and neutron yield for neutrons of various energies, and also on the form of the energy distribution of source neutrons (see Appendix). Let  $G_s(|z|)$  be the particular expression for  $G(|z|)$  corresponding to a source of some specified neutron energy spectrum in a given medium. Similarly let  $G_f(|z|)$  be the expression for  $G(|z|)$  corresponding to a fission source in the same medium. The use made below of a single function  $G_f(|z|)$  for fission sources involves the assumption that the form of the energy spectrum of fission neutrons is independent of the energy of the neutron which causes fission. This is the only restrictive assumption on the nature of the multiplication process required to set up the problem.

The integral of  $G(|z|)$  over all  $z$  gives the total number of primary fission neutrons per source neutron which may in general depend on the energy spectrum of the source. In particular the quantity

$$\int_{-\infty}^{+\infty} G_s(|z|) dz = s \quad (2.1)$$

for source neutrons may be different from

$$\int_{-\infty}^{+\infty} G_f(|z|) dz = k \quad (2.2)$$

for a fission source. The latter quantity  $k$  is defined as the multiplication factor.

We introduce for mathematical convenience

$$F(|z|) = \frac{1}{k} G_f(|z|), \quad (2.3)$$

which is normalized to unity:

$$\int_{-\infty}^{+\infty} F(|z|) dz = 1. \quad (2.4)$$

We use  $F(|z|)$  to define\* a characteristic length  $M$  (usually called a migration length) by means of

$$M^2 = \int_{-\infty}^{+\infty} \frac{z^2}{2} F(|z|) dz. \quad (2.5)$$

$M$  is therefore a measure of the distance a neutron on the average travels away from a plane source of fission neutrons before being captured to give rise to  $k$  primary fission neutrons.

We consider now the physical problem of a given plane source of strength  $Q$  introduced into an infinite multiplying medium and wish to determine the resulting neutron distribution. If we describe the neutron distribution by specifying the number  $f(z)dz$  of fission neutrons to which it gives rise per unit time between  $z$  and  $z+dz$  then  $f(z)$  must satisfy the simple inhomogeneous integral equation

$$f(z) = Q G_s(|z|) + k \int_{-\infty}^{+\infty} f(z') dz' F(|z - z'|), \quad (2.6)$$

since fission neutrons created at a rate  $f(z)dz$  in the interval between  $z$  and  $z+dz$  are due partly to the given source of strength  $Q$  at the origin (first term on the right) and partly to fission sources distributed throughout the infinite medium with a density  $f(z')$  (second term on the right).

If some other property of the neutron distribution were chosen to describe it, e.g., the number of fissions, or the number of neutron captures taking place per unit volume per unit time, then additional restrictive assumptions would have to be made in order to obtain a simple integral equation analogous to (2.6). Thus if the number of fissions per unit volume per unit time is taken as the variable describing the neutron distribution, then not only the *form* of the energy distribution but also the *average number*  $\nu$  of neutrons emitted in a fission process must be assumed to be independent of the energy of the neutrons causing fission (see Appendix). We therefore retain the rate of creation of fission neutrons  $f(z)$  as the variable describing the neutron distribution, and shall have  $f(z)$  in mind when speaking for the sake of brevity simply of neutron distribution.

\* The inclusion of the factor 2 in this definition for the sake of mathematical convenience later is in accord with general usage.

An integral property of  $f(z)$  follows immediately from integrating (2.6) over all  $z$  and applying (2.1) and (2.4):

$$\int_{-\infty}^{+\infty} f(z) dz = \frac{Qs}{1-k}. \quad (2.7)$$

This may also be obtained by summing the number of fission neutrons of all generations to which  $Q$  source neutrons give rise, viz.,  $Qs + Qsk + Qsk^2 + Qsk^3 + \dots$

### 3. Elementary Method of Obtaining the Approximate Solution of the Integral Equation for $(1-k) \ll 1$

If  $(1-k) \ll 1$  then many generations of neutrons will contribute to  $f(z)$ , and it seems plausible that  $f(z)$  will vary much more slowly with  $z$  than  $F(|z|)$  which describes a single neutron generation. It may be expected that this will be true even in the neighbourhood of the given source at the origin since for  $(1-k) \ll 1$  the effect of the given source will be swamped by that of the secondary sources of fission neutrons.

This difference in the rate of variation of  $f(z)$  and  $F(|z|)$  enables us to replace (2.6) approximately by a differential equation. We invert the convolution in (2.6) by introducing a new variable  $u = z - z'$ , and expand  $f(z - u)$  in a Taylor series about  $z$ . In place of (2.6) we obtain:

$$\begin{aligned} f(z) &= Q G_s(|z|) + k \int_{-\infty}^{+\infty} du F(|u|) \left[ f(z) - uf'(z) + \right. \\ &\quad \left. \frac{u^2}{2} f''(z) - \frac{u^3}{3!} f'''(z) + \frac{u^4}{4!} f^{iv}(z) \dots \right] \\ &= Q G_s(|z|) + k \left[ f(z) + M^2 f''(z) + \frac{m_4}{4!} f^{iv}(z) + \dots \right], \end{aligned} \quad (3.1)$$

where

$$m_4 = \int_{-\infty}^{+\infty} u^4 F(|u|) du. \quad (3.2)$$

The odd moments of  $F(|u|)$  are all zero. In view of our assumption, that  $f(z - u)$  changes but little over the region in which  $F(|u|)$  differs appreciably from zero, the successive terms in the square brackets of (3.1) must fall off rapidly, so that by keeping only the first few terms of the expansion we can approximately replace the integral equation (2.6) by a differential equation of low order. The boundary conditions on the solution of this differential equation are:

$$\begin{aligned} f(|z|) \rightarrow 0 \text{ for } |z| \rightarrow \infty, \text{ and } \left[ \frac{d^{2n+1} f(z)}{dz^{2n+1}} \right]_{z=0} \\ = Q \left[ \frac{d^{2n+1} G_s(z)}{dz^{2n+1}} \right]_{z=0} \quad (n = 0, 1, 2, \dots). \end{aligned} \quad (3.3)$$

The second part of (3.3) is obtained by differentiating (2.6) an odd number of times, setting  $z = 0$ , and noting that the resulting integrand is odd.

If we keep only the first two terms in the brackets of (3.1) and consistently let  $k \rightarrow 1$  we obtain the second order differential equation:

$$f''(z) - \frac{1-k}{M^2} f(z) = -\frac{Q G_s(|z|)}{M^2}. \quad (3.4)$$

The solution of (3.4) vanishing at infinity is

$$f(z) = C e^{-\sqrt{1-k} \frac{|z|}{M}} + S(|z|), \quad (3.5)$$

where

$$S(z) = -\frac{Q}{M\sqrt{1-k}} \int_{|z|}^{\infty} \sinh \left[ \sqrt{1-k} \frac{(z' - |z|)}{M} \right] G_s(|z'|) dz' \quad (3.6)$$

is the particular integral of (3.4) which falls off with increasing  $|z|$  at a rate determined by  $G_s(|z|)$  and represents the deviation of  $f(z)$  from the asymptotic exponential solution in the neighbourhood of the given source at the origin.

Since (3.6) falls off with increasing  $z$  at a rate comparable with that of  $G_s(|z|)$  and hence of  $F(|z|)$ , it can at best represent only an order of magnitude estimate\* of the actual deviation near the source of the solution of the integral equation (2.6) from its asymptotic exponential form. The reason for this is that although the expansion of (3.1) converges rapidly for the main slowly varying exponential part of  $f(z)$  it may converge only slowly, or not at all, for the small correction term  $S(|z|)$  which may vary as fast, or faster than  $F(|z|)$ . Therefore to determine  $C$  in (3.5) it is not safe to use  $f'(0) = Q G'_s(0)$  from (3.3), since we depend then on the accurate knowledge of  $S'(0)$ . It is preferable to determine  $C$  by applying (2.7) to (3.5) and neglecting\*\*  $\int_{-\infty}^{+\infty} S(|z|) dz$  in comparison with  $Qs/(1-k)$ . This gives

$$C = \frac{Qs}{2M\sqrt{1-k}}. \quad (3.7)$$

Since for  $(1-k) \ll 1$   $S(0)$  is smaller† than  $C$  by a factor  $\sqrt{1-k}$  and  $S(|z|)$  falls off faster than the exponential of (3.5), we may neglect  $S(|z|)$  everywhere and the approximate solution of (2.6) valid everywhere is

$$f(z) = C \exp(-\mu |z|), \quad (3.8)$$

with  $C$  given by (3.7) and  $\mu = \sqrt{1-k}/M$ .

\* The simple example of case I in Section 5 below shows that for  $\gamma < 1$  (3.6) may even have the wrong sign.

\*\* The order of magnitude of  $\int_{-\infty}^{+\infty} S(|z|) dz$  is  $2M_s S(0) \approx Qs M_s^2/M^2 \approx Qs$ , where  $M_s$  is the characteristic length associated with  $S(|z|)$  or  $G_s(|z|)$ .

† From (3.6) the order of magnitude of  $S(0)$  is  $Qs M_s/2M^2 \approx Qs/2M$ .

The point source solution  $\rho(r)$  is obtained from the plane source solution  $f(z)$  as follows (see reference (2)):

$$\rho(r) = -\frac{1}{2\pi r} \frac{df(r)}{dr} = -\frac{C}{2\pi r} \frac{d}{dr} \exp(-\mu r) = A \frac{\exp(-\mu r)}{r}, \quad (3.9)$$

where

$$A = \frac{C\mu}{2\pi}. \quad (3.10)$$

The value of the exponent  $\mu$  in (3.8) and (3.9), but not of the coefficient  $C$  or  $A$  in front, may be somewhat improved by retaining three terms in the second square brackets of (3.1) to give a fourth order differential equation:

$$\frac{m_4}{4!} f^{(iv)}(z) + M^2 f''(z) - \frac{1-k}{k} f(z) = -\frac{Q}{k} G(z). \quad (3.11)$$

Using the trial solution (3.8) for the complementary function we find that  $\mu$  must satisfy

$$\frac{m_4}{4!} \mu^4 + M^2 \mu^2 - \frac{1-k}{k} = 0, \quad (3.12)$$

which gives for the smallest root  $\mu$

$$\begin{aligned} \mu &= \frac{1}{M} \sqrt{\frac{\sqrt{1 + \frac{1-k}{k} \frac{m_4}{3! M^4}} - 1}{\frac{2m_4}{4! M^4}}} \\ &= \frac{\sqrt{1-k}}{M} \left[ 1 + \frac{1}{2} \left( 1 - \frac{m_4}{4! M^4} \right) (1-k) + 0 \{ (1-k)^2 \} \right]. \end{aligned} \quad (3.13)$$

#### 4. Solution of Integral Equation by Fourier Transforms. Asymptotic Behaviour of the Solution

Let  $\phi(\xi)$ ,  $\Phi(\xi)$ , and  $\Gamma_s(\xi)$  be respectively the Fourier transforms of  $f(z)$ ,  $F(|z|)$ , and  $G_s(|z|)$  defined by

$$\begin{aligned} \phi(\xi) &= \int_{-\infty}^{+\infty} f(z) e^{i\xi z} dz; \quad \Phi(\xi) = \int_{-\infty}^{+\infty} F(|z|) e^{i\xi z} dz; \\ \Gamma_s(\xi) &= \int_{-\infty}^{+\infty} G_s(|z|) e^{i\xi z} dz. \end{aligned} \quad (4.1)$$

Multiplying (2.6) by  $e^{i\xi z}$ , integrating over all  $z$ , and applying the convolution theorem to the integral on the right-hand side we obtain:

$$\phi(\xi) = Q\Gamma_s(\xi) + k\phi(\xi)\Phi(\xi). \quad (4.2)$$

Solving for  $\phi(\xi)$  we get

$$\phi(\xi) = Q \frac{\Gamma_s(\xi)}{1 - k\Phi(\xi)}, \quad (4.3)$$

which on inversion gives:

$$f(z) = \frac{Q}{2\pi} \int_{-\infty}^{+\infty} \frac{\Gamma_s(\xi) e^{-i\xi z} d\xi}{1 - k\Phi(\xi)}. \quad (4.4)$$

In order to determine the asymptotic behaviour of  $f(z)$  for large  $|z|$  we now investigate the poles of the integrand of (4.4) which lie at the roots of

$$\Phi(\zeta) = \frac{1}{k}, \quad (4.5)$$

and at the poles of  $\Gamma_s(\zeta)$  which are not at the same time poles of  $\Phi(\zeta)$ .

From their physical nature  $F(|z|)$  and  $G_s(|z|)$  are positive and even. We also assume that both  $F(|z|)$  and  $G_s(|z|)$  fall off at least exponentially at large  $|z|$  so that  $F(|z|)e^{\eta z}$  and  $G_s(|z|)e^{\eta z}$  are quadratically integrable in the whole interval  $-\infty < z < \infty$  for  $|\eta| < \eta_f$  and  $|\eta| < \eta_s$  respectively, where  $\eta_f$  and  $\eta_s$  are positive quantities characteristic of  $F(|z|)$  and  $G_s(|z|)$ . Considered as a function of the complex variable  $\zeta = \xi + i\eta$ ,  $\Phi(\zeta)$  defined by (4.1) has the following properties.

(a)  $\Phi(\zeta)$  is holomorphic in the strip  $|I(\zeta)| < \eta_f$ ,

$$(b) \Phi(\zeta) = \Phi(-\zeta), \quad \overline{\Phi(\zeta)} = \Phi(\bar{\zeta}), \quad (4.6)$$

which show that  $\Phi(\zeta)$  is real along both the real and the imaginary axes in the  $\zeta$  plane.

$$(c) \Phi(0) = 1, \quad \Phi''(0) = -2M^2, \quad \Phi^{(2n+1)}(0) = 0, \quad (4.7)$$

the first two relations following from (2.4) and (2.6), the last from the fact that  $F(|z|)$  is even.

$$(d) \frac{d}{d\eta} \Phi(i\eta) = 2 \int_0^\infty F(|z|)z \sinh \eta z \, dz > 0 \text{ for } 0 < \eta < \eta_f, \quad (4.8)$$

which shows that  $\Phi(\zeta)$  increases monotonically from 1 to  $\infty$  as  $\zeta$  goes from 0 to  $i\eta_f$  (or from 0 to  $-i\eta_f$ ) along the imaginary axis.

(e) For  $\xi \neq 0$ , and  $0 \leq \eta < \eta_f$

$$R\Phi(\xi + i\eta) = \int_{-\infty}^{+\infty} F(|z|)e^{-\eta z} \cos \xi z \, dz < \int_{-\infty}^{+\infty} F(|z|)e^{-\eta z} \, dz \\ = R\Phi(0 + i\eta). \quad (4.9)$$

In order for  $\zeta$  to be a root of (4.5) it must simultaneously satisfy the two conditions

$$R\Phi(\zeta) = \frac{1}{k} > 1 \quad I\Phi(\zeta) = 0. \quad (4.10)$$

The second of these conditions is satisfied along all points of the imaginary axis in virtue of (4.6). Because of (4.8) the first condition will certainly be satisfied at a pair of points  $\zeta = \pm i\mu$  with  $0 < \mu < \eta_f$ . Since  $\Phi'(\nu\mu) \neq 0$  these will be simple roots of (4.5). Expanding  $\phi(\nu\mu)$  in powers of  $\mu$  we may rewrite (4.5) in the form

$$\frac{1-k}{k} = M^2 \mu^2 + \frac{m_4}{4!} \mu^4 + \dots, \quad (4.11)$$

which we recognize to be the same as (3.12). We see that as  $k \rightarrow 1$  the smallest root  $\mu$  of (4.11) is such that

$$\zeta = \pm i\mu \rightarrow \pm i \frac{\sqrt{1-k}}{M} \quad (4.12)$$

independently of the exact form of  $F(|z|)$  and  $\Phi(\zeta)$ .

If (4.5) has any roots other than  $\zeta = \pm i\mu$  their imaginary parts must be larger than  $\mu$ . This may be seen from the fact that the first of conditions (4.10) cannot be satisfied for  $|\eta| < \mu$  or for  $|\eta| = \mu$ ,  $\xi \neq 0$  because of (4.8) and (4.9).

The singularities of  $\Gamma_s(\zeta)$  must have imaginary parts not smaller than  $\eta_s$  which for  $1-k$  sufficiently small will always be greater than  $\mu$  (otherwise when the multiplication is not sufficiently strong even the asymptotic behaviour of  $f(z)$  will be governed by the neutrons coming from the given source). The integrand of (4.4) consequently has simple poles at  $\zeta = \pm i\mu$ , and all its other singularities, if any, lie further away from the real axis in the  $\zeta$  plane and are situated symmetrically with respect to both the real and the imaginary axes. Let  $\eta_1$  be the magnitude of the imaginary part of the next singularity of the integrand. For  $z > 0$  we shift the path of integration in (4.4) from the real axis to the line  $I(\zeta) = -\eta_1$  (or to the line  $I(\zeta) = +\eta_1$ , for  $z < 0$ ), and obtain the asymptotic expression for large  $|z|$ :

$$f_{as}(z) = Ce^{-\mu|z|} + O(e^{-\eta_1|z|}), \quad (4.13)$$

where  $\mu$  is defined as the positive real root of

$$\Phi(i\mu) = \frac{1}{k} \quad (4.14)$$

and

$$C = \frac{Q \Gamma_s(i\mu)}{k \frac{d\Phi(i\mu)}{d\mu}} = \frac{Q}{k} \frac{\int_0^\infty G_s(|z|) \cosh \mu z \, dz}{\int_0^\infty F(|z|) z \sinh \mu z \, dz}. \quad (4.15)$$

For  $k \rightarrow 1$  (4.14) reduces to (4.12) and (4.15) reduces to

$$C \rightarrow Q \frac{\Gamma_s(0) + O(k-1)^2}{\frac{d}{d\mu} \left[ \Phi(0) - \frac{\mu^2}{2} \Phi''(0) \right]} \rightarrow \frac{Qs}{2M^2\mu} \rightarrow \frac{Qs}{2M\sqrt{1-k}}, \quad (4.16)$$

where  $s$  is defined by (2.1). Thus the  $\mu$  and  $C$  of (4.13) reduce for  $k \rightarrow 1$  to those of (3.7) independently of the nature of  $F(|z|)$ . For  $k$  appreciably less than unity (4.14) and (4.15) give the *exact* expressions for both the inverse relaxation length  $\mu$  and the coefficient  $C$  of the asymptotic form (4.13) of  $f(z)$ .

The asymptotic solution for a *point* source of primary neutrons may again be determined from the plane source case with the aid of (3.9) where  $A$  is now given by:

$$A = \frac{C\mu}{2\pi} = \frac{Q}{2\pi k} \frac{\mu \Gamma_s(i\mu)}{\frac{d\Phi(i\mu)}{d\mu}}. \quad (4.17)$$

If the energy spectrum of the given source is taken to be the same as that of a fission source, so that

$$G_s(|z|) = G_f(|z|) = k F(|z|), \quad (4.18)$$

then  $\Gamma_s(\xi)$  in (4.2) to (4.4) should be replaced by  $k \Phi(\xi)$ , and  $\Gamma_s(i\mu)$  in (4.15) to (4.17) should be replaced by  $k \Phi(i\mu) = 1$  in virtue of (4.14).

Let us denote  $\phi(\xi)$  and  $f(z)$  in the special case (4.18), respectively, by:

$$\phi_0(\xi) = Q \frac{k \Phi(\xi)}{1 - k \Phi(\xi)}, \quad (4.19)$$

and

$$f_0(z) = \frac{Q}{2\pi} \int_{-\infty}^{+\infty} \frac{k \Phi(\xi) e^{-i\xi z}}{1 - k \Phi(\xi)} d\xi. \quad (4.20)$$

Then in the general case  $G_s(|z|) \neq G_f(|z|)$  we have:

$$\begin{aligned} \phi(\xi) &= \frac{Q \Gamma_s(\xi)}{1 - k \Phi(\xi)} = Q \Gamma_s(\xi) \left[ 1 - \frac{k \Phi(\xi)}{1 - k \Phi(\xi)} \right] \\ &= Q \Gamma_s(\xi) + \Gamma_s(\xi) \phi_0(\xi). \end{aligned} \quad (4.21)$$

Inverting (4.21) and applying the convolution theorem we have:

$$f(z) = Q G_s(|z|) + \int_{-\infty}^{+\infty} G_s(|z'|) f_0(z - z') dz'. \quad (4.22)$$

Thus  $f(z)$  may be obtained either from (4.4) in terms of  $\Gamma_s(\xi)$  and  $\Phi(\xi)$ , or from (4.22) in terms of  $G_s(|z|)$  and  $f_0(z)$ .

## 5. Discussion of Special Cases

Four special cases are discussed below in which the distribution  $G_f(|z|)$  of primary fission neutrons is in each case given by a particular model of neutron diffusion. The characteristic length  $M$  defined by (2.5) is used as the unit of length throughout this section.

In the first three cases the complete exact solution  $f_0(z)$  corresponding to  $G_s(|z|) = G_f(|z|)$  is found explicitly, so that the asymptotic term

$$f_{0as}(z) = C_0 \exp(-\mu|z|) \quad (5.1)$$

may be compared directly with the other more rapidly decreasing terms. In the fourth case the asymptotic term is given explicitly, but only the order of the next term is indicated. Table I summarizes the constants  $\mu$  and  $C_0$  of (5.1) for the four cases. The value of  $\mu$  remains unchanged in the more general case  $G_s(|z|) \neq G_f(|z|)$ , while the value of  $C$  may be obtained by multiplying  $C_0$  by  $\Gamma_s(i\mu)$ .  $f(z)$  may be obtained from  $f_0(z)$  and  $G_s(|z|)$  with the aid of (4.22), or directly from (4.4).

Case I. *Elementary Treatment of the One Velocity Problem*

$$F(|z|) = \frac{G_f(|z|)}{k} = \frac{1}{2} \exp(-|z|). \quad (5.2)$$

The migration length chosen throughout this section as the unit of length in this case reduces to the *diffusion length* (see reference (2) for definition). The Fourier transform of (5.2) is

$$\Phi(\xi) = \frac{1}{1 + \xi^2}. \quad (5.3)$$

From (4.19)

$$\phi_0(\xi) = Q \frac{k}{\xi^2 + 1 - k} \quad (5.4)$$

and from (4.20) by contour integration:

$$f_0(z) = \frac{Qk}{2\sqrt{1-k}} \exp\left[-\sqrt{1-k}|z|\right]. \quad (5.5)$$

The *complete* solution is in this case given everywhere by the single exponential term (5.5) which is simply (5.2) with the unit of length rescaled by a factor  $\sqrt{1-k}$ . The integrated value of  $f_0(z)$  over all  $z$  is  $Qk/(1-k)$  which is the same as (2.7) with  $s = k$ .

A simple example of  $G_s(|z|) \neq G_f(|z|)$  may be considered by taking

$$G_s(|z|) = s \frac{\gamma}{2} \exp(-\gamma|z|) \quad \text{with } \gamma \neq 1, s \neq k. \quad (5.6)$$

The Fourier transform of (5.6) is:

$$\Gamma_s(\xi) = \frac{s}{1 + \left(\frac{\xi}{\gamma}\right)^2}. \quad (5.7)$$

This leads to:

$$f(z) = \frac{Qk}{2\sqrt{1-k}} \frac{s\gamma^2}{\gamma^2 - (1-k)} \left[ \exp(-\sqrt{1-k}|z|) - \frac{\sqrt{1-k}(1-\gamma^2)}{k\gamma} \exp(-\gamma|z|) \right]. \quad (5.8)$$

In agreement with the results of Section 3 we can see that for  $(1-k) \ll 1$  the ratio of the second term to the first term of (5.8) near the given source ( $z = 0$ ) is of order  $\sqrt{1-k}$ , and the second term falls off more rapidly than the first as long as  $\sqrt{1-k} < \gamma$ . The second term of (5.8) represents the exact expression for the deviation of  $f(z)$  near the source from its asymptotic form, and the expression to which (3.6) reduces in this case differs from it in the value of the coefficient of  $\exp(-\gamma|z|)$  for reasons outlined in Section 3. The coefficient of  $\exp(-\sqrt{1-k}|z|)$  in (5.8) differs from that in (5.5) by the factor  $\Gamma_s(i\mu)$  in accordance with (4.17).

Case II. *Exact Treatment of the One Velocity Problem with Isotropic Scattering*

$$F(|z|) = \frac{\alpha}{\sqrt{3}\alpha} \left[ \frac{(1-\nu^2)\nu}{(1-\alpha)(\nu^2-\alpha)} e^{-\frac{\nu|z|}{\sqrt{3}\alpha}} + \frac{1}{2} \int_1^\infty \frac{e^{-\eta \frac{|z|}{\sqrt{3}\alpha}} d\eta}{\eta \left( 1 - \frac{1-\alpha}{\eta} \operatorname{arth} \frac{1}{\eta} \right)^2 + \frac{\pi^2(1-\alpha)^2}{4\eta}} \right], \quad (5.9)$$

where  $\alpha = l/l_c$  is the ratio of the total mean free path  $l$  to the capture mean free path  $l_c$ ,  $\nu$  is the positive real root of the transcendental equation\*

$$\frac{1}{1-\alpha} = \frac{\operatorname{arth} \nu}{\nu}. \quad (5.10)$$

The unit of length is the *migration length*  $l/\sqrt{3\alpha}$  which becomes the diffusion length of Case I for  $\alpha \rightarrow 0$ . As  $\alpha \rightarrow 0$  the first term of (5.9) reduces to (5.2) and the second term vanishes so that this case reduces to the preceding one. The Fourier transform of (5.9) is (see reference (1) for derivation of (5.9) and (5.11)):

$$\Phi(\xi) = \frac{\alpha \operatorname{art} [\xi\sqrt{3\alpha}]}{\xi\sqrt{3\alpha} - (1-\alpha) \operatorname{art} [\xi\sqrt{3\alpha}]}. \quad (5.11)$$

From (4.19)

$$f_0(\xi) = Q \frac{k \alpha \operatorname{art} [\xi\sqrt{3\alpha}]}{\xi\sqrt{3\alpha} - (1-\alpha') \operatorname{art} [\xi\sqrt{3\alpha}]} \quad (5.12)$$

with

$$\alpha' = \alpha(1-k). \quad (5.13)$$

This differs from (5.11) only by having the extra factor  $Qk$  in the numerator, and  $\alpha'$  in place of  $\alpha$  in one term of the denominator. Employing the procedure of reference (1) to invert (5.12) we obtain an expression analogous to (5.9), viz.

$$f_0(z) = \frac{Qk\alpha}{\sqrt{3\alpha}} \left[ \frac{(1-\nu'^2)\nu'}{(1-\alpha')(\nu'^2-\alpha')} e^{-\frac{\nu'|z|}{\sqrt{3}\alpha}} + \frac{1}{2} \int_1^\infty \frac{e^{-\eta \frac{|z|}{\sqrt{3}\alpha}} d\eta}{\eta \left( 1 - \frac{1-\alpha'}{\eta} \operatorname{arth} \frac{1}{\eta} \right)^2 + \frac{\pi^2(1-\alpha')^2}{4\eta}} \right], \quad (5.14)$$

where  $\nu'$  is the root of (5.10) with  $\alpha$  replaced by  $\alpha'$ . Although the form of (5.9) is preserved in (5.14), the *relative importance* of the two terms is altered.

\* We use the abbreviated notation  $\operatorname{arth} x \equiv \operatorname{arctanh} x$  and  $\operatorname{art} x \equiv \operatorname{arctan} x$  throughout this paper.

The second term of (5.14), describing the influence of the neutrons coming directly from the given source, is affected relatively little by a change in  $\alpha'$  as  $k \rightarrow 1$ , while the coefficient of the first term contains the factor  $\nu'/(\nu'^2 - \alpha')$  which increases like  $(1 - k)^{-1}$  as  $k \rightarrow 1$ .

Case III. *Elementary Treatment of Multiplication Preceded by Slowing-down*

$$F(|z|) = \frac{1}{\sqrt{4\pi}} e^{-\frac{z^2}{4}}. \quad (5.15)$$

This corresponds to the physical model in which the fission neutron spectrum is represented by a single neutron energy  $E_0$ , and the neutrons are assumed to be captured as soon as they are slowed down to an energy  $E_1 < E_0$ . The age-velocity slowing-down theory (see reference (2)) is used to describe the slowing-down process, and the *slowing-down* length (to which the migration length is equivalent in this case) is used as the unit of length. The Fourier transform of (5.15) is

$$\Phi(\xi) = e^{-\xi^2}. \quad (5.16)$$

From (4.19)

$$\phi_0(\xi) = Q \frac{k}{e^{\xi^2} - k}. \quad (5.17)$$

The denominator of (5.17) has zeros at

$$\xi_n = \pm \xi_n \pm i\eta_n, \quad (n = 0, 1, 2, \dots) \quad (5.18)$$

where

$$\xi_n = \frac{n\pi}{\sqrt{\frac{\ln \frac{1}{k}}{2} + \sqrt{\left(\frac{\ln \frac{1}{k}}{2}\right)^2 + n^2\pi^2}}} \rightarrow \pm \sqrt{n\pi} \text{ for } n \gg \frac{\ln \frac{1}{k}}{2\pi} \quad (5.19)$$

$$\eta_n = \frac{\sqrt{\frac{\ln \frac{1}{k}}{2} + \sqrt{\left(\frac{\ln \frac{1}{k}}{2}\right)^2 + n^2\pi^2}}}{\sqrt{\frac{\ln \frac{1}{k}}{2} + \sqrt{\left(\frac{\ln \frac{1}{k}}{2}\right)^2 + n^2\pi^2}}} \rightarrow \pm \sqrt{n\pi} \text{ for } n \gg \frac{\ln \frac{1}{k}}{2\pi}. \quad (5.20)$$

Contour integration then gives:

$$f_0(z) = Q \left[ \frac{e^{-|z| \sqrt{\ln \frac{1}{k}}}}{2 \sqrt{\ln \frac{1}{k}}} + \sum_{n=1}^{\infty} \frac{e^{-\eta_n |z|}}{4 \sqrt{\left(\ln \frac{1}{k}\right)^2 + 4n^2\pi^2}} \sin \left\{ \tan^{-1} \left( \frac{\eta_n^2}{n\pi} \right) - \frac{n\pi}{\eta_n} |z| \right\} \right]. \quad (5.21)$$

Here the Gaussian form of (5.15) is not at all preserved in (5.21).

TABLE I

VALUES OF  $\mu$ ,  $C_0$  AND  $A_0$  IN  $f_{0,ss}(z) = C_0 \exp(-\mu|z|)$  AND  $\rho_{0,ss}(r) = \frac{A_0}{r} \exp(-\mu r)$ .

THE MIGRATION LENGTH  $M$  IS TAKEN AS THE UNIT OF LENGTH

Case	$\Phi(\xi)$	$\mu$ Defined by $\Phi(\frac{1}{2}\mu) = \frac{1}{k}$	$\frac{C_0}{Q} = \frac{1}{k} \frac{d\Phi(\frac{1}{2}\mu)}{d\mu} = \frac{2\pi A_0}{\mu Q}$
I	$\frac{1}{1 + \xi^2}$	$\sqrt{1 - k}$	$\frac{k}{2\sqrt{1 - k}}$
II	$\frac{\alpha \operatorname{art} \xi \sqrt{3\alpha}}{[\xi \sqrt{3\alpha}] - (1 - \alpha) \operatorname{art}[\xi \sqrt{3\alpha}]}$	Positive real root of: $\frac{1}{1 - \alpha(1 - k)} = \frac{\operatorname{arth}[\mu \sqrt{3\alpha}]}{\mu \sqrt{3\alpha}}$	$\frac{k\alpha}{\sqrt{3\alpha} [1 - \alpha(1 - k)]} \frac{\nu'}{[\nu'^2 - \alpha(1 - k)]}$ with $\nu' = \mu \sqrt{3\alpha}$
III	$e^{-\xi^2}$	$\sqrt{\ln \frac{1}{k}}$	$\frac{1}{2\sqrt{\ln \frac{1}{k}}}$
IV	$\frac{e^{-\delta \xi^2}}{1 + \xi^2(1 - \delta)}$	Positive real root of: $1 - \mu^2(1 - \delta) = k e^{\delta \mu^2}$	$\frac{1}{2\mu [1 - \mu^2 \frac{\delta(1 - \delta)}{1 - \mu^2(1 - \delta)}]}$
All cases ( $1 - k$ ) < 1		$\sqrt{1 - k}$	$\frac{1}{2\sqrt{1 - k}}$

For  $G_s$  ( $|z| \neq G_f$  ( $|z|$ ),  $C$  and  $A$  may be obtained from  $C_0$  and  $A_0$  by multiplying them by  $\Gamma_s$  ( $\frac{1}{2}\mu$ ).

Case IV. *Elementary Treatment of Multiplication Preceded by Slowing-down Which is Followed by Diffusion at Constant Energy*

This is an extension of Case III corresponding to the assumption that a neutron need not be immediately captured on reaching the energy  $E_1$ , but that it may diffuse for some time without further loss of energy. If  $\delta$  denotes the ratio of the slowing-down length to the total migration length, which is taken as the unit of length, then reference (2) gives:

$$F(z) = \frac{\exp\left(\frac{\delta}{1-\delta}\right)}{4\sqrt{1-\delta}} \left\{ \exp\left(-\frac{z}{\sqrt{1-\delta}}\right) \left[1 - \operatorname{erf}\left(\sqrt{\frac{\delta}{1-\delta}} - \frac{z}{2\sqrt{\delta}}\right)\right] + \exp\left(\frac{z}{\sqrt{1-\delta}}\right) \left[1 - \operatorname{erf}\left(\sqrt{\frac{\delta}{1-\delta}} + \frac{z}{2\sqrt{\delta}}\right)\right] \right\}, \quad (5.22)$$

where

$$\operatorname{erf} x \equiv \frac{2}{\sqrt{\pi}} \int_0^x e^{-u^2} du \equiv -\operatorname{erf}(-x). \quad (5.23)$$

This reduces to (5.2) as  $\delta \rightarrow 0$ , and to (5.15) as  $\delta \rightarrow 1$ . The Fourier transform of (5.22) is

$$\Phi(\xi) = \frac{\exp(-\delta \xi^2)}{1 + \xi^2(1-\delta)}. \quad (5.24)$$

From (4.19)

$$\phi_0(\xi) = Qk \frac{1}{[1 + \xi^2(1-\delta)] e^{\delta \xi^2} - k}. \quad (5.25)$$

The denominator of (5.25) has a denumerable infinity of zeros which are discussed in an Appendix of reference (2). The zeros with the smallest imaginary part lie at  $\pm i\mu$ , where  $\mu$  is the only real positive root of

$$1 - \mu^2(1-\delta) = k e^{\delta \mu^2}. \quad (5.26)$$

Inversion of (5.25) gives:

$$f_{0as}(z) = \frac{Q}{2\mu \left[ \frac{1 - \mu^2 \delta(1-\delta)}{1 - \mu^2(1-\delta)} \right]} \exp(-\mu|z|) + 0 [\exp(-\eta_1|z|)], \quad (5.27)$$

where  $\eta_1$  is the real part of the first complex root of (5.26). The form of (5.22) is again not at all preserved in (5.27).

## 6. Acknowledgment

We wish to express our thanks to Dr. R. E. Marshak for helpful discussions of this problem at the time the original work was done.

## 7. Appendix

### *The Nature of $G(|z|)$*

The function  $G(|z|)$  introduced in Section 2 may be explicitly written as:

$$G(|z|) = \int dE' \int dE'' x_s(E') H(|z|, E', E'') \frac{c(E'') \nu(E'')}{\tau(E'')}, \quad (7.1)$$

where

$x_s(E')dE'$  = fraction of neutrons of all energies emitted by the source at  $z = 0$  with energy between  $E'$  and  $E' + dE'$ . The integral of  $x_s(E')$  over all  $E'$  is by definition unity, but the form of the dependence of  $x_s(E')$  on  $E'$  may depend on the nature of the source, e.g., in the case of a fission source it may depend on the energy of the neutron causing the fission.

$H(|z|, E', E'')dz dE''$  = number of neutrons between  $z$  and  $z + dz$  with energy between  $E''$  and  $E'' + dE''$  in a steady state distribution in a non-multiplying infinite medium of the same capture and scattering properties as the multiplying medium under consideration, due to a unit plane source at  $z=0$  of neutrons of energy  $E'$ . This depends on the mechanism of neutron diffusion and slowing-down, on the properties of the medium, and on the initial energy  $E'$  of the neutrons emitted by the source.

$\frac{1}{\tau(E'')}$  = capture probability per unit time of neutrons of energy  $E''$ . This depends on the composition of the medium and the neutron absorption cross-sections of the constituent nuclei.

$c(E'')$  = fraction of captures at energy  $E''$  which lead to fission. This depends on the composition of the medium and the variation with energy of the neutron absorption cross-sections of the various components.

$\nu(E'')$  = average number of fission neutrons of all energies emitted per fission caused by a neutron of energy  $E''$ .

Thus  $G(|z|)$  for a given medium will depend on the nature of the source through the form of  $x_s(E')$ .

Conservation of neutrons in a non-multiplying medium gives:

$$\int dz \int dE'' \frac{H(|z|, E', E'')}{\tau(E'')} = 1, \text{ for all } E' . \quad (7.2)$$

In the multiplying medium

$$\int dz G_f(|z|) = k = \overline{c \nu} = \text{average number of fission neutrons born per neutron captured in the infinite medium.}$$

The average  $\overline{c \nu}$  of  $c(E'') \nu(E'')$  with respect to the energy  $E''$  is taken using

$$\int dE' \int dz \frac{H(|z|, E', E'')}{\tau(E'')} x_f(E') \quad (7.3)$$

as the weighting function, which is normalized to unity in virtue of (7.2) and the definition of  $x_f(E')$ , but the form of whose dependence on  $E''$  might in general depend on the nature of the fission source through the form of  $x_f(E')$ .

*Alternative Forms of the Integral Equation*

Let

$\rho(z, E) dz dE$  = number of neutrons between  $z$  and  $z + dz$  with energy between  $E$  and  $E + dE$ .

We account for this number of neutrons by adding together the contributions of the given source, and of the fission sources distributed throughout the medium. This gives:

$$\rho(z, E) = Q \int dE' x_s(E') H(|z|, E', E) + \int dz' \int dE' \int dE'' \frac{\rho(z', E')}{\tau(E')} c(E') \nu(E') x_{E'}(E'') H(|z - z'|, E'', E). \quad (7.4)$$

To get a simpler integral equation we first assume that  $x_{E'}(E'')$  is independent of the energy  $E'$  of the neutron which causes fission. We may then introduce into (7.4)

$$f(z) = \int dE' \frac{\rho(z', E')}{\tau(E')} c(E') \nu(E'), \quad (7.5)$$

which represents the total number of fission neutrons of all energies emitted per unit time per unit  $z$  at the point  $z$ . Multiplying both sides of (7.4) by

$$\frac{c(E) \nu(E)}{\tau(E)}, \quad (7.6)$$

integrating over  $E$ , and using (7.5) and (7.1) we obtain:

$$f(z) = Q G_s(|z|) + \int dz' f(z') G_f(|z - z'|), \quad (7.7)$$

which is obtained directly as (2.6) in Section 2.

If we wanted to introduce in place of (7.5) a different function

$$g(z) = \int dE' \frac{\rho(z, E')}{\tau(E')} c(E'), \quad (7.8)$$

which represents the number of fissions per unit time per unit  $z$ , or

$$h(z) = \int dE' \frac{\rho(z, E')}{\tau(E')}, \quad (7.9)$$

which represents the number of captures per unit time per unit  $z$ , or

$$n(z) = \int dE' \rho(z, E'), \quad (7.10)$$

which represents the number of neutrons of all energies in a steady state per unit  $z$ , then we would have to assume in the case of (7.8) that  $\nu(E')$ , in

the case of (7.9) that  $\nu(E')c(E')$ , and in the case of (7.10) that  $\nu(E')c(E')/\tau(E')$ , as well as  $x_{E'}(E'')$ , are not functions of  $E'$  in order to obtain a simple integral equation analogous to (7.7).

### References

1. PLACZEK, G. and VOLKOFF, G. M. Notes on diffusion of neutrons without change in energy. 1943. Declassified report available in multilith form from the National Research Council of Canada, Ottawa, Canada.
2. WALLACE, P. R. and LECARNE, J. Elementary approximations in the theory of neutron diffusion. 1943. Declassified report available in multilith form from the National Research Council of Canada, Ottawa, Canada.

# Canadian Journal of Research

Issued by THE NATIONAL RESEARCH COUNCIL OF CANADA

VOL. 25, SEC. A.

SEPTEMBER, 1947

NUMBER 5

## EXCITATION CONDITIONS IN THE UPPER ATMOSPHERE AS DETERMINED FROM A STUDY OF ATOMIC EMISSION LINES IN THE AURORAL SPECTRUM<sup>1</sup>

BY WILLIAM PETRIE<sup>2</sup>

### Abstract

Vegard's identifications of a number of lines appearing in the auroral spectrum are discussed. The conclusion is reached that a good many of these lines may be attributed to the oxygen atom in several stages of ionization. It is shown how measured line intensities and theoretical line strengths are combined to give the excitation temperature of the auroral region. Preliminary results indicate that this temperature is in the range 3000° to 6000° K. The meaning of this result is discussed briefly.

### Introduction

It is well known that the auroral spectrum is dominated by nitrogen bands, and lines arising from the lower levels of the oxygen atom. The extensive observations by Vegard and Tönsberg (12) suggest that a number of the weaker spectral features may be attributed to oxygen and nitrogen atoms in several different stages of ionization. It is important that intensity measures of these features may be obtained, since such data will give information on the excitation conditions of the upper atmosphere. In this paper, Vegard's identification of certain of the weaker lines is discussed, and it is shown how measured intensities and theoretical strengths for these same lines may be used to compute the temperature of the auroral region.

### Discussion of Vegard's Data

In order to decide which oxygen and nitrogen lines are likely to appear in the auroral spectrum, it is necessary to study the energy levels of these atoms, and to consider the transition probabilities between various levels.

#### (a) OI

The ground levels of the neutral oxygen atom are  $^3P$ ,  $^1D$ ,  $^1S$ , the latter two being metastable levels. Transitions between the  $^1D - ^3P$  levels produce the red auroral lines at  $\lambda\lambda$  6364, 6302. Transitions between the levels  $^1S - ^1D$  produce the green auroral line at  $\lambda$  5577. A third transition,  $^1S - ^3P$  gives a line at  $\lambda$  2972, which has not been observed in the auroral spectrum. Consider the 'future' of atoms excited to the  $^1S$  level. Radiative transitions may take place to the levels  $^1D$  and  $^3P$ , forming the lines  $\lambda\lambda$  5577, 2972. Since the

<sup>1</sup> Manuscript received April 15, 1947.

Contribution from the Department of Physics, University of Saskatchewan, Saskatoon, Sask.

<sup>2</sup> Associate Professor of Physics.

transition probabilities to the levels  $^1D$  and  $^3P$  are in the ratio 2 0 : 0 18, we would expect the latter line to be formed with appreciable intensity. The values of the transition probabilities have been calculated by Bowen (2). However, a number of the atoms in the  $^1S$  level will be collisionally de-excited to the  $^1D$  and  $^3P$  levels; these are radiationless transitions. The intensity of the line  $\lambda$  2972 will depend upon the ratio between the two types of transitions.

The theory of collisional excitation and de-excitation has been used by Menzel and colleagues (8), to compute temperatures in the atmospheres of a number of planetary nebulae. Consider two energy levels  $A$  and  $B$ . Let  $N_A$  = the number of atoms per cubic centimetre in level  $A$ , and let  $N_e$  = the number of free electrons per cubic centimetre. Then the number of collisional excitations by electrons from  $A$  to  $B$  per second is (4):

$$N_{AB} = N_A N_e \int_{v_0} \Omega_{AB} v f(v) dv. \quad (1)$$

$\Omega_{AB}$  = the cross-sectional area for collisional excitation by electrons from levels  $A$  to  $B$ .  $f(v)$  = the fraction of the electrons with velocities between  $v$  and  $(v + dv)$ . If we assume that a Maxwellian velocity distribution holds for the free electrons, then,

$$f(v) dv = 4\pi \left( \frac{m}{2\pi k T_e} \right)^{\frac{3}{2}} v^2 e^{-\frac{1}{2}mv^2/kT_e} dv. \quad (2)$$

$T_e$  is called the electron temperature, that is, the temperature controlling the velocity distribution among the free electrons.  $v_0$  is the smallest electron velocity capable of exciting the atom from level  $A$  to  $B$ , and is defined by

$$\frac{1}{2} m v_0^2 = \chi_{AB}. \quad (3)$$

$\chi_{AB}$  = the difference in excitation potential between the levels  $A$  and  $B$ . Carrying out the integration and substituting the values of the constants, we find for inelastic collisions,

$$N_{AB} = 8.54 \times 10^{-6} \frac{N_A N_e}{T_e^{\frac{3}{2}}} \frac{\Omega_{AB}}{\tilde{\omega}_A} e^{-\chi_{AB}/kT_e}. \quad (4)$$

$\tilde{\omega}_A$  = the statistical weight of level  $A$ . For superelastic impacts, the number of collisional de-excitations per second from levels  $B$  to  $A$  is,

$$N_{BA} = 8.54 \times 10^{-6} \frac{N_B N_e}{T_e^{\frac{3}{2}}} \frac{\Omega_{AB}}{\tilde{\omega}_B}. \quad (5)$$

$\tilde{\omega}_B$  = the statistical weight of level  $B$ . The exponential does not appear since electrons of any velocity may bring about de-excitation.

We will now use Equation (5) to calculate the number of collisional de-excitations from the levels  $^1S$  to  $^3P$ . Collisional cross-sections for the OI atom have been calculated by Yamanouchi *et al.* (14). Their value for

$\Omega_{SP} = 2.5$ . The value of  $\tilde{\omega} = (2J + 1) = 1$  for the  $^1S_0$  level. Martyn and Pulley (7) give the electron density in the auroral region as  $10^5$  per  $\text{cm}^3$ . The work of the same authors indicates that the electron temperature in the auroral region is  $1200^\circ \text{K}$ . Substituting these values in Equation (5) we have

$$N_{SP} = 8.54 \times 10^{-6} \frac{N_s \times 10^5}{(1200)^{\frac{1}{2}}} \frac{2.5}{1} = 0.06 N_s.$$

This result indicates that 6% of the atoms in the  $^1S$  level are collisionally de-excited to the  $^3P$  levels. A similar calculation shows that about the same percentage are collisionally de-excited to the  $^1D$  level. Hence the greatest number of the atoms in the  $^1S$  level experience radiative transitions to the  $^1D$  and  $^3P$  levels, and the line  $\lambda 2972$  should appear with appreciable intensity. It is likely that this radiation is absorbed by the ozone layer, which would account for its non-appearance. It is intended to carry out a laboratory investigation of this point at the University of Saskatchewan.

In addition to the red and green auroral lines, Vegard and Tönsberg (12) list several others as being due to OI. Four of these appear to arise from the following transitions.

$$2p^35s(^5S^0) - 2p^33p(^5P) \text{ giving } \lambda 6453.7$$

$$2p^34p(^5P) - 2p^33s(^5S^0) \text{ giving } \lambda 3947.3$$

$$2p^34p(^3P) - 2p^33s(^3S^0) \text{ giving } \lambda 4368.3$$

$$2p^33s(^3P^0) - 2p^33p(^3P) \text{ giving } \lambda 3954.6$$

The identifications are doubtful with the exception of the line  $\lambda 4368.3$ . The lines  $\lambda\lambda 6453.7, 3947.3$  are moderately strong, but fall very close to nitrogen bands of the first and second positive group. These will be denoted by  $1P.G.$  and  $2P.G.$  The line  $\lambda 3954.6$  has a small theoretical strength, and is listed as a weak feature in the M.I.T. wave-length tables. The identification of the line  $\lambda 4368.3$  is probably correct; it is the strongest line in the multiplet formed by the transitions  $^3P - ^3S$ , and is listed as a high intensity line in the M.I.T. tables.

There are strong lines arising from other levels of the OI atom. Since these lines have not been recorded in the auroral spectrum, their absence must be satisfactorily explained if the identification of  $\lambda 4368.3$  is correct. An examination of these levels shows that the lines arising from them are either in the region of nitrogen bands, or else appear in the near infrared beyond the present recorded auroral spectrum. The detection in the auroral spectrum of the line  $\lambda 8446.4$  from the transition  $2p^33p(^3P) - 2p^33s(^3S^0)$ , would greatly strengthen the identification of the other OI permitted lines. This feature should be searched for carefully, since it has a large theoretical strength,

appears as a strong line in the M.I.T. tables, probably falls in a clear region between members of the  $1P.G.$  nitrogen bands, and would not be strongly absorbed by the atmosphere below the auroral region. The transitions producing the OI lines discussed here are shown in Fig. 1.

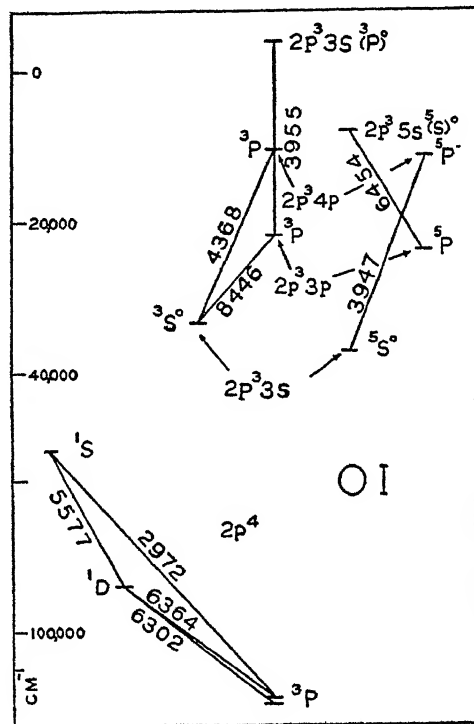


FIG. 1. Partial energy level diagram of OI.

### (b) OII

The ground configuration of the OII atom is  $2p^3$ , giving the terms  $^4S$ ,  $^2D$ ,  $^2P$ , the latter two being metastable. The transition  $^2D - ^4S$  gives a line at  $\lambda 3728.9$ , which is observed in the auroral spectrum. Lines from the transition  $^2P - ^2D$  would probably be recorded, but they fall in the region of the  $1P.G.$  nitrogen bands. Vegard lists 25 lines as due to the OII atom, and 14 of these have been assigned to definite energy levels. Table I lists these lines and the transitions from which they arise. The words first, second, and third mean that the line in question is the strongest, second strongest, etc., in the multiplet to which it belongs.

The evidence generally favours Vegard's identifications. Most of these lines have large theoretical strengths, and are listed as strong lines in the M.I.T. tables. The identification of the lines  $\lambda\lambda 3954.4$  and  $3982.7$  is in doubt, since these features have small theoretical strengths, and are listed as weak lines in the M.I.T. tables. Strong lines from other levels fall in the

region of nitrogen bands, and hence do not appear. We must explain the absence of the line  $\lambda 4943.0$  from the transition  $2p^23d(^2D) - 2p^23p(^2P^0)$ . This line has a large theoretical strength and appears to be in a region free from nitrogen bands.

TABLE I

Transition	Wave-length, Å	Remarks
$2p^23p(^4P^0) - 2p^23s(^4P)$	4319.6	Second. Strongest in region 2PG bands
$2p^23p(^2P^0) - 2p^23s(^2P)$	3954.4	Second. Strongest in region Vegard-Kaplan bands
$2p^23p(^2P^0) - 2p^23s(^2P)$	3982.7	Third
$2p^23p(^2D^0) - 2p^23s(^2P)$	4414.9	First
$2p^23p(^2D^0) - 2p^23s(^2P)$	4417.0	Second
$2p^23p(^2D^0) - 2p^23s(^2P)$	4452.4	Third
$2p^23d(^4F) - 2p^23p(^4D^0)$	4075.9	First
$2p^23d(^4F) - 2p^23p(^4D^0)$	4072.2	Second
$2p^23d(^4D) - 2p^23p(^4D^0)$	3857.2	Second. Strongest in region of Negative Group nitrogen bands
$2p^23d(^4D) - 2p^23p(^4P^0)$	4119.2	First
$2p^23d(^2G) - 2p^23p(^2F^0)$	4185.5	Second. Strongest in region of Negative Group nitrogen bands
$2p^24f(^4F^0) - 2p^23d(^4F)$	4048.2	Second. Strongest in region of 2PG bands
$2p^24f(^4D^0) - 2p^23d(^4P)$	4303.8	First
$2p^24f(^4D^0) - 2p^23d(^4P)$	4294.7	Second

## (c) OIII

The ground configuration of the OIII atom is  $2p^2$ , giving the terms  $^3P$ ,  $^1D$ ,  $^1S$ , the latter two being metastable. The transition  $^1D - ^3P$  gives two lines at  $\lambda\lambda 4959.0, 5006.8$ ; the latter is listed by Vegard as appearing in the auroral spectrum. The ratio of the transition probabilities of these lines is 0.006 : 0.018, which probably explains the absence of the former line. The line at  $\lambda 4363.2$  from the transition  $^1S - ^1D$  is listed as appearing in the auroral spectrum with considerable intensity. Lines arising from transitions between the lower permitted levels either fall in the region of nitrogen bands, or are beyond the recorded spectral region, with the exception of  $\lambda 3962.7$  from the transition  $2p3p(^1S) - 2p3s(^1P^0)$ . This line is given in Vegard's list.

## (d) NI

The ground configuration of NI is  $2p^3$ , giving the terms  $^4S$ ,  $^2D$ ,  $^2P$ . The transitions  $^2D - ^4S$  give a pair of lines with wave-lengths  $\lambda\lambda 5198.5$  and  $5200.7$ . These lines should be looked for carefully; they do not appear in

Vegard's list. The transition  $^2P - ^4S$  gives a line at  $\lambda$  3466.4 which is included in Vegard's list. Vegard attributes six additional lines to the NI atom, and three of these appear to arise from the following transitions—

$$2p^24p(^2S^0) - 2p^23s(^2P) \text{ giving } \lambda 4935.0$$

$$2p^24p(^2S^0) - 2p^23s(^2P) \text{ giving } \lambda 4914.9$$

$$2p^24p(^4P^0) - 2p^23s(^4P) \text{ giving } \lambda 4223.0$$

These identifications are in doubt, since all three have small theoretical strengths, and only the first appears as a reasonably strong line in the M.I.T. tables. The line at  $\lambda$  5560.4 from the transition  $2p^25d(^4F) - 2p^23p(^4D^0)$  should be searched for carefully, since it has a large theoretical strength and is listed as an intense line in the M.I.T. tables.

#### (e) NII

The ground configuration of the NII atom is  $2p^2$ , giving the terms  $^3P$ ,  $^1D$ ,  $^1S$ . The transitions  $^1D - ^3P$  give lines with wave-lengths  $\lambda\lambda$  6548.1 and 6583.6. The line at  $\lambda$  6548.1 is listed by Vegard, but the other does not appear. This second line should be searched for carefully since it has the greater transition probability of the pair. It may be obscured by a member of the 1 P.G. nitrogen band system. The transition  $^1S - ^1D$  gives a line at  $\lambda$  5754.8, which appears in Vegard's list. A number of additional lines are attributed to NII. One of these, at  $\lambda$  5679.6, appears to arise from the transition  $2p3p(^3D) - 2p3s(^3P^0)$ . The identification is probably correct, since this line has a large theoretical strength and appears as an intense line in the M.I.T. tables.

#### (f) NIII

The lower forbidden transitions of the NIII atom are not in the observable region of the spectrum. Two lines listed by Vegard appear to arise from the following transitions  $2s2p3p(^4D) - 2s2p3s(^4P^0)$  giving  $\lambda$  4510.7,  $2s2p3p(^4S) - 2s2p3s(^4P^0)$  giving  $\lambda$  3772.2.

In summary, we may say that the evidence generally favours Vegard's identification as regards the atomic oxygen lines. The case for the appearance of atomic nitrogen lines is not nearly so strong. It is suggested that useful information may be obtained by studying the relative intensities of certain oxygen and nitrogen lines appearing in a discharge through air at various pressures. Such an investigation is being undertaken at the University of Saskatchewan.

Assuming that Vegard's identifications are correct in certain cases, the question arises as to the mechanism of excitation which is operating. A good deal has been written on this subject, since it was necessary to explain the appearance of the forbidden oxygen lines from the ground levels of the atom,

and the absence of all permitted lines from higher levels. Kaplan (6) has suggested that oxygen atoms are excited to the lower metastable levels through collisions with nitrogen molecules in metastable levels. Since Kaplan has observed the auroral green line in a discharge produced mainly by nitrogen molecules in metastable levels, his argument is fairly conclusive. Chapman (3) has suggested that the nitrogen molecules are excited by the energy available from the recombination of oxygen atoms. However, if atomic oxygen lines arising from permitted levels are present, a more general mechanism of excitation must be operating. It is suggested that the most probable mechanism is excitation by electron collision. It is well known that oxygen and nitrogen atoms in both the neutral and ionized forms present large cross-sectional areas for collisional excitation by electrons. Regardless of the method of excitation, the relative populations of a number of energy levels will give information on excitation conditions.

### Line Intensities and Line Strengths

The strength of a line is defined as the sum of the absolute squares of the matrix elements of electric moment joining the sets of states in question. On the other hand, the intensity of a line is proportional to the number of atoms in any one of the states of its initial level, the fourth power of its frequency, and its strength. A quantitative expression for the intensity of a spectral line is given by Equation (6) :

$$I = \frac{64\pi^4\nu^4}{3c^3} N_0 \frac{\tilde{\omega}}{\tilde{\omega}_0} e^{-\chi_n/kT} s, \quad (6)$$

where  $\nu$  = the frequency of the line,

$N_0$  = the number of atoms in the ground level for a particular stage of ionization of the element in question,

$\tilde{\omega}$  = the statistical weight of the level from which the line originates,

$\tilde{\omega}_0$  = the statistical weight of the ground level,

$\chi_n$  = the excitation potential of the upper energy level involved in the production of the line,

$T$  = the excitation temperature of the emitting volume,

$s$  = the theoretical line strength.

The strength of a line in terms of the strength of the multiplet to which the line belongs may be obtained from the tables computed by Russell (11). That is, we obtain the quantity  $\frac{s}{\sum s}$ , where  $s$  is the line strength and  $\sum s$  the multiplet strength. Relative multiplet strengths in terms of a quantity  $\sigma^2$  have been calculated by Goldberg (5).  $\sigma$  is a function of the total and orbital quantum numbers,  $n, l$  and  $n', l'$  of the jumping electron, and is given by

$$\sigma = \frac{e}{\sqrt{4l^2 - 1}} \int_n^\infty r \cdot R(n, l) R(n', l') dr, \quad (7)$$

where  $e$  is the charge on the electron in electrostatic units, and  $R(n, l)$  and  $R(n', l')$  are the normalized radial eigenfunctions of the jumping electron. The quantity  $\sigma$  is a constant for all the multiplets arising from a transition between two electron configurations. Multiplet strengths in terms of  $\sigma^2$  are denoted by  $S$ . Menzel and Goldberg (9) have computed factors which reduce the relative multiplet strengths to absolute values. We denote these factors by  $a$ . The strength of a line is now the product of the three quantities,  $\frac{S}{\sum S} Sa$ , since  $\sum S$  and  $S$  cancel each other.

It should be pointed out that the calculations for both line and multiplet strengths are accurate only if Russell-Saunders coupling holds. The sum rule provides a check on the accuracy of this type of coupling in any given case. The rule states that the sum of the strengths of all the lines of a multiplet which arise from a common initial level is proportional to the weight  $(2J + 1)$  of the initial level. This rule has been applied to the multiplets in which we are interested, and Russell-Saunders coupling appears to hold quite accurately.

### Excitation Conditions in the Auroral Region

We have stated that a number of auroral lines can be attributed with a good deal of certainty to the oxygen atom. For certain of these lines Vegard and Tonsberg (12) have published measured intensities. It will now be shown how these intensities are combined with values of the theoretical strengths to determine the excitation temperature of the emitting volume. From Equation (7) the relative intensity of two spectral lines is given by

$$\frac{I_1}{I_2} = \left(\frac{\nu_1}{\nu_2}\right)^4 \frac{\tilde{\omega}_1}{\tilde{\omega}_2} e^{-(\chi_{n_1} - \chi_{n_2})/kT} \frac{S_1}{S_2}. \quad (8)$$

Strictly speaking, we should use different temperatures  $T_1$  and  $T_2$  in the equation, to allow for a likely non-Boltzmann distribution of atoms in the various energy levels. However, since we have insufficient data on intensity measures to determine what type of distribution exists, we assume that  $T$  will be the same for the various energy levels. Using the intensity values given by Vegard, and the line strengths obtained as we have indicated, and substituting both in Equation (8) it is found that  $T$  varies from  $3000^\circ \text{K}$  to  $6000^\circ \text{K}$ . This result is from four OII lines. These temperatures cannot be considered accurate owing to the limited intensity data available, but the method will give useful information on excitation conditions in the auroral region, when more measured line intensities are obtained. The same calculations applied to energy levels covering a considerable range in excitation potential will give the distribution of atoms in these levels, and hence information on the excitation temperature.

It is perhaps misleading to use the word temperature in this case. If we consider an atmosphere in thermal equilibrium, all methods of computing the temperature give the same results. This condition does not apply to the

earth's upper atmosphere, and the temperature will vary with the method of computation. From the intensity distribution in a number of nitrogen bands, Vegard has obtained a temperature of around  $300^{\circ}$  K. This means that the particles exciting the nitrogen molecules have a velocity distribution characteristic of  $300^{\circ}$  K. On the other hand, as indicated above, the intensities of a number of OII lines indicate that the exciting particles have a velocity distribution characteristic of much higher temperatures, in the range  $3000^{\circ}$  K. to  $6000^{\circ}$  K. These differences indicate that the earth's atmosphere is far from a condition of thermal equilibrium. Calculations applied to the intensities of OIII lines would undoubtedly give a still different value. The meaning of the different types of temperature used in the field of astrophysics has been given by Petrie (10).

Other investigations have indicated that the temperature obtained depends upon the method used. From a study of the luminosities of meteors as a function of height, Whipple (13) has found that temperatures increase considerably with height. Martyn and Pulley (7) have studied collisional frequencies between electrons and molecules at the 250 km. level, and find a temperature of  $1200^{\circ}$  K. From measurements of the width of the auroral green line, Babcock (1) estimates the temperature to be  $900^{\circ}$ . All this evidence from a number of investigations leaves little doubt as to the reality of the high temperature conditions. We must remember, however, that temperature can have different meanings when dealing with an atmosphere not in thermal equilibrium.

In a later communication, the author will indicate a different method of obtaining temperatures from the relative intensities of atomic lines.

### References

1. BABCOCK, H. D. *Astrophys. J.* 57 : 209-221. 1923.
2. BOWEN, I. S. *Rev. Mod. Phys.* 8 : 55-81. 1936.
3. CHAPMAN, S. *Proc. Roy. Soc., London, A*, 132 : 353-374. 1931.
4. FOWLER, R. H. *Statistical mechanics; the theory of the properties of matter in equilibrium.* The Macmillan Company, New York. 1929.
5. GOLDBERG, L. *Astrophys. J.* 82 : 1-25. 1935.
6. KAPLAN, J. *Phys. Rev.* 49 : 67-69. 1936.
7. MARTYN, D. F. and PULLEY, O. O. *Proc. Roy. Soc., London, A*, 154 : 455-486. 1936.
8. MENZEL, D. H., ALLER, L. H., and HEBB, M. H. *Astrophys. J.* 93 : 230-235. 1941.
9. MENZEL, D. H. and GOLDBERG, L. *Astrophys. J.* 84 : 1-13. 1936.
10. PETRIE, W. *J. Roy. Astron. Soc. Can.* 38 : 137-142. 1944.
11. RUSSELL, H. N. *Astrophys. J.* 83 : 129-139. 1936.
12. VEGARD, L. and TÖNDSBERG, E. *Geofys. Publikasjoner*, 13 (1) : 3-22. 1940.
13. WHIPPLE, F. L. *Rev. Mod. Phys.* 15 : 246-264. 1943.
14. YAMANOUCHI, T., INUI, T., and AMEMIYA, A. *Proc. Phys.-Math. Soc. Japan*, 22: 847-854. 1940.



## NOTICE

The Author and Subject Indexes for each of the sections, A, B, C, D, E, and F, of the *Canadian Journal of Research* for the year 1947 will be issued with the first number of the section in 1948.



# Canadian Journal of Research

Issued by THE NATIONAL RESEARCH COUNCIL OF CANADA

VOL. 25, SEC. A.

NOVEMBER, 1947

NUMBER 6

## THE ABSORPTION OF GAMMA-RAYS FROM $\text{Co}^{60}$ <sup>1</sup>

BY W. V. MAYNEORD<sup>2</sup> AND A. J. CIPRIANI<sup>3</sup>

### Abstract

Measurements of the absorption of gamma-rays from  $\text{Co}^{60}$  and radium have been made in a number of materials. Variation of absorption coefficient of the gamma-rays from radium with thickness of lead absorber is in agreement with recent experimental determinations. The gamma-rays from  $\text{Co}^{60}$  are approximately monochromatic and are therefore suitable for testing theoretical absorption formulae. The absorption coefficient per electron for materials of atomic number equal to or less than that of aluminium was in agreement with the Klein-Nishina formula, assuming the cobalt radiation to consist of two lines at 1.10 and 1.30 Mev. respectively. The photoelectric absorption coefficients per electron for heavy elements are in good agreement with the theory developed by Hulme, McDougall, Buckingham, and Fowler. This coefficient varies approximately as  $Z^3$ .

### Introduction

Among the artificial radioactive substances  $\text{Co}^{60}$ , owing to its relatively long life, is a convenient laboratory gamma-ray standard and a possible substitute for radium in certain therapeutic applications. It was therefore thought of importance to determine the absorption coefficients of its radiations in a number of materials, particularly as the approximate homogeneity of these radiations affords an opportunity to test theoretical formulae for absorption coefficients much more accurately and conveniently than by the use of the complex radiations from radium preparations.

Preliminary experiments were, however, carried out with Ra (B + C) sources as a check on the experimental arrangements adopted.

### Sources of Radiation

The Ra (B + C) source consisted of a Monel cylinder 6.3 mm. diameter and approximately 7.0 mm. long containing 100 mgm. radium element, the whole constituting a standard industrial radiographic source. The active material was enclosed in a cylindrical volume 4 mm. long and 4 mm. diameter, the wall being approximately 1 mm. Monel.

<sup>1</sup> Manuscript received May 9, 1947.

*Contribution from the Biological and Medical Research Branch of the Atomic Energy Project, National Research Council of Canada, Chalk River, Ont. Issued as N.R.C. No. 1610.*

<sup>2</sup> *Physicist, Royal Cancer Hospital, London, England. Adviser to the Biological and Medical Research Branch of the Atomic Energy Project, Chalk River, Ont., 1945-1946.*

<sup>3</sup> *Chairman, Biological and Medical Research Branch of the Atomic Energy Project, Chalk River, Ont.*

The beam of gamma-rays was canalized by placing the source at one end of a tapered hole in a lead block as shown in Fig. 1. This tapered hole was cast in a simple cylinder of lead that fitted inside a larger cylinder of lead of

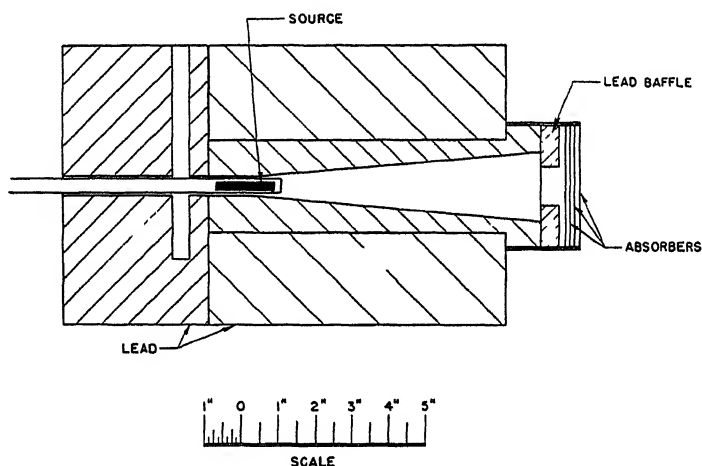


FIG. 1. Longitudinal section through collimating block used in absorption measurements.

the dimensions indicated; a third cylinder of lead was placed behind the collimator for shielding purposes. For convenience in handling, the 100 mgm. source was held in the end of a brass rod turned and sprung to grip it tightly. The cylindrical protective lead block rested on two strips of angle iron, welded to a steel plate. Duralumin tubes, slipped into the angle iron, served as convenient handles and also as adjustable supports for a small wooden table on which absorbers could be supported. Lead baffles having various apertures were machined and placed in the mouth of the taper so as to absorb secondary radiation from the inside of the tapered hole, but these baffles were found to have little effect on the observed absorption coefficients. The distance from centre of radium source to centre of ionization chamber was approximately 72 cm. and the distance between the aperture of the tapered hole and chamber, 51 cm. In these circumstances the scattered radiation from the absorber reaching the chamber was not greater than 2% of the total scatter, but, when necessary, appropriate corrections have been made.

The cobalt source consisted of about 20 gm. of metallic cobalt of total gamma-ray activity equivalent to that of 255 mgm. radium. This material was packed as tightly as possible into a brass cylinder of wall thickness 0.8 mm., which was then soldered. The active volume measured 5.5 cm. long and 1.0 cm. diameter. When placed in the tapered hole so as to give the optimum canalization, the position was as shown in Fig. 1. Most of the measurements were thus made with the radiation emerging from the end of the source, but some observations are also made of the radiation emerging at right angles as also indicated in Fig. 1, thus largely avoiding the absorption loss in the material itself.

### Measuring System

The measuring system, originally designed for gamma-ray dosimetry, usually consisted of a small cylindrical ionization chamber, 2.540 cm. internal diameter and 2.540 cm. internal length, on the end of a long lead evacuated with a rotary oil pump to avoid stray ionization in the system. The apparatus, Fig. 2, was so designed that chambers of any size, shape, or material could readily be screwed into position, the outside of the chamber being raised to the necessary saturation potential. The insulated central lead of the chamber

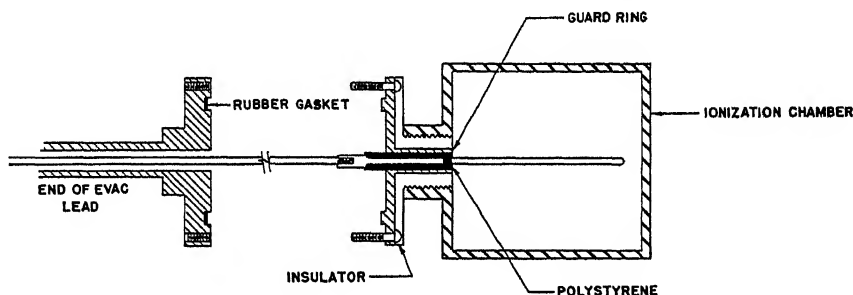


FIG. 2. *Mid-section through ionization chamber and end of evacuated lead.*

was connected to the grid of an FP-54 tube in a slightly modified DuBridge-Brown balanced circuit (2), the deflection of the galvanometer being a measure of the ionization current in the chamber. In preliminary experiments the balance of the circuit and its characteristics were investigated and found satisfactory. After the tube had been aged by continuous running for a fortnight, the stability of zero was satisfactory over times of the order of a few hours. The galvanometer deflection increased linearly with grid potential change (as determined with a Leeds Northrup type K potentiometer) over the whole galvanometer range (maximum current approximately  $0.3 \mu\text{a.}$ ) to within 1%. Consequently, the quicker direct deflection method was usually employed during absorption measurements in place of potentiometer compensation. A Victoreen grid leak of the order of  $10^{11}$  ohms was used in most experiments but  $10^{12}$  ohms was also available if higher sensitivity was required. Both FP-54 and grid leak were enclosed in a heavy brass chamber, which was evacuated with the ionization chamber lead. The high speed of response with the  $10^{11}$  ohms grid leak (full deflection in approximately 10 sec.) and the slow nature of the zero drifts made the operation of measuring radiation absorption very quick, so that in a few minutes the whole absorption curve of a given substance could be investigated, and frequent repetition experiments were possible. In general, the repetition of percentage transmissions is better than 1% and the final absorption coefficients are estimated to be accurate to approximately  $\pm 1\%$ .

Most of the absorption coefficients have been determined using an aluminium ionization chamber of the internal dimensions indicated and 3 mm. wall thickness to avoid so far as possible the complex variation of ionization

function due to photoelectric effect in the chamber wall and to build up the appropriate electronic equilibrium. For a monochromatic radiation the observed absorption coefficient should be independent of chamber material, and we have found for  $\text{Co}^{60}$  radiation good agreement between absorption coefficients in light elements as measured in chambers of carbon, aluminium, and even lead. Small differences are observed during measurements of absorption in heavy elements with a lead chamber (Fig. 5).

### The Absorption of Gamma-rays from Ra (B + C)

Measurements have been made of the absorption coefficients in aluminium and lead for the gamma-rays of Ra (B + C) using the canalized beam as described. A number of experimenters have investigated this subject (7, pp. 466-480) and it is well known that the observed coefficients depend upon the experimental conditions adopted, the main difficulties lying in the assessment of the effects of the ionization functions of the ionization chambers, initial uncertainties in the energy distribution in the complex Ra (B + C) gamma-ray spectra, the initial filtrations of the primary beam, and the magnitude of scatter corrections depending on the geometry of the experimental set-up. The radium source is, in fact, fundamentally unsuited to any attempt to test theoretical formulae for variation of absorption coefficient with atomic number and quantum energy.

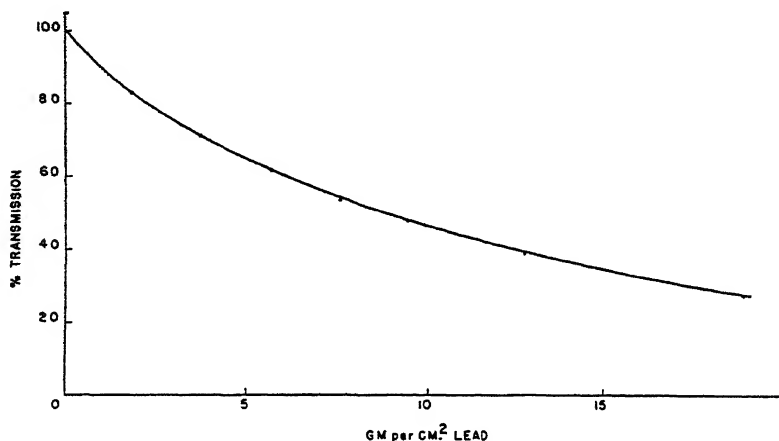


FIG. 3. *Transmission curve in lead for gamma-rays from Ra (B + C) obtained with an aluminium ionization chamber.*

The lead absorbers employed were machined lead disks approximately 1.68 mm. thick and  $7.620 \pm 0.005$  cm. diameter, each of which was weighed. The mean transmission curve as measured in an aluminium chamber is shown in Fig. 3. The logarithmic transmission curve is not straight so that the definition of absorption coefficient at a given filtration becomes of importance. The absorption coefficient should be defined by the tangent to the logarithmic

transmission curve at the filtration of interest, but in view of the uncertainties of drawing such curves the values adopted are those obtained by considering the decrease of transmission caused by three of the experimental filters, namely, a total of 5.76 gm. per  $\text{cm}^2$  of lead. The initial filtration due to 1/16 in. copper sheet placed over the aperture of the beam to remove secondary electrons and soft radiation and the 1 mm. of Monel in the wall of the source itself was regarded as equivalent to 2.0 mm. lead (2.3 gm. per  $\text{cm}^2$ ).

The variation of absorption coefficient with thickness of lead absorber is shown in Fig. 4. The absorption coefficients agree at high filtrations with the

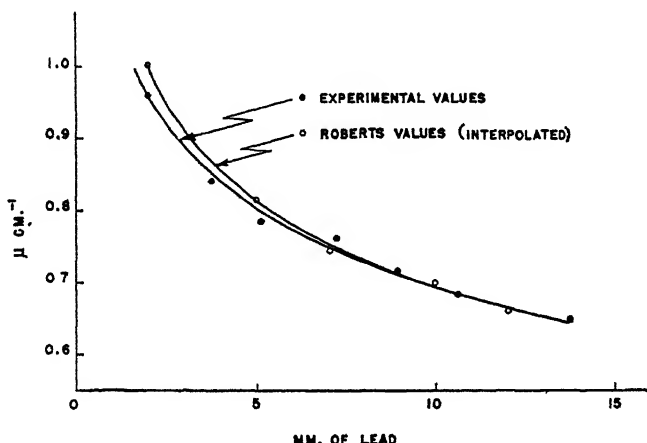


FIG. 4. Variation of linear absorption coefficient with thickness of lead filter for gamma-rays from Ra (B + C).

recent careful measurements by Roberts (6), but are lower at low filtrations, possibly owing to the thickness of standard absorber chosen. In agreement with Roberts we find absorption coefficients below those given by Rutherford, Chadwick, and Ellis, probably owing to the choice of a low atomic number for the ionization chamber. It is, however, interesting to note that if the absorption coefficients measured by us were regarded as corresponding to a filtration equal to the initial filtration plus 2.5 mm. of lead (half the thickness of the test absorber) then our experimental results agree fairly well with the Rutherford, Chadwick, and Ellis curve.

It is clear that great care is required in the definition and measurement of the absorption coefficient of a beam containing such varied quanta as those emitted by Ra (B + C).

### Experimental Results for the Gamma-rays of $\text{Co}^{60}$

The absorption coefficients of a number of substances have been measured for the gamma-rays of  $\text{Co}^{60}$  using an aluminium chamber and radioactive source end-on as already described. The results of these measurements are given below. All absorbers with the exception of mercury were carefully

weighed and their mass absorption coefficients determined directly, electronic and linear absorption coefficients being subsequently deduced. The linear absorption coefficient of liquid mercury was measured directly as described below.

### *Beryllium*

Metallic beryllium was available in large, approximately rectangular blocks of assorted sizes which could be combined to make suitable absorbers. The mean percentage transmissions through varying thickness are given below.

Absorber, gm. per cm. <sup>2</sup>	% Transmission
0.00	100.0
5.80	75.1
11.85	55.0
17.58	41.4
23.42	30.9

The logarithmic transmission curve is accurately straight to 30% transmission, and leads to an observed mass absorption coefficient  $\mu/\rho = 0.0505$  cm.<sup>2</sup> per gm. The uncorrected electronic absorption coefficient is therefore:

$$\mu_e = 1.89 \times 10^{-25} \text{ cm.}^2 \text{ per electron,}$$

$$\text{since } \mu_e = \mu/\rho \times A/Z \times 6.02 \times 10^{23},$$

where  $A$  is the atomic weight and  $Z$  the atomic number of the element considered,  $\rho$  the density in gm. per cm.<sup>3</sup>

Measurements were also made of the absorption of the gamma-rays from radium in beryllium using two 100 mgm. Monel enclosed sources in tandem.

The corrected absorption coefficients were  $\mu/\rho = 0.0535$  or  $\mu_e = 2.01 \times 10^{-25}$  cm.<sup>2</sup> per electron.

With a filter of 12 mm. lead the mass absorption coefficient was 0.0445 or  $\mu_e = 1.67 \times 10^{-25}$  cm.<sup>2</sup> per electron.

### *Carbon*

The absorption was measured in accurately cylindrical blocks of pure graphite machined to  $3.000 \pm 0.002$  in. diameter and of various thicknesses. All filters were weighed. The mean logarithmic transmission curve shows no deviation from a straight line to 25 gm. per cm.<sup>2</sup> and leads to uncorrected absorption coefficients,

$$\mu/\rho = 0.0549 \text{ cm.}^2 \text{ per gm. and } \mu_e = 1.83 \times 10^{-25} \text{ cm.}^2 \text{ per electron.}$$

In the experiments on beryllium and carbon the thickness of absorber required was such as to bring the scattering material appreciably nearer the ionization chamber than the exit of the taper hole, and it became necessary to consider scatter corrections to the observed absorption coefficients.

The theory of such scattering corrections has been studied by a number of workers, both Tarrant (9) and Tandberg (8) having given formulae for the corrections involved. Under the conditions here considered the correction is

small and may be made using Tarrant's formula for the difference between the true and apparent electronic coefficients, namely:

$$\mu_e \text{ true} - \mu_e \text{ app.} = \frac{\pi e^4}{m^2 c^4} \cdot \theta^2 \left\{ 1 + \frac{\theta^2}{4} (5.5 \alpha - 1) \right\},$$

where  $\theta$  is the maximum angle of scatter into the chamber,  $\alpha = h\nu/mc^2$ .

For the cobalt radiation  $\alpha = 2.4$  and the maximum angle of scatter in the carbon experiments 0.13 radians, so that the maximum scatter correction is  $0.04 \times 10^{-25}$ . Taking into account the appropriate geometry for each element, the corrected values of the electronic absorption coefficients for beryllium and carbon respectively are  $1.92 \times 10^{-25}$  and  $1.87 \times 10^{-25}$  cm.<sup>2</sup> per electron.

### Water

From a biological and medical point of view the absorption in water is clearly of great importance and observations were, therefore, made of the absorption coefficient in water. Several lucite cells were constructed, a typical example having a watertight lid held in position by 12 screws and containing a cylinder of liquid 3.000 in. diameter and 1.000 in. long. The dimensions were verified by weighing, the mass of water per square centimetre in this instance being found to be 2.54 gm. per cm.<sup>2</sup> In preliminary experiments on the empty cells the absorption in the ends, 1.00 mm. thick, was found and allowance made in the final results. The mean of a number of experiments gave the percentage transmission of the Co<sup>60</sup> gamma-rays through 2.54 gm. per cm.<sup>2</sup> of water as 85.2%, with corresponding coefficients  $\mu/\rho = 0.0632$  cm.<sup>2</sup> per gm. or  $\mu_e = 1.90 \times 10^{-25}$  cm.<sup>2</sup> per electron.

It was also thought of interest to measure the absorption coefficients in heavy water, since the experiment affords an opportunity to investigate the abnormally high mass absorption coefficient of hydrogen compared to that of other light elements. On substituting deuterium for normal hydrogen, the number of electrons per molecule remains constant but the mass is, of course, increased.

The lucite cell was carefully filled with heavy water (99.7% purity), and the transmission again measured. The observed percentage transmission through the cell was now 85.3%, in good agreement with the result for normal water and demonstrating that the linear absorption coefficients in water and heavy water are identical. The mass of heavy water filling the cell was 128.13 gm. as compared to 115.78 gm. of water, the relative densities being therefore 1.107. The measured absorption coefficients for water and heavy water were as follows:

Water

$\mu/\rho = 0.0632$  cm.<sup>2</sup> per gm.  
 $\mu_e = 1.90 \times 10^{-25}$  cm.<sup>2</sup> per electron  
 $\mu = 0.0632$  cm.<sup>-1</sup>

Heavy water

$\mu/\rho = 0.0568$  cm.<sup>2</sup> per gm.  
 $\mu_e = 1.89 \times 10^{-25}$  cm.<sup>2</sup> per electron  
 $\mu = 0.0630$  cm.<sup>-1</sup>

It is interesting to note that for gamma-ray absorption deuterium is the 'normal' element and 'ordinary' hydrogen the abnormal material. (See Table I.) These conclusions are in agreement with experiments carried out some years ago (5) by one of us using X-rays produced at 400 kv.

### *Aluminium*

The absorption of  $\text{Co}^{60}$  gamma-rays was measured in carefully machined disks of pure aluminium of varying thicknesses and diameter  $3.000 \pm 0.002$  in. The straight logarithmic absorption curve gave  $\mu/\rho = 0.0550 \text{ cm}^2$  per gm. and  $\mu/\epsilon = 1.90 \times 10^{-25} \text{ cm}^2$  per electron.

A lead ionization chamber was also used for the absorption measurements. The results were the same, within experimental error, as those obtained with an aluminium ionization chamber. This would, of course, be expected for a homogeneous radiation and a light element. It was later shown that the apparent absorption coefficient in lead is different when measured in lead and aluminium chambers, even for  $\text{Co}^{60}$  radiations.

### *Heavy Elements*

Measurements have also been made with a number of heavier elements in order to investigate the photoelectric absorption coefficients. The method of measurement was as previously described and calls for no further comment.

The elements investigated were in the form of accurately machined circular disks and included mild steel, pure electrolytic copper, fine silver, platinum, lead, bismuth, and uranium. The absorption in metallic mercury was found

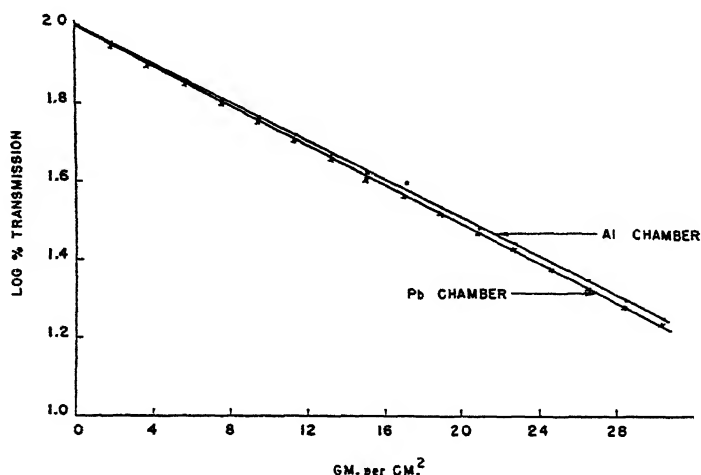


FIG. 5. Logarithmic transmission curve in lead for gamma-rays from  $\text{Co}^{60}$  obtained with an aluminium ionization chamber and a lead chamber.

by filling a glass cell whose absorption when empty was known, and inserting lucite blocks of known absorbing properties so as to give varying thicknesses of mercury, care being taken to ensure complete displacement of the

liquid. By measuring the dimensions of the glass cell and lucite blocks the thickness of the mercury layer could be found and hence the linear absorption coefficient.

A number of measurements have also been made with metallic uranium which was available in the form of disks of thickness approximately 7 gm. per cm.<sup>2</sup> This material is of particular interest as it affords the opportunity to test the variation of photoelectric coefficient with atomic number for the highest atomic numbers, in which region experimental results have hitherto been uncertain. From a practical point of view the high density and high absorption per electron combine to give metallic uranium a high linear absorption coefficient, which makes it a particularly valuable shielding material with considerable application in medicine and experimental work generally. Fig. 5 shows the logarithmic absorption curves in lead as measured with aluminium and lead chambers respectively. The absorption curve in lead of radiation emitted at right angles to the axis of the cobalt source and measured in an aluminium chamber is indistinguishable from the mean of these two curves.

### Experimental Results and Discussion

We give below (Table I) the experimental absorption coefficients, corrected where necessary for scatter, while Fig. 6 shows a few examples of the logarithmic transmission curves from which the coefficients were derived. No evidence of high energy ( $> 1.5$  Mev.) components in the Co<sup>60</sup> gamma-ray spectrum was obtained, but such components, if weak, might still be revealed by a study of transmissions at larger thickness of absorber than that used by us.

TABLE I

Material	Atomic No., <i>Z</i>	Atomic wt., <i>A</i>	Experimental $\mu/\rho$ , cm. <sup>2</sup> per gm.	Corrected $\mu_e$ , cm. <sup>2</sup> per electron $\times 10^{25}$	$\tau_e$
Be	4	9.02	0.0505	1.92	0.00
C	6	12.01	0.0549	1.87	0.00
H <sub>2</sub> O	'5'	'9.008'	0.0632	1.90	0.00
D <sub>2</sub> O	'5'	'10.015'	0.0568	1.89	0.00
Al	13	26.97	0.0550	1.90	0.00
Steel	26	55.85	0.0538	1.92	0.02
Cu	29	63.57	0.0531	1.94	0.04
Ag	47	107.88	0.0519	1.98	0.08
Pt	78	195.32	0.0576	2.41	0.51
Hg	80	200.61	0.0578	2.41	0.51
Pb	82	207.21	0.0573	2.42	0.52
Bi	83	209.00	0.0588	2.47	0.57
U	92	238.07	0.0638	2.74	0.84

The values given in Table I are for absorber thicknesses up to 10 gm. per cm.<sup>2</sup> For heavy elements (e.g., lead and bismuth) there is some evidence that the logarithmic transmission curve departs from linearity at greater thicknesses by an amount in agreement with the theory discussed below.

It will be seen that elements of low atomic number for which photoelectric absorption is negligible yield a constant value of electronic coefficient whose mean value is  $1.90 \times 10^{-25}$  cm.<sup>2</sup> per electron. The absorption coefficient

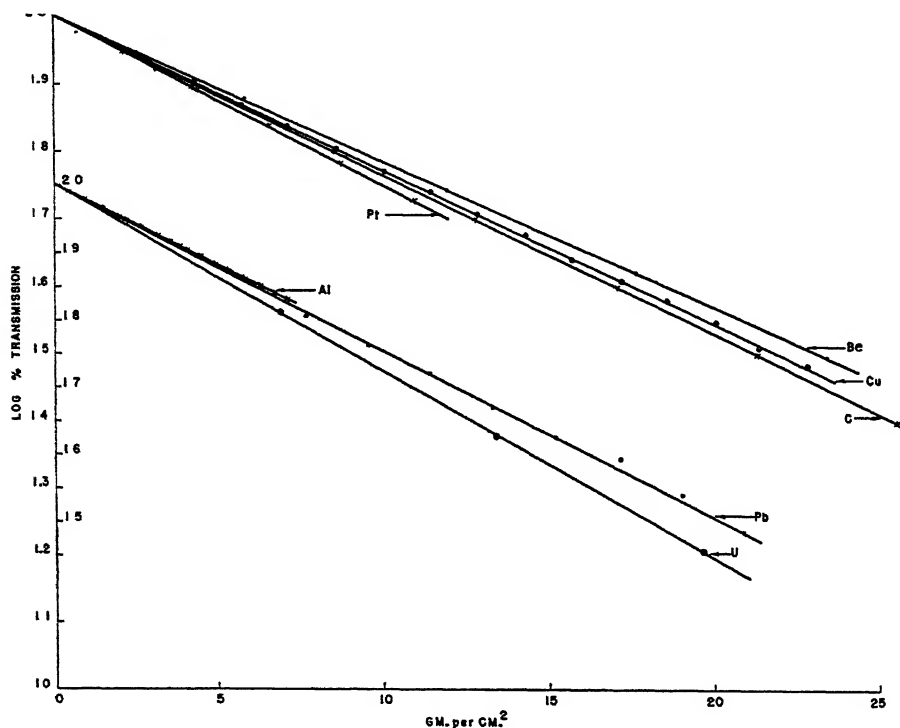


FIG. 6. Logarithmic transmission curve in some of the elements studied for the gamma-rays from  $\text{Co}^{60}$ .

would correspond, according to the Klein-Nishina formula (4), to a value of  $h\nu/mc^2$  equal to 2.40 or an average quantum energy of 1.22 Mev. As the result of beta-ray studies, Deutsch, Elliott, and Roberts (1) gave the energies of the  $\text{Co}^{60}$  lines as  $1.10 \pm 0.03$  and  $1.30 \pm 0.03$  Mev., respectively, which would correspond to a mean energy of 1.21 Mev. Our absorption measurements are, therefore, in good agreement with the beta-ray results and lie within the experimental error of those experiments. Alternatively, the agreement may be regarded as verifying the Klein-Nishina calculations of scattering absorption coefficients. Comparison may also be made with the theory of photoelectric absorption given by Hulme, McDougall, Buckingham, and Fowler who give their results (3) in the form of a graph of a calculated function

of the photoelectric absorption coefficient per atom over a range of atomic number and quantum energies. Values of photoelectric absorption coefficients per electron, deduced by graphical interpolation from their results for the elements measured by us, are given in the Table II below for  $\alpha = 2.40$ .

The experimental values of  $\tau_e$  are obtained by subtracting  $1.90 \times 10^{-25}$  from the measured total absorption coefficient per electron, pair formation being negligible for  $\text{Co}^{60}$  radiation.

The Hulme theory does not lead to any simple relation between  $\tau_e$  and  $Z$ , but suggests a variation of  $\tau_e$  roughly proportional to  $Z^{3.56}$ , which is distinctly faster than  $Z^3$ , over the region of  $Z$  from 10 to 80 for the radiation having  $\alpha = 2.40$ . The theoretical and experimental values of  $\mu$  per electron are plotted against  $Z$  in Fig. 7 and the values of  $\tau_e$  given in Table II

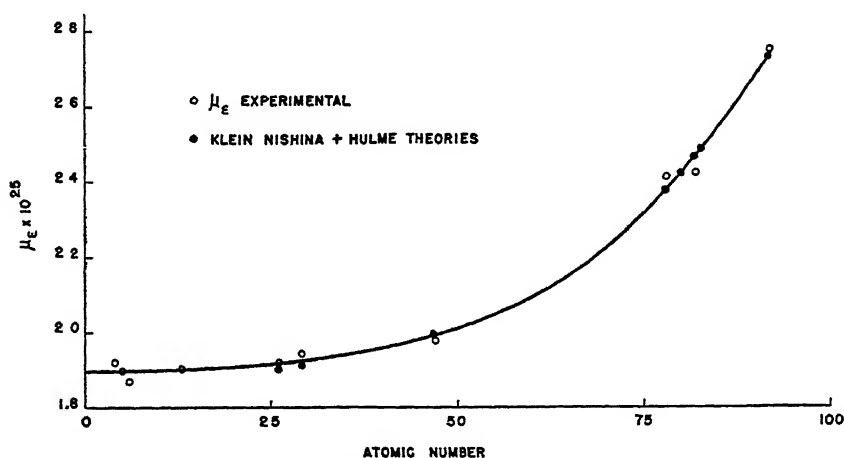


FIG. 7. Theoretical and experimental values of the absorption coefficient per electron plotted against atomic number  $Z$

TABLE II

$Z$	$\tau_e \times 10^{25}$		$Z$	$\tau_e \times 10^{25}$	
	Theoretical	Experimental		Theoretical	Experimental
26	0.01	0.02	80	0.51	0.51
29	0.02	0.04	82	0.56	0.52
47	0.09	0.08	83	0.57	0.57
78	0.47	0.51	92	0.83	0.84

It will be seen that the experimental and theoretical results for  $\tau_e$  are also in good agreement. We conclude, therefore, that both scattering and photoelectric theories are satisfactory in the region of 1.2 Mev. It would be of considerable interest to repeat the experiments with a substantially monochromatic radiation in a different energy region.

## References

1. DEUTSCH, M., ELLIOTT, L. G., and ROBERTS, A. *Phys. Rev.* 68 : 193-197. 1945.
2. DUBRIDGE, L. A. and BROWN, H. *Rev. Sci. Instruments*, 4 : 532-536. 1933.
3. HULME, H. R., MCDUGALL, J., BUCKINGHAM, R. A., and FOWLER, R. H. *Proc. Roy. Soc., London*, A149 : 131-151. 1935.
4. KLEIN, O. and NISHINA, Y. *Z. Physik*, 52 : 853-868. 1929.
5. MAYNEORD, W. V. and ROBERTS, J. E. *Nature*, 136 : 793. 1935.
6. ROBERTS, J. E. *Proc. Roy. Soc., London*, A183 : 338-355. 1945.
7. RUTHERFORD, E., CHADWICK, J., and ELLIS, C. D. *Radiations from radioactive substances*. Cambridge Univ. Press, London. 1930.
8. TANDBERG, J. *Inaugural Dissertation*, University of Uppsala. 1937.
9. TARRANT, G. T. P. *Proc. Cambridge Phil. Soc.* 28 : 475-489. 1932.

# THE *E*-PLANE RADIATION PATTERN OF SHORT ELECTROMAGNETIC HORNS OF LARGE APERTURE<sup>1</sup>

BY G. A. WOONTON<sup>2</sup> AND J. G. TILLOTSON<sup>3</sup>

## Abstract

The relation between the power received by a short, rectangular, electromagnetic horn, and its angular position in a plane electromagnetic field can be calculated, for rotation in the plane of the electric vector, from ordinary optical theory by assuming that the aperture produces at the throat a Fresnel diffraction pattern appropriate to the angular position of the aperture. Experimental results for four horns of slant lengths 25, 50, 100, and 176 cm, but all of the same aperture,  $10\lambda$  to a side at a wave length of 3.2 cm, are in good agreement with the theoretical predictions at angles up to  $\frac{1}{4}$  radian from the axis, for slant lengths down to 50 cm but not down to 25 cm.

## Introduction

The diffraction pattern of an aperture as discussed in physical optics and the radiation pattern of an antenna both result from the same physical phenomena; the close relation between the two is particularly apparent if the antenna is a microwave electromagnetic horn. In that case the electromagnetic wave which falls on the mouth of the horn and converges on the throat, or which diverges from the throat to be radiated from the mouth, can be identified with a light wave that falls on a slit in a screen, to be diffracted to a field point, or which diverges from a point source to fall on a slit and form a diffraction pattern.

Mathematical relations which are adequate for the prediction of optical diffraction patterns must be used with caution when applied to the prediction of microwave radiators. This is not due to any difference in phenomena; the discrepancies appear because of the very great difference in the relative dimensions of the waves and the apparatus in the two cases. The approximations which are inherent in the optical, Huygens-Kirchhoff method of calculation are of two kinds: fundamental approximations which are essentially a misstatement of the nature of the phenomena, and superficial approximations of trigonometry and algebra, which are introduced to simplify mathematical manipulations. Errors due to the first kind of approximation are most serious when the dimensions of the aperture are comparable with the wave length; errors due to trigonometrical and algebraic approximations become important when the point at which the field is to be predicted is taken at a relatively few wave lengths from the aperture.

The radiation patterns of apertures of various shapes have been predicted by Barrow and collaborators, by Chu, and by Schelkunoff (1; 2; 3; 4, Chap. IX), by methods which are exact in the statement of boundary conditions,

<sup>1</sup> Manuscript received June 20, 1947

Contribution from the Department of Physics, University of Western Ontario, London, Ont.

<sup>2</sup> Research Professor.

<sup>3</sup> Demonstrator.

$$\frac{b}{a+b} \doteq 1; \quad \phi \doteq \alpha; \quad \overline{TC} \doteq a\phi; \quad \overline{TU} \doteq \frac{W}{\gamma} - a\phi; \quad \overline{TR} \doteq \frac{W}{\gamma} + a\phi$$

length of the horn from its vertex. In the illustration it has been rotated through an angle  $\phi$  so that a ray from the source,  $S$ , directed at the vertex of the horn,  $P$ , meets the equiphase locus  $UTCR$  at  $T$ , which is then the pole of the system. According to well known theory (5, p. 228) one can write:

$$|E|^2 = \frac{ab\lambda}{2(a+b)} \left\{ \int_{-V_1}^{V_2} \cos \frac{\pi v^2}{2} dv \right\}^2 + \left\{ \int_{-V_1}^{V_2} \sin \frac{\pi v^2}{2} dv \right\}^2$$

In these relations,

$|E|$  = the absolute value of the electric field strength;

$a$  = the slant length of the horn from mouth to vertex;

$b$  = the distance from the source to the pole of the system;

$\lambda$  = wave length of the radiation;

$W$  = width of the horn mouth, here taken equal to the arc  $UTCR$  as a convenient approximation;

$$V_2 = \sqrt{\frac{2(a+b)}{ab\lambda}} \cdot \overline{TU}$$

$$V_1 = \sqrt{\frac{2(a+b)}{ab\lambda}} \cdot \overline{TR}$$

When radiation patterns are measured, the source,  $S$ , is made very distant so that all rays from the source are approximately parallel at the mouth of the horn. Then

$$b \rightarrow \infty, \quad \frac{b}{a+b} = 1 \quad \text{and} \quad \phi = \alpha,$$

$$\text{so that } \overline{TC} = \alpha a = \phi a, \quad \overline{TR} = \left( \frac{W}{2} + a\phi \right) \quad \text{and} \quad \overline{TU} = \left( \frac{W}{2} - a\phi \right).$$

With these changes  $\frac{ab\lambda}{2(a+b)}$  becomes approximately  $\frac{a\lambda}{2}$  and the limits take on the simple forms:

$$V_2 = \sqrt{\frac{2}{a\lambda}} \left( \frac{W}{2} - a\phi \right) = \sqrt{\frac{2a}{\lambda}} \left( \frac{W}{2a} - \phi \right),$$

$$V_1 = \sqrt{\frac{2}{a\lambda}} \left( \frac{W}{2} + a\phi \right) = \sqrt{\frac{2a}{\lambda}} \left( \frac{W}{2a} + \phi \right).$$

Since the wave guide at the throat of the horn imposes a sinusoidal variation on the amplitude of the received radiation in the  $H$ -plane and since the Fresnel integrals imply uniform field across the aperture, this method can be used to calculate  $E$ -plane patterns only.

The horns were measured by rotating them on a turntable, mounted about 15 ft. above the ground, in a location free of any obstruction, at a distance of 88.5 m. from the source of the 3.2 cm. waves. The distant source,  $S$  (see Fig. 1), of the radiation consisted of a 3.2 cm. Shepherd klystron coupled through wave guide to a dipole array at the focus of a paraboloid mirror; the aperture of the mirror was chosen small enough to produce a uniform patch of nearly plane waves over the whole region in which the horn was rotated. The output of the klystron was square wave modulated at 150 c.p.s. The radiation was detected by a silicon crystal at the throat of the horn and the

modulation component passed on through a tuned amplifier stage to an attenuation box and thence to other tuned stages and an output meter. The noise bandwidth of the system was 8 c.p.s. and the whole system including the crystal was found to be linear with power over a range of 30 db.

At each change in the angle  $\phi$  of  $1^\circ$  the attenuation box was adjusted to bring the output of the system to a standard value. The attenuation in decibels in each case was used as a measure of the relative power received.

## Results and Conclusions

All of the electromagnetic horns which were used in these experiments were built with the same aperture, 32 cm. square or  $10\lambda$  at the operating wave length of 3.2 cm. The slant lengths, that is, the values for  $a$  of the horns, are 176, 100, 47.5, and 25 cm. The horns are of approximately square cross section but all are subject in some measure to irregularities in construction which produce asymmetries in their radiation patterns. Measurement shows a slight departure from the assumed constant field at the horn mouth in the  $E$ -plane of the longer horns and a pronounced departure in the shortest, 25 cm. horn; it is assumed that these irregularities are due to horn modes other than the  $TE_{01}$  generated by discontinuities at the horn throat.

Figs. 2, 3, 4, and 5 are the  $E$ -plane radiation patterns of the horns; both measured and calculated values of relative power at the horn throat are plotted in these graphs as a function of the angular displacement of the horn from the line joining horn and source. Of all the measured patterns that for the shortest horn alone bears no relation to the predicted values; in view of the probable presence of other modes this is not conclusive evidence of the complete failure of the Kirchhoff approximations at a distance appropriate to the length and aperture of this horn. The figures show that measured and predicted values are in agreement up to an angular displacement of  $15^\circ$  or  $\frac{1}{4}$  radian for horns as short as 50 cm. (16 wave lengths); there is some evidence that for horns longer than 50 cm. even the minor disagreements within the  $\frac{1}{4}$  radian limit are due to horn asymmetries rather than to failure of the optical theory.

FIG. 2. *Measured and calculated radiation patterns of a rectangular horn radiator. Rotation is in the plane of the electric vector. The slant length of the horn (dimension  $a$  of Fig. 1) is 176 cm. The aperture of the horn is 10 wave lengths square = 32 cm. Wave length = 3.2 cm. Theoretical values ——— Measured values + ——— + ———*

FIG. 3. *Measured and calculated radiation patterns of a rectangular horn radiator. Rotation is in the plane of the electric vector. The slant length of the horn (dimension  $a$  of Fig. 1) is 100 cm. The aperture of the horn is 10 wave lengths square = 32 cm. Wave length = 3.2 cm. Theoretical values ——— Measured values + ——— + ———*

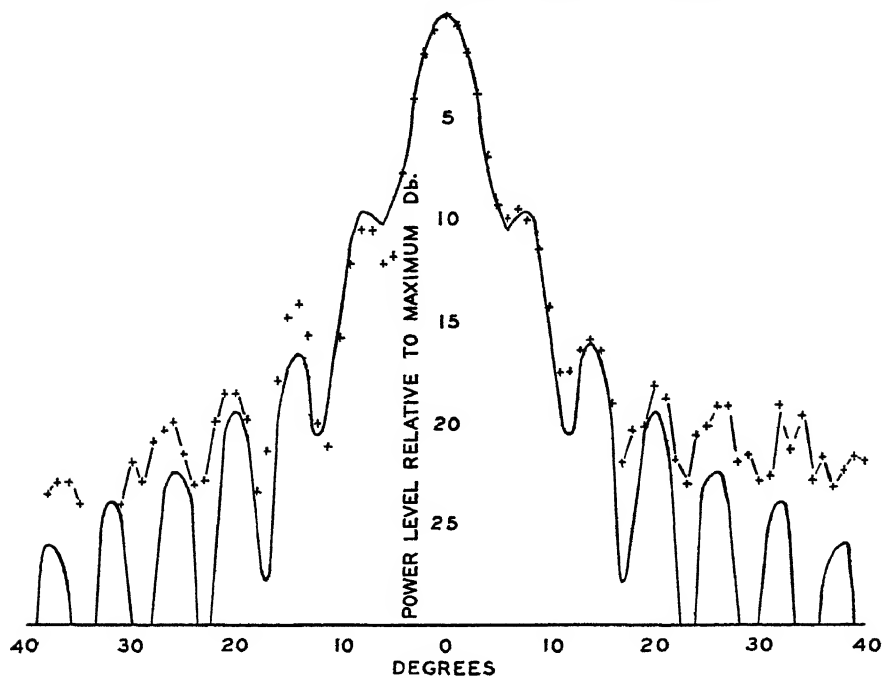


FIG. 2.

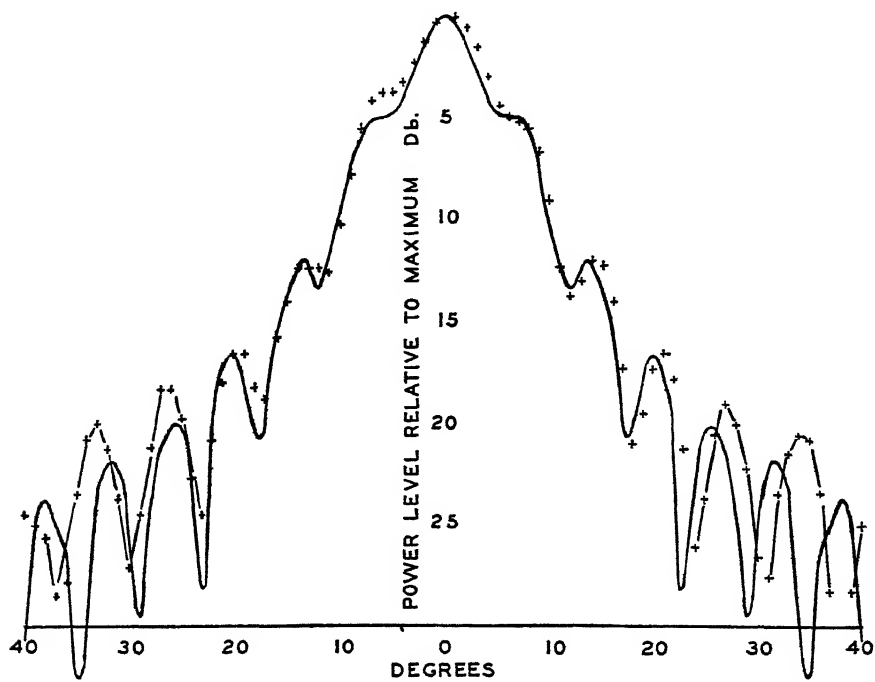


FIG. 3.

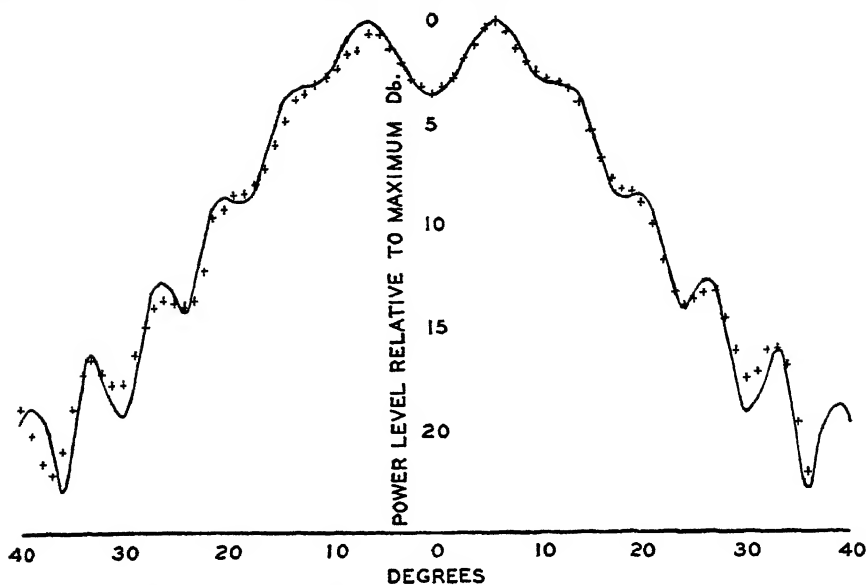


FIG. 4. Measured and calculated radiation patterns of a rectangular horn radiator. Rotation is in the plane of the electric vector. The slant length of the horn (dimension  $a$  of Fig. 1) is 47.5 cm. The aperture of the horn is 10 wave lengths square = 32 cm. Wave length = 3.2 cm.

Theoretical values ——— Measured values + ——— + ———

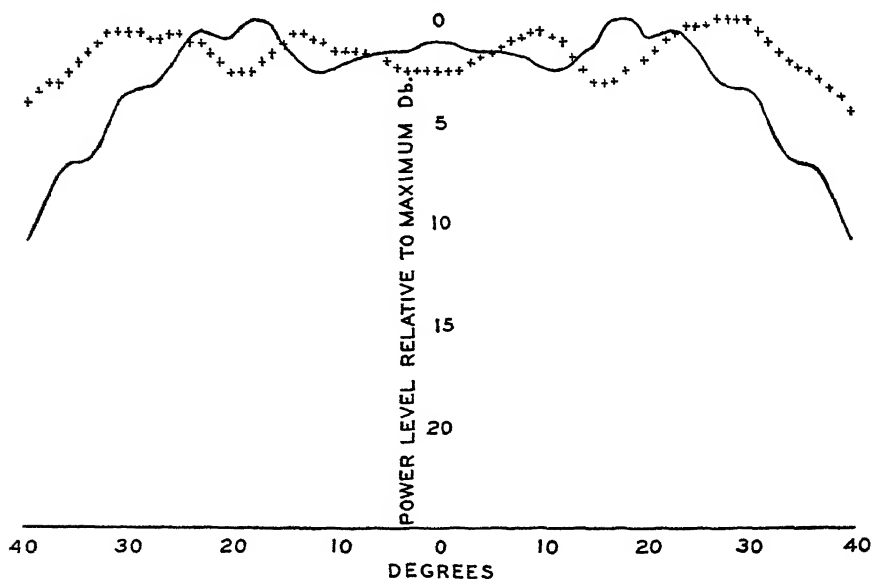


FIG. 5. Measured and calculated radiation patterns of a rectangular horn radiator. Rotation is in the plane of the electric vector. The slant length of the horn (dimension  $a$  of Fig. 1) is 25.0 cm. The aperture of the horn is 10 wave lengths square = 32 cm. Wave length = 3.2 cm.

Theoretical values ——— Measured values + ——— + ———

### Acknowledgment

This research was made possible by a grant from the National Research Council of Canada.

### References

1. BARROW, W. L. and CHU, L. J. Proc. Inst. Radio Engrs. 27 : 51-64. 1939.
2. BARROW, W. L. and GREENE, F. M. Proc. Inst. Radio Engrs. 26 : 1498-1519. 1938.
3. CHU, L. J. J. Applied Phys. 11 : 603-610. 1940.
4. SCHELKUNOFF, S. A. Electromagnetic waves. D. Van Nostrand Company, Inc., New York. 1943.
5. WOOD, R. W. Physical optics. 3rd ed. The Macmillan Company, New York. 1934.

# THE USE OF DIAPHRAGMS IN THE ELECTRON MICROSCOPE<sup>1</sup>

BY S. G. ELLIS<sup>2</sup>

## Abstract

A method is described for deducing electron trajectories from optical measurements made on the electron microscope. A device for centring and changing apertures while the microscope is in operation is described. The choice of the size and position for diaphragms is discussed, together with other factors involved in their use.

Diaphragms, when used in the electron microscope, act either as field limiting or aperture limiting diaphragms. The objective diaphragm acts as an aperture limiting diaphragm by removing from the beam leaving the specimen electrons whose trajectories made more than a certain angle  $\alpha_0$  with the axis of the lens at the specimen. This angle  $\alpha_0$  is called the angular aperture of the lens. More precisely it may be called the physical angular aperture of the lens. The objective diaphragm will also prevent, to a certain extent, electrons from reaching the final image if they have been inelastically scattered by parts of the specimen not conjugate with that image. The objective diaphragm therefore increases the contrast in the final image, and in principle might be expected to increase the resolution in micrographs.

## Theory of Diaphragm Sizes and Positions

When the 1944 Toronto electron microscope (2) was constructed, provision was made for putting diaphragms in the three magnetic lenses at any point on the axis and for centring the diaphragms while the microscope was in operation. The design of this microscope was made by Drs. L. Newman and J. H. L. Watson (12). It fell to the writer to determine the best sizes and axial positions for the diaphragms. It was evident that the solution of this problem depended on discovering the electron trajectories in the lenses.

From the work of Dosse (3) it was known that the axial field of an objective lens with two identical pole pieces could be described with fair accuracy by the empirical formula

$$H = H_0 / (1 + z^2/a^2) . \quad (1)$$

Here, an  $Oz$  axis has been chosen, positive in the direction of electron motion, and with origin at the field maximum.  $H_0$  is the maximum axial magnetic field, and  $a$  is the distance along the axis at which the field falls to  $H_0/2$ .

Glaser had solved the paraxial ray equation for this field distribution and had given a very complete account of the optics of the lens (4).

<sup>1</sup> Manuscript received June 27, 1947.

Contribution from the Department of Physics, University of Toronto, Toronto, Ont.

<sup>2</sup> Research Assistant and Lecturer. Holder of a Fellowship under the National Research Council of Canada, 1945-1946. Now at RCA Laboratories, Princeton, N. J.

If  $r$  is the radial displacement of the electron, the general solution of the paraxial ray equation for the above field is,

$$r = a[1 + z^2/a^2]^{\frac{1}{2}} \left\{ C_1 \sin ([1 + k^2]^{\frac{1}{2}} \operatorname{arccot} z/a) + C_2 \cos ([1 + k^2]^{\frac{1}{2}} \operatorname{arccot} z/a) \right\}, \quad (2)$$

$$\text{where } k^2 = -\frac{eH_0^2 a^2}{8mV}, \quad (3)$$

$V$  = speed of the electrons in electron volts,

$e$  = charge of electron,

$m$  = mass of electron.

Marton and Hutter (10) have used this equation in a discussion of the optimum size and position for an objective diaphragm. Briefly, they determine the path of an electron leaving the centre of the specimen at a supposedly optimum angular aperture, after elastic collision with the specimen. They recommend that a diaphragm be placed in the plane where the radial displacement of such an electron reaches a maximum value ( $r_0''$  say) and that the diaphragm have this radius  $r_0''$ .

Two objections may be raised to this theory. In the first place such a diaphragm would exert an aperture limiting effect on electrons proceeding from the periphery of that part of the specimen imaged on the photographic plate, different from the effect on the electrons from the centre of the specimen. Second, the method of determining  $H_0$  and  $a$  is not clearly specified. The accurate determination of the axial field distribution is difficult because of the small size of the objective pole pieces, and the calculation of electron trajectories from such measurements notoriously inaccurate because of the cumulative nature of the errors (5). The method described below was evolved to obviate these difficulties.

If  $u_0$  = distance from specimen to the origin at the field maximum,

$v_0$  = distance from the origin to the intermediate image, then it can be shown from Equation (2) that

$$\frac{1}{v_0} - \frac{1}{u_0} = \frac{1}{z_f} + \frac{a^2}{u_0 v_0 z_f}, \quad (4)$$

where

$$z_f = -a \cot (\pi/[1 + k^2]^{\frac{1}{2}}), \quad (5)$$

the sign convention introduced above being maintained. Further, the magnification  $M_0$  is given by

$$M_0 = -\left[ \frac{a^2 + v_0^2}{a^2 + u_0^2} \right]^{\frac{1}{2}}, \quad (6)$$

the minus sign indicating inversion of the image in the meridional plane. It is supposed here that

$$1 < [1 + k^2]^{\frac{1}{2}} < 2.$$

If the position of the field maximum can be estimated from the pole piece configuration, and  $u_0$ ,  $v_0$ , and  $M_0$  are measured for the objective\*,  $a$  can be calculated from Equation (6),  $z_f$  from Equation (4), and then  $[1 + k^2]^{\frac{1}{2}}$  from Equation (5).

If the pole pieces of the objective are not identical, or if for any other reason the position of the maximum axial field is uncertain, the following procedure may be employed.

Let  $u_0'$  be the distance from the object to some arbitrarily chosen level, such, for example, as the upper surface of the upper pole piece. Then

$$u_0 = u_0' + z'$$

and

$$M_0 = - \left[ \frac{v_0^2}{a^2 + (u_0' + z')^2} \right]^{\frac{1}{2}}, \quad (7)$$

neglecting  $a$  in comparison with  $v_0$ .

Then 
$$\left( \frac{v_0^2}{M_0^2} - u_0'^2 \right) = 2z' u_0' + (a^2 + z'^2). \quad (8)$$

Plotting  $\left( \frac{v_0^2}{M_0^2} - u_0'^2 \right)$  against  $u_0'$  for different values of the latter, a straight line will be obtained if the range of objective currents is small enough that  $a$  remains unchanged. The slope of the line is  $2z'$  and its intercept  $(a^2 + z'^2)$ , from which  $a$  may be found.

The numerical calculation of the trajectory is facilitated by rewriting Equation (2) in the form

$$y = [1 + x^2]^{\frac{1}{2}} A \sin(\omega \theta + \epsilon), \quad (9)$$

where  $x = z/a$

$$y = r/a$$

$$\theta = \operatorname{arccot} z'/a$$

$$\omega = [1 + k^2]^{\frac{1}{2}}. \quad (10)$$

The angular aperture of the lens is

$$\alpha = \frac{dr}{dz} = \frac{dy}{dx}$$

measured at the object, where

$$\frac{dy}{dx} = [1 + x^2]^{-\frac{1}{2}} \cdot [x A \sin(\omega \theta + \epsilon) - \omega A \cos(\omega \theta + \epsilon)]. \quad (11)$$

For any assumed value of the aperture, the values of  $r$ ,  $z$ , and  $\alpha_0$  at the specimen may be substituted in Equations (9) and (11), and the specific values of  $A$  and  $\epsilon$  deduced. Corresponding values of  $x$  and  $y$  for  $z$  in the range

$$u < z < 2z_f$$

can be calculated, the trajectories plotted, and the axes converted to values of  $r$  and  $z$ . This has been done in Figs. 1 and 2 for an objective used in the

\* The intermediate image is usually formed below the intermediate screen, a fact which must be kept in mind if magnification measurements are made at the intermediate screen.

1944 Toronto microscope. In effect, trajectories of the form given by Equation (2) have been fitted to the known initial and final trajectories for the objective.

It is seen in Figs. 1 and 2 that the trajectories pass through an exit pupil or crossover at  $z = 0.4$  cm. and that a diaphragm placed there will exert the same aperture limiting effect on electrons from all of the observed parts of

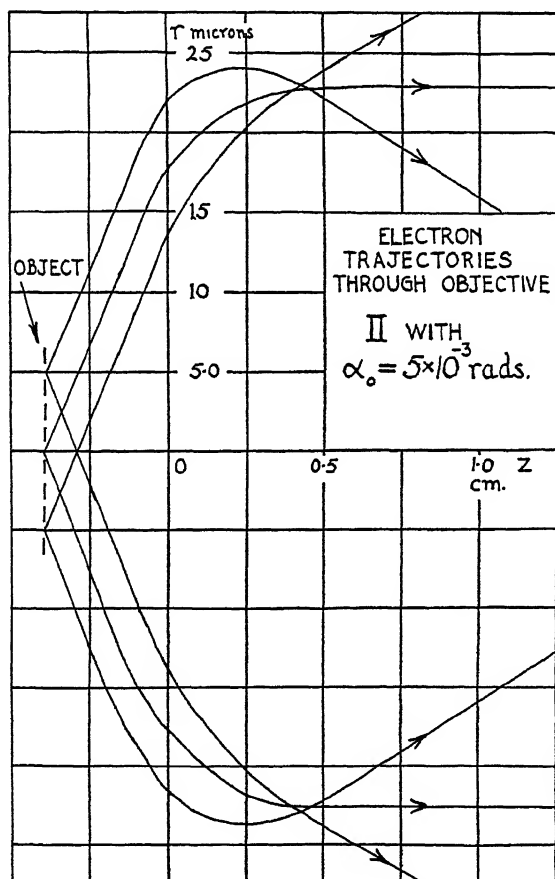


FIG. 1.

the specimen. It may be mentioned that for the trajectories shown in Figs. 1 and 2 the aperture  $\frac{dr}{dz}$  at  $z = u$  is 2% greater than at  $z = -\infty$ . That is, the field of this objective does not exert a noticeable converging effect on the illuminating beam.

The radius of the diaphragm depends on the angular aperture at which it is desired to operate the objective. A number of courses are open. For example, the angular aperture may be made equal to the maximum angular

aperture of the illuminating beam. This will permit focusing with a smaller depth of field than that used in making micrographs. Another course is to make the physical aperture equal to the calculated optimum angular aperture. At present, however, decisive experimental proof of the existence of an

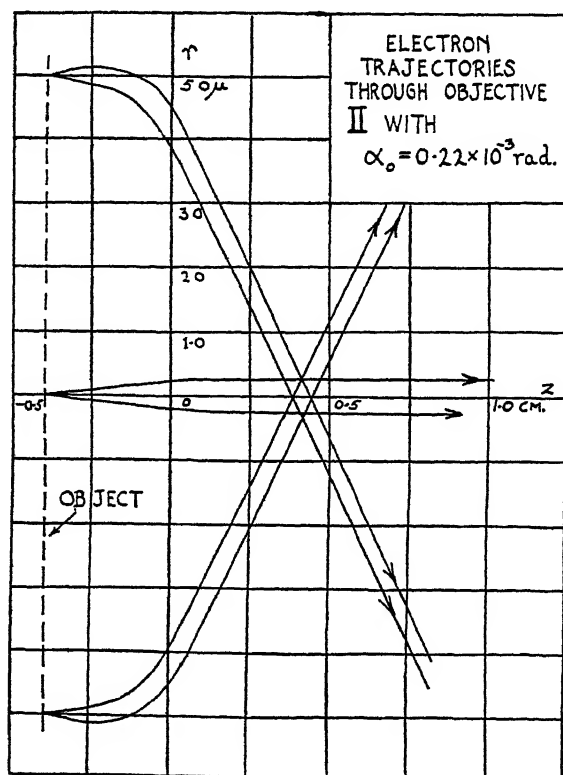


FIG. 2.

optimum angular aperture, as predicted by theory, is lacking. So long as the diaphragm is used primarily to increase contrast, the size of the diaphragm is not too critical, and the latter course mentioned above will lead to an acceptable solution.

### Choice of Angular Aperture

The optimum angular aperture  $\alpha_{OPT}$  is usually calculated by combining the diffraction defect  $\delta_{DIFF}$  and the spherical aberration defect  $\delta_{SPH}$  either arithmetically

$$\delta = \delta_{DIFF} + \delta_{SPH}, \quad (12)$$

or by the error law

$$\delta = (\delta_{DIFF}^2 + \delta_{SPH}^2)^{\frac{1}{2}}. \quad (13)$$

If  $C_{SPH}$  is the spherical aberration coefficient of the objective then

$$\delta_{SPH} = C_{SPH} \alpha^3 \quad (14)$$

and

$$\delta_{DIFF} \doteq \lambda/2 \alpha, \quad (15)$$

where  $\lambda$  is the de Broglie wave length of the illuminating electrons. When  $\alpha$  and  $k^2$  are known, the coefficient  $C_{SPH}$  can be estimated from the formula given by Glaser (4). Fig. 3 shows the variation of  $\delta$  with  $\alpha$  according to Equations (12) and (13) for an objective used in this laboratory. This

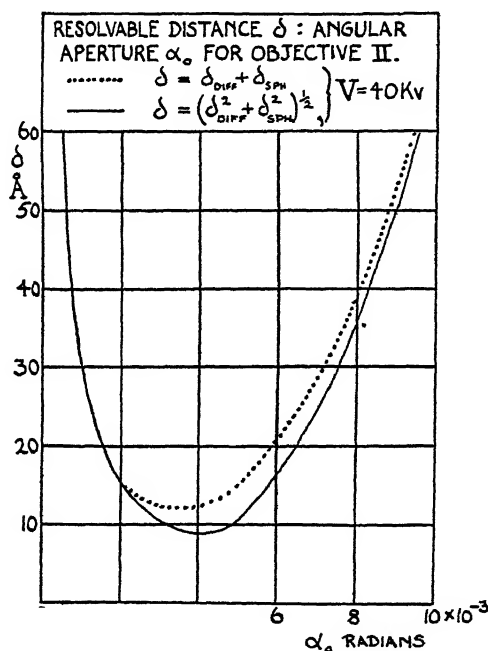


FIG. 3.

indicates that for  $\alpha$  between  $2$  and  $6 \times 10^{-3}$  the calculated resolving power of the microscope is less than  $20 \text{ \AA}$ . In other words, a  $50 \mu$  diameter diaphragm should be suitable for such a lens if one wished to attain the highest resolution in examining thin specimens with well defined variations in mass thickness.

With thicker specimens, the value of  $\alpha_{OPT}$  will differ from that given above, yet in practice a diaphragm chosen on the above considerations will prove a suitable compromise.

With many specimens the effective resolution is conditioned by contrast limitations in the image caused by the fact that different parts of the specimen have little difference in electron scattering power. It should be noticed, however, that the inner potential of the specimen may contribute effects that tend to enhance the contrast in the image.

Consider, for example, a specimen in the form of a film with surfaces that have concave and convex parts. Such a specimen is shown in section in Fig. 4. For our present purposes it is sufficient if the equipotentials showing

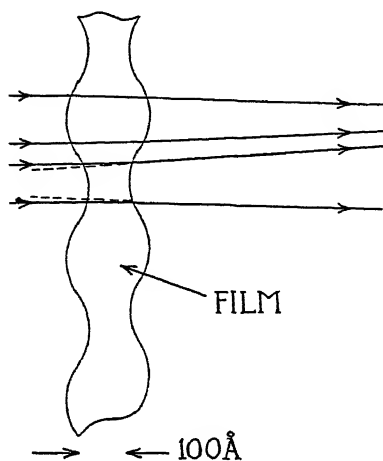


FIG. 4. Refraction in thin film.

the transition to the inner potential have the form shown in the figure. Let the radius of curvature of these surfaces be  $R$  and the inner potential be  $V_i$ . If biconvex parts of the film exist they will act as a converging lens on the electrons of focal length

$$f_i = V_i R / V_i. \quad (16)$$

For  $V_i = 10$  v.,  $V = 50$  kv., and  $R = 100 \text{ Å}$ ,  $f_i = 50 \mu$ . If then the objective is underfocused (objective current low) by  $50 \mu$ , bright regions will be formed in the image at points conjugate to biconcavities in the film; or if overfocused by  $50 \mu$ —at points conjugate to biconvexities.\* The in-focus image should show less contrast.

If one wishes to gain information about the specimen by employing this effect it would seem desirable to employ the smallest aperture that will still permit adequate resolution according to Equation (15). For in this way the confusing effect of the scattered electrons, reasonably uniform for the whole specimen, will be avoided and the refraction effect enhanced in comparison.

It may be noted here that the objective diaphragm size and position may be determined rapidly by the following approximate method. If  $\alpha_0$  is the maximum angular aperture to be permitted for the objective, the diaphragm radius  $r_0''$  is given approximately by

$$r_0'' = \alpha_0 f = \alpha_0 (a^2 + z_f^2)^{\frac{1}{2}}. \quad (17)$$

The diaphragm may be placed at a distance  $z_f$  below the centre of the lens.

\* It is possible that some of the contrast in Fig. 2, reference (9), is due to this effect.

Since the condenser lens may be treated as a thin lens, and since the electron trajectories near the lens are effectively parallel to the axis, the diaphragm radius can be calculated from

$$r_c'' = v_c \alpha_c (\max),$$

where  $\alpha_c (\max.)$  = maximum angular aperture of the illuminating beam,

$v_c$  = distance from the centre of the condenser lens to the specimen.

### Method of Manufacture

A steel needle is ground on a fine oilstone block until the point, viewed at  $\times 100$  in a light microscope, has the appearance shown in Fig. 5. To obtain a very fine point, the needle is held very obliquely to the surface of the oilstone and moved in the direction of its length. The needle is rotated during grind-



FIG. 5. Profile of needle point for making diaphragms.

ing to ensure that the point shall be free from flat surfaces. Abrasive is removed from the needle by dipping it in dilute nitric acid (one volume of concentrated acid to two volumes of distilled water), then washing in distilled water, and then scrubbing it with a lint-free lens paper.\* This is a variation on a method first described by Hillier (6).

The condenser diaphragm is made from 0.005 in. bronze sheet, and the objective diaphragm from 0.002 in. copper or brass foil. The diaphragm blank is cut to size with a suitable punch, flattened, and placed on a glass microscope slide. The holes are then gently drilled with a needle, using a rotary motion. In the case of the objective diaphragm one large hole (1 or

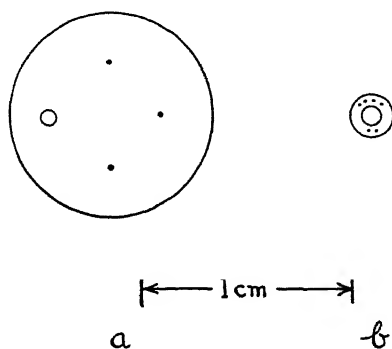


FIG. 6. Two forms of objective diaphragm.

2 mm. diameter) is made with a punch and the smaller holes are drilled around it as shown in Fig. 6, *a* and *b*. Holes down to  $30 \mu$  diameter can be made in this way. With practice, holes down to  $5 \mu$  diameter can be produced.

\* Ross-Adams Lens Tissue is suitable.

The finished diaphragm is cleaned by etching in dilute nitric acid and washing in distilled water. It can be dried on lint-free lens paper. Both sides of the diaphragm are then examined in a light microscope to ensure that it is free from dirt and lint. The diaphragm should be completed as shortly as possible before its inclusion in the microscope so that it is exposed to air-borne dust for the minimum time. The final test of the cleanliness of the diaphragm is made when the microscope is in operation.

A more elaborate arrangement for making diaphragms has been described by von Ardenne and Reibedanz (1).

### Method of Mounting

The diaphragm, *D* (Fig. 7), is mounted on the top of a brass chimney, *C*, which has a base, *B*, that bears on the lower surface of the lens. This base is held to the lens by a retaining ring, *P*. The chimney is moved, transversely

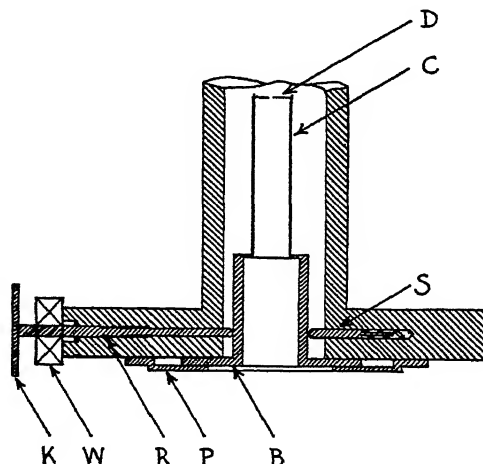


FIG. 7. *Diaphragm moving mechanism. Vertical centre section, not to scale.*

to the axis of the lens, by a rod, *R*, which has a threaded section, and is kept in contact with *B* by a sprung rod, *S*, bearing on the other side of the chimney. The rod, *R*, can be turned from outside the microscope by the knob, *K*, the Wilson seal, *W*, maintaining the vacuum (14). A similar rod for movement perpendicular to the plane of Fig. 7 is also provided.

Fig. 8 shows a detail of the top of a diaphragm chimney. In Fig. 8*a* the lower surface of the lower pole piece has been hollowed to permit the lateral movement of the diaphragm. The diaphragm in this case consists of one large hole (1 mm. diameter) and several smaller ones, as shown in Fig. 6*a*. The diaphragm is held to the chimney by a retaining ring. In Fig. 8*b*, which shows a lens of shorter focal length, the diaphragm is soldered with Wood's metal to two wires projecting from the top of the chimney. No flux is used in this soldering. Here the diaphragm is smaller but still consists of one large

hole surrounded by several smaller holes (Fig. 6b). Where the diaphragm is soldered to the supports, a final etching with nitric acid is done after the soldering is completed.

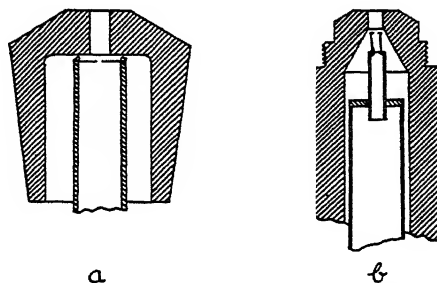


FIG. 8. Diaphragms in position beneath lower pole piece of objectives.

If the diaphragm is made large enough to accommodate several holes as shown in Fig. 6a then it will have to be situated somewhat below the exit pupil of the lens. In order that rays from the periphery of the field of view shall not be obstructed, the radius of the diaphragm hole has to be increased. If plots such as those shown in Figs. 1 and 2 have been made, the required diaphragm radius is readily determined. Alternatively, an approximate value for the diaphragm radius may be calculated from

$$r_0'' = \alpha_0 (a^2 + z_f^2)^{\frac{1}{2}} + r_0' (d + z_f)/z_f, \quad (18)$$

where  $r_0'$  = radius of that part of specimen that is to be imaged on the photographic plate,

$d$  = distance from lens centre to the diaphragm.

While the objective lens is removed from the column it is convenient to record the number of turns of the knobs,  $K$  (Fig. 7), required to change from one hole to another of the diaphragm. It is very important that the large hole be sufficiently well centred by eye that the axis of the objective passes through it. If this condition is not observed, the intermediate screen may receive no electrons when the microscope is brought into operation, and the subsequent centring of the diaphragms and alignment of the lenses will be possible only if good fortune attends the attempt.

### Method of Centring

The condenser diaphragm is centred as accurately as possible by eye when it is introduced into the lens. The procedure for centring the condenser diaphragm can be best described with Fig. 9. With the diaphragm off the axis of the condenser lens the illumination, as viewed at the intermediate screen, follows a curved path as the condenser lens current is varied through the value giving the maximum aperture of illumination, i.e., varied through focus. With the condenser lens out of focus, the condenser diaphragm is moved until the enlarged area of illumination on the intermediate screen is

concentric with the position of the in-focus area of illumination. If the plane of the condenser diaphragm is not in the plane of the condenser lens centre, the above adjustment may have to be repeated after the usual procedure for aligning the illuminating system of the microscope has been performed. The centring of the condenser diaphragm can easily be done with a specimen in the microscope.

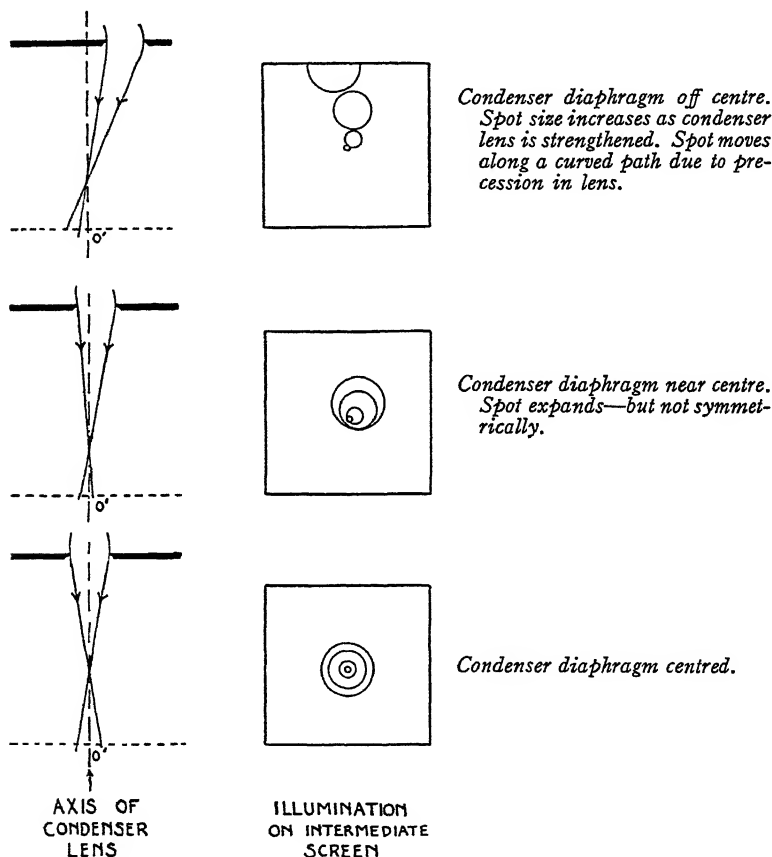


FIG. 9.

To centre one of the small holes in the objective diaphragm, the knobs,  $K$  (Fig. 7), are turned the appropriate number of revolutions as previously determined when the lens was removed from the column. This will generally bring the hole near to but not on to the axis of the lens. Since the exit pupil of the objective is about  $50\ \mu$ , or less, in diameter (See Figs. 1 and 2) it will act as a nearly point source of electrons, and if the diaphragm is  $d$  cm. below the exit pupil, will throw a shadow image of the diaphragm on the intermediate screen. The magnification  $M_0'$  of this image will be given by

$$M_0' = \frac{v_0 - z_f}{d} \doteq \frac{v_0}{d}. \quad (19)$$

Equation (19) provides an independent method for checking the accuracy of the measurement of  $z_f$ , since it permits the calculation of the position of the exit pupil when  $M_0'$  and  $v_0$  are known. For objectives in which the two pole pieces do not have the same form, Equation (19) provides the most accurate method of finding the position of the exit pupil. The diaphragm is next moved carefully until the shadow image of the hole coincides with the hole in the intermediate screen. This adjustment is easier if the condenser is out of focus, so that a large area of the intermediate screen is illuminated.

Dark field observation can be obtained by moving the objective diaphragm transversely as shown in Fig. 10, so that only scattered electrons can pass through to form the final image

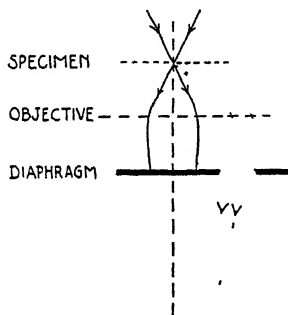


FIG 10 Objective diaphragm moved sideways so as to pass only scattered electrons and give dark field observation.

A final check on the cleanliness of the diaphragm can be made by making a double exposure and moving the diaphragm a small distance (less than  $r_0''$ ) sideways between the exposures. Under these conditions non-conducting bodies on the diaphragm will be charged to different amounts, producing image shifts, so that doubling of the image will appear in the doubly exposed plate.

In one method of using the 1944 Toronto electron microscope as an electron diffraction camera, the specimen is placed close below the projector lens. It is desirable to delimit the electron beam so that it will not strike the projector pole faces and also to decrease the effect of spherical aberration in the projector lens. This can be achieved by placing a diaphragm above the objective in the specimen cartridge. It can be centred by the object moving screws

The radius of the beam at the projector pole pieces will be approximately  $r_0'' v_0/u_0$ , where  $r_0''$  is the diaphragm radius. It is therefore advantageous to make  $u_0$  large in this case in order that  $r_0''$  shall not have to be very small.

### Observations

The most noticeable effect of the objective diaphragm is to increase the contrast in the image. A  $50 \mu$  diameter diaphragm has been customarily used in the 1944 Toronto microscope. This diaphragm has aided in the

examination of thick specimens and also specimens such as Formvar replicas, and soaps (without shadow casting) in which the contrast is low.

It cannot be said from the results obtained that the objective diaphragm has led to an increase in resolution. However, the instrument resolving power has been limited by lack of symmetry in the field of the objective and by the difficulty of obtaining exact focus, so that the above point remains undecided.

Dark field observation by the method shown above does not produce good resolution. This is in part due to the large chromatic error with the scattered electrons and in part due to the non-symmetric nature of the imaging beam. Dark field observation does, however, provide a sensitive method of observing the Bragg reflections from crystalline bodies if the diaphragm is so situated as to pass only the diffracted beam. This then provides a sensitive method for detecting small crystals in the specimen. Dark field observation also provides a method of observing qualitatively the scattering power of the specimen.

### Discussion

Some objections to the use of an objective diaphragm have been raised. Since the diaphragm is grounded to the body of the microscope, charges will be induced upon it that will deflect those electrons passing close to the diaphragm. While a precise mathematical treatment of the problem is difficult, an approximate calculation (15, pp. 700-701) shows that the error introduced amounts to  $10\text{\AA}$  (when referred to the object) for electrons passing within  $1\text{ }\mu$  of the wall in a typical case. It should be mentioned, however, that less than 10% of the imaging electrons pass within  $1\text{ }\mu$  of the wall if the diaphragm radius is greater than  $21\text{ }\mu$  even when the current per unit solid angle leaving the object is independent of direction.

Another objection that has been made is that if the objective aperture is made considerably less than the maximum aperture of the illumination, then the depth of focus does not decrease when the aperture of the illumination is brought to its maximum value as much as it would if  $\alpha_0$  was not defined by a diaphragm. As a consequence of this the visual focusing is made more difficult. This objection carries less weight now that electron microscopes can be focused at reduced aperture (8).

Finally, Hillier (7) has pointed out that a diaphragm situated at the exit pupil of the objective is in a position of maximum current density and that polarizing layers (11, 13) will form on the diaphragm, charge up from the electron beam, and lead to a decrease in the resolution by deflecting the imaging electrons. These polarization layers have been observed on diaphragms removed from the Toronto microscope. However, with several small holes in the diaphragm it is easy to change to a clean one if it is needed, and in any case the large hole, 1 mm. diameter, in the diaphragm can be used if any disturbing effect, either from polarizing layers or induced charge, is suspected.

It may be mentioned that the effect of the induced charges noted above is in opposition to the effect of the spherical aberration of the objective. In principle then, the spherical aberration of the objective could be corrected if a diaphragm at the exit pupil exerted on the electrons passing through it a centrifugal impulse proportional to the cube of their radial displacement up to a certain limiting value, and completely blocked electrons of greater radial displacement. It is evident that the design and construction of such a diaphragm would introduce very considerable difficulties and might well be unjustified by the ends to be secured.

Hillier (9) has described an objective using two components. The first is a weak lens giving approximately unit magnification, the second is a conventional objective of short focal length. Fig. 11 shows the approximate electron trajectories through such a lens for  $\alpha_0 = 5 \times 10^{-3}$ . It will be seen that a

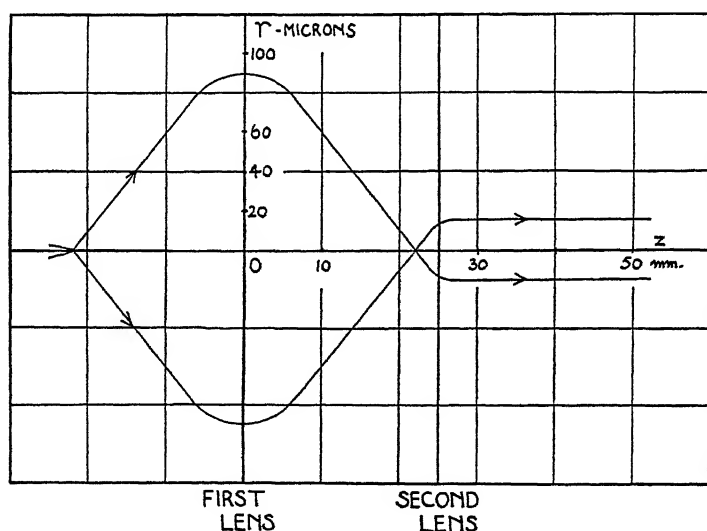


FIG. 11. *Approximate electron trajectories through double objective described by Hillier (9).*

diaphragm placed in the first component could have a diameter of nearly  $200 \mu$  and still exert the same limiting effect as a  $30 \mu$  diameter diaphragm in the second component. Moreover, by considering the paths of rays from the periphery of the specimen area examined it will be seen that the axial position of the diaphragm is not critical when considered in terms of its field limiting effect. Hillier reports, however, that a diaphragm when used in this lens causes asymmetries in the image. If, to consider a simple case, the disturbing effect of a diaphragm is to cause a deviation,  $\theta$ , in a marginal ray, irrespective of which component the diaphragm is in, then its effect on the intermediate image is greater by a factor  $2f_1/f_2$  if it is placed in the first component. Here  $f_1$  is the focal length of the first component and  $f_2$  that of the second. In so far as the disturbing effects are caused by the charging up of dust or polarizing

layers by scattered electrons, the deviation  $\theta$  will be less for a given particle of dirt and a given ray with the dirt on a diaphragm in the first component. This is because the current density at the midplane of the first component is less than at the second component. The net result is that from the point of view of disturbing effects on the beam there is little difference between the two positions of the diaphragm.\* Despite the greater spherical and chromatic aberrations of this system, this lens has the notable advantages of a greater working distance and a larger diaphragm size. The micrographs published by Hillier attest its virtues.

## Conclusions

Experience gained over the last three years with objective diaphragms in the 1944 electron microscope has led to the conclusion that despite their defects they are of great assistance in the examination of samples giving low contrast. With some samples their use has been imperative in visual observation and choice of field.

Now that high resolution micrographs of samples possessing well defined spacial variations of electron scattering power can be consistently produced, it will be important to try to improve the resolution when working with samples such as bacteria and viruses in which the various parts of the structure do not differ greatly in their ability to scatter electrons. For this reason it seems desirable to investigate further the influence of diaphragms on the resolution. If the cleanliness of the diaphragm is found to be a limiting factor then a mechanism such as that described above will be one way of providing a clean diaphragm whenever critical work is encountered. Alternatively, progress may be made only when the formation of the polarizing layers noted above can be suppressed, or when they can be removed from the diaphragm by heating it *in situ*.

## Acknowledgments

The author wishes to express his gratitude to Prof. E. F. Burton of the McLennan Laboratory for encouragement during the prosecution of this work, and to the National Research Council of Canada for a Fellowship.

## References

1. ARDENNE, M. v. and REIBEDANZ, H. Z. Instrumentenk. 60 : 22-26. 1940.
2. BURTON, E. F. and KOHL, W. H. The electron microscope; an introduction to its fundamental principles and applications. 2nd ed. Reinhold Publishing Corporation New York. 1946.
3. DOSSE, J. Z. Physik, 117 : 437-443. 1941.
4. GLASER, W. Z. Physik, 117 : 285-315. 1941.
5. GODDARD, L. S. and KLEMPERER, O. Proc. Phys. Soc., London, 56 : 378-396. 1944.
6. HILLIER, J. Ph.D. Thesis, University of Toronto. 1941.
7. HILLIER, J. Private communication
8. HILLIER, J. J. Applied Phys. 17 : 307-309. 1946.
9. HILLIER, J. R.C.A. Rev. VIII : 29-42. 1947.

\* I am indebted to Dr. Hillier for a discussion of the effects of contamination in this lens.

10. MARTON, L. and HUTTER, R. G. E. Phys. Rev. 65 : 161-167. 1944.
11. STEWART, R. L. Phys. Rev. 45 : 488-490. 1934.
12. WATSON, J. H. L. Ph.D. Thesis, University of Toronto. 1943.
13. WATSON, J. H. L. J. Applied Phys. 18 : 153-161. 1947.
14. WILSON, R. R. Rev. Sci. Instruments, 12 : 91-93. 1941.
15. ZWORYKIN, V. K., MORTON, G. A , RAMBERG, E. G , HILLIER, J., and VANCE, A. W.  
Electron optics and the electron microscope. John Wiley & Sons, Inc., New York,  
and Chapman & Hall, Ltd., London. 1945.

# A LOW-PRESSURE GLOW-DISCHARGE PROTON SOURCE<sup>1</sup>

BY PAUL LORRAIN<sup>2</sup>

## Abstract

A cold cathode proton source operating at about 200 v. at a pressure of a few microns is described. The discharge is essentially similar to that of a Philips vacuum gauge. The characteristics of the discharge, the ion extraction, and the proton production have been investigated. The addition of 10% of oxygen to the hydrogen increased the proton content of the ion beam from 10 to 50% while introducing only about 1% of oxygen and other foreign ions. The ionization processes are discussed.

## Introduction

The problem of the positive ion source for ion accelerators, and in particular of the proton source, has been stated by a number of authors (1, 5, 7, 13, 17, 21, 33, 36, 41, 42). It will suffice here to enumerate the desirable characteristics for such a source. They are: (a) ion beam current of the order of 1 ma. or more, depending on the accelerator, beam cross section of the order of 10 sq. mm., and low angular spread; (b) low energy spread in the ion beam; (c) high percentage of atomic ions; (d) low gas flow from the ion source to the accelerator; (e) small size; (f) low power dissipation; (g) stability, simplicity of operation and of power supplies. The relative importance of these characteristics depends on the accelerator and on the measurements contemplated.

For simplicity of operation, it is important that the source should not require a heated filament because (a) the filament is gradually destroyed by the positive ion bombardment and has a life span at most of the order of 100 hr., and (b) a filament power supply is required. Since the filament of a cyclotron ion source must be operated perpendicularly to a high magnetic field, it is usually heated with a high frequency current to reduce the mechanical strain, and the power supply required is elaborate and expensive. Most positive ion sources require a heated filament. The high voltage canal ray tube (7), the F. M. Penning (32), and the T. Franzini sources (14, 15, 19) are notable exceptions.

The type of discharge used in the present source appears to have been originated by L. R. Maxwell in 1931 (28). In his discharge, the electron path length from cathode to anode, and thus the number of ion pairs produced per electron emitted at the cathode, at low pressure, was multiplied by a large factor through electron oscillations. In this way, a low voltage discharge could be maintained even at very low pressures when the mean free path of the electrons for ionization was much larger than the dimensions of the discharge tube. Fig. 1 shows a schematic diagram of the Maxwell source.

<sup>1</sup> Manuscript received June 13, 1947.

*This work was performed partly at the Montreal Laboratory of the National Research Council and partly in the Département de Physique of the Université Laval, Quebec, Canada. Issued as N.R.C. No. 1629.*

<sup>2</sup> Physicist. Present address: Physics Department, Cornell University, Ithaca, N.Y., U.S.A.

A heated filament,  $F$ , was used as cathode and a plate,  $P$ , pierced with a hole opposite the filament, was used as anode. Parallel to the anode and on the side opposite to that of the filament was a second similar plate,  $Q$ , negative

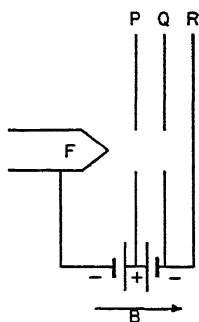


FIG. 1. *The Maxwell source.*

with respect to the anode. The electrons emitted by the filament were focused by a powerful axial magnetic field through the hole in the anode and reflected back to the filament by the second plate. The electrons were again reflected at the filament and thus described a large number of oscillations before reaching the anode. Positive ions were collected on a third parallel plate,  $R$ , through a hole in the second plate,  $Q$ . This source could produce 3 ma. of positive ions at a pressure of  $3 \mu$ , which is excellent, even today. It does not seem to have attracted much attention, however, probably because it required a magnetic field of 12,000 gauss and because the ions were collected immediately behind the second plate and were not available as a beam. Also, at the time, positive ion sources were of much less interest than they are today.

In 1937, F. M. Penning investigated two different types of low-pressure glow discharges in which electrons were made to oscillate in a magnetic field. One type was the 'inverted magnetron' (30). The other was essentially similar to L. R. Maxwell's source, but operated with a cold cathode. Using this latter type, F. M. Penning designed a vacuum gauge, now known as the Philips gauge (31), and an ion source (32). The discharge for his ion source occurred between three parallel plates, the two outside ones being the cathodes and the centre one, with a hole in its centre, being the anode. The magnetic field was axial. Electrons described oscillations between the two cathodes along the magnetic lines of force. The ion beam emerged from a hole in one of the cathodes. F. M. Penning's original paper seems to be the only one in the literature on this type of ion source. The operating voltage and the energy spread of the ion beam were very high, of the order of 10,000 v.

In 1940, A. T. Finkelstein (12) designed a source similar to that of Maxwell's, but operating at magnetic fields of a few hundred gauss and producing a maximum ion beam current of 150 ma. The operating voltage was low, about 50 v. This was followed in Germany by a number of similar sources (1, 2, 17, 41), notably those of M. von Ardenne (1, 2).

A. G. Ward, of the Montreal Laboratory of the National Research Council, undertook, in the spring of 1945, the design of a positive ion source of the Penning type for a Van de Graaff accelerator. With brass or steel electrodes, ion beam currents of 3.5 ma. were obtained at a pressure of 5 to 10  $\mu$  for a discharge current of 10 ma. and a discharge voltage of 1 to 2 kv. A later source gave ion beams of 100 to 150  $\mu$ a. at 1 or 2  $\mu$  with 500  $\mu$ a. and 5 kv. at the discharge. The main difficulties were the rapid variation of the source characteristics with pressure, the apparent existence of widely different modes of operation at a given pressure (42), and the fact that the proton percentage in the ion beam was unknown.

## I. Apparatus

### 1. The Vacuum System

Fig. 2 shows the ion source and the mass spectrograph used. Fig. 11a shows a schematic diagram of the discharge tube. Electrolytic hydrogen, supplied in tanks by the Dominion Oxygen Company, Montreal, and containing 99.7% hydrogen and 0.3% oxygen, was piped through a copper tube and admitted to the system through a needle valve. The pressure in the hydrogen line was kept slightly above the atmospheric pressure to avoid the possible introduction of air. Water and other vapors could be added to the hydrogen by bubbling it in a flask near the needle valve. Hydrogen could be mixed with various percentages of oxygen by collecting the gases over water in an inverted beaker serving as a gasometer. The water was at room temperature. When pure hydrogen was required, the needle valve was replaced by a palladium diffusion tube (20).

An RCA 1946 thermocouple vacuum gauge and a Distillation Products VG-2 ionization vacuum gauge were used. The calibration of the thermocouple gauge was assumed to be the same for pure hydrogen and for the mixture of about 90% of hydrogen, 10% of oxygen, and 2% of water vapor which was used in the latter part of the work.

Fig. 2 shows the position of the gas inlet and of the vacuum gauges. The upper cathode,  $K_1$ , had holes around its circumference such that their aggregate pumping speed was much larger than that of the hole in  $K_2$ . The gauge pressure was thus approximately equal to that in the discharge. For small anode diameters, the pumping speed at  $K_1$  was not sufficiently high and the gauge pressure was higher than the discharge pressure.

### 2. The Discharge Tube and the Beam Forming Lens

The discharge tube was designed with the experimental work described below in mind. The cathodes,  $K_1$  and  $K_2$ , and the anode,  $A$ , were made from 99.95% magnesium sticks supplied by Dominion Magnesium Limited, Toronto. The electrodes were supported on brass rings and glass spacers, and the whole was enclosed in a coaxial glass tube.  $R$  was evacuated directly, as shown, and provided a low pressure region for the electrode leads. The brass rings supporting the electrodes were water cooled by means of loops of fine copper tubing replacing the wire leads shown in Fig. 2. This discharge

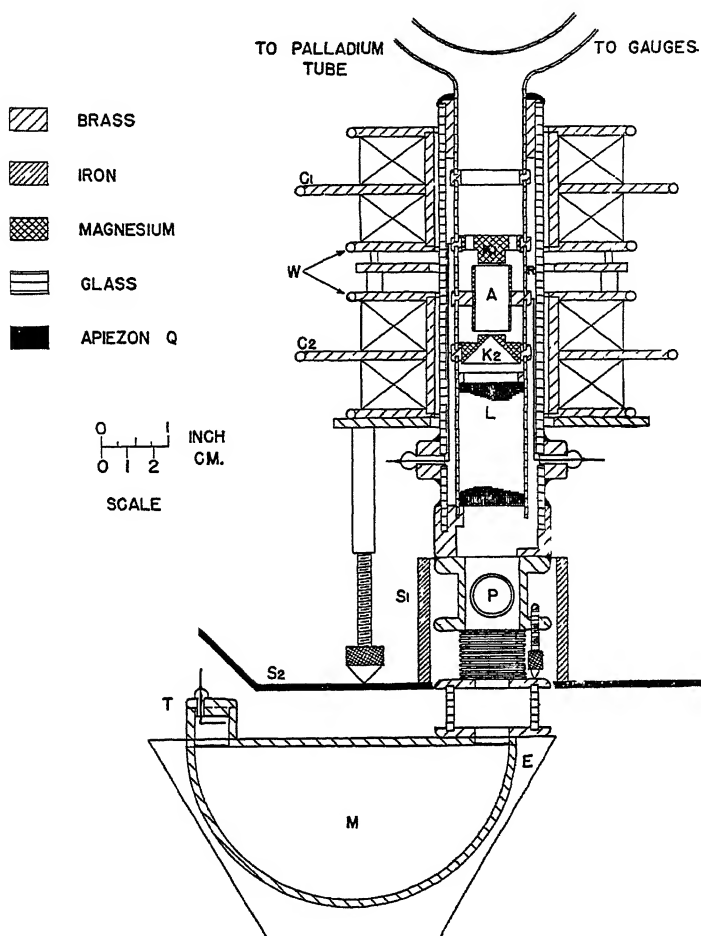


FIG. 2. Ion source and mass spectrograph.  $C_1$ ,  $C_2$ , coils for producing the magnetic field for the discharge;  $W$ , water cooling;  $A$ , anode;  $K_1$ ,  $K_2$ , cathodes;  $R$ , low pressure region for the electrode leads;  $L$ , accelerating lens electrode;  $P$ , to pumps;  $M$ , mass spectrograph;  $S_1$ ,  $S_2$ , magnetic shields;  $E$ , electromagnet pole piece;  $T$ , collector.

tube was particularly convenient because: (a) dismantling or reassembling it involved only two Apiezon cement seals and thus required only a few minutes, (b) no trouble was experienced from spurious discharges at the leads, (c) the gauge pressure was approximately equal to the discharge pressure, and (d) the incoming gas was exposed only to glass and metal.

The cathodes were always the ones shown, but anodes of various diameters and lengths were used.

The electrodes, glass spacers, and brass rings were cleaned by dipping them for a fraction of a second in concentrated hydrochloric acid, rinsing in tap water and distilled water, and drying with alcohol. To avoid contact with the hands, the cleaned parts were assembled with a glass rod.

The magnetic field required for the discharge was produced by a pair of specially designed water cooled coils shown in Fig. 2. Each of the four sections was wound with 370 turns of No. 17½ B & S gauge HF Formex wire. The magnetic induction along the axis was calculated to be 129 gauss per amp. within  $\pm 1\%$  over a distance of 3.3 cm. on either side of the centre. These coils could operate continuously at magnetic fields of 1,000 gauss, and, for short periods, at fields up to 4,000 gauss.

The ions emerging from the lower cathode were formed into a beam by means of the electrostatic lens action of the lower conical surface of the cathode,  $K_2$ , and the cylinder,  $L$ . Accelerating voltages of about 5,000 v. were used.

### 3. The Mass Spectrograph

The mass spectrograph used was of the Dempster type (8) with an ion path radius of 6.0 cm. The ion energy was held constant and the magnetic field was varied to focus the various types of ions on the slit of the collector,  $T$ . Narrow slits, about 1/64 in. wide, were used so that the energy spread of the ion beam could be estimated.

To reduce secondary electron emission from the collector, it was biased at +300 v. with respect to the body of the mass spectrograph. Two iron blocks resting on the electromagnet pole pieces on either side of the collector provided a magnetic field which also served to reduce secondary emission. The variation of the collector current with the collector bias indicated that under these conditions secondary emission was negligible. The 300 v. bias actually had no appreciable effect on the percentage composition of the ion beam.

The curve of collector current against magnet current showed sharp maxima corresponding to the different types of ions in the beam. With the magnet current set for a maximum detector current, a change of about 1% in the former reduced the latter to one-half its maximum value.

The collector current was measured with a vacuum tube voltmeter with a full scale sensitivity of  $1.33 \times 10^{-7}$  amp. on the lowest range. The ion beam currents used for the mass analyses were of the order of 500  $\mu$ a.

The percentage composition of the ion beam under a given set of conditions was always determined two or three times in succession and the mean percentages were used. With pure hydrogen, a mass analysis could be reproduced from one day to another within approximately the experimental error. For example, the points shown on Fig. 5 were taken on two different days, both sets of points covering the whole range of pressure. When a mixture of hydrogen, oxygen, and water vapor was used, the reproducibility was not as good, but satisfactory. The points for any given curve were always determined in random order to eliminate any possible time variation in the composition of the ion beam.

Direct observation of the mass spectrum on an oscillograph screen was made possible in the following manner. The mass spectrograph magnetic field was swept automatically at a frequency of about 1 c.p.s. by opening and

closing the circuit of the electromagnet with a switch operated by an electric motor and a cam. This provided a satisfactory approximation of a saw-tooth sweep of the magnetic field because of the inductance of the electromagnet. The voltage across a resistance in series with the electromagnet provided a horizontal sweep for a DuMont type 208 oscillograph arranged for d-c. amplification. The current from the collector,  $T$ , was passed through a resistance of a few megohms and the voltage across this was fed to the  $Y$ -axis amplifier of the oscillograph. The oscillograph therefore displayed a graph of the detector current as a function of the magnetic field, i.e., the mass spectrum. The accuracy of this method is limited by: (a) unavoidable 'noise' in the discharge, producing rapid variations in the beam current; (b) non-linearity of the oscillograph response; (c) frequency dependence of the oscillograph response, since the sweep is not strictly saw-tooth and the peaks are not all swept at the same speed. The effect of (a) is reduced by taking the average heights of the peaks for a few sweeps; (b) and (c) are relatively negligible. The agreement between the oscillograph and the vacuum tube voltmeter results was within the experimental error. This method has the great advantage of providing a continuous indication of the ion beam composition. It was extremely useful, especially for rapid qualitative observations. It permitted direct observation of time variations in the beam composition, which would have been difficult to observe otherwise.

## II. Results

### 1. The Discharge

The behavior of the discharge is highly satisfactory at pressures above a few microns; ignition is instantaneous and the operation is very reliable. The magnetic field does not need to be uniform or accurately axial, and can be supplied by a permanent magnet.

Magnesium was used for the cathodes because of its low work function and low sputtering, and also because of its availability and its machinability.

Cathodes of the shape shown in Fig. 2 concentrate positive ion bombardment of the cathodes and electron emission near the axis of the discharge. With flat cathodes, electrons emitted at their periphery reach the anode directly without oscillating and simply heat the anode without ionizing the gas. The green cathode light which is characteristic of magnesium (10) occurs only on that part of the cathodes that projects in the anode cylinder, except at high discharge currents.

It was observed that when the discharge was operated at potentials of the order of 1000 v., the anode material sputtered on to the cathode. It is thus desirable to use the same material for both the anode and cathode if such high discharge voltages are expected to occur.

The operation of the discharge was not changed appreciably when the anode was a ring instead of a cylinder as in Fig. 2. A cylindrical anode was used here because it lends itself to ion source designs which are mechanically very satisfactory.

With hydrogen, a bluish-white plasma fills the anode cylinder. There is no definite dark-space near the cathodes when magnesium is used, but with brass cathodes the plasma shows a definite convex surface facing the cathodes. With cathodes as in Fig. 2, the plasma is more luminous near the axis of the discharge tube. At very low pressures, of the order of  $0.01 \mu$ , the luminous part of the discharge is a very fine line, about 1 mm. in diameter, along the axis of the discharge tube. With magnesium, the green cathode light is then concentrated in a small spot at the centre of the cathode.

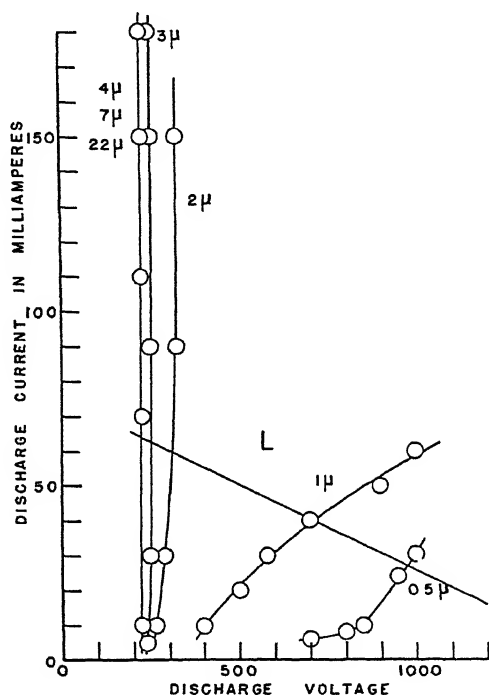


FIG. 3. Typical set of curves of the discharge current as a function of the discharge voltage, at various pressures, with pure hydrogen. Magnetic induction, 1300 gauss. Anode length, 60 mm.; anode diameter, 20 mm.

Fig. 3 shows a typical set of curves of the discharge current as a function of the discharge voltage at various pressures. The discharge tube was similar to that of Fig. 2 but with an anode cylinder 60 mm. in length and 20 mm. in inner diameter. These curves are similar to those of a cold cathode discharge between plane parallel electrodes in the absence of a magnetic field (35). The constant voltage curves correspond to the 'normal' discharge and the others to the 'abnormal' discharge. The part of the characteristics which occurs at currents of a few milliamperes is not shown. For the constant voltage characteristics, the ignition voltage was a few hundred volts higher than the voltage shown. With duralumin cathodes (AC17ST), the curves were similar but the minimum discharge voltage was about 350 v.

The discharge voltage varies with the state of the cathode surfaces. For the 4, 7, and 22  $\mu$  characteristic, the voltage can vary from 150 to 300 v., with magnesium. If the cathodes are well outgassed by operating the discharge at low pressure and high wattage without providing for heat dissipation, the minimum operating voltage may rise to 500 v. or more. It resumes its usual value of about 200 v. if the electrodes are exposed to air at a pressure of a few hundred microns for a few seconds. Thorough outgassing of the electrodes is thus not desirable. On the other hand, the discharge voltage was observed in many cases to decrease from an initial value of about 450 v. to about 250 v. after a few minutes of operation.

The 1 and 0.5  $\mu$  curves must be considered as qualitative; in this region, the characteristics cannot be reproduced satisfactorily. This can be attributed to the outgassing of the cathodes, which changes their electron emission properties. Outgassing also provides an erratic source of gas of uncertain composition.

Fig. 4 shows the discharge voltage and the discharge current at various pressures and magnetic fields. This curve shows the intersection of families of curves of the type of those of Fig. 3 with the resistance line,  $L$ . A supply voltage of 1500 v. and a series resistance of 20,000 ohms (including the internal resistance of the power supply) were used. The points corresponding to low pressures and high voltages must again be considered as qualitative.

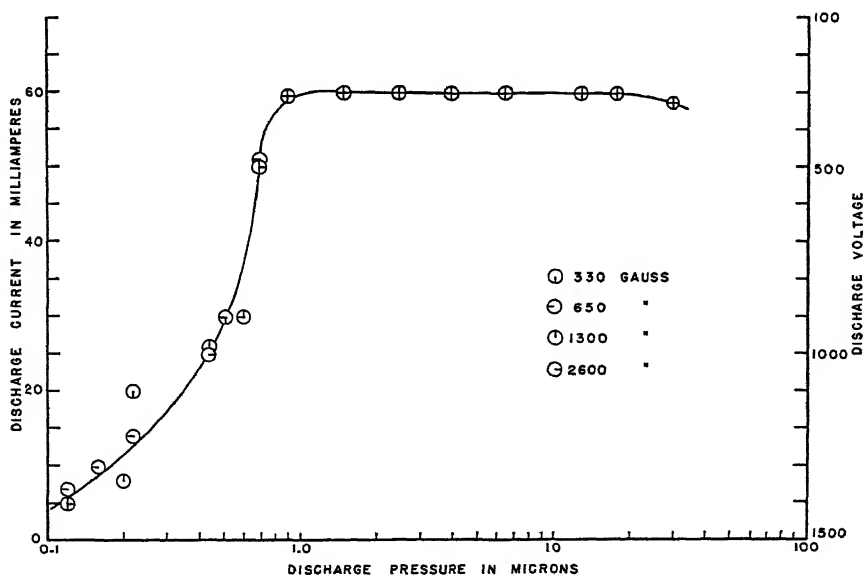


FIG. 4. Discharge voltage and discharge current for various pressures and magnetic fields, with a mixture of 90% of hydrogen and 10% of oxygen collected over water. Power supply voltage, 1500 v.; series resistance, 20,000 ohms. Anode length, 26 mm.; anode diameter, 20 mm.

Experience with many different discharge tubes of the same type and of the same order of size as the present ones has shown that the voltage—

pressure characteristic, as in Fig. 4, is determined mainly by the cathode material, and not by the geometry of the electrodes or by their spacing.

## 2. Proton Production

Figs. 5 and 6 show the percentage composition of the ion beam as a function of the pressure, with pure hydrogen, for anodes of two different sizes. The true discharge pressures for Fig. 5 are about the same as for Fig. 6; they are lower than the gauge pressures shown because of the small anode diameter used. The optimum proton content with pure hydrogen was about 10%. The percentage of  $H_{2-1}^+$  and  $H_{3-1}^+$  ions in the beam was of the order of 1%.

With electrolytic tank hydrogen, the beam composition was extremely variable, the proton content varying, for example, from 10 to 80% for apparently similar discharge conditions. The beam composition was especially variable at the beginning of a run when the discharge had not been operating for some time. No appreciable improvement was observed when the electrodes were water cooled. Similar inconsistencies have been observed by previous workers in this field (22). A set of curves of the percentage composition of the ion beam obtained under fairly steady conditions with electrolytic tank hydrogen was similar to those of Figs. 7 and 8 with a maximum proton content of 12%.

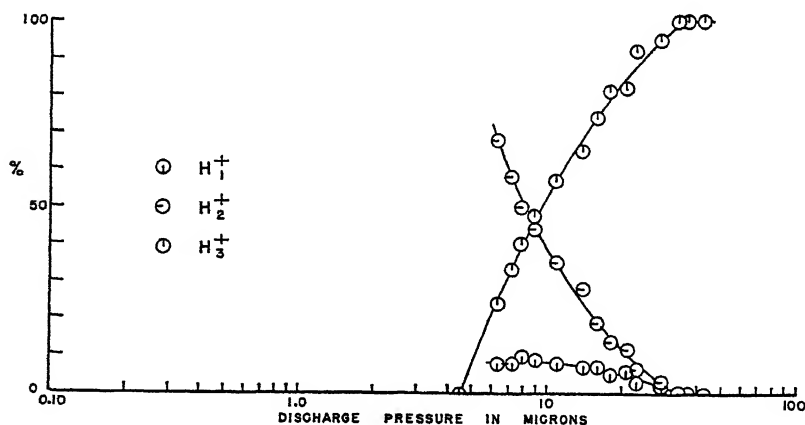


FIG. 5. Percentage composition of the ion beam as a function of the pressure, with pure hydrogen. The gauge pressures shown are higher than the true pressures by a factor of about 3. Magnetic induction, 780 gauss; discharge current, 30 ma. Anode length, 26 mm; anode diameter, 13 mm.

The very high proton percentages were highly encouraging, even though erratic. It appeared that the 0.3% of oxygen present in the electrolytic hydrogen reduced the recombination of atomic hydrogen at the walls of the discharge tube and thus provided a higher concentration of atomic hydrogen (see below).

Various poisons were added to the electrolytic hydrogen in the hope of obtaining a reliable high proton percentage in the ion beam. Air, water

vapor, and hydrogen chloride vapor had no appreciable effect. The hydrogen chloride vapor was added by bubbling the hydrogen in concentrated hydrochloric acid at 0° C.

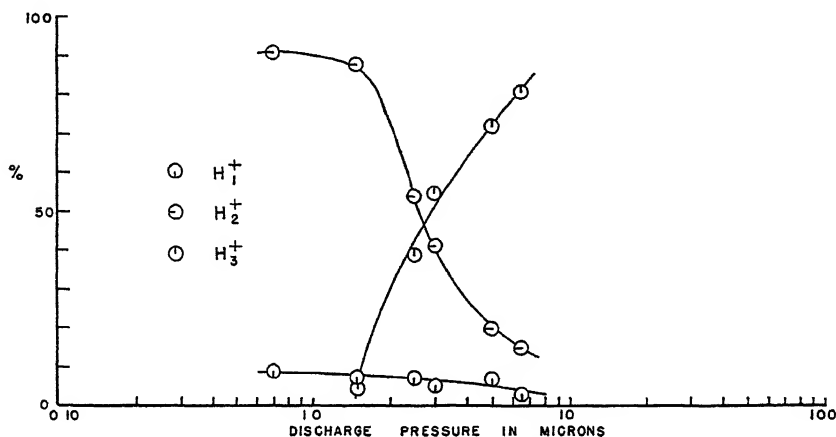


FIG. 6. Percentage composition of the ion beam as a function of the pressure, with pure hydrogen. Magnetic induction, 780 gauss, discharge current, 30 ma. Anode length, 60 mm.; anode diameter, 20 mm.

The addition of oxygen produced a definite improvement. For given discharge conditions, the proton percentage in the ion beam increased until the gas contained 10% of oxygen. Further addition of oxygen had little effect. Fig. 7 shows the ion beam composition for the same discharge tube as that of

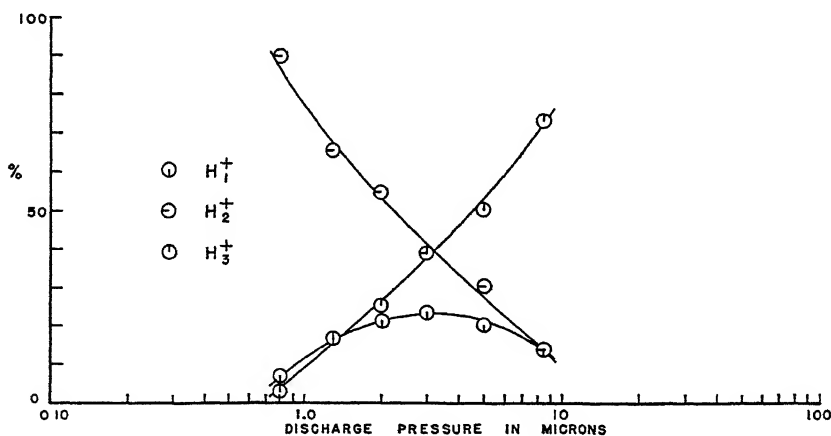


FIG. 7. Percentage composition of the ion beam as a function of the pressure, with a mixture of 90% of hydrogen and 10% of oxygen collected over water. Magnetic induction, 780 gauss, discharge current, 30 ma. Anode length, 60 mm.; anode diameter, 20 mm.

Fig. 6 and for the same operating conditions, but with a mixture of 90% of electrolytic tank hydrogen and 10% of tank oxygen collected over water at room temperature. Fig. 8 shows a similar set of curves for a shorter anode.

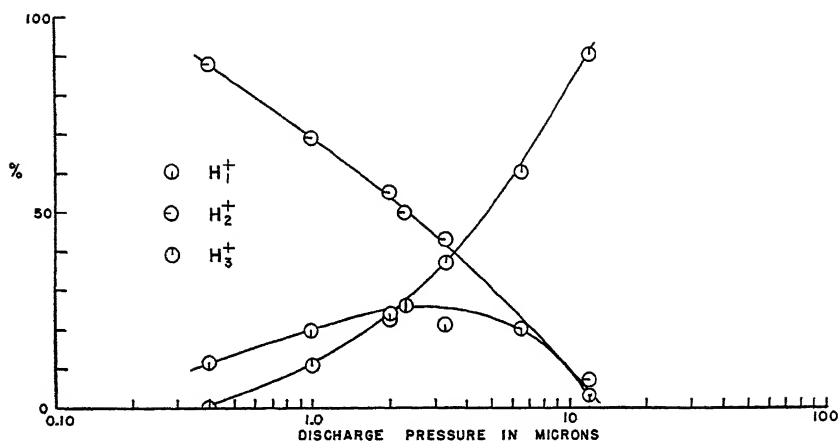


FIG. 8. Percentage composition of the ion beam as a function of the pressure, with a mixture of 90% of hydrogen and 10% of oxygen collected over water. Magnetic induction, 780 gauss; discharge current, 30 ma. Anode length, 26 mm.; anode diameter, 20 mm.

The percentage of oxygen and other foreign ions in the beam was only about 1%. It is to be noted that the increase in the proton percentage was *not* accompanied by a corresponding decrease in the total ion current.

Fig. 9 shows the percentage composition of the ion beam for the same discharge tube and for the same gas mixture as for Fig. 8, at a pressure of 2  $\mu$ , for various discharge currents and magnetic fields.

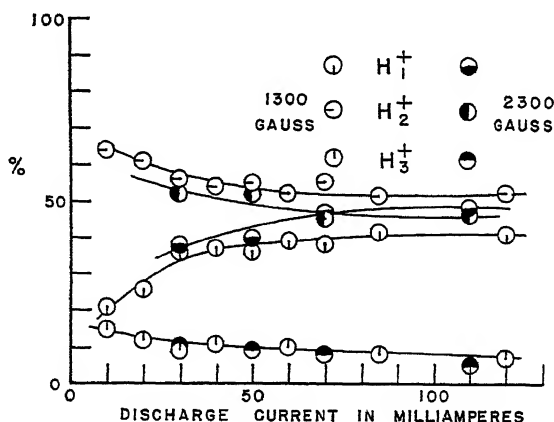


FIG. 9. Percentage composition of the ion beam as a function of the discharge current, with a mixture of 90% of hydrogen and 10% of oxygen collected over water. Discharge pressure, 2  $\mu$ . Anode length, 26 mm, anode diameter, 20 mm.

Fig. 10 shows the variation in the ion beam composition at a discharge current of 30 ma., as the magnetic field is increased from 400 to 3200 gauss.

When the ion beam is extracted from the edge of the cathode, its composition is about the same as when it is extracted from the centre, as in Fig. 2.

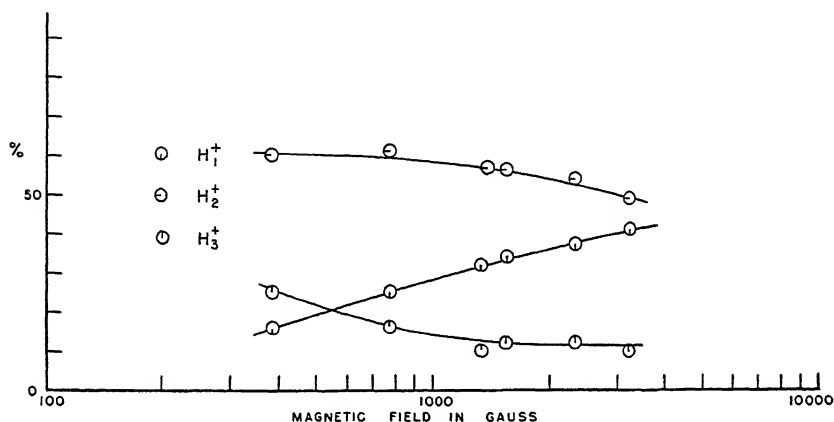
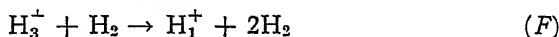
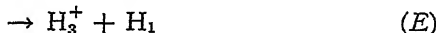
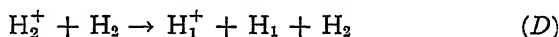
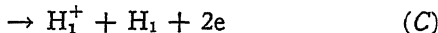
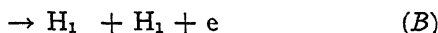


FIG. 10. Percentage composition of the ion beam as a function of the magnetic field at the discharge, with a mixture of 90% of hydrogen and 10% of oxygen collected over water. Discharge pressure, 2  $\mu$ ; discharge current, 30 ma. Anode length, 26 mm.; anode diameter, 20 mm.

### 3. Ionization Processes

The probable ionization and dissociation processes in hydrogen are as follows (3, 9, 16, 18, 27, 29, 36, 37, 38).



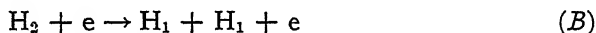
The ionization potentials for (A) and (C) are about 17 v. (3, 4, 38). Molecular ions from (A) have energies of a few electron volts, while atomic ions from (C) have thermal energies (29). The cross section for (A) is a maximum for electrons of about 75 v. and is about 200 times that for (C) (29). Process (C) thus probably has little importance for a proton source. Reaction (B) has been investigated both experimentally (9, 18) and theoretically (27). Its cross section is particularly high for 15 volt electrons, about 6 times the maximum cross section for Reaction (A). Reactions (D) and (F) are observed in mass spectrographs when accelerated  $\text{H}_2^+$  and  $\text{H}_3^+$  ions collide with neutral molecules before entering the magnetic field, giving rise to ions whose apparent mass is  $\frac{1}{2}$  or  $\frac{1}{3}$  of that of a proton, usually designated as  $\text{H}_{2-1}^+$  or  $\text{H}_{3-1}^+$  (16, 37).

Glass and metallic surfaces catalyze the recombination of atomic hydrogen to molecular hydrogen, but glass can be poisoned by mixing oxygen or water vapor with the hydrogen or by coating it with metaphosphoric acid. Tungsten surfaces can be poisoned with oxygen (43). The absence of dust and of organic matter is important, and the surfaces should preferably be

cool to reduce the recombination (11, 39, 43). Under optimum conditions, a hydrogen discharge tube operating at a pressure of 200 to 500  $\mu$  can contain 20 to 50% of atomic hydrogen (39, 43).

In Figs. 5 and 6, the curves for  $H_2^+$  and  $H_3^+$  show the high probability of Reaction (E): as the pressure is increased, the percentage of  $H_2^+$  ions decreases while that of  $H_3^+$  ions increases until the beam is composed almost exclusively of  $H_3^+$ . The  $H_3^+$  ions appear to be formed mainly through Reaction (E). The competing reaction (D) cannot thus be the main source of atomic ions, since the  $H_1^+$  and  $H_3^+$  curves are entirely different in shape. The 8% of atomic ions which is found at the lower pressures when the percentage of  $H_3^+$  is negligible cannot be attributed to (F). Also, from the fact that the percentage of  $H_3^+$  rises to 100 at the higher pressures, it must be inferred that Reaction (F) is quite rare in the present discharge. Then the atomic ions must originate mainly from (G). The atomic hydrogen required can be produced either through (B) or through (E). The latter reaction obviously contributes very little to the formation of atomic ions here, since the percentage of  $H_1^+$  decreases as that of  $H_3^+$  increases.

By a process of elimination, one is thus led to believe that, in the present source, the atomic ions are formed mainly through (B) and (G):



The importance of these two reactions is confirmed by the fact that much higher percentages of atomic ions are found when the walls of the discharge tube are poisoned to reduce the rate of recombination of atomic hydrogen and thus increase its concentration in the gas.

The results of other workers in this field hardly agree with each other and with the present results. This can be attributed to differences in the energy distribution of the ionizing electrons, and in the discharge tube surfaces.

H. D. Smyth's results on the primary and secondary products of ionization in hydrogen (37), when plotted as in Figs. 5 and 6 give for the ion  $H_2^+$  a curve that is entirely similar to the present ones, but his curve for  $H_3^+$  shows no discontinuity at the low pressures, and his maximum percentage of  $H_3^+$  is only about 80. He observed an *increase* in the percentage of atomic ions with pressure and attributed their formation to Reaction (D).

L. P. Smith and G. W. Scott (34, 36) have reported a proton source for which the atomic ion percentage *decreased* sharply with pressure. These authors explain the formation of atomic hydrogen in their source by Reactions (B) and (G) at low pressures and also by (C) and by (A), (E), and (G). They do not give data on the  $H_2^+$  and  $H_3^+$  ions.

O. Luhr (26) has observed that hydrogen ions aged to  $10^5$  collisions in hydrogen at a pressure of 300  $\mu$  contain 10% of  $H_1^+$ , 10% of  $H_2^+$ , and 80% of  $H_3^+$ . This is not in agreement with the present results nor with H. D. Smyth's curves.

The marked increase in the proton percentage that occurs upon the addition of oxygen and of water vapor to the hydrogen (Figs. 7 and 8) is presumably due to a decrease in the rate of recombination of atomic hydrogen at the walls of the discharge tube. At the lower pressures, the metal surfaces are probably outgassed so that the surfaces favor the recombination of atomic hydrogen as if the oxygen and the water vapor were not present.

The curves of Figs. 9 and 10, showing the composition of the ion beam as a function of the discharge current and of the magnetic field, can be explained qualitatively. The rate of production of atomic hydrogen should increase with the density of the slow electrons available for dissociation in the discharge tube, and thus with the discharge current. When the magnetic field is increased at constant discharge current, the rate of drift of the electrons toward the anode is reduced and the density of slow electrons increases. Then, increasing either the discharge current or the magnetic field should (a) increase the percentage of atomic ions; (b) reduce the percentages of both the  $H_2^+$  and  $H_3^+$  ions, if these are formed according to Equations (A) and (E); (c) reduce the ratio of the percentage of  $H_3^+$  to the percentage of  $H_2^+$  if the  $H_3^+$  ions are formed according to Equation (E).

#### 4. Ion Extraction

A positive ion beam can be extracted from a gas discharge either in the form of a canal ray through a hole in the cathode or directly from the discharge plasma. Figs. 11 (a) and 11 (b) show schematically these two types of extraction with the present type of discharge. Fig. 11 (c) is a proposed modification of Fig. 11 (b) for the cyclotron. The first two types were investigated very briefly. Unfortunately, time did not allow a more thorough

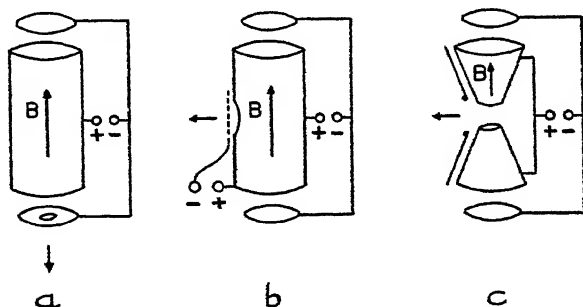


FIG. 11. The extraction of the ion beam.

investigation of the ion extraction. No attempt was made to obtain large ion beam currents. The results obtained, however, will indicate orders of magnitude, if not optimum conditions.

For the former case, discharge tubes similar to that shown in Fig. 2 and varying only as to the dimensions of the anode cylinder, were used. The hole in  $K_2$  had a diameter of 2 mm. and its area was  $2\sigma_0$  of that part of the cathodes

that projects in the anode cylinder. Under these conditions, the ratio of the total ion beam current (including secondary electrons from the target) to the discharge current varied from 2 to 1% as the discharge current was increased from 10 to 100 ma. The dimensions of the anode had but little effect on this ratio. The pressure also had little effect, as long as the discharge was operated in the constant voltage region.

A small hole was used in  $K_2$  so as to maintain a low pressure in the mass spectrograph. A somewhat larger hole would presumably have given a higher ratio of ion beam current to discharge current.

The extraction was much more efficient at low pressures and high discharge voltages. In one case, for instance, the ratio of the ion beam current to the discharge current was 1.3% when the discharge was operated at 300 v., while it was 16% at 1000 v. Unfortunately, this high efficiency of extraction cannot be utilized, as it is accompanied by a relatively low efficiency of proton production.

An ion beam can also be extracted from the discharge plasma through a side hole in the anode cylinder by means of a grid maintained at a negative potential with respect to the anode, as in Fig. 11*b*. In the one source of this type that was built, the anode cylinder was 25 mm. long and 13 mm. in diameter, and was drilled with a side hole 6 mm. in diameter. The grid was at a distance of a few millimetres from the hole and its transparency was roughly 25 or 50%. The ion beam current increased as the grid was made more negative with respect to the anode, until the extracting potential was about 500 v. A further increase in the extracting potential had little effect on the ion beam current.

Under these conditions, the ratio of the ion beam current (including the current to the grid and secondary electrons from the target) to the discharge current was about 10%. The grid intercepted most of the ions, but with a proper design, the current to the extracting electrode could probably be less than one-half of the total ion current. The effective ratio of the ion beam current (including secondary electrons) to the total discharge current can thus be taken as 5% for the above discharge tube.

The ratio of the number of protons to the number of unionized particles emitted by the source can be calculated approximately as follows. Let

$N_u$  = Number of unionized particles emitted by the source per second;

$N_i$  = Number of ionized particles emitted per second;

$N_p$  = Number of protons emitted per second;

$i_m$  = Measured ion beam current, in milliamperes;

$i$  = True ion beam current in milliamperes;

$d$  = Diameter of the orifice through which the ion beam is extracted;

$p$  = Pressure in the discharge tube, in microns;

$M$  = Average molecular weight of the gas used.

Then

$$N_i = 6.3 \times 10^{15} i. \quad (H)$$

Assuming that the pressure in the discharge tube is much higher than that in the mass spectrograph (or in the ion accelerator),

$$N_u = 1.3 \times 10^{16} \frac{d^2 p}{\sqrt{M}}. \quad (J)$$

The gas mixture (composed of about 90% of hydrogen, 10% of oxygen, and 2% of water vapor) which was used, had an average molecular weight of about 4, assuming that 50% of the hydrogen in the discharge tube was in the atomic state. We thus have

$$\frac{N_i}{N_u} = \frac{i}{d^2 p}. \quad (K)$$

In the present case, the measured ion beam current  $i_m$  included the secondary electron current; a rough correction for this can be made by writing  $i = i_m/1.5$ . Then, since about 50% of the ions formed were protons, under optimum conditions,

$$\frac{N_p}{N_u} = \frac{i_m}{3d^2 p}. \quad (K)$$

For the case of endwise extraction through one of the cathodes, we had, in one case,  $i_m = 1$  ma.,  $d = 2$  mm., and  $p = 2 \mu$ , and

$$\frac{N_p}{N_u} = 4\%. \quad (L)$$

This is not a maximum value; higher values of  $N_p/N_u$  could be obtained by using a higher discharge current. A change in the size of the orifice in the cathode at constant discharge current would not produce a large change in this ratio, since  $N_i$  and  $N_p$  are proportional to the area of the orifice, like  $N_u$ , at least to a first approximation.

With sidewise extraction through a hole in the anode cylinder, the discharge currents used were low, about 10 ma. and the resulting value of  $N_p/N_u$  was about one-tenth of the above value. The ion beam current per unit area of the extraction hole and per unit discharge current was about 2.5 times lower for sidewise extraction than for endwise extraction.

The ratio of the proton current  $i_p$ , in microamperes, in the ion beam, to the wattage,  $W_d$ , dissipated in the discharge for endwise extraction, with 250 v. and 100 ma. at the discharge, and 1 ma. in the ion beam, was  $13 \mu$ a. per watt. Again, this is not the maximum value; higher values could be obtained by using a larger extraction hole.

For sidewise extraction, with 250 v. and 10 ma. at the discharge, and 0.5 ma. in the ion beam, the above ratio was  $67 \mu$ a. per watt. This is probably about the optimum value for sidewise extraction. The dissipation of the heat developed in the source for either type of extraction presents no serious problem.

The energy of the extracted ions, for endwise extraction, is given approximately by the discharge voltage. The energy spread was low, as could be judged by the sharpness of the maxima of the mass spectrum, less than 1% of

the mean energy, i.e., less than about 2 v. When the discharge was operated at high voltages, the energy spread was very much larger and increased with the discharge voltage.

The intensity of the ion beam current can be varied, for both types of extraction, by varying the discharge current with a rheostat in series with the discharge.

An electron beam can be extracted from the discharge by applying a positive potential on the cylinder  $L$  (Fig. 2). The electrons give a much more luminous beam than the positive ions because of their higher efficiency for excitation and ionization (6). A fine sharp beam was obtained with an accelerating potential of only 20 v. on  $L$ , indicating that the energy of the electrons as they emerged from  $K_2$  was very low. M. von Ardenne has designed a source that can supply either a positive ion or an electron beam, for use with a Van de Graaff accelerator (2).

The ion source shown in Fig. 2 was designed purely for the purpose of investigating its discharge characteristics and its mass spectrum. It would not be convenient as an ion source for an accelerator.\* In designing such a source, a choice will have to be made between endwise and sidewise extraction of the ion beam. The latter type of extraction has the distinct advantage that it permits the use of the high magnetic field of a C-type permanent magnet. A mass analysis of the ion beam could probably be made in the field of a second C-type magnet near the discharge tube where the ion beam has an energy of only a few hundred volts. M. von Ardenne has described a mass monochromator which could be used with either type of extraction (1).

With endwise extraction, it seems that the magnetic field for the discharge would have to be provided by one or two coils, as in Fig. 2. A tubular permanent magnet surrounding the discharge tube could also be used (42), but then the magnetic induction would only be a few hundred gauss and the optimum proton percentage probably about 20%.

The discharge tube should present only magnesium, brass, and glass surfaces to the gas, since it is doubtful that many other surfaces are poisoned by oxygen and water vapor in the manner described above (43).

A deuteron source would not require a higher magnetic field than a proton source, since the main action of the magnetic field is on the electrons.

## Conclusions

The ion source described above possesses to a satisfactory degree the desirable characteristics enumerated in the Introduction.

The table shown below will serve to compare the present source with the various other types. In cases where a number of papers have been published on the same type of source, reference is made to the most recent one. The figures shown are necessarily approximate, since the operating conditions can vary; they have been chosen to represent the average characteristics.

\* A further paper will be published shortly describing an ion source of the present type for use with a linear accelerator and providing a high ion beam current.

TABLE I  
APPROXIMATE CHARACTERISTICS OF VARIOUS TYPES OF POSITIVE ION SOURCE

Type	Year	Filament	Energy spread, v.	$z$ , ma.	$\frac{i_p}{i}$ , %	$\frac{i_p}{W_d}$ , $\mu\text{a.}/\text{w.}$	$\frac{N_p}{N_u}$ , %
Low-pressure glow-discharge (Penning) (32)	1937	No	10,000	0.5	Very low <sup>1</sup>	Very low <sup>1</sup>	Very low <sup>1</sup>
Palladium tube (14, 15)	1938		0.2	0.2	?	?	$10^{-4}$
Electron beam (36)	1939	Yes	500	1	60	3	6
Low-pressure arc (Finkelstein) (12)	1940	Yes	$<2^1$	150	?	?	?
Pyrex capillary (22)	1941	Yes	30	1.5	60	6.7	3.6
Canal ray tube (7)	1942	No	25,000	1.5	45	1	0.2
Low-pressure arc (von Ardenne) (1, 2)	1943	Yes	$<2^1$	0.1	50	5	0.4
High-frequency discharge (40)	1946	No	20,000	0.3	?	?	?
Cyclotron (23)	1946	Yes	50	100 <sup>1</sup>	10 <sup>1</sup>	5.6 <sup>1</sup>	4 <sup>1</sup>
Low-pressure glow-discharge (present work)	1947	No	$<2$	1	50	67	4

<sup>1</sup> Probable value.

### Acknowledgments

The writer wishes to express his thanks to Dr. J. S. Foster and to Dr. B. W. Sargent for suggesting the problem, and to Mr. A. G. Ward for his valuable advice in the first few months of this work. The writer also wishes to express his indebtedness to the National Research Council of Canada for the award of a Grant for Research which greatly facilitated the progress of the work.

### References

1. ARDENNE, M. v. *Physik. Z.* 43 : 91-101. 1942.
2. ARDENNE, M. v. *Z. Physik*, 121 : 236-267. 1943.
3. BLEAENEY, W. *Phys. Rev.* 35 : 1180-1186. 1930.
4. BRODE, R. B. *Rev. Modern Phys.* 5 : 257-279. 1933.
5. BURCHAM, W. E. Unpublished report MP-176. The development of a source of fast neutrons of variable energy. National Research Council of Canada. 1945.
6. COBINE, J. D. *Gaseous conductors; theory and engineering applications.* McGraw-Hill Book Co., Inc., New York. 1941.
7. CRAGGS, J. D. *Proc. Phys. Soc., London*, 54 : 245-265. 1942.
8. DEMPSTER, A. J. *Phys. Rev.* 11 : 316-325. 1918.
9. DORSCH, K. E. and KALLMANN, H. *Z. Physik*, 53 : 80-91. 1929.
10. DRUYVESTEYN, M. J. and PENNING, F. M. *Rev. Modern Phys.* 12 : 87-174. 1940.
11. FARKAS, A. and MELVILLE, H. W. *Experimental methods in gas reactions.* Macmillan & Co., Ltd., London. 1939.
12. FINKELSTEIN, A. T. *Rev. Sci. Instruments*, 11 : 94-97. 1940.
13. FOWLER, R. D. and GIBSON, G. E. *Phys. Rev.* 46 : 1075-1086. 1934.

14. FRANZINI, T. *Nuovo cimento*, 15 : 88-99. 1938.
15. FRANZINI, T. *Atti accad. Lincei*, 27 : 292-297. 1938.
16. FRIEDLÄNDER, E., KALLMANN, H., LASAREFF, W., and ROSEN, B. *Z. Physik*, 76 : 60-69, 1932.
17. HEIL, H. *Z. Physik*, 120 : 212-226. 1942.
18. HUGHES, A. LL. and SKELLETT, A. M. *Phys. Rev.* 30 : 11-25. 1927.
19. HULUBEI, H. *Compt. rend.* 199 : 199-201. 1934.
20. JOSSEM, E. L. *Rev. Sci. Instruments*, 11 : 164-166. 1940.
21. KORSCHING, H. *Physik. Z.* 42 : 74-79. 1941.
22. LAMAR, E. S., BUECHNER, W. W., and VAN DE GRAAFF, R. J. *J. Applied Phys.* 12 : 132-140. 1941.
23. LIVINGSTON, M. S. *Rev. Modern Phys.* 18 : 293-299. 1946.
24. LIVINGSTON, M. S., HOLLOWAY, M. G., and BAKER, C. P. *Rev. Sci. Instruments*, 10 : 63-67. 1939.
25. LORRAIN, P. Unpublished report PD-158. A cold cathode discharge for use in an ion source. National Research Council of Canada. 1945.
26. LUHR, O. *Phys. Rev.* 44 : 459-462. 1933.
27. MASSEY, H. S. W. and MOHR, C. B. O. *Proc. Roy. Soc., London*, A135 : 258-275. 1932.
28. MAXWELL, L. R. *Rev. Sci. Instruments*, 2 : 129-140. 1931.
29. NEWHALL, H. F. *Phys. Rev.* 62 : 11-18. 1942.
30. PENNING, F. M. *Physica III* : 873-894. 1936.
31. PENNING, F. M. *Physica IV* : 71-75. 1937.
32. PENNING, F. M. and MOUBIS, J. H. A. *Physica IV* : 1190-1199. 1937.
33. RITSCHL, R. *Physik. Z.* 38 : 141-157. 1937.
34. SCOTT, G. W., JR. *Phys. Rev.* 55 : 954-959. 1939.
35. SEELIGER, R. *Einführung in die Physik der Gasentladungen*. J. A. Barth, Leipzig. 1927.
36. SMITH, L. P. and SCOTT, G. W., JR. *Phys. Rev.* 55 : 946-953. 1939.
37. SMYTH, H. D. *Phys. Rev.* 25 : 452-468. 1925.
38. SMYTH, H. D. *Rev. Modern Phys.* 3 : 347-391. 1931.
39. STEACIE, E. W. R. *Atomic and free radical reactions; the kinetics of gas phase reactions involving atoms and organic radicals*. Reinhold Publishing Corporation, New York. 1946.
40. THONEMANN, P. C. *Nature*, 158 : 61. 1946.
41. WALCHER, W. *Z. Physik*, 122 : 62-85. 1944.
42. WARD, A. G. Unpublished report PM-148. Notes on positive ion sources. National Research Council of Canada. 1945.
43. WOOD, R. W. *Proc. Roy. Soc., London*, A102 : 1-9. 1922.

## THERMAL CONDUCTIVITY OF METALS AT HIGH TEMPERATURES<sup>1</sup>

### I. DESCRIPTION OF THE APPARATUS AND MEASUREMENTS ON IRON

BY L. D. ARMSTRONG<sup>2</sup> AND T. M. DAUPHINEE<sup>2</sup>

#### Abstract

An apparatus for measuring the thermal conductivity of metals in the temperature range 0° to 800° C. is described. The method utilizes unidirectional heat flow in a cylindrical sample in a vacuum. The advantages of the method are outlined and a comprehensive analysis of possible errors in the measurements is included. Measurements on Armco iron indicate that results with an absolute error of less than 2% may be obtained. The results of measurements on a sample of Armco iron gave thermal conductivities of 0.181, c.g.s. units at 0° C. and 0.069, c.g.s. units at 800° C. A change in slope of the thermal conductivity - temperature curve was found at a temperature of approximately 375° C., and is tentatively attributed to the presence of 0.03% nickel impurity.

#### Description of the Apparatus

##### *Introduction*

The thermal conductivity of metals at high temperatures has considerable theoretical and practical interest. It provides a valuable check on the theories of the solid state, which are still in a condition of considerable uncertainty. Its practical value is well demonstrated by the demand for thermal conductivity data that has arisen as a result of recent developments in nuclear physics and jet propulsion. For these and other reasons, additional information on thermal conductivities would be very valuable.

An apparatus for the measurement of thermal conductivity at high temperatures should be adaptable to the measurement of conductivities of a large number of metals and it should operate over as wide a temperature range as possible. Since some metals are very active chemically, a vacuum apparatus is desirable. Moreover, some metals are not available in large quantities and consequently the apparatus should use the smallest samples with which accurate results can be obtained. The presence of transition points and the non-linearity of the thermal conductivity - temperature relation necessitate the use of small temperature intervals.

##### *Method of the Experiment*

The measurement of the temperature, heat flow, and dimensions is complicated by a number of factors. As the temperature interval must be measured between points in a temperature gradient, thermocouples are generally required instead of the more sensitive resistance thermometers. This limits the accuracy with which the small temperature intervals can be measured. In general, it is not feasible to measure the heat flow in the same

<sup>1</sup> Manuscript received in original form June 7, 1947, and, as revised, August 27, 1947.

Contribution from the Division of Physics and Electrical Engineering, National Research Laboratories, Ottawa, Canada Issued as N.R.C. No. 1620.

<sup>2</sup> Physicist.

region as the temperature gradient. Consequently, precautions have to be taken to prevent undesirable heat exchanges from radiation and conduction. Many other considerations arising from the criteria previously outlined must be taken into account.

The method selected is one using axial, unidirectional heat flow in a cylindrical sample, between a measurable heat source and a heat sink, with appropriate shielding to prevent errors due to radiation and conduction. The temperature gradient is measured by thermocouples peened into the sample a known distance apart, and the entire unit is operated in a vacuum. The thermal conductivity is then calculated using the formula:

$$K_T = \frac{Q \times L}{A (T_2 - T_1)}, \quad (1)$$

where  $K_T$  = thermal conductivity in calories per square centimetre per second for a temperature gradient of  $1^\circ \text{C.}$  per centimetre at temperature  $T^\circ \text{C.}$ ,

$Q$  = heat input in calories per second,

$L$  = separation of measuring thermocouples in centimetres,

$A$  = cross sectional area of sample in square centimetres,

$T_2 - T_1$  = temperature interval in  $^\circ \text{C.}$ ,

$T = \frac{T_2 + T_1}{2}.$

### Apparatus

A cross sectional view of the apparatus is shown in Fig. 1. The sample,  $A$ , is a solid cylinder 8.00 cm. long and 2.50 cm. in diameter, and rests on the centre portion of the heat sink,  $B$ . The sample heater element (10 w.) is a helix of platinum-10% rhodium wire cemented in grooves in the sample heater,  $C$ . The sample cap,  $D$ , covers the exposed sides of the sample heater. The guard sleeve,  $E$ , is a cylindrical iron tube concentric with the sample and, like it, resting on the heat sink. It has two heating coils of platinum-rhodium wire, one at the top and the other near the bottom. The guard cap,  $F$ , supported by ceramic insulators on the guard sleeve, surrounds the exposed sides of the sample cap. The guard cap has a heating element of platinum-rhodium wire in grooves on the top. The heat sink,  $B$ , is a machined gold block, with a non-inductive heating coil wound in ceramic cement in the lower portion. It is securely attached to the supporting column,  $G$ , by a cone joint and screw.

The supporting column is a thin walled iron tube that passes through the bottom of the 'pyrostat'.\* Its upper section contains a spiral coil through which air or water may be circulated. The pyrostat encloses the main part of the apparatus and may be maintained at the desired temperature by the furnace,  $H$ , while cooling coils prevent the ends from overheating. The

\* The authors have been unable to find any simple term to represent the container that surrounds the apparatus. Since this container performs the same function at high temperatures as a cryostat does at low temperatures it has been given the name of 'pyrostat'.

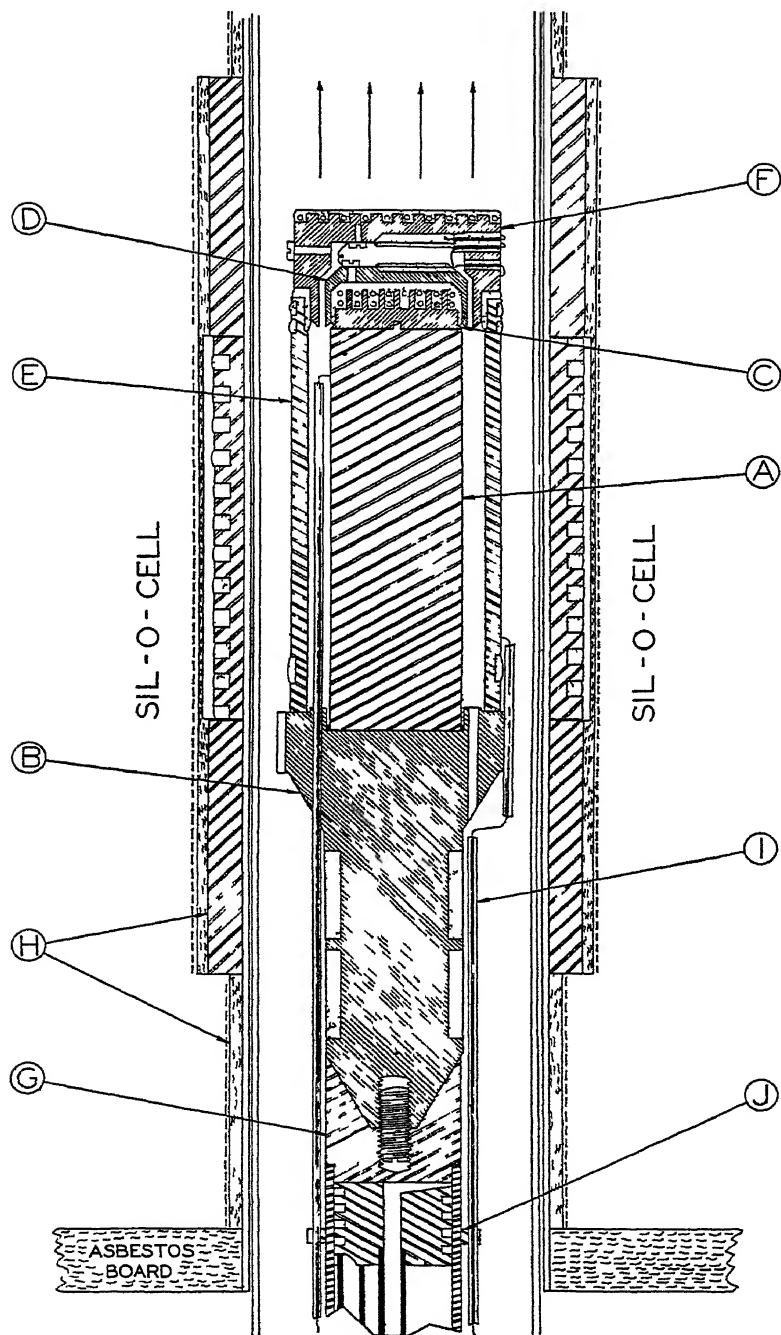


FIG. 1.

vacuum connections are made at the top of the pyrostat and the lead wires are taken out at the bottom.

All lead wires are taken to the base of the apparatus in fine bore ceramic tubing, *I*, which acts both as an insulator and as a rigid support. Above the supporting column this tubing is fitted into holes drilled in the heat sink, while along the supporting column it is held in slotted collars, *J*, by spring clips.

### *The Furnace*

The furnace, *H* (Fig. 1), which fits loosely over the pyrostat, consists of a five section winding on a stainless steel tube. In order to provide a uniform temperature region the three centre sections are wound over  $\frac{1}{4}$  in. thick steel sleeves. A 200 ohm platinum resistance thermometer is embedded in a spiral groove cut into the centre sleeve, and thermocouples are installed under the winding of each section. The outer wall is a galvanized iron cylinder on which are mounted terminal strips for the electrical connections. The ends are closed with asbestos board disks and the furnace is insulated with diatomaceous silica.

### *Vacuum Connections*

The vacuum line to an oil diffusion pump is joined to the apparatus by a faced metal-to-metal seal. A sylvon bellows allows for thermal expansion

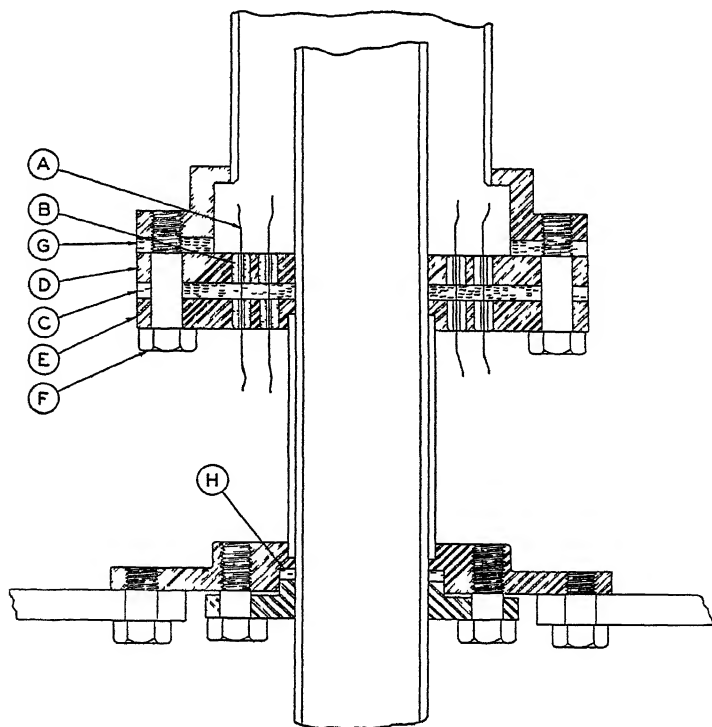


FIG. 2. *Vacuum seal.*

of the pyrostat. The bottom of the pyrostat is sealed with rubber gaskets as shown in Fig. 2. The lead wires, *A*, are threaded through the insulating beads, *B*, and the rubber gasket, *C*. The beads are set into the steel plates, *D*, *E*, which are clamped together by means of screws, *F*, compressing the rubber and making an effective vacuum seal. Other rubber gaskets, *G*, *H*, are used to seal the centre column and the pyrostat tube. This assembly has functioned very satisfactorily and no difficulty has been encountered in maintaining pressures of less than  $1\ \mu$ .

### Power Circuits

The power for the sample, guard sleeve, and guard cap heaters is taken from a common source regulated to maintain voltage constant to 0.1%. The circuits may be adjusted simultaneously by controlling this source, or independently by rheostats in the individual circuits (Fig. 3). To prevent

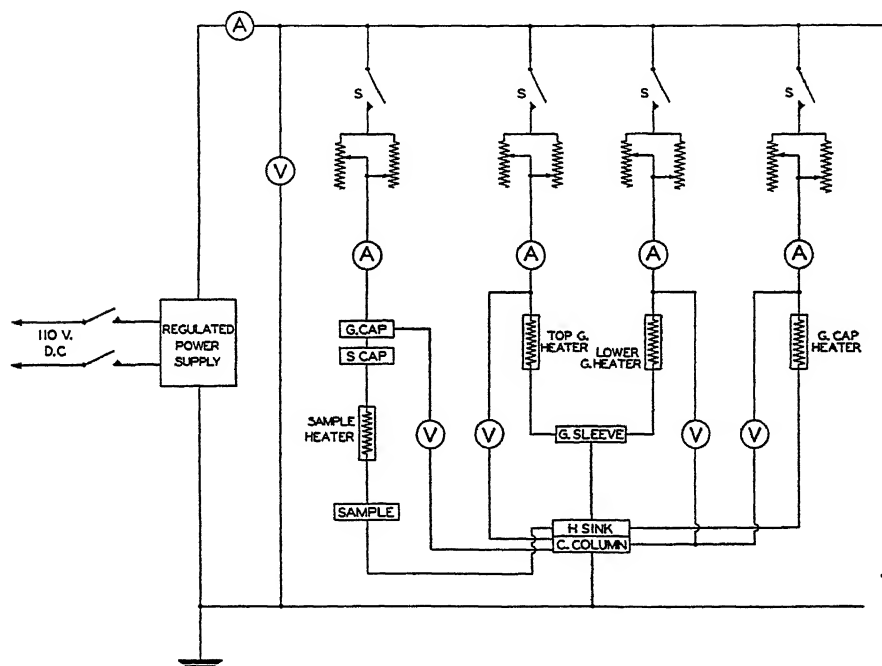


FIG. 3. Heater control circuits.

heat conduction errors, current and potential leads are not attached directly to the sample heater element. The connections are made to the guard cap. Short wires connect the guard cap to the sample cap and the sample cap to the heater element. The centre column serves as ground. Since the guard cap is part of the sample heater circuit, the ground lead for the guard cap heater element is connected to the heat sink. The sample heater current and voltage are shown by accurate meters calibrated to 1/10% full scale, while large panel meters are used for all other circuits.

The sink heater is fed from the 110 v. d-c. mains through a rheostat control with fine and coarse adjustment. A reversing relay is connected in this circuit to check for magnetic effects due to the heater.

The furnace wiring circuit is shown in Fig. 4. Power is supplied from the 110 v. a-c. mains and controlled by means of a 5 kva. variable voltage transformer. A saturable reactor in series provides fine control, and may, if desired, be used in conjunction with the resistance thermometer for automatic temperature regulation. Uniform furnace temperatures can be established by adjusting the variable transformers in series with each of the five sections of the winding.

### *Thermal Contacts*

In Equation (1) it is assumed that rectilinear heat flow exists throughout the region in which the temperatures are measured. For this to be true in regions close to an interface it is essential that the heat flow across the interface be uniform. One of the simplest ways of securing this uniformity is to reduce the thermal resistance to a minimum by means of a low melting point intermediate metal that will 'wet' both surfaces. Tin is satisfactory for many materials and has been used in the preliminary measurements on Armco iron. At the conclusion of the tests it was found that the joints had become so strong that they could be broken only with difficulty even at high temperatures.

### *The Use of Gold*

An interesting point came up during the preliminary experiments on the apparatus. At that time the heat sink was made of copper, and it was found that after the apparatus had been evacuated and maintained at 500° C. for some time the regions around the sink became coated with a reddish deposit of copper, owing to the formation of unstable volatile hydrides or nitrides. The small amounts of hydrogen and nitrogen present in the pyrostat react with the copper, and the compounds formed subsequently dissociate to leave a metallic deposit. Since evaporated copper on the fine thermocouples in the apparatus might easily cause errors in temperature measurement, it was advisable to eliminate such evaporation. Investigation showed that many other metals behave similarly at high temperatures. Gold appeared to be the only metal having the desired characteristics, namely, small evaporation under working conditions, relatively high thermal conductivity, and a melting point well above 900° C. Consequently, gold was used for all parts of the apparatus requiring these characteristics; namely, for the sample heater, sample cap, guard cap, and heat sink.

Observations at the conclusion of the first series of experiments showed that some evaporation of the gold had taken place. In addition, any excess of tin around the edges of the contacts had spread over the neighboring surfaces of the gold, forming a low melting point alloy which crystallized on subsequent cooling.

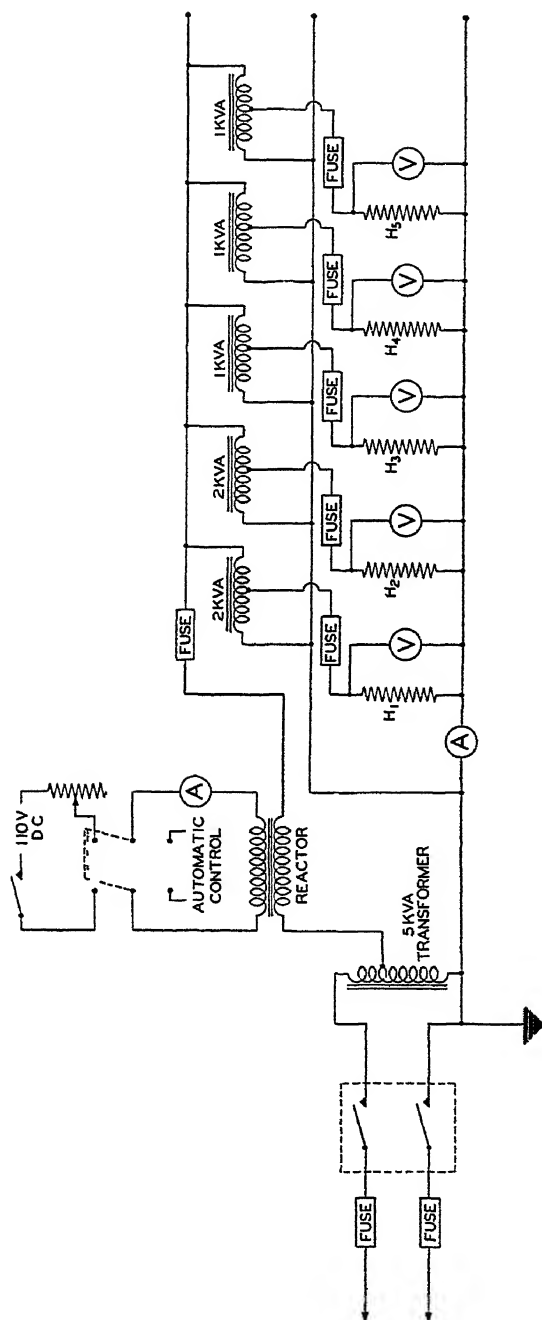


FIG 4. Furnace control circuit

### *Temperature Measurement*

Except for the use of the resistance thermometer in the furnace, temperatures are measured by means of platinum-platinum-rhodium thermocouples. The sample, guard sleeve, and heat sink thermocouples are attached by making a shallow and very narrow groove on the surface of the metal perpendicular to the axis, and, after laying in the thermocouple, peening down the sides of the groove until the thermocouple is completely enclosed and wedged in place. The sample thermocouples are spaced approximately 5 cm. apart, the upper one being 1 cm. from the top. Since the position of these thermocouples must be known very accurately, 0.003 in. wire and very small butt-welded junctions (1) are used; the separation of the thermocouples is measured with a travelling microscope. Similar thermocouples are attached to the outside of the guard sleeve opposite those on the sample. In order that no heat will be conducted along the wires to the junction, the leads of these four thermocouples are taken halfway around the sample or guard sleeve at the same level before being taken to the base of the apparatus. Fine wire thermocouples are embedded in ceramic cement in grooves on the top of the sample cap and the underside of the guard cap. The leads are brought out through holes in the guard cap and down outside the guard sleeve.

Two thermocouples are mounted in the air space between the guard sleeve and the pyrostat wall, one near the top of the guard sleeve and the other near the bottom, to give an indication of the temperature gradient in the pyrostat. The five thermocouples mentioned in the description of the furnace are used to determine the temperatures and gradients in the furnace itself. Since their response to changes in the furnace heating current is considerably more rapid than that of the thermocouples inside the pyrostat, these thermocouples are used in conjunction with the resistance thermometer in the control of the furnace temperature.

The leads of all thermocouples are taken to a felt insulated metal zone box where they are connected to copper lead wires. To cut down parasitic e.m.f.'s. the remainder of the circuit (Fig. 5), including the selector switches, is composed entirely of copper. The guard, sample, and cap thermocouples are read with a Leeds and Northrup type K2 potentiometer. Provision is made for simultaneous reversal of the thermocouple, reference junction, and supply, and for a small compensating e.m.f. to neutralize the rather high thermals of the instrument. Two other potentiometers are used, one for heat sink and furnace thermocouples, and the other for the sample top, sample cap, and guard cap thermocouples. A variable e.m.f. is included in the circuit of the centre furnace thermocouple and is used to equalize the e.m.f. from it and the heat sink thermocouple, so that they may be compared without changing the setting of the potentiometer. The resistance thermometer is read with a portable Wheatstone bridge.

### *Electrical Shielding*

All possible precautions were taken to eliminate errors arising from electromagnetic effects of other circuits, electrostatic charging, leakage currents or

ceramic conduction at high temperatures. Electromagnetic effects are prevented by using non-inductive windings for all heater elements and by using alternating current only where it is separated from the measuring section

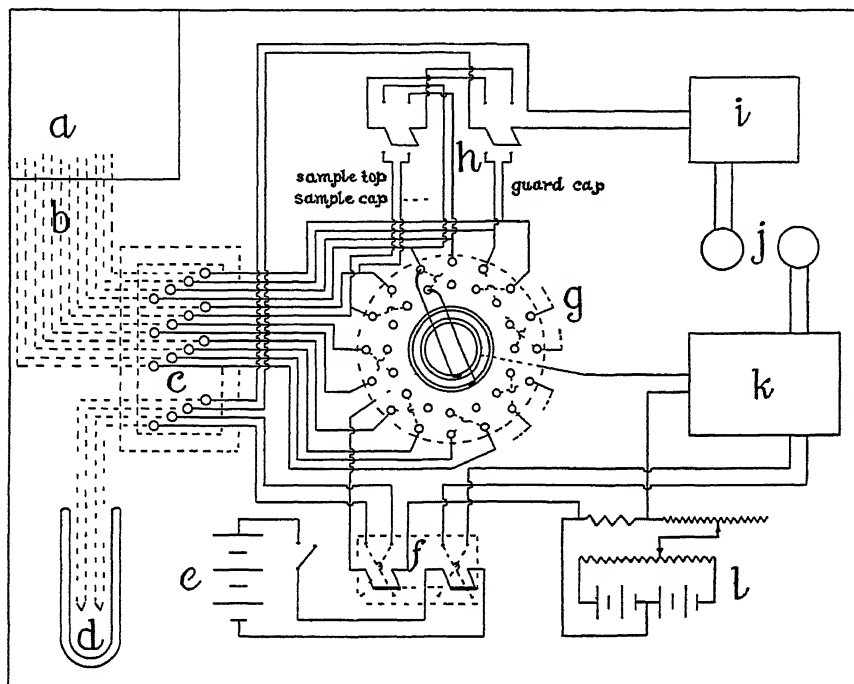


FIG. 5. *Measuring unit thermocouple circuit.*

by the iron pyrostat tube and the iron sleeves inside the furnace. Electrostatic charging arising from low humidity in the winter and from leakage currents due to high humidity in the summer are neutralized by complete shielding of all important leads, by maintaining the apparatus at ground potential, by placing the potentiometers, standard cells, storage batteries, and galvanometers on grounded plates, and by grounding the metal shells of the thermocouple switches and zone box. On the panel all power circuits are kept well separated from the thermocouple circuits. Since the centre column is grounded, and since the thermocouples, connected directly to the column at the tips, are within a few millivolts of ground at all times, there is little possibility of appreciable leakage through the ceramic tubing when readings are being taken. However, the two caps are in the neighborhood of  $+20$  v. while for shielding purposes it is desirable that their thermocouples be at ground potential. To accomplish this and at the same time neutralize the effect of conduction through the cement in which these thermocouples are embedded, they are grounded at the tips by 0.005 platinum wires that run parallel to the leads as far as the heat sink.

### *Thermal Shielding and Lead Losses*

Heat exchange between the sample and sample cap and other parts of the apparatus can be prevented only by complete matching of temperatures. In this apparatus, radiation is the greatest problem, the most vulnerable areas being the top of the sample heater and the upper part of the sample. An isothermal surface is obtained on the heater by a cap of high conductivity material (i.e., gold). Radiation losses are then prevented by means of a second isothermal surface (the inside of the guard cap) at the same temperature. Radiation losses from the sample are prevented by matching the temperature gradients along the sample and the guard sleeves. Heaters are provided on the guard sleeve for this purpose.

Heat losses along the thermocouple leads are kept small by using very fine wire (0.003 in.) and correspondingly small ceramic tubing. Only one other lead need be considered, that to the sample heater, and since it connects the sample and guard caps, which are at the same temperature, heat conduction along it does not occur. The vacuum serves to prevent conduction through the gas, as well as chemical action.

### *Assembly of the Apparatus*

After the supporting column and heat sink are installed, the other parts and their associated leads are put in place in the following order. The sample, with heater and cap already attached, is tinned to the heat sink and the sample thermocouples are installed. The guard sleeve is similarly joined to the heat sink. The sample cap thermocouple is threaded through the guard cap, which is then placed on top of the guard sleeve. After the two thermocouples between the guard sleeve and the pyrostat wall are installed, the pyrostat tube is put in place and the furnace is then lowered to a position midway along the pyrostat tube.

### *Experimental Procedure*

In order to measure the thermal conductivity it is necessary to adjust the various heater currents in such a way that a steady temperature gradient ( $2^{\circ}$  to  $4^{\circ}$  C. per cm.) is set up in the sample and that the temperatures of the guard thermocouples are matched to the corresponding ones of the sample. After steady conditions have been maintained for some time, the required quantities may be measured.

It is necessary to regulate the temperature of the heat sink quite accurately if steady conditions are to be maintained in the sample. This is accomplished by means of the heat sink heater in conjunction with the cooling coil. This dual control system enables measurements to be taken over the full temperature range with a single apparatus.

The following sequence of operations was found most satisfactory:

1. The heat sink and furnace are brought to the desired temperatures and maintained constant.
2. The desired gradient is established in the sample.

3. Using the top guard heaters, the temperature of the top guard thermocouple is matched and held to that of the top sample.
4. The guard cap temperature is adjusted until the sample cap thermocouple gives the same reading at equilibrium conditions as the guard cap thermocouple.
5. The furnace and lower guard heater are adjusted until the temperature of the bottom guard thermocouple matches that of the bottom sample.
6. The matching conditions are maintained until the sample comes to thermal equilibrium.
7. Several complete sets of readings are taken. From these results the thermal conductivity is calculated.

### Calculations

$Q$  as required in Equation (1) is determined from the meter readings by the formula

$$Q = \frac{V}{J} \left( I - \frac{V}{r_1} \right) \left( 1 + \frac{r_2}{r_1} - \frac{r_3}{R} \right) \text{ cal. per sec.} \quad (2)$$

where  $V$  and  $I$  are the voltmeter and ammeter readings,  $r_1$  = voltmeter resistance,  $r_2$  = resistance of voltmeter leads,  $r_3$  = effective resistance of power lead joining the caps,  $R$  = heating element resistance, and  $J$  = the electrical equivalent of heat.  $T_2$  and  $T_1$  are the temperatures at the positions of the two thermocouples on the sample, as calculated from the thermocouple e.m.f.'s.

The conductivity was therefore obtained from the formula:

$$K_T = \frac{L_0 V \left( 1 - \frac{V}{r_1} \right) \left( 1 + \frac{r_2}{r_1} - \frac{r_3}{R} \right)}{A_0 J (1 + \alpha T) (T_2 - T_1)}, \quad (3)$$

where  $K_T$  is the average thermal conductivity over the temperature interval  $T_2 - T_1$  and is considered to apply to the temperature

$$T = (T_2 + T_1)/2.$$

The parameters  $L$  and  $A$  in Equation (1) are functions of temperature. For most metals the ratio  $\frac{L}{A}$  may be determined with sufficient accuracy from the relation  $\frac{L}{A} = \frac{L_0}{A_0 (1 + \alpha T)}$ , where  $L_0$  and  $A_0$  are the dimensions at  $0^\circ \text{C}$ . and  $\alpha$  = mean linear coefficient of expansion from  $0^\circ$  to  $800^\circ \text{C}$ .

### Calibration

The method used in this experiment of intercalibrating thermocouples could, with modifications, have many other applications, and therefore a full description is included here.

The method is based on the fact that the only information required for a measurement of the thermal conductivity is the magnitude of the change in the temperature gradient brought about by a change in the heat input. It is

not necessary that the initial temperature gradient, heat exchange with surroundings, or power input be zero, nor is it necessary to know the absolute temperature accurately. However, the change in temperature gradient must be the result of the change in the power input alone, and this requires that the exchange between the sample and its surroundings must remain constant.

The procedure in comparing thermocouples is as follows. The furnace and heat sink are brought to the desired temperature and held at this temperature with no power delivery to the sample and guard sleeve heaters. The guard cap temperature is then adjusted until the guard cap and sample cap thermocouples give identical and constant readings. The furnace temperature is then adjusted until the sample top and guard top thermocouples give identical readings. These conditions (constant temperature of heat sink, equality of cap thermocouples, and equality of guard and sample top thermocouples) are held until the e.m.f. difference between the top and bottom sample thermocouples becomes constant. As soon as stable conditions have been reached the differences of e.m.f. between the top and bottom sample thermocouples and the bottom guard and bottom sample thermocouples are measured, using galvanometer deflections to avoid potentiometer errors. It has been found that intercalibration at 60° to 100° C. intervals is usually sufficient.

During a measurement, conditions are arranged so that the heat exchange from any small area of surface of the sample is the same as it was during the intercalibration. This is accomplished by matching the readings of the guard cap and sample cap, the guard top and sample top, and the guard bottom and sample bottom thermocouples, respectively, in the last case making due allowance for the calibration differences. Thus the change in the temperature gradient along the sample is due to the measured heat input alone. In the calculations the necessary correction is applied to the bottom sample thermocouple reading.

#### *Experimental Error*

The following are possible sources of error in this apparatus:

1. Heat loss from the sample and sample cap by radiation.
2. Heat loss by conduction along power leads, thermocouple leads, and ceramic tubing.
3. Non-linearity of heat flow in the sample.
4. Errors in measurement of power input.
5. Errors in measurement of the temperature interval.
6. Errors due to the apparatus not being at equilibrium.
7. Errors in measurement of dimensions.
8. Errors arising from the variation of conductivity with temperature.

1. The methods used to reduce the heat loss from the sample by radiation were discussed previously. Matching between thermocouples during a run was maintained to better than 0.1° C. Taking the entire effective radiation area into consideration and using Stefan's law of radiation with an assumed

effective emissivity of 0.6 between close surfaces, the total loss at  $1000^{\circ}\text{A}$  from radiation amounts to less than 0.30% of the heat input, and decreases as the cube of the absolute temperature.

2. Total conduction of heat along the 0.003 in. thermocouple leads and 2 mm. ceramic tubing with the maximum gradient of  $4^{\circ}\text{C.}$  per cm. and along the 0.010 in. lead wire with a gradient of less than  $0.03^{\circ}\text{C.}$  per cm. could not possibly cause an error greater than 0.05%.

3. Non-linearity of heat flow in the sample would be caused primarily by poor thermal contact between the sample heater and the sample, or between the sample and the heat sink, and to a lesser extent by radiation from the surface. As tin is used at the interfaces, large discontinuities are prevented. In addition, the measuring thermocouples are spaced 1 cm. and 2 cm. from the top and bottom surfaces, respectively, a distance that should be sufficient to allow the local disturbances to level out. Radiation losses from the surface of the sample are kept small by the shielding sleeve, and it can be shown that the effect of radiation on linearity would introduce a maximum error of less than 0.05%.

4. Errors in measurement of power input could arise from the resistance of the voltmeter lead, loss of heat generated in the lead between the two caps, power losses between the sample heater and the ground connection, and limitations of accuracy of meter readings. The voltmeter lead resistance is allowed for in Equation (3) for  $K_T$ . Power generated in the lead between the caps is 0.7% of the total and for purposes of Equation (1) it is assumed that approximately 0.4% is lost to the guard cap. The net correction applied by these terms in the equation is 0.25% with an uncertainty in the order of 0.20%. Power losses from the heater to ground have been measured using the top sample thermocouple as potential lead, and are negligible. By setting one meter on a scale graduation, by careful calibration, and by using only the top part of the scales, the error due to meter readings may be kept below 0.25%.

5. Errors in the measurement of the temperature interval can arise from thermocouple calibration, potentiometer readings, parasitic e.m.f.'s in the potentiometer and circuits, or lead conduction. On account of the method of intercalibration of thermocouples it is unnecessary to calibrate accurately with respect to the international temperature scale. An error in this respect creates corresponding errors in the calculated temperature interval and in the temperature to which the determination is applied. For a substance whose conductivity decreases with increasing temperature (e.g., most pure metals) these two errors tend to cancel each other, and the net effect would not be more than 0.1% under any reasonable conditions. It should be noted here that the sample top, sample cap, and guard cap thermocouples provide a useful check on one another since an error in e.m.f. of any one of the three would make it impossible to match them when calibrating. In the measurements on Armco iron, the difference in reading between any two never exceeded  $2\text{ }\mu\text{v.}$  at the highest temperatures, and therefore it seems unlikely that any

effective contamination occurred. The relative calibration of the sample thermocouples was reproducible at all temperatures to less than  $0.2 \mu\text{v.}$ , which represents a possible error of less than 0.2%. Because of the compensating e.m.f. and the provision for reversal in the potentiometer circuit, it is possible to reproduce readings to the full sensitivity of the potentiometer (approximately 0.05% of the interval). The slide-wire of the potentiometer has been checked and the error does not exceed 0.1%. Since both thermocouples were carried around the sample for a distance of 4 cm. in a constant temperature area and the subsequent gradient was less than  $4^\circ \text{C. per cm.}$ , and since both are subjected to identical conditions, the errors in reading due to lead conduction should be negligible and certainly would not be more than 0.05%. The total of these errors is less than 0.5%.

6. At higher temperatures the time required to reach equilibrium is greater on account of the lower conductivity and greater heat capacity of the sample. In order to be certain that conditions are in equilibrium at the time of measurement, readings were not accepted until three successive sets showed no appreciable drift. Using accepted values for the specific heat of iron, gold, and ceramic cement, it can be shown that for an iron sample a drift of  $1/100^\circ \text{C. per min.}$  corresponds to a heat absorption or emission of approximately  $1/60 \text{ w.}$ , or 0.1% of the power input. No readings were accepted where over a period of 15 min. there was an average drift of more than  $1/200^\circ \text{C. per min.}$

7. The diameter of the sample is measured at room temperatures to an accuracy of 0.1%, and the separation of the thermocouples is measured by means of a travelling microscope to approximately 0.2%. After correction for thermal expansion of the sample the total error in dimensions would not exceed 0.4%. This error does not affect relative readings.

8. For substances with a linear conductivity-temperature relation, use of a large temperature interval introduces no error in the conductivity, as calculated from Equation (3). However, if the relation is non-linear, an error is introduced which varies as the square of the temperature interval. The advantage of being able to make accurate measurements using a small interval is obvious. The apparatus herein described can be used with temperature intervals as small as  $5^\circ \text{C.}$

Effects due to work hardening on the surfaces of the sample are negligible under ordinary conditions. In any event the past history of the specimen does not influence the accuracy of any one thermal conductivity measurement. However, changes caused by annealing would affect the consistency with which results could be reproduced, and should immediately become evident.

The sum of errors from all sources is 1.95%. Of this, 0.90% is systematic and 0.95% random error. The estimate of random error is well verified by the results of measurements on Armco iron. In this case the maximum deviation from the average curve is 0.6% and the standard deviation 0.35%.

## Measurements on Armco Iron

### *Introduction*

Armco ingot iron was selected as the test metal for several reasons. It may be readily obtained in a state of reasonable purity. Therefore the results of previous determinations (2, 3) could serve as a check on the accuracy of the apparatus. The thermal conductivity shows no sharp anomalies in the range  $0^{\circ}$  to  $800^{\circ}$  C. and is reasonably close to that of many of the materials that will later be tested. Aside from oxidation, iron is not subject to appreciable change of properties as a result of heating and should give reproducible results if a sufficiently high vacuum is maintained.

### *The Sample*

The sample was a solid cylinder 2.50 cm. in diameter and 8.00 cm. in length, machined from a hot rolled  $1\frac{1}{2}$  in. rod. Chemical analysis gave the following composition:

Copper	0.067%
Manganese	0.035
Nickel	0.024
Sulphur	0.039
Carbon	0.028
Iron (by difference)	99.808

### *Results and Discussion*

The results are tabulated in the Appendix in the order in which the measurements were taken. In Fig. 6 the thermal conductivity is plotted against temperature for the range  $0^{\circ}$  to  $730^{\circ}$  C. with extrapolation to  $800^{\circ}$  C. Readings were not taken above  $730^{\circ}$  C. because a thermocouple broke in a place that would require partial dismantling of the apparatus. As measurements on Armco iron were made chiefly to test the reliability of the apparatus it was not felt necessary to reassemble it for further readings at high temperatures.

From the experimental results, values have been determined at  $100^{\circ}$  intervals from  $0^{\circ}$  to  $800^{\circ}$  C., and these values are shown in Table I. Included in the table are values obtained by Powell (2) and van Dusen and Shelton (3) for iron of comparable purity.

The results of this determination agree well with those of Powell but are higher than those of van Dusen and Shelton at low temperatures. From the plotted results of the latter it would appear as if a curve with larger slope at low temperatures would have fitted the experimental points as well as the straight line that was used, and would have brought the average values closer to those of the other determinations. However, none of the differences are greater than those that might be expected from experimental error and variations in the samples.

It will be noted in Fig. 6 that a change of slope in the curve of conductivity against temperature occurs at about  $375^{\circ}$  C., while the sections of the curve above and below this point are relatively linear. Straight lines have been fitted to the experimental points by the method of least squares, giving

$K = 0.1819 - 1.631 \times 10^{-4} T$  below  $375^\circ \text{C.}$  and  $K = 0.1656 - 1.197 \times 10^{-4} T$  from  $375^\circ$  to  $800^\circ \text{C.}$  The two lines intersect at  $T = 377^\circ \text{C.}$  The deviations of the experimental points from these lines have been plotted in

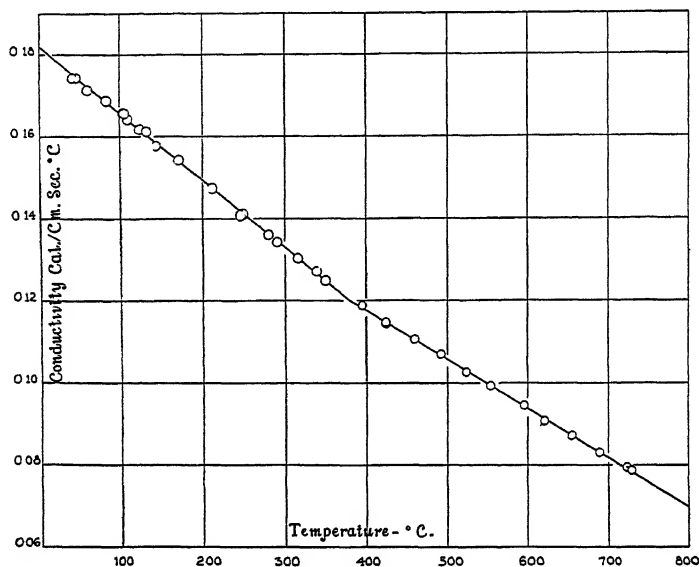


FIG. 6. Thermal conductivity of Armco iron.

TABLE I  
THERMAL CONDUCTIVITY OF ARMCO IRON

Temperature, °C.	Thermal conductivity, c.g.s. units		
	Armstrong and Dauphinee	Powell	van Dusen and Shelton
0	0.181 <sub>9</sub>	0.177	0.172 (estimate)
100	0.165 <sub>8</sub>	0.163	0.159
200	0.149 <sub>3</sub>	0.147	0.145
300	0.133 <sub>0</sub>	0.132	0.131
400	0.117 <sub>7</sub>	0.116	0.1175
500	0.105 <sub>7</sub>	0.1035	0.104
600	0.093 <sub>7</sub>	0.093	—
700	0.081 <sub>7</sub>	0.082	—
800	0.069 <sub>8</sub>	0.071	—

Fig. 7, with differences from the first line being shown over the full range  $0^\circ$  to  $800^\circ \text{C.}$  in order to amplify the change in slope. The maximum deviation from the calculated lines is 0.6% and the standard deviation is 0.35%. It is thought that the change of slope in the conductivity-temperature curve may be due to the effect of the nickel impurity in the sample, the intersection of the two lines falling almost exactly at the Curie point of nickel ( $376^\circ \text{C.}$ ).

However, the magnitude of the effect (a change in slope of 25%) is rather large for the amount of impurity present (0.024%). It should be noted that Powell's results show a bend in the curve in the neighborhood of 405° C. but

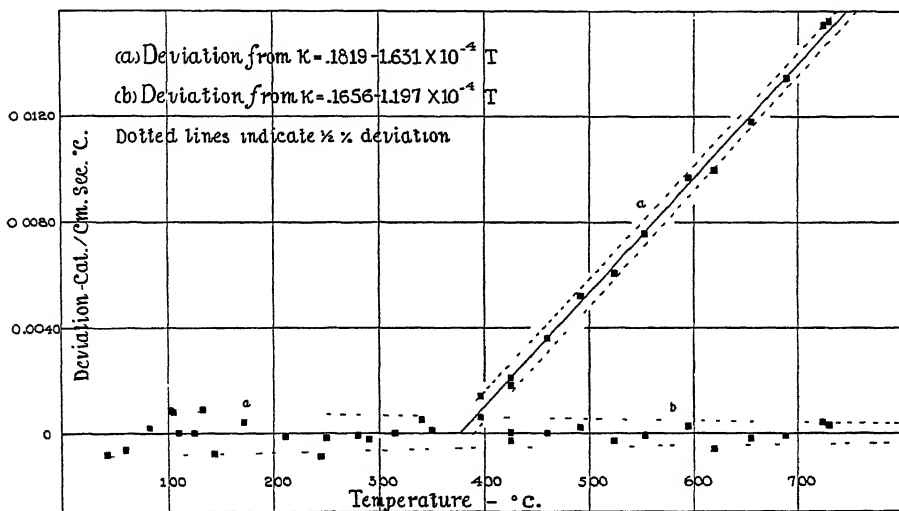


FIG. 7. Deviation from calculated curves.

the analysis of his sample showed no detectable nickel impurity. However, Powell's sample was nickel-plated, and the bend in his curve might be explained by either thermal diffusion or by error in the values for the conductivity of nickel used in the corrections. Further conclusions are not justified at present. Proposed work on the electrical and thermal conductivities of this sample and others of higher purity should indicate more definitely the reason for such an anomaly.

### Conclusions

An apparatus has been described for accurate measurement of thermal conductivities of metals in vacuum for the temperature range 0° to 800° C. Measurements on a sample of Armco iron indicate that absolute error in measurements is not more than 2% and the relative error considerably less than 1%. The results on the iron sample agree well with those of other determinations on iron of comparable purity.

### Acknowledgments

In conclusion the authors wish to acknowledge their indebtedness to Dr. J. D. Babbitt for his interest and constructive criticism at all stages of the work, and to Mr. C. St. Jacques, Mr. P. Huot, and Mr. J. MacDonald for excellent co-operation and technical skill in the construction and assembly of the apparatus, and in the wiring of the control circuits.

## References

1. ARMSTRONG, L. D. and DAUPHINEE, T. M. Can. J. Research, F, 25 : 221-225. 1947.
2. POWELL, R. W. Proc. Phys. Soc., London, 46 : 659-674. 1934.
3. VAN DUSEN, M. S., and SHELTON, S. M. Bur. Standards J. Research, 12 : 429-440. 1934.

## APPENDIX

## THERMAL CONDUCTIVITY OF METALS

Date	Run No.	$T_2$	$T_1$	$T_2 - T_1$	$T = \frac{T_2 + T_1}{2}$	$V$ , corr.	$I$ , corr.	$K_t$
Jan. 8	1	108.77	99.54	9.23	104.1	14.16	0.444	0.1658
	2	112.28	98.07	14.21	105.2	17.78	0.543	0.1656
Jan. 9	3	177.05	166.40	10.65	171.7	15.38	0.439	0.1543
	4	137.79	127.61	10.18	132.7	14.98	0.450	0.1612
	5	218.09	204.59	13.50	211.4	17.44	0.469	0.1473
Jan. 10	6	253.59	239.70	13.89	246.7	17.65	0.456	0.1408
	7	287.20	273.53	13.67	280.3	17.48	0.438	0.1361
Jan. 11	8	323.27	307.91	15.36	315.6	18.53	0.445	0.1304
	9	46.28	38.23	8.06	42.2	12.92	0.446	0.1742
	10	67.66	54.77 <sub>s</sub>	12.88 <sub>s</sub>	61.2	16.64	0.544	0.1713
	11	89.77 <sub>s</sub>	76.29	13.48 <sub>s</sub>	83.0	17.19	0.543	0.1686
Jan. 13	12	358.27	341.92	16.35	350.1	18.99	0.443	0.1249
	13	403.20	385.35	17.85	395.3	19.77	0.442	0.1188
	14	433.25	416.53	16.71	424.8	18.97	0.417	0.1147
	15	470.11	449.74	20.37	459.6	20.88	0.445	0.1105
	16	502.81	481.29	21.52	491.9	21.35	0.445	0.1069
	17	535.48	512.53	22.95	523.0	21.87	0.445	0.1026
	18	563.89	542.33	21.56	553.1	21.04	0.420	0.0992
Jan. 15	19	433.66	416.85	16.81	424.7	18.97	0.418	0.1144
	20	347.23	331.06	16.17	339.1	18.96	0.447	0.1272
Jan. 16	21	257.69	241.06	16.63	249.3	19.41	0.497	0.1411
	22	607.15	583.93	23.22	595.5	21.61	0.420	0.0945
	23	631.43	609.70	21.73	620.5	20.64	0.395	0.0907
	24	666.04	642.78	23.26	654.3	21.21	0.395	0.0870
	25	700.72	676.85	23.87	688.7	21.23	0.386	0.0830
	26	736.35	711.18	25.17	723.7	21.56	0.384	0.0793
	27	742.33	715.33	27.00	728.8	22.29	0.395	0.0786
Jan. 20	28	132.38	117.30	15.08	124.7	18.43	0.543	0.1616
	29	116.89	103.00	13.89	109.9	17.58	0.532	0.1640
Jan. 24	30	151.14	136.74	14.40	143.9	17.98	0.519	0.1577
	31	298.32	284.09	14.23	291.1	17.94	0.438	0.1342

SECTION A  
INDEX TO VOLUME 25

Authors

- Armstrong, L. D.**—The use of high permeability materials in magnetometers. The application of a saturated core type magnetometer to an automatic steering control, 124.  
——— and Dauphinee, T. M.—Thermal conductivity of metals at high temperatures.  
I. Description of the apparatus and measurements on iron, 357.
- Arnell, J. C.**—Permeability studies. II. Surface area measurements of inorganic pigment powders, 191.
- Auger, P., Munn A. M., and Pontecorvo, B.**—The transport mean free path of thermal neutrons in heavy water, 143.
- Batho, H. F.**—See Langstroth G. O.
- Booker, D. V.**—See Sargent, B. W.
- Cavanagh, P. E.**—See Sargent, B. W.
- Cipriani, A. J.**—See Mayneord, W. V.
- Dauphinee, T. M.**—See Armstrong, L. D.
- Demers, P.**—New photographic emulsions showing improved tracks of ionizing particles, 223.
- Dixon, W. R.**—See Hushley, W. J.
- Ellis, S. G.**—A note on the electron microscope examination of greases, 119. The use of diaphragms in the electron microscope, 322.
- Fenning, F. W., Graham, G. A. R., and Seligman, H.**—The ratio of the capture cross sections of lithium and boron for thermal neutrons, 73.
- Ferguson, A. J.**—A note on phase correction in electrical delay networks, 68.
- Graham, G. A. R.**—See Fenning, F. W.; Whitehouse, W. J.
- Graham, R. L.**—See Thode, H. G.
- Hereward, H. G., Laurence, G. C., Munn, A. M., Paneth, H. R., and Sargent, B. W.**—The diffusion length of thermal neutrons in heavy water containing lithium carbonate, 26.  
———, Laurence, G. C., Paneth, H. R., and Sargent, B. W.—Measurement of the diffusion length of thermal neutrons in graphite, 15.  
See Sargent, B. W.
- Hincks, E. P.**—See May, A. N.
- Hushley, W. J. and Dixon, W. R.**—The gamma-ray measurement of radium ore concentrates, 210.
- Johns, M. W.**—See Langstroth, G. O.
- Langstroth, G. O., Johns, M. W., Wolfson, J. L., and Batho, H. F.**—A laboratory study of visibility through clouds, 49. The recognition of objects nearly obscured by a cloud, 58.  
——— and Wolfson, J. L.—A note on the determination of the extinction coefficient of aerosols, 62.
- Larose, P.**—The effect of wind on the thermal resistance of clothing with special reference to the protection given by coverall fabrics of various permeabilities, 169.

- Laurence, G. C.**—See Hereward, H. G.
- Lorrain, P.**—A low-pressure glow-discharge proton source, 338.
- May, A. N. and Hincks, E. P.**—Evidence for an  $(n, \alpha)$  reaction induced in  $O^{17}$  by thermal neutrons, 77.
- Mayneord, W. V. and Cipriani, A. J.**—The absorption of gamma rays from  $Co^{60}$ , 303.
- Munn, A. M. and Pontecorvo, B.**—Spatial distribution of neutrons in hydrogenous media containing bismuth, lead, and iron, 157.  
See Auger, P.; Hereward, H. G.
- Niemi, N. J.**—See Sargent, B. W.
- Northwood, T. D.**—Sonic determination of the elastic properties of ice, 88.
- Paneth, H. R.**—See Hereward, H. G.
- Petrie, W.**—The calculation of line strengths from laboratory data, 42    Excitation conditions in the upper atmosphere as determined from a study of atomic emission lines in the auroral spectrum, 293.
- Placzek, G. and Volkoff, G.**—A theorem on neutron multiplication, 276.
- Pontecorvo, B.**—See Auger, P.; Munn, A. M.
- Sargent, B. W., Booker, D. V., Cavanagh, P. E., Hereward, H. G., and Niemi, N. J.**—The diffusion length of thermal neutrons in heavy water, 134.  
See Hereward, H. G.
- Seligman, H.**—See Fenning, F. W.
- Shu, S.**—The foundations and philosophical implications of wave mechanics, 96.
- Thode, H. G. and Graham, R. L.**—A mass spectrometer investigation of the isotopes of xenon and krypton resulting from the fission of  $U^{235}$  by thermal neutrons, 1.
- Tillotson, J. G.**—See Woonton, G. A.
- Volkoff, G.**—See Placzek, G.
- Watson, W. H.**—A method for computing transformations in radioactive series, 252.
- Whitehouse, W. J. and Graham, G. A. R.**—Ratio of neutron absorption cross sections of boron and hydrogen, 261.
- Wolfson, J. L.**—See Langstroth, G. O.
- Woonton, G. A. and Tillotson, J. G.**—The  $E$ -plane radiation pattern of short electromagnetic horns of large aperture, 315.

SECTION A  
INDEX TO VOLUME 25

Subjects

**Absorption**

cross sections, Neutron, Ratio of, of boron and hydrogen, 261.

See also Capture cross sections.

of gamma rays from Co<sup>60</sup>, 303.

**Aerosols**, Determination of extinction coefficient of, 62.

**Area, Surface**, Measurements of, of inorganic pigment powders, 191.

**Atmosphere, Upper**, Excitation conditions in, as determined from a study of atomic emission lines in the auroral spectrum, 293.

**Atomic emission lines** in the auroral spectrum, Excitation conditions in the upper atmosphere as determined from a study of, 293.

**Auroral spectrum**, Atomic emission lines in, Excitation conditions in the upper atmosphere as determined from a study of, 293.

**Bismuth**, lead, and iron in hydrogenous media, Spatial distribution of neutrons in, 157.

**Boron**

and hydrogen, Ratio of neutron absorption cross sections of, 261.

and lithium, Ratio of capture cross sections of, for thermal neutrons, 73.

**Capture cross sections**

of lithium and boron, Ratio of, for thermal neutrons, 73.

See also Absorption cross sections.

**Carbonate, Lithium**, See Lithium carbonate.

**Clothing**, Thermal resistance of, Effect of wind on, with special reference to the protection given by coverall fabrics of various permeabilities, 169.

**Clouds**

A laboratory study of visibility through, 49.

Recognition of objects nearly obscured by, 58.

**Cobalt**, Absorption of gamma rays from Co<sup>60</sup>, 303.

**Coefficient, Extinction**, See Extinction coefficient.

**Conductivity, Thermal**, of metals at high temperatures. I. Description of the apparatus and measurements on iron, 357.

**Cross sections**

Capture, of lithium and boron, Ratio of, for thermal neutrons, 73.

Neutron absorption, of boron and hydrogen, Ratio of, 261.

**Diaphragms**, Use of, in the electron microscope, 322.

**Diffusion length** of thermal neutrons

in graphite, Measurement of, 15.

in heavy water, 134

in heavy water containing lithium carbonate, 26.

**Elastic properties of ice**, Sonic determination of, 88.

**Electrical delay networks**, A note on phase correction in, 68.

**Electromagnetic horns**, Short, of large aperture, *E*-plane radiation pattern of, 315.

**Electron microscope**

Note on the examination of greases by means of, 119.

Use of diaphragms in, 322.

**Emission lines, Atomic**, in the auroral spectrum, Excitation conditions in the upper atmosphere as determined from a study of, 293.

**Emulsions**, New photographic, showing improved tracks of ionizing particles, 223.

**Extinction coefficient** of aerosols, A note on the determination of, 62.

**Fabrics**, Coverall, of various permeabilities, Effect of wind on the thermal resistance of clothing with special reference to the protection given by, 169.

**Fission** of U<sup>235</sup> by thermal neutrons, A mass spectrometer investigation of the isotopes of xenon and krypton resulting from, 1.

### **Gamma-rays**

Absorption of, from Co<sup>60</sup>, 303.

Measurement of radium ore concentrates by means of, 210.

**Graphite**, Measurement of the diffusion length of thermal neutrons in, 15.

**Greases**, Note on the electron microscope examination of, 119.

**Heavy water**, See Water, Heavy.

**Hydrogen** and boron, Ratio of neutron absorption cross sections of, 261.

**Hydrogenous media**, containing bismuth, lead, and iron, Spatial distribution of neutrons in, 157.

**Ice**, Sonic determination of the elastic properties of, 88.

**Inorganic pigment powders**, Surface area measurements of, 191.

**Ionizing particles**, New photographic emulsions showing improved tracks of, 223.

### **Iron**

bismuth, and lead in hydrogenous media, Spatial distribution of neutrons in, 157.

See under Conductivity, Thermal.

**Isotopes**, See Cobalt; Krypton; Oxygen; Uranium; Xenon.

**Krypton**, A mass spectrometer investigation of isotopes of, resulting from the fission of U<sup>235</sup> by thermal neutrons, 1.

**Lead**, bismuth, and iron in hydrogenous media, Spatial distribution of neutrons in, 157.

**Line strengths**, Calculation of, from laboratory data, 42.

### **Lithium**

and boron, Ratio of capture cross sections of, for thermal neutrons, 73.

carbonate, Diffusion length of thermal neutrons in heavy water containing, 26.

**Magnetometers**, Use of high permeability materials in, The application of a saturated core type magnetometer to an automatic steering control, 124.

**Mass spectrometer**, Investigation of the isotopes of xenon and krypton resulting from fission of U<sup>235</sup> by thermal neutrons by means of, 1.

**Mean free path, Transport**, of thermal neutrons in heavy water, 143.

**Mechanics, Wave**, See Wave mechanics.

**Metals**, Thermal conductivity of, at high temperatures, I. Description of the apparatus and measurements on iron, 357.

**Microscope, Electron**, See Electron microscope.

**Multiplication, Neutron**, Theorem on, 276.

**( $n$ ,  $\alpha$ ) reaction**, induced in O<sup>17</sup> by thermal neutrons, Evidence for, 77.

**Networks, Electrical delay**, A note on phase correction in, 68.

### **Neutron(s)**

absorption cross sections of boron and hydrogen, Ratio of, 261.

multiplication, Theorem on, 276.

Spatial distribution of, in hydrogenous media containing bismuth, lead, and iron, 157.

#### **Thermal**

Evidence for an ( $n$ ,  $\alpha$ ) reaction induced in O<sup>17</sup> by, 77.

Fission of U<sup>235</sup> by, Mass spectrometer investigation of the isotopes of xenon and krypton resulting from, 1.

Measurement of diffusion length of in graphite, 15.

in heavy water, 134.

in heavy water containing lithium carbonate, 26.

Ratio of capture cross sections of lithium and boron for, 73.

Transport mean free path of, in heavy water, 143.

**Oxygen**, Evidence for an ( $n$ ,  $\alpha$ ) reaction induced in O<sup>17</sup> by thermal neutrons, 77.

### **Permeability**

of coverall fabrics, Effect of wind on the thermal resistance of clothing with special reference to, 169.

studies. II. Surface area measurements of inorganic pigment powders, 191.

Use of high permeability materials in magnetometers, 124.

**Phase correction** in electrical delay networks, A note on, 68.

**Photographic emulsions**, New, showing improved tracks of ionizing particles, 223.

**Pigment powders**, Inorganic, Surface area measurements of, 191.

- Powders**, Inorganic pigment, Surface area measurements of, 191.
- Protection** given by coverall fabrics of various permeabilities, Effect of wind on the thermal resistance of clothing with special reference to, 169.
- Proton source**, Low-pressure glow-discharge, 338.
- Radiation pattern**, *E*-plane, of short electromagnetic horns of large aperture, 315.
- Radioactive series**, Method for computing transformations in, 252.
- Radium** ore concentrates, Gamma-ray measurement of, 210.
- Resistance, Thermal**, of clothing, Effect of wind on, with special reference to the protection given by coverall fabrics of various permeabilities, 169.
- Sonic** determination of the elastic properties of ice, 88.
- Spectrometer, Mass**, See Mass spectrometer.
- Spectrum, Auroral**, See Auroral spectrum.
- Steering control**, Automatic, Application of a saturated core type magnetometer to, 124.
- Surface area** measurements of inorganic pigment powders, 191.
- Temperatures**, High, See under Thermal conductivity.
- Thermal conductivity** of metals at high temperatures. I. Description of the apparatus and measurements on iron, 357.
- Thermal neutrons**, See Neutrons, Thermal.
- Thermal resistance** of clothing, See Resistance, Thermal.
- Tracks** of ionizing particles, Improved, New photographic emulsions showing, 223.
- Transformations in radioactive series**, Method for computing, 252.
- Transport mean free path** of thermal neutrons in heavy water, 143.
- U<sup>235</sup>**, See Uranium.
- Uranium**, Fission of U<sup>235</sup> by thermal neutrons, A mass spectrometer investigation of isotopes of xenon and krypton resulting from, 1.
- Visibility** through clouds, A laboratory study of, 49.
- Water, Heavy**  
Containing lithium carbonate, Diffusion length of thermal neutrons in, 26.  
Diffusion length of thermal neutrons in, 134.  
Transport mean free path of thermal neutrons in, 143.
- Wave mechanics**, Foundations and philosophical implications of, 96.
- Wind**, Effect of, on the thermal resistance of clothing with special reference to the protection given by coverall fabrics of various permeabilities, 169.
- Xenon**, A mass spectrometer investigation of isotopes of, resulting from the fission of U<sup>235</sup> by thermal neutrons, 1.

L.A. R I 75

INDIAN AGRICULTURAL RESEARCH  
INSTITUTE LIBRARY, NEW DELHI

[illegible]

GIPNLK-H-40 I.A.R.I.-29-4- 5-15,000

